

Wireless Communications and Mobile Computing

Underwater Wireless Communications and Networks

Lead Guest Editor: Haixin Sun

Guest Editors: Xuebo Zhang and Hamada Esmail





Underwater Wireless Communications and Networks

Wireless Communications and Mobile Computing

Underwater Wireless Communications and Networks

Lead Guest Editor: Haixin Sun


Guest Editors: Xuebo Zhang and Hamada Esmail





Copyright © 2022 Hindawi Limited. All rights reserved.

This is a special issue published in “Wireless Communications and Mobile Computing.” All articles are open access articles distributed under the Creative Commons Attribution License, which permits unrestricted use, distribution, and reproduction in any medium, provided the original work is properly cited.

Chief Editor

Zhipeng Cai , USA

Associate Editors

Ke Guan , China
Jaime Lloret , Spain
Maode Ma , Singapore

Academic Editors

Muhammad Inam Abbasi, Malaysia
Ghufran Ahmed , Pakistan
Hamza Mohammed Ridha Al-Khafaji ,
Iraq
Abdullah Alamoodi , Malaysia
Marica Amadeo, Italy
Sandhya Aneja, USA
Mohd Dilshad Ansari, India
Eva Antonino-Daviu , Spain
Mehmet Emin Aydin, United Kingdom
Parameshchhari B. D. , India
Kalapaveen Bagadi , India
Ashish Bagwari , India
Dr. Abdul Basit , Pakistan
Alessandro Bazzi , Italy
Zdenek Becvar , Czech Republic
Nabil Benamar , Morocco
Olivier Berder, France
Petros S. Bithas, Greece
Dario Bruneo , Italy
Jun Cai, Canada
Xuesong Cai, Denmark
Gerardo Canfora , Italy
Rolando Carrasco, United Kingdom
Vicente Casares-Giner , Spain
Brijesh Chaurasia, India
Lin Chen , France
Xianfu Chen , Finland
Hui Cheng , United Kingdom
Hsin-Hung Cho, Taiwan
Ernestina Cianca , Italy
Marta Cimitile , Italy
Riccardo Colella , Italy
Mario Collotta , Italy
Massimo Condoluci , Sweden
Antonino Crivello , Italy
Antonio De Domenico , France
Floriano De Rango , Italy

Antonio De la Oliva , Spain
Margot Deruyck, Belgium
Liang Dong , USA
Praveen Kumar Donta, Austria
Zhuojun Duan, USA
Mohammed El-Hajjar , United Kingdom
Oscar Esparza , Spain
Maria Fazio , Italy
Mauro Femminella , Italy
Manuel Fernandez-Veiga , Spain
Gianluigi Ferrari , Italy
Luca Foschini , Italy
Alexandros G. Fragkiadakis , Greece
Ivan Ganchev , Bulgaria
Óscar García, Spain
Manuel García Sánchez , Spain
L. J. García Villalba , Spain
Miguel Garcia-Pineda , Spain
Piedad Garrido , Spain
Michele Girolami, Italy
Mariusz Glabowski , Poland
Carles Gomez , Spain
Antonio Guerrieri , Italy
Barbara Guidi , Italy
Rami Hamdi, Qatar
Tao Han, USA
Sherief Hashima , Egypt
Mahmoud Hassaballah , Egypt
Yejun He , China
Yixin He, China
Andrej Hrovat , Slovenia
Chunqiang Hu , China
Xuexian Hu , China
Zhenghua Huang , China
Xiaohong Jiang , Japan
Vicente Julian , Spain
Rajesh Kaluri , India
Dimitrios Katsaros, Greece
Muhammad Asghar Khan, Pakistan
Rahim Khan , Pakistan
Ahmed Khattab, Egypt
Hasan Ali Khattak, Pakistan
Mario Kolberg , United Kingdom
Meet Kumari, India
Wen-Cheng Lai , Taiwan

Jose M. Lanza-Gutierrez, Spain
Pavlos I. Lazaridis , United Kingdom
Kim-Hung Le , Vietnam
Tuan Anh Le , United Kingdom
Xianfu Lei, China
Jianfeng Li , China
Xiangxue Li , China
Yaguang Lin , China
Zhi Lin , China
Liu Liu , China
Mingqian Liu , China
Zhi Liu, Japan
Miguel López-Benítez , United Kingdom
Chuanwen Luo , China
Lu Lv, China
Basem M. ElHalawany , Egypt
Imadeldin Mahgoub , USA
Rajesh Manoharan , India
Davide Mattera , Italy
Michael McGuire , Canada
Weizhi Meng , Denmark
Klaus Moessner , United Kingdom
Simone Morosi , Italy
Amrit Mukherjee, Czech Republic
Shahid Mumtaz , Portugal
Giovanni Nardini , Italy
Tuan M. Nguyen , Vietnam
Petros Nicolaitidis , Greece
Rajendran Parthiban , Malaysia
Giovanni Pau , Italy
Matteo Petracca , Italy
Marco Picone , Italy
Daniele Pinchera , Italy
Giuseppe Piro , Italy
Javier Prieto , Spain
Umair Rafique, Finland
Maheswar Rajagopal , India
Sujan Rajbhandari , United Kingdom
Rajib Rana, Australia
Luca Reggiani , Italy
Daniel G. Reina , Spain
Bo Rong , Canada
Mangal Sain , Republic of Korea
Praneet Saurabh , India

Hans Schotten, Germany
Patrick Seeling , USA
Muhammad Shafiq , China
Zaffar Ahmed Shaikh , Pakistan
Vishal Sharma , United Kingdom
Kaize Shi , Australia
Chakchai So-In, Thailand
Enrique Stevens-Navarro , Mexico
Sangeetha Subbaraj , India
Tien-Wen Sung, Taiwan
Suhua Tang , Japan
Pan Tang , China
Pierre-Martin Tardif , Canada
Sreenath Reddy Thummaluru, India
Tran Trung Duy , Vietnam
Fan-Hsun Tseng, Taiwan
S Velliangiri , India
Quoc-Tuan Vien , United Kingdom
Enrico M. Vitucci , Italy
Shaohua Wan , China
Dawei Wang, China
Huaqun Wang , China
Pengfei Wang , China
Dapeng Wu , China
Huaming Wu , China
Ding Xu , China
YAN YAO , China
Jie Yang, USA
Long Yang , China
Qiang Ye , Canada
Changyan Yi , China
Ya-Ju Yu , Taiwan
Marat V. Yuldashev , Finland
Sherali Zeadally, USA
Hong-Hai Zhang, USA
Jiliang Zhang, China
Lei Zhang, Spain
Wence Zhang , China
Yushu Zhang, China
Kechen Zheng, China
Fuhui Zhou , USA
Meiling Zhu, United Kingdom
Zhengyu Zhu , China



Contents

Energy and Path-Aware-Reliable Routing in Underwater Acoustic Wireless Sensor Networks

Munsif Ali , Anwar Khan , Massimo Bertozzi , Ubaid Ullah , Saleh M. Altowaijri , Ihsan Ali , and Salman Iqbal






Research Article (17 pages), Article ID 8535244, Volume 2022 (2022)

A Viterbi Decoder under Class A Modeled Noise in Shallow Water

Yifei Wang , Huili Fan, Xuebo Zhang , Tian Tian, Shaohua Hong, Zhuofan Xie, Ruiping Song, Mingzhang Zhou, Xiao Feng, Yiting Liang, and Shu Zhang

Research Article (10 pages), Article ID 1956938, Volume 2022 (2022)

Data-Driven Signal Detection for Underwater Acoustic Filter Bank Multicarrier Communications

Yunan Zhu , Biao Wang , Fangtong Xie , Chengxi Wu , and Peng Chao 


Research Article (9 pages), Article ID 4943442, Volume 2022 (2022)

Sea Experimental for Compressive Sensing-Based Sparse Channel Estimation of Underwater Acoustic TDS-OFDM System

Naveed Ur Rehman Junejo , Hamada Esmail , Mariyam Sattar , Haixin Sun , Muhammad Amir Khalil , and Ihsan Ullah 

Research Article (14 pages), Article ID 2523196, Volume 2022 (2022)

Reinforcement Learning-Based Adaptive Switching Scheme for Hybrid Optical-Acoustic AUV Mobile Network

Hanjiang Luo , Ziyang Xu, Jinglong Wang, Yuting Yang, Rukhsana Ruby, and Kaishun Wu



Research Article (14 pages), Article ID 9471698, Volume 2022 (2022)

Research on Towed Linear Array Shape Measurement Method Based on Biorthogonal Signal

Sen Zhang , Ming-Zhi Wang , Jun Yuan , and Chen-Lin Zhou 


Research Article (9 pages), Article ID 8676849, Volume 2022 (2022)

Sensor Selection for Hybrid AOA-TOA Localization with Correlated Measurement Noise in Underwater Wireless Sensor Networks

Rongyan Zhou, Jianfeng Chen , Weijie Tan , Haobo Yuan, and Chang Cai





Research Article (11 pages), Article ID 2779760, Volume 2022 (2022)

A Vibration Signal Denoising Method of Marine Atomic Gravimeter Based on Improved Variational Mode Decomposition

Wenbin Gong , An Li, An Liao, Hao Che, Chunfu Huang, and Fangjun Qin 

Research Article (13 pages), Article ID 1744689, Volume 2022 (2022)

Supervised Contrastive Learning-Based Modulation Classification of Underwater Acoustic Communication

Daqing Gao , Wenhui Hua , Wei Su , Zehong Xu , and Keyu Chen 

Research Article (10 pages), Article ID 3995331, Volume 2022 (2022)




Underwater Localization Using Differential Doppler Scale and TDOA Measurements with Clock Imperfection

Bingbing Zhang, Jiahua Zhu , Yanqun Wu, Weihua Zhang, and Min Zhu
Research Article (13 pages), Article ID 6597132, Volume 2022 (2022)

Precoded IM-OFDM-SS for Underwater Acoustic Communication

Zeyad A. H. Qasem , Hussein A. Leftah , Haixin Sun , and Hamada Esmail 
Research Article (12 pages), Article ID 7940993, Volume 2022 (2022)





Time-Domain Channel Estimation Scheme for OFDM over Fast Fading Channels

Sami Asharjabi , Hefdhallah Sakran , and Azzam Al-nahari 
Research Article (9 pages), Article ID 7839430, Volume 2022 (2022)

Reinforcement Learning for Distributed Energy Efficiency Optimization in Underwater Acoustic Communication Networks

Liejun Yang, Hui Wang , Yexian Fan, Fang Luo, and Wei Feng
Research Article (12 pages), Article ID 5042833, Volume 2022 (2022)





A Directional Selective Power Routing Protocol for the Internet of Underwater Things

Manal Al-Bzoor , Ahmed Musa , Khawla Alzoubi , and Taha Gharaibeh 
Research Article (13 pages), Article ID 3846621, Volume 2022 (2022)

MuLSi-Co: Multilayer Sinks and Cooperation-Based Data Routing Techniques for Underwater Acoustic Wireless Sensor Networks (UA-WSNs)

Munsif Ali, Sahar Shah , Mahnoor Khan , Ihsan Ali , Roobaea Alroobaea , Abdullah M. Baqasah, and Muneer Ahmad 
Research Article (16 pages), Article ID 4840481, Volume 2022 (2022)

Analysis of Security Attacks and Taxonomy in Underwater Wireless Sensor Networks

Irfan Ahmad , Taj Rahman , Asim Zeb , Inayat Khan , Inam Ullah , Habib Hamam , and Omar Cheikhrouhou 
Review Article (15 pages), Article ID 1444024, Volume 2021 (2021)

Research Article

Energy and Path-Aware-Reliable Routing in Underwater Acoustic Wireless Sensor Networks

Munsif Ali ¹, Anwar Khan ², Massimo Bertozzi ¹, Ubaid Ullah ³,
Saleh M. Altowaijri ⁴, Ihsan Ali ⁵ and Salman Iqbal⁶

¹Department of Engineering and Architecture, University of Parma, Italy

²Department of Electronics, University of Peshawar, Peshawar, 25120 Khyber Pakhtunkhwa, Pakistan

³Faculty of Engineering, University of Deusto, Spain

⁴Department of Information Systems, Faculty of Computing and Information Technology, Northern Border University, Rafha 91911, Saudi Arabia

⁵Department of Computer System and Technology, Faculty of Computer Science and Information Technology, Universiti Malaya, 50603 Kuala Lumpur, Malaysia

⁶Computer Science, Vehari Campus COMSATS University Islamabad, Pakistan

Correspondence should be addressed to Saleh M. Altowaijri; saleh.altowaijri@nbu.edu.sa and Ihsan Ali; ihsanalichd@siswa.um.edu.my

Received 20 January 2022; Accepted 9 August 2022; Published 6 September 2022

Academic Editor: A.H. Alamoodi

Copyright © 2022 Munsif Ali et al. This is an open access article distributed under the Creative Commons Attribution License, which permits unrestricted use, distribution, and reproduction in any medium, provided the original work is properly cited.

In underwater acoustic sensor networks (UASNs), energy awareness, best path selection, reliability, and scalability are among the key factors that decide information delivery to the sea surface. Existing protocols usually do not combine such performance-affecting factors in information routing. As a result, the performance of such protocols usually deteriorates if multiple performance factors are taken into account. To cope with such performance deterioration, this article proposes two routing protocols for UASNs: energy and path-aware reliable routing (EPRR) and cooperative EPRR (Co-EPRR). Compared with the counterpart systems, the proposed protocols have been designed to deal with the problem of long propagation delays and achieve network reliability. The EPRR scheme uses nodes' physical distance from the surface with its depth, which minimized the delay of packet transmission. The channel interaction time has been reduced, therefore, reducing unwanted channel effects on the data. Furthermore, the density of the nodes in the upper part of the network prevents data loss and limits the rapid death of the nodes. The second proposed scheme, Co-EPRR, uses the concept of routing information from the source to the destination on multiple paths. In Co-EPRR routing, the destination node can receive more than one copy of the data packet. This reduces unfavorable channel effects during data delivery. Both the schemes show good performance in terms of packet delivery ratio, received packet analysis, and end-to-end delay.

1. Introduction

Energy awareness, best route selection, reliability, and scalability are among the principal factors that determine the performance of underwater acoustic sensor networks (UASNs) [1] in information routing to the desired target, as these factors are directly linked with performance evaluation. In addition, these performance factors play a key role in undersea applications such as underwater exploration, monitoring, submarine tracking, and navigation and are used for military purposes

[2–5]. Unfortunately, existing schemes usually do not consider these factors altogether in information routing, which leads to compromised network performance since one or the other performance parameter can get compromised.

Channel noise and bit error rate can be looked into channel conditions during data routing in order to minimize to a certain extent [6, 7] that the channel impairments affecting data delivery. As described in [6], cooperative communication is one of the techniques that could be exploited to deal with channel properties. This technique is based on multiple

paths and on the combination of data at the destination; this approach has been used to increase the reliability of data delivery. In cooperative communication, a relay forwards data to the destination by amplifying or decoding the received signal. The first is known as amplify and forward (AF), and the second is known as decode and forward (DF) [8]. The AF scheme is simpler and forwards data with a lower latency than DF, as DF completely decodes the signal before forwarding [9]. In general, two cooperative methods, called fixed and incremental cooperative relay schemes, are used [10, 11]. In fixed cooperation, the relay always cooperates. While in incremental relaying, the cooperation is done when a destination needs to send the desired signal. In incremental relaying, instantaneous information from the channel reduces data forwarding by limiting the feedback packets to a few bits. In fixed relaying, data are transmitted to the destination regardless of the channel condition [12]. In cooperative communication, The receiver can get more than one copy of the same data packets. All these data packets are then combined using one of the combining techniques to improve the correct reception of the data [13].

Using multiple antennas at a sensor node provides data reliability. However, in the case of UASNs, adding antennas is difficult and expensive. Therefore, to improve reliability, cooperative communication is usually used instead of multiple antennas. In such a case, overhearing of the data by neighboring nodes can lead to high data reliability [14] even when a single antenna node is used. Anyway, in cooperative communication, data retransmission by a relay is used to have error-free data. However, multiple data transmission leads to additional energy consumption and increases latency.

Protocols that do not consider channel awareness and noise in data routing generally do not guarantee reliable data delivery, since there is no retransmission of data packets. On the other hand, cooperative routing protocols enhance data reliability, since data are transmitted by sender and relay nodes as well. Many cooperative [15, 16], noncooperative [17], and different other types of routing protocols are proposed for UASNs [18, 19]. These routing algorithms achieve high reliability at the cost of high latency and excessive energy consumption.

The selection of the best and shortest path during data routing takes into account the overall time to transmit the packet from the source to the desired target. This not only shortens the time of data delivery, which is necessary in emergency and military applications, but also makes the data affected by the channel properties for a short period of time. As a result, reliability is also increased. Scalability ensures that new nodes can be added to the network so that the network can be easily extended when desired.

The existing schemes that route data in UASNs do not consider energy awareness, shortest path selection, reliability, and scalability together [15, 16]. Instead, the proposed methods generally exploit a single parameter or indicator in the routing of information [20–22]. Even when more than one parameter is considered, if the computation of the Euclidean distance for route determination is needed, the network scalability is affected [23, 24]; the calculation of Euclidean distance is, in fact, cumbersome in UASNs, as it

involves the computation of nodes' position coordinates and nodes constantly change their positions. As a result, one or more performance indicators are not always optimal when the network operates.

This work proposes two approaches (EPRR and Co-EPRR) to cope with these limitations. In EPRR, data are reached to the sink along the shortest links, so less time is taken by the data. This minimizes the propagation delay and shortens the time it takes for the channel properties to affect the data. As a result, the data transfer reliability is improved. Moreover, consideration of energy and noise parameters further improves routing strategies and data forwarding. The Co-EPRR also adds cooperative routing to EPRR to make data communication even more reliable. In Co-EPRR, data overhearing of the node is exploited and the relay cooperates with the destination. If the destination fails to receive the correct data, then, a relay retransmits the data on request of the destination. The Co-EPRR utilizes amplify and forward incremental cooperation; data retransmission is controlled by using the bit error rate (BER) threshold. Cooperation of the nodes provides data reliability and increases the chances of a successful reception of the data.

Both the proposed schemes have promising performance in data delivery to the desired target and do not affect the scalability of the network as they do not require the Euclidean distance computation in route computation. Instead, nodes' physical distance is involved, which is computationally less complex.

To summarize, the contributions of the proposed work are as follows:

- (i) The nodes are deployed in the network in such a way as to avoid early death of the nodes and improve performance. Specifically, the density of nodes in the upper area of the network is greater than other lower part of the network
- (ii) The proposed EPRR scheme considers the shortest and best routes, which are the paths that provide the least time from a source to the desired target. The choice of the shortest path is based on the distance amongst nodes and sinks. Channel noise, residual energy, and depth are considered as well for further improving successful delivery
- (iii) In the proposed Co-EPRR scheme, to ensure reliable delivery of data packets, cooperative routing is added to the EPRR protocol. Desired information amongst the nodes is shared to advance throughput and reliable data exchange. The relay cooperates with the destination node if the data have an error greater than a given threshold. The relay node retransmits the same data again on request of the destination. Data are processed using maximum ratio combining (MRC) to obtain the required data at the destination
- (iv) Both EPRR and Co-EPRR use timer-based operations to compute the distance rather than the

computationally complex Euclidean distance. This reduces the complexity of computation and avoids the loss of scalability. As a result, network performance is improved without compromising scalability, as is the usual case with existing schemes

2. Related Work

A routing algorithm presented in [17] uses depth information for data delivery and is a receiver-based approach. The data is exchanged with the nodes having low depth. The lowest depth node accepts data for further transmission to the next step. The node having the lowest depth then informs all other neighbors by transmitting the same packet with the highest preference. When the neighbors receive the same packet, they discard the old one and consider successful delivery of the packet. This algorithm performs very well. However, high traffic on the upper nodes creates data overhead and leads to early death of nodes.

A recent approach [25] that improves the most popular existing algorithm [17] is presented. The fuzzy logic and the bloom filter are utilized to improve the existing routing strategy. The fuzzy logic is used for the uncertainty of energy estimation and hop count. Moreover, for the memory improvement of the DBR, a bloom filter is utilized. This algorithm performs best in terms of many performance metrics, such as energy, data delivery, and node lifetime.

The algorithm in [26] utilized an opportunistic technique for data routing and titled as “confined energy depletion (CED) opportunistic routing (OR) mechanism”. The data is routed in steps in order to achieve better performance such as energy utilization and packet reception. Firstly, the data advanced towards the next nodes. Then, the best forwarder is selected to advance the data. Next, the signal-to-noise ratio (SNR) and link quality are determined for the next step to advance the data.

The author suggested a clustered routing method, the location, and energy-aware k-means clustered routing (LE-KCR) algorithm, in [27]. K-means technology is used to determine the location of each node and the remaining energy of each node. Cluster-head selection considers both the situated site and the remaining energy of a prospective cluster-head, as well as the distance between it and its sink node. Compared with the traditional low-energy adaptive clustering hierarchy (LEACH) protocol and the enhanced LEACH protocol based on K-means clustering technology, the LE-KCR scheme consumes less energy and has fewer dead nodes.

To enable time-saving and reliable routing for UWSN, [28] offers the energy-efficient guiding-network-based routing (EEGNBR) protocol. It considers the beneficial distance-vector technique and creates a guiding network to give underwater sensor nodes the shortest route (least hop counts) toward the sinks in order to reduce network latency. Furthermore, it combined classic opportunistic routing with a revolutionary data forwarding technique known as a concurrent working mechanism, which also significantly minimizes forwarding delay while ensuring reliable routing. In terms of network latency, the protocol outperforms certain

related traditional protocols while maintaining an equivalent or even superior energy usage and packet delivery ratio.

An energy-aware multilevel clustering scheme is suggested in [29], to increase the lifetime of the underwater wireless sensor network. The undersea network area is composed of 3D concentric cylinders with many layers, and each level is separated into several blocks, each of which represents a cluster. The proposed algorithm employs a vertical communication route from the sea floor to the surface region. Simulations are used to demonstrate the efficacy of the proposed approach, which performs well in terms of network lifespan and residual energy.

A delay-tolerant algorithm with sink mobility is presented in [30]. In order to minimize duplicate data and energy cost, this scheme uses different variations of the depth threshold. For further improvements, the algorithm uses mobile sinks. The deployment of mobile sinks reduces the path length between two nodes. Reducing path length tends to minimize latency and improve successful data exchange. However, the path trajectories for sinks are difficult and costly underwater. Moreover, the depth threshold increases the computational complexity of the algorithm.

The algorithm in [31] tries to maximize the network throughput and data reception by using the novel incremental cooperation. In this case, the retransmission of data by the relay occurs when the receiver fails to retrieve the correct data. Moreover, the algorithm implements a multilayer network structure and uses courier nodes. The courier nodes move in each layer for the collection of data, which maximizes the network throughput and latency. However, the courier nodes increase the cost of network deployment. Due to the cooperation, the energy cost is also high.

A delay-sensitive-energy efficient scheme for UWSNs called FVBF is proposed in [23]. The FVBF enhances the performance of the VBF [24] by using the fuzzy logic technique, where the best forward node is selected by considering the position of the node and the energy information in the cylinder. In FVBF, consideration of the residual energy ratio (RER) and fuzzy logic interference system reduces energy consumption and interference. The lowest distance and highest remaining energy are considered for selection of the destination to forward the information to the desired sink node through the multihop path. The fuzzy logic interference system reduces the contribution of the other nodes during the routing and follows the shortest path to reach the sink node. FVBF minimizes delay during the information forwarding and reduces energy consumption. However, the nodes have a large data burden on the cylinder.

To reduce latency and improve network energy, Ali et al. introduced DVRP [20]. DVRP forwards the information in the network in a diagonal or vertical manner to reduce the path length and decreases the latency. Moreover, the horizontal flow of information in the existing schemes increases the routing path, which increases the energy cost and latency. The best forwarder selection is made on energy and flood angle. Data to the next node are delivered in the same manner. The information is forwarded only in the flooding zones vertically or diagonally to decrease the path

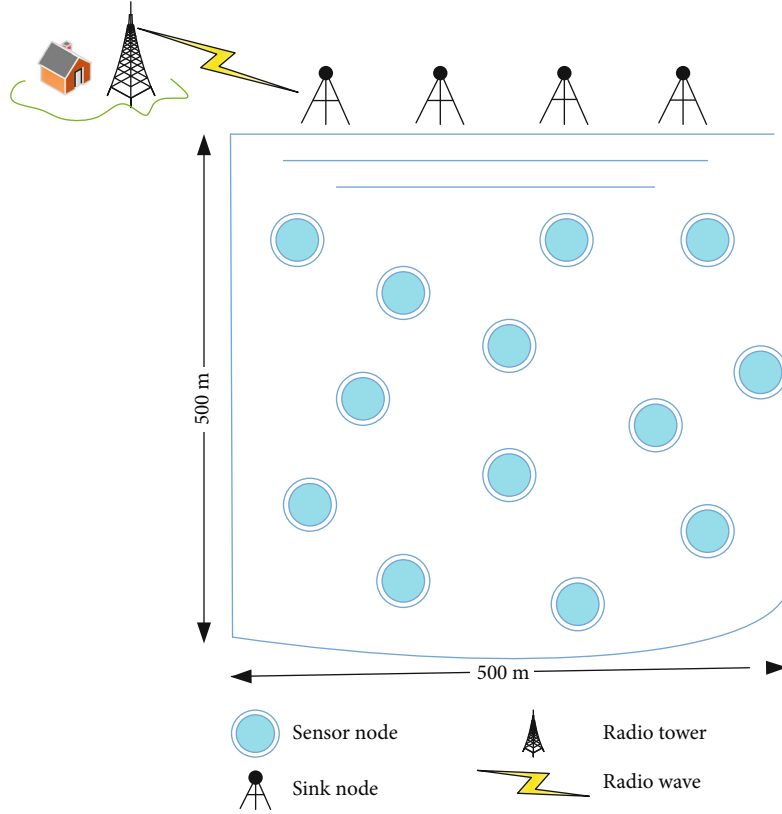


FIGURE 1: Network model.

```

1 Initialization;
2  $S_{source}$ : Source node;
3  $D_i$ : Depth possesses by sensor node  $i$ ;
4  $S_{source}$  broadcast a hello packet;
5 Calculate response time  $t$ ;
6  $d_{s,n}$ : distance between sender and neighbor node;
7  $d_{s,n} = (v \times t)/2$ ;
8  $d_{n,sink}$ : distance between sink and neighbor node;
9  $d_{s,sink} = ds, n_1 + \dots + dn_1, n_i + dn_i, sink$ ;
10 Neighbor nodes reply;
11 for round=1:end do
12   if  $S_{source}$  receives reply then
13     compute  $d_{s,n}$  and  $d_{n,sink}$ ;
14     compute weight function  $W_s(n)$ ;
15      $W_s(n) = R/d_{s,n} + d_{n,sink} + D_n + N$ 
16   end
17 end
18 Find maximum value of the  $W_s(n)$  to choose relay node;
19 The Best relay having the highest value of the weight function

```

ALGORITHM 1: Network initialization and destination selection.

length and allow the node to forward the information to the upper sink node with a small delay. DVRP reduces the network energy consumption and minimizes the latency during packet forwarding. However, the flooding angle updating is required for data forwarding.

In [21], an efficient energy and delay minimization algorithm named PBR for underwater UWSNs is presented. The information flows in two different ways, one is a regular information packet and the other is an emergency information packet, and it is transmitted by the path which leads to

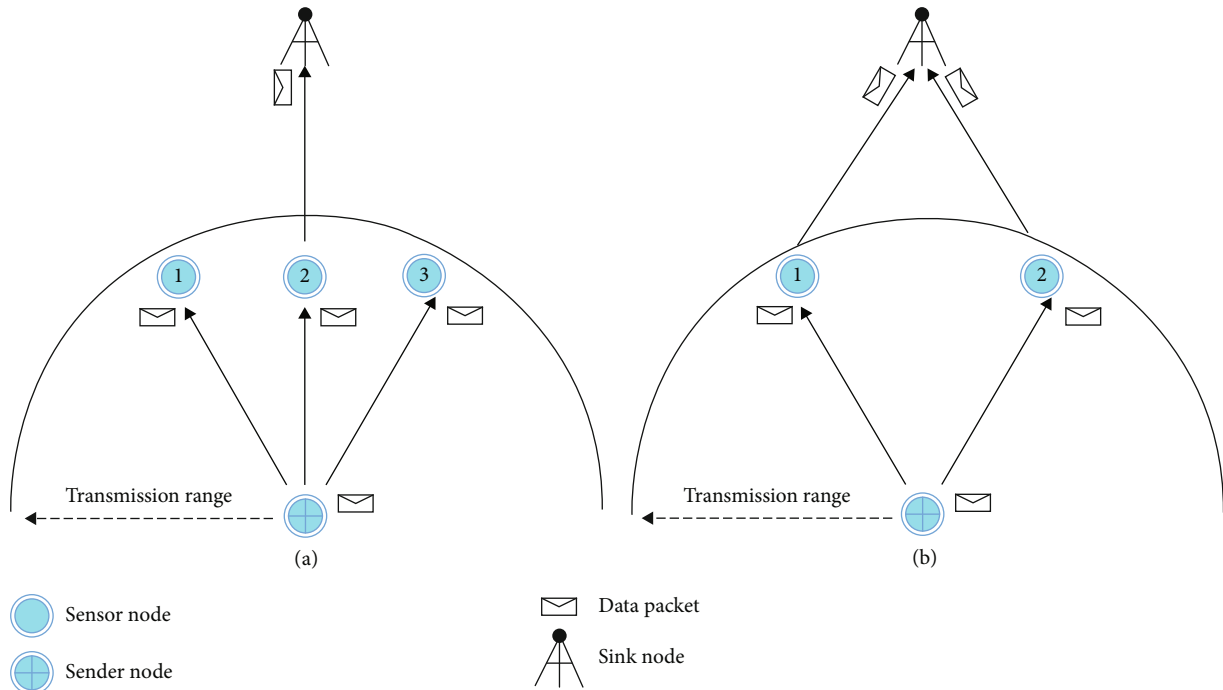


FIGURE 2: Data forwarding in EPRR.

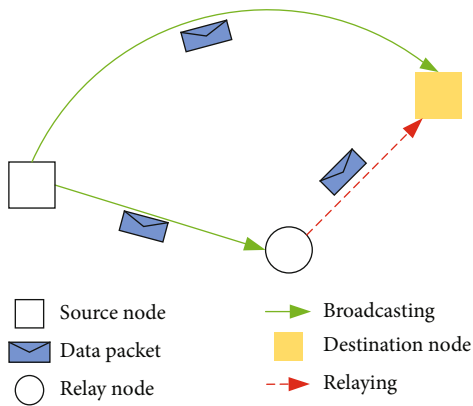


FIGURE 3: Data forwarding technique.

deliver data through the shortest path. The picking of the best forwarder node is based on the desired attributes such as the remaining energy, delay, and number of hops. The node having a minimum number of hops, delay, and high residual energy which lies within the communication range is considered the best forwarder node which forwards the information further to the sink node. By taking the desired parameters, it reduces the path length and increases the information that reached the sink node with low cost of energy and taking less time as compared to the counterpart schemes. However, the regular information is received with a high latency compared to the emergency packet. An efficient mechanism for the video and image transmission using acoustic waves is discussed in [32].

The UMDR [22] algorithm forwards the information with a small latency and uses a directional antenna. Instead of the broadcast nature of the data transmission, the nodes

use a directional antenna to deliver data in less time. In addition, it reduces the energy cost and the overhead of the control message due to the directional antenna. However, the computational complexity due to the directional antenna is high.

The idea is introduced in [33] to obtain an efficient algorithm in energy consumption and reliability of the network by considering nodes' depth and minimum number of neighbors. The selection of the best forwarder node is established on the function parameter; minimum depth, and number of neighbors to reduce the interference between the nodes. In this algorithm, the source node first broadcasts a hello packet to collect the information of all the nodes. The node close to the sink node having the least number of neighbors is selected as the destination node. Selecting the node which has the minimum number of neighbors as a forwarder reduces the interference and collision of the data packets. The algorithm sounds superior in energy consumption, remaining energy, packets received at the sink node, packets dropped, PDR, and delay. However, the data load at the lowest depth is greater in the network and tends to die soon.

A cooperative depth-based routing (CoDBR) is presented in [15]. Data are forwarded to the destination using the fixed relaying cooperative technique. Three copies of the data are received by the destination, one is transferred directly to the destination by the sender, and the other two copies of the data are transmitted by the relay nodes. The data are then combined utilizing the MRC technique. The relay and destination selection is based on the depth information. The node that has the lowest depth is selected as a destination. The CoDBR improves the network throughput and reliability with high latency and high energy

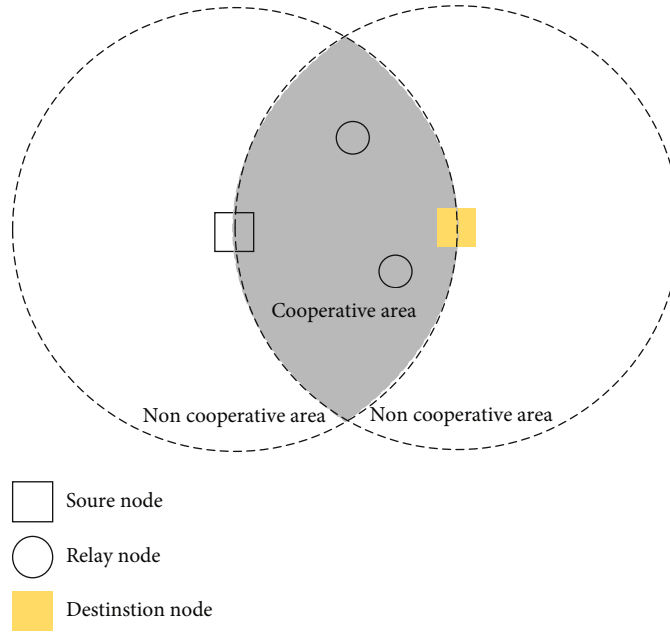


FIGURE 4: Relay selection.

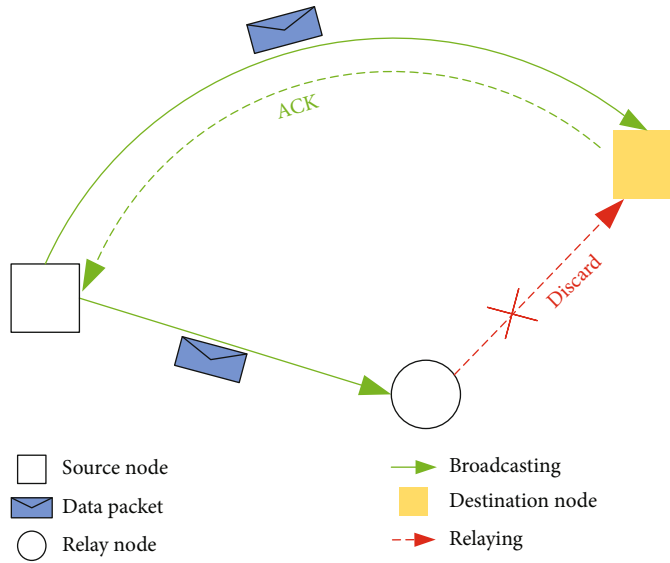


FIGURE 5: Data transmission (ACK).

consumption. Lee and his colleagues propose an automatic repeat request (ARQ) cooperative algorithm in [16]. All relay nodes transmit the data one by one on the destination request for correct data reception to achieve high throughput. However, the request of the destination to all the relay nodes one by one for retransmission consumes excessive energy and increases latency.

A cooperative void avoiding routing that requires the location information of the nodes for data forwarding is presented in [34]. For data forwarding, the sender considers an imaginary pipeline to the sink node to avoid data flooding. Nodes within the cylinder are eligible for data forwarding. The redundant packet forwarding is restricted using data

holding mechanism. The protocol achieves a better packet delivery ratio by utilizing a minimum amount of energy. However, this routing algorithm requires the location of the sensor nodes for information exchange.

In the region-based cooperative routing protocol (RBCRP) [35], the whole network is divided into four regions. In each region, a mobile sink moves horizontally in the network and collects data from the nodes in its own region. The source transmits data directly or through a relay node to the MS. Direct transmission is done when the source node finds MS in its transmission range. Otherwise, the data are transmitted through a relay node to the MS. The RBCRP is an energy-efficient and reliable algorithm in terms of PDR.

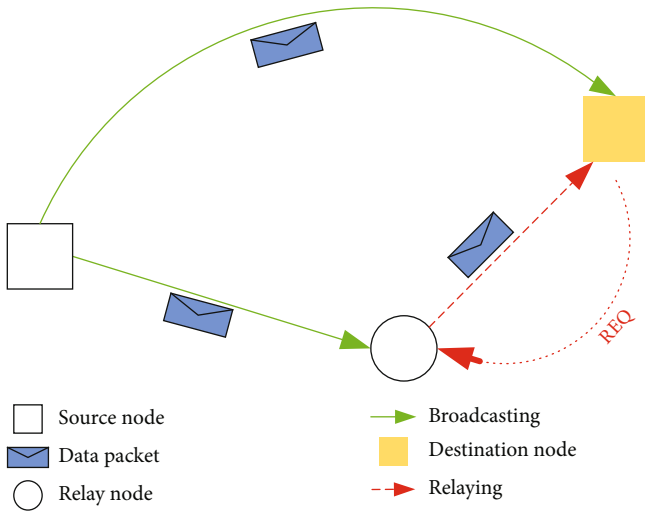


FIGURE 6: Data transmission (REQ).

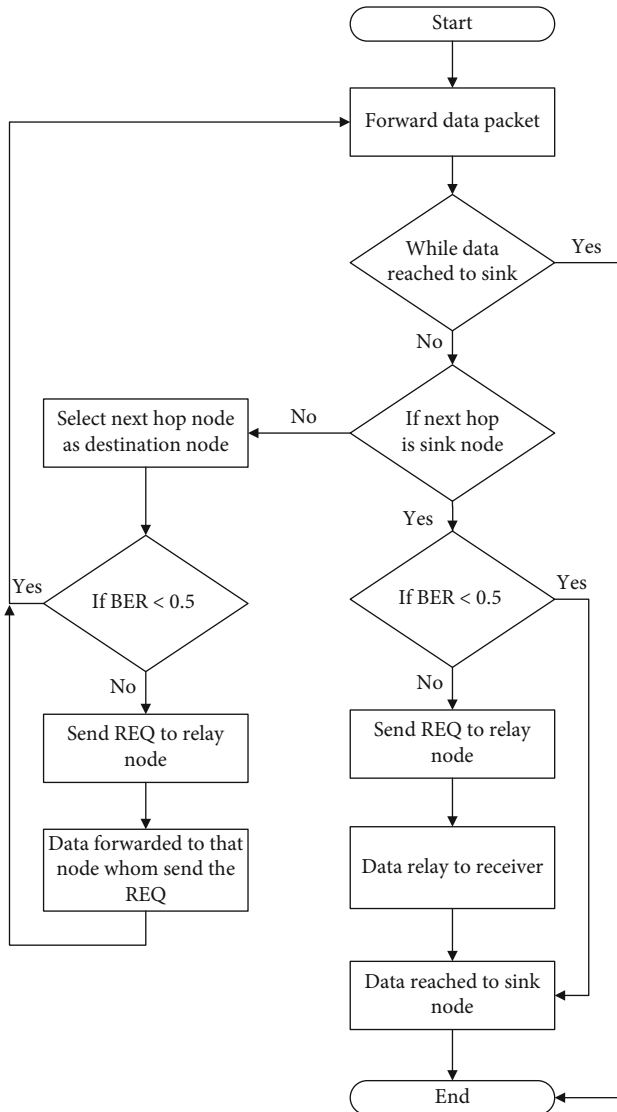


FIGURE 7: Flow chart.

```

1  $S_{sender}$ : Sender node;
2  $N_i$ : Neighbor node  $i$  of the sender node;
3  $S_{sender}$  send a data packet;
4 for round=1:end do
5   while data packet not reached to sink node do
6     if Next hop = Sink node then
7       if BER < 0.5 then
8         data packet accepted;
9         send ACK to sender;
10        Data reached to sink node = true
11      else
12        Select  $N_1$  as relay node;
13        Send REQ to  $N_1$  by the sink node;
14        Forward data by  $N_1$ ;
15        data packet accepted;
16        Data reached to sink node = true;
17      end
18    else
19      Select  $N_1$  as destination;
20      if BER < 0.5 then
21        data packet accepted;
22         $S_{sender} = N_1$ .
23      else
24        Select  $N_2$  as a relay node;
25        send REQ to  $N_2$  by  $N_1$ ;
26        Forward data by  $N_2$ ;
27        data packet accepted;
28         $S_{sender} = N_1$ 
29      end
30    end
31  end
32 end
    
```

ALGORITHM 2: Routing mechanism.

TABLE 1: Parameters choice.

Parameters	Size	Unit
Network size	$500 \times 500 \times 500$	Meter
Sink nodes	4	
Sensor nodes	225	
Transmission range	100	Meter
Depth threshold	60	Meter
Data packet	50	Bytes
Threshold	0.5	
Frequency	30	kHz

However, the movement of the mobile sink node is difficult underwater in terms of defining its path.

An algorithm in [36] is proposed for cooperative data transmission to the sink with a minimum energy consumption. The fuzzy logic chooses the best relay among the neighboring nodes. The proposed scheme improves the PDR and delay of the network. Packet collision minimization is done using the holding time. However, the remaining energy of the node is used for relay selection which is updated after a short time interval causes communication overhead and high latency.

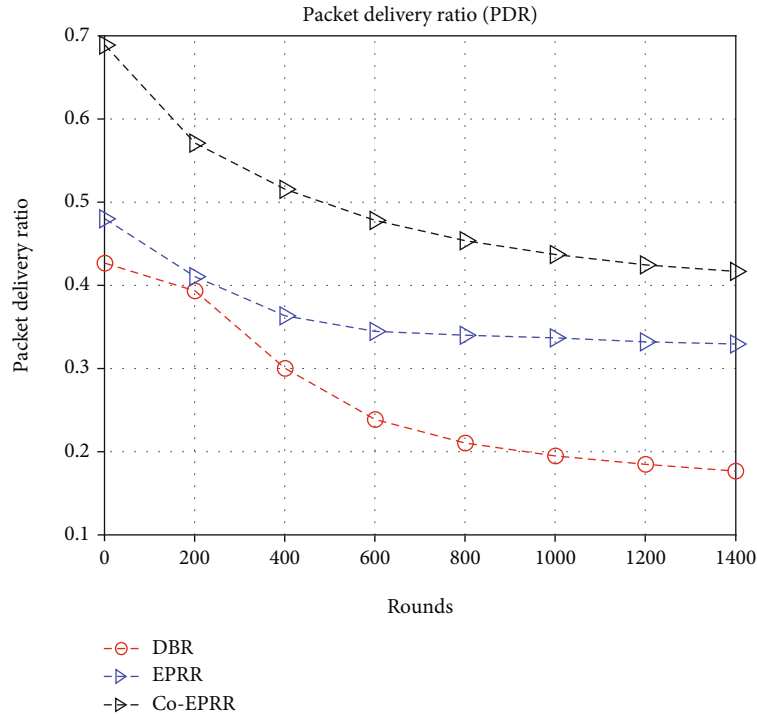


FIGURE 8: Packet delivery ratio (PDR).

TABLE 2: Packet delivery ratio (PDR) analysis.

Protocol	PDR at round 1	PDR at round 200	PDR at round 400	PDR at round 600	PDR at round 800	PDR at round 1000	PDR at round 1200	PDR at round 1400
Co-EPRR	0.688	0.571	0.515	0.478	0.453	0.437	0.424	0.416
EPRR	0.480	0.410	0.363	0.344	0.340	0.336	0.332	0.329
DBR	0.426	0.393	0.300	0.238	0.210	0.195	0.184	0.176

The cooperative routing that uses fixed ratio combining (FRC) is proposed in [37]. The selection of the relay is made on the channel noise, the distance of the source to the relay node, and the remaining energy of the node. The protocol achieves better energy consumption, delay, and network lifetime than its counterpart schemes. However, acknowledgment consumes excessive energy. The same routing metrics such as SNR, time of arrival, and distance between are used also in the algorithm presented in [38]. The relay node cooperates with the destination node whenever it does not receive the correct data. PDR and delay are improved. However, using CTS, RTS, and ACK causes communication overhead.

A cooperative communication is presented in [39], in which the relay regenerates the data followed by its transfer further to destination. The best relay node is selected using the SNR, time of arrival (TOA), and hop count information. In this approach, a better packet delivery ratio is achieved with minimal energy usage and delay. The sink node broadcasts an advertising packet to obtain the hop count information. However, this needs to be updated after specific intervals of time that cause delay.

In [40], a cooperative algorithm is proposed. The relay and destination nodes are chosen using three parameters: link quality, time of arrival, and hop count information.

The data are retransmitted by the sender when it receives a request from the destination. If the sender does not receive a request from the receiver, then after some time intervals the sender forwards the same packet to the receiver. This scheme achieves better PDR with minimum energy consumption and latency. However, information updating is required for relay and destination node selection and location information is needed for data routing. A most recent approach that used both acoustic and optical waves is presented in [41]. The acoustic waves are used for the control signal transmission, while data is exchanged using optical waves.

3. Proposed EPRR Algorithm

3.1. Network Architecture. Below the water surface, a sensor network setup is installed as shown in Figure 1. The deployment of the nodes affects the performance of the network, especially underwater. In particular, nodes are deployed to have a bigger number in the upper part of the network than in the other part of the area to be monitored. The nodes are capable of detecting attributes such as temperature, pressure, and light. These sensor nodes are powered by a limited battery. The communications among sensor nodes are done

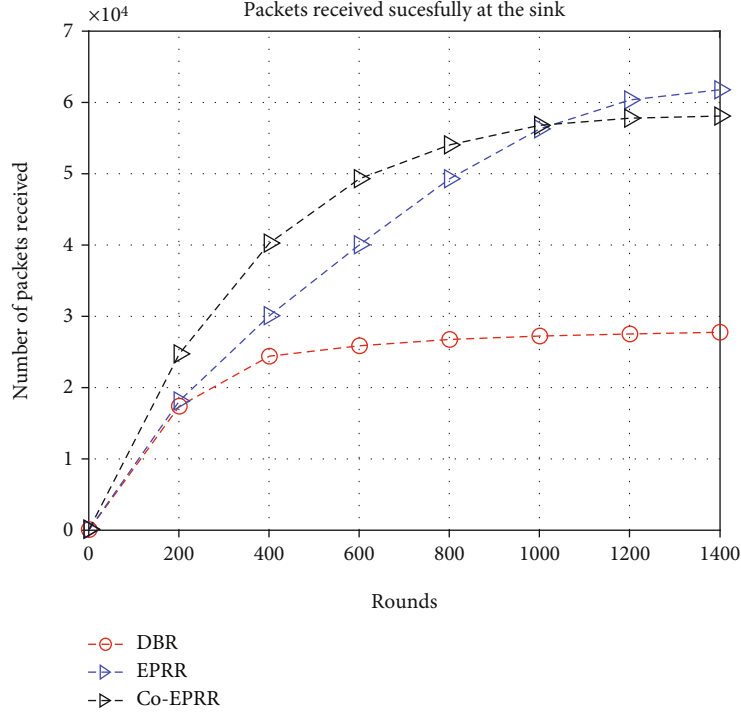


FIGURE 9: Received packet analysis.

TABLE 3: Successful packet reception analysis.

Protocol	Received data at round 1	Received data at round 200	Received data at round 400	Received data at round 600	Received data at round 800	Received data at round 1000	Received data at round 1200	Received data at round 1400
Co-EPRR	155	24632	40199	49275	54039	56783	57789	58091
EPRR	108	18039	30047	40000	49259	56280	60344	61778
DBR	96	17300	24351	25865	26753	27235	27522	27766

using acoustic waves. Each sensor node acts as a relay or source node. On the other hand, on the sea surface, sinks are placed at a fixed position. The sink nodes are different from the sensor nodes and communicate with each other through radio waves, while still using acoustic waves to communicate with the sink nodes. The acoustic modem is installed to communicate between sensor nodes at each sensor node. The sink nodes gather information from the sensor nodes; for further processing, the data is then delivered to the base station.

3.2. Network Initialization and Forwarder Selection. After network setup, the depth information of every sensor node is obtained by a pressure sensor attached to it. The depth value of the node i is denoted by D_i . Each node finds the distance from their neighbor nodes sending a specific “hello” packet. When a node receives the broadcasted hello packet from a sender, it sends a response. The sender, once it receives a response from a neighbor node, can calculate the roundtrip time taken t and then calculate the distance. The neighbors also share their depth with the sender in the hello packet. The sender s finds that its distance from every neighbor node n is represented by $d_{s,n} = (v \times t)/2$, where v repre-

sents the speed of acoustic waves in water. Then, the next forwarder finds its distance in the same manner from the next nodes and shares that distance value with the sender. At the end of the process, each node knows the distance value from the sink $d_{s,\text{sink}} = ds, n_1 + \dots + dn_1, n_i + dn_i$, sink, where n_i is the last node which communicates directly with the sink. In other words, the sink lies in the coverage area of the node. Based on the parameters $D_n, d_{s,n}, d_{n,\text{sink}}$, noise N , and residual energy R a sender node can also compute a weight function for the neighbor node as follows:

$$W_s(n) = \frac{R}{d_{s,n} + d_{n,\text{sink}} + D_n + N}. \quad (1)$$

The weight function for each neighbor node is determined by equation (1). The source then determines the next forwarder on the basis of the maximum value of the weight function. The best forwarder node is selected as the one with the highest value of the weight function. Algorithm 1 depicts the selection of the forwarder node.

The sender calculates the weight function for every neighbor and selects the node that follows the shortest route

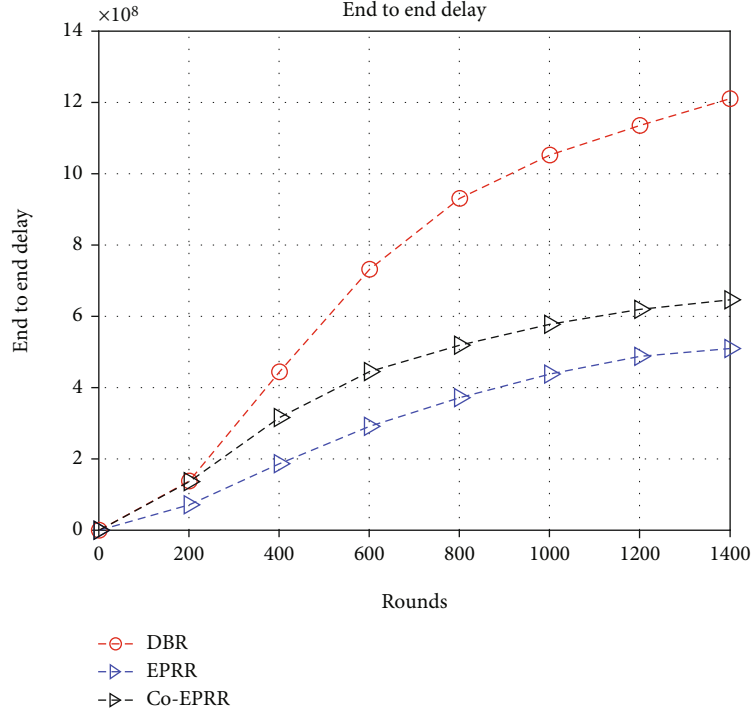


FIGURE 10: Network delay.

TABLE 4: End to end latency analysis.

Protocol	Delay at round 1	Delay at round 200	Delay at round 400	Delay at round 600	Delay at round 800	Delay at round 1000	Delay at round 1200	Delay at round 1400
Co-EPRR	5.62×10^3	1.35×10^8	3.15×10^8	4.44×10^8	5.18×10^8	5.77×10^8	6.19×10^8	6.46×10^8
EPRR	2.43×10^3	7.07×10^7	1.86×10^8	2.91×10^8	3.71×10^8	4.37×10^8	4.87×10^8	5.09×10^8
DBR	2.74×10^3	1.36×10^8	4.42×10^8	7.30×10^8	9.30×10^8	1.05×10^9	1.13×10^9	1.21×10^9

to the sink. Two different scenarios are depicted in Figure 2 in which all neighbors have the same depth. When using only depth information, all neighbors will direct data to the next stage because of having the same depth value. Therefore, the proposed approach chooses the best forwarder using the distance with the depth information of the nodes. In the scenario depicted in part a, node 2 is selected as the next forwarder, because it has the highest value of the weight function than the other neighbors. In other words, it is the shortest route to the sink than the others. In part b, both nodes have the same depth and distance from the source and the sink. So, both hold the same value of the weight function. Therefore, in this case, the sender has an open choice to select any of these nodes. And one of them directs data toward the sink.

3.3. Data Forwarding. When a source needs to exchange a data, it first checks the sink in its proximity. If a sink is available, then, direct exchanging of data with the sink node is performed without any other indirect path. When a sink is not present, the data are routed through other nodes until they reach the sink node. Namely, the source node gives

the packet to be sent to its neighbor nodes in case of not finding any sink node in its neighborhood. When the source to destination link fails, the data are dropped. From these neighbor nodes, a destination is selected on the basis of equation (1) which has the maximum value. Then, the sender sends the data with their unique ID and also embed the ID of the destination to the data packet. The same process is followed at every next hop until the data reach the sink node.

4. Proposed Co-EPRR Algorithm

The EPRR does not guarantee reliable data delivery, because if the source to destination link fails, then, the data is lost. The Co-EPRR is proposed, which provides data reliability whenever the source to the destination link is failed and then relays the data to the destination. The cooperation of the relay node and the combining technique is discussed in this section. The network architecture, network initialization, and destination selection are the same in Co-EPRR as in EPRR.

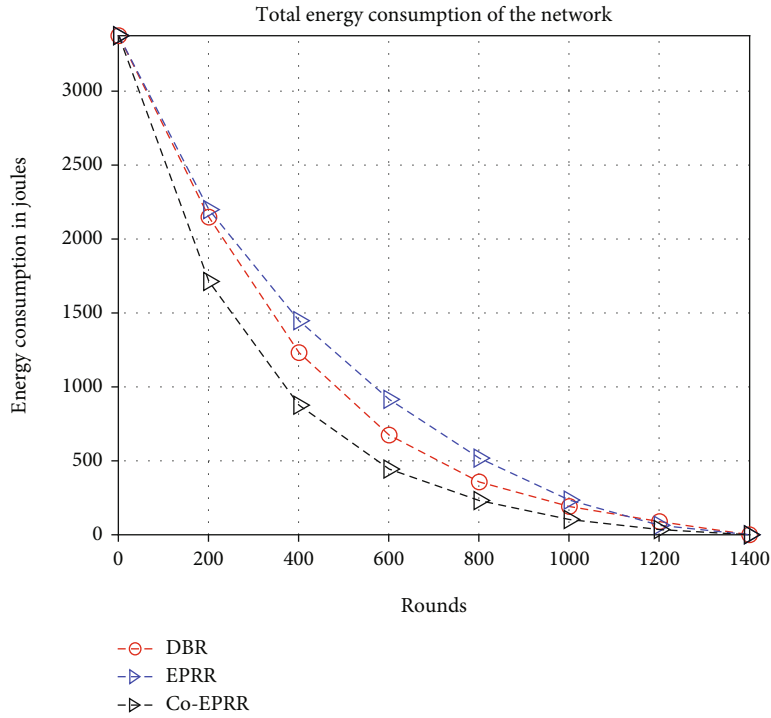


FIGURE 11: Residual energy analysis.

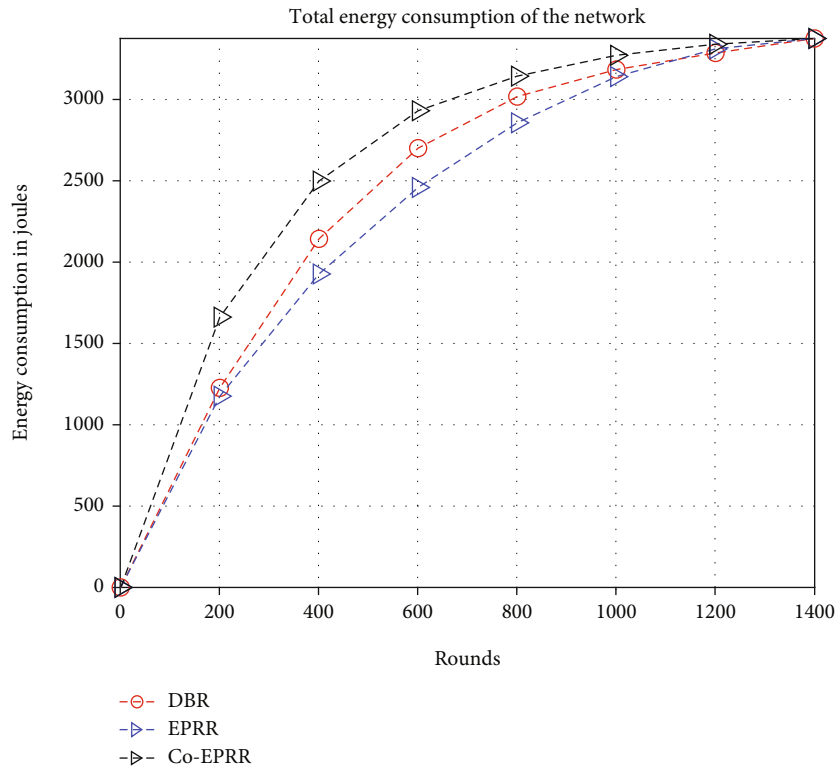


FIGURE 12: Energy expenditure analysis.

4.1. *Relay Selection Using Cooperation.* For cooperation, three nodes are considered: the source, the relay, and the destination nodes as depicted in Figure 3. In cooperative

schemes, data is received at the destination from the sender as well as by the relay node. The first one is known as broadcasting, and the second is relaying. In the first phase, the

TABLE 5: Remaining energy analysis.

Protocol	Residual energy at round 1	Residual energy at round 200	Residual energy at round 400	Residual energy at round 600	Residual energy at round 800	Residual energy at round 1000	Residual energy at round 1200	Residual energy at round 1400
Co-EPRR	3.37×10^3	1.71×10^3	880.00	445.84	232.27	103.85	35.49	0
EPRR	3.37×10^3	2.20×10^3	1.45×10^3	918.23	520.10	235.62	64.68	0
DBR	3.37×10^3	2.15×10^3	1.23×10^3	676.52	358.38	191.74	89.66	0

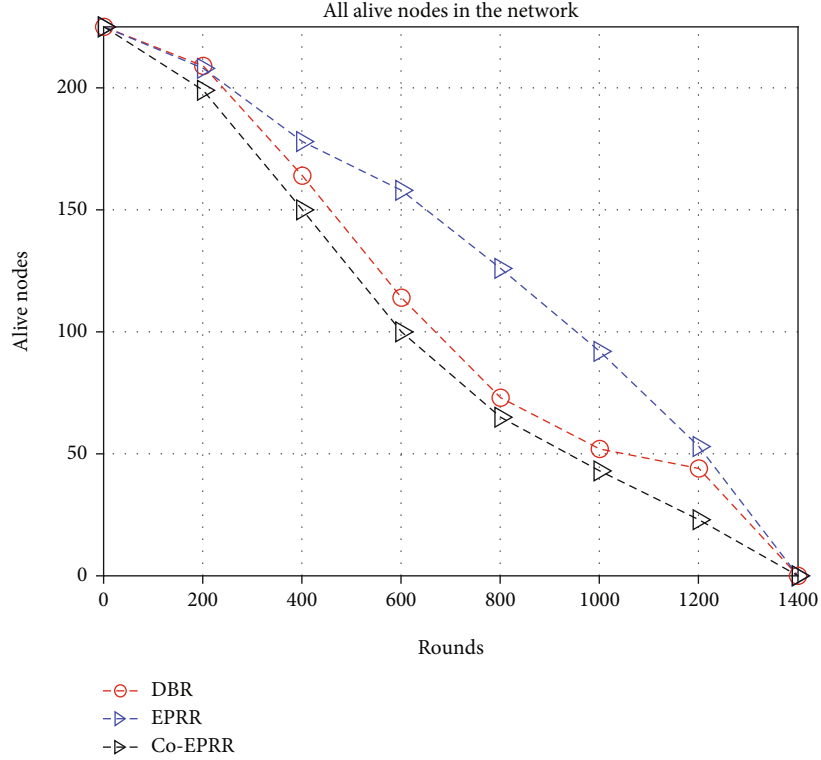


FIGURE 13: Alive node analysis.

destination and relay nodes receive data directly from the source node. In the second phase, the data received by the relay node is directed toward the destination.

The data forwarding from source S to relay R and destination D is formulated as

$$\begin{aligned} y_{sd}(t) &= h_{sd}X_s(t) + N_{sd}(t), \\ y_{sr}(t) &= h_{sr}X_s(t) + N_{sr}(t), \end{aligned} \quad (2)$$

where h_{sd} and h_{sr} are the channel gains between $S-D$ and $S-R$, respectively. The signal that S transmits at time t is X_s . The y_{sd} and y_{sr} are signals from $S-D$ and $S-R$, respectively. The N_{sd} and N_{sr} are the channel noise added to the desired signal from the $S-D$ and $S-R$ links, respectively.

Data communications from R to D are formulated as follows:

$$y_{rd}(t) = h_{rd}f(y_{sr}(t)) + N_{rd}(t), \quad (3)$$

where h_{rd} is the channel gain from $R-D$. The N_{rd} is the channel noise along the $R-D$ link. R processes the signal received from S represented by a function $f(y_{sr})$. In this paper, the AF technique (amplify and forward) is used. R amplifies the desired signal by a factor of β before sending it to D and receives the signal as follows:

$$y_{rd}(t) = h_{rd}\beta(h_{sr}X_s(t) + N_{sr}(t)) + N_{rd}(t). \quad (4)$$

The channel is modeled as Rayleigh fading and AWGN is used to simulate the channel noise. The sequence of bit generated by a sender using binary phase shift keying (BPSK) is sent over the AWGN channel directly to a destination. Then the destination checks the bit error rate (BER) and is given as [42]

$$\text{BER} = \frac{1}{2} \left(1 - \sqrt{\frac{\text{SNR}}{1 + \text{SNR}}} \right), \quad (5)$$

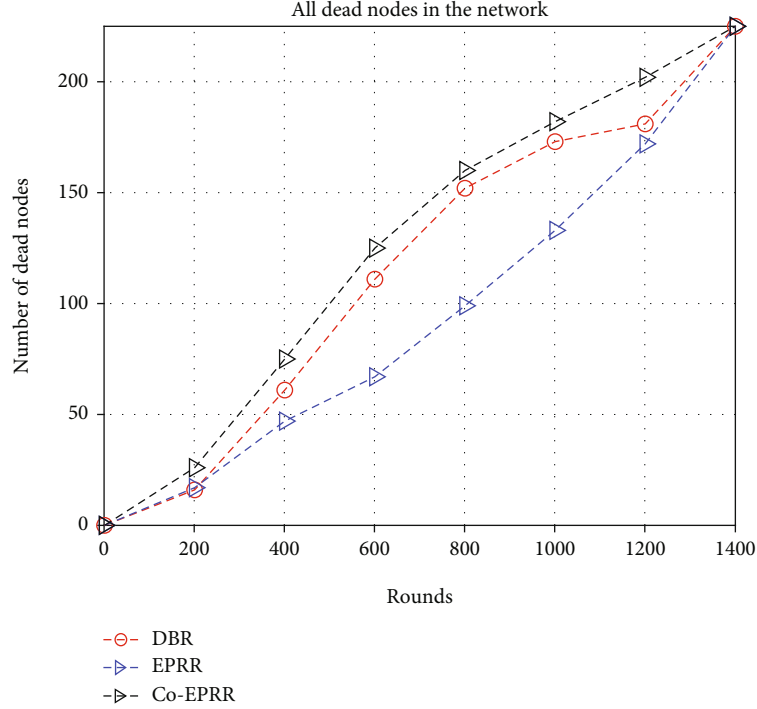


FIGURE 14: Dead node analysis.

TABLE 6: Analysis of the number of alive nodes in the network.

Protocol	Alive nodes at round 1	Alive nodes at round 200	Alive nodes at round 400	Alive nodes at round 600	Alive nodes at round 800	Alive nodes at round 1000	Alive nodes at round 1200	Alive nodes at round 1400
Co-EPRR	225	199	150	100	66	43	23	0
EPRR	225	209	178	158	127	92	53	0
DBR	225	209	165	114	73	52	44	0

where

$$\bar{\text{SNR}} = 10^{\text{SNR}/10},$$

$$\text{SNR} = \frac{P_t}{A(d,f)N(f)}, \quad (6)$$

where P_t represents the transmitted power of the source. The $A(d,f)$ and $N(f)$ represent the attenuation and noise associated with the underwater channel.

The relay is selected from the nodes which lie in the common transmission range (cooperative area) of both S and D as shown in Figure 4. The relay and destination selection criterion is the same as for the destination selection in the EPRR. Based on the weight function, two nodes are selected: one serves as a relay and the other as a destination (equation (1)). The destination is selected which has the highest value of the weight function, and the second node is selected as a relay which holds the highest value of the weight function. The relay forwards data only once to the destination to reduce the data collision and delay time.

When a data is received by the destination, it analyzes the BER. If the BER is less than 0.5, then, the destination responds to the sender and sends an acknowledgment

(ACK) as shown in Figure 5. When the data packet BER is greater than 0.5, then, D requests R for retransmission as shown in Figure 6. The sender node embeds relay ID information when transmitting the hello packet. Whenever the destination needs for retransmission of the data, then, the destination requests to relay which is close to it. The relay node amplifies and forwards (AF) the desired data packet and sends it to the destination.

4.2. Combining Technique. When a destination has multiple replica of the same data packet, all these data packets are combined using one of the diversity combining techniques. In this paper, the MRC technique is used. At the destination, the received signal y_d is the combination of all relaying and directly transmitted signals, which is combined by using the MRC technique and is given as [43]

$$y_d(t) = \sum_{k=1}^L h_{kd}^* \times y_{kd}(t), \quad (7)$$

where y_{kd} is the received signal through multiple paths and h_{kd}^* represents the conjugate of the channel gain. In this case,

D combines two signals: one from S and one from R ; therefore, $L = 2$ and is expressed as follows:

$$y_d(t) = h_{rd}^* \times y_{rd}(t) + h_{sd}^* \times y_{sd}(t). \quad (8)$$

The flow chart in Figure 7 shows the detail of the data transmission of the proposed algorithm. Algorithm 2 also explains the whole process of the proposed scheme.

5. Simulation Results and Discussion

MATLAB is used for simulation purposes to authenticate the results of the EPRR and Co-EPRR. The EPRR and Co-EPRR schemes are compared with DBR, because the DBR considers the depth of the node for data routing. For fair comparison, the mobility model and the MAC scheme considered in DBR are also taken into consideration by the proposed schemes. A network having a size of $500 \text{ m} \times 500 \text{ m} \times 500 \text{ m}$ is considered which distributes nodes randomly. The density in the upper area of the network is kept higher than that of the rest of the network. It is due to the high traffic load on the upper nodes, in which the death ratio is greater than the highest depth nodes. Among 225 nodes, 100 of them are deployed in the upper 100 m^3 . The sinks are placed at the top of the networks. The sink node has an infinite energy source, because it can be easily powered on the sea surface. The sensor node consumes 2 W, 0.8 W, and 8 mW power in transmission, reception, and idle mode, respectively. A hello packet contains 48 bits and is broadcasted to establish a connection. The transmission range and depth threshold of the sensor nodes are 100 m and 60 m, respectively. Table 1 shows metrics under consideration.

In Co-EPRR, the packet delivery ratio is the highest than EPRR and DBR. Because when data are received by a destination, it is checked. When the BER is less than the threshold value, it is accepted. However, if BER exceeds the limits, then, the destination requests are relayed for retransmission, which enhances the packet delivery ratio. The cooperation is helpful in advancing packets to the surface that raises PDR. Moreover, the greater number of nodes in the upper area of the network provides a path for the data. The path providing by the upper nodes leads to enhance the packet reception probability. Also, the selection of the shortest path is another reason for the highest PDR. The effects of the channel are less due to the shortest path. Due to all these reasons, the PDR of the Co-EPRR is the highest than that of the rest of the algorithms. The results of PDR are shown in Figure 8.

The PDR of the proposed EPRR is better than the DBR. Because in the former, the shortest path is followed toward the sink node in which the probability of packet loss is less. Also, the packet is less affected by the channel noise and attenuation which is received correctly at the destination and the packet drop probability is less than DBR. Another reason for better PDR is the density of the network. In the upper area of the network, the number of nodes is kept greater in order to increase the packet delivery probability. So, the proposed algorithms get good performance with respect to PDR.

The DBR has the lowest PDR. It is due to the high traffic on the upper nodes that the death ratio is high. The death of the nodes leads to break the communication between sinks and the lower nodes. Moreover, DBR considers the depth for path selection which does not guarantee the shortest path and the data may be corrupted by noise and tend to reduce the PDR. The PDR performance analysis is also shown in Table 2.

The received packet analysis is shown in Figure 9. The number of packets received in Co-EPRR is higher than that in EPRR and DBR. Due to the cooperation of the nodes, it maximizes the number of received packets. The proposed cooperative scheme requests to relay for retransmission of the data. Retransmission of data increases the chances of successful reception. Another reason for the highest data reception is the best possible route for the data exchange. Moreover, the network topology also contributes. The greater number of nodes provides multiple paths to the surface which enhances the reception of the data. At round 1000, the reception of the packets performance goes down than the EPRR. It is due to the death of the node. The death of the nodes reduces the chances of cooperation. Reduction in the cooperation process leads to fewer packet reception.

The EPRR has a higher packet reception than DBR. Due to the distribution of nodes in the network, multiple paths are available for data exchange, which increases the reception of the packets. Also, the shortest path selection leads to reduce channel effects on the data. The less channel effects on the data tend to the correct data reception and increase them. At the start up to 200 rounds, the packet reception in both EPRR and DBR is the same. It is due to the flooding of the data in DBR. After that, the nodes die, leading to reduction of packet reception. The analysis is also shown in Table 3.

The EPRR delay is the lowest than the others as shown in Figure 10, because it follows the shortest path to the sink node which deliver data with small latency, while the Co-EPRR has a greater delay than the proposed EPRR scheme. The reason is that the destination takes time to check the received data through multiple paths and to combine these data packets. The cooperation at every next hop node takes time, which results in delay. Therefore, in the Co-EPRR, the data is received at the sink node with high latency.

In the counterpart DBR scheme, redundant packets are transmitted, which increases packet collision, energy consumption, and latency. Also, the selection parameter only considers the nodes' depth for data routing, which does not guarantee the shortest route to the destination. In the proposed EPRR and Co-EPRR schemes, the shortest route is used for data transmission by considering the distance with the depth value of the node. The decision for the forwarder selection is made by the sender which selects only one forwarder which leads to reducing the packet collision probability and redundant transmission. The delay performance is further elaborated in Table 4.

In Figures 11 and 12, the residual energy and energy consumption results are shown. The Co-EPRR residual energy is the lowest than the counterpart schemes as it checks the BER prior to packet advancing. If BER is greater

than 0.5, then, the destination requests to relay for retransmission. In short, two sensor nodes are used to transmit the same data packet and both sensor nodes consume energy. The cooperation is done at every next hop node, which consumes excessive energy. So, in Co-EPRR, the energy consumption is greater than that of the proposed EPRR and the counterpart scheme. Conversely, the residual energy is minimum than the counterpart schemes.

The EPRR has a higher residual energy than the counterpart scheme. The shortest path is followed to the sink node, which reduces energy consumption as few nodes are involved in data forwarding. Also, multipath transmission is avoided which consumes less energy and its residual energy is higher than the counterpart schemes. While in the competitor DBR algorithm, redundant data transmission tends the more energy consumption and reduces the network lifetime. Table 5 shows more detail about the energy of the network.

In Co-EPRR, nodes die soon as cooperation makes them use of their energy rapidly. Therefore, cooperative schemes have the lowest alive nodes and the highest dead nodes compared to DBR and EPRR as shown in Figures 13 and 14, respectively. In EPRR, the nodes do not die soon due to the lower energy usage. In DBR, the higher energy consumption leads to rapid death of the nodes. Therefore, the number of alive nodes in DBR is lower than that of the proposed EPRR. As a result, the number of alive nodes is higher in EPRR than in the counterpart scheme as shown in Figure 13 and also in Table 6.

6. Conclusion and Future Work

Two routing algorithms are proposed for UASNs: EPRR and Co-EPRR. The former used delay-sensitive paths for data routing. This reduced the delay and shortened the time for which data are affected by channel properties, which improved the reliability of data delivery. The latter algorithm added cooperative routing to EPRR to further counteract adverse properties of the channel in the data, which involved sending data over multiple links from a source to a destination. This increased the probability of successful data delivery to the desired target, even if some links failed to deliver the data. Both protocols maintained scalability of the network by computing physical distance rather than the computationally complex Euclidean distance. Network scalability is lost when Euclidean distance is computed, as it involves nodes' coordinate computations, and nodes constantly change their positions. Furthermore, the higher density of the nodes provides stable operation in the proposed schemes. Extensive simulations proved that the proposed schemes performed better in delivering packets to the desired target. The delay of the EPRR scheme was shorter than that of the counterpart scheme. However, the delay of Co-EPRR was greater than that of the counterpart scheme due to the routing data over multiple paths in the former. In the future, energy harvesting techniques will be used to energize the surface nodes to prolong the network lifetime.

Data Availability

The data used to support the findings of this study are available from the corresponding author upon request.

Conflicts of Interest

The authors declare that they have no conflicts of interest.

Acknowledgments

The author wishes to acknowledge the approval and support of this research work from the deanship of the scientific research in Northern Border University, Arar, Kingdom of Saudi Arabia. This research work was also partially supported by a faculty grant (GPF096A-2020), University of Malaya, Malaysia.

References

- [1] Y. W. Hong, W. J. Huang, F. H. Chiu, and C. C. J. Kuo, "Cooperative communications in resource-constrained wireless networks," *IEEE Signal Processing Magazine*, vol. 24, no. 3, pp. 47–57, 2007.
- [2] J. Heidemann, M. Stojanovic, and M. Zorzi, "Underwater sensor networks: applications, advances and challenges," *Philosophical Transactions of the Royal Society A*, vol. 370, no. 1958, pp. 158–175, 2012.
- [3] I. F. Akyildiz, D. Pompili, and T. Melodia, "Underwater acoustic sensor networks: research challenges," *Ad Hoc Networks*, vol. 3, no. 3, pp. 257–279, 2005.
- [4] I. F. Akyildiz, D. Pompili, and T. Melodia, "State-of-the-Art in Protocol Research for Underwater Acoustic Sensor Networks," *Proceedings of the 1st ACM International Workshop on Underwater Networks*, , pp. 7–16, ACM, 2006.
- [5] J. Heidemann, W. Ye, J. Wills, A. Syed, and Y. Li, "Research challenges and applications for underwater sensor networking," in *IEEE Wireless Communications and Networking Conference, 2006. WCNC 2006*, Las Vegas, NV, 2006, April.
- [6] A. Agustin and J. Vidal, "Amplify-and-forward cooperation under interference-limited spatial reuse of the relay slot," *IEEE Transactions on Wireless Communications*, vol. 7, no. 5, pp. 1952–1962, 2008.
- [7] H. Esmail, Z. A. H. Qasem, H. Sun, J. Wang, and N. U. R. Junejo, "Underwater image transmission using spatial modulation unequal error protection for internet of underwater things," *Sensors*, vol. 19, no. 23, p. 5271, 2019.
- [8] D. Simmons, D. Halls, and J. P. Coon, "OFDM-based nonlinear fixed-gain amplify-and-forward relay systems: SER optimization and experimental testing," in *Networks and Communications (EuCNC), 2014 European Conference on* (pp. 1-5). *IEEE*, Bologna, Italy, 2014, June.
- [9] M. Fadoul, M. B. Morsin, C. Y. Leow, and A. A. Eteng, "Using amplify-and-forward relay for coverage extension in indoor environments," *Journal of Theoretical and Applied Information Technology*, vol. 91, no. 2, 2016.
- [10] Q. Song and M. Garcia, "Cooperative OFDM underwater acoustic communications with limited feedback: part I," *International Journal of Computer Applications*, vol. 54, no. 16, pp. 42–46, 2012.

- [11] J. N. Laneman, D. N. Tse, and G. W. Wornell, "Cooperative diversity in wireless networks: efficient protocols and outage behavior," *IEEE Transactions on Information Theory*, vol. 50, no. 12, pp. 3062–3080, 2004.
- [12] M. O. Hasna and M. S. Alouini, "A performance study of dual-hop transmissions with fixed gain relays," *IEEE Transactions on Wireless Communications*, vol. 3, no. 6, pp. 1963–1968, 2004.
- [13] H. Hourani, *An overview of diversity techniques in wireless communication systems*, IEEE JSAC, 2004.
- [14] P. Liu, Z. Tao, Z. Lin, E. Erkip, and S. Panwar, "Advances in smart antennas - cooperative wireless communications: a cross-layer approach," *IEEE Wireless Communications*, vol. 13, no. 4, pp. 84–92, 2006.
- [15] H. Nasir, N. Javaid, H. Ashraf et al., "CoDBR: cooperative depth based routing for underwater wireless sensor networks," in *Broadband and Wireless Computing, Communication and Applications (BWCCA), 2014 Ninth International Conference on*, pp. 52–57, Guangdong, China, 2014, November.
- [16] J. W. Lee, J. Y. Cheon, and H. S. Cho, "A Cooperative ARQ Scheme in Underwater Acoustic Sensor Networks," in *OCEANS 2010 IEEE-Sydney*, pp. 1–5, IEEE, 2010.
- [17] H. Yan, Z. J. Shi, and J. H. Cui, "DBR: Depth-Based Routing for Underwater Sensor Networks," in *International Conference on Research in Networking*, pp. 72–86, Springer, Berlin, Heidelberg, 2008.
- [18] Z. A. H. Qasem, J. Wang, X. Kuai, H. Sun, and H. Esmail, "Enabling unique word OFDM for underwater acoustic communication," *IEEE Wireless Communications Letters*, vol. 10, no. 9, pp. 1886–1889, 2021.
- [19] H. Esmail, Z. A. H. Qasem, H. Sun, J. Qi, J. Wang, and Y. Gu, "Wireless information and power transfer for underwater acoustic time-reversed NOMA," *IET Communications*, vol. 14, no. 19, pp. 3394–3403, 2020.
- [20] T. Ali, L. T. Jung, and I. Faye, "Diagonal and vertical routing protocol for underwater wireless sensor network," *Procedia-Social and Behavioral Sciences*, vol. 129, pp. 372–379, 2014.
- [21] S. Shetty, R. M. Pai, and M. M. Pai, "Energy efficient message priority based routing protocol for aquaculture applications using underwater sensor network," *Wireless Personal Communications*, vol. 103, no. 2, pp. 1871–1894, 2018.
- [22] J. Yang, S. Liu, Q. Liu, and G. Qiao, "UMDR: multi-path routing protocol for underwater ad hoc networks with directional antenna," in *Journal of Physics: Conference Series (Vol. 960, No. 1, p. 012010)*, IOP publishing, 2018.
- [23] R. Bu, S. Wang, and H. Wang, "Fuzzy logic vector-based forwarding routing protocol for underwater acoustic sensor networks," *Transactions on Emerging Telecommunications Technologies*, vol. 29, no. 3, article e3252, 2018.
- [24] P. Xie, J. H. Cui, and L. Lao, "VBF: Vector-Based Forwarding Protocol for Underwater Sensor Networks," in *International Conference on Research in Networking*, pp. 1216–1221, Springer, Berlin, Heidelberg, 2006.
- [25] H. Karimi, K. Khamforoosh, and V. Maihami, "Improvement of DBR routing protocol in underwater wireless sensor networks using fuzzy logic and bloom filter," *PLoS One*, vol. 17, no. 2, article e0263418, 2022.
- [26] S. Ashraf, M. Gao, Z. Chen, H. Naeem, and T. Ahmed, "CED-OR based opportunistic routing mechanism for underwater wireless sensor networks," *Wireless Personal Communications*, vol. 125, no. 1, pp. 487–511, 2022.
- [27] L. Li, Q. Yang, and X. Jing, "A K-means clustered routing algorithm with location and energy awareness for underwater wireless sensor networks," *In Photonics*, vol. 9, no. 5, p. 282, 2022.
- [28] Z. Liu, X. Jin, Y. Yang, K. Ma, and X. Guan, "Energy-efficient guiding-network-based routing for underwater wireless sensor networks," *IEEE Internet of Things Journal*, 2022.
- [29] S. Chinnasamy, J. Naveen, P. J. A. Alphonse, C. Dhasarathan, and G. Sambasivam, "Energy-aware multilevel clustering scheme for underwater wireless sensor networks," *Access*, vol. 10, pp. 55868–55875, 2022.
- [30] K. Latif, N. Javaid, I. Ullah, Z. Kaleem, Z. Abbas Malik, and L. D. D. I. E. E. R. Nguyen, "DIEER: delay-intolerant energy-efficient routing with sink mobility in underwater wireless sensor networks," *Sensors*, vol. 20, no. 12, p. 3467, 2020.
- [31] A. Yahya, S. U. Islam, M. Zahid et al., "Cooperative routing for energy efficient underwater wireless sensor networks," *IEEE Access*, vol. 7, pp. 141888–141899, 2019.
- [32] A. Ezzat, H. Esmail, and H. S. Hussein, "Efficient real time image transmission over underwater acoustic mmwave channel," in *In 2018 International Conference on Computing, Electronics & Communications Engineering (iCCECE)*, pp. 230–235, IEEE, Southend, UK, 2018.
- [33] A. Khan, N. Javaid, I. Ali et al., "An energy efficient interference-aware routing protocol for underwater WSNs," *KSII Transactions on Internet and Information Systems*, vol. 11, no. 10, pp. 4844–4864, 2017.
- [34] N. Javaid, T. Hafeez, Z. Wadud, N. Alrajeh, M. S. Alabed, and N. Guizani, "Establishing a cooperation-based and void node avoiding energy-efficient underwater WSN for a cloud," *IEEE Access*, vol. 5, pp. 11582–11593, 2017.
- [35] N. Javaid, S. Hussain, A. Ahmad, M. Imran, A. Khan, and M. Guizani, "Region based cooperative routing in underwater wireless sensor networks," *Journal of Network and Computer Applications*, vol. 92, pp. 31–41, 2017.
- [36] M. A. Rahman, Y. Lee, and I. Koo, "EECOR: an energy-efficient cooperative opportunistic routing protocol for underwater acoustic sensor networks," *IEEE Access*, vol. 5, pp. 14119–14132, 2017.
- [37] S. Ahmed, N. Javaid, F. A. Khan et al., "Co-UWSN: cooperative energy-efficient protocol for underwater WSNs," *International Journal of Distributed Sensor Networks*, vol. 11, no. 4, Article ID 891410, 2015.
- [38] Y. Wei and D. S. Kim, "Cooperative relay for reliable communications in underwater acoustic sensor networks," in *Military Communications Conference (MILCOM)*, pp. 518–524, Baltimore, MD, USA, October 2014.
- [39] D. D. Tan, T. T. Le, and D. S. Kim, "Distributed cooperative transmission for underwater acoustic sensor networks," in *2014 IEEE Military Communications Conference*, pp. 205–210, Baltimore, MD, USA, April 2013.
- [40] H. Tran-Dang and D. S. Kim, "Efficient relay selection algorithm for cooperative routing in underwater acoustic sensor networks," in *2018 14th IEEE international workshop on factory communication systems (WFCS)*, pp. 1–9, Imperia, Italy, June 2018.
- [41] M. Mostafa, H. Esmail, and O. A. Omer, "Hybrid energy efficient routing protocol for UWSNs," in *2020 2nd International Conference on Computer and Information Sciences (ICCS)*, pp. 1–6, Sakaka, Saudi Arabia, Oct 2020.

- [42] J. G. Proakis, *Digital Communications*, McGraw-Hill, New York, 1995.
- [43] P. Wang, L. Zhang, and V. O. Li, "Asynchronous cooperative transmission for three-dimensional underwater acoustic networks," *IET Communications*, vol. 7, no. 4, pp. 286–294, 2013.

Research Article

A Viterbi Decoder under Class A Modeled Noise in Shallow Water

Yifei Wang^{1,2,3}, Huili Fan,⁴ Xuebo Zhang^{2,5,6}, Tian Tian,^{1,2,3} Shaohua Hong,^{1,2,3} Zhuofan Xie,^{1,2,3} Ruiping Song,^{1,2,3} Mingzhang Zhou,^{1,2,3} Xiao Feng,^{1,2,3} Yiting Liang,¹ and Shu Zhang⁴

¹School of Informatics, Xiamen University, Xiamen, China

²Key Laboratory of Southeast Coast Marine Information Intelligent Perception and Application, Ministry of Natural Resources, Xiamen, China

³Key Laboratory of Underwater Acoustic Communication and Marine Information Technology, Ministry of Education, Xiamen, China

⁴China Ship Development and Design Center, China

⁵College of Physics and Electronic Engineering, Northwest Normal University, Lanzhou, China

⁶Acoustic Signal & Electronics Science and Technology Corporation, Lanzhou, China

Correspondence should be addressed to Xuebo Zhang; xby_zhang@nwnu.edu.cn

Received 19 November 2021; Revised 15 May 2022; Accepted 4 June 2022; Published 23 June 2022

Academic Editor: Gianluigi Ferrari

Copyright © 2022 Yifei Wang et al. This is an open access article distributed under the Creative Commons Attribution License, which permits unrestricted use, distribution, and reproduction in any medium, provided the original work is properly cited.

A traditional Viterbi decoder is primarily optimized for additive white Gaussian noise (AWGN). With the AWGN channel, it offers good decoding performance. However, the underwater acoustic communication (UAC) channel is extremely complicated. In addition to white noise, there are a variety of artificial and natural impulse noise that occur suddenly. The traditional Viterbi decoder cannot obtain the optimum performance under this case. In order to solve this problem, this paper introduces a novel Viterbi decoder with the impulsive noise, which is considered to be subjected to Middleton Class A distribution in shallow ocean. Since Middleton Class A noise is very complicated, a simplified model is first introduced. Then, the error analysis of simplified model under various parameters is discussed in detail. The analysis shows that the simplified one just leads to slight error. Hereafter, a novel Viterbi decoder using the simplified model is discussed. Compared to a traditional decoder, a preprocessing is just required. The performance of soft decision-based decoder in the Middleton Class A noise channel (MAIN) and AWGN are further compared. Based on our simulations, the new decoder can significantly improve the performance in comparison with conventional one, which further validates our presented method.

1. Introduction

The noise distribution [1, 2] plays an important role in developing underwater signal processors. Traditional signal processors such as underwater localization [3–13], underwater tracking [9, 14, 15], sonar imaging [16–27], direction of arrival (DOA) estimation [28–32], and underwater acoustic communication (UAC) are mostly based on Gaussian noise, which can be supported by a central limit theorem. Besides, the Gaussian model is just determined by the first-order and second-order statistics [33]. Under this case, the linear processors can be obtained with Gaussian noise. Using the linear processors, the signal processing can be significantly

simplified. In practice, the shallow ocean often suffers from ambient noise from shipping vessels, marine life, activity on the surrounding land, and so on. This noise is impulsive [34, 35], and it is called non-Gaussian noise [36–41], which exhibits heavier tails than the Gaussian noise. Consequently, this noise cannot be directly described by using the probability density function (PDF) of Gaussian distribution. Compared to traditional Gaussian noise, the PDF of non-Gaussian noise is extremely complicated [42–46].

Nowadays, the non-Gaussian noise [36–41, 47–49] in shallow ocean has attracted much attention in the underwater field. The related work of non-Gaussian noise, especially impulse noise, has been widely researched. The receiver

performance under different impulse noise models is also inconsistent. The duration of impulse noise is very short while its amplitude is quite high. The energy of impulse noise is almost dozens of times higher than Gaussian noise in dB. Impulse noise models can be divided into memory noise channels, such as Gilbert-Elliott channel [50] and Markov-Gaussian channel models [51–53]. GE memory impulse channel belongs to the first order two state Markov process. It assumes that the channel has one good state and one bad state. The two different states are distinguished by setting the threshold. Until now, there has been a lot of literature on the and research of Markov memory channel. For instance, the literature [51] designed a quasicyclic low-density parity-check (QC-LDPC) code to resist Markov memory impulse noise and improve the robustness. In [53], Tseng et al. added the Polar Code over Markov Gaussian memory impulse noise channels and compared the performance of SC and BP algorithms. A previous work was only Polar Code over memoryless impulse noise channels. In [54], the α -sub-Gaussian noise model with memory order m (α SGN(m)) was applied in the description of snapping shrimp noise in shallow water. The scheme tackled the optimal detection of transmitted symbols in catching shrimp noise. In this paper, we consider the impulse noise is independent of each other in the underwater acoustic channel. Therefore, we consider using the memoryless noise model.

Impulse noise also includes memoryless models such as the Gaussian Mixture Model (GMM), symmetric α -stable (S α S) distribution, and additive Middleton class A and B models. The Gaussian Mixture Model (GMM) is a parametric probability density function defined as a weighted sum of Gaussian component densities. In [55], the GMM is used to model the ocean noise, and the expectation-maximization (EM) iteration method is exploited to estimate the GMM parameters. In [56], the performance of underwater communication system in noise with GMM statistics is discussed in detail. However, the heavier tail of non-Gaussian noise cannot be comprehensively described by this statistic. To solve this problem, symmetric α -stable (S α S) distribution [57] is proposed to model the shallow ocean noise. However, this model does not have the closed-form distribution except for the Cauchy, Levy, and Gaussian distributions. This is not convenient for the performance analysis of signal processors. In addition, Middleton class A noise has a strict probability density function(PDF) which simplifies the algorithmic complexity. The major advantage is that Middleton class A noise is a generalized GMM model. We can adjust the parameters of Middleton Class A impulse noise models to fit the underwater acoustic environment.

Actually, traditional processors are often discussed based on the empirical non-Gaussian models. To some degree, the statistics of ocean ambient noise are just fitted by using empirical non-Gaussian models, and the parameters of non-Gaussian noise model do not have physical meaning. Based on the physical mechanism of noise source and noise propagation characteristic, Middleton noise [58] possessing physical meaning is proposed. In [39], a parameter estimation method based on characteristic function for the Middleton Class A model is presented. In [38], the parameter

estimation of Middleton Class B noise is discussed based on the least-square estimation method. In [59], the mixture noise including $S\bar{I} \pm S$ distribution and Gaussian distribution is discussed. In practice, their model is a simplification of Middleton Class B model. In general, Middleton Class A is a general GMM model. Compare to the Class A model, the Class B model is very complicated. In this paper, we mainly concentrate on the Viterbi decoder and its performance with the Middleton Class A model.

The remainder of this work is arranged in the following. Section 2 introduces the PDF of Middleton Class A model and simplified one. In Section 3, the convolutional code and Viterbi decoder are presented. Then, the performance of the Viterbi decoder with Class A model is discussed in detail. Lastly, some conclusions are reported in the last section.

2. Middleton Class A Impulsive Model

In this section, an impulsive noise model named Middleton Class A is introduced.

2.1. The PDF of the Middleton Class A Noise. The one-dimensional PDF of normalized Middleton's Class A noise model can be expressed as

$$f_{A,\Gamma}(n) = \sum_{m=0}^{\infty} C_m \cdot \frac{1}{\sqrt{2\pi\sigma_m^2}} \exp\left(-\frac{n^2}{2\sigma_m^2}\right), \quad (1)$$

$$C_m = \frac{e^{-A} A^m}{m!}, \quad (2)$$

where the impulse index A is the product of the average number of pulses received per unit time and the pulse duration. It determines that the noise can be arbitrarily close to Gaussian noise and the Poisson process. The Gaussian coefficient Γ is the ratio of the average power of the Gaussian noise to the average power of the impulse noise. It is defined as

$$\Gamma = \frac{\sigma_G^2}{\sigma_I^2}, \quad (3)$$

where the receiver variance $0, 0, 1 \sigma_m^2$ can be described by

$$\sigma_m^2 = \sigma_G^2 + \sigma_I^2 \frac{m}{A} = \sigma^2 \frac{m/A + \Gamma}{1 + \Gamma}. \quad (4)$$

The total noise variance of the receiver σ^2 can be calculated as

$$\sigma^2 = \sigma_G^2 + \sigma_I^2. \quad (5)$$

The PDF of Class A noise is the sum of numerous zero-mean Gaussian PDFs with different weights. As shown by Equation (1), the noise source distribution obeys the Poisson distribution. In general, the impulse of noise is influenced by A and Γ . The Middleton Class A noise model is very close to Gaussian noise when the values of A and Γ are relatively large. The impulse of noise will

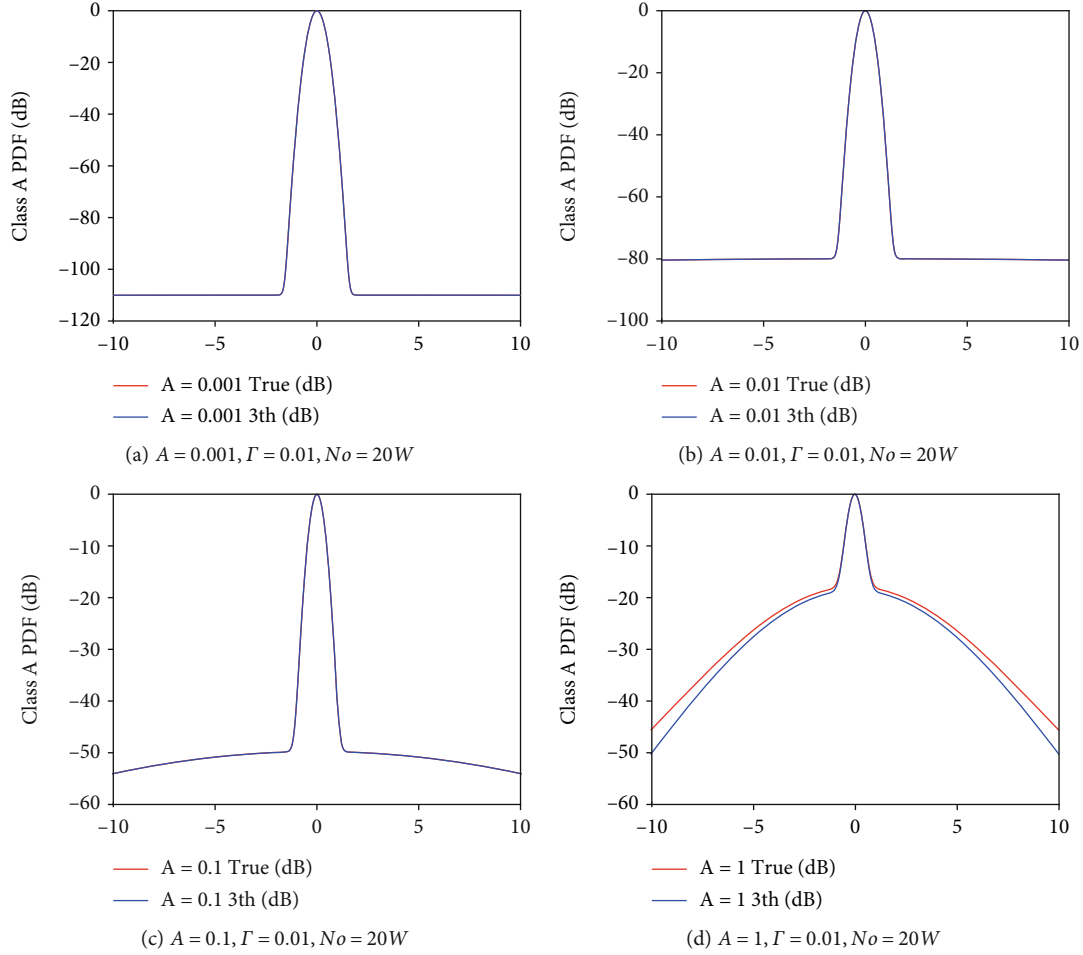


FIGURE 1: PDF of Middleton Class A with the different parameter A ($\Gamma = 0.01, N_o = 20W$).

become stronger as A and Γ decrease. Thus, the total noise interference can be influenced through A and Γ .

2.2. The Error Analysis of Truncated Model of Class A Noise. Since the PDF of Class A noise consists of infinite series, it is undesirable in reality. We explore the truncation model for Class A noise. Experiments indicate that the finite terms of noise can be adopted when A is small enough [60].

A truncation to the first three terms of the PDF is as follows:

$$\hat{f}_{A,\Gamma}(n) = \sum_{m=0}^2 C_m \cdot \frac{1}{\sqrt{2\pi\sigma_m^2}} \exp\left(-\frac{n^2}{2\sigma_m^2}\right). \quad (6)$$

The impact of parameters A , Γ , and N_o on the PDF between the simplified model and true one (Approximate replacement of the first 300,000 terms) is then discussed.

2.2.1. Error Analysis with Different Parameter A . Before discussion, we need to normalize the probability density function and then take the logarithm.

When $\Gamma = 0.01$, $N_o = 20W$, and $A = [0.001 \ 0.01 \ 0.1 \ 1]$, respectively, the error between the simplified model and the true one of the Class A noise PDF is discussed in Figure 1.

As depicted in Figure 1, the order m of the Middleton Class A noise approximate model is related to A . When A is small enough, the error of the approximation model in Equation (6) is close to 0. When A is in the range from 0.1 to 1, the simplified model can not be a good substitution. The reason is owed to the impulsive weakening of non-Gaussian noise, bringing it closer to Gaussian noise.

2.2.2. Error Analysis with Different Parameter Γ . When $\Gamma = [0.001 \ 0.01 \ 0.1 \ 1]$, the error between the simplified model and the true one of Class A noise PDF is shown in Figures 2–4. In the simulations, N_o is set to $20W$, and A is $[0.001 \ 0.01 \ 0.1 \ 1]$.

By comparing Figures 2–4, it can be observed that the value of Γ has no effect on the error of the PDF approximate model in Middleton Class A noise.

2.2.3. Error Analysis with Different Parameter N_o . In this subsection, the differences between the simplified model and the true model of the Class A noise PDF will be discussed. The results are exhibited in Figure 5, where $\Gamma = 0.01$, $N_o = [20 \ 20.2]$, and $A = 0.01$.

In Figure 5, note that the error of the PDF simplified model has nothing to do with the parameter N_o . When N_o takes different values, the error is always around 0.

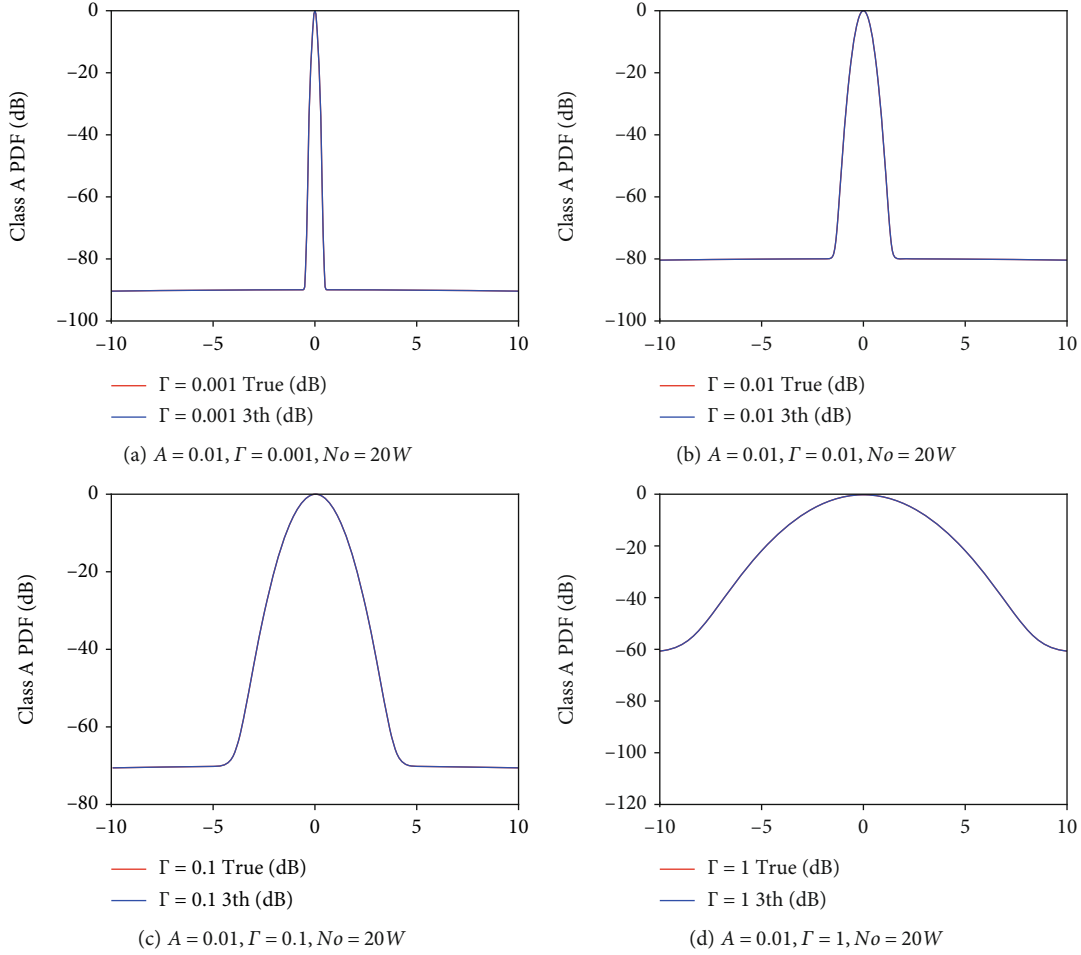


FIGURE 2: PDF of Middleton Class A with the different parameter Γ ($A = 0.01, N_o = 20W$).

3. Convolutional Code and Viterbi Decoding

Convolutional coding is a very promising coding technique proposed by Elias et al. in 1955. It has been widely used in communication systems, especially in satellite communication systems. Among them, the Odenwalder convolutional coding with code rates of $1/2$ and $1/3$ and constraint length $K = 7$ has become the standard coding method in commercial satellite communication systems. In 1967, Viterbi proposed a probabilistic decoding algorithm for convolutional encoding—the Viterbi algorithm. When the constraint degree of the code is small, it is more efficient and faster than other probabilistic decoding algorithms. Besides, the decoder is simpler. Since the Viterbi algorithm was proposed, it has been developed quickly in both theory and practice. The Viterbi algorithm has been widely used in various digital communication systems.

3.1. Generation of Convolutional Code. Convolutional code is a channel code with error correction capability, which can effectively reduce transmission error [61]. The decoding method is Viterbi decoding. Convolutional code can be described by (n, k, L) . In this way, n represents the code length corresponding to the output of the encoder. k is the length of the effective information group, which is the input

of the encoder. L denotes the constraint length. The code rate of the convolutional code is k/n . The n bits of the encoding output not only depend on the k bits but also depend on the $k - 1$ bit input before this. So the convolutional encoder has the property of “memory.”

Take $(2, 1, 3)$ convolutional code as an example.

By using the delay factor, the information sequence $M_0 M_1 M_2 \dots M_{l-1}$ and convolutional code series $C_0 C_1 C_2 \dots C_{l-1}$ can be described by

$$a_i = M_i \oplus M_{i-1} \oplus M_{i-2}, \quad 0 \leq i \leq l-1, \quad (7)$$

$$b_i = M_i \oplus M_{i-2}, \quad 0 \leq i \leq l-1. \quad (8)$$

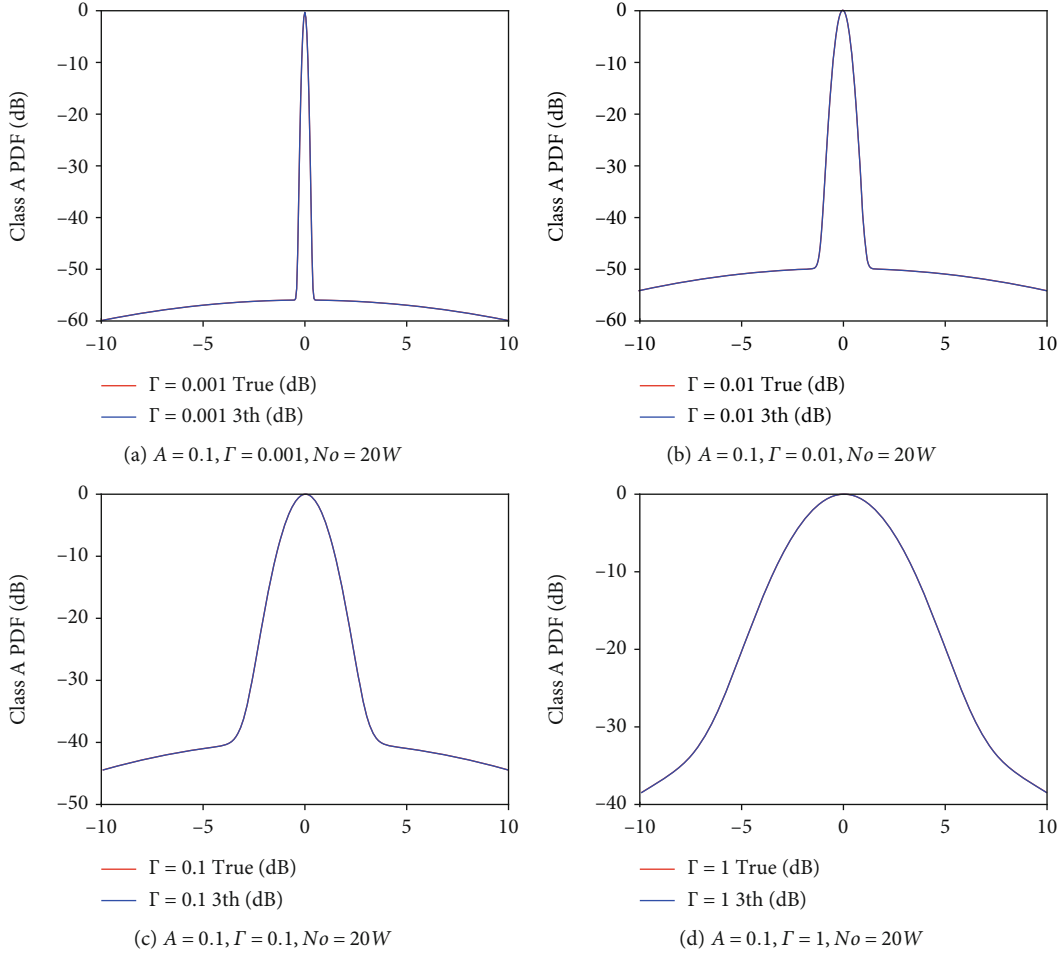
$$\mathbf{C}_i = \mathbf{a}_i \mathbf{b}_i, \quad (9)$$

where M_i is current input information bit and M_{i-1} and M_{i-2} are the first and the first two information bits. When $i \leq 0, M_i = 0$, set the initial state of the delay register to 0.

The generator polynomial of the Convolutional code is expressed as

$$G(Z) = [1 + Z^{-1} + Z^{-2} \quad 1 + Z^{-2}], \quad (10)$$

where Z represents delay register.


 FIGURE 3: PDF of Middleton Class A with the different parameter Γ ($A = 0.1, N_o = 20W$).

3.2. Trellis Diagram. Trellis graphs are used in the Viterbi decoding. It cannot be a representation of a single state. The trellis graphs are joined in a chronological sequence to define the relationship between time and state transition, generating a network of convolutional codes. The encoding process of the convolutional encoder is dynamic.

The following are the important concepts in the trellis diagram:

- (i) Calculate the branch metric (BM)

Calculate the Hamming distance (hard decision) or Euclidean distance (soft decision) between the input symbol and the output symbol corresponding to two paths, which is the branch metric of two paths.

- (ii) Calculate the path metric (PM)

To obtain the two metrics at time t , the BM of the two pathways is added to the state metrics recorded in the appropriate state at time $t - 1$.

- (iii) Select the surviving path

Compare the path metrics and maintain the smallest one as the state metric at time t , as well as the formation path.

- (iv) Traceback depth

Generally, the Viterbi decoder's backtracking depth is 6 times the constraint length. Set the traceback depth to 18 in this document.

In Figure 6, the uncoded sequence is $\mathbf{M} = M_0 M_1 M_2 \cdots M_{L-1}$. The output sequence of convolutional code is $\mathbf{C} = C_0 C_1 C_2 \cdots C_{L-1}$. Assume that the sequence after binary modulation is $\mathbf{V} = V_0 V_1 V_2 \cdots V_{L-1}$ and the channel output sequence is $\mathbf{R} = R_0 R_1 R_2 \cdots R_{L-1}$. The decoder must generate an estimate of the code sequence $\hat{\mathbf{V}}$ based on the accepted sequence \mathbf{R} . The maximum likelihood decoding is to choose maximize the log likelihood function $\log P(r|c)$ as $\hat{\mathbf{V}}$.

$$P(r|v) = \prod_{l=0}^{N-1} P(r_l|v_l). \quad (11)$$

Hence,

$$\log P(r|v) = \sum_{l=0}^{N-1} \log P(r_l|v_l), \quad (12)$$

where $P(r_l|v_l)$ is the channel transition probability. Log-

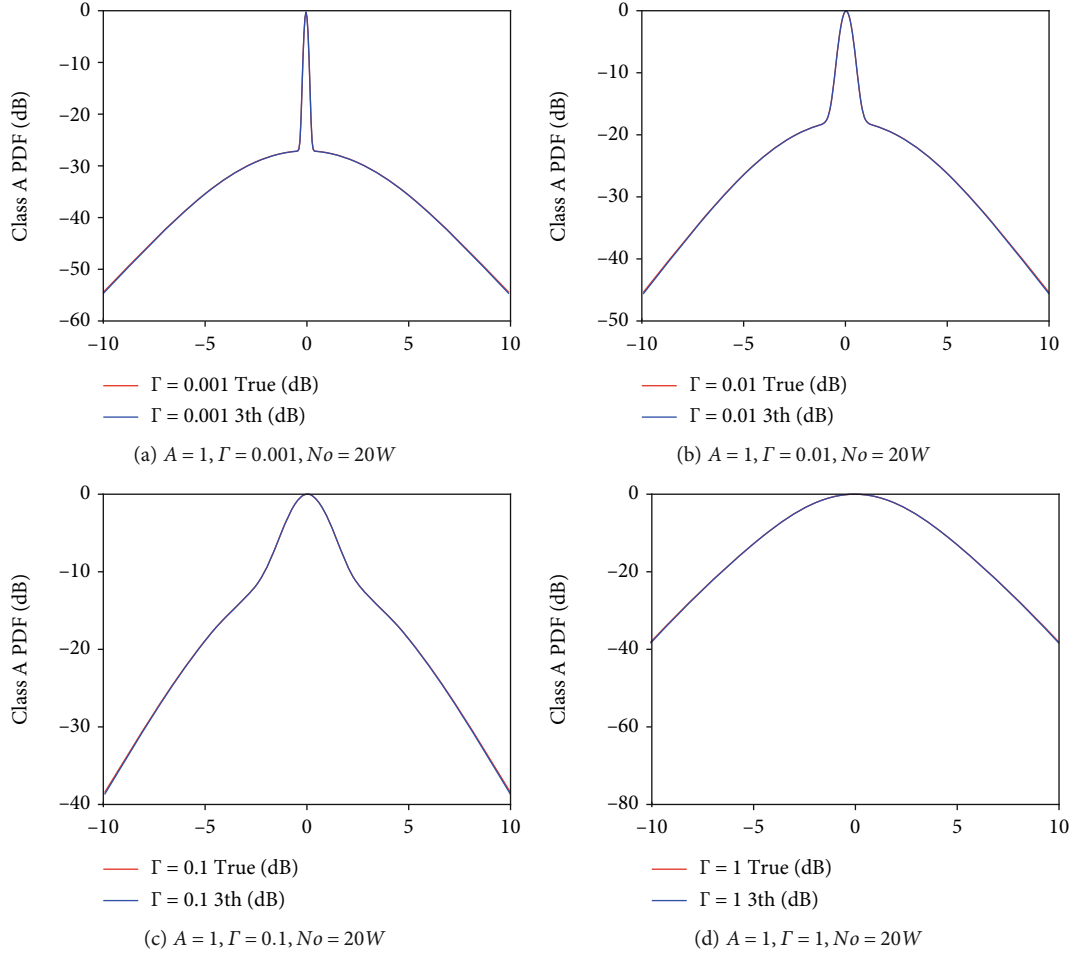


FIGURE 4: PDF of Middleton Class A with the different parameter Γ ($A = 1, N_o = 20W$).

likelihood function $\log P(r|v)$ is the metric of \mathbf{C} , where $\log P(r_l|v_l)$ is called the branch metric.

4. Performance of Viterbi Decoder under Class A Noise

The system block diagram and bit error rate formula under BPSK modulation are presented in this section. In addition, we pay specific attention to the effect on the best receivers after the Class A noise channel.

The full simulation system is presented in Figure 7.

As a soft decision symbol, the log-likelihood ratio is introduced to the Viterbi decoder input [62].

$$\text{LLR} = \ln f_{A,\Gamma}(r_l - \sqrt{E_b}) - \ln f_{A,\Gamma}(r_l + \sqrt{E_b}). \quad (13)$$

We first introduce the branch metric and LLR formula of Viterbi decoding under the Gaussian channel.

In BPSK modulation, we use the bit energy E_b to normalize the Gaussian pdf, where the mapping rule $1 \rightarrow +\sqrt{E_b}$, $1 \rightarrow -\sqrt{E_b}$. Denote $E_b = v_l^2$ and $N_G = 2\sigma^2$ as bit energy and total noise power, respectively. The code rate of convolutional code is $R_c = 1/2$. We consider the value of ± 1

sequence $\mathbf{V} = V_0 V_1 V_2 \cdots V_{l-1}$ and accepted sequence $\mathbf{R} = R_0 R_1 R_2 \cdots R_{l-1}$.

The PDF of Gaussian noise can be expressed as

$$P_G(n) = \frac{1}{\sqrt{2\pi}\sigma} \exp\left(-\frac{n^2}{2\sigma^2}\right). \quad (14)$$

The branch metric and LLR under the traditional Gaussian decoder can be expressed as

$$\mathbf{r} \times \mathbf{v} = \sum_{l=0}^{N-1} r_l \cdot v_l, \quad (15)$$

$$L(y_k) = \frac{2}{\sigma_G^2} y_k. \quad (16)$$

The bit error rate formula under the influence of Gaussian noise can be written as

$$\text{BER}_{\text{AWGN}} = \frac{1}{2} \text{erfc}\left(\sqrt{\frac{E_b}{N_G}}\right). \quad (17)$$

The PDF of Class A noise consists of infinite terms,

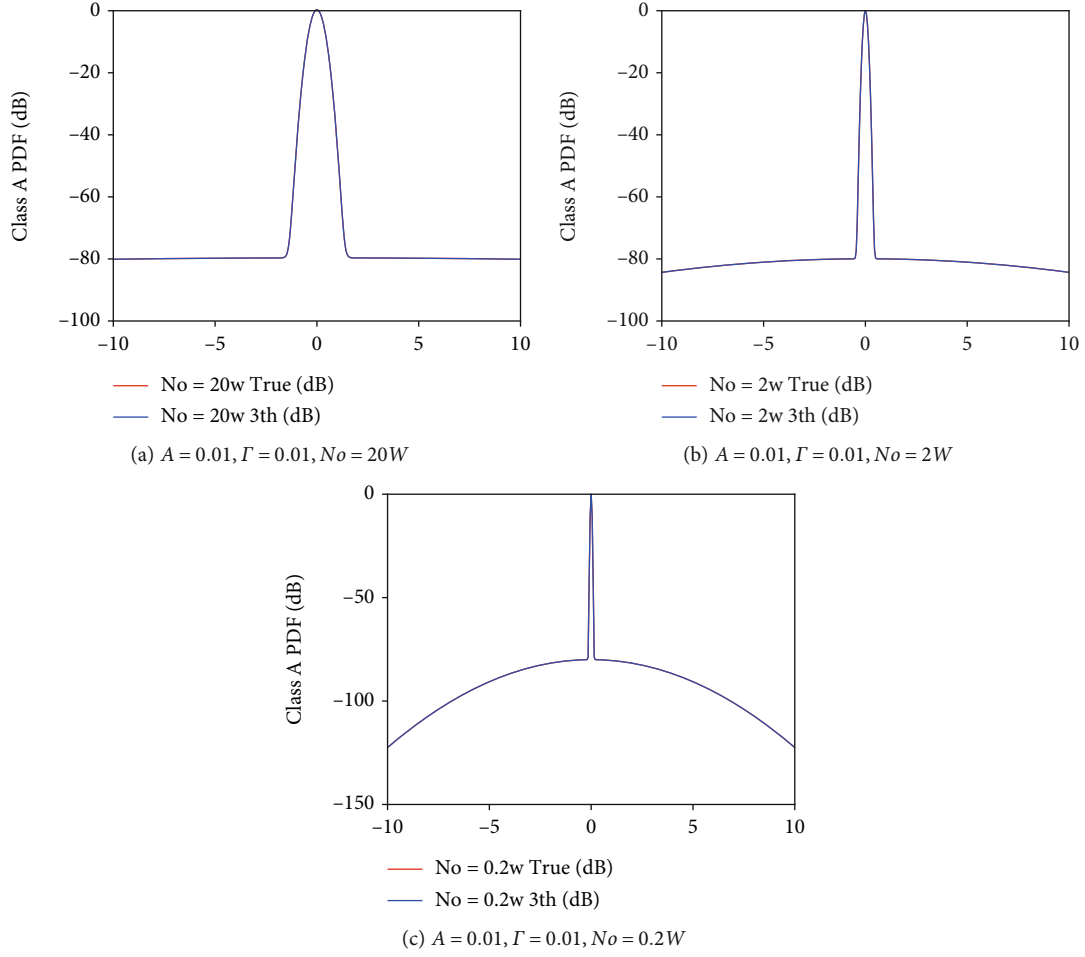
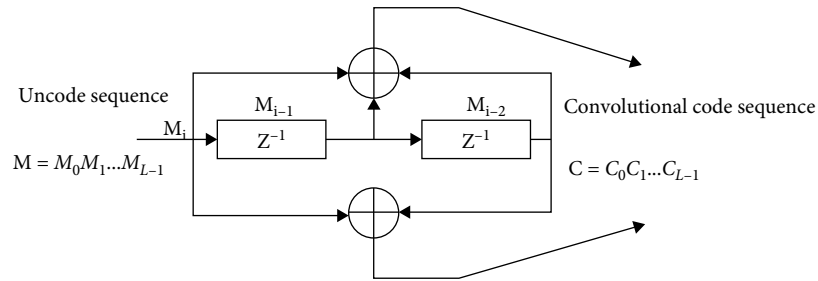

 FIGURE 5: PDF of Middleton Class A with the different parameter N_o ($A = 0.01, \Gamma = 0.01$).


FIGURE 6: (2, 1, 3) convolutional encoder.

leading to the enormous complexity of logarithmic. We use the 3-order approximate model and Equation (13) to simplify the soft symbol.

$$\ln \hat{f}_{A,\Gamma}(n) = \ln_{\max_{m=0,1,2}} \frac{\left[C_m \cdot \left(1/\sqrt{2\pi}\sigma_m \right) e^{-(r_i - \sqrt{E_b})^2 / 2\sigma_m^2} \right]}{\left[C_m \cdot \left(1/\sqrt{2\pi}\sigma_m \right) e^{-(r_i + \sqrt{E_b})^2 / 2\sigma_m^2} \right]}. \quad (18)$$

The Class A noise Viterbi decoder can be established by

Equation (13). The algorithm equation can be depicted as soft decision based on Class A noise PDF simplified model, as shown in Equation (18).

The bit error rate formula under the influence of Class A noise can be obtained as

$$\text{BER}_{\text{MAIN}} = \frac{1}{2} \sum_{m=0}^{+\infty} \frac{e^{-A} A^m}{m!} \text{erf} c \left(\sqrt{\frac{A\Gamma + A E_b}{A\Gamma + m N_0}} \right). \quad (19)$$

When A is very small, we take the first 3 orders as an approximation

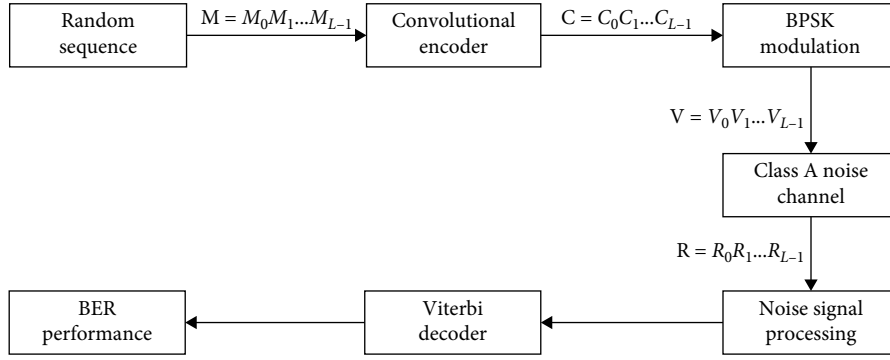
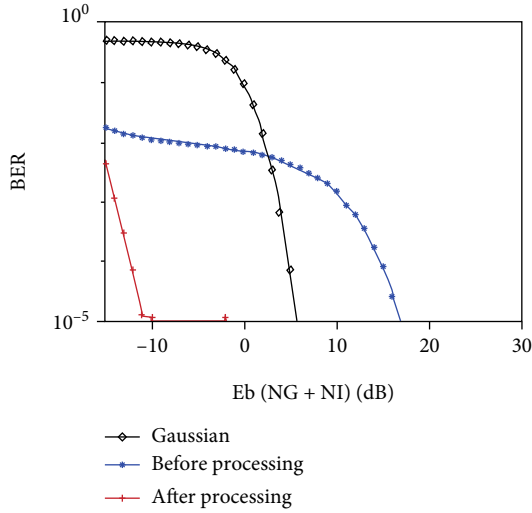
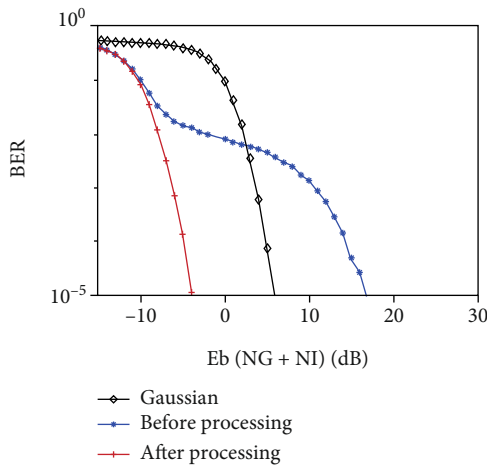


FIGURE 7: Block diagram of signal processing.

FIGURE 8: BER performance soft decision before and after processing ($A = 0.01, \Gamma = 0.01$).FIGURE 9: BER performance soft decision before and after processing ($A = 0.01, \Gamma = 0.1$).

$$\text{BER}_{\text{MAIN}} = \frac{1}{2} \sum_{m=0}^2 \frac{e^{-A} A^m}{m!} \text{erfc} \left(\sqrt{\frac{A\Gamma + A E_b}{A\Gamma + m N_0}} \right). \quad (20)$$

Finally, based on our simplified model, we present the soft decision of BER performance in the proposed decoder after signal processing Middleton Class A noise under different parameters.

According to Figure 8, the proposed decoder outperforms the signal processing of soft decision in the Class A noise channel. It is worth noting that when the noise has a higher impulse, the BER performance improves significantly. When the BER approaches 10^{-5} , the gain of $A = 0.01$ and $\Gamma = 0.01$ is around 25-30 dB. As shown in Figure 9, the gain of $A = 0.01$ and $\Gamma = 0.1$ is only 20 dB, which is owing to the noise trending to Gaussian noise at this time. It can be seen that the coefficient of the Gaussian Γ will also affect the performance of the decoder.

5. Conclusion

In this paper, a method of processing Middleton Class A noise by the Viterbi decoder is introduced in the field of shallow water acoustic communication. The effects of the three parameters A , N_0 , and Γ of Middleton class A noise on the third-order approximate model are also investigated. It can be concluded that parameters N_0 and Γ just influence the curve's shape but have no effect on the third-order approximate model, while parameter A influences the approximate model. When A is less than 0.1, the third-order model can be a good approximation to replace the real model in the curve of probability density probability. At the same time, the BER performance in the final section proves its feasibility under various parameters.

Additionally, the Class A noise decoder's system block diagram is constructed in the paper. The noise processing algorithm is derived from the optimum reception theory of Class A noise. After signal processing, the decoder overcomes the drawbacks of traditional decoders in Class A noise channel reception and enhances soft decision performance.

Data Availability

The data used to support the findings of this study were supplied by Yifei Wang under license and so cannot be made freely available. Requests for access to these data should be made to Yifei Wang (23320201154028@stu.xmu.edu.cn).

Conflicts of Interest

The authors declare no conflicts of interest.

Acknowledgments

This work was supported by the National Natural Science Foundation of China (61971362), Marine Defense Innovation Fund (JJ-2020-701-09), and the Natural Science Foundation of Fujian Province (No. 2020J01003).

References

- [1] H. Paik, N. Sastry, and I. SantiPrabha, "Effectiveness of noise jamming with white Gaussian noise and phase noise in amplitude comparison monopulse radar receivers," in *2014 IEEE International Conference on Electronics, Computing and Communication Technologies (CONECCT)*, pp. 1–5, Bangalore, India, 2014.
- [2] S. V. Uppala and J. D. Sahr, "Computing probability of errors of linear multiuser detectors in white Gaussian noise and Rayleigh fading channels," in *ICC '98. 1998 IEEE International Conference on Communications. Conference Record. Affiliated with SUPERCOMM'98 (Cat. No.98CH36220)*, vol. 1, pp. 360–364, Atlanta, GA, USA, 1998.
- [3] J. Kim, "3D path planner of an autonomous underwater vehicle to track an emitter using frequency and azimuth–elevation angle measurements," *IET Radar, Sonar & Navigation*, vol. 14, no. 8, pp. 1236–1243, 2020.
- [4] X. Zhang, J. Tang, F. Wang, S. Bai, and D. Liu, "Accurate back projection imaging algorithm for multi-receiver SAS in engineering application," *Journal of Naval University of Engineering*, vol. 26, no. 2, pp. 20–24, 2014.
- [5] C. Zhao, W. Zhu, G. Qiao, and F. Zhou, "Optimisation method with node selection and centroid algorithm in underwater received signal strength localisation," *IET Radar, Sonar & Navigation*, vol. 14, no. 11, pp. 1681–1689, 2020.
- [6] X. Zhang, J. Tang, and J. Ouyang, "Imaging processor for multi-receiver sas in the presence of partially failed receivers," *Applied Mechanics and Materials*, vol. 543-547, no. 2, pp. 2225–2228, 2014.
- [7] X. Zhang, W. Ying, and Y. Liu, "Processing multireceiver SAS data based on the PTRS linearization," in *2021 IEEE International Geoscience and Remote Sensing Symposium (IGARSS)*, pp. 5167–5170, Brussels, Belgium, 2021.
- [8] B. Zhu, D. Li, Z. Li, H. He, and X. Li, "Robust adaptive Kalman filter for strapdown inertial navigation system dynamic alignment," *IET Radar, Sonar & Navigation*, vol. 15, no. 12, pp. 1583–1593, 2021.
- [9] X. Zhang, P. Yang, and X. Dai, "Focusing multireceiver SAS data based on the fourth-order legendre expansion," *Circuits, Systems, and Signal Processing*, vol. 38, no. 6, pp. 2607–2629, 2019.
- [10] C. Wang, B. Wang, Z. Ding, and M. Fu, "A co-occurrence matrix-based matching area selection algorithm for underwater gravity-aided inertial navigation," *IET Radar, Sonar & Navigation*, vol. 15, no. 3, pp. 250–260, 2021.
- [11] C. Tan, X. Zhang, P. Yang, and M. Sun, "A novel sub-bottom profiler and signal processor," *Sensors*, vol. 19, no. 22, p. 5052, 2019.
- [12] H. Li, A. Jakobsson, D. Sun, and C. Zheng, "Underwater source localization in the presence of strong interference," *IET Radar, Sonar & Navigation*, vol. 15, no. 3, pp. 226–239, 2021.
- [13] X. Zhang, P. Yang, and M. Sun, "Experiment results of a novel sub-bottom profiler using synthetic aperture technique," *Current Science*, vol. 122, no. 4, pp. 461–464, 2022.
- [14] H. Son, "Smart tracking algorithm for multi-static sonar based on expectation maximisation," *IET Radar, Sonar & Navigation*, vol. 14, no. 10, pp. 1624–1630, 2020.
- [15] J. Kim, "Filter re-start strategy for angle-only tracking of a highly manoeuvrable target considering the target's destination information," *IET Radar, Sonar & Navigation*, vol. 14, no. 6, pp. 935–943, 2020.
- [16] G. Delyon, "Clutter map detector for active diver detection sonar," *IET Radar, Sonar & Navigation*, vol. 14, no. 1, pp. 177–186, 2020.
- [17] X. Zhang, H. Wu, H. Sun, and W. Ying, "Multireceiver sas imagery based on monostatic conversion," *IEEE Journal of Selected Topics in Applied Earth Observations and Remote Sensing*, vol. 14, pp. 10835–10853, 2021.
- [18] X. Zhang, X. Dai, and B. Yang, "Fast imaging algorithm for the multiple receiver synthetic aperture sonars," *IET Radar, Sonar & Navigation*, vol. 12, no. 11, pp. 1276–1284, 2018.
- [19] M. Rashed, M. Meijer, and P. Teal, "Performance of the matched filter in sonar systems having time variable gain," *IET Radar, Sonar & Navigation*, vol. 14, no. 3, pp. 425–430, 2020.
- [20] X. Zhang, J. Tang, H. Zhong, and S. Zhang, "Wavenumber-domain imaging algorithm for wide-beam multi-receiver synthetic aperture sonar," *Journal of Harbin Engineering University*, vol. 35, no. 1, pp. 93–101, 2014.
- [21] X. Zhang, C. Tan, and W. Ying, "An imaging algorithm for multireceiver synthetic aperture sonar," *Remote Sensing*, vol. 11, no. 6, p. 672, 2019.
- [22] J. Mei, Y. Pei, Y. Zakharov, D. Sun, and C. Ma, "Improved underwater acoustic imaging with non-uniform spatial resampling RL deconvolution," *IET Radar, Sonar & Navigation*, vol. 14, no. 11, pp. 1697–1707, 2020.
- [23] X. Zhang and P. Yang, "Imaging algorithm for multireceiver synthetic aperture sonar," *Journal of Electrical Engineering and Technology*, vol. 14, no. 1, pp. 471–478, 2019.
- [24] X. Zhang and P. Yang, "An improved imaging algorithm for multi-receiver sas system with wide-bandwidth signal," *Remote Sensing*, vol. 13, no. 24, p. 5008, 2021.
- [25] D. Gillis, "An underwater target detection framework for hyperspectral imagery," *IEEE Journal of Selected Topics in Applied Earth Observations and Remote Sensing*, vol. 13, pp. 1798–1810, 2020.
- [26] X. Zhang, P. Yang, P. Huang, H. Sun, and W. Ying, "Wide-bandwidth signal-based multireceiver SAS imagery using extended chirp scaling algorithm," *IET Radar, Sonar & Navigation*, vol. 16, no. 3, pp. 531–541, 2022.
- [27] Y. Xie, N. Bore, and J. Folkesson, "Inferring depth contours from sidescan sonar using convolutional neural nets," *IET Radar, Sonar & Navigation*, vol. 14, no. 2, pp. 328–334, 2020.
- [28] X. Zhang and W. Ying, "Influence of the element beam pattern on synthetic aperture sonar imaging," *Geomatics and Information Science of Wuhan University*, vol. 47, no. 1, pp. 133–140, 2022.
- [29] F. Jiang, Z. Zhao, H. Najafabadi, and Y. Yang, "Underwater TDOA/FDOA joint localisation method based on cross-

- ambiguity function," *IET Radar, Sonar & Navigation*, vol. 14, no. 8, pp. 1256–1266, 2020.
- [30] X. Zhang, X. Dai, and B. Fang, "An imaging Algorithm for multireceiver synthetic aperture sonar," *Geomatics and Information Science of Wuhan University*, vol. 11, no. 6, pp. 672–1673, 2019.
- [31] M. Rajan and A. Mohanty, "Time delay estimation using wavelet denoising maximum likelihood method for underwater reverberant environment," *IET Radar, Sonar & Navigation*, vol. 14, no. 8, pp. 1183–1191, 2020.
- [32] R. Naus and Y. Toh, "Time difference of arrival localisation exploiting all available time differences," *IET Radar, Sonar & Navigation*, vol. 14, no. 2, pp. 252–256, 2020.
- [33] A. Tollkuhn, F. Particke, and J. Thielecke, "Gaussian state estimation with non-gaussian measurement noise," in *2018 Sensor data fusion: trends, solutions, applications (SDF)*, pp. 1–5, Bonn, Germany, 2018.
- [34] M. Chunxia, S. Dan, C. Feng, Z. Xuegang, H. Jing, and B. Jin, "Statistical characteristic of spectrum for ambient noise at high frequencies in shallow water," in *2017 IEEE International Conference on Signal Processing, Communications and Computing (ICSPCC)*, pp. 1–4, Xiamen, China, 2017.
- [35] S. Kassam, *Signal Detection in Non-Gaussian Noise*, Springer Science & Business Media, 2012.
- [36] Y. Fangyuan, Q. Guo, and D. Li, "Performance of iterative ofdm receiver in doubly spread underwater acoustic communication channel," in *2014 12th International Conference on Signal Processing (ICSP)*, pp. 1579–1583, Hangzhou, China, 2014.
- [37] I. Prokopenko and N. Babanska, "Detection algorithm of non-Gaussian character of sample 1 distribution and its implementation in radar data processing," in *2015 Signal Processing Symposium (SPSymposium)*, pp. 1–4, Debe, Poland, 2015.
- [38] X. Zhang, W. Ying, P. Yang, and M. Sun, "Parameter estimation of underwater impulsive noise with the class B model," *IET Radar, Sonar & Navigation*, vol. 14, no. 7, pp. 1055–1060, 2020.
- [39] X. Zhang, W. Ying, and B. Yang, "Parameter estimation for class a modeled ocean ambient noise," *Journal of Engineering and Technological Sciences*, vol. 50, no. 3, pp. 330–345, 2018.
- [40] X. Zhang, C. Tan, and W. Ying, "Characteristic function based parameter estimation for ocean ambient noise," in *2018 IEEE 3rd International Conference on Image, Vision and Computing (ICIVC)*, pp. 817–820, Chongqing, China, 2018.
- [41] S. Banerjee and M. Agrawal, "Underwater acoustic communication in the presence of heavytailed impulsive noise with bi-parameter cauchyGaussian mixture model," in *2013 Ocean Electronics (SYMPOL)*, pp. 1–7, Kochi, India, 2013.
- [42] N. Guney, H. Delic, and M. Koca, "Robust detection of ultrawideband signals in non-Gaussian noise," *IEEE Transactions on Microwave Theory and Techniques*, vol. 54, no. 4, pp. 1724–1730, 2006.
- [43] G. Guo, M. Mandal, and Y. Jing, "A robust detector of known signal in non-Gaussian noise using threshold systems," *Signal Processing*, vol. 92, no. 11, pp. 2676–2688, 2012.
- [44] F. Duan, F. Chapeau-Blondeau, and D. Abbott, "Non-Gaussian noise benefits for coherent detection of narrowband weak signal," *Physics Letters A*, vol. 378, no. 26–27, pp. 1820–1824, 2014.
- [45] V. Hari, G. Anand, A. Premkumar, and A. Madhukumar, "Design and performance analysis of a signal detector based on suprathreshold stochastic resonance," *Signal Processing*, vol. 92, no. 7, pp. 1745–1757, 2012.
- [46] D. Rousseau, G. Anand, and F. Chapeau-Blondeau, "Noise-enhanced nonlinear detector to improve signal detection in non-Gaussian noise," *Signal Processing*, vol. 86, no. 11, pp. 3456–3465, 2006.
- [47] S. Yang, Y. Yang, and Y. Ma, "Investigation of the horizontal directivity of underwater ambient noise with the circular hydrophone array," *The Journal of the Acoustical Society of America*, vol. 131, no. 4, pp. 3484–3484, 2012.
- [48] P. Akimov, P. Bakut, and V. Bogdanovich, *Theory of Signal Detection*, vol. 440, Radio i svyaz, Moscow, 1984.
- [49] W. Ying, P. Yang, C. Li, and J. Liu, "A comparison between two parameter estimation methods for non-Gaussian noise models," in *2020 IEEE 5th International Conference on Signal and Image Processing (ICSIP)*, pp. 623–627, Nanjing, China, 2020.
- [50] T. Farjam, T. Charalambous, and H. Wymeersch, "Timer-based distributed channel access in networked control systems over known and unknown Gilbert-Elliott channels," in *2019 18th European Control Conference (ECC)*, pp. 2983–2989, Naples, Italy, 2019.
- [51] D.-F. Tseng and S.-S. Lin, "Robust low density parity check decoding over markov gaussian channels," in *2019 IEEE 89th Vehicular Technology Conference (VTC2019-Spring)*, pp. 1–5, Kuala Lumpur, Malaysia, 2019.
- [52] D.-F. Tseng, F. G. Mengistu, Y. S. Han, M. Abera Mulatu, L.-C. Chang, and T.-R. Tsai, "Robust turbo decoding in a Markov Gaussian channel," *IEEE Wireless Communications Letters*, vol. 3, no. 6, pp. 633–636, 2014.
- [53] S.-M. Tseng, W.-C. Hsu, and D.-F. Tseng, "Deep learning based decoding for polar codes in Markov Gaussian memory impulse noise channels," *Wireless Personal Communications*, vol. 122, no. 1, pp. 737–753, 2022.
- [54] A. Mahmood and M. Chitre, "Viterbi detection of psk signals in markov impulsive noise," in *2018 OCEANS - MTS/IEEE Kobe Techno-Oceans (OTO)*, pp. 1–6, Kobe, Japan, 2018.
- [55] X. Xia, X. Zhang, and X. Chen, "Parameter estimation for gaussian mixture processes based on expectation-maximization method," in *2016 4th International Conference on Machinery, Materials and Information Technology Applications*, 2016.
- [56] S. Banerjee and M. Agrawal, "On the performance of underwater communication system in noise with Gaussian mixture statistics," in *2014 Twentieth National Conference on Communications (NCC)*, Kanpur, India, 2014.
- [57] K. Pelekanakis and M. Chitre, "Adaptive sparse channel estimation under symmetric alpha-stable noise," *IEEE Transactions on Wireless Communications*, vol. 13, no. 6, pp. 3183–3195, 2014.
- [58] D. Middleton, *An Introduction to Statistical Communication Theory*, vol. 960, McGraw-Hill New York, 1960.
- [59] J. Wang, J. Li, S. Yan et al., "A novel underwater acoustic signal denoising algorithm for Gaussian/non-Gaussian impulsive noise," *IEEE Transactions on Vehicular Technology*, vol. 70, no. 1, pp. 429–445, 2021.
- [60] H. Kusao, "Optimum coherent receiver for impulsive rf noise," *Transactions of IEICE Japan*, vol. 68, no. 6, 1985.
- [61] S. Mishra and R. R. Tripathi, "Vdhl implementation of Viterbi algorithm for decoding of convolutional code," in *2015 International Conference on Computational Intelligence and Communication Networks (CICN)*, pp. 1367–1370, Jabalpur, India, 2015.
- [62] Y. Nakano, D. Umehara, M. Kawai, and Y. Morihiro, "Viterbi decoding for convolutional code over class a noise channel," in *Proceedings of the 7th International Symposium on Power-Line Communications and Its Applications*, pp. 97–102, Kyoto, Japan, 2003.

Research Article

Data-Driven Signal Detection for Underwater Acoustic Filter Bank Multicarrier Communications

Yunan Zhu , Biao Wang , Fangtong Xie , Chengxi Wu , and Peng Chao 

Ocean College, Jiangsu University of Science and Technology, Zhenjiang 212100, China

Correspondence should be addressed to Biao Wang; wangbiao@just.edu.cn

Received 12 September 2021; Revised 14 October 2021; Accepted 20 April 2022; Published 16 May 2022

Academic Editor: Alessandro Bazzi

Copyright © 2022 Yunan Zhu et al. This is an open access article distributed under the Creative Commons Attribution License, which permits unrestricted use, distribution, and reproduction in any medium, provided the original work is properly cited.

By contraposing the signal detection for filter bank multicarrier (FBMC) communications with the underwater acoustic (UWA) channel, this paper analyzes the traditional imaginary interference problem and proposes a deep learning-based method. The neural network with feature extraction and automatic learning ability is employed to replace the demodulation modules to recover transmitted signals without explicit channel estimation and equalization. Sufficient data sets are generated according to the measured channel conditions in Qingjiang river, the optimization of network parameters is finished by constraining cost function in offline training, and the signal detection is carried out directly with the well-trained network in online testing. The system performance of various supervised learning models such as multilayer perceptron (MLP), convolutional neural network (CNN), and bidirectional long short-term memory (BLSTM) network is compared under different data sizes, network parameters, and prototype filters. The simulation results show that the bit error rate (BER) performance of the proposed signal detection is better than that of the classic one, which indicates that deep learning is a promising tool in UWA communication systems.

1. Introduction

Compared with other transmission media, UWA channel is much more complicated due to strict bandwidth limitation, Doppler frequency shift, and background noise. Orthogonal frequency division multiplexing (OFDM) is currently an effective method to realize high-rate UWA communication due to its ability to handle long multipath broadening and frequency selectivity [1–4]. However, the orthogonality of the subcarriers in OFDM system is easily affected by Doppler effect, which will cause difficulties in channel estimation and signal detection [5–7].

As a new force in 5G multicarrier modulation, FBMC introduces filter bank in OFDM to ensure the independence between subchannels without cyclic prefix that provides protection interval, which greatly improves the spectrum efficiency. The prototype filter bank has excellent time-frequency (TF) focusing characteristics to make FBMC more robust against both ISI and ICI [8–10]. The subcarriers of

FBMC only meet the orthogonality in the real domain, resulting in the inherent imaginary interference between adjacent subcarriers and symbols. Furthermore, the classical signal processing method cannot be directly used, which makes the signal detection of FBMC system more challenging. Researchers have proposed many signal detection approaches based on pilot to counter imaginary interference including interference approximation method [11, 12] and interference cancellation method [13–15], so as to maximize the symbol amplitude at the pilot after demodulation. The interference approximation method is designed to calculate the value of the neighborhood symbol interference, and the interference cancellation method makes full use of the odd symmetry of the filter fuzzy function, but the performance of these systems still depends on the accuracy of channel estimation and the pilot overhead is high.

Recently, deep learning has sprung up in speech processing [16], real-time vision [17], and other engineering fields. The concept of applying deep learning to wireless communi-

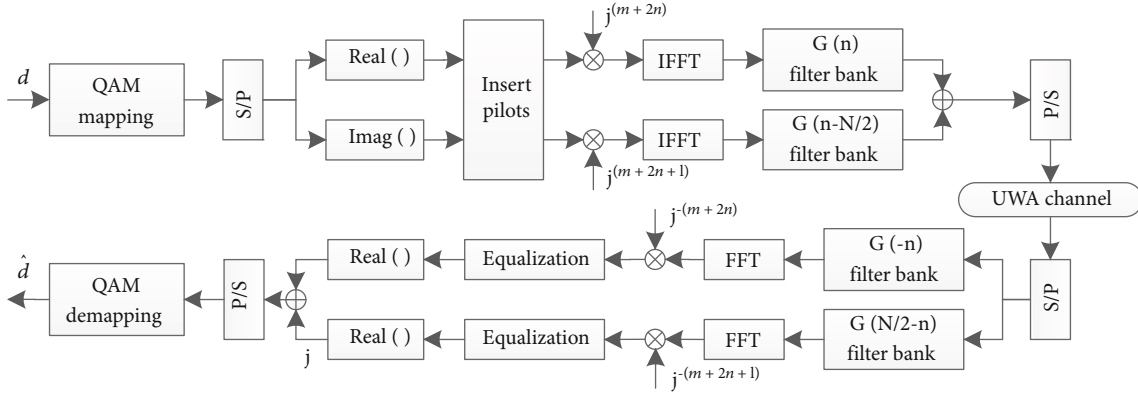


FIGURE 1: Block diagram of an equivalent UWA FBMC system. The SFB in transmitter includes phase transformation, M/2 upsampling, prototype filter forming, subcarrier modulation, and stack. The AFB in the receiver includes subcarrier demodulation, matched filtering, M/2 downsampling, and phase demodulation.

cation systems, especially UWA communication systems, has just begun to emerge in public. According to [18], a symbol demodulation and detection model based on twice training network is proposed whose performance is far better than that of the maximum likelihood algorithm. According to [19], a linear channel coding and decoding algorithm based on deep neural network has been proved to be superior to the classical belief propagation algorithm. MLP is the most basic deep learning model, which consists of multiple fully connected neural layers [20]. Ye et al. introduce MLP into the receiver of OFDM system for channel estimation and signal detection and reveal that deep learning method can obtain the analogous BER performance compared with the traditional OFDM system [21]. Inspired by the above, Zhang et al. propose a deep learning-based OFDM communication system and analyze the robustness under the UWA channel [22]. Qasem et al. propose a new scheme called deep learning-coded index modulation-spread spectrum to deal with the increasing data rate restriction of limited user number [23].

Stimulated by the potential of neural network in the UWA communication field, this paper proposes a deep learning-based receiver for FBMC system. By regarding FBMC signal detection as label prediction of neural networks, several supervised learning models such as feedforward MLP, CNN [24], and BLSTM [25, 26] have been adopted to realize implicit channel estimation and equalization. The performance of the proposed method is quantitatively analyzed with sufficient amount of transmitted data which is simulated by the channel impulse response (CIR) measured in Qingjiang river. Simulation results demonstrate that compared to classical channel estimation methods such as least square (LS), the signal detection method based on deep learning is more effective in improving the BER performance of UWA FBMC communication.

The rest of this paper is organized as follows. In Section 2, the model of FBMC and the problem of imaginary interference are introduced. In Section 3, several supervised learning models are reviewed, and then, the deep learning-based signal detection for UWA FBMC systems is presented.

In Section 4, the system performance analysis and comparison are provided. The conclusions are made in Section 5.

Notations: $(\cdot)_{m,n}$ denotes the (m, n) th TF point. $\Re\{\cdot\}$ denotes the real part of complex number. $(\cdot)^*$ denotes the conjugate. $*$ denotes the convolution. \circ denotes the Hadamard product.

2. System Model and Problem Formulation

2.1. UWA FBMC System Model. Different from OFDM, the transmitted symbol of FBMC system is offset quadrature amplitude modulation (QAM) symbol; namely, the real and imaginary parts of complex QAM symbols are extracted, respectively, and then sent after misplacing half symbol period. Figure 1 shows the block diagram of FBMC system implemented by filter bank and IFFT. The output of the transmitted symbol through the synthesis filter bank (SFB) can be expressed as [27]

$$s(l) = \sum_{m=0}^{M-1} \sum_n a_{m,n} \underbrace{g\left(l - n \frac{M}{2}\right) e^{j2\pi ml/M} e^{j\varphi_{m,n}}}_{g_{m,n}(l)}, \quad (1)$$

where M is the subcarrier number, $a_{m,n}$ is real data on the m th subcarrier of the n th FBMC symbol, and phase factor $\varphi_{m,n}$ is set to $(\pi/2)(m+n)$. $g(l)$ denotes the prototype filter with length $L_g = KM$, where K denotes the overlap factor. $g_{m,n}(l)$ represents the synthesis basis obtained from the TF transformation of $g(l)$. After channel and analysis filter bank (AFB), the demodulation symbol at TF point (p, q) is

$$y_{p,q} = \sum_{m=0}^{M-1} \sum_n a_{m,n} \sum_l g_{m,n}(l) g_{p,q}^*(l), \quad (2)$$

where the orthogonal condition of $g(l)$ for perfect signal reconstruction satisfies $\Re\{\sum_l g_{m,n}(l) g_{p,q}^*(l)\} = \delta_{m,p} \delta_{n,q}$. $\delta_{m,p}$ denotes the Kronecker delta function which equals 1 if

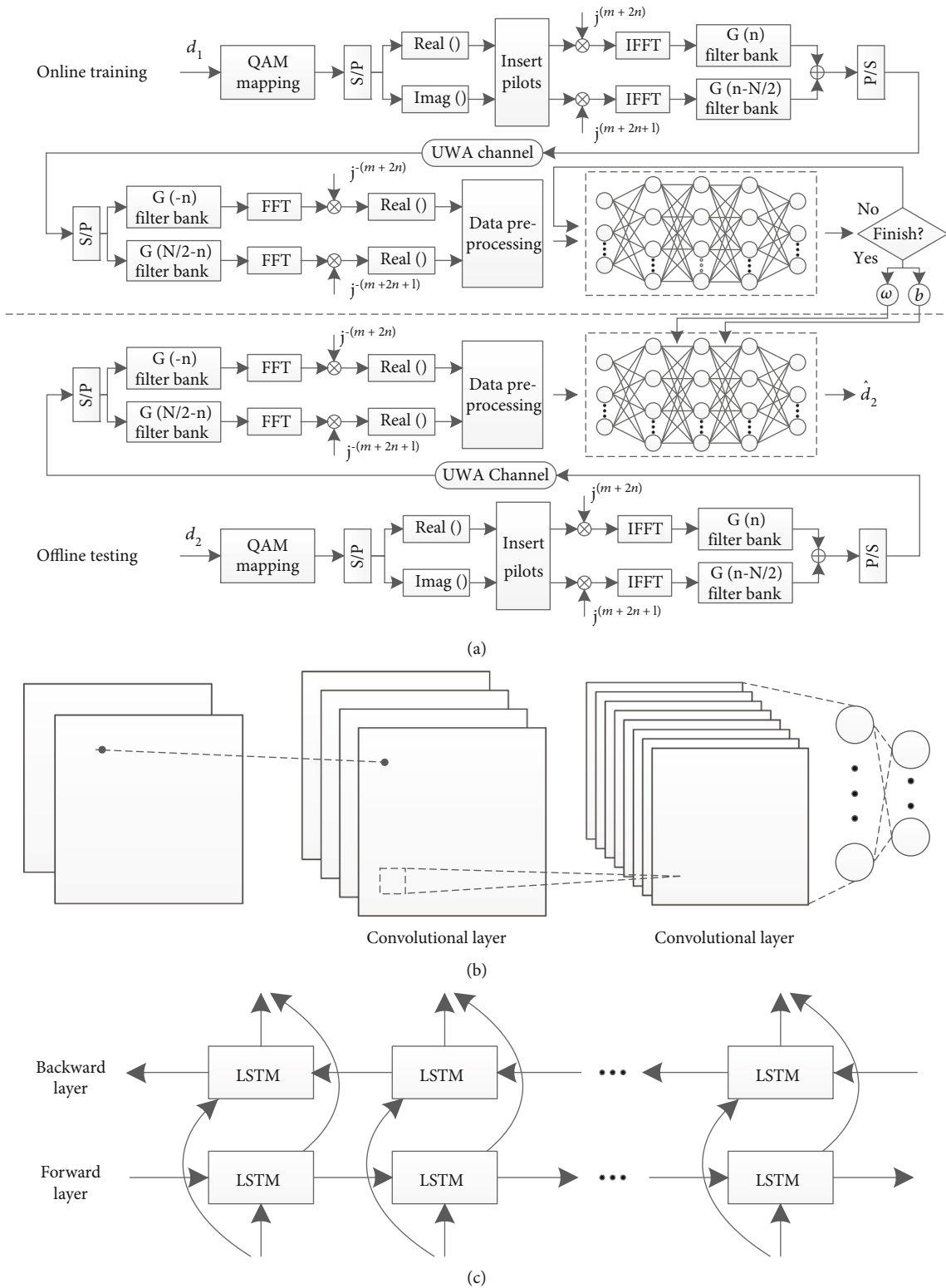


FIGURE 2: (a) Block diagram of deep learning-based UWA FBMC system, in which the structure of MLP is shown in the dotted line box. (b) The structure of CNN. (c) The structure of BLSTM consists of 2 LSTM layers.

$m = p$ and equals 0 if $m \neq p$. Thus, the transmitted symbol can be accurately recovered at FBMC receiver after taking the real part of the demodulated symbol.

2.2. *The Problem of Imaginary Interference.* It is worth noting that FBMC systems satisfy orthogonality only in the real field, which implies that even under ideal channel

conditions, there will be inherent imaginary interference $\zeta_{m,n}^{p,q} = \sum_l g_{m,n}(l)g_{p,q}^*(l)$ in the AFB if any $(m, n) \neq (p, q)$. The distribution of $\zeta_{m,n}^{p,q}$ varies according to the filter bank employed.

We assume that the channel is frequency flat and unchanged over the duration of the prototype filter, so the output of the AFB at (p, q) can be shown as [12]

$$y_{p,q} = H_{p,q}a_{p,q} + \underbrace{j \sum_{(m,n) \neq (p,q)} H_{m,n}a_{m,n}\zeta_{m,n}^{p,q}}_{I_{p,q}} + \eta_{p,q}, \quad (3)$$

where $H_{p,q}$ is the channel frequency response and $I_{p,q}$ and $\eta_{p,q}$ denote the imaginary interference and noise component. Considering that imaginary interference mainly comes from adjacent TF points, the first-order neighborhood of (p, q) is defined as $\Omega_{p,q} = \{(p \pm 1, q \pm 1), (p, q \pm 1), (p \pm 1, q)\}$, where $H_{p,q} \approx H_{m,n}$. Then, Equation (3) can be further expressed as

$$y_{p,q} = H_{p,q} \underbrace{\left(a_{p,q} + j \sum_{(m,n) \in \Omega_{p,q}} a_{m,n} \zeta_{m,n}^{p,q} \right)}_{c_{p,q}} + \eta_{p,q}, \quad (4)$$

where $c_{p,q}$ is the symbol virtually transmitted. When data at (p, q) and $\Omega_{p,q}$ are known, $c_{p,q}$ can be treated as a pseudopilot to estimate channel frequency response by the LS principle, as $\hat{H}_{p,q} = y_{p,q}/c_{p,q} \approx H_{p,q} + \eta_{p,q}/c_{p,q}$.

3. Supervised Learning Models and Deep Learning-Based Signal Detection

3.1. Multilayer Perceptron. As shown in the dashed box in Figure 2(a), a MLP can be summarized as an artificial neural network with multiple hidden layers between input and output layers [28]. The output of the j th neuron in the i th layer can be expressed as

$$z_j^i = f \left(\sum_k \omega_{jk}^i z_k^{i-1} + b_j^i \right), \quad (5)$$

where ω_{jk}^i is the weight between the j th neuron in the i th layer and the k th neuron in the $(i-1)$ th layer, b_j^i is the bias of the j th neuron in the i th layer, and $f(\cdot)$ is the selected activation function of this layer. $f_{\text{leakyReLU}}(x) = \max(\alpha x, x)$, $\alpha = 0.05$, an improved ReLU function, is employed for the hidden layers, and the output layer applies the function $f_{\text{sigmoid}}(x) = 1/(1 + e^{-x})$ to make the network output in the interval $(0, 1)$. In addition, each hidden layer adopts dropout regularization to prevent the network from favoring certain features with iterative training, so as to guarantee the generalization ability of the system.

3.2. Convolutional Neural Network. The CNN in Figure 2(b) uses shared convolution kernels to automatically extract local spatial correlation features of input data

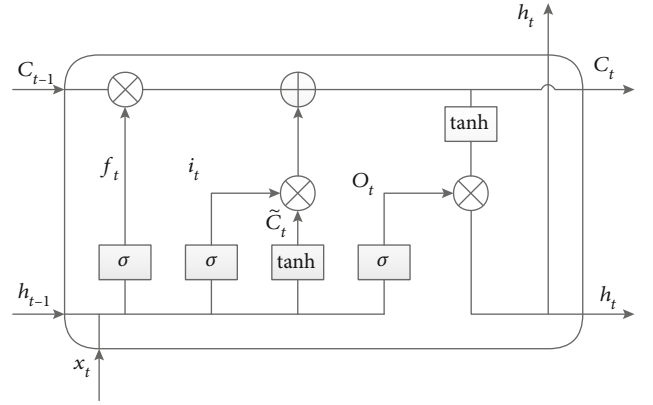


FIGURE 3: The inner structure of LSTM neurons.

[29]. The weight sharing method greatly reduces the number of parameters and makes the whole training process easier. The output of the i th convolutional layer can be expressed as [30]

$$Z^i = f \left(W^i * Z^{i-1}(p, q) + b^i \right) = f \left(\sum_m \sum_n Z^{i-1}(p-m, q-n) W^i(m, n) + b^i \right), \quad (6)$$

where W^i is the convolution kernel with adjustable weights of the i th layer, b^i is the bias, and $W^i * Z^{i-1}(p, q)$ represents the result of two-dimensional convolution. Batch normalization, an efficient regularization method with faster convergence speed, is adopted in the convolutional layer to prevent gradient disappearance and overfitting. Pooling layer is not taken in this article because the input tensor is not large. The whole convolution process can be regarded as a special feature extraction, in which the feature data is output through a few fully connected layers after flattening.

3.3. Bidirectional Long Short-Term Memory. Recurrent neural network is a kind of recursive neural network which characterizes the time correlation of input sequence. As shown in Figure 3, LSTM introduces gate mechanism and storage units to neurons to address the long-term dependence challenge of sequences. At time t , the input gate, forget gate, output gate, LSTM input, LSTM output, cell state, and the candidate are, respectively, represented as i_t , f_t , o_t , x_t , h_t , C_t , and \tilde{C}_t ; the operational processes are as follows [31]:

$$\begin{aligned} i_t &= f_{\text{sigmoid}}(W_{ix}x_t + W_{ih}h_{t-1} + b_i), \\ f_t &= f_{\text{sigmoid}}(W_{fx}x_t + W_{fh}h_{t-1} + b_f), \\ \tilde{C}_t &= f_{\text{tanh}}(W_{cx}x_t + W_{ch}h_{t-1} + b_c), \\ C_t &= i_t \circ \tilde{C}_t + f_t \circ C_{t-1}, \\ o_t &= f_{\text{sigmoid}}(W_{ox}x_t + W_{oh}h_{t-1} + b_o), \\ h_t &= o_t \circ f_{\text{tanh}}(C_t), \end{aligned} \quad (7)$$

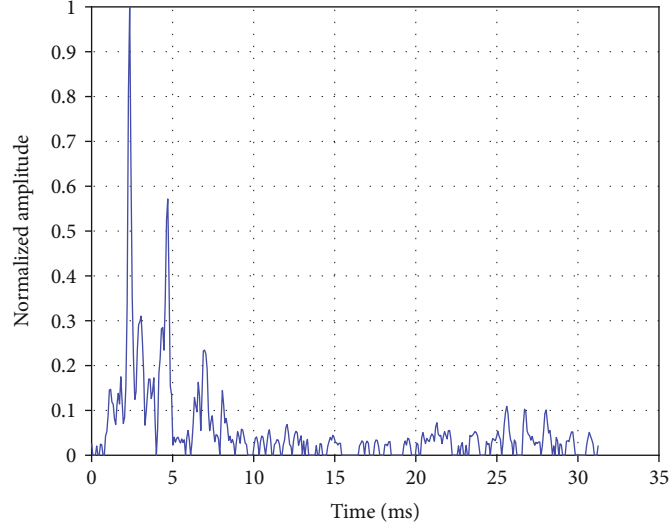


FIGURE 4: Channel impulse response of Qingjiang river measured by LFM signal at a certain moment.

where W and b represent weights and biases, C_{t-1} is the state of the cell at the previous moment, and $f_{\tanh}(x) = (e^x - e^{-x}) / (e^x + e^{-x})$ is also an activation function. Figure 2(c) shows that a BLSTM layer consists of two LSTM layers stacked in opposite directions, whose output is calculated jointly through two layers of hidden state by

$$Z_t = f\left(W_{Zh} \vec{h}_t + W_{Zh} \overleftarrow{h}_t + b_Z\right), \quad (8)$$

where \vec{h}_t is the forward sequence and \overleftarrow{h}_t is the backward sequence. So the final prediction depends not only on the past input but also on the future input.

3.4. Neural Network-Driven UWA FBMC Systems. Figure 2 shows the structure of the deep learning-based UWA FBMC system, in which the neural network models replace the channel estimation, equalization, and demapping modules at the receiver of the traditional system, while the transmitter remains unchanged. In each simulation, the frequency domain data received after FFT and the random binary sequence transmitted are recorded as a set of input and corresponding label d . The models are trained by viewing FBMC demodulation and UWA channels as black boxes [21]. With the network iteration, the weights W (or ω) and biases b of the neural network are adjusted, and the difference between output \hat{d} and label d is continuously reduced.

In this paper, we take signal detection as binary label classification and adopt crossentropy (CE) cost function to measure the difference

$$CE = -\frac{1}{N} \sum_{k=1}^N \left[d(k) \ln \hat{d}(k) + (1 - d(k)) \ln (1 - \hat{d}(k)) \right], \quad (9)$$

where N represents the number of neurons in the output layer. When the cost function meets the preset threshold condition or the network iteration reaches the maximum



FIGURE 5: Layout of Qingjiang river experiment.

epoch limit, the neural network finishes the training process, and W (or ω) and b stop updating and are saved accordingly. The online neural network directly outputs the predicted binary sequence after loading the new received frequency domain signal.

4. System Performance

4.1. Simulation Configuration. In order to carry out offline training more realistically and effectively, we use the measured underwater acoustic channel of Qingjiang river (as shown in Figure 4) to generate enough communication data. Figure 5 depicts the layout of this experiment. The river depth at the experimental site is about 100 m, the hanging depth of the transmitting transducer is about 30 m, and the hanging depth of the receiving hydrophone is about 10 m. During the experiment, both the sending ship and the receiving ship are in a free-drifting state, with a distance of about 1.5 km.

TABLE 1: Parameter setting of deep learning models.

		MLP	CNN	BLSTM
Hyperparameter	Learning rate		10^{-4}	
	Optimizer		Adam	
	Dropout rate		0.5	
	Minibatch size		1000	
	Input tensor	(None, 2048)	(None, 32, 32, 2)	(None, 2, 1024)
Network structure	Fully connected layers	5	2	1
	Convolutional layers	—	2	—
	LSTM layers	—	—	2

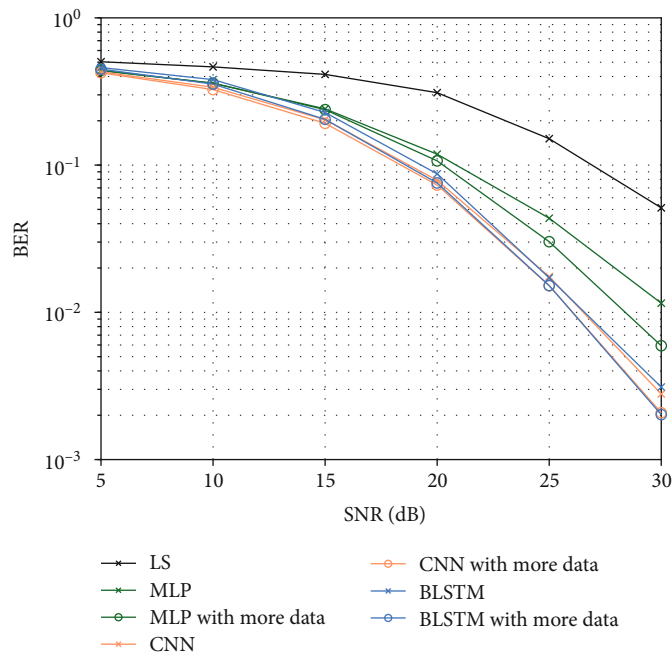


FIGURE 6: BER performance comparison among various signal detection methods.

The input number depends on the number of real and imaginary parts of 2 FBMC blocks with 512 subcarriers. The networks involved in this paper extract features from the amplitude, space, and time dimensions, respectively, whose input tensor, selection of the network layer, and settings of hyperparameter are shown in Table 1. A rate $R_c = 1/2$ convolutional coder with generator polynomial [5, 7] in octal format and 4-QAM is considered. The PHYDYAS filter [32] is adopted as prototype filter, and a total of 50000 sets of obtained communication data are divided into training set and test set by 9:1.

4.2. BER versus the Data Size. Several supervised learning models are first compared with LS method for signal detection in Figure 6, where the LS method performs the worst because the accuracy of channel estimation is easily affected by imaginary interference. The MLP method (the number of neurons in each layer is 2048, 512, 128, 32, and 16) significantly improves BER performance through data-driven implicit channel estimation. In addition, CNN (the number

of channels in each kernel is 4 and 8) and BLSTM methods further explore the spatial correlation and temporal correlation among the input data, respectively, which perform state-of-the-art signal detection.

We also double the communication data and maintain the original proportion to explore the impact of data size on the proposed system. The MLP method seems to achieve greater gain than CNN and BLSTM do due to the more space for learning caused by the amplitude feature extraction only, but the latter two still have better BER performance when more data is provided. The results indicate that the characteristics of UWA channel are efficiently learned by deep learning-based methods and the BER performance is sensitive to the data size.

4.3. BER versus the Network Parameters. The accuracy of deep learning-based signal detection mainly depends on the complexity of its model. According to the structural characteristics of different networks, the network parameters such as hidden layer neurons of MLP, channels in the

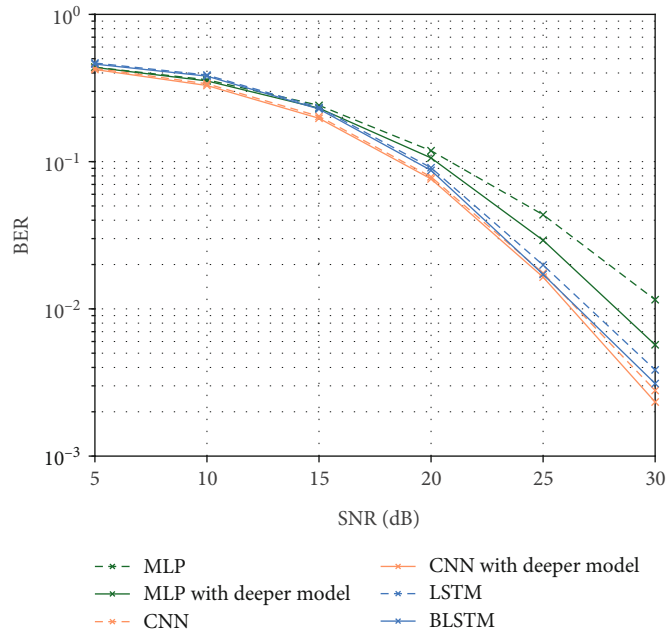


FIGURE 7: BER performance comparison with various network parameters.

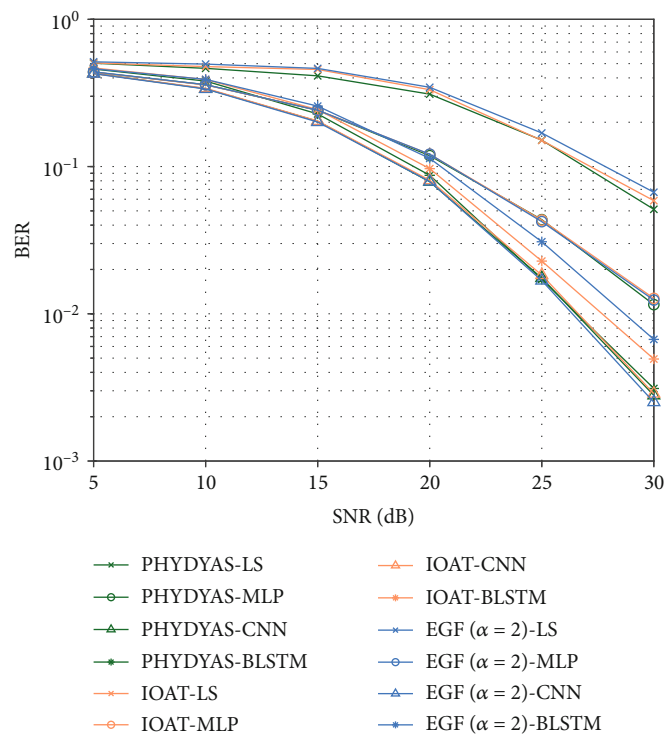


FIGURE 8: BER performance comparison with various prototype filters.

convolution kernel of CNN, and direction of propagation of LSTM are regulated to make them deeper. The number of neurons in MLP is reset to 2048, 1024, 512, 64, and 16; the number of kernel channels in CNN is reset to 8 and 16; and BLSTM is compared with unidirectional LSTM. From Figure 7, the BER performance of the deeper model is gener-

ally improved. It is noted that the gain of BLSTM indicates that the transmitted symbols in the future also have an impact on the current signal detection.

4.4. BER versus the Prototype Filter. Wondering how the BER performance of the deep learning-based signal detection and

LS-based signal detection is affected by the selection of prototype filter, we add EGF ($\alpha = 2$) and IOAT filters in simulation. For fair comparison, the settings of UWA communication system and network parameters remain fixed. As depicted in Figure 8, MLP and CNN methods own more stable performance and better robustness than LS algorithm under different communication scenarios, but the BLSTM method presents an obvious performance difference. That is, BLSTM is sensitive to the degree of matching between filter banks and underwater acoustic channels.

5. Conclusion

This paper presents a deep learning-based FBMC signal detection for UWA communications, which only need to collect received symbols for implicit channel estimation and equalization in a data-driven way. Furthermore, CNN with spatial correlation and BLSTM with temporal correlation are analyzed for deeper feature extraction. The proposed receiver has been tested with CIR measured in Qingjiang river at a range of 1.5 km. Results of comparison show that the proposed methods outperform classical algorithms in detection accuracy, which leads a flexible design for future UWA communications.

Data Availability

The data used to support the findings of this study are available from the corresponding author upon request.

Conflicts of Interest

The authors declare that there is no conflict of interest regarding the publication of this paper.

Acknowledgments

This research was supported in part by the National Natural Science Foundation of China under Grant 52071164 and in part by the Postgraduate Research & Practice Innovation Program of Jiangsu Province under Grant KYCX20_3161.

References

- [1] A. Radosevic, R. Ahmed, T. M. Duman, J. G. Proakis, and M. Stojanovic, "Adaptive OFDM modulation for underwater acoustic communications: design considerations and experimental results," *IEEE Journal of Oceanic Engineering*, vol. 39, no. 2, pp. 357–370, 2014.
- [2] D. Jiang and H. Esmaili, "Zero-pseudorandom noise training OFDM," *Electronics Letters*, vol. 50, no. 9, pp. 650–652, 2014.
- [3] Z. A. H. Qasem, J. Wang, X. Kuai, H. Sun, and H. Esmaili, "Enabling unique word OFDM for underwater acoustic communication," *IEEE Wireless Communications Letters*, vol. 10, no. 9, pp. 1886–1889, 2021.
- [4] Z. A. H. Qasem, H. A. Leftah, H. Sun, J. Qi, and H. Esmaili, "X-transform time-domain synchronous IM-OFDM-SS for underwater acoustic communication," *IEEE Systems Journal*, pp. 1–12, 2021.
- [5] Z. Wang, S. Zhou, J. C. Preisig, K. R. Pattipati, and P. Willett, "Clustered adaptation for estimation of time-varying underwater acoustic channels," *IEEE Transactions on Signal Processing*, vol. 60, no. 6, pp. 3079–3091, 2012.
- [6] Y. H. Zhou, F. Tong, and G. Q. Zhang, "Distributed compressed sensing estimation of underwater acoustic OFDM channel," *Applied Acoustics*, vol. 117, pp. 160–166, 2017.
- [7] N. U. R. Junejo, H. Esmaili, M. Zhou, H. Sun, J. Qi, and J. Wang, "Sparse channel estimation of underwater TDS-OFDM system using look-ahead backtracking orthogonal matching pursuit," *IEEE Access*, vol. 6, pp. 74389–74399, 2018.
- [8] Q. He and A. Schmeink, "Comparison and evaluation between FBMC and OFDM systems," *19th International ITG Workshop on Smart Antennas (WSA)*, pp. 1–7, 2015.
- [9] N. Junejo, J. Yan, S. Adnan, H. Chen, and H. Sun, "Channel estimation using pilot method for underwater filter bank multicarrier system," *International Conference in Communications, Signal Processing, and Systems*, 2019.
- [10] H. Esmaili, Z. Qasem, H. Sun, J. Qi, J. Wang, and Y. Gu, "Wireless information and power transfer for underwater acoustic time-reversed NOMA," *IET Communications*, vol. 14, no. 19, pp. 3394–3403, 2020.
- [11] C. L  l  , J. P. Javaudin, R. Legouable, A. Skrzypczak, and P. Siohan, "Channel estimation methods for preamble-based OFDM/OQAM modulations," *European Transactions on Telecommunications*, vol. 19, no. 7, pp. 741–750, 2008.
- [12] E. Kofidis, D. Katselis, A. Rontogiannis, and S. Theodoridis, "Preamble-based channel estimation in OFDM/OQAM systems: a review," *Signal Processing*, vol. 93, no. 7, pp. 2038–2054, 2013.
- [13] W. Cui, D. Qu, T. Jiang, and B. Farhang-Boroujeny, "Coded auxiliary pilots for channel estimation in FBMC-OQAM systems," *IEEE Transactions on Vehicular Technology*, vol. 65, no. 5, pp. 2936–2946, 2016.
- [14] K. Chen-Hu, J. C. Estrada-Jim  nez, M. J. F. G. Garc  a, and A. G. Armada, "Continuous and burst pilot sequences for channel estimation in FBMC-OQAM," *IEEE Transactions on Vehicular Technology*, vol. 67, no. 10, pp. 9711–9720, 2018.
- [15] N. U. R. Junejo, H. Esmaili, H. Sun, Z. A. H. Qasem, and J. Wang, "Pilot-based adaptive channel estimation for underwater spatial modulation technologies," *Symmetry*, vol. 11, no. 5, pp. 711–728, 2019.
- [16] D. Wang and J. Chen, "Supervised speech separation based on deep learning: an overview," *IEEE/ACM Transactions on Audio, Speech, and Language Processing*, vol. 26, no. 10, pp. 1702–1726, 2018.
- [17] H. Li, X. Wang, F. Shen, Y. Li, F. Porikli, and M. Wang, "Real-time deep tracking via corrective domain adaptation," *IEEE Transactions on Circuits and Systems for Video Technology*, vol. 29, no. 9, pp. 2600–2612, 2019.
- [18] L. Fang and L. Wu, "Deep learning detection method for signal demodulation in short range multipath channel," *IEEE International Conference on Opto-electronic Information Processing*, pp. 16–20, 2017.
- [19] E. Nachmani, Y. Beery, and D. Burshtein, *Learning to decode linear codes using deep learning*, 2016.
- [20] Y. Lecun, Y. Bengio, and G. Hinton, "Deep learning," *Nature*, vol. 521, no. 7553, pp. 436–444, 2015.
- [21] H. Ye, G. Y. Li, and B. Juang, "Power of deep learning for channel estimation and signal detection in OFDM systems," *IEEE Wireless Communications Letters*, vol. 7, no. 1, pp. 114–117, 2018.

- [22] Y. Zhang, J. Li, Y. Zakharov, X. Li, and J. Li, "Deep learning based underwater acoustic OFDM communications," *Applied Acoustics*, vol. 154, pp. 53–58, 2019.
- [23] Z. Qasem, H. A. Leftah, H. Sun, J. Qi, J. Wang, and H. Esmail, "Deep learning-based code indexed modulation for autonomous underwater vehicles systems," *Vehicular Communications*, vol. 28, article 100314, 2021.
- [24] S. Lawrence, C. L. Giles, A. C. Tsoi, and A. D. Back, "Face recognition: a convolutional neural-network approach," *IEEE Transactions on Neural Networks*, vol. 8, no. 1, pp. 98–113, 1997.
- [25] S. Hochreiter and J. Schmidhuber, "Long short-term memory," *Neural Computation*, vol. 9, no. 8, pp. 1735–1780, 1997.
- [26] M. Schuster and K. K. Paliwal, "Bidirectional recurrent neural networks," *IEEE Transactions on Signal Processing*, vol. 45, no. 11, pp. 2673–2681, 1997.
- [27] P. Siohan, C. Siclet, and N. Lacaille, "Analysis and design of OFDM/OQAM systems based on filterbank theory," *IEEE Transactions on Signal Processing*, vol. 50, no. 5, pp. 1170–1183, 2002.
- [28] J. Deng, J. Sun, W. Peng, Y. Hu, and D. Zhang, "Application of neural networks for predicting hot-rolled strip crown," *Applied Soft Computing*, vol. 78, pp. 119–131, 2019.
- [29] Y. Zhu, B. Wang, Y. Zhang, J. Li, and C. Wu, "Convolutional neural network based filter bank multicarrier system for underwater acoustic communications," *Applied Acoustics*, vol. 177, no. 2, article 107920, 2021.
- [30] I. Goodfellow, Y. Bengio, and A. Courville, *Deep Learning*, MIT Press, 2016.
- [31] Y. Xie, R. Liang, H. Tao, Y. Zhu, and L. Zhao, "Convolutional bidirectional long short-term memory for deception detection with acoustic features," *IEEE Access*, vol. 6, pp. 76527–76534, 2018.
- [32] "Maurice Bellanger.: 'FBMC physical layer: a primer'," *PHY-DYAS EU FP7 Project*, 2010.

Research Article

Sea Experimental for Compressive Sensing-Based Sparse Channel Estimation of Underwater Acoustic TDS-OFDM System

Naveed Ur Rehman Junejo ^{1,2}, Hamada Esmail ^{1,3}, Mariyam Sattar ⁴, Haixin Sun ¹,
Muhammad Amir Khalil ² and Ihsan Ullah ²

¹Department of Information and Communication, School of Informatics, Xiamen University, Xiamen 316005, China

²Department of Computer Engineering, The University of Lahore, 1-KM Defence Road, Lahore, Pakistan

³Electrical Engineering Department, Faculty of Engineering, Aswan University, Aswan 81542, Egypt

⁴Department of Mechanical Engineering, Institute of Space Technology, Islamabad, Pakistan

Correspondence should be addressed to Hamada Esmail; h.esmail@aswu.edu.eg

Received 20 January 2022; Revised 24 March 2022; Accepted 7 April 2022; Published 5 May 2022

Academic Editor: Miaowen Wen

Copyright © 2022 Naveed Ur Rehman Junejo et al. This is an open access article distributed under the Creative Commons Attribution License, which permits unrestricted use, distribution, and reproduction in any medium, provided the original work is properly cited.

Due to the high spectral efficiency (SE) and fast synchronization, the time-domain synchronization orthogonal frequency division multiplexing (TDS-OFDM) system has gotten much more attraction of researchers as compared to cyclic-prefix (CP) and zero padding (ZP) OFDM in terrestrial as well as underwater acoustic communication. Inter-block interference (IBI) degrades the TDS-OFDM performance due to its long-delay multiple channels. In TDS-OFDM, dual pseudo-random noise (DPN) sequences utilize two PN sequences as a guard interval (GI) after every data block to cope with interference from the OFDM data block to the next PN sequence resulting in compromising the energy efficiency (EE) and spectral efficiency. We have proposed compressed sensing-based technique compressive sensing matching pursuit (CoSaMP), orthogonal matching pursuit (OMP), and look-ahead and backtracking OMP (LABOMP) for TDS-OFDM over the real-time underwater channel in this paper. Moreover, prior to estimating the channel, the received PN sequence is considered in the time domain to compensate for the Doppler shift of the UWA channel. The real-time data experiment has been initially conducted for testing in a water tank in our laboratory. Furthermore, it has been tested on the sea for long communications under the water at the Wuyuan sea area in Xiamen, China. Simulations and experimental results evident that the compressed sensing techniques have better performance over the conventional TDS-OFDM and DPN-TDS-OFDM, even LABOMP outperform OMP and CoSaMP in terms of bit-error-rate (BER), SE, and EE.

1. Introduction

The water has covered the major area of Earth's surface; nearly 71% of the earth is water covered. Such water is split into various principles such as small-scale seas, oceans, and rivers. Ocean tenderness commands the wind originals and the environment changes that make different lifestyles on top of the earth's surface. Lakes and rivers include no more than 1% of freshwater over the earth's surface. Its disease seriously harms ecosystems. The internet of underwater things (IoUT), the control of enormous areas of uncharted water [1]. The purpose of this study proposal is to propose a green underwater multicarrier modulation technique.

The full design supporting the accepted data rate with reliable communication IoUT nodes has been considered among one of the most challenging underwater communication problems due to the weak spread of electromagnetic waves in the water and the low data rate future in the case of acoustic waves propagation [2]. Recently, magnetic induction was proposed for underground and underwater data transmission, but unfortunately, ocean conductivity makes harsh attenuation for both the magnetic induction and electromagnetic signals. To prevail over that kind of attenuation problem, ultra-low frequency bands with very low data transmission rates should be used. With a high potential data rate, optical data transmission has been proposed for

underwater data transmission. Unfortunately, optical-based underwater communication systems suffer from modeling the chemical and physical traits of the water. Due to all the above, the acoustic-based underwater communication system is considered the broadest technology [3]. Research on underwater communication was mainly focused on increasing data rate over the limited acoustic bandwidth and solving acoustic-based problems such as high ambient noise, Doppler shift, and propagation delay [4].

The designing acoustic-based communication system should consider the natural features of the ocean media. Such features such as high attenuation power and such attenuation restrict and limit the communication distance. Plus, the transmitter and receiver motion due to water waves increase the Doppler Effect. Also, due to the variations in geography, underwater communication considers environmental-based communication and provides a non-uniformly fluctuated acoustic propagation [5]. To obtain reliable acoustic-based underwater communication researchers and industry go-to multicarrier modulation. Thanks to the multicarrier modulation, the data rate can be increased even over limited channel bandwidth such as acoustic-based underwater channels. Also mitigates the Doppler shift and unwanted inter symbol interference (ISI). Another advantage point of the multicarrier modulation technique is the easy equalization [6, 7]. The multicarrier technique is a reserve to defeat the long-time interval which creates a greater symbol period but shrinks the ISI. Due to all the above, the channel estimation technique can be a key parameter in providing reliable underwater and deserved great attention [8–10].

The multicarrier communication technique, i.e., orthogonal frequency division multiplexing (OFDM), is considered among the key notable underwater multicarrier modulation techniques. The OFDM technique is further divided into three main categories including (1) zero padding (ZP - OFDM), (2) cyclic-prefix (CP - OFDM), and (3) time-domain synchronization (TDS - OFDM) [11–13]. The difference between the three schemes is the inter-block interference (IBI) mitigation way over the multipath channels [11, 12]. Each way has its advantage and disadvantages. CP provides linear convolution and can be used for channel estimation at the expense of transmitted power. Unfortunately, saving the IoUT node's power is a very important point due to the hard recharging capability. ZP-OFDM solves the channel null problem and saves the transmitted power at the expense of the on-off problem [14]. TDS-OFDM technique, at the cost of the bit-error rate (BER) in the functioning of the system, presents exceptional power and energy efficiency [11, 15, 16]. In the present era, the system data rate has been increased following the technique of index modulation [17–20]. Unfortunately, the index modulation technique cannot support the long underwater communication distance as the multipath nature of the acoustic underwater channel can destroy the indexed data plus data recovery needs high receiver complexity.

In the multicarrier modulation, the guard interval technique is required to circumvent the inter-carrier interference (ICI) in the underwater acoustic channel, such long guard interval wastes the channel utilization. Such spectral loss will be more severe as the long tap delay underwater channel

needs long pilots' signals. The overhead information of pilot's and guard interval waste IoUTs nodes as well as spectral. Energy saving is very important for a new modern communication system, and such importance is very effective in the IoUT nodes as the recharging capability is hard in the underwater communication and saving energy increases the battery lifetime. Therefore, based on that, the TDS-OFDM schemes and the ZP-OFDM systems are the utmost desired multicarrier modulation techniques. However, the energy-saving capability and the spectral efficiency of the ZP-OFDM system are low in comparison to the TDS-OFDM scheme. The primary disadvantage of the TDS-OFDM systems is the excessive BER owing to the IBI amid the OFDM data blocks and the pseudo-noise (PN) sequences introduced in the guard intervals. The researchers focused on reducing and removing such IBI with different methods such as interference cancelation based on the iterative algorithm [21], and with addition without fluctuations in the frame construction of the TDS-OFDM scheme [22]. Unfortunately, these schemes slightly improve the TDS-OFDM BER performance [23], and such schemes cannot support a reliable TDS-OFDM-based underwater acoustic communication. Different BER improvement methods of the TDS-OFDM are changing the frame structure, and the modified frame structure is based on interference cancelation [23]. In the proposed unique word (UW) OFDM system, the time domain guard interval is produced by assigning the redundant pilots in the frequency domain [24]. Unfortunately, the UW-OFDM complexity is high without interference-free for the OFDM data blocks. Dual PN sequences have been used for TDS-OFDM in [23, 25, 26] to receive OFDM without inference. Dual PN simplified the channel estimation and equalization, but duplicate guard interval reduces the spectral efficiency. Duplication for guard interval is inapplicable for IoUT, as a duplicate of the guard interval is a waste of energy and spectrum.

Owing to the reduced length of multipath intervals than the channel spread, the channel impulse response (CIR) is sparse in the channel of underwater acoustics [27]. Therefore, the compressive sensing theory is applied for sparse channel estimation because of the sparse performance of the underwater channel [3, 28–30]. This paper applies the methods of CS theory to estimate the underwater CIR by using a small region free from the IBI. This arrangement at first approximates the Doppler factor followed by balancing through the collected PN structure. The later step predicts the channel with the aid of sparse recovery greedy algorithm, look-ahead, and backtracking orthogonal matching pursuit (LABOMP). The LABOMP was applied to the chosen small IBI-free region to get better recovery and ignore the IBI effect. LABOMP is used as multistage estimation providing better signal recovery. The proposed CS-based schemes are applied in real field measurements and show better energy, spectral, and BER performance. Compared to convention TDS-OFDM schemes, the proposed one provides reliable underwater communication.

The paper is structured to discuss the detailed model of the system in Section II while Section III explains the technique for channel estimation applied to the underwater

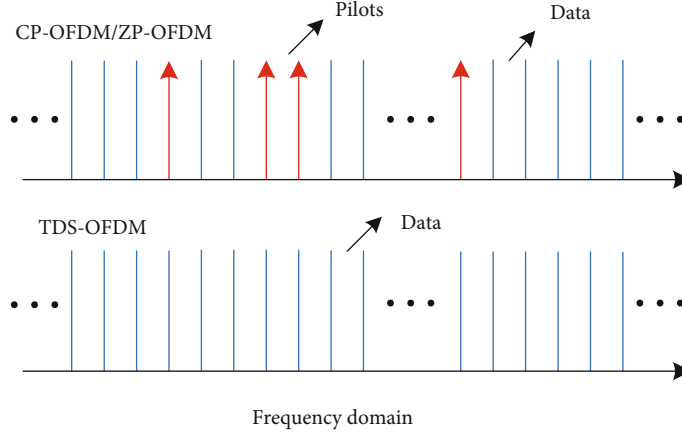


FIGURE 1: The frequency domain response of the OFDM standard signal structure.

acoustic channel based on compressive sensing. Section IV provides the simulation results followed by their validation through experimental results and discussion in Section V. Finally, the conclusive summary of the article is given in Section VI.

2. Model of the System

As we know, CP-OFDM, TDS-OFDM, and ZP-OFDM are the three different types of the OFDM system that are widely applicable in the technology of wireless communication [13, 31]. CP has been used as guard interval for CP-OFDM, ZP has been considered in ZP-OFDM as guard interval, and PN sequences are inserted as guard interval in TDS-OFDM. The comparative analysis of the structure of the signal, for the ZP-OFDM, TDS-OFDM, and CP-OFDM, in the frequency domain is shown in Figure 1 [23]. In comparison to the maximum delay of the time-varying multipath channel, the length of the guard interval (GI) must be larger so the information data block is not affected by ISI or IBI [3]. To evade the IBI issue in the multipath channel, the IBI-free region i^{th} transmitted OFDM block can be mathematically formulated as:

$$\mathbf{x}_i = [\mathbf{p}_i, \mathbf{d}_i]_{M+NX1}^T, \quad (1)$$

where $\mathbf{p}_i = \{p_{i,k}\}_{k=0}^{M-1}$, M is the PN sequence length, $\mathbf{d}_i = \{d_{i,k}\}_{k=0}^{N-1}$, k signifies the k^{th} constituent of the i^{th} block of the TDS-OFDM, and N specifies the length of the block for the OFDM information data.

3. Channel Estimation Based on CS for Underwater Communication

The interference in TDS-OFDM comprises several characteristics in a way that the perfect detection over multiple channels is difficult to achieve for the unknown OFDM data blocks. Figure 2 depicts this response behavior. Owing to the

data block of the OFDM, it is a difficult task to anticipate and mitigate IBI completely in support of the perfectly employed channel estimation techniques. Furthermore, because of the large size of the data block for the OFDM, the computational complexity is increased while calculating IBI. The training sequence is exploited on the receiver end besides knowing the training sequences; therefore, the IBI can then be computed only after the successful and accurate achievement of channel estimation [3]. While estimating channels accurately and overlooking the effects of the data block for OFDM on the sequence of training, there will be a resulting unmanageable mutual interference. The small IBI-free region exists because of the margin design of the system within the training received and is also analyzed in some practical applications. The worst case for the CP-OFDM and TDS-OFDM is observed in the equivalent channel length and guard interval. To avoid such a scenario, it is better to increase the guard size and minimize the channel length to achieve perfect estimation while avoiding the IBI. Figure 3 shows the proposed transceiver model.

The perfect channel estimation results in the complete elimination of the interference induced mutually from the data block of the TDS-OFDM. The ZP-OFDM system and the TDS-OFDM scheme, after ignoring the PN sequence, depict the same results. The technique of the DPN-TDS-OFDM dealt with the problem of the mutual interference, in the conventional TDS-OFDM system, arising from the data block to the PN sequence. The perfect channel estimation while ignoring the IBI and duplication of the guard interval to get a PN sequence is achieved in the DPN-TDS-OFDM frame. Figure 2 depicts the results of the TDS-OFDM schemes for multipath channels. The IBI affected the received PN sequence due to the former data block of the OFDM in the multipath channel resulting in channel estimation. The channel estimation is obtained in the time domain for the TDS-OFDM system, and the PN sequence received can be expressed as:

$$\mathbf{r}_i = \boldsymbol{\varphi}_i \mathbf{h}_i + \mathbf{u}_i, \quad (2)$$

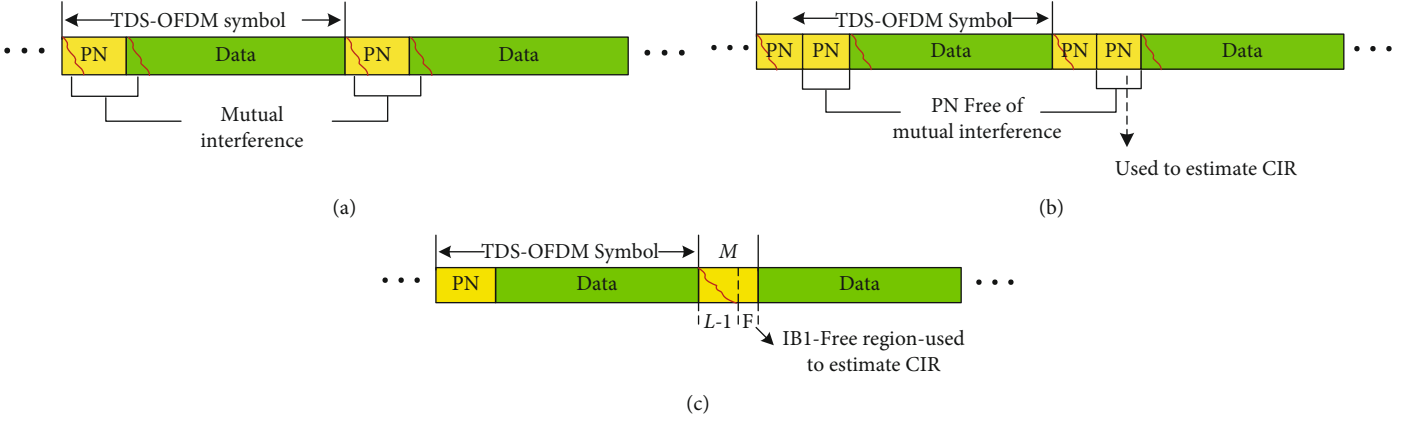


FIGURE 2: Received frame signal structure of different TDS-OFDM systems. (a) Conventional TDS-OFDM. (b) DPN-TDS-OFDM. (c) TDS-OFDM based on CS.

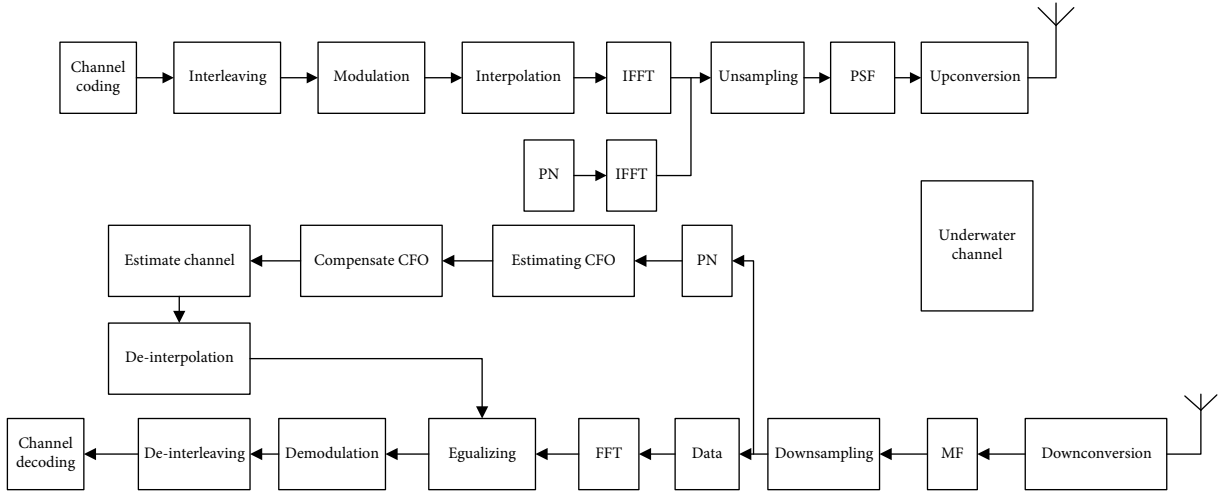


FIGURE 3: Block diagram of the transceiver proposed for the real underwater experiment.

where u_i signifies the AWGN noise having a mean value of zero and variance σ^2 . φ_i can be mathematically represented as:

$$\varphi_i = \begin{bmatrix} p_{i,0} & d_{i-1,N-1} & \cdots & d_{i-1,N-L+1} \\ p_{i,1} & p_{i,0} & \cdots & d_{i-1,N-L+2} \\ \vdots & \vdots & \ddots & \vdots \\ p_{i,L-1} & p_{i,L-2} & \cdots & p_{i,0} \\ p_{i,L} & p_{i,L-1} & \cdots & p_{i,1} \\ \vdots & \vdots & \ddots & \vdots \\ p_{i,M-1} & p_{i,M-2} & \cdots & p_{i,M-L} \end{bmatrix}_{MXL} \quad (3)$$

The $i-1$ th element shows the last transmitted block that interferes with the present symbol of the TDS-OFDM in eq. (3). It can be observed that the preceding samples, i.e., $M-L+1$, show no corrupted signals generating from the previous data blocks of the TDS-OFDM. Therefore, the CS theory

utilizes the IBI-free region for the estimation of the channel. The observation matrix is introduced by extracting the preceding $F = M - L + 1$. A new sub-matrix is developed and is mathematically expressed as:

$$\Phi = \begin{bmatrix} p_{i,L-1} & p_{i,L-2} & \cdots & p_{i,0} \\ p_{i,L} & p_{i,L-1} & \cdots & p_{i,1} \\ \vdots & \vdots & \ddots & \vdots \\ p_{i,M-1} & p_{i,M-2} & \cdots & p_{i,M-L} \end{bmatrix}_{FXL} \quad (4)$$

The PN sequence is used to obtain the observation matrix $F \times L$ size. Eventually, the noise in IBI-free region corrupts the received signal and thus can be denoted as under:

$$y_i = \Phi_i h_i + u_i \quad (5)$$

3.1. Proposed Algorithm. The energy and spectrum in the UWA communication can be saved by minimizing the free IBI regions in TDS-OFDM. Thus, a small IBI-free region is

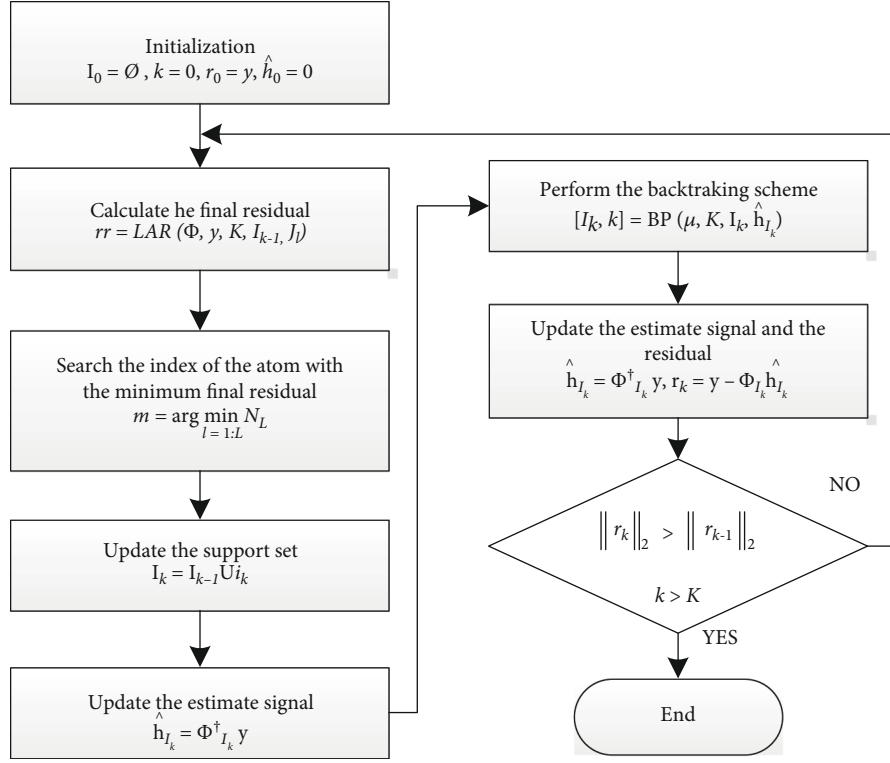


FIGURE 4: Flow chart of our proposed LABOMP algorithm for underwater acoustic channel estimation.

used and a LABOMP algorithm is proposed in this paper to address this issue. The backtracking pruning (BP) and look-ahead residue (LAR) functions are utilized in the LABOMP algorithm [3], by implementing the backtracking and look-ahead scheme, respectively. In the LABOMP algorithm flow chart depicted in Figure 4, the steps of the LAR function are presented in algorithm 1. In the first part, the potential l atoms are chosen that are more correlative with the residue of the last loop using a fixed look-ahead parameter l . In the second step, the support set is obtained by selecting the best one before predicting the effects of each potential atom. The residue and estimated signals are updated in the third step. Finally, the termination condition of the algorithm is evaluated by determining the current iteration status.

Functions 1 and 2 are defined by utilizing the flow chart of LABOMP in Figure 4. The second step of the LABOMP flow chart shows that K is the sparsity level and Function 1 is the look-ahead residual set, where $\mathbf{r} \in R^{FX1}$ and $\Phi \in R^{FXL}$. The parameter I and i represent the set of intermediate support and optimal atom index in the current iteration, respectively. Hence, the given algorithmic function is used to find the output residual $\mathbf{r} \in R^F$. Function 2 is the backtracking pruning and is shown in step 6 of the LABOMP flow chart, where K is the sparsity level and $\mu \in [0, 1]$ by considering that the \hat{h}_{I_k} is the estimated signal passing LAR function and I_k is the present selected set of intermediate support. Thus, the backtracking k and the new index of atoms I_k are obtained by using the following algorithmic function. The total iterations are divided into two types by the backtracking scheme that comprises cascade backtracking and a dominant look-ahead convergence. The stage of

the cascade backtracking is triggered by the preset constant threshold, i.e., $\lambda = \mu \cdot K$, that deletes the incorrect selected atoms in the last iteration. Moreover, the rule for adding atoms and signal structure has been associated with λ and the anticipated empirical value for LABOMP algorithm is $0.8K \sim 0.9K$. Algorithm 2 depicts the twofold idea of the BP function. In the first step, dominant look-ahead convergence provides the correct large coefficient atoms. The mismatched atoms that are selected in the previous iteration are not strictly orthogonal due to small coefficients. Therefore, to prune the maximum mismatching atoms, the scheme of backtracking utilizes the support set in the second step [3].

4. Simulation Results and Discussion

4.1. Spectral Efficiency. The mathematical formulation of spectral efficiency for OFDM systems has been presented in [23]:

$$\text{SpectralEfficiency} = \left(\frac{N_{\text{Data}}}{N_{\text{Data}} + P_{\text{Pilots}}} \times \frac{N_{\text{Frame}}}{N_{\text{Frame}} + M} \right) \times 100\%, \quad (6)$$

where N_{Data} denotes the data size (data subcarriers) and P_{Pilots} signifies the pilot sub-carriers, M shows the guard interval length, and N_{Frame} is the length of the frame (data subcarriers and pilots subcarriers). Figure 5 relates the spectral efficiency of our proposed method LABOMP with DPN-TDS-OFDM, TDS-OFDM, and conventional CP-OFDM.

Input: Sparsity K , $\mathbf{y} \in \mathbb{R}^{F \times 1}$, $\Phi \in \mathbb{R}^{F \times L}$, newly selected index i , previous support set \mathbf{I} ;
Initialization: The approximate coefficient $\hat{\mathbf{h}}_{I_k} = \Phi_{I_k}^\dagger \mathbf{y}$, residual $\mathbf{r}_k = \mathbf{y} - \Phi_{I_k} \cdot \hat{\mathbf{h}}_{I_k}$, the intermediate support set $\mathbf{I}_k = \mathbf{I}_{k-1} \cup i$, counter $k = |\mathbf{I}_k|$;
Repeat:
 $k = k + 1$;
 $i_k = \underset{i=1}{\operatorname{argmax}}^N \Phi_i^T \mathbf{r}_{k-1}$, $i \notin \mathbf{I}_{k-1}$; matching the filter values
 $\mathbf{I}_k = \mathbf{I}_{k-1} \cup i$; updating support set
 $\hat{\mathbf{h}}_{I_k} = \Phi_{I_k}^\dagger \mathbf{y}$;
 $\mathbf{r}_k = \mathbf{y} - \Phi_{I_k} \cdot \hat{\mathbf{h}}_{I_k}$;
Until $\|\mathbf{r}_{k-1}\|_2 < \|\mathbf{r}_k\|_2$ or $k > K$
Output: $\mathbf{r}_k = \mathbf{y} - \Phi_{I_k} \Phi_{I_k}^\dagger \mathbf{y}$;

ALGORITHM 1: LAR algorithm

Input: K , $\hat{\mathbf{h}}_{I_k}$, μ , \mathbf{I}_k ;
Initialization: $\lambda = \mu K$;
while $k \geq \lambda$ & $k \% 2 = 1$
 $[v, pp] = \underset{i \in \mathbf{I}_k}{\operatorname{argmin}} |\hat{\mathbf{h}}_{I_k}|$;
 $\mathbf{I}_k = \mathbf{I}_k \setminus pp$ the minimum value of $\hat{\mathbf{h}}_{I_k}$ to eliminate
end while
Output: \mathbf{I}_k , pp ;

ALGORITHM 2: BP algorithm

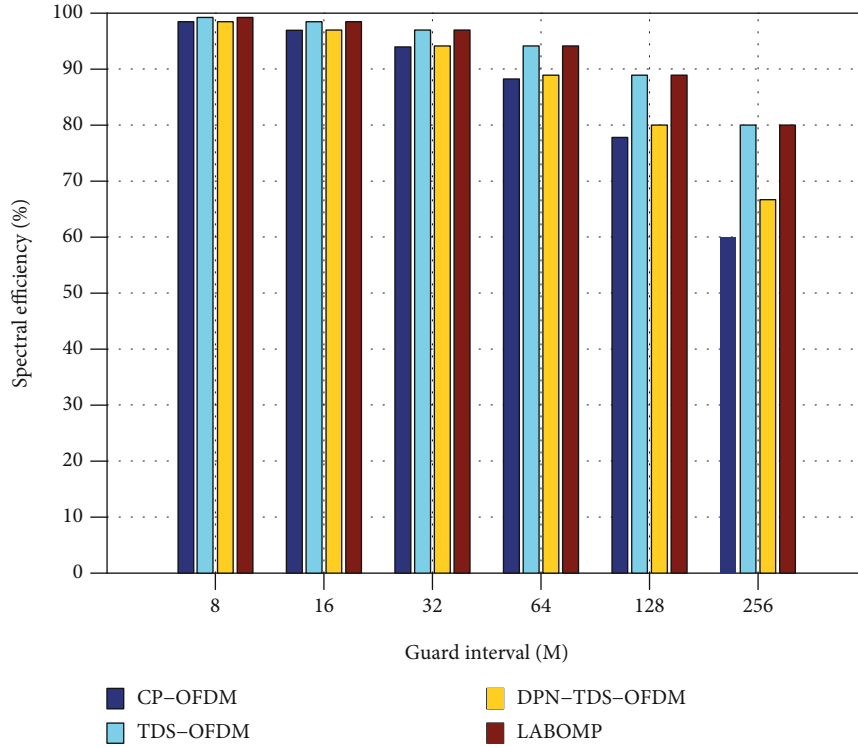


FIGURE 5: Spectral efficiency comparison of CP-OFDM, TDS-OFDM, DPN-TDS-OFDM, and proposed LABOMP-TDS-OFDM.

Despite the consistent and fast synchronization, TDS-OFDM, due to the removal of pilots, shows more spectral efficiency in comparison to CP-OFDM systems. Here, the

consequence of these advantages is more critical and crucial to revoke the iterative interfering because of the mutual interference in between the PN sequence (guard interval) and the

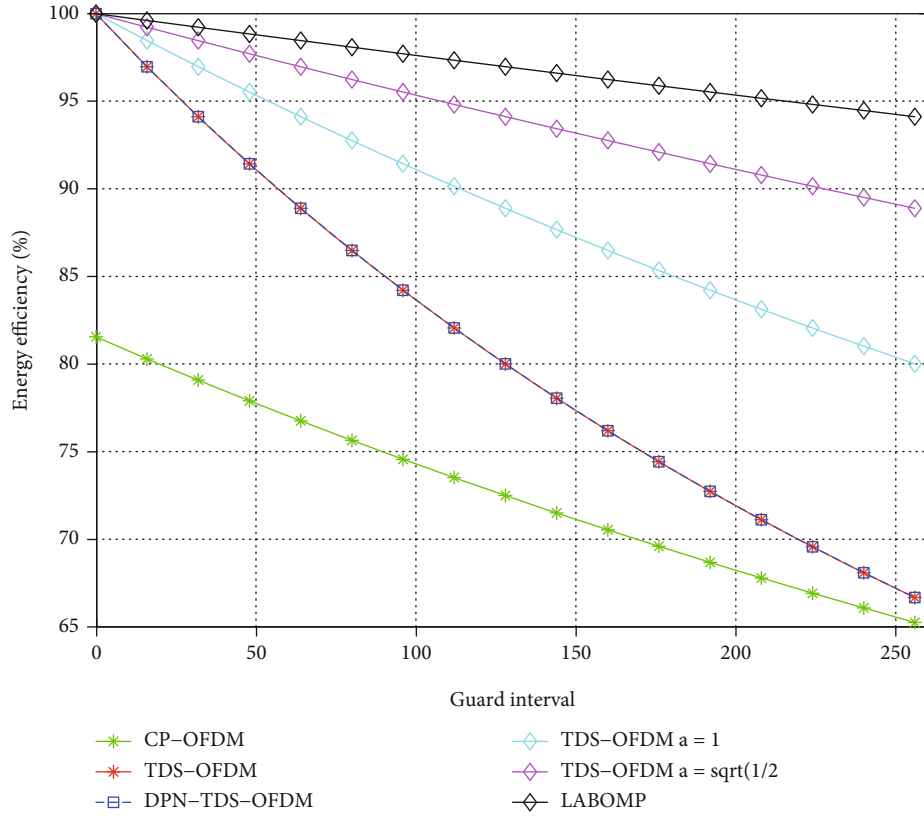


FIGURE 6: Energy efficiency comparison of CP-OFDM, conventional TDS-OFDM, DPN-TDS-OFDM, TDS-OFDM a=1, TDS-OFDM a= sqrt (1/2), and proposed LABOMP-TDS-OFDM.

TABLE 1: System specifications of parameters.

Parameters	Values
PN sequence (M)	255
Data block (N)	1024
Free-region length in channel (F)	75
Channel size (L)	255
Bandwidth	6KHz
Carrier frequency	20KHz
Sampling frequency	96KHz
Central frequency	30KHz
Modulation	QPSK
Data rate	11.99 kbits/sec
OFDM symbol duration	170.67 msec
CFO	0.2

data block of OFDM. Double the PN sequences in DPN-TDS-OFDM cancel out the interferences but the spectral efficiency was highly affected. There is no alteration required in the structure of the TDS-OFDM system while using the CS concept into TDS-OFDM, so the spectral efficiency has been improved concerning BER and MSE with high performance. Figure 5 depicts the spectral efficiency comparison of LABOMP-TDS-OFDM with conventional TDS-OFDM, conventional CP-OFDM, and DPN-TDS-OFDM.

4.2. *Energy Efficiency.* The energy efficiency for OFDM systems has been formulated in [23]:

$$\text{EnergyEfficiency} = \left(\frac{N_{\text{Data}}}{N_{\text{Data}} + b^2 P_{\text{Pilots}}} \times \frac{N_{\text{Frame}}}{N_{\text{Frame}} + a^2 M} \right) \times 100\% \quad (7)$$

where a and b signify the amplitude factor imposed on the guard interval and the amplitude factor imposed on the pilots in the time and frequency domain, respectively. The pilot's amplitudes have been increased for CP-OFDM requirement which increases the receiver channel estimation performance such as $b=4/3$ has been identified by the digital video broadcasting second generation terrestrial (DVB-T2) standard [23, 32]. Similarly, to guarantee the reliable channel estimation in TDS-OFDM, the amplitude of PN sequences has been increased; DTMB standard indicated the value of $a = \sqrt{2}$ [23, 33]. Alternatively, channel estimation performance of CS-based proposed LABOMP-TDS-OFDM has been improved with IBI-free region. IBI-free region has been employed in the LABOMP-TDS-OFDM so the guard interval does not require a high power; hence, the used PN training sequence amplitude is designated as $a = 0.5$. Figure 6 depicts the energy efficiency performance of TDS-OFDM, DPN-TDS-OFDM, CP-OFDM, and LABOMP-TDS-OFDM CS-based IBI-free region. In

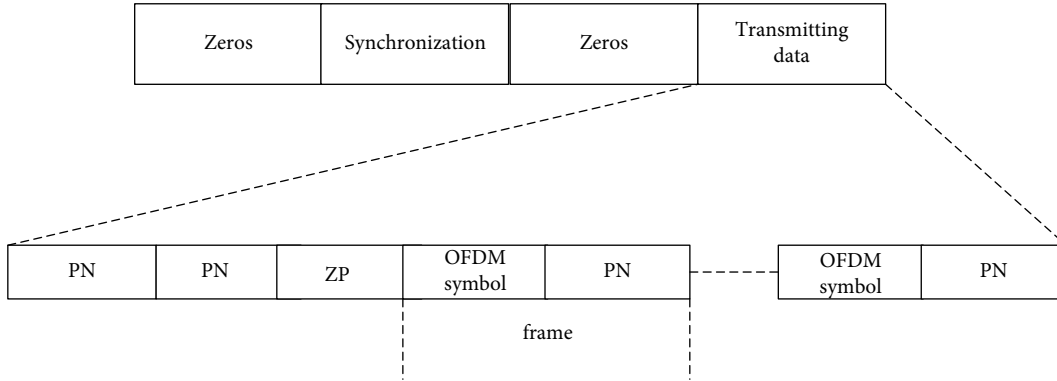


FIGURE 7: Frame structure of the transmitting signal.

TABLE 2: BER of OFDM received symbols at short distance.

Symbols	DPN	OMP	CoSaMP	LABOMP
1	0.0045	0.0032	0.0032	0.0018
2	0.0073	0.0053	0.0050	0.0042
3	0.0117	0.0086	0.0073	0.00671
4	0.0081	0.0053	0.0050	0.0039
5	0.0092	0.0072	0.0061	0.0048

TABLE 3: BER of OFDM received symbols with different distances.

Symbols	DPN	OMP	CoSaMP	LABOMP
1 m	0	0	0	0
10 m	0.0033	0.0019	0.0012	0.0008
30 m	0.0107	0.0062	0.0050	0.0031
100 m	0.0866	0.0583	0.0466	0.0311
1 km	0.0988	0.0662	0.0574	0.0446

CP-OFDM, the 4K mode of the DVB-T2 is used that result in the pilot occupation ratio of 11.29% [32]. The standard amplitude factor selected for DPN-TDS-OFDM and DTMB is 1 and $\sqrt{2}$, respectively [25].

4.3. Computational Complexity. We have noted from the proposed method that its performance mainly depends upon two parameters, present constant threshold λ and look-ahead parameter l . The better performance has been attained by increasing the value of l but it has a trade-off with computational complexity. Moreover, the performance can be not significantly improved with a small value of λ . The fact is that in the initial many iterations, atoms have been chosen with the larger value of coefficients, though the early matching backtracking has been suppressed. If the value of $l=1$ and $\lambda=K$, LABOMP will behave like OMP. The complexity of LABOMP has been analyzed. It is known that multiplication operation is slower than summation so multiplication is mainly reported. The standard multiplication requires for matching filter FL while for estimating the spares channel requires $O(SF)$ multiplication by using least square (LS).

The total iterations performed by LABOMP is $2S - \lambda + 1$. LABOMP computational complexity is $O(IS^2[1 + (S - \lambda)^2/S^2](SF + FL))$. In LAR, the LS estimator and matching filter multiplication cost are $O(IS^2[1 + (S - \lambda)^2/S^2])$ and total backtracking LS estimation cost is $(S - \lambda + 1)$.

The overall computational complexity of CoSaMP containing iterations equal to the sparsity level S is $O(4FS^3 + 8S^4)$ [34], and OMP is $O(FLS)$. In the conventional TDS-OFDM and DPN-OFDM, the channel is estimated based on the good features of the training sequence without interference cancelation. In these schemes, the received PN sequence directly correlated with the local PN sequence to generate the channel impulse response by efficiently implementing M -point fast Fourier transform; hence, these schemes have $\mathcal{O}((M/2) \log_2 M)$ [21, 22, 35].

5. Experimental Results and Discussion

The real data experiment was first conducted in the water tank for testing. Furthermore, it was also conducted in the sea at Wuyuan sea area Xiamen, China. The experimental field depth in the tank is almost 1 m. We have transmitted the signal from one transducer at the water depth of 1 m, and the signal was received by another transducer at the depth of 1 m also. The experimental depth of both transmitter and receiver was almost 3 m in the sea, and the distances between transmitter and receivers were almost 1 m, 10 m, 30 m, 100 m, and 1 Km, respectively. The sea experiment was done on different distances.

In the TDS-OFDM system, the total number of carriers only contained data subcarriers and there is no pilot subcarrier. The channel is estimated by guard interval (PN sequences). The parameters' specification of real sea testing is shown in Table 1. The transmitting frame structure of OFDM data is shown in Figure 7. The frame structure includes zeros vector with length of 120, linear frequency modulation (LFM) pulse vector has the 4096 sizes, after LFM there are zeros that has the length of 12000, and in the end is the transmitting data (OFDM symbols). There are five symbols, each symbol has five frames, and every frame size is 2560. For synchronization, auto-correlation

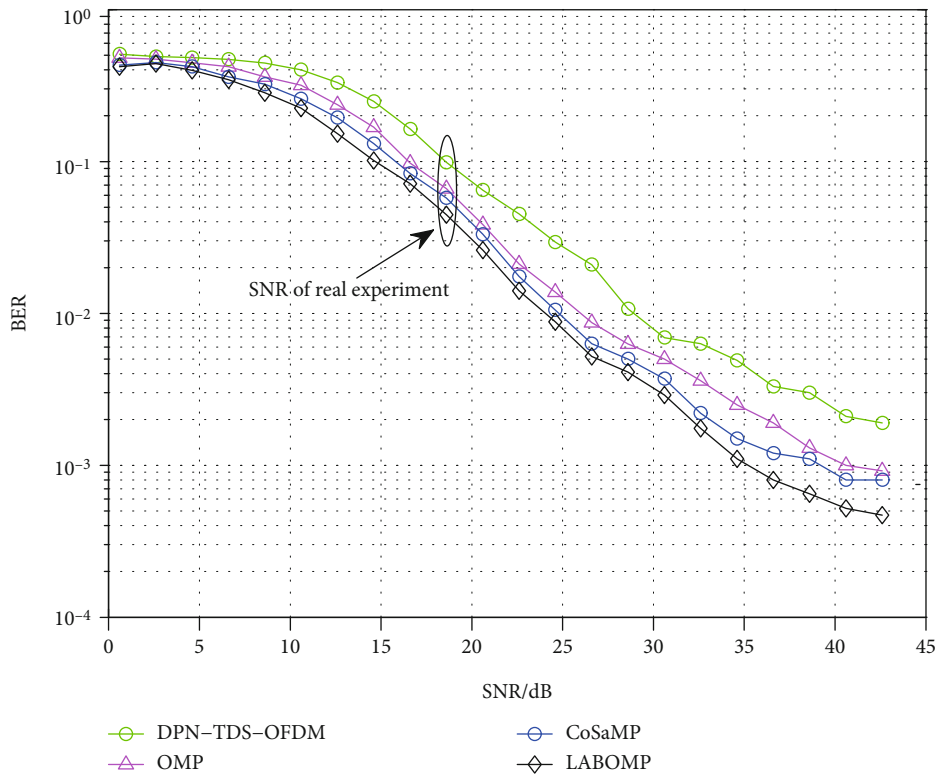


FIGURE 8: BER comparison of semi experiment DPN-TDS-OFDM, OMP, CoSaMP, and LABOMP.

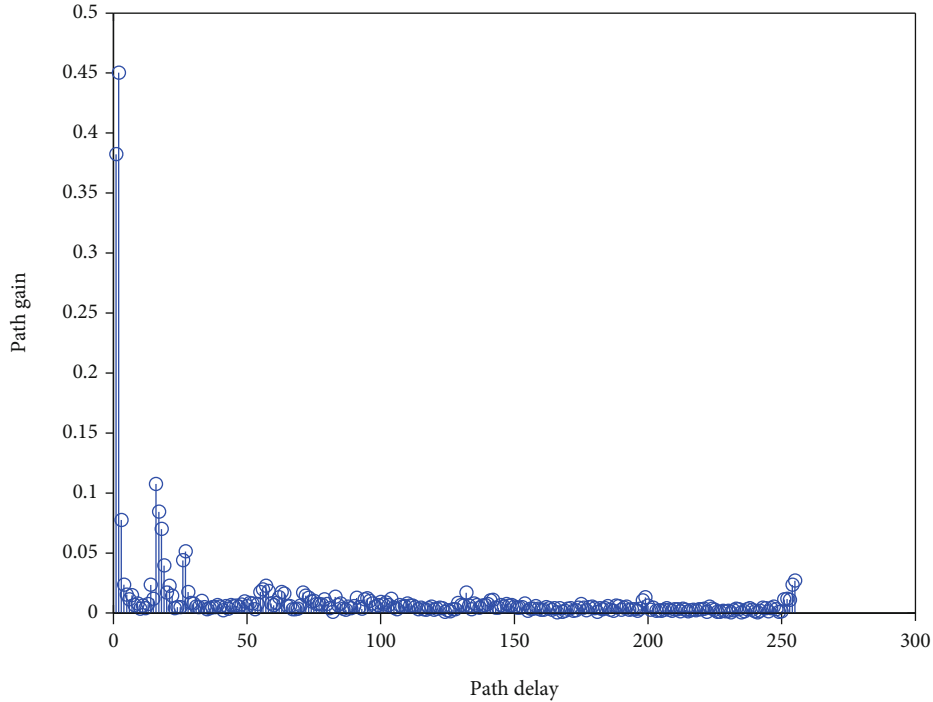


FIGURE 9: Underwater estimated CIR by known PN sequence.

method has been utilized to find the starting point of the signal for exact data recovery after channel estimation.

The performance evaluation of the TDS-OFDM system in the UWA channel has compared the DPN-TDS-OFDM

and compressed sensing-based methods, namely, OMP, CoSaMP, and LABOMP. First, the channel is estimated by all these methods in the time domain. After the channel estimation, the results are for data demodulation in the form

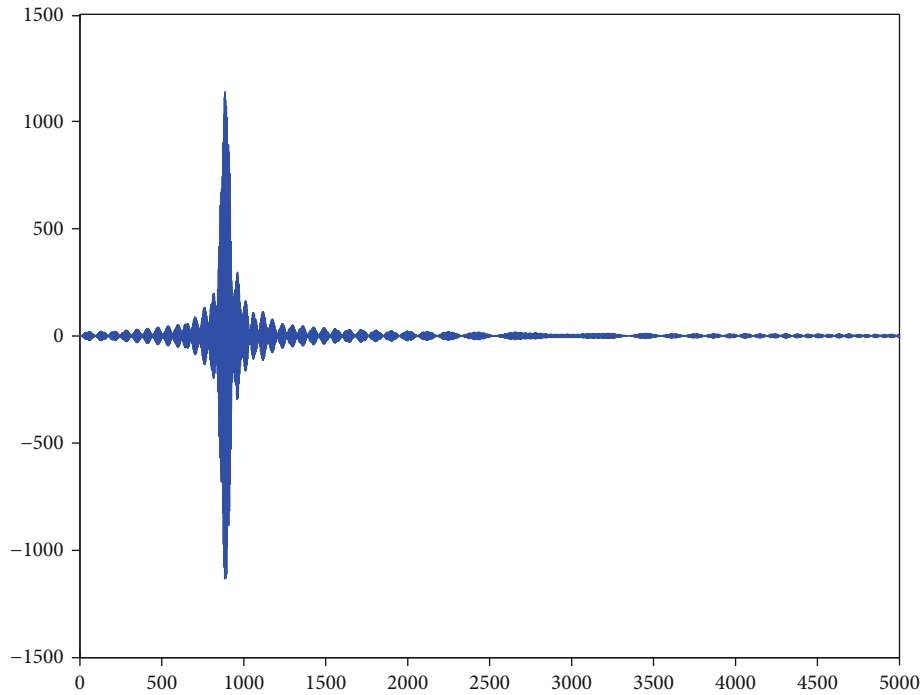


FIGURE 10: LFM-based auto-correlation.

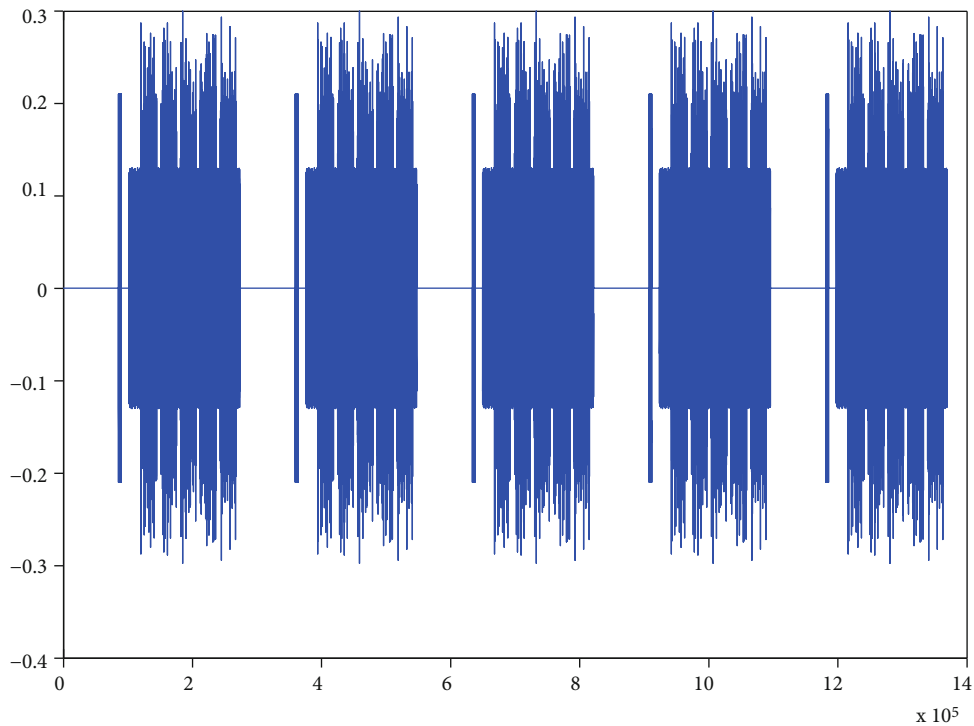


FIGURE 11: OFDM transmitting signal before sending over the underwater acoustic channel.

MMSE equalizer to ease the channel estimation method performance evaluation. In last, data is detected in the frequency domain. The LABOMP is for the first time proposed for underwater TDS-OFDM system which outperforms in comparison of DPN, OMP, and CoSaMP. The different

channel estimation method's performance has been analyzed using PN sequences. In DPN-TDS-OFDM channel, it is estimated by using two repeated PN sequences; for OMP, CoSaMP, and LABOMP channel, estimation is done by using IBI-free region in the received PN sequence.

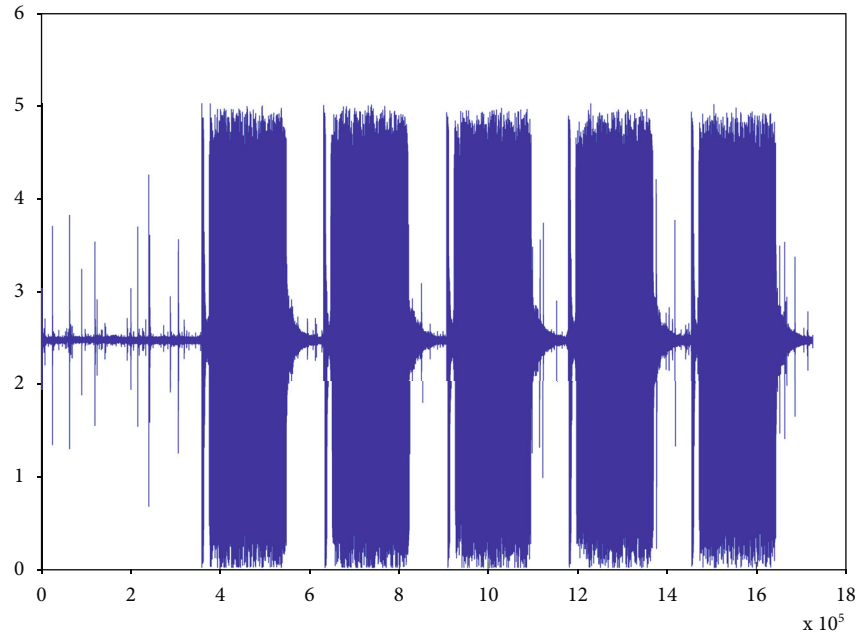


FIGURE 12: OFDM received signal through the underwater acoustic channel.



FIGURE 13: Field area of a real experiment.

Table 2 shows the BER of five received OFDM data symbols. These results of BER have been attained at a short distance of almost 10 m between transmitter and receiver. It is clearly shown that all techniques give better BER performance at a short distance. All CS-based methods outperform DPN-TDS-OFDM in terms of BER, but LABOMP gives better

performance than OMP and CoSaMP. Table 3 depicts the BER performance of DPN-TDS-OFDM, OMP, CoSaMP, and LABOMP at different distances as 1 m, 10 m, 30 m, 100 m, and 1 Km. At a distance of 1.5 m, all methods give outstanding performance in terms of BER. As the distance is going to increase, the BER is affected. Our proposed CS-



FIGURE 14: Instruments used for real sea experiment.

based greedy algorithm, namely, LABOMP, gives better performance in terms of BER as compared to other methods including DPN-TDS-OFDM, OMP, and CoSaMP.

The BER performance of the semi experiment with DPN-TDS-OFDM, OMP, CoSaMP, and LABOMP is shown in Figure 8. Thanks to the sparse nature of the UWA channel, it is seen that greedy algorithms outperform DPN-TDS-OFDM in terms of BER with different SNR gains. But, luckily the LABOMP algorithm also gives better performance in terms of BER compared to OMP and CoSaMP. The SNR of the channel is 18.6 dB. Figure 9 depicts the CIR of the OFDM data symbol which is estimated by a known PN sequence. As we say, the UWA channel is multipath and sparse, so it is seen in Figure 9.

Figure 10, Figure 11, and Figure 12 show the auto-correlation, OFDM transmitted signal, and received signal from the UWA channel, respectively. In Figure 10, LFM has been used to find the synchronization point. As we know auto-correlation gives the highest point at the beginning of the signal, so in this way, we get the starting point of the signal at receiving side. It is seen from Figure 12, that signal is affected by UWA channel and noise also, even there is a delay in received signal as compared to transmitted signal as seen in Figure 11. In real-time, the receiver has to wait for the information which will be sent by the transmitter.

Figure 13 depicts the map of the allocation where we have tasted underwater real-time experiments. The experiment was tested at different distances from 1 m to almost 1 Km. The black straight line in Figure 13 shows the long-distance experiment is 967 m which is almost equal to 1

Km. Figure 14 illustrates the hardware system which has been used for the sea experiment. The hardware system contains a laptop, battery, power amplifier, and analog to digital (A/D) converter. For a real sea experiment, the transmitting data has been saved in a MATLAB file (.m). After that, the data format has been converted to .bin format. That.bin file has been transmitted wireless from one computer to another using LABVIEW on both sides.

6. Conclusion

In this paper, algorithms for the UWA TDS-OFDM have been proposed based on CS to curtail the IBI for sparse channel estimation between PN training sequence and data frames. The IBI-free region in PN sequences plays a vital role; the channel has been properly reconstructed by CS-based techniques to attain higher EE and SE. PN sequence has been utilized to estimate and compensate the Doppler shift. In the real sea testing, experimental results show that the performance of the CS-based algorithms is much better than the DPN-TDS-OFDM and TDS-OFDM. A relevant comparison is performed among LABOMOP, CoSaMP, and OMP to observe the effectiveness of each CS-based algorithm. It is evident from the simulation and experimental results that the LABOMOP outperforms the conventional CS algorithms such as CoSaMP and OMP. Furthermore, the proposed CS-based methods achieved better spectral SE, EE, and substantial BER improvement for TDS-OFDM in comparison with conventional systems.

Data Availability

The data used to support the findings of this study are available from the corresponding author upon request.

Conflicts of Interest

The authors declare no conflict of interest.

Acknowledgments

This paper is based upon work supported by Science, Technology & Innovation Funding Authority (STDF) under grant number 46143.

References

- [1] H. Esmail, Z. A. H. Qasem, H. Sun, J. Wang, and N. U. Rehman Junejo, "Underwater image transmission using spatial modulation unequal error protection for internet of underwater things," *Sensors*, vol. 19, no. 23, pp. 5271–5284, 2019.
- [2] X. Ma, F. Yang, S. Liu, and J. Song, "Channel estimation for wideband underwater visible light communication: a compressive sensing perspective," *Optics Express*, vol. 26, no. 1, pp. 311–321, 2018.
- [3] N. U. R. Junejo, H. Esmail, M. Zhou, H. Sun, J. Qi, and J. Wang, "Sparse channel estimation of underwater TDS-OFDM system using look-ahead backtracking orthogonal matching pursuit," *IEEE Access*, vol. 6, pp. 74389–74399, 2018.
- [4] M. Mostafa, H. Esmail, and E. M. Mohamed, "A comparative study on underwater communications for enabling C/U plane splitting based hybrid UWSNs," in *2018 IEEE Wireless Communications and Networking Conference*, pp. 1–6, Barcelona, Spain, April 2018.
- [5] I. Iglesias, A. Song, J. Garcia-Frias, M. Badiey, and G. R. Arce, "Image transmission over the underwater acoustic channel via compressive sensing," in *2011 45th Annual Conference on Information Sciences and Systems*, pp. 1–6, Baltimore, MD, USA, March 2011.
- [6] J. Li and Y. V. Zakharov, "Efficient use of space-time clustering for underwater acoustic communications," *IEEE Journal of Oceanic Engineering*, vol. 43, no. 1, pp. 173–183, 2018.
- [7] Y. V. Zakharov and A. K. Morozov, "OFDM transmission without guard interval in fast-varying underwater acoustic channels," *IEEE Journal of Oceanic Engineering*, vol. 40, no. 1, pp. 144–158, 2015.
- [8] C. R. Berger, Z. Wang, J. Huang, and S. Zhou, "Application of compressive sensing to sparse channel estimation," *IEEE Communications Magazine*, vol. 48, no. 11, pp. 164–174, 2010.
- [9] S. Kaddouri, P.-P. J. Beaujean, and P.-J. Bouvet, "High-frequency acoustic estimation of time-varying underwater sparse channels using multiple sources and receivers operated simultaneously," *IEEE Access*, vol. 6, pp. 10569–10580, 2018.
- [10] Z. Yang and Y. R. Zheng, "Iterative channel estimation and turbo equalization for multiple-input multiple-output underwater acoustic communications," *IEEE Journal of Oceanic Engineering*, vol. 41, no. 1, pp. 232–242, 2016.
- [11] X. Ma, F. Yang, S. Liu, W. Ding, and J. Song, "Structured compressive sensing-based channel estimation for time frequency training OFDM systems over doubly selective channel," *IEEE Wireless Communications Letters*, vol. 6, no. 2, pp. 266–269, 2017.
- [12] L. Dai, Z. Wang, and Z. Yang, "Time-frequency training OFDM with high spectral efficiency and reliable performance in high speed environments," *IEEE Journal on Selected Areas in Communications*, vol. 30, no. 4, pp. 695–707, 2012.
- [13] H. Esmail and D. Jiang, "Zero-pseudorandom noise training OFDM," *Electronics Letters*, vol. 50, no. 9, pp. 650–652, 2014.
- [14] B. Muquet, Z. Wang, G. B. Giannakis, M. De Courville, and P. Duhamel, "Cyclic prefixing or zero padding for wireless multicarrier transmissions," *IEEE Transactions on Communications*, vol. 50, no. 12, pp. 2136–2148, 2002.
- [15] J. Wu, Y. Chen, X. Zeng, and H. Min, "Robust timing and frequency synchronization scheme for DTMB system," *IEEE Transactions on Consumer Electronics*, vol. 53, no. 4, pp. 1348–1352, 2007.
- [16] W. Ding, F. Yang, W. Dai, and J. Song, "Time-frequency joint sparse channel estimation for MIMO-OFDM systems," *IEEE Communications Letters*, vol. 19, no. 1, pp. 58–61, 2015.
- [17] E. Başar, Ü. Aygözü, E. Panayırçı, and H. V. Poor, "Orthogonal frequency division multiplexing with index modulation," *IEEE Transactions on Signal Processing*, vol. 61, no. 22, pp. 5536–5549, 2013.
- [18] M. Wen, B. Ye, E. Basar, Q. Li, and F. Ji, "Enhanced orthogonal frequency division multiplexing with index modulation," *IEEE Transactions on Wireless Communications*, vol. 16, no. 7, pp. 4786–4801, 2017.
- [19] J. Li, S. Dang, M. Wen, X.-Q. Jiang, Y. Peng, and H. Hai, "Layered orthogonal frequency division multiplexing with index modulation," *IEEE Systems Journal*, vol. 13, no. 4, pp. 3793–3802, 2019.
- [20] M. Wen, X. Cheng, L. Yang, Y. Li, X. Cheng, and F. Ji, "Index modulated OFDM for underwater acoustic communications," *IEEE Communications Magazine*, vol. 54, no. 5, pp. 132–137, 2016.
- [21] J. Wang, Z.-X. Yang, C.-Y. Pan, J. Song, and L. Yang, "Iterative padding subtraction of the PN sequence for the TDS-OFDM over broadcast channels," *IEEE Transactions on Consumer Electronics*, vol. 51, no. 4, pp. 1148–1152, 2005.
- [22] M. Liu, M. Crussiere, and J.-F. Hélar, "A novel data-aided channel estimation with reduced complexity for TDS-OFDM systems," *IEEE Transactions on Broadcasting*, vol. 58, no. 2, pp. 247–260, 2012.
- [23] L. Dai, J. Wang, Z. Wang, P. Tsiaflakis, and M. Moonen, "Spectrum-and energy-efficient OFDM based on simultaneous multi-channel reconstruction," *IEEE Transactions on Signal Processing*, vol. 61, no. 23, pp. 6047–6059, 2013.
- [24] M. Huemer, C. Hofbauer, and J. B. Huber, "Non-systematic complex number RS coded OFDM by unique word prefix," *IEEE Transactions on Signal Processing*, vol. 60, no. 1, pp. 285–299, 2012.
- [25] J. Fu, J. Wang, J. Song, C.-Y. Pan, and Z.-X. Yang, "A simplified equalization method for dual PN-sequence padding TDS-OFDM systems," *IEEE Transactions on Broadcasting*, vol. 54, no. 4, pp. 825–830, 2008.
- [26] L. Dai, Z. Wang, and Z. Yang, "Next-generation digital television terrestrial broadcasting systems: key technologies and research trends," *IEEE Communications Magazine*, vol. 50, no. 6, pp. 150–158, 2012.
- [27] L. Dai, Z. Wang, and Z. Yang, "Spectrally efficient time-frequency training OFDM for mobile large-scale MIMO systems," *IEEE Journal on Selected Areas in Communications*, vol. 31, no. 2, pp. 251–263, 2013.

- [28] W. Ding, F. Yang, C. Pan, L. Dai, and J. Song, "Compressive sensing based channel estimation for OFDM systems under long delay channels," *IEEE Transactions on Broadcasting*, vol. 60, no. 2, pp. 313–321, 2014.
- [29] X. Ma, F. Yang, S. Liu, J. Song, and Z. Han, "Design and optimization on training sequence for mmWave communications: a new approach for sparse channel estimation in massive MIMO," *IEEE Journal on Selected Areas in Communications*, vol. 35, no. 7, pp. 1486–1497, 2017.
- [30] X. Ma, F. Yang, W. Ding, and J. Song, "Novel approach to design time-domain training sequence for accurate sparse channel estimation," *IEEE Transactions on Broadcasting*, vol. 62, no. 3, pp. 512–520, 2016.
- [31] H. Esmail and D. Jiang, "Spectrum and energy efficient OFDM multicarrier modulation for an underwater acoustic channel," *Wireless Personal Communications*, vol. 96, no. 1, pp. 1577–1593, 2017.
- [32] E. Etsi, "Digital video broadcasting," *Frame Structure Channel Coding and Modulation for a Second Generation Digital Terrestrial Television Broadcasting System*, vol. 1, 2012.
- [33] B. T. Series, "Error-correction, data framing, modulation and emission methods for digital terrestrial television broadcasting," *International Telecommunication Union*, vol. 2011, 2011.
- [34] L. Dai, Z. Wang, and Z. Yang, "Compressive sensing based timing domain synchronous OFDM transmission for vehicular communication," *IEEE Journal on Selected Areas in Communications*, vol. 31, no. 9, pp. 460–469, 2013.
- [35] Z. Yang, X. Wang, Z. Wang, J. Wang, and J. Wang, "Improved channel estimation for TDS-OFDM based on flexible frequency-binary padding," *IEEE Transactions on Broadcasting*, vol. 56, no. 3, pp. 418–424, 2010.

Research Article

Reinforcement Learning-Based Adaptive Switching Scheme for Hybrid Optical-Acoustic AUV Mobile Network

Hanjiang Luo ¹, Ziyang Xu,¹ Jinglong Wang,¹ Yuting Yang,¹ Rukhsana Ruby,² and Kaishun Wu²

¹College of Computer Science and Engineering, Shandong University of Science and Technology, Qingdao, China

²College of Computer Science and Software Engineering, Shenzhen University, Shenzhen, China

Correspondence should be addressed to Hanjiang Luo; luo.hj@foxmail.com

Received 13 November 2021; Revised 10 April 2022; Accepted 11 April 2022; Published 2 May 2022

Academic Editor: Xuebo Zhang

Copyright © 2022 Hanjiang Luo et al. This is an open access article distributed under the Creative Commons Attribution License, which permits unrestricted use, distribution, and reproduction in any medium, provided the original work is properly cited.

In an autonomous underwater vehicles– (AUVs–) based optical-acoustic hybrid network, it is critical to achieve ultra high-speed reliable communications, in order to reap the benefits of the complementary systems and perform high-bandwidth and low-latency operations. However, as the mobile AUVs operate in harsh oceanic environments, it is essential to design an effective switching algorithm to execute flexible hybrid acoustic-optical communications and increase the network throughput. In this paper, we propose a Q-learning-based adaptive switching scheme to maximize the network throughput by capturing the dynamics of the varying channels as well as the mobility of AUVs. In order to address the challenge associated with partial observations of the optical channel and improve the switching efficiency in extreme conditions, a blind optical channel estimation method is designed and implemented with the Extended Kalman Filter (EKF), in which the relationship between the underwater acoustic and optical channels is utilized to improve the channel prediction accuracy. Based on this environmental status, a reinforcement learning approach is leveraged to build a near-optimal switching strategy for the hybrid network. We conduct numerical simulations to verify the performance of the scheme, and the simulation results demonstrate that the proposed switching scheme is effective and robust.

1. Introduction

The deployment of underwater sensor networks (USNs) has enabled extensive marine activities of ocean monitoring and exploring [1, 2], in which both underwater acoustic communication (UAC) and underwater wireless optical communication (UWOC) are utilized for underwater networking. Although UAC is the only reliable and dominated technology that currently enables medium and long-range underwater wireless communications, it also suffers from several shortcomings (e.g., limited bandwidth, low-speed, high propagation delay, and high energy consumption [3]), which may make it difficult to meet growing application demands, such as transferring underwater real-time ultra high-definition videos and conducting real-time remotely controlled operations [4, 5].

To alleviate the limitations of UAC, as an alternative and complementary technology, UWOC has developed rapidly recently that enables high-speed, low-delay, and low-energy consumption networks, which may compensate for the deficiencies of UAC in terms of latency and bandwidth [6]. Nevertheless, UWOC has its own drawbacks communicating only with relatively short range, and it is also affected by hazardous oceanic environments (e.g., underwater obstacles, turbulence, turbidity, and light noise) [7]. To address these problems, a paradigm of multimodal networking is proposed to integrate multiple communicating systems (e.g., optical and acoustic) in a hybrid network, in order to mitigate shortcomings and take advantage of complementary technologies [8–10]. Along this line, the integration of optical and acoustic systems has been explored in both simulations and experiments [11–14], and these optical-acoustic hybrid systems

are leveraged to retrieve monitored data [9, 15], control coordination [16], build multiple routing paths [17, 18], and transfer real-time video [9], which demonstrate the benefit and effectiveness of such hybrid optical-acoustic systems [19].

Since a fleet of AUVs are desirable mobile vehicles to perform flexible underwater tasks under operational scenarios, such as environment monitoring, security surveillance, and underwater asset investigation [1, 20], the study focused on leveraging a swarm of AUVs to form underwater mobile networks has been developing rapidly in the recent years [3, 21]. By networking a swarm of AUVs equipped with both optical and acoustic communication systems, such a hybrid network enables high-bandwidth and low-latency underwater video transmission and real-time underwater operation and control [9, 22]. However, implementing such a network is not trivial as the associated challenges should be addressed carefully due to the limitations of the system, the hostile environments, as well as the mobility of AUVs [23, 24]. Among them, one critical issue is to maximize the hybrid network throughput by exploiting the complementary communicating technologies in terms of both acoustic and optical, especially the optical waves, as UWOC suffers from limited communication range [23]. Therefore, the optical link needs to be switched ON or OFF complementarily to the acoustic link in an automatic manner [13]. However, the optical system is affected by the communication distance, beam width, and the mobility of AUVs. Moreover, as the AUVs are operated in the harsh environments, the temporal and spatial dynamics of the channel (e.g., the turbidity of the seawater, the obstacles, and the turbulence and currents) may degrade the performance of the communication significantly [7]. Consequently, it is desirable to monitor and even predict the changing conditions of the channels in order to carry out the switching scheme in an adaptive and effective manner [25, 26].

There are a few pioneering studies dealing with the switching issue and providing precious investigations of underwater multimodal wireless networks [13, 27–29]. In [13], the authors explored the multimodal switching issue to maximize instantaneous network throughput using the range-based triggering mechanism to proactively switch among different physical layers (PHYs). However, the switching strategy uses a preset threshold to execute the switching policy. In [27], the authors discussed the statistical relationship between acoustic and optical channels and proved feasibility of predicting the optical channel state based on the properties of acoustic channels. Although a switching scheme based on optical signal-to-noise ratio (SNR) threshold was presented, no further specific experiments and simulations were conducted to validate the performance. Nevertheless, an effective switching strategy should be adaptive to the environmental dynamics, and as reinforcement learning (RL) has the capability of interacting with the environment and could gradually learn an optimal or near-optimal action policy, it is a promising artificial intelligence (AI) tool to develop switching strategy for underwater sensor networks. In a recent research, a model-free RL method is adopted to deal with the dynamics of the channels in order to smoothly switch among different types of acoustic modems

in an adaptive manner [28, 29]. However, the switching policy in a hybrid optical-acoustic communication system, involving two different types of links, has not been studied much. Furthermore, as the UWOC has more restrictions compared to the acoustic communication, these limitations should be carefully addressed in the switching scheme.

To tackle the aforementioned challenges, in order to maximize the throughput of the hybrid AUV mobile network, as depicted in Figure 1, in this paper, we leverage the Q-learning and Extended Kalman Filter (EKF) tools to deal with the severe oceanic environments and propose an adaptive switching scheme. Compared to these learning-ignorant schemes, the proposed scheme does not require prior knowledge of the environments. Furthermore, we leverage the relationship between the acoustic and optical channels to enhance the effectiveness of switching strategy by capturing the dynamics of the varying channels [27]. To the best of our knowledge, this is the first study to provide an adaptive switching scheme for the AUV-based hybrid optical-acoustic network. To summarize, the major contributions of this paper are listed as follows:

- (1) We propose an adaptive switching scheme for an AUV-based optical-acoustic hybrid network that leverages both the Q-learning and EKF tools to increase the network throughput
- (2) A blind estimation method for underwater optical channel state is implemented with the EKF tool to improve the channel prediction accuracy for effective proactive switching
- (3) The critical factors (e.g., acoustic and solar noise, water turbidity, AUV mobility, and optical beam width) which affect the effectiveness and robustness of the switching scheme are investigated via numerical simulations

2. Preliminaries

In this section, we introduce the preliminaries for the proposed adaptive switching scheme, which include the following: network model, acoustic channel, optical channel, and localization of AUVs.

2.1. Basics of Network Model. The hybrid underwater acoustic-optical network includes a swarm of AUVs and an underwater positioning system, as shown in Figure 1. Each AUV is equipped with both the acoustic and optical communication technologies. Moreover, the positioning system is deployed either on an assistant ship or on a floating buoy, which is near the AUV operating area. As depicted in Figure 2, the hybrid system consists of an underwater wireless acoustic communication (UWAC) link and an UWOC link. The UWAC link is dedicated for conveying the feedback information of channel states and the positioning information of the AUVs. Therefore, the acoustic channel is used for both the control and low-rate data transmission purposes.

As the swarm of AUVs are mobile, the designated switching scheme aims to choose the UWAC link or UWOC link

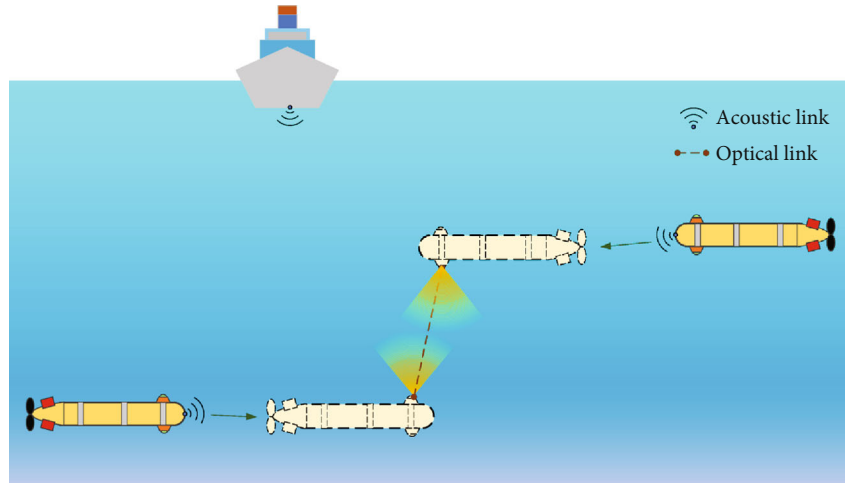


FIGURE 1: A sample structure of the hybrid optical-acoustic network.

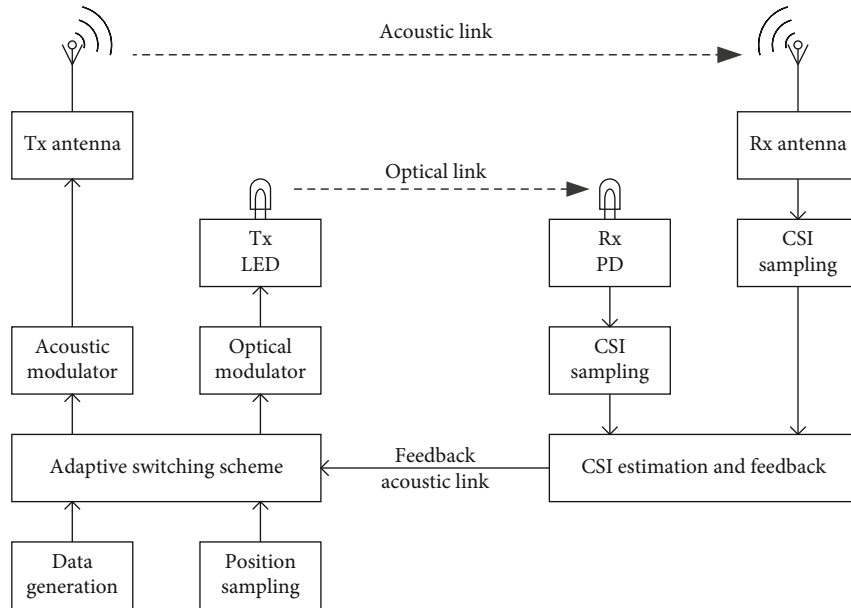


FIGURE 2: A sample block diagram of hybrid optical-acoustic systems.

for data transmission in an adaptive manner based on the channel conditions and the AUV positions. Once the conditions for the optical link are favorable, a well-designed scheme should switch it ON, which means the initiation of optical transmission for many tasks, such as pointing, acquisition, and tracking (PAT) system [30]. During the process, the receiver sends back the feedback information (e.g., channel state information (CSI)) into the acknowledge string (ACK) via acoustic links until the UWOC link has been established.

2.2. Basics of Acoustic Channel. To monitor the channel state and measure the noise level, the signal-to-noise ratio (SNR) is selected as CSI to characterize the channel. The path loss in the underwater acoustic channel is given by [31]: $A(r, f) = A_0 r^b a(f)^r$, where A_0 is the normalizing constant, r is the

distance between the transmitter and the receiver, b is the spreading factor, f is the acoustic signal frequency, and $a(f)$ is the absorption coefficient estimated by Thorp's derivation which is constant for the specific frequency sound wave.

By ignoring the changes of noise and transmission power in a short time period, the observation of SNR of time-varying and frequency-selective channel can be formalized as Markov chains in discrete time domain, which implies that the current theoretical prediction of SNR depends on the past prediction. The SNR of transmission performed at frequency over distance between a transmitter and a receiver can be expressed as follows [31]:

$$SNR_A = \frac{P}{A(r, f)N_0(f)B}, \quad (1)$$

where P is the transmit power, N_0 is the noise power, and B is the narrow band around the signal frequency.

Although the underwater acoustic noise can be described as the white Gaussian noise, the received signal always suffers from Non-Gaussian noise (e.g., alpha noise and Middleton Class A and Class B noise) consisting of short spike pulses generated by external interference in the underwater channel [32, 33], which result in the probability density function (PDF) of the noise with longer and extended tails. According to these studies, it is known that the Non-Gaussian noise follows the symmetrical alpha-stable (SaS) distribution class [34]. The characteristic function of the SaS distribution class is given by

$$\varphi(x) = \exp(i\mu x - \gamma|x|^\alpha) \quad (2)$$

where α is the characteristic exponent that determines the degree of pulse characteristic of the distribution and $0 < \alpha \leq 2$ holds. The terms μ and γ are the location and dispersion parameters, which are similar to the mean and variance of the Gaussian distribution. When $\alpha = 2$ holds, the α stable distribution is equivalent to the Gaussian distribution.

To suppress the spikes and make the noise conform to the Gaussian distribution, some filters have been proposed such as U-filter's Gaussianization process [35] and median filter [36]. By leveraging the aforementioned filters, the noise of the acoustic channel $Noise_A$ is defined as

$$Noise_A \sim N(SNR_A, \sigma_{AC}^2), \quad (3)$$

where σ_{AC}^2 represents the mean error variance.

2.3. Basics of Optical Channel. To build an UWOC link among the mobile AUVs, an LED is adopted as the transmitter in this work, which has a wide beam angle to reduce the strict alignment requirement and guarantee the communication between AUVs [27].

Correspondingly, we also choose SNR as the main feature of the optical CSI, since in a real-time control system (RTCS), the optical PAT is driven by affluent SNR. Note that when the AUV is equipped with an optical noise sensor, the short-term noise dynamics can be taken into consideration. The SNR can be modelled as a Markov chain [37] as follows:

$$SNR_O = \left[\frac{P_t e^{-c(\lambda)r} D^2 \cos \phi}{4r^2 NEP \tan^2 \theta} \right]^2, \quad (4)$$

where P_t is the optical transmit power, r is the distance between the transmitter and the receiver, $c(\lambda)$ stands for the attenuation coefficient which consists of absorption coefficient $a(\lambda)$ and scattering coefficient $b(\lambda)$: $c(\lambda) = a(\lambda) + b(\lambda)$, λ is the beam wavelength, D is the receiver aperture diameter, ϕ is the incident angle between the optical axis of the receiver and the line-of-sight (LOS) direction, θ is the half angle transmitter beam width, and NEP is the noise equivalent power.

Under the consumption of unchanged transmit power and fixed optical system parameters, the noise of optical channel $Noise_O$ is defined by

$$Noise_O \sim N(SNR_O, NEP^2), \quad (5)$$

where the noise of optical NEP^2 can be modelled as the sum of a series of Gaussian noises. It includes the thermal noise in the signal amplification process, the quantum shot noise generated at the receiving end, the photodetector dark current noise generated by the photodetector electrical current leakage, and the background noise caused by environment optical clutter.

2.4. Localization of AUVs. Since both the acoustic and the optical channels are affected by the communication distance, a positioning system is required to determine the positions of AUVs [3]. As shown in Figure 3, we use the ultra short baseline positioning (USBL) technique to locate AUVs by measuring the phase difference of the target's acoustic signal to the hydrophone through the shipborne array probe as follows:

$$\begin{cases} x = d \cos \alpha \\ y = d \cos \beta \end{cases}, \quad (6)$$

where d represents the distance between the shipborne base station and the positioning target, α is the azimuth angle along the x -axis, and β is the azimuth angle along the y -axis. Then, the position information is broadcast to the transmitter AUV Tx and the receiver AUV Rx . After that, Tx can calculate the relative position $P_{Tx \rightarrow Rx}^t$ by the following formula [38]:

$$P_{Tx \rightarrow Rx}^t = \begin{bmatrix} x_{Rx} - x_{Tx} \\ y_{Rx} - y_{Tx} \\ z_{Rx} - z_{Tx} \end{bmatrix}, \quad (7)$$

where z_{Tx} is the depth of the transmitter and z_{Rx} is the depth of the receiver, which are updated after completing each communication round. We assume that the trajectory of the AUV is preset by the shipborne base station. Thus, the relative position in the next time slot can be predicted in advance.

3. Adaptive Switching Scheme

In this section, we present the adaptive switching scheme design based on the RL technique. The overall diagram of switching scheme is shown in Figure 2. We first provide the fundamental mechanism of the proposed switching policy, then propose an optical channel estimation based on the EKF in detail, and finally provide the switching algorithm at the end of the section.

3.1. The Design of the Switching Scheme. As shown in Figure 4, we briefly describe the primary mechanisms of

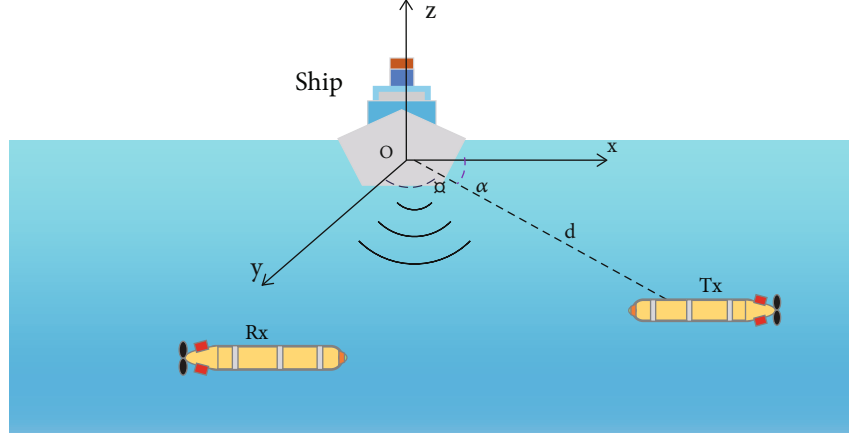


FIGURE 3: The positioning system by ultra short baseline positioning technology.

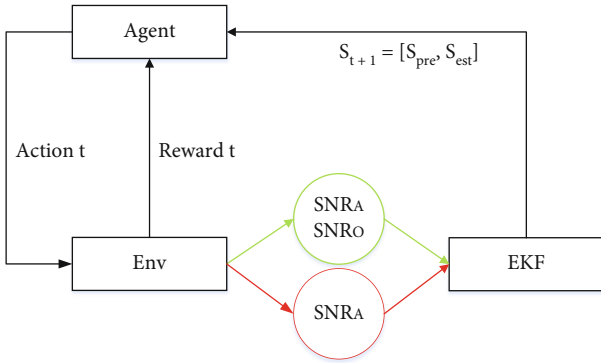


FIGURE 4: The illustration of the adaptive switching scheme.

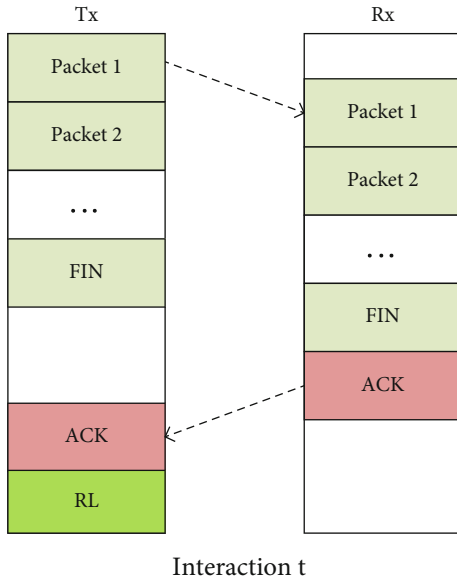


FIGURE 5: Illustration of CSI estimation and feedback process.

the switching scheme. To design an effective switching policy, the AUV should consider the positioning of the target transmitter, the states of acoustic and optical channels. The channel states are denoted as SNR_A and SNR_O , respectively.

These sensed information are then fed into the EKF tool for further processing before sending to the agent as part of the environment states. It should be noted that SNR_O is only measured and collected after the UWOC link is switched ON.

More precisely, the agent in an AUV generates and updates the policy function $\pi(s)$. The inputs to the policy function come from the communications with the target AUV via acoustic link, including state S and reward R . The state set S consists of acoustic channel state estimation outcome S_{pre} and the optical channel state estimation outcome S_{est} as shown in Figure 4. The output of the policy function is only a single action, which affects the measurement of the next state.

Optical state information is more difficult to acquire compared to acoustic channel states because of the extra cost of alignments. Therefore, we keep apart the acoustic and optical communications in the learning process, which in turn requires a reward function R specifically for the optical communication, but not for the acoustic communication. Subsequently, the AUV alternating policy function $\pi(s)$ is equivalent to the exploration of the successful connections for the optical communications. To realize the exploration, we design a blind estimation model for the optical channel. The basic idea of the estimation process is that the receiver estimates the optical CSI by combining the theoretical value of optical CSI and the acoustic measurement outcome when the optical information is not available via the relationship between the acoustic and optical channel states [27].

The proposed optical channel state estimation model is developed based on the EKF tool, and the optical CSI measurement is used to estimate the optical channel SNR_O . When the optical CSI measurement is not available, we obtain the optical estimation state S_{est} by updating the observation matrix with the acoustic CSI tracking information SNR_A and its theoretical value.

3.2. Design of the RL Technique. The interaction between an AUV and the optical channel can be formulated as a Markov Decision Process (MDP). The UWOC channel state transition matrix is estimated and updated by acoustic channel

TABLE 1: The settings of the SNR levels.

State	dB	Setting	Level
S_{pre}	$SNR_A \leq 5$		0
	$5 < SNR_A \leq 10$		1
	$10 < SNR_A \leq 15$		2
	$SNR_A > 15$		3
S_{est}	$SNR_O \leq 5$		0
	$5 < SNR_O \leq 10$		1
	$10 < SNR_O \leq 15$		2
	$15 < SNR_O \leq 20$		3
	$SNR_O > 20$		4

observations while switching. Therefore, there is a trade-off between exploration and exploitation in AUV. Exploration implies updating the model frequently so as to obtain a more accurate future prediction, which incurs additional costs. On the other hand, the higher degree of exploitation may result in a local optimal solution. For this reason, an effective quantification function is proposed to adjust ε , which urges the agent to have more explorations when the constructed model is ineffective. The following elements are included in the design of the proposed scheme:

- (i) Environment: The environment contains the acoustic and optical channels and the receiver, and it generates reward when the optical communication is ON
- (ii) State: The state S describes the current environment. We combine the SNR S_{pre} of the acoustic channel and the optical estimated SNR S_{est} obtained by the EKF tool as states S , which is denoted as $S = [S_{pre}, S_{est}]$. To simplify the design, the state quantities are discretized into N and M levels in a total of $N \times M$ states
- (iii) State value function: The estimated value of current state $V_\pi(s)$ is calculated as the expectations of the future rewards
- (iv) Action: The action set $Action = [0, 1]$ is the UWOC link binary controller bit, where 0 means OFF and 1 means ON
- (v) Reward: The reward function R_t can be set according to the different tasks of the AUV. An agent seeks the optimal policy to maximize the value function V_π while leveraging the feedback information from the environment. As there is only a unique task, the reward function R_t is set to a fixed value, which is only obtained during the UWOC link. If the UWOC is successfully established, the agent will get the reward χ to update Q-value of action ON. While UWOC is failed to set up, the agent will get the reward φ to modify Q-value of action OFF:

$$R_t = \begin{cases} \chi, & \text{Success} \\ \varphi, & \text{Fail} \\ 0, & \text{Otherwise} \end{cases}, \quad (8)$$

The policy function π is a greedy strategy, which balances the relationship between the exploration and exploitation as follows:

$$\pi(s) = \begin{cases} \operatorname{argmax}_{\tau \in Action} Q(s, \tau), & 1 - \varepsilon \\ \text{random}, & \varepsilon \end{cases}, \quad (9)$$

where the action τ to maximize the Q-value is chosen with probability $1 - \varepsilon$ and the action is selected randomly with probability ε .

Bellman equation is used to describe the relationship between the current state value and the consequent state value that the current state value is equal to the expectation of the sum of discount next state value and the instantaneous reward [29]:

$$V_\pi(s) = E_\pi(R_{t+1} + \gamma V_\pi(S_{t+1}) | S_t = s), \quad (10)$$

where γ is the discount factor. The learned action value function Q directly approximates the optimal action and maximizes over all possible actions in the next state as follows:

$$Q(s, \tau) = (1 - \delta)Q(s, \tau) + \delta \left(R_{t+1} + \gamma \max_{\tau'} Q(s', \tau') \right); \quad (11)$$

where δ is the learning rate. We assume that the environmental information is observable. Then, we set the reward function R_t according to the network requirement. For example, as we want to increase the successful trial of the switching process, we continuously update Q-table in interaction with the environment. The Q-function $\pi(s)$ uses a tabular approximation method, and the CSI information is approximated into several levels.

3.3. Optical Channel Estimation. As discussed earlier, the state of the RL technique consists of two kinds of information: SNR_A and SNR_O . Since the acoustic link is used for the control channel, its SNR can be easily obtained. The actual optical SNR, especially when there is no optical communicating link, cannot be obtained directly. In [27], the possibility of using acoustic SNR to predict optical SNR is discussed. Inspired by this research, we use the EKF tool to estimate optical SNR from the acoustic SNR which require a small amount of prior knowledge and is adapted to the AUV movement.

Initialization: Learning rate δ , exploration and exploitation threshold ε state-action-value-function $Q(s, \tau) = 0$.

- 1: **for** $t = 1, 2, 3, \dots$ **do**:
- 2: Obtain the relative position $P_{Tx \rightarrow Rx}^t$ using the relation in (7)
- 3: Predict the hybrid channel state mean $\hat{X}_{t|t-1}$
- 4: Predict the variance $P_{t|t-1}$ using the relation in (23).
- Blind Estimation Stage
- 5: **if** $\tau = 0$ **then**
- 6: Estimate the observation Z_t^b using the relation in (17).
- 7: Obtain the channel estimation $\hat{X}_{t|t}$ using the relation in (24).
- 8: **end if**
- Feedback Stage
- 9: **if** $\tau = 1$ **then**
- 10: Observe the channel state Z_t^f using the relation in (20).
- 11: Estimate the channel state $\hat{X}_{t|t}$ using the relation in (24).
- 12: Obtain the reward R_t .
- 13: **end if**
- Online Learning Stage
- 14: Update $S_{t+1} = [S_{pre}, S_{est}]$
- 15: Update Q-Value $Q(s, \tau)$ using the relation in (11).
- 16: Choose action $\tau \in Action$ using the relation in (9).
- 17: Update the EKF parameters.
- 18: **end for**

ALGORITHM 1: The proposed adaptive switching algorithm.

TABLE 2: UWOC parameters.

Parameters		Value
Receiver sensitivity	\mathfrak{R}	$0.26 A/W$
Receiver aperture diameter	D	$1.1 mm^2$
Half angle transmitter beam width	θ	$0.5 rad$
Electron charge	q	$1.6 \times 10^{-19} C$
Wavelength	λ	$532 nm$
Downwelling irradiance	E	$1440 watts/m^2$
Radiance factor	L_{fac}	2.9
Diffuse attenuation coefficient	T_A	$\exp(-\tau_0)$
Boltzmann's constant	k	1.381×10^{-23}
Equivalent temperature	T_e	$290 K$
Dark noise	I_{DC}	$1.226 \times 10^{-9} Ampere$
Transmit power		$30 W$
Beam attenuation coefficient		1.0
Signal bandwidth		$100 kHz$
Planck's constant		$6.6261 \times 10^{-34} Js$
Underwater reflectance		1.25%
Speed of light		2.25257×10^8
Radiant absorption factor		0.5
Noise figure of system		4
Load resistance		100Ω

We first define the state space vector X_t at time slot t as follows [38]:

$$X_t = \begin{bmatrix} P_{A \rightarrow B}^t \\ SNR_O^t \\ SNR_A^t \end{bmatrix}_{5 \times 1}, \quad (12)$$

where $P_{A \rightarrow B}^t$ is the relative position vector of AUVs and SNR_O^t and SNR_A^t are the SNRs of optical and acoustic channels, respectively. Then, we derive the state transition function from (4) as follows:

$$\begin{aligned} X_t &= f(X_{t-1}) = F_t X_{t-1} + \omega_t, \\ &= \begin{bmatrix} I_{3 \times 3} & 0 & 0 \\ \cdots & G_O^t & 0 \\ 0 & \cdots & G_A^t \end{bmatrix}_{5 \times 5} X_{t-1} + \omega_t, \end{aligned} \quad (13)$$

$$\begin{aligned} G_O^t &= \frac{1}{(e^{c(|P_t| - |P_{t-1}|)} \times (|P_t|/|P_{t-1}|))^3 \times (x_{t-1}^2 + y_{t-1}^2/x_t^2 + y_t^2)^2}, \\ G_A^t &= \frac{1}{(1 + (\Delta r/r_{t-1}))^b \times a(f)^{\Delta r}}, \end{aligned} \quad (14)$$

where F_t is the transfer matrix and is used to adjust the prior estimation covariance matrix $P_{t|t-1}$ and ω_t is the process noise which obeys the Gaussian distribution with mean 0 and covariance Q . Secondly, the observations can be divided into two stages based on the availability of optical channel

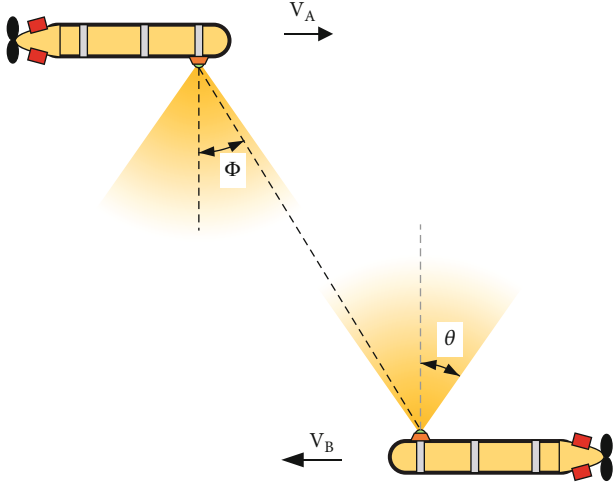


FIGURE 6: A sample optical communication scenario between two AUVs.

observations, such as blind estimation stage and feedback stage.

In the blind estimation stage, due to the lack of the optical channel observation, we resort to the relationship between acoustic and optical channels to estimate the optical SNR via the acoustic measurements. At this stage, the observation (or measurement) vector Z_t^b at time t can be expressed as

$$Z_t^b = \begin{bmatrix} P_{A \rightarrow B}^t \\ SNR_A^t \end{bmatrix}_{4 \times 1}, \quad (15)$$

where $P_{A \rightarrow B}^t$ and SNR_A^t are the measurement of relative positions of AUVs and the acoustic SNR. Then, the observation is expressed as

$$Z_t^b = h_b(X_t) = H_t^b X_t + v_t^b = \begin{bmatrix} I_{3 \times 3} & 0 & 0 \\ 0 & 0 & L^t \end{bmatrix}_{4 \times 5} X_t + v_t^b, \quad (16)$$

$$L^t = C_b SNR_O \frac{r^{A-b} \exp^{2cr} NE P^2}{a^r \cos^2 \theta}, \quad (17)$$

where $h_b(\bullet)$ represents the mapping at the blind estimation stage, which converts the 5×1 state vector X to the corresponding 4×1 measurement vector Z_b . H_t^b is observation matrix and v_t^b is the observation noise, which is assumed to be zero mean Gaussian white noise with covariance R . C_b is a constant related to signal amplifier circuits and the underwater environment.

In the feedback stage, we use the optical channel measurement as feedback to the EKF tool, in order to improve the accuracy of the estimation. The observation (or measurement) vector Z_t^f at time t of this stage can be expressed as

$$Z_t^f = \begin{bmatrix} P_{A \rightarrow B}^t \\ SNR_O^t \\ SNR_A^t \end{bmatrix}_{5 \times 1}, \quad (18)$$

where SNR_A^t is the measured value of the optical SNR. Afterwards, the observation is expressed as

$$Z_t^f = h_f(X_t) = H_t^f X_t + v_t^f, \quad (19)$$

$$H_t^f = I_{5 \times 5}. \quad (20)$$

where $h_f(\bullet)$ represents the mapping at the feedback stage, which converts the 5×1 state vector X to the corresponding 5×1 measurement vector Z^f . H_t^f is an identity matrix and v_t^f is the observation noise, which is assumed to be zero mean Gaussian white noise with covariance R . According to the aforementioned descriptions, the observation function $h(\bullet)$ and the observation matrix H_t of the system can be abbreviated as the following relation:

$$Z_{t+1} = h(X_t) = \begin{cases} h_b(X_t) + v_t^b, & \text{at Blind Stage} \\ h_f(X_t) + v_t^f, & \text{at Feedback Stage} \end{cases}, \quad (21)$$

$$H_t = \begin{cases} H_t^b, & \text{at Blind Stage} \\ H_t^f, & \text{at Feedback Stage} \end{cases}, \quad (22)$$

Due to the nonlinearity nature of the system view state and observation function, EKF is employed for channel state estimation since it is a nonlinear version of Kalman filter. Standard EKF tool generally consists of two phases: prediction and updating. There are three covariance matrices: P , Q , and R [39]. The Q and R are both positive definite matrices which depended on the environment settings, and the $P_{0|0}$ is initialized as an identity matrix. The state vector and its covariance matrix can be iteratively updated by the following relations [39]:

Prediction:

$$\begin{aligned} \hat{X}_{t|t-1} &= f(\hat{X}_{t-1|t-1}), \\ P_{t|t-1} &= F_t P_{t-1|t-1} F_t^T + Q. \end{aligned} \quad (23)$$

Updating:

$$\begin{aligned} \tilde{y}_t &= z_t - h(\hat{X}_{t|t-1}), \\ S_t &= H_t P_{t|t-1} H_t^T + R, \\ K_t &= P_{t|t-1} H_t^T S_t^{-1}, \\ \hat{X}_{t|t} &= \hat{X}_{t|t-1} + K_t \tilde{y}_t, \\ P_{t|t} &= (I - K_t H_t) P_{t|t-1}. \end{aligned} \quad (24)$$

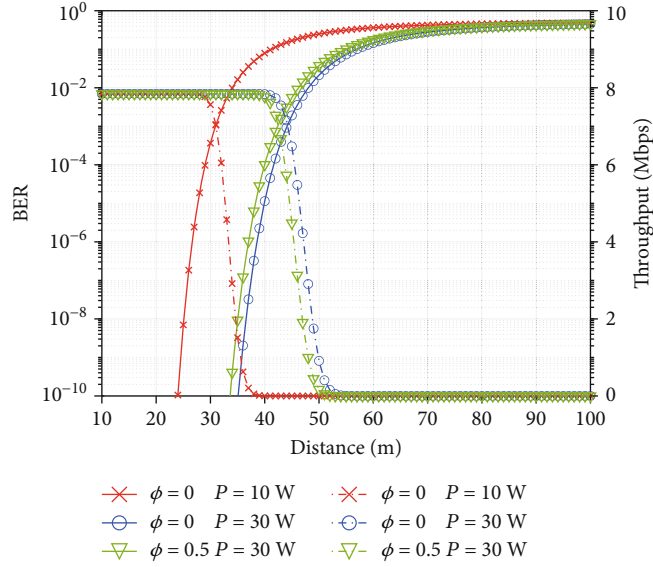


FIGURE 7: The characteristic of UWOC with different distances.

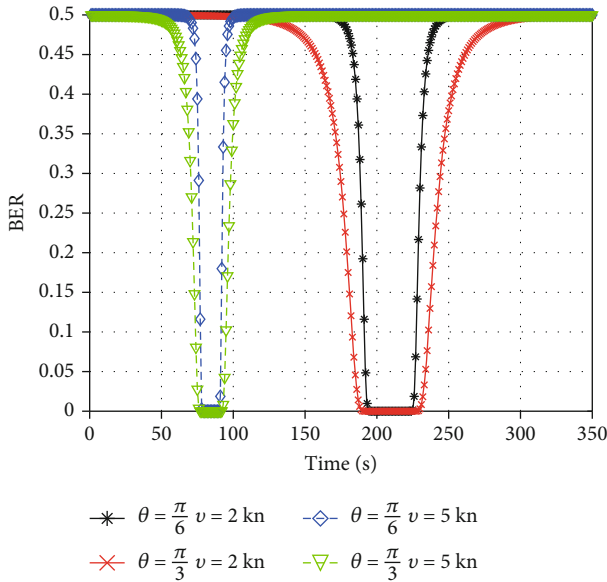


FIGURE 8: The characteristic of UWOC with different AUV speeds and half angles.

After the observations, such as relative position, acoustic SNR, or optical SNR, have been processed, the EKF tool provides an estimation of X as the input state for the RL technique to make decisions.

3.4. The Description of the Proposed Switching Algorithm. The proposed algorithm is deployed in the controllers of the AUVs, and the switching policy is stored in a Q-table and updated by communicating with other AUVs. The discrete time slot is denoted as the period which begins at the packet transmission until Tx has received the ACK from Rx and updates the Q-table, and the sequences are related to the packet transmission process as shown in Figure 5.

We assume that the environment remains relatively stable over a short period of time. At the beginning of each interaction, the transmitter first receives the positioning information $P_{Tx \rightarrow Rx}$, and the receiver tracks and estimates the channel state X_t using the EKF tool while receiving the packets. Once the transmission is initiated, the receiver estimates the optical channel state \hat{X}_t and places the estimation value into the ACK. Finally, the transmitter progresses to the online learning stage and updates the policy function $\pi(s)$. The initial parameters are the learning rate δ , the exploration constant ϵ , and the system error σ . Before the packet transmission, the position of the target is determined by the positioning system which resides in the shipborne base station or a buoy.

Then, the receiver calculates the prediction of the hybrid channel state \hat{X}_t using the relation in (23) and collects the observations. The value of the observation function is defined in (21). While the optical communication is OFF, the measurement function Z_t is obtained by the blind estimation which combines the theoretical value of optical SNR_O and the acoustic measurement SNR_A using the relation in (17). Then, the observation is updated with the optical measurement outcome using the relation in (20) under the process of optical communication. We choose SNR to represent CSI [23]; thus, we have a double state tuple S_t consisting of both the acoustic SNR estimation outcome SNR_A^t and the optical SNR estimation outcome SNR_O^t. The quantified levels are shown in Table 1, and we set the state $S_t = [S_{pre}^t, S_{est}^t]$ for the RL algorithm.

The condition for judging optical communication successful is based on an SNR threshold which the PD on the receiver conceives the optical signal is real [23]. It should be noted that the optical signal measurement of the receiver is sent back to the transmitter via the acoustic channel. Therefore, the online learning stage can be reached at both the transmitter and the receiver ends through the bi-directional

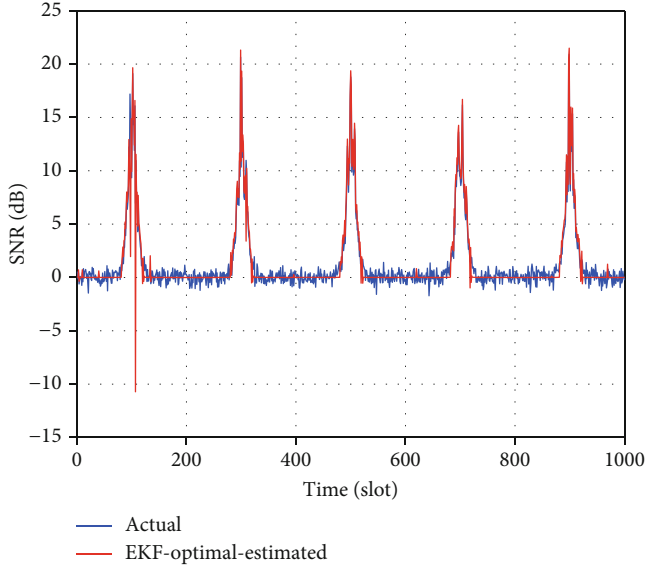


FIGURE 9: The convergence of the estimation and the actual state.

communication process, and it reduces the costs of learning. After the successful switching operation, the optical SNR is used to assist the PAT procedure [39].

The adaptive switching process is summarized in Algorithm 1. Once the system is initialized, the algorithm is mainly divided into three parts: blind estimated stage, feedback stage, and online learning stage. At the beginning of each interaction, the relative position P of each agent is obtained to predict the channel state $\hat{X}_{t|t-1}$ and the covariance P . When the optical channel is not obtained by the agent, the blind estimation stage is used to estimate the optical channel observation Z by the acoustic observations using the relation in (17). Otherwise, when the UWOC is switched ON, the feedback stage is used to estimate the optical channel state Z by the optical observations. Subsequently, the corresponding agent obtains the reward R at the end of UWOC switching trials. After getting the channel estimation $\hat{X}_{t|t}$ from the blind estimation stage or the feedback stage where the optical state is measured at the feedback stage but absent at the blind estimation stage, the agent updates the next state S_{t+1} using SNR_A and SNR_O in Table 1. In the online learning stage, the agent updates the Q-table and EKF parameters, and then the action of the next interaction is chosen using the relation in (9).

4. Performance Evaluation

In this section, we evaluate the performance of the proposed switching scheme through simulations. The operating area of AUVs is set to $2000\text{ m} \times 2000\text{ m} \times 500\text{ m}$. The primary simulation parameters and settings are provided in Table 2. We first simulate the characteristics of optical communication between mobile AUVs. Then, we verify the effectiveness of the proposed switching algorithm. Finally, we testify the robustness of the proposed scheme.

4.1. The Characteristics of Optical Communication between Mobile AUVs. The performance of the optical communication of mobile AUVs is affected by several factors. As shown in Figure 6, when two mobile AUVs encounter, the chance of performing reliable visible light communication (VLC) via LOS link depends on several factors (e.g., the distance between two AUVs, the transmit power P , the half-angle FOV θ , the incident angle of the receiver \emptyset , and the speed of AUV v).

As shown in Figure 7, we illustrate the performance variations under different communication distances between two AUVs, and also with different levels of transmit power P and the incident angle \emptyset . The half angle is fixed to $\theta = \pi/6$. The collision avoidance range of AUVs is set to 10 m [40].

As shown in the figure, the solid lines describe the throughput, and the dotted lines represent the bit error rate (BER). The distance between two AUVs is varying from 10 m to 100 m. We take different settings of transmit power and incident angle to compare the performance, such as the transmit power is set to 10 W and 30 W, and the incident angle is set to 0 rad and 0.5 rad. Figure 7 shows that the optical communication throughput has good performance which can reach the magnitude of Mbit. However, the throughput declines rapidly when the distance is larger than a number in between the range of 30 m and 50 m. Consequently, we can take some measures to improve the optical transmission capability, such as improving the transmit power. The figure also shows that the BER has a significant performance for applications associated with the communication distance of 40 m.

Figure 8 shows the UWOC characteristics of two mobile AUVs with respect to different speeds and half angles. The speed of AUVs is set to 2 and 5 knots, and the half angle θ is set to $\pi/6$ and $\pi/4$. As shown in the figure, it can be observed that under the same half angle θ , the time window is larger with a slow speed of AUVs in terms of BER communication performance. The delay that an AUV experiences while communicating with another one via the optical link is longer with a wide half angle compared to the narrow half angle under the same speed.

4.2. The Effectiveness of the Switching Scheme. In order to verify the effectiveness of the proposed scheme, we simulate the performance of the EKF and Q-learning tools. In the simulations, two AUVs are deployed in the depth of 15 m and 25 m. The trajectories of these AUVs are in a linear roundtrip patrol along a straight line with a range span about 500 m. The initial positions of the AUVs are on the left and right sides of their patrol lines, and the AUVs are moving towards each other at a speed of 2 knot and 4 knot, respectively. Each interaction process is defined as a time slot as shown in Figure 5. When the two AUVs patrol along the preset lines, the SNR of UWOC gradually increases and decreases in accordance with the change of distance between two AUVs.

As shown in Figure 9, the EKF tool has a good performance when the optical SNR is large enough, and both states are generated under the simulated environments. Overall, the EKF is relatively stable when estimating the states, and

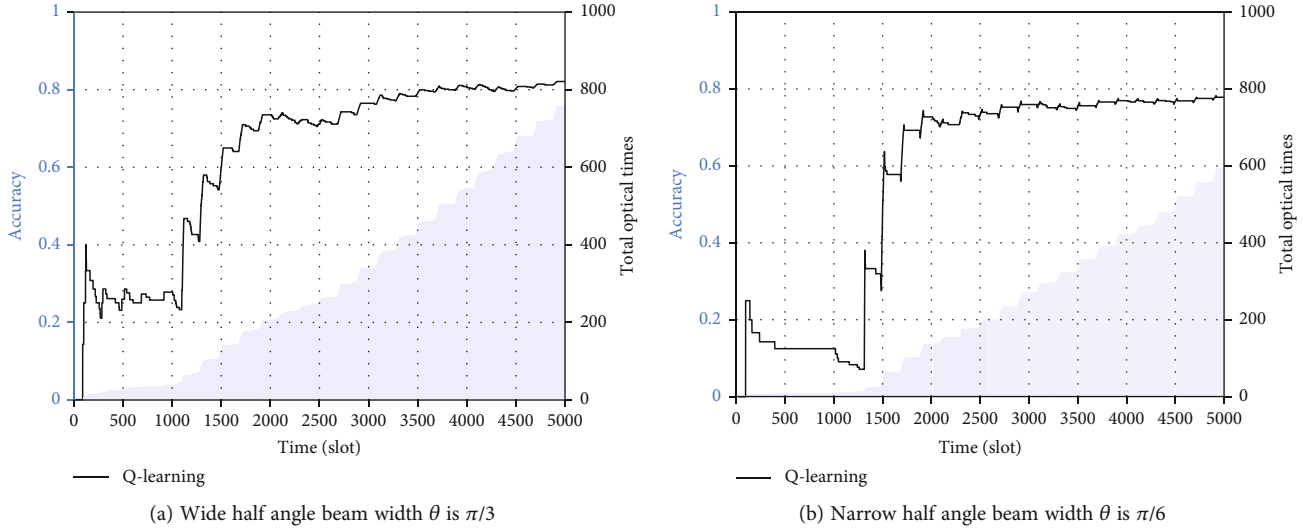
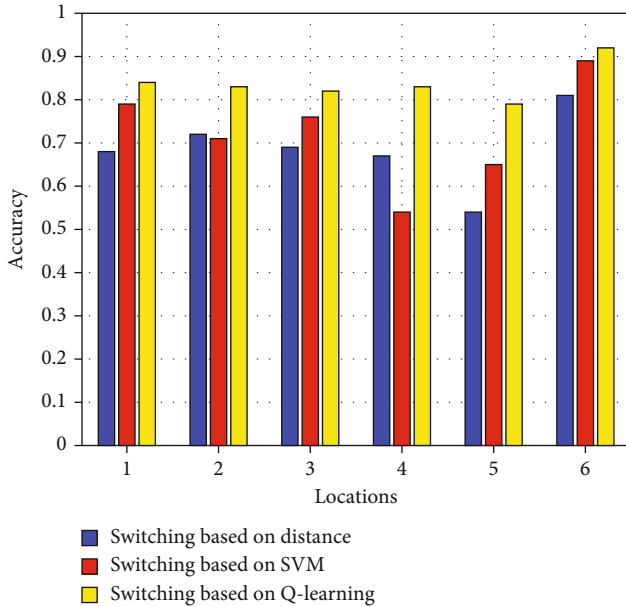
FIGURE 10: The convergence of Q-learning process with the varying half angle beam width θ .

FIGURE 11: The comparison of the proposed method with other switching methods.

the actual states are generally match the estimated states, especially when there is no optical measured values.

The effectiveness of the Q-learning process is simulated and analyzed, and the corresponding results are shown in Figure 10. The accuracy is defined as the ratio of the successful switching time to the total switching trials. The initial learning rate δ is set to 0.01, and the reward discount γ is 0.7. When the optical communication is successful, the corresponding AUV gets the reward $\chi = 1$, and the punishment is $\varphi = 0.8$ for the other case. The ϵ of the greedy strategy is initially set to 0.06, and it decreases with the increasing level of accuracy.

To compare the performance of the learning process, we set different half angles in Figures 10(a) and 10(b) to

evaluate the convergence process of Q-function. Overall, Figure 10 shows that the accuracy of the switching scheme has significant improvement with the increasing training rounds. During the beginning stage of the training process, the optical communication delay becomes less due to the few number of training samples. However, after the convergence of the policy function, the optical communication delay is increasing, while the accuracy of switching policy is stabilized.

The figures also show that the half angle has an impact on the learning process. Compared to Figures 10(a) and 10(b), the narrow half angle means the shorter switching time window, and so the exploration trials at the beginning of the learning process are fewer. However, with the increasing of the training trials, the accuracy with narrow half angle converges to 80%, which is almost identical to the wide one.

Figure 11 shows the switching accuracy performance of the proposed method in yellow color compared with traditional methods which include distance-based method in blue color [41] and SVM-based switching method in red color [27]. There are six different underwater communication locations considered in our simulation which include harbor, rough sea, calm sea, calm sea with working boat, turbid waters, and clear waters corresponding to locations 1, 2, 3, 4, 7, and 8 in [27]. It is worth noting that there are different kinds of mechanical noise interference in the harbor, obvious spikes in the rough sea, fixed frequency noise in the calm sea with working boat, and large attenuation coefficient of beam in turbid water. As shown in Figure 11, the distance-based switching method is insensitive to acoustic noise but vulnerable to the turbidity of the water, and the SVM-based method depending on acoustic SNR is mainly affected by the acoustic noise. Compared to these traditional methods, our proposed method achieves more than 75% switching accuracy in all cases.

4.3. The Robustness for Switching Scheme. In this part, we evaluate the robustness of the switching scheme under

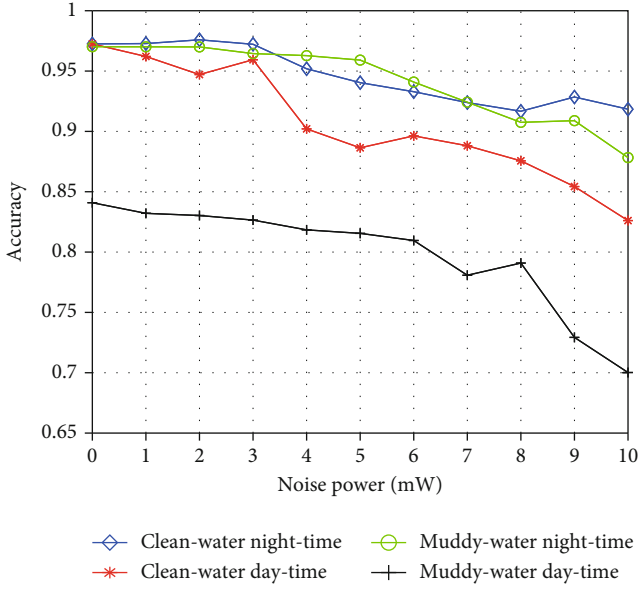


FIGURE 12: The switching accuracy under different environmental conditions.

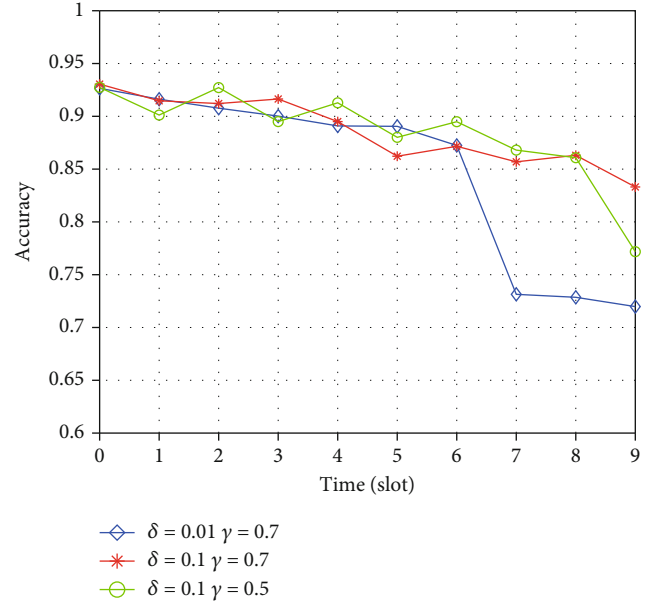


FIGURE 14: The performance under different delays, learning rates, and discount factors.

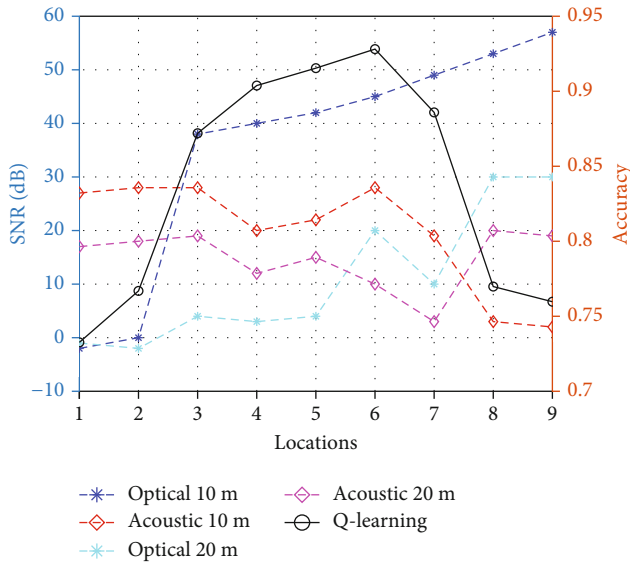


FIGURE 13: The switching accuracy under different SNR levels.

different types of water and sunlight-noise levels for realistic underwater wireless communication environments.

As the real underwater wireless communication environment is very complex, we focus on evaluating the robustness of the switching scheme under different noises and optical attenuation coefficients. The parameters related to the underwater environment are taken from the work in [42]. The simulated results are shown in Figure 12, and we can observe that the environmental noise affects the overall performance of the switching scheme. Moreover, as the radiation noise of sunlight increases, the performance of the switching scheme decreases. However, under the condition of strong noise, increasing the transmit power alleviates the

influence and thus improves the adaptivity caused by the variation of optical attenuation coefficient.

Figure 13 shows the performance of the proposed scheme under different SNR levels. The left y-axis is the value of SNR sorting the optical SNR from the smallest to the largest according to the open dataset in [27] corresponding to locations 7, 8, 4, 5, 6, 3, 2, 9, and 1, respectively. The dotted line is defined as the mean value of SNR of the acoustic and optical channels in the communication range of 10 m and 20 m. The right y-axis is the switching accuracy, and the solid line shows the performance of the proposed method. It can be seen that the switching accuracy is lower when either the acoustic or optical SNR is weak. This is because the high attenuation coefficient of the optical channel can lead to transmission link instability, while the low acoustic SNR can lead to poor estimation of the optical channel. Overall, the proposed method has a good performance under different SNR levels.

The learning process generally involves the optical alignment procedure, and as the alignment process of the optical system needs a certain duration of time to perform the task, it requires the switching scheme to remain effective for that duration of time. Therefore, the time delay caused by the alignment procedure affects the successful ratio of the switching. As shown in Figure 14, the time tolerance of the Q-learning-based strategy is tested with a greedy coefficient of 0.01, and the average value of the accuracy is calculated with different time delays, learning rates, and discount factors. As depicted in the figure, the larger time delay leads to less belief in the past experience, which implies that a larger learning rate has a better time tolerance. Since the discount factor indicates the weight to the future reward, as shown in the figure, a large discount factor γ has a better adaptation to time delay.

5. Conclusions

In this paper, we proposed an adaptive switching scheme for the underwater AUV-based acoustic-optical hybrid mobile network while combining the long-range but low-rate acoustic and the high-rate but short-range optical communications. In this scheme, we leveraged a RL-based method and the EKF tool to improve the adaptivity of the switching method. In response to the challenge associated with the intermittent feature of the optical channel, a blind estimation method based on EKF was proposed to estimate the optical channel state using the acoustic channel measurement. To deal with the harsh ocean environments, in the scheme, the relationship between the acoustic and optical channels, the channel variations and the mobility of the AUVs were considered and integrated into the learning process of the agent. We also conducted numerous simulations to verify the effectiveness and robustness of the proposed switching algorithm by considering the AUV speed, the environmental noise, the half angle beam width, and the optical alignment delay. In the future, we will apply multi-agent RL techniques in the switching scheme to improve the overall throughput further.

Data Availability

The data used to support the findings of this study are included within the article.

Conflicts of Interest

The authors declare that they have no conflicts of interest.

Acknowledgments

This work was supported in part by the Shandong Provincial Natural Science Foundation, China under Grant ZR2020MF059, in part by the China NSFC under Grant 62072287, and in part by the Scientific Research Foundation of Shandong University of Science and Technology for Recruited Talents under Grant 2019RCJJ011.

References

- [1] H. Luo, K. Wu, R. Ruby, Y. Liang, Z. Guo, and L. M. Ni, "Software-defined architectures and technologies for underwater wireless sensor networks: a survey," *IEEE Communications Surveys & Tutorials*, vol. 20, no. 4, pp. 2855–2888, 2018.
- [2] H. Luo, J. Wang, B. Fanfeng, R. Ruby, K. Wu, and Z. Guo, "Recent progress of air/water cross-boundary communications for underwater sensor networks: a review," *IEEE Sensors Journal*, pp. 1–23, 2022.
- [3] A. Peter, J. Sticklus, and A. Harlakin, "Underwater optical wireless communications in swarm robotics: a tutorial," *IEEE Communications Surveys & Tutorials*, vol. 23, no. 4, pp. 1–30, 2021.
- [4] H. Esmail, Z. A. H. Qasem, H. Sun, J. Qi, J. Wang, and Y. Gu, "Wireless information and power transfer for underwater acoustic time-reversed Noma," *IET Communications*, vol. 14, no. 19, pp. 3394–3403, 2020.
- [5] Z. A. H. Qasem, H. Esmail, H. Sun, J. Qi, and J. Wang, "Deep learning-based spread-spectrum fgsM for underwater communication," *Sensors*, vol. 20, no. 21, pp. 6123–6134, 2020.
- [6] N. Saeed, A. Celik, T. Y. al-Naffouri, and M.-S. Alouini, "Underwater optical wireless communications, networking, and localization: a survey," *Ad Hoc Networks*, vol. 94, p. 101935, 2019.
- [7] A. Celik, N. Saeed, B. Shihada, T. Y. Al-Naffouri, and M.-S. Alouini, "End-to-end performance analysis of underwater optical wireless relaying and routing techniques under location uncertainty," *IEEE Transactions on Wireless Communications*, vol. 19, no. 2, pp. 1167–1181, 2019.
- [8] R. Ruby, S. Zhong, B. M. ElHalawany, H. Luo, and K. Wu, "SDN-Enabled energy-aware routing in underwater multimodal communication networks," *IEEE/ACM Transactions on Networking*, vol. 29, no. 3, pp. 965–978, 2021.
- [9] S. Han, Y. Noh, U. Lee, and M. Gerla, "Optical-acoustic hybrid network toward real-time video streaming for mobile underwater sensors," *Ad Hoc Networks*, vol. 83, pp. 1–7, 2019.
- [10] F. Campagnaro, R. Francescon, P. Casari, R. Diamant, and M. Zorzi, "Multimodal underwater networks: recent advances and a look ahead," in *In Proceedings of the International Conference on Underwater Networks & Systems*, pp. 1–8, New York, 2017.
- [11] C. Moriconi, G. Cupertino, S. Betti, and M. Tabacchiera, "Hybrid acoustic/optic communications in underwater swarms," in *In OCEANS 2015-Genova*, pp. 1–9, Genova, Italy, 2015.
- [12] N. Farr, A. Bowen, J. Ware, C. Pontbriand, and M. Tivey, "An integrated, underwater optical/acoustic communications system," in *In OCEANS 2010 IEEE-Sydney*, pp. 1–6, Sydney, NSW, Australia, 2010.
- [13] F. Campagnaro, F. Guerra, F. Favaro et al., "Simulation of a multimodal wireless remote control system for underwater vehicles," in *In Proceedings of the 10th International Conference on Underwater Networks & Systems*, pp. 1–8, New York, 2015.
- [14] F. Campagnaro, F. Favaro, F. Guerra, V. S. Calzado, M. Zorzi, and P. Casari, "Simulation of multimodal optical and acoustic communications in underwater networks," in *In OCEANS 2015-Genova IEEE*, pp. 1–7, Genova, Italy, 2015.
- [15] D. Zhang, I. N'Doye, T. Ballal, T. Y. Al-Naffouri, M. S. Alouini, and T. M. Laleg-Kirati, "Localization and tracking control using hybrid acoustic-optical communication for autonomous underwater vehicles," *IEEE Internet of Things Journal*, vol. 7, no. 10, pp. 10048–10060, 2020.
- [16] T. Hu and Y. Fei, "Murao: a multi-level routing protocol for acoustic-optical hybrid underwater wireless sensor networks," in *In 9th Annual IEEE Communications Society Conference on Sensor, Mesh and Ad Hoc Communications and Networks (SECON)*, pp. 218–226, Seoul, Korea (South), 2012.
- [17] E. P. M. C. Júnior, L. F. M. Vieira, and M. A. M. Vieira, "Captain: a data collection algorithm for underwater optical-acoustic sensor networks," *Computer Networks*, vol. 171, no. 2020, p. 107145, 2020.
- [18] A. Celik, N. Saeed, B. Shihada, T. Y. Al-Naffouri, and M.-S. Alouini, "Opportunistic routing for opto-acoustic internet of underwater things," *IEEE Internet of Things Journal*, vol. 9, no. 3, pp. 1–15, 2021.
- [19] J. Wang, W. Shi, L. Xu, L. Zhou, Q. Niu, and J. Liu, "Design of optical-acoustic hybrid underwater wireless sensor network,"

- Journal of Network and Computer Applications*, vol. 92, pp. 59–67, 2017.
- [20] Z. A. Qasem, H. A. Leftah, H. Sun, J. Qi, J. Wang, and H. Esmail, “Deep learning-based code indexed modulation for autonomous underwater vehicles systems,” *Vehicular Communications*, vol. 28, no. 3, p. 100314, 2021.
- [21] J. Connor, B. Champion, and M. A. Joordens, “Current algorithms, communication methods and designs for underwater swarm robotics: a review,” *IEEE Sensors Journal*, vol. 21, no. 1, pp. 153–169, 2021.
- [22] C. Lodovisi, P. Loreti, L. Bracciale, and S. Betti, “Performance analysis of hybrid optical–acoustic auv swarms for marine monitoring,” *Future Internet*, vol. 10, no. 7, pp. 1–13, 2018.
- [23] N. D. Hardy, H. G. Rao, S. D. Conrad et al., “Demonstration of vehicle-to-vehicle optical pointing, acquisition, and tracking for undersea laser communications,” *In Free-Space Laser Communications SPIE*, vol. 10910, pp. 205–214, 2019.
- [24] M. Kong, Y. Guo, M. Sait et al., “Toward automatic subsea operations using real time underwater optical wireless sensor networks,” *IEEE Photonics Journal*, vol. 14, no. 1, pp. 1–9, 2021.
- [25] S. K. Shrivastava, S. Sengar, and S. P. Singh, “A new switching scheme for hybrid fso/rf communication in the presence of strong atmospheric turbulence,” *Photonic Network Communications*, vol. 37, no. 1, pp. 53–62, 2019.
- [26] S. K. Shrivastava, S. Sengar, and S. P. Singh, “On the effect of incorrect channel condition information on modified switching scheme of hybrid fso/rf system,” *IEEE Transactions on Cognitive Communications and Networking*, vol. 5, no. 4, pp. 1208–1217, 2019.
- [27] R. Diamant, F. Campagnaro, M. De Filippo De Grazia et al., “On the relationship between the underwater acoustic and optical channels,” *IEEE Transactions on Wireless Communications*, vol. 16, no. 12, pp. 8037–8051, 2017.
- [28] J. Lin, S. Wei, X. Liang, and X. Jiang, “Adaptive modulation switching strategy based on q-learning for underwater acoustic communication channel,” in *In Proceedings of the Thirteenth ACM International Conference on Underwater Networks & Systems*, pp. 1–5, New York, 2018.
- [29] S. Wei, J. Lin, K. Chen, X. Liang, and E. Cheng, “Reinforcement learning-based adaptive modulation and coding for efficient underwater communications,” *IEEE Access*, vol. 7, pp. 67539–67550, 2019.
- [30] X. Sun, C. H. Kang, M. Kong et al., “A review on practical considerations and solutions in underwater wireless optical communication,” *Journal of Lightwave Technology*, vol. 38, no. 2, pp. 421–431, 2020.
- [31] M. Stojanovic, “On the relationship between capacity and distance in an underwater acoustic communication channel,” *ACM SIGMOBILE Mobile Computing and Communications Review*, vol. 11, no. 4, pp. 34–43, 2007.
- [32] X. Zhang, W. Ying, and B. Yang, “Parameter estimation for class a modeled ocean ambient noise,” *Bandung Institute of Technology*, vol. 50, no. 3, pp. 330–345, 2018.
- [33] X. Feng, M. Zhou, X. Zhang, K. Ye, J. Wang, and H. Sun, “Variational Bayesian inference based direction of arrival estimation in presence of shallow water non-Gaussian noise,” *Journal of Electronics and Information Technology*, vol. 44, pp. 1–10, 2022.
- [34] X. Zhang, W. Ying, P. Yang, and M. Sun, “Parameter estimation of underwater impulsive noise with the class B model,” *IET Radar, Sonar & Navigation*, vol. 14, no. 7, pp. 1055–1060, 2020.
- [35] P. Wang and L. Feng, “U-filter’s Gaussianization function for interference background,” in *In 2009 International Conference on Wireless Communications & Signal Processing*, pp. 1–4, Nanjing, China, 2009.
- [36] J. Wang, J. Li, S. Yan et al., “A novel underwater acoustic signal denoising algorithm for Gaussian/non-Gaussian impulsive noise,” *Transactions on Vehicular Technology*, vol. 70, no. 1, pp. 429–445, 2021.
- [37] J. W. Giles and I. N. Bankman, “Underwater optical communications systems. part 2: basic design considerations,” in *In MILCOM 2005-2005 IEEE Military Communications Conference*, pp. 1700–1705, Atlantic City, NJ, USA, 2005.
- [38] G. Cario, A. Casavola, G. Gagliardi, M. Lupia, U. Severino, and F. Bruno, “Analysis of error sources in underwater localization systems,” in *In OCEANS 2019-Marseille*, pp. 1–6, Marseille, France, 2019.
- [39] A. Alalwan, T. Mohamed, M. Chakir, and T. M. Laleg, “Extended Kalman filter based linear quadratic regulator control for optical wireless communication alignment,” *IEEE Photonics Journal*, vol. 12, no. 6, pp. 1–12, 2020.
- [40] H. Bjørn-Olav, M. B. Eriksen, K. Y. Pettersen, and M. S. Wiig, “A modified dynamic window algorithm for horizontal collision avoidance for AUVs,” in *In 2016 IEEE Conference on Control Applications (CCA)*, pp. 499–506, Buenos Aires, Argentina, 2016.
- [41] F. Campagnaro, F. Guerra, P. Casari, R. Diamant, and M. Zorzi, “Implementation of a multi-modal acoustic-optical underwater network protocol stack,” in *In OCEANS 2016-Shanghai*, pp. 1–6, Shanghai, China, 2016.
- [42] L. J. Johnson, R. J. Green, and M. S. Leeson, “Underwater optical wireless communications: depth dependent variations in attenuation,” *Applied Optics*, vol. 52, no. 33, pp. 7867–7873, 2013.

Research Article

Research on Towed Linear Array Shape Measurement Method Based on Biorthogonal Signal

Sen Zhang , Ming-Zhi Wang , Jun Yuan , and Chen-Lin Zhou 

School of Electronic Engineering, Naval University of Engineering, Wuhan 430033, China

Correspondence should be addressed to Sen Zhang; johnson_xh@sina.com

Received 20 January 2022; Revised 15 March 2022; Accepted 18 March 2022; Published 20 April 2022

Academic Editor: Hamada Esmaiel

Copyright © 2022 Sen Zhang et al. This is an open access article distributed under the Creative Commons Attribution License, which permits unrestricted use, distribution, and reproduction in any medium, provided the original work is properly cited.

Systematic error and random error are main factors affecting the positioning of biorthogonal signal underwater positioning system. Based on the operation theory of USBL, this paper quantitatively analyzes a theoretical analysis and simulation calculations on influence of different error sources on the positioning accuracy and qualitatively analyzes the effectiveness of the towed linear array shape measurement method based on biorthogonal signal through practical experiments. By comparing the measurement effect after correction by using the measurement array with the measurement effect based on the linear array, the effectiveness of the method is verified.

1. Introduction

With the development of marine resources, underwater acoustic positioning and navigation system have received extensive attention and research. According to the length of array, it can be divided into long baseline LBL, short baseline SBL, and ultrashort baseline USBL [1]. This kind of underwater acoustic navigation and positioning system is very similar to the radio navigation system with the shore radio beacon as the reference point. The distance between the two sides is determined by measuring the phase difference and time delay between the reference point and the moving carrier, and then, the position of the moving carrier is calculated to realize the function of navigation and positioning. The advantages of long baseline are high positioning accuracy and long operating distance, but the disadvantages are high cost and difficult to place and recover. The short baseline is longer, and the positioning accuracy and operating distance of the baseline are poor, so the cost is reduced. The ultrashort baseline array has small size and convenient installation [2].

Based on the principle of ultrashort baseline positioning system, this paper analyzes the research on towed linear array shape measurement method based on biorthogonal signal, which mainly measures the influence of positioning error under different array element radius, depth error

caused by pressure sensor, attitude angle error caused by attitude sensor, and signal-to-noise ratio error in random error on positioning accuracy. This paper quantitatively analyzes a theoretical analysis and simulation calculations on influence of different error sources on the positioning accuracy and qualitatively analyzes the effectiveness of the towed linear array shape measurement method based on biorthogonal signal through practical experiments. By comparing the measurement effect after correction by using the measurement array with the measurement effect based on the linear array, the effectiveness of the method is verified.

2. Working Principle

The system consists of transmitting terminal and receiving terminal. The transmitting terminal consists of two transmitting transducers connected by rigid connection and two transmitting transducers to launch different orthogonal signal at the same time; a receiving transducer is used as the receiver to receive the two signals, by processing the separation and obtaining the time delay between the signal and phase difference. Thus, the azimuth of the receiver relative to the transmitter is obtained. Then, measure the distance between the transmitting terminal and the receiving terminal (the depth difference between the transmitting terminal

and the receiving terminal can be obtained with the help of the depth sensor), and the position of the receiving terminal relative to the transmitting terminal can be obtained.

Set A and B as two transmitting array, take the connecting line between them as the x -axis, the midpoint between them as the origin O , and the vertical downward as the z -axis, and establish the coordinate system as shown in Figure 1. T is the target terminal, and $[x, y, z]$ is its coordinates. The receiver terminal T with the launch of the distance between A and B , respectively, is R_A and R_B , the distance between the origin O , and the target terminal T is R . The angle between attachment OT and X axis is α , and the angle between the ABT plane and the XOY plane is β [3–5].

Assuming that the located target end meets the far-field assumption conditions, then:

$$\cos \alpha = \frac{R_{BA}}{L} = \frac{t_{BA}c}{L}, \quad (1)$$

where L is the interval between the array elements, d is the radius of the element, $R_{BA} = R_B - R_A$ is the range difference between the two transmitting terminal and the positioning target terminal T , t_{BA} is the corresponding propagation time difference, and c is the sound speed. The coordinates of the targeted terminal T are as follows:

$$\begin{cases} x = R \cos \alpha, \\ y = R \sin \alpha \cos \beta, \\ z = R \sin \alpha \sin \beta. \end{cases} \quad (2)$$

When t is the propagation time of acoustic wave propagating from the origin O to the targeted terminal T , then $R = c * t$; at this point, the x -axis coordinate of t point is

$$x = R \cos \alpha = c^2 t \frac{t_{BA}}{2d}. \quad (3)$$

The depth z of the target terminal to be located is measured by the depth sensor, set $z = D$, and then:

$$\sin \beta = \frac{D}{R \sin \alpha}. \quad (4)$$

After simplification, the coordinate value of T can be solved:

$$\begin{cases} x = c^2 t \frac{t_{BA}}{2d}, \\ y = \sqrt{c^2 t^2 - x^2 - D^2}, \\ z = D. \end{cases} \quad (5)$$

According to trigonometry, the distance between the target terminal and the origin of coordinates can be expressed as follows:

$$R = \frac{1}{2} \sqrt{2R_A^2 + 2R_B^2 - 4d^2}. \quad (6)$$

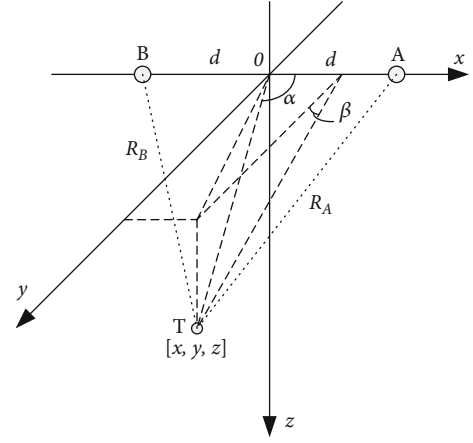


FIGURE 1: Principle of ranging and positioning.

At this point, the propagation delay can be expressed as follows:

$$t = \frac{R}{c} = \frac{1}{2} \sqrt{2t_A^2 + 2t_B^2 - \frac{4d^2}{c^2}}. \quad (7)$$

3. System Composition

The system consists of transmitter and receiver, as shown in Figure 2. The transmitter is located on the towed body and consists of transducer array, transmitter subsystem, and attitude measurement subsystem. The receiving terminal is located on the ship and consists of towed line array subsystem and receiving and processing subsystem. The time synchronization between the transmitter and the receiver is realized by the synchronization clock module [3].

3.1. Control and Processing Center. The control and processing center mainly performs the following functions: (1) receive PPS and UTC clock data output by GPS receiver, synchronize with internal thermostatic crystal oscillator, and maintains its own time; (2) read the attitude sensor data, add the time stamp, and save it; (3) generate two channel phase coded signals and output them to the power amplifier; and (4) the attitude sensor data and temperature and depth sensor data stored in the control center can be read externally through Ethernet.

3.2. Power Amplifier. The power amplifier mainly performs the following functions: (1) power amplification of the transmitted signal generated by the signal source; and (2) complete the impedance matching with the transmitting transducer.

3.3. Transmitting Transducer Array. The transmitting terminal is composed of two transmitting transducers through rigid connection, and the two transmitting transducers simultaneously emit different orthogonal signals.

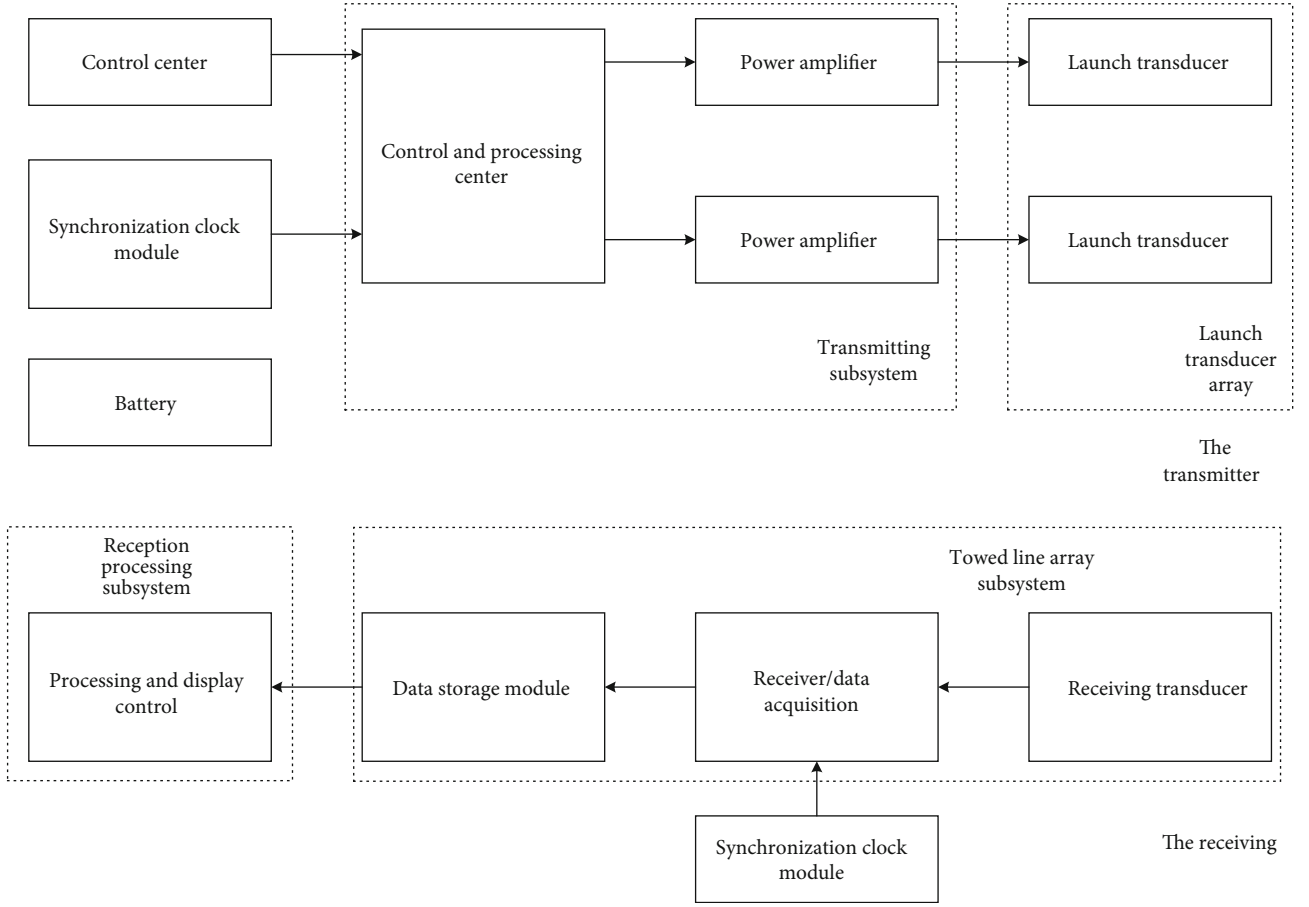


FIGURE 2: Schematic diagram of transmitter and receiver.

3.4. Receiving Terminal. The receiver terminal amplifies and filters the received weak electrical signal. The synchronization clock generates the trigger clock at the agreed time (i. e., the launch time), which triggers the data acquisition unit to start collecting. The data acquisition module converts analog signals into digital signals and sends them to the data storage module for storage. The data storage module contains gigabit Ethernet ports. After being reclaimed, the data stored on the data storage module is read through gigabit Ethernet ports and processed offline.

4. Positioning Error Analysis

4.1. System Error. Systematic error is caused by factors that are fixed or change according to a certain law. Under the same measurement conditions, this law can be repeated and expressed by functions or curves in principle.

Firstly, the positioning error in the horizontal direction is analyzed and obtained from Equation (3):

$$x = c^2 t \frac{t_{BA}}{2d}, \quad (8)$$

where t is the propagation delay from the transmitting terminal to the receiving terminal and the synchronous

ranging method is adopted in this paper and is the one-way time difference. Let us differentiate both sides completely,

$$\Delta x = \frac{ctt_{BA}}{d} \Delta c + \frac{c^2 t_{BA}}{2d} \Delta t + \frac{c^2 t}{2d} \Delta t_{BA} - \frac{c^2 t t_{BA}}{2d^2} \Delta d. \quad (9)$$

Similarly, the positioning error of the y -axis can be obtained:

$$\Delta y = \frac{ct^2 \Delta c}{\sqrt{c^2 t^2 - x^2 - D^2}} + \frac{c^2 t \Delta t}{\sqrt{c^2 t^2 - x^2 - D^2}} - \frac{x \Delta x}{\sqrt{c^2 t^2 - x^2 - D^2}} - \frac{D \Delta D}{\sqrt{c^2 t^2 - x^2 - D^2}}. \quad (10)$$

The depth information D of z -axis can be obtained from the pressure sensor:

$$\Delta z = \Delta D. \quad (11)$$

As for the positioning of the receiving terminal, the total position error is caused by the errors in the three directions of x -axis, y -axis, and z -axis, so the relative deviation is

$$\frac{\Delta P}{R} = \sqrt{\left(\frac{\Delta x}{R}\right)^2 + \left(\frac{\Delta y}{R}\right)^2 + \left(\frac{\Delta z}{R}\right)^2}. \quad (12)$$

According to Equations (9)–(12), the main error sources are sound velocity error, delay measurement error, array element radius error, and depth measurement error caused by array installation.

After the array is installed and fixed, the radius error caused by the array installation can be ignored. At present, the sound velocity error can usually be controlled within 0.1% distance, so it has little influence. However, the phase measurement error caused by sound bending depends on the sound velocity structure in the operation area and is mainly caused by the temperature density change of water in the sound propagation path [6, 7]. In the simulation experiment, it is assumed that the sound velocity is constant, which is 1500 m/s. According to Equations (9)–(12), the larger the radius of the array element is, the smaller the mean square positioning error is. However, the radius of the array element should be controlled according to the actual needs. The depth error generated by the pressure sensor can be seen from Equation (11), which will have an impact on the positioning error, mainly determined by the performance parameters of the pressure sensor.

In addition to acoustic positioning errors, joint transmitter attitude information is required in the conversion to the geodetic coordinate system. The attitude angle error generated by the attitude sensor causes the deviation of the array coordinate system, which need to be converted into actual coordinates through the rotation matrix, as shown in the following formula [8–10]:

$$P = \begin{bmatrix} \cos \theta & -\sin \theta & 0 \\ \sin \theta & \cos \theta & 0 \\ 0 & 0 & 1 \end{bmatrix}^{-1} [x^* \ y^* \ z^*]. \quad (13)$$

In Equation (13), P is the actual coordinate, α is the attitude angle error, and $[x^*, y^*, z^*]$ is the measured coordinate without attitude angle error. The change of attitude angle error will affect the positioning error.

4.2. Random Error. The random error mainly includes delay measurement error and phase measurement error caused by noise. The timing error consists of clock error and pulse front measurement error. The clock error is very small and can not be considered. The measurement error of pulse front is caused by ocean noise and related to SNR.

Δt , the error caused by time delay measurement, and as can be known from signal detection and estimation knowledge, the time delay measurement error through correlation processing is

$$\Delta t \approx \frac{1}{2\pi f_0 \sqrt{BT} \sqrt{SNR}}, \quad (14)$$

where B is the transmitted signal bandwidth (Hz), SNR is the signal-to-noise ratio, and T is the duration. Since acoustic

wave propagation can be regarded as spherical expansion, SNR approximation is inversely proportional to the square of the distance under the condition of constant transmitting power; then, \sqrt{SNR} approximation is inversely proportional to the distance. Δt can be approximately regarded as proportional to distance change, while $1/t$ is inversely proportional to distance change. The combination of the two can approximately offset the error effect caused by propagation loss in distance variation. Therefore, the error of time delay measurement is mainly determined by the center frequency of the system. The farther the distance is, the greater the error is (SNR decreases due to the propagation loss). At present, the relative error of experimental measurement can be controlled within 0.1%, so the influence is not significant [10].

For the phase measurement error, the optimality of the estimated value can be determined by using the Cramer-Rao lower bound:

$$\Delta \varphi \approx \frac{1}{\sqrt{SNR}}. \quad (15)$$

It can be seen from Equation (15) that the phase measurement error is inversely proportional to the square root of SNR. The effective method to improve the phase measurement accuracy is to improve SNR. It is more advantageous to use lower frequency and broadband signal. Therefore, the greater the noise in the propagation process of underwater acoustic signal, the greater the random error of measurement. Improving SNR can effectively reduce the influence of ocean noise on measurement results and improve the performance of the whole system.

In this paper, the experimental system error mainly considers the array radius error caused by the array installation, the depth error caused by the pressure sensor, and the attitude angle error caused by the attitude sensor.

5. Simulation Analysis of Positioning Error

In this section, the influence of different error sources on positioning accuracy was compared by simulation. The MATLAB 2016a software was used for simulation. The specific simulation environment was $z = 300$ m at the receiving terminal, SNR was 20 dB, and the influence on positioning accuracy of the system when the array element radius changed within the range of 0.5–3 m was considered. We used Monte Carlo method to calculate the radius error of each element 100 times. When the receiver was at different positions (100,600) and (200,600), the mean square positioning error changed with the radius of array element, as shown in Figure 3.

Considering the influence of attitude angle error on positioning accuracy of the system when it varied within 0–0.2°, when the receiver was at different positions (100,600) and (200,600), the change of the mean square positioning error with attitude angle error was shown in Figure 4.

Considering that the depth measurement error z varies between 0 and 0.1 m, when the receiving terminal is at different depths, namely, $z = 300$ m and $z = 500$ m, the change of

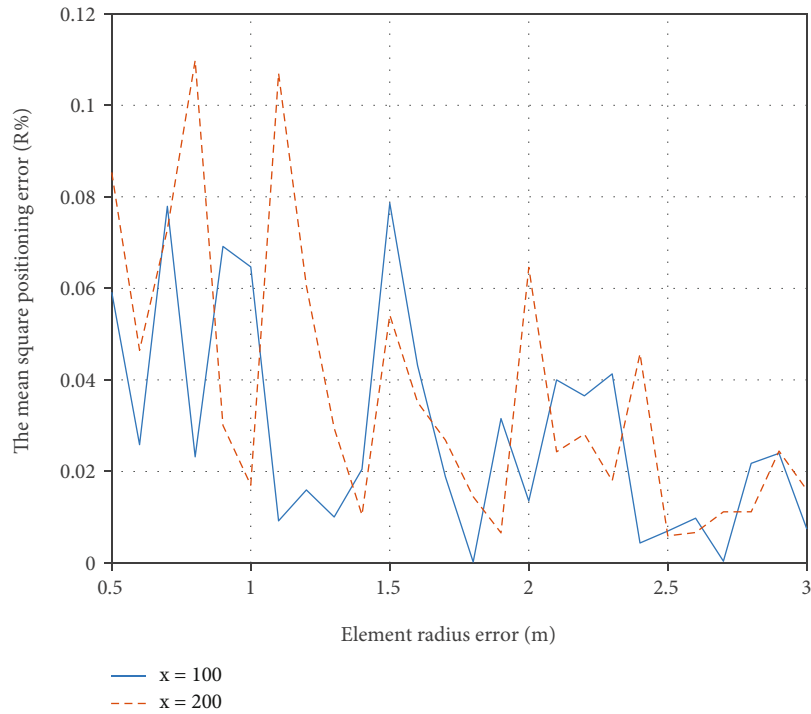


FIGURE 3: Element radius error.

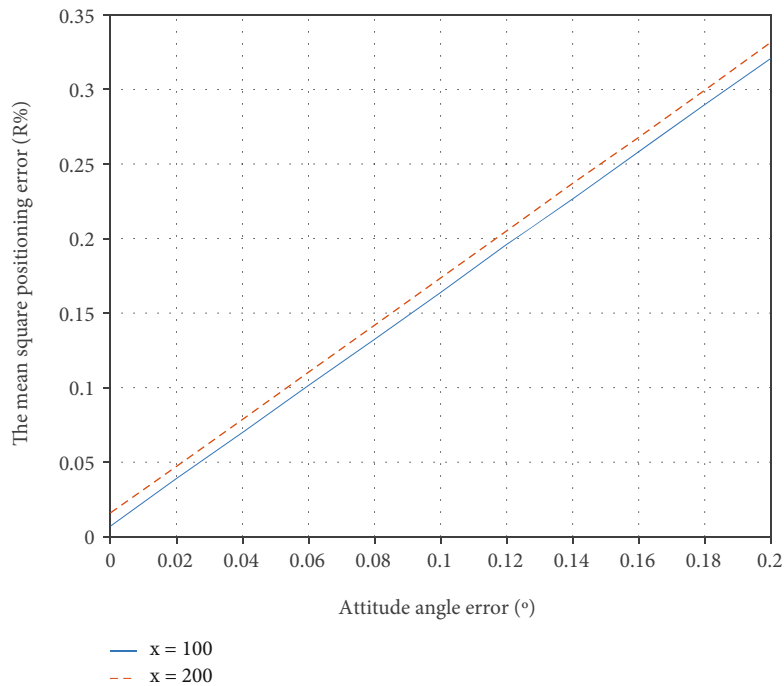


FIGURE 4: Attitude angle error.

the mean square positioning error with depth measurement error is shown in Figure 5.

Similarly, when the SNR error varies within the range of -5-20 dB, the influence on the positioning accuracy of the system is considered. When the receiver is at different positions (100,600) and (200,600), the change of the mean

square positioning error with the SNR error is shown in Figure 6.

As shown in Figure 3, in the general trend, the mean square positioning error gradually decreases as the radius error of array element increases, and the error is less than 0.1%. Due to the influence of signal coherence, the error will

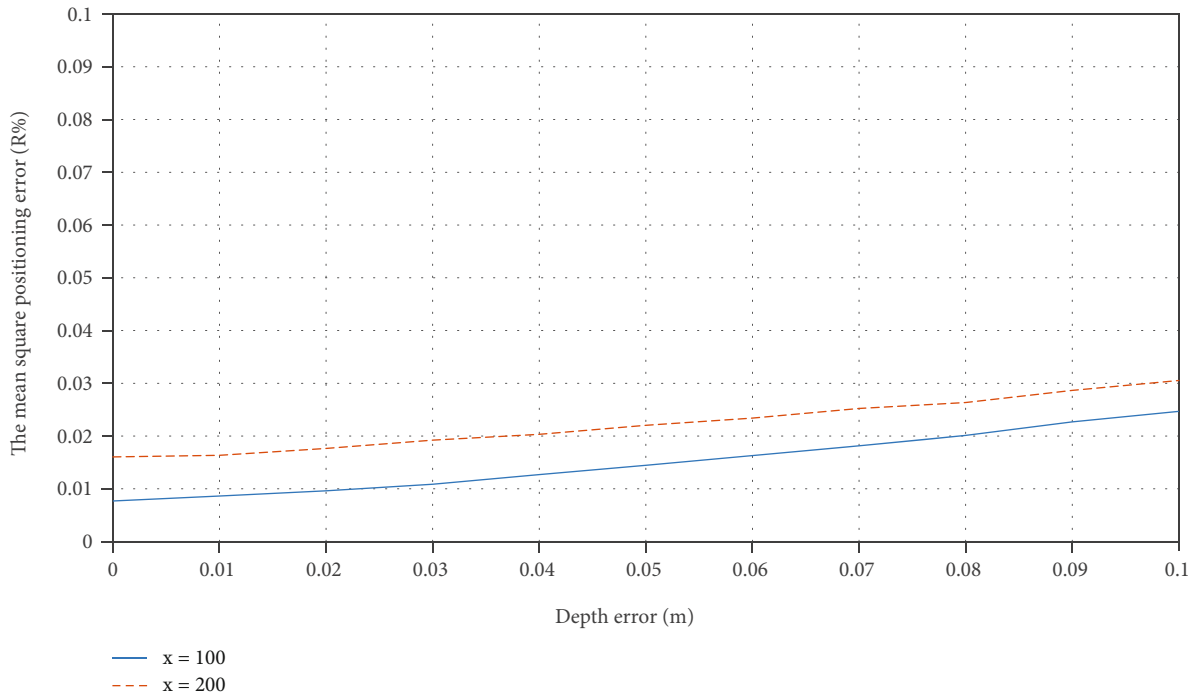


FIGURE 5: Depth error.

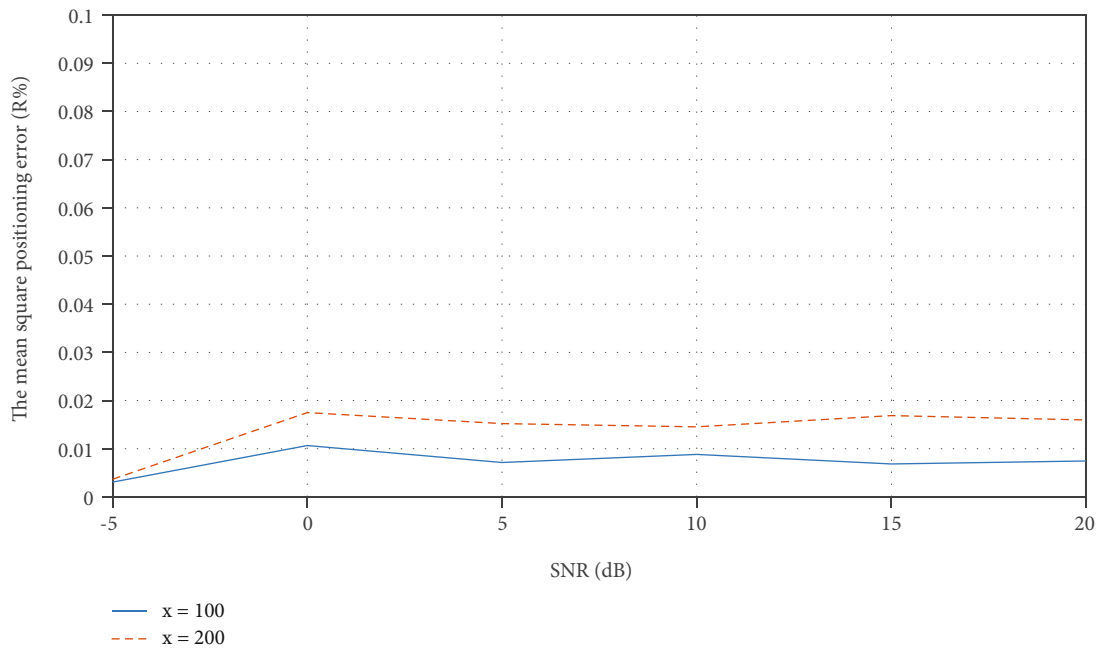


FIGURE 6: SNR error.

show certain ups and downs when the receiver is at different positions. As shown in Figure 4, the mean square positioning error increases with the increase of attitude angle error, showing an approximate linear relationship. As shown in Figure 5, the mean square positioning error increases as the depth measurement error increases, and the mean square positioning error does not exceed 0.03%. As shown

in Figure 6, the mean square positioning error tends to be stable with the increase of SNR. The main reason is that the positioning signals are multiple orthogonal signals with large time broadband and wide product. At a certain SNR, the cross-correlation sidelobe level signal is higher than the noise signal after matched filtering, so the change of SNR has little influence on the positioning error.

TABLE 1: Towed body roll angle and inclination angle data.

	Amount of data	Average	Standard deviation	Minimum value	Median	Maximum
Inclination angle	205153	5.21631	1.06777	8.63	5.36	0.94
Roll angle	205153	1.1049	0.40981	0.56	1.09	2.7

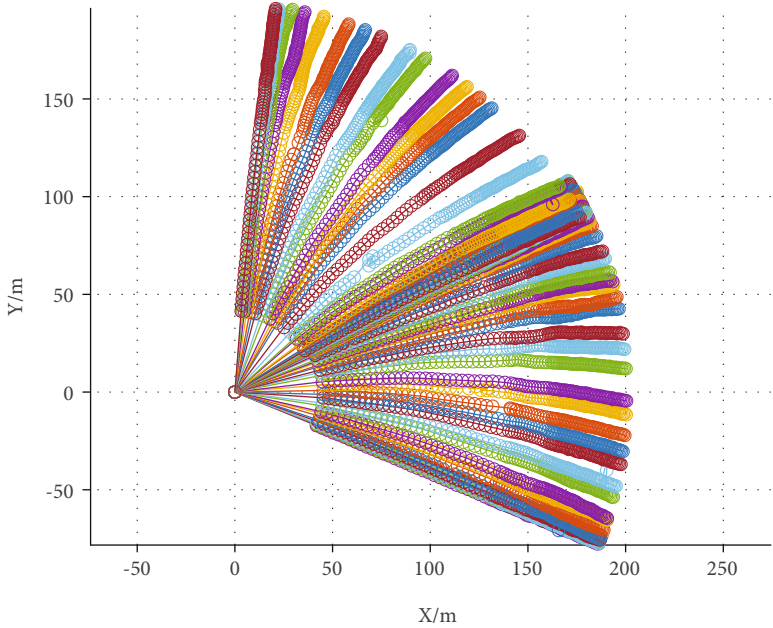


FIGURE 7: Formation measurement results during sea test.

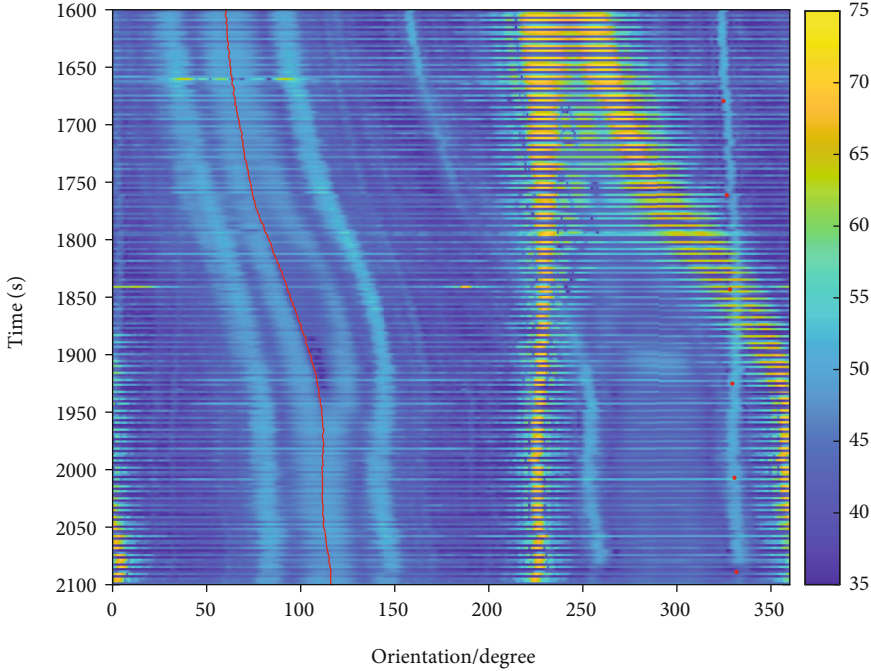


FIGURE 8: Process diagram after array correction by measuring array.

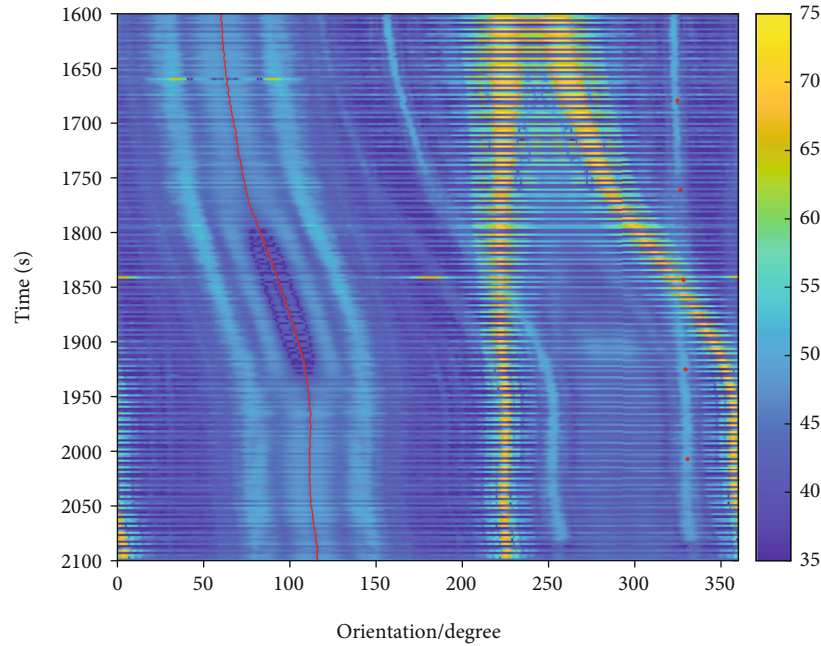


FIGURE 9: Process diagram based on linear array.

6. Positioning Test Certificate

In April 2021, sea trials were carried out in the South China Sea in four stages: launching of the towed vehicle, operation stability test of towed vehicle under different ship speed, operation stability test of towed body and receiving array cable, and measurement test of towed line array under maneuvering steering condition of towed body cable.

The test of the towed body under the condition of maneuvering steering of the cable was conducted for 348 minutes in total. After entering the water for 20 minutes, the towed body gradually dived to a depth of 27 m and continued to run at a depth of about 27 m for about 130 min. The heading gradually changed from 180° to about 0° . From the 150th minute, the dive reached a depth of about 35~40 m, and the operation lasted for 200 min. The heading gradually changed from 0° to -180° , completing a circle. In the stable operation stage, the roll angle and inclination angle of the towed body changed in a small range, as shown in Table 1.

During the sea test in South China Sea, the measurement formation was shown in Figure 7 during the turning process.

It can be seen from Figure 7 that the spacing of array elements is obviously different, which is consistent with the actual situation. At the same time, it can be clearly seen that the dragging array turns from the left side of the array to the right side of the array during the steering process, which is consistent with the dragging state.

It can be seen from Figures 8 and 9 that the red line is the heading of the towboat, which turns from 58° to 113° (about 50°) within 500 s. The red point is the heading of the target ship measured by GPS. As shown in Figure 9, when using linear array for beamforming, the heading course of the target is blurred and divergent. As shown in Figure 8, after cor-

rection, the target is more concentrated and can achieve accurate and steady direction finding in the process of turning.

7. Conclusion

To sum up, the error of attitude sensor has a great impact on the measurement accuracy and limit the positioning accuracy of the system. At present, the heading measurement error of the fiber optic inertial navigation sensor is usually about 0.1° , so the overall positioning accuracy is about 0.2% slant distance. At the same time, the experiment proves that the technique of using orthogonal signal to measure the formation is feasible, which can measure the position of each element of the line array effectively in the state of dragging.

The experiment still has the following deficiencies:

- (1) In the actual experiment in the South China Sea, due to the difficulty of controlling different influence sources, the effectiveness of the experiment can only be qualitatively analyzed by comparing the measurement effect after correction by using the measurement array with the measurement effect based on the linear array. The influence of different error sources on positioning accuracy is quantitatively analyzed through simulation experiments
- (2) In order to measure real-time data, we need to install a measuring device on the towed cable, so it will have an impact on the layout and salvage process of the towed cable

We will continue to improve relevant experiments in the follow-up work.

Data Availability

The equipment data used to support the findings of this study have not been made available because the equipment data belongs to the confidentiality requirements of Naval University of engineering, Wuhan.

Conflicts of Interest

The authors declare that they have no conflicts of interest.

References

- [1] T. Jiang, "Analysis and simulation of positioning error in ultra-short baseline positioning system," *Mine Warfare & Ship Self-Defence*, vol. 4, 2012.
- [2] Y. Han, C. Zheng, and D. Sun, "A high precision calibration method for long baseline acoustic positioning systems," *Chinese Journal of Acoustics*, vol. 4, pp. 489–500, 2017.
- [3] S. Zhang, J. Guo, and Z. Tian, "An underwater navigation system based on multi-orthogonal signals and its lake trial," in *2017 IEEE 17th International Conference on Communication Technology (ICCT)*, Chengdu, China, 2017.
- [4] S. Zhang, J. Guo, and W. U. Yuanyuan, "Calibration algorithm for underwater navigation system based on Rodrigues matrix transformation," *Acta Armamentarii*, vol. 41, no. 2, p. 8, 2020.
- [5] J. Guo and S. Zhang, "Research on CRLB for position calibration of underwater navigation system with multiple orthogonal signals," *Ship Electronic Engineering*, vol. 39, no. 4, p. 5, 2019.
- [6] Q. H. Tang, Y. T. Wu, J. S. Ding, L. Yang, and Y. X. Liu, "Calibration of ultra-short baseline acoustic positioning system," *Technical Acoustics*, vol. 25, 2006.
- [7] C. H. Tian, "Error analysis and experiment of USBL positioning," *Journal of Waterway and Harbor*, vol. 36, 2015.
- [8] H. C. Sui, C. H. Tian, D. Z. Han, and C. M. Wang, "Error analysis of underwater positioning system," *Journal of Waterway & Harbor*, vol. 31, 2010.
- [9] S. L. Zhang, "Applied of Rodrigues matrix on rigorous solution to collinear equation," *Journal of Wuhan Technical University of Surveying and Mapping*, vol. 1, pp. 81–91, 1987.
- [10] W. U. Yuanyuan, S. Zhang, and J. Guo, "Calibration algorithm of underwater navigation system based on Gauss-Newton algorithm," *Ship Electronic Engineering*, vol. 38, no. 11, 2018.

Research Article

Sensor Selection for Hybrid AOA-TOA Localization with Correlated Measurement Noise in Underwater Wireless Sensor Networks

Rongyan Zhou,^{1,2} Jianfeng Chen ¹, Weijie Tan ³, Haobo Yuan,⁴ and Chang Cai¹

¹School of Marine Science and Technology, Northwestern Polytechnical University, Xi'an 710072, China

²School of Information Engineering, Nanyang Institute of Technology, Nanyang 473004, China

³Guizhou Big Data Academy, Guizhou University, Guiyang 550025, China

⁴School of Engineering, University of South Australia, Adelaide 5095, Australia

Correspondence should be addressed to Jianfeng Chen; chenjf@nwpu.edu.cn

Received 2 October 2021; Revised 25 November 2021; Accepted 23 March 2022; Published 11 April 2022

Academic Editor: Hamada Esmail

Copyright © 2022 Rongyan Zhou et al. This is an open access article distributed under the Creative Commons Attribution License, which permits unrestricted use, distribution, and reproduction in any medium, provided the original work is properly cited.

Underwater target localization is the most crucial part of the underwater wireless sensor network (UWSN). Due to limited communication range and energy constraints in underwater scenarios, only a subset of sensors can be selected to localize. This paper investigates the sensor selection schemes for hybrid angle-of-arrival (AOA) and time-of-arrival (TOA) localization in the underwater scenario. We first develop the Cramér-Rao lower bound (CRLB) for the hybrid AOA-TOA localization with correlated measurement noise model with Gaussian priors, and a Boolean vector is introduced to denote the selected sensors for hybrid measurement. Secondly, the sensor selection schemes are formulated as an optimization problem, and the optimality criterion is to minimize the trace of CRLB. The original nonconvex problem has been modified to the semidefinite problem program (SDP) by convex relaxation, and then, a randomization algorithm is chosen to advance the result of the SDP method. Finally, simulations verify that the proposed algorithm approaches the exhaustive search algorithm, and the effect of correlated measurement noise on the estimation performance in the hybrid localization system is proved.

1. Introduction

Target localization technology plays a significant role in marine target detection and tracking, marine environment monitoring, underwater vehicle navigation, etc. [1, 2]. However, owing to the limitations are high power consumption, severe propagation delay, and so on [3–6]; it is not feasible to active all sensors to localize or track the unknown target in the underwater wireless sensor network (UWSN). Thus, the problems of sensor selection for target localization in UWSN have been considered; the goal is to make a compromise solution between the localization estimation accuracy and the best subset of activated sensors [7, 8].

Several localization methods have been developed using different localization measurements, e.g., time-difference-of-arrival (TDOA) or time-of-arrival (TOA) [9], angle-of-arrival (AOA) [10], received signal strength (RSS) [11],

and frequency difference of arrival (FDOA) [12]. The AOA-based and TOA-based localization are the most popularly used ones. The AOA-based localization can be easily obtained using triangulation approaches, but the estimation accuracy is lower than the TOA localization. A reduced-complexity algorithm based on a pseudo maximum likelihood (ML) estimation is presented in [13]; an AOA-based mechanism that associates the line-of-sight (LOS) over time for a given trial location was described. Recently, a novel AOA-based approximately unbiased estimation is derived by using semidefinite relaxation (SDR) in [14]. In contrast, the TOA can achieve better localization performance when the high-precision timing measurements are acquired [15]. In [16], a new algebraic localization method was derived based on a minimum number of localization measurements. On this basis, an optimal linear unbiased estimator is designed to calculate the final position estimation.

Extensive research has been conducted to investigate the sensor selection schemes in [17–21]. Generally, sensor selection schemes are transformed as an optimization issue by using different optimality criterion. Two frequently used optimization criteria are minimizing the trace of Cramér-Rao lower bound (CRLB) (A-optimality criterion) and maximizing the determinant of the Fisher information matrix (FIM) (D-optimality criterion). On this basis, the scheme of sensor selection is transformed into an integer programming (IP) scheme with an optimization variable. However, owing to the IP scheme is an NP-hard scheme. The direct way to acquire the best sensor subset is the exhaustive search algorithm, which has high computational complexity and does not apply to broad sensor networks. For these reasons, several suboptimal algorithms have been presented to deal with the sensor selection schemes.

The sensor selection scheme was formulated based on minimizing the log-determinant of the estimated error covariance matrix, and the convex relaxation was adopted to solve the problem in [17]. The authors proposed a sparsity-promoting method by minimizing the number of sensors to be selected with the limitation of the estimation performance in [18]. Thus, the original nonconvex optimization issue can be transformed to a sparse vector design scheme. The problem of sensor scheduling in the linear system with correlated measurement noise was presented in [19], which was transformed to minimize the trace of the inverse of the Bayesian FIM. Recently, the sensor selection issue for TDOA-based localization was formulated by minimizing the trace of CRLB and two independent Boolean vectors as the selected reference sensors and ordinary sensors in [20]. The convex relaxation methods are utilized to formulate the nonconvex problem as an SDP. The two suboptimal sensor selection algorithms were designed for DOA-based and TOA-based localization algorithms to minimize the trace of CRLB, which only used one Boolean vector as the optimization variable in [21]. Both of the nonconvex problems were relaxed as convex SDP.

In the literature mentioned above, sensor selection schemes usually utilize only one kind of measurement. The key to locating a target is obtaining sufficient measurement from the multiple sensors to improve estimation accuracy. Therefore, an intuitive method, known as hybrid measurements, has attracted considerable attention recently [22, 23]. Besides, since the underwater channel has the features of low communication channel bandwidth, serious multipath effect, and variable acoustic velocity [24], it is necessary to improve the localization performance using the hybrid localization method. Plenty of hybrid target location methods are implemented based on different combinations of mixed measurements, e.g., TDOA-RSS, AOA-TOA, and RSS-AOA [22, 23, 25–28]. The authors derived the CRLB for the hybrid method using both AOA and TOA estimates in [25]. Lately, a joint TOA and AOA estimator was proposed for UWB indoor ranging under LOS operating conditions [26]. In [27], the authors focus on the energy-efficient localization strategy using hybrid TOA/AOA measurements, and a joint resource allocation and an antenna selection framework were presented to minimize the estimation error. In

[28], the authors extend the sensor selection method to a mixed TDOA and AOA localization scenario with the presence of sensor location error. However, the sensor selection schemes with correlated noise measurement were little considered in the above literature due to the FIM being a non-linear function. Besides, the FIM becomes more complicated by using more types of measurements. Therefore, the sensor selection problems for the hybrid measurements with correlated noise in UWSN are nontrivial tasks. Moreover, the inaccurate sensor locations can also cause a considerable reduction of localization accuracy, which should be considered in the sensor selection schemes.

This paper investigates sensor selection strategies for hybrid AOA-TOA-based localization in underwater scenario. The key contributions are summarized as follows:

- (1) The CRLB for the hybrid AOA-TOA cooperative localization measurement model is presented for Gaussian priors, and one Boolean vector is used for the expressions of sensor selection scheme with the hybrid AOA-TOA measurement under correlated measurement noise
- (2) To mitigate the localization error caused by uncertainty in sensor locations, a calibration source with precisely known location is introduced. The sensor selection scheme is formulated by a nonconvex optimization problem based on minimizing the trace of CRLB, and the convex relaxation techniques are adopted to transform the original problem as SDP problem. Besides, a randomization algorithm is also approved to improve the result

The rest of this paper is organized as follows: In Section 2, the CRB for the hybrid AOA-TOA-based localization is derived, and sensor selection scheme is formulated. Section 3 investigates the method to reduce the sensor location error and then transform the original scheme to the nonconvex optimization schemes. The convex relaxation and a randomization algorithm are developed to solve the sensor selection problems in Section 4. The comprehensive simulation results are presented in Section 5. Finally, Section 6 is devoted to our conclusions and future research directions.

2. Problem Formulation

This section introduces the hybrid AOA-TOA measurement model and the CRLB for the hybrid AOA-TOA-based localization in UWSN, and the sensor selection scheme is introduced.

2.1. The Hybrid AOA-TOA Measurement Model. We consider a two-dimensional underwater scenario composed of multiple sensors with known locations and an unknown stationary target. Assuming that the unknown target follows a given prior probability density function (PDF) $\mathbf{p} \sim \mathcal{N}(\mathbf{p}_0, \mathbf{C}_0)$, where \mathbf{p}_0 and \mathbf{C}_0 are the mean and covariance matrix of \mathbf{p} . The unknown target location is $\mathbf{p} = (p_x, p_y)^T$, and the k th mutiple sensor is $\mathbf{s}_k = (s_{xk}, s_{yk})^T, k = 1, \dots, N$. Each

multiple sensors can achieve the hybrid AOA and TOA measurements. Consequently, the hybrid measurement can acquire an estimator for the unknown target. The calibration source is located at $\mathbf{c} = (c_x, c_y)^T$, which is utilized to correct the sensor location errors.

The k th sensor has the measurement model as follows:

$$\tilde{z}_k = z_k + \alpha_k = f_k(\mathbf{p}, \mathbf{s}_k) + \alpha_k, \quad (1)$$

and $f_k(\mathbf{p}, \mathbf{s}_k)$ denotes a nonlinear measurement model with \mathbf{p} and \mathbf{s}_k . We assume that the measurement noise is α_k .

Stacking \tilde{z}_k for $k = 1, \dots, N$. The vector form of the above (1) is

$$\tilde{\mathbf{z}} = \mathbf{z} + \alpha, \quad (2)$$

with

$$\begin{aligned} \tilde{\mathbf{z}} &= [\tilde{z}_1, \dots, \tilde{z}_N]^T, \\ \mathbf{z} &= [z_1, \dots, z_N]^T = [f_1(\mathbf{p}, \mathbf{s}_1), \dots, f_N(\mathbf{p}, \mathbf{s}_N)]^T, \\ \alpha &= [\alpha_1, \dots, \alpha_N]^T, \end{aligned} \quad (3)$$

and we assume that α is white, Gaussian, zero-mean random vectors. Owing to the noise experienced is correlated among different sensors; the covariance matrix \mathbf{R}_α of α is a nondiagonal matrix.

Without loss of generality, different sensor types obtain different measurements and parameter expressions. Hence, we first introduce the AOA and TOA measurements, respectively.

The measurement model of AOA-based localization at the k th sensor is given [29]

$$z_k = f_k(\mathbf{p}, \mathbf{s}_k) = \tan^{-1} \frac{p_y - s_{yk}}{p_x - s_{xk}}, \quad (4)$$

and \tan^{-1} denotes the 4-quadrant arctangent; and the noisy AOA measurement of the k th sensor is $\tilde{\theta}_k$. We assume AOA measurement noise vector $\beta \sim \mathcal{N}(0, \sigma_A^2 \mathbf{R}_A)$, with σ_A^2 denoting the noise power, while $\Sigma_A = \sigma_A^2 \mathbf{R}_A$ represents the covariance matrix.

For the noisy circular-based TOA measurement of the k th sensor, we obtain [30]

$$\tilde{t}_k = t_k + l_k = \frac{\|\mathbf{p} - \mathbf{s}_k\|}{v} + l_k, \quad (5)$$

where t_k ignores the presence of distance errors, v is the signal velocity, and l_k denotes the measurement noise. Writing the range measurement equation in the (5) form gives

$$z_k = f_k(\mathbf{p}, \mathbf{s}_k) = \|\mathbf{p} - \mathbf{s}_k\|, \quad (6)$$

where $d_k = \|\mathbf{p} - \mathbf{s}_k\|$ denotes the distance of the target and sensor, and we also assume the TOA measurement noise vector $\chi \sim \mathcal{N}(0, \sigma_T^2 \mathbf{R}_T)$, with σ_T^2 denoting the noise, while $\Sigma_T = \sigma_T^2 \mathbf{R}_T$ represents the covariance matrix.

Therefore, the hybrid AOA-TOA measurement noise vector can be expressed as

$$\zeta = [\beta, \chi], \quad (7)$$

the hybrid AOA-TOA measurement noise covariance matrix with $2N$ measurements is given by

$$\begin{aligned} \Sigma &= \mathbb{E}\{\zeta\zeta^T\} = \text{diag}\left\{\mathbb{E}\{\beta\beta^T\}, \mathbb{E}\{\chi\chi^T\}\right\} \\ &= \text{diag}\{\Sigma_A, \Sigma_T\} = \text{diag}\{\sigma_A^2 \mathbf{R}_A, \sigma_T^2 \mathbf{R}_T\}. \end{aligned} \quad (8)$$

The Jacobian matrices of the N sensor for the AOA measurement errors and the TOA measurement errors can be expressed as, respectively

$$\begin{aligned} \mathbf{J}_{\text{AOA}} &= \left[\begin{array}{cc} \frac{\partial \tilde{\theta}_1}{\partial p_x} & \frac{\partial \tilde{\theta}_1}{\partial p_y} \\ \vdots & \vdots \\ \frac{\partial \tilde{\theta}_N}{\partial p_x} & \frac{\partial \tilde{\theta}_N}{\partial p_y} \end{array} \right]_{\mathbf{p}} = \left[\begin{array}{cc} \frac{-\sin \theta_1}{d_1} & \frac{\cos \theta_1}{d_1} \\ \vdots & \vdots \\ \frac{-\sin \theta_N}{d_N} & \frac{\cos \theta_N}{d_N} \end{array} \right]_{N \times 2}, \\ \mathbf{J}_{\text{TOA}} &= \left[\begin{array}{cc} \frac{\partial \tilde{t}_1}{\partial p_x} & \frac{\partial \tilde{t}_1}{\partial p_y} \\ \vdots & \vdots \\ \frac{\partial \tilde{t}_N}{\partial p_x} & \frac{\partial \tilde{t}_N}{\partial p_y} \end{array} \right]_{\mathbf{p}} = \left[\begin{array}{cc} 2 \cos \theta_1 & 2 \sin \theta_1 \\ \vdots & \vdots \\ 2 \cos \theta_N & 2 \sin \theta_N \end{array} \right]_{N \times 2}. \end{aligned} \quad (9)$$

Thus, we can get the Jacobian matrix of the hybrid AOA-TOA measurements as

$$\mathbf{J} = \begin{bmatrix} \mathbf{J}_{\text{AOA}} \\ \mathbf{J}_{\text{TOA}} \end{bmatrix}_{2N \times 2}. \quad (10)$$

Using (8) and (10), the FIM for the hybrid AOA-TOA localization with Gaussian priors yields [31]

$$\text{FIM} = \mathbf{C}_0^{-1} + \mathbf{J}^T \Sigma^{-1} \mathbf{J}, \quad (11)$$

$$\text{CRLB} = \text{FIM}^{-1}. \quad (12)$$

2.2. Sensor Selection Problem. The goal of the sensor selection scheme is to select the best nonredundant set of sensors for localization tasks while satisfying some performance. We consider a localization problem, which chooses a specific subclass with M sensors of N ($N > M$) sensors to satisfy a range of demand. We assume N sensors can obtain N AOA and N TOA measurements in the UWSN. Consequently, two different measurements are obtained by the

same sensor. A Boolean vector can be defined as

$$\mathbf{r} = [\mathbf{w}^T, \mathbf{v}^T]^T, \quad (13)$$

$$\begin{aligned} \mathbf{w} &= [w_1, w_2, \dots, w_N]^T, w_i \in \{0, 1\}, i = 1, 2, \dots, N, \\ \mathbf{v} &= [v_1, v_2, \dots, v_N]^T, v_j \in \{0, 1\}, i = 1, 2, \dots, N, \end{aligned} \quad (14)$$

and i th element of \mathbf{w} denotes if the i th sensor is selected or not for the AOA measurement, and the i th element of \mathbf{v} denotes if the i th sensor is selected or not for the TOA measurement. It assumed that when the i th sensor is selected, both the AOA and TOA measurements from that sensor are jointly considered for the localization task.

More specifically, we define two sensing matrices Φ_w ($\Phi_w \in \mathbb{R}^{M \times N}$) and Φ_v ($\Phi_v \in \mathbb{R}^{M \times N}$) [17], where Φ_w is a sub-matrix of $\text{diag}(\mathbf{w})$ ($\text{diag}(\mathbf{w}) \in \mathbb{R}^{N \times N}$) that only contains all rows corresponding to the selected sensors, $\text{diag}(\mathbf{w})$ is a diagonal matrix, and the diagonal elements are obtain by \mathbf{w} . The similarly definition is available for Φ_v and \mathbf{v} . Note that the links of them are associated by

$$\begin{aligned} \Phi_w \Phi_w^T &= \mathbf{I}_w, \Phi_w^T \Phi_w = \text{diag}(\mathbf{w}), \\ \Phi_v \Phi_v^T &= \mathbf{I}_v, \Phi_v^T \Phi_v = \text{diag}(\mathbf{v}), \end{aligned} \quad (15)$$

thus

$$\Phi_r \Phi_r^T = \mathbf{I}_r, \Phi_r^T \Phi_r = \text{diag}(\mathbf{r}). \quad (16)$$

Based on the above definitions, the covariance matrix of the hybrid measurements for the selected sensor is given by

$$\Sigma_r = E[\Phi_r \zeta (\Phi_r \zeta)^T] = \Phi_r \Sigma \Phi_r^T. \quad (17)$$

With the above hybrid measurement model and the definitions, the FIM for selected sensors is expressed as

$$\text{FIM}_r = \mathbf{C}_0^{-1} + \mathbf{J}^T \Phi_r^T \Sigma_r^{-1} \Phi_r \mathbf{J}. \quad (18)$$

3. Sensor Selection Method for the Hybrid AOA-TOA-Based Localization

This section introduces a calibration source with a precisely known location to alleviate the localization performance degeneration caused by the sensor position errors. The sensor selection issue for hybrid AOA-TOA-based localization is transformed into an optimization issue. The optimality criterion chosen is to minimize the inverse of the FIM, which is also known as the A-optimality criterion. Other criteria are also available such as the D-optimality criterion (maximizing the determinant of the FIM or minimizing the volume of the localization error ellipsoid), which may be cause large estimation error with volume minimization in some cases, and the E-optimality criterion (minimizing the maximum eigenvalue of the CRLB matrix), and the A-optimality criterion is the most commonly used criteria for

performance measurement, which is equivalent the estimation mean squared error (MSE).

3.1. The Method to Correct Sensor Location Errors. To mitigate the localization inaccuracy caused by sensor position error in the underwater scenario, a calibration source is introduced to correct the sensor location errors. Assuming that the calibration source location in the localization model is precisely known, the signal for sensor position compensating is sent to sensors through the calibration source. According to the received signal and the calibration source location, the sensors can use the arrival time to realize the correction of position error.

On the premise that the calibration source is completely synchronized with the sensor clock in the UWSN, the time delay of the sensors that received the signal is sent by the calibration source and can be expressed as

$$\tau_k = \frac{1}{v} \|\mathbf{s}_k - \mathbf{c} + \Delta \mathbf{s}_k\| + \varepsilon_k = \Delta \tau_k + \varepsilon_k, \quad (19)$$

where v represents the transmission speed of underwater acoustic signal and $\Delta \mathbf{s}_k$ denotes the position error contained in the k th sensor. ε_k denotes the measurement noise, which follows $\varepsilon_k \sim \mathcal{N}(0, \alpha_k^2)$. We assume that $\varepsilon = (\varepsilon_1, \varepsilon_2, \dots, \varepsilon_N)^T$, $\tau = (\tau_1, \tau_2, \dots, \tau_N) \Delta \tau = (\Delta \tau_1, \Delta \tau_2, \dots, \Delta \tau_N)$. When the noise variance of each sensor is different, $\mathbf{Q} = \text{cov}(\varepsilon \varepsilon^T) = \text{diag}(\alpha_1^2, \alpha_2^2, \dots, \alpha_N^2)$, which is the covariance matrix of the time of arrival measurement error.

The likelihood function of sensor measurement can be expressed as

$$f(\tau|\mathbf{s}) = \frac{1}{(2\pi)^{N/2} \sqrt{\det \mathbf{Q}}} \exp \left[-\frac{1}{2} (\tau - \tau(\mathbf{s}))^T \mathbf{Q}^{-1} (\tau - \tau(\mathbf{s})) \right]. \quad (20)$$

The maximum likelihood estimation of target location is

$$\hat{\mathbf{s}}_\tau = \arg \min_{\mathbf{s}_\tau} f(\mathbf{s}_\tau), \quad (21)$$

where the $f(\mathbf{s}_\tau)$ is denoted as cost function.

$$f(\mathbf{s}_\tau) = (\tau - \tau(\mathbf{s}_\tau))^T \mathbf{Q}^{-1} (\tau - \tau(\mathbf{s}_\tau)). \quad (22)$$

It assumed that the variable estimation \mathbf{s}_τ has the initial estimation \mathbf{s}_τ^0 , and the k th estimation obtained by iteration is \mathbf{s}_τ^k . We denote the residual error as

$$\mathbf{e}(\mathbf{s}_\tau) = \tau(\mathbf{s}_\tau^k) - \tau. \quad (23)$$

To compute the residual error, the first-order Taylor series approximation is used for $\mathbf{e}(\mathbf{s}_\tau)$ in \mathbf{s}_τ^k . Therefore,

(23) can be rewritten as

$$\mathbf{e}(\mathbf{s}_\tau) \approx \mathbf{e}\left(\mathbf{s}_\tau^k\right) + \left. \frac{\partial \tau(\mathbf{s}_\tau)}{\partial \mathbf{s}_\tau} \right|_{\mathbf{s}_\tau=\mathbf{s}_\tau^k} \left(\mathbf{s}_\tau - \mathbf{s}_\tau^k \right) = \mathbf{e}\left(\mathbf{s}_\tau^k\right) + \mathbf{J}\left(\mathbf{s}_\tau^k\right) \Delta \mathbf{s}_\tau^k. \quad (24)$$

By substituting (24) into (22), we obtain

$$\begin{aligned} f(\mathbf{s}_\tau) &= (\tau - \tau(\mathbf{s}_\tau))^T \mathbf{Q}^{-1} (\tau - \tau(\mathbf{s}_\tau)) \\ &\approx \left(\mathbf{e}\left(\mathbf{s}_\tau^k\right) + \mathbf{J}\left(\mathbf{s}_\tau^k\right) \Delta \mathbf{s}_\tau^k \right)^T \mathbf{Q}^{-1} \left(\mathbf{e}\left(\mathbf{s}_\tau^k\right) + \mathbf{J}\left(\mathbf{s}_\tau^k\right) \Delta \mathbf{s}_\tau^k \right) \\ &= \mathbf{e}^T\left(\mathbf{s}_\tau^k\right) \mathbf{Q}^{-1} \mathbf{e}\left(\mathbf{s}_\tau^k\right) + 2\mathbf{e}^T\left(\mathbf{s}_\tau^k\right) \mathbf{Q}^{-1} \mathbf{J}\left(\mathbf{s}_\tau^k\right) \Delta \mathbf{s}_\tau^k + \Delta \mathbf{s}_\tau^{kT} \mathbf{J}^T\left(\mathbf{s}_\tau^k\right) \mathbf{Q}^{-1} \mathbf{J}\left(\mathbf{s}_\tau^k\right) \Delta \mathbf{s}_\tau^k. \end{aligned} \quad (25)$$

We take the derivative of $\Delta \mathbf{s}_\tau^k$ to the above formula and make it zero to obtain

$$\Delta \mathbf{s}_\tau^k = - \left(\mathbf{J}^T\left(\mathbf{s}_\tau^k\right) \mathbf{Q}^{-1} \mathbf{J}\left(\mathbf{s}_\tau^k\right) \right)^{-1} \mathbf{J}^T\left(\mathbf{s}_\tau^k\right) \mathbf{Q}^{-1} \mathbf{e}\left(\mathbf{s}_\tau^k\right). \quad (26)$$

Thus, the $k+1$ estimation of the variable can be expressed as

$$\mathbf{s}_\tau^{k+1} = \mathbf{s}_\tau^k + \Delta \mathbf{s}_\tau^k. \quad (27)$$

Hence, we can adopt the above method to modify the sensor position error before sensor selection. For simplify, we still use \mathbf{s}_k to represent the precise sensor position.

3.2. Sensor Selection for Correlated Noises. We shall investigate the sensor selection scheme for hybrid AOA-TOA-based localization with the correlated noises. Using [31], the noise covariance matrix can be decomposed as

$$\begin{aligned} \Sigma_A &= \lambda_A \mathbf{I}_N + \mathbf{Z}_A, \\ \Sigma_T &= \lambda_T \mathbf{I}_N + \mathbf{Z}_T, \end{aligned} \quad (28)$$

where the positive scalar is λ_A , λ_T is selected to make sure the matrix \mathbf{Z}_A , \mathbf{Z}_T is all positive definite, and \mathbf{I} denotes the identity matrix. The hybrid AOA-TOA measurement for the decomposition can be expressed as

$$\Sigma = \Gamma_N + \mathbf{Z}, \quad (29)$$

with $\Gamma = \text{diag}\{\lambda_A \mathbf{I}_N, \lambda_T \mathbf{I}_N\}$ and $\mathbf{Z} = \text{diag}\{\mathbf{Z}_A, \mathbf{Z}_T\}$.

Using (29) in (17), we can obtain

$$\Sigma_r = \Phi_r (\Gamma_N + \mathbf{Z}) \Phi_r^T = \Gamma_r + \Phi_r \mathbf{Z} \Phi_r^T, \quad (30)$$

with $\Gamma_r = \text{diag}\{\lambda_A \mathbf{I}_M, \lambda_T \mathbf{I}_M\}$. Substituting (30) into (18), with the matrix lemma [32], we have

$$\begin{aligned} &= \Phi_r^T (\Gamma_r + \Phi_r \mathbf{Z} \Phi_r^T)^{-1} \Phi_r \\ \Phi_r^T \Sigma_r^{-1} \Phi_r &= \mathbf{Z}^{-1} - \mathbf{Z}^{-1} (\mathbf{Z}^{-1} + \Gamma_r^{-1} \Phi_r^T \Phi_r)^{-1} \mathbf{Z}^{-1} \\ &= \mathbf{Z}^{-1} - \mathbf{Z}^{-1} (\mathbf{Z}^{-1} + \Gamma_r^{-1} \text{diag}(\mathbf{r}))^{-1} \mathbf{Z}^{-1}. \end{aligned} \quad (31)$$

Substituting (31) into (18), it derives

$$\mathbf{FIM}_r = \begin{aligned} &\mathbf{C}_0^{-1} + \mathbf{J}^T \mathbf{Z}^{-1} \mathbf{J} \\ &- \mathbf{J}^T \mathbf{Z}^{-1} (\mathbf{Z}^{-1} + \Gamma_r^{-1} \text{diag}(\mathbf{r}))^{-1} \mathbf{Z}^{-1} \mathbf{J}. \end{aligned} \quad (32)$$

As discussed above, the relationship between \mathbf{FIM}_r and \mathbf{r} is created absolutely by (32). We adopt the A-optimality criterion as the optimization objective, which is equivalent to minimize the trace of inverse of the FIM; thus, the sensor selection issue in the hybrid AOA-TOA-based localization is given by

$$\begin{aligned} \min_{\mathbf{r}} \quad &\text{tr}(\mathbf{FIM}_r^{-1}) \\ \text{s.t.} \quad &1^T \mathbf{r} = 2M \\ &\mathbf{r} \in \{0, 1\}^{2N} \end{aligned} \quad (33)$$

It is clear from the (33) is a nonconvex optimization scheme because of the last Boolean constraints. In the following sections, we propose employing the convex relaxation to approximately solve it.

4. Semidefinite Relaxation for Sensor Selection Problem

This section we analyze and present the method to settle the above nonconvex problem. The sensor selection scheme described in Section 3 is a nonconvex and NP-hard problem. We present a convex relaxation solution for the hybrid AOA-TOA sensor selection. What is more, a randomization algorithm is approved to advance the achievement of the SDP.

4.1. The SDP Method. To simplify the problem and facilitate theoretical analysis, we construe $\mathbf{A} = \mathbf{C}_0^{-1} + \mathbf{J}^T \mathbf{Z}^{-1} \mathbf{J}$ and $\mathbf{B} = \mathbf{Z}^{-1} \mathbf{J}$ in (32). Hence, the optimization issue in (33) is transformed as

$$\begin{aligned} \min_{\mathbf{r}} \quad &\text{tr}(\mathbf{X}) \\ \text{s.t.} \quad &\mathbf{A} - \mathbf{B}^T (\mathbf{Z}^{-1} + \Gamma_r^{-1} \text{diag}(\mathbf{r}))^{-1} \mathbf{B} \mu \mathbf{X}^{-1} \\ &1^T \mathbf{r} = 2M \\ &\mathbf{r} \in \{0, 1\}^{2N} \end{aligned} \quad (34)$$

and the $\mathbf{X} \in \mathbb{R}^{M \times M}$ in the above optimization issue is an auxiliary variable; the first constraint in (34) is given by [17]

$$\left(\mathbf{A} - \mathbf{B}^T (\mathbf{Z}^{-1} + \Gamma_r^{-1} \text{diag}(\mathbf{r}))^{-1} \mathbf{B} \right)' \mathbf{X}. \quad (35)$$

Here, we introduce the other one variable $\mathbf{Y} \in \mathbb{R}^{M \times M}$ and the inequality constraint in (35) can be equivalently transformed to

$$\mathbf{A} - \mathbf{Y} \mu \mathbf{X}^{-1}, \quad (36)$$

$$\mathbf{Y}\mu\mathbf{B}^T(\mathbf{Z}^{-1} + \Gamma_r^{-1} \text{diag}(\mathbf{r}))^{-1}\mathbf{B}. \quad (37)$$

Here, the $\mathbf{U} \leq \mathbf{V}$ (or $\mathbf{U} \geq \mathbf{V}$) shows that $\mathbf{V} - \mathbf{U}$ (or $\mathbf{U} - \mathbf{V}$) is the positive semidefinite matrix. Applying to the Schurs complement, the first constraint in (34) is transformed to the below linear matrix inequality (LMI)

$$\begin{bmatrix} \mathbf{A} - \mathbf{Y} & \mathbf{I} \\ \mathbf{I} & \mathbf{X} \end{bmatrix} \mu 0, \quad \begin{bmatrix} \mathbf{Y} & \mathbf{B}^T \\ \mathbf{B} & \mathbf{Z}^{-1} + \Gamma_r^{-1} \text{diag}(\mathbf{r}) \end{bmatrix} \mu 0, \quad (38)$$

Substituting (38) into (34), and the original optimization issue is rewritten as

$$\begin{aligned} & \min_{\mathbf{r}, \mathbf{X}, \mathbf{Y}} \quad \text{tr}(\mathbf{X}) \\ \text{s.t.} \quad & \text{LMIs in (38)} \\ & \mathbf{1}^T \mathbf{r} = 2M \\ & \mathbf{r} \in \{0, 1\}^{2N} \end{aligned} \quad (39)$$

We can find that the above optimization problem is non-convex owing to the Boolean selection vector \mathbf{r} . Thus, we utilize (16) and introduce an auxiliary variable $\mathbf{R} = \mathbf{r}\mathbf{r}^T$; the number of sensor selection and Boolean constraints in (39) is given by

$$\text{tr}(\mathbf{R}) = M, \text{diag}(\mathbf{R}) = \mathbf{r}, \quad (40)$$

and then, the $\mathbf{R} = \mathbf{r}\mathbf{r}^T$ can be relaxed to $\mathbf{R}\mu\mathbf{r}\mathbf{r}^T$; we reach the following optimization problem

$$\begin{aligned} & \min_{\mathbf{r}, \mathbf{X}, \mathbf{Y}} \quad \text{tr}(\mathbf{X}) \\ \text{s.t.} \quad & \text{LMIs in (38)} \\ & \text{tr}(\mathbf{R}) = M \\ & \text{diag}(\mathbf{R}) = \mathbf{r} \\ & \begin{bmatrix} \mathbf{R} & \mathbf{r} \\ \mathbf{r}^T & 1 \end{bmatrix} \mu 0 \end{aligned} \quad (41)$$

For the SDP (41) problem, the interior point algorithm is utilized to solve it quickly, and then, the fractional \mathbf{r} can be obtained. Thus, the \mathbf{w} and \mathbf{v} also can be extracted from the \mathbf{r} as defined before. The convenient method is to select the M largest sum of a fractional element w_k and v_k , and the corresponding index denotes the selected sensors.

We also can use a randomization algorithm to get a better solution, which consists of an iterative procedure. The aforementioned procedure is called ‘‘SDP,’’ and the details of the randomization algorithm are shown in Algorithm 1, which is called ‘‘SDP with randomization.’’

5. Number Results

In this section, we first analyze the complexities of the proposed approach, and then, extensive simulations prove that

the proposed approach can obtain high estimation performance for the hybrid TOA-AOA-based localization.

The commonly used method is the interior point method for the SDP solution, which the computational complexity is $\mathcal{O}(N^3)$ [33]. Furthermore, the SDP with the randomization algorithm should be considered. Due to the additional multiplication operations are needed for the randomization algorithm is $S\mathcal{O}_M$, and S denotes the number of random vectors. The exhaustive search algorithm itemizes all the possible sensor subsets with M from the total N sensors; thus, all possible sensor subsets are $N!/(N-M)!M!$, and we can choose the sensor subset with the minimum trace of CRLB. The exhaustive search algorithm that has high computational complexity is $\mathcal{O}(N!)$. It is noticeable that the proposed algorithm has lower computational complexity compared to the exhaustive algorithm.

In what follows, the proposed algorithm validity is demonstrated by simulation results. In the simulation experiment, let us assume that N sensors are randomly arranged in a region of size $1000 \text{ m} \times 1000 \text{ m}$. The prior PDF of \mathbf{p} is given by $\mathbf{p} \sim \mathcal{N}(\mathbf{p}_0, \mathbf{C}_0)$, and $\mathbf{p}_0 = (0, 0)^T$, $\mathbf{C} = \text{diag}(50, 50)$. The calibration source location is $\mathbf{c}_0 = (30, -20)^T$. The positive definite is \mathbf{Z}_A and \mathbf{Z}_T , and we set $\lambda = 0.9\lambda_{\min}$, where λ_{\min} is the minimum eigenvalue of Σ_A and Σ_T . Two general approaches, the closest sensor algorithm and exhaustive search algorithm are recommended to contract with the proposed approach in this paper. The exhaustive algorithm can obtain the best result and is also used for comparison. In the closest sensor algorithm, the M shortest distance between the sensors and target of sensors is chosen. For simplicity, ‘‘Exhaustive search’’ is used to represent the exhaustive search algorithm, and ‘‘Closest sensors’’ is used to represent the M closest sensors. ‘‘SDP’’ and ‘‘SDP with randomization’’ are utilized to indicate our proposed SDP algorithm and SDP with Algorithm 1. Besides, we also use ‘‘All sensors’’ to represent the total activated sensors, and ‘‘Random selection’’ is utilized to represent randomly selected M sensors.

In the first experiment, we investigate the algorithm’s performance to correct the sensor location errors using the calibration source. We assume that noise variance of the TOA measurement is $\sigma_1 = \dots = \sigma_N = 1 \text{ m}$, and the noise variance of the AOA measurement is $\gamma_1 = \dots = \gamma_N = 1^\circ$. The errors of the sensor position are within a 2-mile radius of the true position. Figure 1 depicts the localization accuracy with the different number of sensors. We observe that the $\text{tr}(\text{CRLB})$ of the corrected sensor position is close to $\text{tr}(\text{CRLB})$ of the true sensors; the conclusion can be realized under the SDP solution and SDP with randomization algorithm. The effectiveness of the sensor position error correction method is proved, and the SDP with randomization obtains a high localization accuracy with the different number of selected sensors.

Next, we consider that the simulation scenarios are composed of $M = 5$ and $M = 10$ selected sensor, and the noise variance of AOA measurement remains constant while the noise variance of TOA measurement is a variable from 1 m^2 to 10 m^2 . Figure 2 presents the $\text{tr}(\text{CRLB})$ increase as the noise variance growing of all these algorithms. However, the SDP with randomization algorithm always has better

Input: The fractional solution \mathbf{w} and \mathbf{v} ;

- 1: **for** $k = 1, 2, \dots, N$ **do**
- 2: Generate two random vectors: $\mathbf{w}_\zeta^k \sim \mathcal{N}(\mathbf{w}^O, \mathbf{W}_w - \mathbf{w}^o \mathbf{w}^{oT})$, $\mathbf{v}_\zeta^k \sim \mathcal{N}(\mathbf{v}^O, \mathbf{V}_v - \mathbf{v}^o \mathbf{v}^{oT})$.
- 3: set the largest M elements as 1 and the rest as 0 to generate two feasible vectors $(\mathbf{w}_\zeta^k)_N$ and $(\mathbf{v}_\zeta^k)_N$
- 4: Obtain the selected sensor index from $(\mathbf{w}_\zeta^k)_N$ and $(\mathbf{v}_\zeta^k)_N$, select the same sensor index of the two vectors as 1.
- 5: select the rest $(M - a)$ sensors from the rest of "1" sensors.
- end for**
- 6: Substitute each possible combination into objective function and choose vectors with the minimum value.
- 7: **Output:** the solved Boolean vector to choose with the minimum value

ALGORITHM 1: A randomization algorithm.

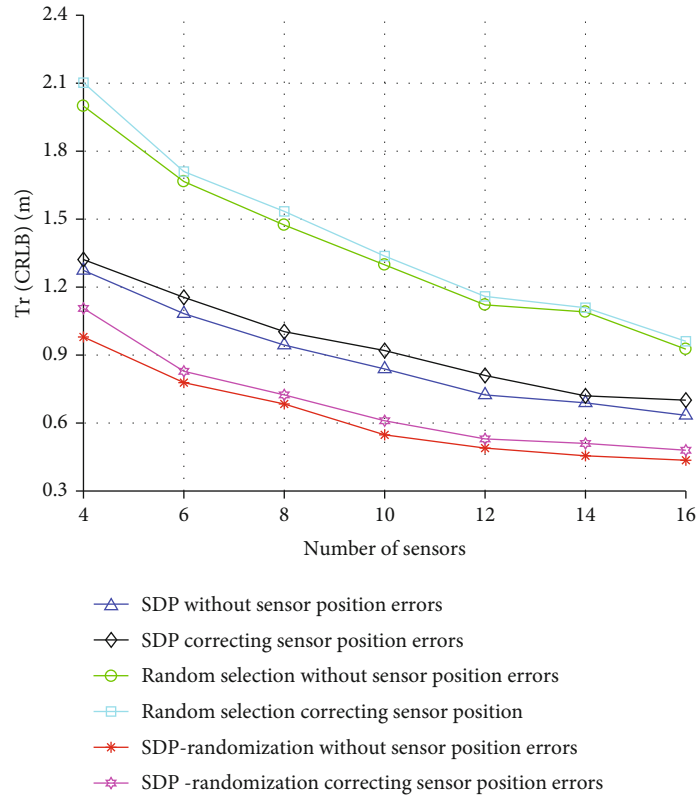


FIGURE 1: Comparison with different number of sensors.

localization accuracy and is close to the exhaustive search algorithm.

To further demonstrate the efficiency of the proposed method, we also consider the simulation scenarios in that the noise variance of TOA measurement remains constant. In contrast, the noise variance of AOA measurement varies from 1° to 10° . Other parameter settings remain unchanged as Figure 2.

We observe in Figure 3 that the $\text{tr}(\text{CRLB})$ does not increase significantly as γ^2 increases, which is consistent with the results in [34].

Furthermore, we consider the sensor selection scenario with each sensor having different noise variance while the number of the selected sensor varies from 4 to 16. Figure 4 plots the $\text{tr}(\text{CRLB})$ corresponding to these algorithms. It is

observed from Figure 4 that the $\text{tr}(\text{CRLB})$ decreases with the selected sensor number from 4 to 16. The SDP with randomization algorithm yields a lower estimation error than other algorithms and almost achieves the exhaustive search algorithm.

Finally, the correlated measurement noise scenario is considered. The correlation parameter $\lambda_A = \lambda_T = \lambda$ varies from 0.1 to 0.9, and the remaining parameters of this simulation unchanged as above. Figure 5 depicts the $\text{tr}(\text{CRLB})$ comparison of different number of selected sensors, and it can be observed that the $\text{tr}(\text{CRLB})$ curve of the SDP with randomization algorithm has the same variation tendency when the different selected sensors. That is the localization accuracy is raising as the correlation gets stronger, which is consistent with the results in [35]. Due to the strongly

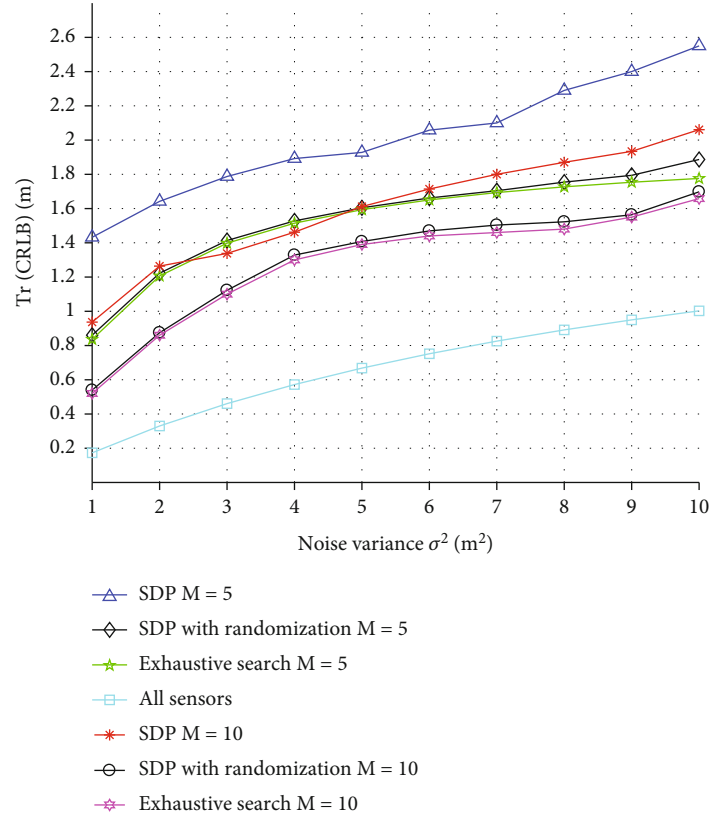


FIGURE 2: Comparison with different noise variance of TOA as $M=5$ and $M=10$.

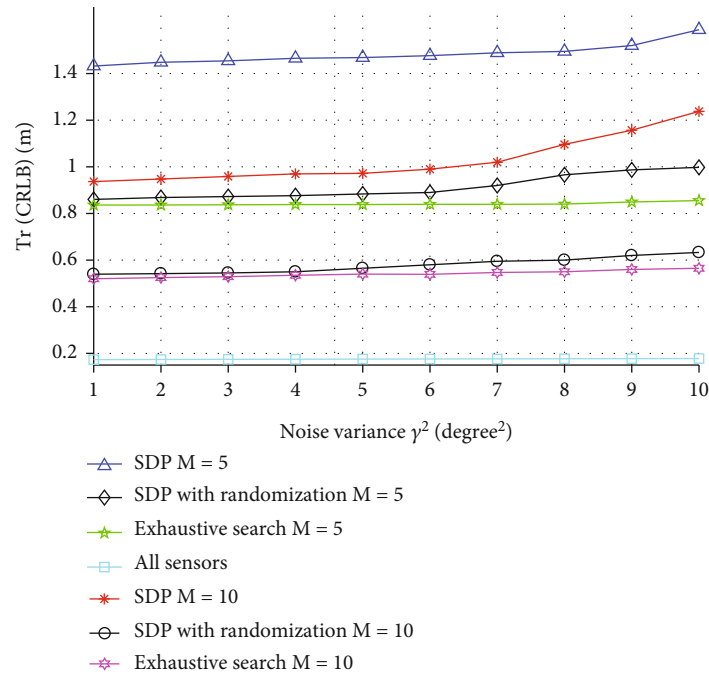


FIGURE 3: Comparison with different noise variance of AOA as $M=5$ and $M=10$.

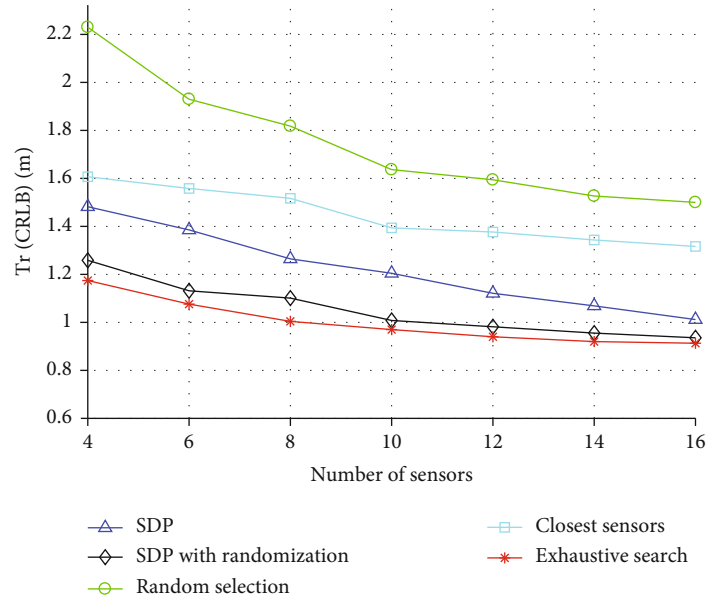


FIGURE 4: Comparison with different numbers of sensors and noise variance.

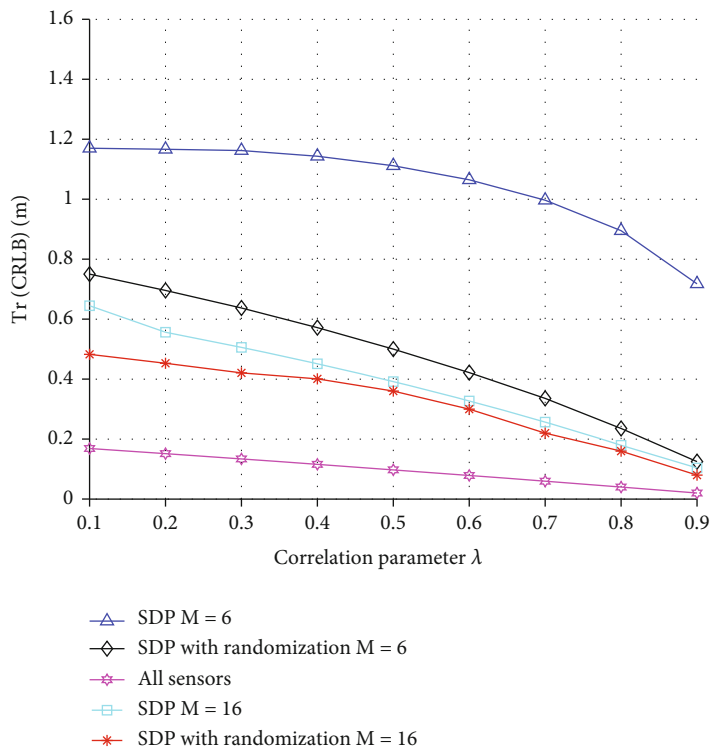


FIGURE 5: Comparison with different correlation parameter as $M = 6$, $M = 16$, and all sensors.

correlated noise, noise cancellation is achieved by subtracting one sensor from the rest. Furthermore, it is observed that SDP with randomization approach obtained better localization accuracy than the SDP solution.

6. Conclusion

This paper explores the sensor selection scheme for an uncertain target localization based on hybrid AOA-TOA measurements with the correlated noise in the underwater scenario. Considering that the original nonconvex optimization problem is formulated by minimizing the $\text{tr}(\text{CRLB})$, the optimization issue can be relaxed by convex relaxation and solved by the SDP method. The randomization algorithm is utilized to refine the results. Besides, a calibration source with a precise position is used to correct the sensor position. Simulation studies confirm that the superiority of the proposed algorithm over the existing algorithms; besides, the influence of the noise correlation on the sensor selection scheme is also discussed.

In the future work, we will investigate the sensor selection scheme for multiple underwater unknown targets with correlated noise, which will be formulated as a convex combination problem. We will develop the SDP solution for sensor selection for TDOA, AOA, and/or RSS. Furthermore, it is interesting to devise the sensor selection scheme with hybrid localization for target tracking in the underwater scenario. Sensor selection in the presence of non-line-of-sight propagation is also a challenging research topic.

Data Availability

The data used to support the finding of this study are included in the article.

Conflicts of Interest

The authors declare that they have no conflicts of interest.

References

- [1] H. P. Tan, R. Diamant, W. K. Seah, and M. Waldmeyer, "A survey of techniques and challenges in underwater localization," *Ocean Engineering*, vol. 38, no. 14-15, pp. 1663–1676, 2011.
- [2] M. Erol-Kantarci, H. T. Mouftah, and S. Oktug, "A survey of architectures and localization techniques for underwater acoustic sensor networks," *IEEE Communications Surveys and Tutorials*, vol. 13, no. 3, pp. 487–502, 2011.
- [3] H. Esmail, Z. A. Qasem, H. Sun, J. Qi, J. Wang, and Y. Gu, "Wireless information and power transfer for underwater acoustic time-reversed NOMA," *IET Communications*, vol. 14, no. 19, pp. 3394–3403, 2020.
- [4] M. Calvo-Fullana, J. Matamoros, and C. Antón-Haro, "Sensor selection and power allocation strategies for energy harvesting wireless sensor networks," *IEEE Journal on Selected Areas in Communications*, vol. 34, no. 12, pp. 3685–3695, 2016.
- [5] Z. A. H. Qasem, H. Esmail, H. Sun, J. Wang, Y. Miao, and S. Anwar, "Enhanced fully generalized spatial modulation for the Internet of Underwater Things," *Sensors*, vol. 19, article 1519, 2019.
- [6] S. Anwar, C. Yuen, H. Sun, Y. L. Guan, and Z. Babar, "Novel receiver design of nonorthogonal FDM systems in underwater acoustics communication," *IEEE Systems Journal*, vol. 14, no. 3, pp. 3875–3884, 2020.
- [7] E. Cheng, L. Wu, F. Yuan, C. Gao, and J. Yi, "Node selection algorithm for underwater acoustic sensor network based on particle swarm optimization," *IEEE Access*, vol. 7, pp. 164429–164443, 2019.
- [8] A. Nordio, A. Tarable, F. Dabbene, and R. Tempo, "Sensor selection and precoding strategies for wireless sensor networks," *IEEE Transactions on Signal Processing*, vol. 63, no. 16, pp. 4411–4421, 2015.
- [9] Y. T. Chan and K. C. Ho, "A simple and efficient estimator for hyperbolic location," *IEEE Transactions on Signal Processing*, vol. 42, no. 8, pp. 1905–1915, 1994.
- [10] H. J. Shao, X. P. Zhang, and Z. Wang, "Efficient closed-form algorithms for AOA based self-localization of sensor nodes using auxiliary variables," *IEEE Transactions on Signal Processing*, vol. 62, no. 10, pp. 2580–2594, 2014.
- [11] L. A. C. Najarro, I. Song, S. Tomic, and K. Kim, "Fast localization with unknown transmit power and path-loss exponent in WSNs based on RSS measurements," *IEEE Communications Letters*, vol. 24, no. 12, pp. 2756–2760, 2020.
- [12] Y. Wang and Y. Wu, "An efficient semidefinite relaxation algorithm for moving source localization using TDOA and FDOA measurements," *IEEE Communications Letters*, vol. 21, no. 1, pp. 80–83, 2017.
- [13] A. Fascista, A. Coluccia, and G. Ricci, "A pseudo maximum likelihood approach to position estimation in dynamic multipath environments," *Signal Processing*, vol. 181, article 107907, 2021.
- [14] X. Chen, W. Gang, and K. C. Ho, "Semidefinite relaxation method for unified near-field and far-field localization by AOA - ScienceDirect," *Signal Processing*, vol. 181, article 107916, 2021.
- [15] T. Jia, K. C. Ho, H. Wang, and X. Shen, "Effect of sensor motion on time delay and Doppler shift localization: analysis and solution," *IEEE Transactions Signal Processing*, vol. 67, no. 22, pp. 5881–5895, 2019.
- [16] S. S. Al-Samahi, Y. Zhang, and K. C. Ho, "Elliptic and hyperbolic localizations using minimum measurement solutions," *Signal Processing*, vol. 167, article 107273, 2020.
- [17] S. Joshi and S. Boyd, "Sensor selection via convex optimization," *IEEE Transactions on Signal Processing*, vol. 57, no. 2, pp. 451–462, 2009.
- [18] S. P. Chepuri and G. Leus, "Sparsity-promoting sensor selection for non-linear measurement models," *IEEE Transactions on Signal Processing*, vol. 63, no. 3, pp. 684–698, 2015.
- [19] S. Liu, S. P. Chepuri, M. Fardad, E. Maşazade, G. Leus, and P. K. Varshney, "Sensor selection for estimation with correlated measurement noise," *IEEE Transactions on Signal Processing*, vol. 64, no. 13, pp. 3509–3522, 2016.
- [20] Y. Zhao, Z. Li, B. Hao, and J. Shi, "Sensor selection for TDOA-based localization in wireless sensor networks with non-line-of-sight condition," *IEEE Transactions on Vehicular Technology*, vol. 68, no. 10, pp. 9935–9950, 2019.
- [21] Z. Dai, G. Wang, X. Jin, and X. Lou, "Nearly optimal sensor selection for TDOA-based source localization in wireless

- sensor networks,” *IEEE Transactions on Vehicular Technology*, vol. 69, no. 10, pp. 12031–12042, 2020.
- [22] A. Coluccia and A. Fascista, “Hybrid TOA/RSS range-based localization with self-calibration in asynchronous wireless networks,” *Journal of Sensor and Actuator Networks*, vol. 8, article 31, 2019.
- [23] Y. Zhao, W. Qi, P. Liu, L. Chen, and J. Lin, “Accurate 3D localisation of mobile target using single station with AoTDoA measurements,” *IET Radar Sonar & Navigation*, vol. 14, no. 6, pp. 954–965, 2020.
- [24] Z. A. Qasem, H. A. Leftah, H. Sun, J. Qi, and H. Esmail, “X-Transform time-domain synchronous IM-OFDM-SS for underwater acoustic communication,” *IEEE Systems Journal*, vol. 99, pp. 1–12, 2021.
- [25] A. Mallat, J. Louveaux, and L. Vandendorpe, “UWB based positioning in multipath channels: CRBs for AOA and for hybrid TOA-AOA based methods,” in *2007 IEEE international conference on communications*, pp. 5775–5780, Glasgow, UK, June 2007.
- [26] Y. Y. Li, G. Q. Qi, and A. D. Sheng, “Performance metric on the best achievable accuracy for hybrid TOA/AOA target localization,” *IEEE Communications Letters*, vol. 22, no. 7, pp. 1474–1477, 2018.
- [27] P. Yuan, T. Zhang, N. Yang, H. Xu, and Q. Zhang, “Energy efficient network localisation using hybrid TOA/AOA measurements,” *IET Communications*, vol. 13, no. 8, pp. 963–971, 2019.
- [28] Y. Zhao, Z. Li, B. Hao, P. Wan, and L. Wang, “How to select the best sensors for TDOA and TDOA/AOA localization?,” *China Communications*, vol. 16, no. 2, pp. 134–145, 2019.
- [29] K. Doğançay and H. Hmam, “Optimal angular sensor separation for AOA localization,” *Signal Processing*, vol. 88, no. 5, pp. 1248–1260, 2008.
- [30] N. H. Nguyen and K. Dogancay, “Optimal geometry analysis for multistatic TOA localization,” *IEEE Transactions on Signal Processing*, vol. 64, no. 16, pp. 4180–4193, 2016.
- [31] N. H. Nguyen, “Optimal geometry analysis for target localization with Bayesian priors,” *IEEE Access*, vol. 9, pp. 33419–33437, 2021.
- [32] S. P. Chepuri and G. Leus, “Sparse sensing for distributed Gaussian,” in *IEEE International Conference on Acoustics, Speech and Signal Processing (ICASSP)*, pp. 2394–2398, South Brisbane, QLD, Australia, April 2015.
- [33] A. Ben-Tal and A. Nemirovski, *Lectures on Modern Convex Optimization: Analysis, Algorithms, and Engineering Applications*, Ser. MPS-SIAM Series on Optimization, SIAM, Philadelphia, PA, USA, 2001.
- [34] S. Xu, “Optimal sensor placement for target localization using hybrid RSS, AOA and TOA measurements,” *IEEE Communications Letters*, vol. 24, no. 9, pp. 1966–1970, 2020.
- [35] B. Xue, L. Zhang, W. Zhu, and Y. Yu, “A new sensor selection scheme for Bayesian learning based sparse signal recovery in WSNs,” *Journal of the Franklin Institute*, vol. 355, no. 4, pp. 1798–1818, 2018.

Research Article

A Vibration Signal Denoising Method of Marine Atomic Gravimeter Based on Improved Variational Mode Decomposition

Wenbin Gong ¹, An Li,¹ An Liao,² Hao Che,¹ Chunfu Huang,¹ and Fangjun Qin ¹

¹College of Electrical Engineering, Naval University of Engineering, Wuhan 430033, China

²Training Base, Army Logistics Academy, Chongqing 400000, China

Correspondence should be addressed to Fangjun Qin; haig2005@126.com

Received 18 January 2022; Revised 3 March 2022; Accepted 10 March 2022; Published 27 March 2022

Academic Editor: Xuebo Zhang

Copyright © 2022 Wenbin Gong et al. This is an open access article distributed under the Creative Commons Attribution License, which permits unrestricted use, distribution, and reproduction in any medium, provided the original work is properly cited.

As a high-precision gravity measuring device, a marine atomic gravimeter is highly sensitive to vibration signals. Accurate measurement and analysis of vibration signal is the primary condition to realize vibration compensation and vibration suppression. Denoising plays a crucial role in the processing of these vibration signals. The vibration signals of a marine gravimeter contain numerous nonlinear and nonstationary components. In this paper, a vibration signal denoising method of marine atomic gravimeter based on improved variational mode decomposition (VMD) was put forward to effectively suppress the noise. An improved genetic particle swarm optimization (GPSO) was first adopted for the parametric optimization of VMD by taking minimum permutation entropy (PE) as fitness function and adaptively determining the optimal parameters of VMD. PE was then utilized to calculate the proportion of noise-containing components in the intrinsic mode function (IMF) components obtained by VMD. The components were classified into noise and signal components by searching for the mutation points of two adjacent IMF permutation entropies. On this basis, noise components were denoised by Savitzky-Golay (SG) filter. In the end, the denoised components were reconstructed with the signal components to generate denoised vibration signals. To verify the effectiveness, the proposed method was applied in denoising, simulated and measured vibration signals of a marine atomic gravimeter, and compared with Daubechies (db) wavelet, Symlets (sym) wavelet, and empirical mode decomposition (EMD). The results showed that the proposed method could effectively remove the noise from nonlinear vibration signals and retain the authentic and useful information, so that it was able to provide the supporting data for gravity compensation of marine atomic gravimeter.

1. Introduction

As a high-precision absolute gravimeter, an atomic gravimeter may be applied in inertial navigation and earth gravity field measurement [1]. In terms of marine measurement, Bidet et al. [2] employed an atomic gravimeter in marine gravity measurement for the first time. An atomic gravimeter was attached to a gyroscope stabilized platform, so that it could always measure the actual virtual component of gravity field regardless of waves and sways. The platform overcame effectively the poor verticality of a ship-borne atomic gravimeter in measurement. Based on an inertial stabilized platform, Cheng et al. [3] conducted an absolute

measurement experiment with a ship-borne atomic gravimeter when the ship was moored, and Li et al. [4] performed a further lake test of an atomic gravimeter in absolute gravity measurement.

During measurement, an atomic gravimeter is severely affected by the vibration of Raman retroreflection mirror since its measurement precision and reliability are highly restricted by vibration noise. For this reason, vibration noise isolation and attenuation are crucial to obtaining accurate atomic interference phase and realizing accurate gravity field information detection. In order to guarantee the measurement precision of an atomic gravity, vibration isolation techniques [5, 6] and vibration compensation methods [7–9] are

often employed for vibration noise suppression. The noise in the marine environment is very complex and vulnerable to impulse noise, so it is difficult to process the signal [10]. In the structure of a ship, noise is mainly caused by the vibration of main engine, diesel engine, main propulsion system, main propeller, and other devices. The noise caused by crew activities intermittently is also coupled into the signals of main vibration noise. These vibration signals are nonlinear and nonstationary [11–14]. For the purpose of vibration noise suppression in measurement with an atomic gravimeter, accurate measurement and analysis of vibration signals lays a basis for vibration compensation and suppression. Normally, an accelerometer is utilized to gather vibration signals, but these vibration signals are inevitably mingled with ambient noise and circuit noise in the process. Denoising analysis must be therefore conducted with the gathered vibration data to extract the actual vibration information of vibration sources, so as to provide the reliable data for vibration isolation design and vibration compensation [15].

Wavelet transform denoising is a denoising method suitable for nonstationary signals. It has been widely applied in engineering, but its final effect is affected by the selection of threshold and wavelet basis function [16]. In 1998, Huang et al. put forth an analysis method for nonlinear and nonstationary signals based on Hilbert-Huang transform, that is, empirical mode decomposition (EMD), which could adaptively decompose a signal into a number of intrinsic mode functions (IMFs) with actual physical implications. The method had been widely applied in denoising nonlinear and nonstationary signals. Kopsinis and McLaughlin combined wavelet decomposition with EMD to denoise signals and used different thresholds for IMFs in filtering and reconstruction to realize signal denoising [17]. Rezaee and Osguei [18] made an improvement to EMD by introducing a new parameter to obtain a new local mean. In this way, they enhanced the precision and efficiency of EMD and effectively applied it in the analysis of vibration signals. Nevertheless, the application of EMD was also troubled by end effect and mode mixing especially when the signal to noise ratio (SNR) was low. In order to resolve this problem, some improvements of EMD have been explored including ensemble empirical mode decomposition (EEMD), improved complete ensemble empirical mode decomposition (ICEEMD), and partial ensemble empirical mode decomposition (PEEMD) [16, 19, 20]. Nevertheless, these methods can inhibit mode mixing to some extent but intrinsically extract local extremum and interpolate envelopes. They are still empirical and lack a solid mathematic basis.

In order to effectively inhibit the mode mixing of EMD, Dragomiretski and Zosso [21] put forward variational mode decomposition (VMD) in 2014. Based on the three-dimensional variational constraint theory, this algorithm estimated multiple modes simultaneously by virtue of nonrecursion and improved the computational efficiency while guaranteeing the integrity of features. Hence, it could satisfactorily resist noise and reduce mode mixing. With its solid mathematic basis for the

decomposition of nonstationary signals, VMD has been applied in earthquake time-frequency analysis, signal filter denoising, and ground vibration attenuation, which is a sufficient proof of its effectiveness and superiority in signal decomposition [22–24]. Nevertheless, number of decomposed modes K and penalty term α must be artificially set in the VMD of signals. If the value of K is set too high, overdecomposition may be caused to generate false components. If it is set too low, underdecomposition occurs and results in the mixing of modes close to frequency. Moreover, the penalty factor α also affects the extraction of single-component modes. If it is set too large, the bandwidth will be narrower for single modes, causing to intercept the effective frequency components outside bandwidth. If it is set too small, the bandwidth will be wider, and the two adjacent modes will share the center frequency and result in information redundancy [25, 26].

In order to adaptively decompose signals, some methods have been developed to determine the K value based on kurtosis [27] and energy factor [28]. In these methods, only the number of decomposed modes K is optimized while the penalty factor α is ignored. Therefore, optimal decomposition cannot be achieved with these methods. Along with the emergence of intelligent optimization algorithms, attempts have been made to apply some optimization algorithms in the optimization of VMD parameters, and satisfying results have been obtained [24, 29, 30]. Zhou et al. [31] put forward the particle swarm optimization (PSO) to optimize the VMD parameters. In this method, they used mean permutation entropy (MPE) as its fitness function and determined the optimal combination of K and α by searching for the minimum of the fitness function. It was an efficient search algorithm because of its fast convergence while requiring the setting of fewer parameters. Nevertheless, the PSO is troubled by premature convergence and faces slower convergence in the late stage since population diversity disappears in the searched space. Meanwhile, it cannot be further optimized after reaching a certain precision of convergence, so that its final precision is not good. Based on genetic algorithm (GA), Kumar et al. took kernel-based mutual information (KEMI) as fitness function to find out the optimal parameters K and α of VMD [29]. The GA algorithm has strong global search capability and avoids local optimum, but it may be easily affected by such problems as premature convergence, numerous computations, slow convergence, and poor stability.

To solve the above problems, a vibration signal denoising method combining improved VMD parameter optimization algorithm and Savitzky-Golay (SG) filter is proposed in this paper. Firstly, the improved genetic particle swarm optimization (GPSO) is applied to VMD, and the permutation entropy (PE) is used as the fitness function to optimize the VMD parameters and decompose the noisy vibration signal. Secondly, the noise proportion in IMF is calculated by PE, and the IMF component is divided into noise component and the signal component. SG filter was applied for denoising noisy components. Finally, the denoised component and signal component

are reconstructed to obtain the denoised vibration signal. The method is applied to the analysis of vibration simulation signals and measured signals.

2. Theoretical Background

2.1. Variational Mode Decomposition. As for the structural variation of signals in VMD, Wiener filter is introduced to solve variation by virtue of iterative computation. Each input signal is decomposed into K IMFs with different center frequencies ω_k . The variational model is correspondingly described by Equation (1).

$$\left\{ \min_{\{u_k\}, \{\omega_k\}} \left\{ \sum_{k=1}^K \left\| \partial_t \left[\left(\delta(t) + \frac{j}{\pi t} \right) * u_k(t) \right] e^{-j\omega_k t} \right\|_2^2 \right\} \text{ s.t. } \sum_{k=1}^K u_k = f, \right. \quad (1)$$

where $\{u_k\} = \{u_1, \dots, u_K\}$ is K IMF components after decomposition, $\{\omega_k\} = \{\omega_1, \dots, \omega_K\}$ is the center frequency of each component, $\delta(t)$ is the unit pulse function, j is the imaginary unit, $*$ is the convolution operation, and ∂_t is the partial derivative with respect to t . Lagrangian multiplier λ and secondary penalty term α are introduced to obtain the optimal solution of constrained variation as follows:

$$\begin{aligned} L(\{u_k\}, \{\omega_k\}, \lambda) = & \alpha \sum_k \left\| \partial_t \left[\left(\delta(t) + \frac{j}{\pi t} \right) * u_k(t) \right] e^{-j\omega_k t} \right\|_2^2 \\ & + \left\| f(t) - \sum_i u_i(t) + \frac{\lambda(t)}{2} \right\|_2^2 \\ & + \left\langle \lambda(t), f(t) - \sum_k u_k(t) \right\rangle. \end{aligned} \quad (2)$$

The alternation of multiplication operators is conducted to iteratively update u_k , ω_k , λ and obtain the optimal mode component u_k , center frequency ω_k , and Lagrangian multiplier λ .

$$\hat{u}_k^{n+1}(\omega) = \frac{\hat{f}(\omega) - \sum_{i \neq k} \hat{u}_i(\omega) + \hat{\lambda}(\omega)/2}{1 + 2\alpha(\omega - \omega_k)^2}, \quad (3)$$

$$\omega_k^{n+1} = \frac{\int_0^\infty \omega |\hat{u}_k(\omega)|^2 d\omega}{\int_0^\infty |\hat{u}_k(\omega)| d\omega}, \quad (4)$$

$$\hat{\lambda}^{n+1}(\omega) = \hat{\lambda}^n(\omega) + \tau \left(\hat{f}(\omega) - \sum_k \hat{u}_k^{n+1}(\omega) \right), \quad (5)$$

where \wedge is the Fourier transform, τ is the fidelity coefficient, and n is the iteration times. Iteration is constantly updated but halted when relative error is less than convergence precision. The decomposition result u_k is eventually outputted.

$$\sum_k \frac{\|\hat{u}_k^{n+1}(\omega) - \hat{u}_k^n(\omega)\|_2^2}{\|\hat{u}_k^n\|_2^2} < \varepsilon. \quad (6)$$

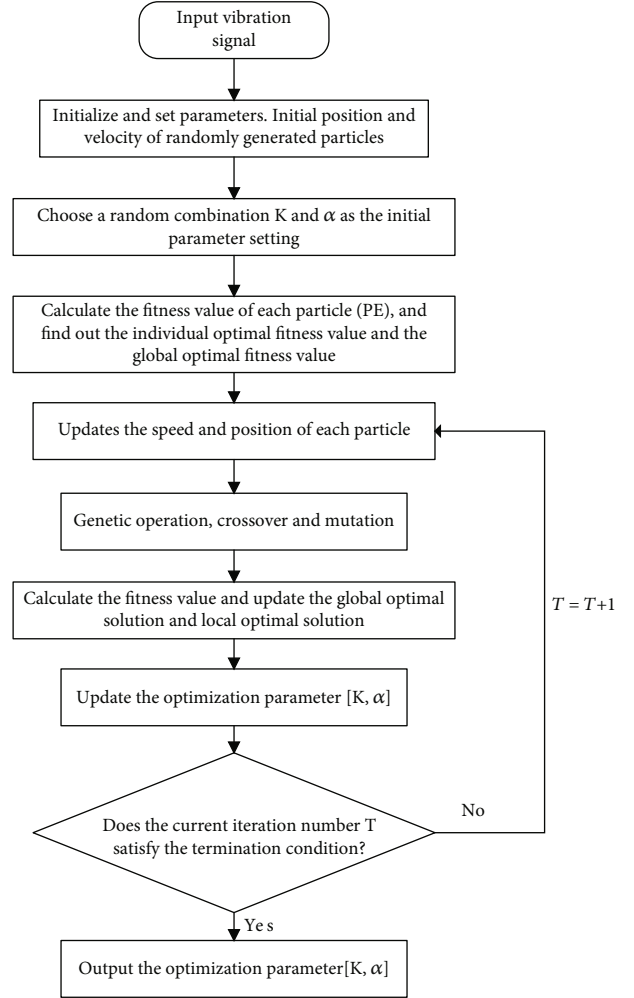


FIGURE 1: Process flow of VMD parametric optimization by GPSO.

2.2. GPSO Optimized VMD. The effect of VMD depends significantly on the number of decomposed modes K and penalty term α . Considering their limitations in VMD, GA and PSO are combined in this paper. In this way, genetic computation is adopted to obtain the optimal solution of PSO. Under specific conditions, genetic operations including reproduction, crossover, and mutation are carried out for particles and their displacement rate, so that the particles can be alienated from local optimal to obtain the global optimal solution. The GPSO has quicker convergence and better grouping quality than traditional PSO. The combined algorithm makes full use of the advantages of both GA and PSO, so as to guarantee the quick convergence to global optimal solution. The process flow is presented in Figure 1. The specific steps are given as follows:

- (1) Randomly initialize the particles in a population and set their corresponding parameters. Generate n particles randomly with $X_i = \langle p_i, v_i \rangle (i = 1, 2, \dots, n)$, where p_i and v_i are the geometrical location and velocity vector. So the initial generation of particle swarm $t = 0$ is identified as

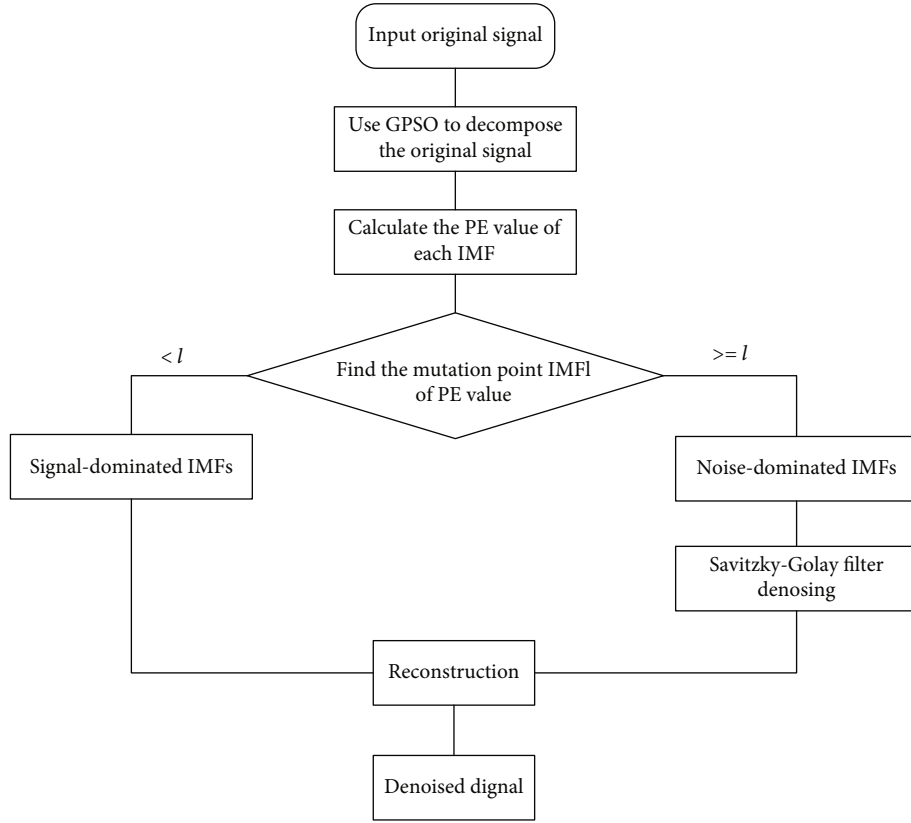


FIGURE 2: Process flow of the proposed denoising method.

$$\begin{aligned}
 X(0) &= (X_1(0), X_2(0), \dots, X_n(0)) \\
 &= (\langle p_1(0), v_1(0) \rangle, \langle p_2(0), v_2(0) \rangle, \dots, \langle p_n(0), v_n(0) \rangle).
 \end{aligned} \tag{7}$$

- (2) *VMD Decomposition.* Calculate the fitness of individuals in the initial population, and select the individual's optimal value $P_{pb}(t)$ and the global optimal value $P_{gb}(t)$ in the particle swarm. In this paper, PE is taken as the fitness function, and minimum PE is employed to determine optimal solution. By calculating the fitness function, the complexity of the signal is obtained from the PE value. The more complex the signal is, the greater the calculated PE value is, vice versa. After the vibration signal is decomposed by VMD, if there are many noise components included in the IMF component, the higher the complexity of the signal is, the greater the PE value is. If a few noise components are included in the IMF component, the stronger the regularity of the signal, the simpler the signal, and the lower the PE value.

- (3) Update the position and velocity of each particle. For each particle $X_i(t) = \langle p_i(t), v_i(t) \rangle$, we let

$$p_i(t+1) = p_i(t) + v_i(t+1), \tag{8}$$

$$\begin{aligned}
 v_i(t+1) &= C_1 v_i(t) + C_2 r_1(0, 1) [P_{pb}(t) - P_i(t)] \\
 &\quad + C_3 r_2(0, 1) [P_{gb}(t) - P_i(t)],
 \end{aligned} \tag{9}$$

where $r_1(0, 1)$ and $r_2(0, 1)$ are the random numbers in $(0, 1)$, C_1 is the inertia weight, and C_2 and C_3 are the learning factors. Therefore, the $t+1$ th generation of particle swarm is formed as follows:

$$\begin{aligned}
 X(t+1) &= (X_1(t+1), X_2(t+1), \dots, X_n(t+1)) \\
 &= (\langle p_1(t+1), v_1(t+1) \rangle, \langle p_2(t+1), v_2(t+1) \rangle, \dots, \langle p_n(t+1), v_n(t+1) \rangle).
 \end{aligned} \tag{10}$$

Larger inertia weight helps get out of local minimum point and facilitates global search, while smaller inertia weight is conducive to precise local search in the current region of search and helpful to the convergence of algorithm. For this reason, a linearly changing weight can be employed. An inertia weight decreases linearly from the maximum value C_{\max} to the minimum value C_{\min} . It varies with the iteration times of the algorithm as follows:

$$C_1 = C_{\max} - \frac{t * (C_{\max} - C_{\min})}{t_{\max}}, \tag{11}$$

where t is the current iteration steps, t_{\max} is the maximum iteration steps, and C_{\max} and C_{\min} are the maximum and minimum inertia weights, respectively, which are set to 1.2 and 0.6 in this paper.

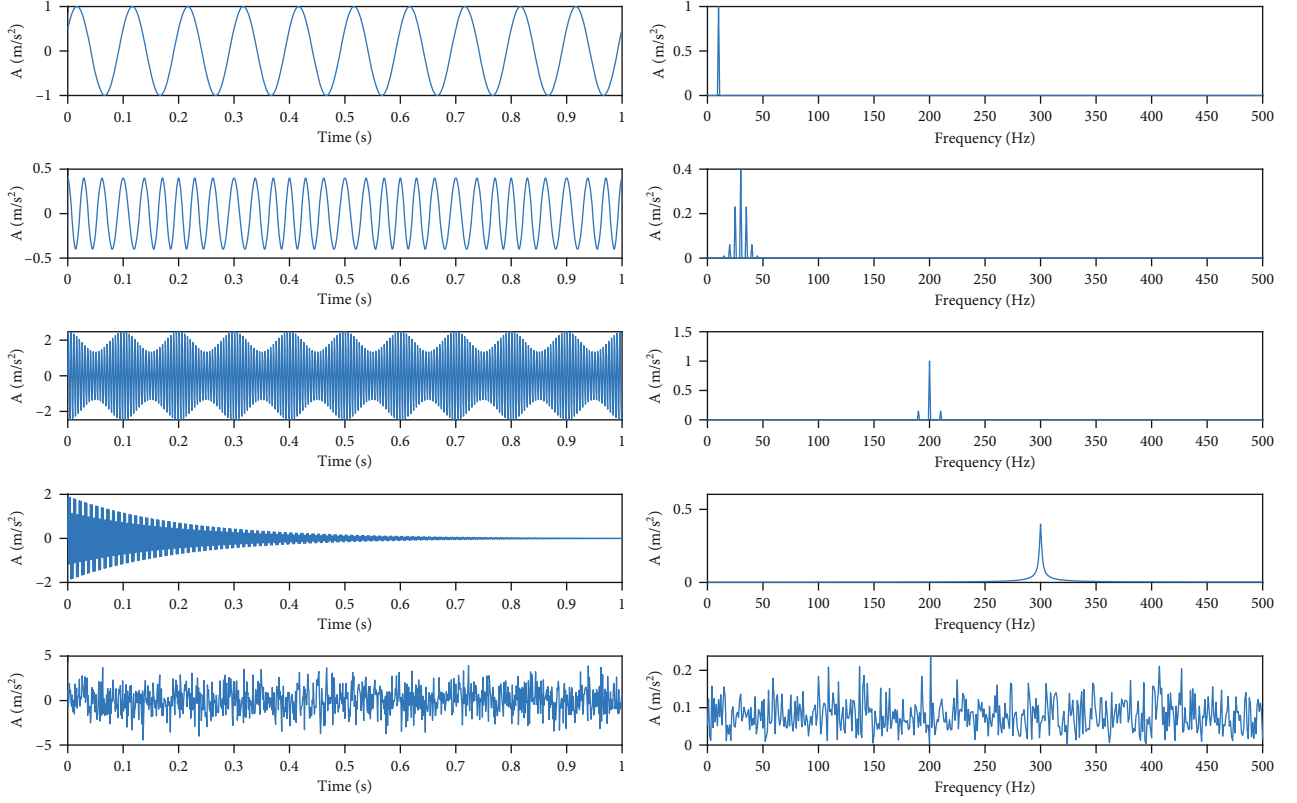


FIGURE 3: Time-frequency waveform of each subsignal in simulation signals.

- (4) *Crossover Operation.* Apply a crossover operator to a population, and switch some chromosomes in each selected pair of individuals at a probability to generate new individuals. The crossover probability is set to 0.8 in this paper.
- (5) *Mutation Operation.* Apply a mutation operator to the population. Change any or some genes of the selected individuals to other allele(s) at a probability. For a population $P(t)$, selection, crossover, and mutation operations are conducted to obtain its next-generation population $P(t+1)$, whose fitness is calculated. The fitness is then used for sequencing. These genetic operations will be repeated. The crossover probability is set to 0.3 in this paper.
- (6) Recalculate the fitness of particles in the new population, update the optimal solution ($P_{pb}(t)$ and $G_{gb}(t)$) of the population based on the fitness, and calculate the optimal particles $X_{pb}(t) = \langle P_{pb}(t), v_{pb}(t) \rangle$ that have been found so far for each particle i . Calculate the optimal particles $X_{gb}(t) = \langle P_{gb}(t), v_{gb}(t) \rangle$ that have been found so far for the current population $X(t)$.
- (7) Determine whether the conditions for the end of iteration are satisfied. If not, return to Step 3.

2.3. Fitness Function. When the GPSO is employed to optimize the VMD parameters, a fitness function must be deter-

mined to evaluate its optimization results. PE is a mean entropy parameter to measure the complexity of one-dimensional time series, which can be used to detect dynamic mutation and time series randomness [32]. Phase space reconstruction is carried out for a set of time series $\{X(i), i = 1, 2, \dots, N\}$ to obtain a matrix \mathbf{Y} :

$$\mathbf{Y} = \begin{pmatrix} x(1) & x(1+\tau) & \cdots & x(1+(d-1)\tau) \\ x(2) & x(2+\tau) & \cdots & x(2+(d-1)\tau) \\ x(j) & x(j+\tau) & \cdots & x(j+(d-1)\tau) \\ \vdots & \vdots & & \vdots \\ x(K) & x(K+\tau) & \cdots & x(K+(d-1)\tau) \end{pmatrix}, j = 1, 2, \dots, K, \quad (12)$$

where d is the embedding dimensions, τ is the delay time, K is the number of reconstructed components, and $x(j)$ is the components in the j th column of the reconstruction matrix. The elements in each column of the reconstruction matrix \mathbf{Y} are reorganized in ascending order, so that a group of symbol sequence $S_{(l)} = \{j_1, j_2, \dots, j_d\}$ can be obtained for each column of the matrix \mathbf{Y} . The occurrence probability of each symbol sequence P_1, P_2, \dots, P_k can be calculated. At this time, the PE H_p of K different symbol sequences for the time series $X(i)$ can be defined in the form of Shannon entropy as $H_p(d) = -\sum_{j=1}^k P_j \ln(P_j)$.

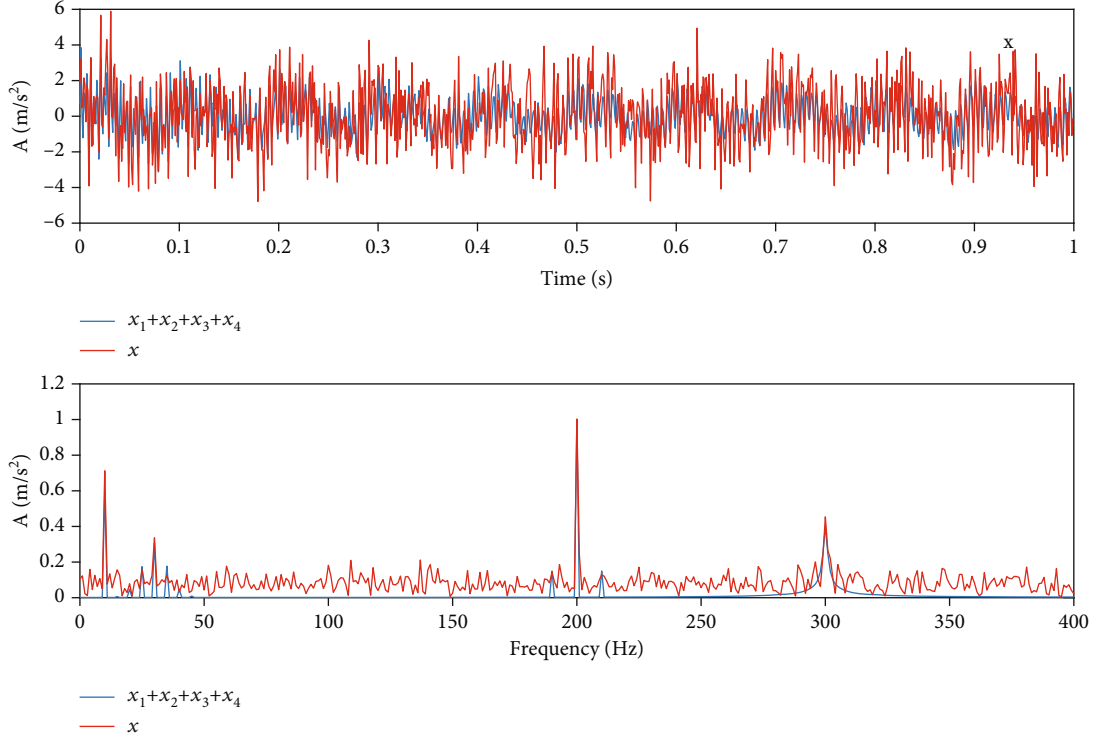


FIGURE 4: Time-frequency waveform of simulation signals.

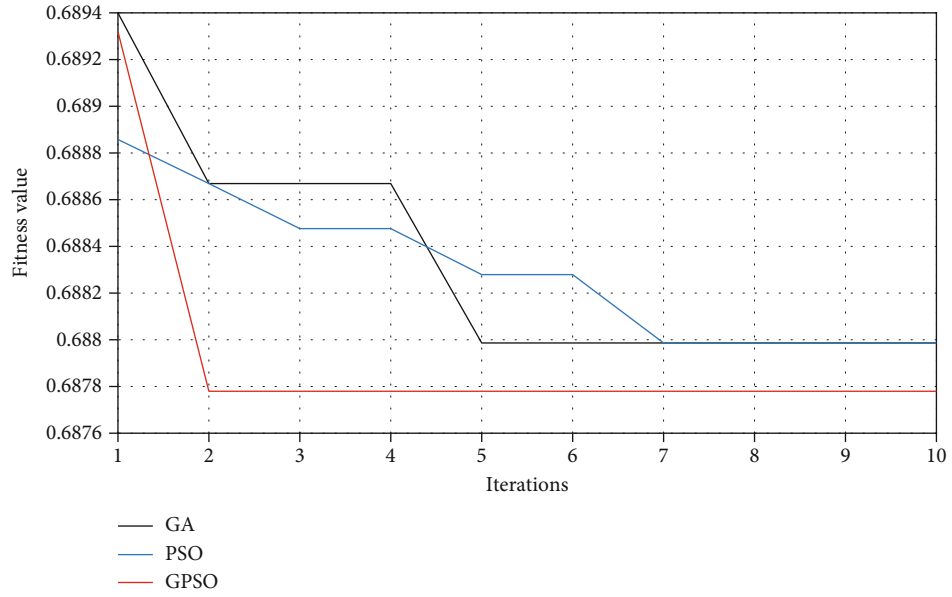


FIGURE 5: Comparison of fitness function convergence curves.

TABLE 1: Comparison of optimization results.

Method	Best parameter (α/K)	Time (s)
GA-VMD	2077.6/5.5	2262
PSO-VMD	2359.8/4.4	1805
GPSO-VMD	2219.4/5.1	1627

In the above definition, the value of H_p represents how time series is stochastic. A smaller value implies simpler time series, while a larger value leads to more complex and stochastic time series. Hence, minimum PE is taken as a fitness function in this paper and then solved to determine optimal decomposition parameters.

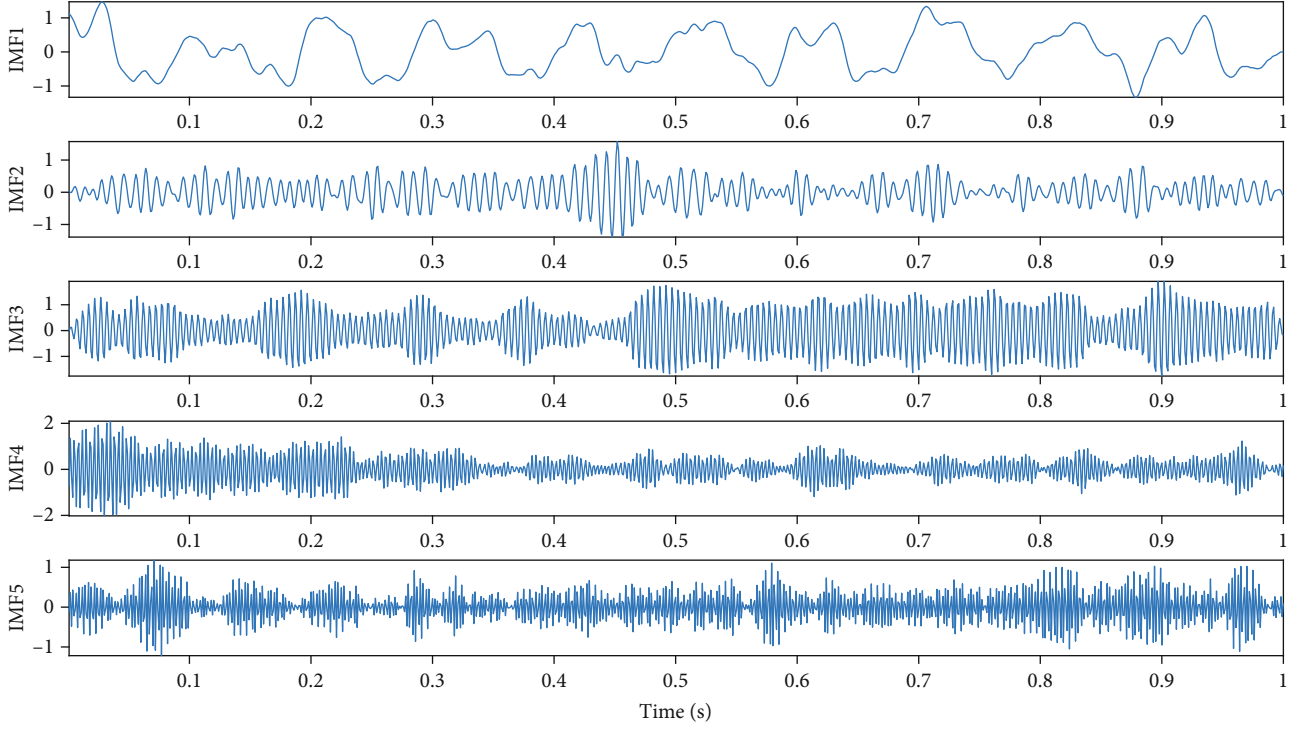


FIGURE 6: Decomposition results of simulation signals by VMD.

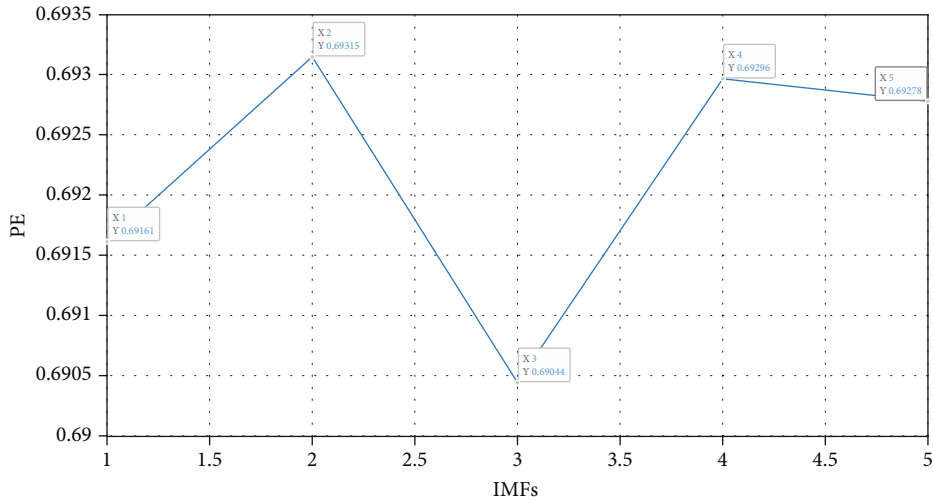


FIGURE 7: PE of each IMF component.

2.4. Savitzky-Golay Filter. SG filter, a method put forth by Savitzky and Golay, is widely applied in denoising the nonstationary signals containing non-Gaussian noise [33]. In the method, univariate P-order polynomials are adopted to fit the fixed length neighborhood of each data point in the selected data. Least squares criterion is followed to determine the polynomial coefficients by minimizing fitting error, so as to obtain the optimal fitted value of the data point, which is the value obtained after denoising. In this way, signals are denoised. At the time of denoising, the SG filter method can effectively retain the variation information of signals.

$$\begin{aligned}
 & \min \sum_{j=-m}^m (Y_j - y_j)^2, \\
 & \text{s.t. } Y_i = c_0 + c_1 i + c_2 i^2 + \dots + c_p i^p.
 \end{aligned} \tag{13}$$

3. The Proposed Vibration Signal Denoising Method

In this paper, a vibration signal denoising method combining improved VMD parameter optimization algorithm and

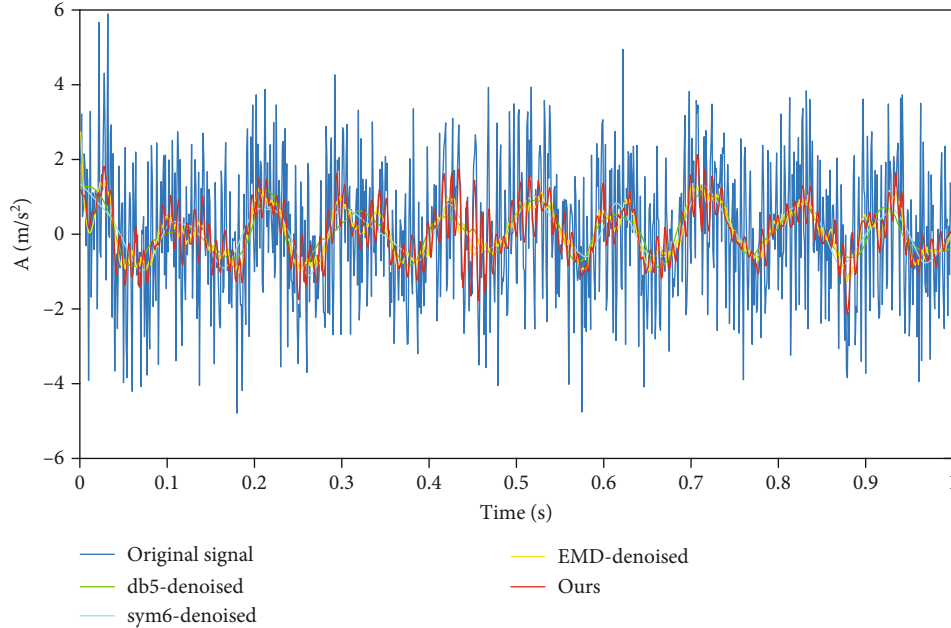


FIGURE 8: Simulation signals denoised by different algorithms.

TABLE 2: Denoising results with different algorithms.

Methods	SNR (dB)	MSE
Original signal	-7.2690	2.0352
db5	-4.4865	2.1325
sym6	-4.4810	2.1436
EMD-PE-SG	-0.4277	1.1413
The proposed method	1.2517	0.7204

SG filter is proposed. This method adopts the improved heuristic method GPSO and takes PE as the fitness function to automatically determine the number K of modal components and the penalty factor α of VMD. The optimal parameters K and α are used to perform the VMD of noise-containing vibration signals and obtain a number of IMFs. Subsequently, PE is employed to calculate the portion of noise in decomposed signal components. The components are classified into noise and signal components by searching for the mutation points of two adjacent IMF permutation entropies. Noise components are denoised by virtue of SG filter. In the end, the denoised components are reconstructed with signal components to eventually obtain denoised vibration signals. Through decomposition and reconstruction, the main information of the signal is retained and a large amount of noise contained in the signal is eliminated. This method can be adaptively select optimization parameters and noise components. We do not directly abandon noise-containing components but optimize them to prevent overfiltering from causing signal distortion. The signals reconstructed after denoising contain more signal information. The denoising process of the proposed algorithm is given in Figure 2. The exact procedures of the proposed algorithm can be expressed as follows:

Step 1. Taking PE as the fitness function, GPSO-VMD is applied to decompose the vibration signal, and K and α at the minimum PE value are taken as the optimal decomposition values.

Step 2. Set the obtained K and α as VMD parameters and decompose the vibration signal into K IMFs.

Step 3. Calculate the PE of IMF obtained by decomposition. The signal-dominated IMF and noise-dominated IMF are distinguished by the mutation point of PE of two adjacent IMF.

Step 4. Apply SG filter to denoise the noise component.

Step 5. Reconstruct the IMFs dominated by the signal and the IMF component after denoising to obtain the final denoised signal.

4. Simulation

4.1. Construction of Simulation Signals. The vibration signals measured by an atomic gravimeter in a ship environment are very complicated, nonlinear, and nonstationary. These signals actually contain lots of unpredictable disturbance noises. In order to verify the effectiveness of the proposed method, vibration simulation signals were designed with nonlinear and nonstationary features. The simulation signals $x(t)$ consisted of sinusoidal signal $x_1(t)$, frequency-modulated signals $x_2(t)$, amplitude-modulated signals $x_3(t)$, exponentially decayed sinusoidal signals $x_4(t)$, and other random noises with mean 0, standard deviation 1, and amplitude 1.4. Moreover, they had $t = [0, 0.001]$ and sampling frequency 1000 Hz. These simulation signals are defined by Equation (14).

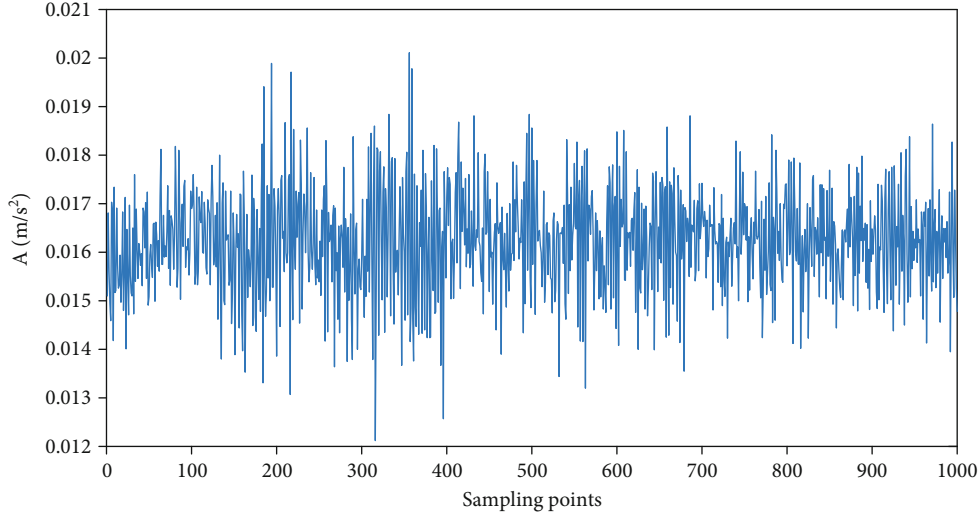


FIGURE 9: Time domain waveform of vibration signals of a marine atomic gravimeter.

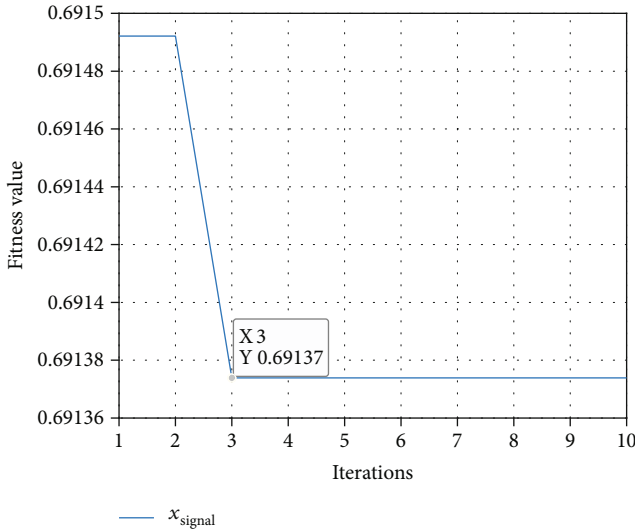


FIGURE 10: Convergence curve of vibration signal fitness function.

$$\begin{cases} x_1(t) = 0.6 \sin(20\pi t + \pi/6), \\ x_2(t) = 0.4 \cos(60\pi t + \sin 10\pi t), \\ x_3(t) = (1 + 0.3 \cos 20\pi t) \cdot \sin(400\pi t), \\ x_4(t) = 2e^{-5t} \cdot \sin 600\pi t, \\ x = x_1 + x_2 + x_3 + x_4 + 1.4 \cdot \text{rand}(n). \end{cases} \quad (14)$$

The time-frequency domain waveform of each subsignal is given in Figure 3, and the mixed signal is presented in Figure 4. As revealed in the frequency domain waveform of mixed signals, noises had higher power than signals, so that signals were submerged in a highly noisy environment. Moreover, noises were evenly distributed in the entire frequency domain of signals, which makes it very difficult to accurately extract feature signals.

Prior to VMD, number of decomposed modes K and penalty term α should be properly selected. The improved GPSO was adopted to optimize the VMD algorithm. Thus, we set population size 50, crossover 0.8, and mutation probability 0.3. The number of decomposed modes K was set in the range [2, 10], while the penalty term α was set in the range [200, 3000]. Minimum PE was adopted as the fitness function. The fitness function convergence curve of GPSO is shown in Figure 5. Convergence was achieved at the time of the second iteration, when the optimal VMD parameters K and α were 5.1 and 2219.4, respectively, and rounded to 5 and 2219 since they must be integral. In order to prove its superiority, the GPSO was compared with GA and PSO algorithms, respectively. All optimization methods employed minimum PE as fitness function and had the same population size and maximum iteration times. The experiment used Windows 10 operating system, Intel Corei7-8750H and matlab2019a for simulation. The convergence results of the fitness function for these three algorithms are presented in Figure 5 and summed up in Table 1.

As shown in Figure 5, the GPSO, GA, and PSO converged after the second, fifth, and seventh iteration, respectively. The GPSO had the lowest fitness after convergence and achieved the fastest convergence among them, which proves the strong global search capability and fast convergence rate.

4.2. Denoising Analysis of Simulation Signals. Noise simulation signals were decomposed in VMD based on the K and α values obtained by GPSO, so as to gain a number of IMF components as shown in Figure 6. Obviously, signals could be effectively decomposed in VMD. The decomposition results were greatly consistent with simulation signals, proving the efficacy of the parameters obtained by GPSO.

The IMF components obtained by VMD were arranged from low frequency to high frequency. Noises were mainly concentrated in high-frequency components, but there were still some effective IMF components. If they were simply

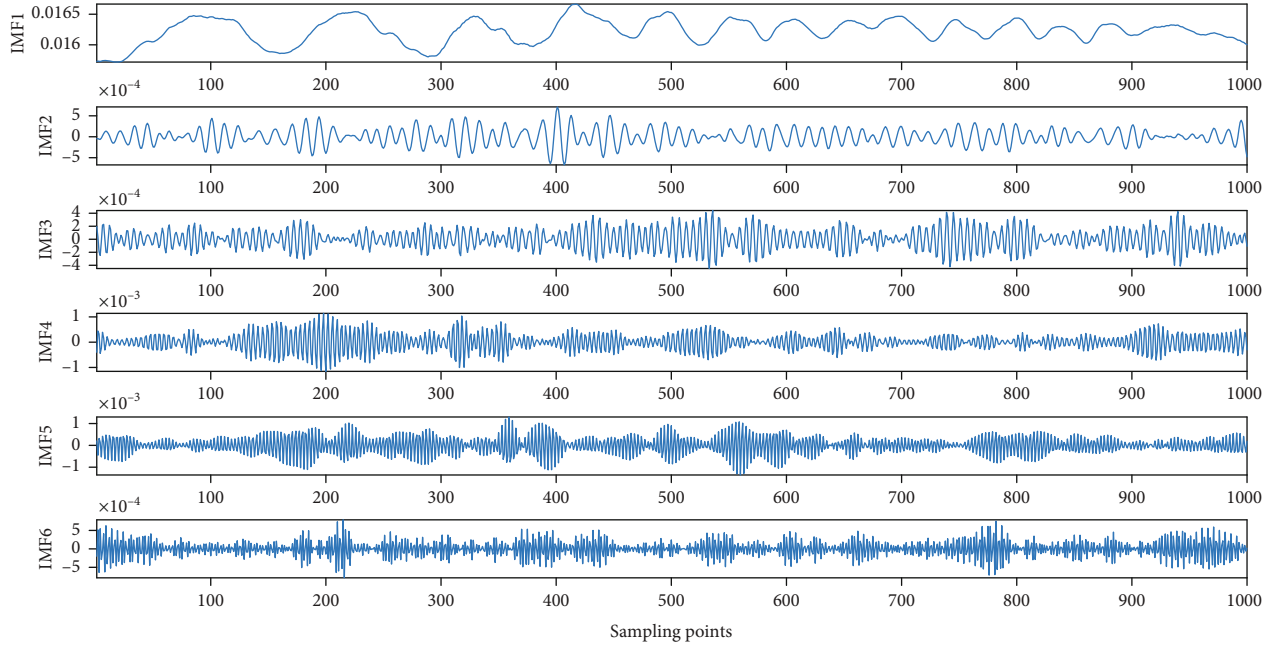


FIGURE 11: Decomposition by VMD.

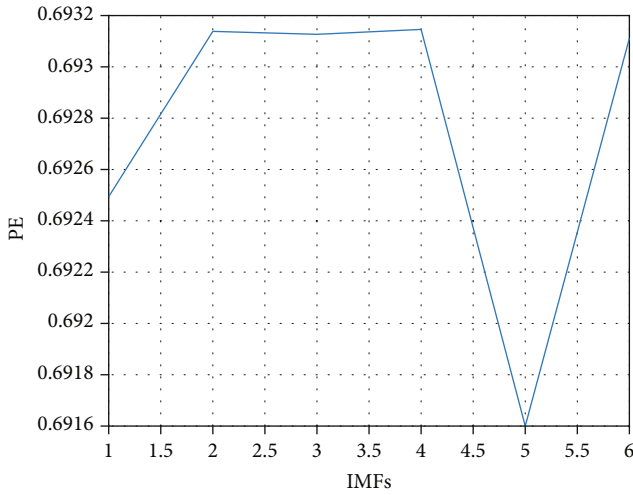


FIGURE 12: PE of each IMF for the vibration signal.

abandoned, some effective signals would be lost. For this reason, effective components must be separated from noise-containing components, so as to denoise the latter. For this purpose, PE of each IMF component was calculated separately and used to determine the proportion of noise-containing components in the IMF components. This was achieved by calculating the mutation point in the PE of two adjacent components, that is, $\beta = \max |H_p(\text{IMF}_{l+1}) - H_p(\text{IMF}_l)|$ with l for mutated IMF components. The noise-containing components were denoised by SG filter and then reconstructed with the effective IMF components to finally obtain denoised signals. A simulation signal $x(t)$ was decomposed into five IMF components, whose permutation entropies were calculated separately.

Based on the PE of each IMF component in Figure 7, the difference between the permutation entropies of adjacent IMF components was 0.00154, 0.00271, 0.00252, and 0.00018, respectively. The difference between IMF2 and IMF3 was the largest. Hence, IMF3 was a mutation point, which helped identify IMF3-IMF5 as high-frequency noise-containing components. These high-frequency noise-containing components were treated by SG filter to obtain a signal. In this paper, the SG filter parameters are set as polynomial order 3 and data frame length 41. This signal was reconstructed with other signal components including IMF1 and IMF2 to obtain denoised vibration signal.

We also compared the proposed method with the classic wavelet denoising and empirical mode decomposition (EMD) to verify its effectiveness. Daubechies (db) wavelet and Symlets (sym) wavelet with good orthogonality in the wavelet transform denoising were selected to denoise simulation signals. The green and cyan signals in Figure 8 show the results of wavelet transform denoising with five layers of soft threshold by db5 and sym6 wavelets, respectively. After analyzing these results, it was found that the denoising by db5 and sym6 wavelets might achieve the desired effect of denoising but filtered lots of useful high-frequency information, resulting in information distortion. The yellow signal in Figure 8 shows the result of denoising by EMD. In order to highlight the advancement of the proposed VMD algorithm, the denoising by EMD was performed in the same way as the proposed algorithm. A noise was first decomposed by EMD to obtain a number of IMF components. The PE of each component was calculated to find out the mutation point. The SG filtering was carried out for the IMF components in front of the mutation point. At last, the denoised signal was obtained through reconstruction. Based on the denoising results presented in Figure 8,

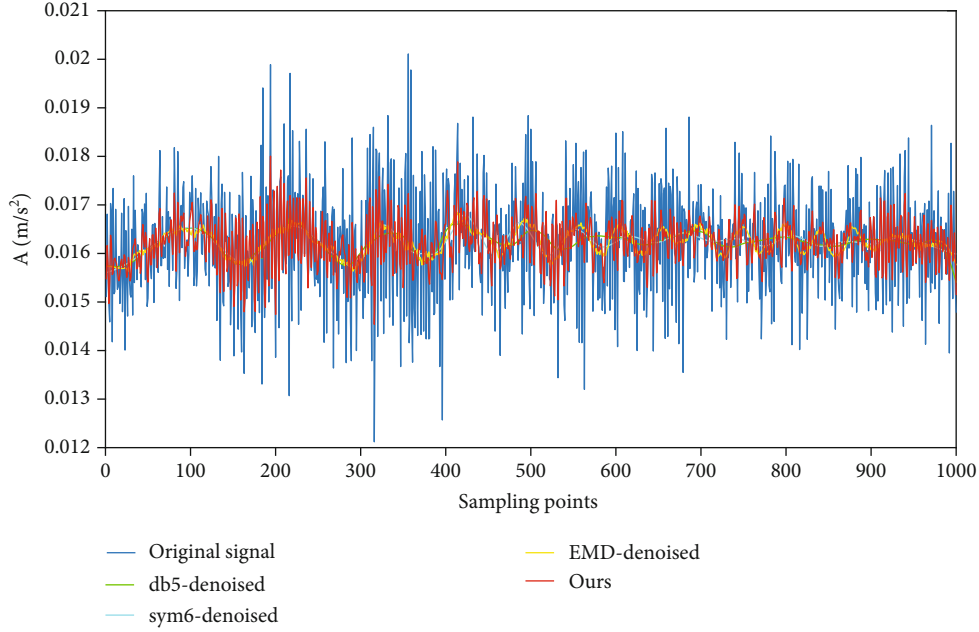


FIGURE 13: Comparison of denoised vibration signals.

EMD was more effective than db5 and sym6 wavelets in terms of denoising but still troubled by severe information distortion, causing the excessive loss of useful information. The denoising results of the proposed VMD algorithm are shown in the red signal in Figure 8. Obviously, the proposed algorithm could effectively retain the information of signals, achieve good denoising effect, and achieve high consistency regardless the denoised signal or the original signal.

In order to quantitatively analyze the denoising effect of the proposed method, we took signal-to-noise ratio (SNR) and Mean Square Error (MSE) as the indicators to evaluate the denoising effect with denoised signals and noise-containing signals [34]. The greater SNR, the better effect of denoising. The lower MSE, the poorer effect of denoising. The SNR and MSE values are expressed by

$$\text{SNR} = 10 \lg \frac{\sum_{i=1}^n x_i^2}{\sum_{i=1}^n (y_i - x_i)^2}, \quad (15)$$

$$\text{MSE} = \sum_{i=1}^n \frac{1}{n} (x_i - y_i)^2, \quad (16)$$

where x_i indicates the signals that do not contain noise and y_i means the denoised signals. The SNR and MSE values in the test of algorithms with simulation signals are presented in Table 2.

As revealed in Table 2, SNR was -7.2690 after adding random noise into a simulation signal $x(t)$. It was evident that the signal had lower power than noise, so that it was entirely submerged by the latter, making it very difficult to perform denoising. After being denoised by db5, sym6, EMD, and the proposed method, the proposed method achieved SNR 1.2517, which was the largest among them. Moreover, the proposed method realized the lowest MSE,

revealing the most remarkable improvement by the proposed method. The proposed algorithm proves that denoising can be significantly achieved even in a highly noisy environment.

5. Vibration Signal Denoising of Marine Atomic Gravimeter

5.1. Data Collection. The vibration data of an atomic gravimeter was collected by navigation test. The test platform was composed of an atomic gravimeter, an inertial stabilized platform, and a vibration measuring device. The collection of vibration data was performed by a collecting unit formed by a data collector, an accelerometer, and a computer. The accelerometer was attached to the atomic gravimeter placed on the inertial stabilized platform. The accelerometer converted the vibration information into analog voltage output. The data collector performed the analog-to-digital conversion of analog signals collected by sensors and transferred the digital information to the computer. Data collection software was installed in the computer to store and process the received digital information. We selected the vibration signal x_{signal} and took the data from 1000 sampling points for analysis, as shown in Figure 9.

5.2. Implementation of Denoising. The GPSO was employed to optimize the VMD parameters in the proposed method, so as to obtain the optimal number of decomposed modes K and penalty term α . We set population size 50, crossover probability 0.8, mutation probability 0.3, number of decomposed modes in [2, 10], and penalty term in [200, 3000]. PE was used as the fitness function. At the third iteration, the fitness function has completed convergence, and the minimum PE value is 0.69137. The corresponding optimization

results were [6, 2301]. The convergence curve of the fitness function is shown in Figure 10.

Subsequently, the parameters optimized by GPSO were used in the decomposition by VMD to obtain six IMF components. Based on these components, it was found that noise signals were concentrated in IMF5 and IMF6.

The PE of each IMF component was calculated. Then the maximum difference between the permutation entropies of two adjacent IMF components was calculated to find out a mutation point and classify IMF components into effective signal IMF components and noise-containing IMF components as shown in Figure 11. As revealed in the slope of PE in Figure 12, the mutation point of PE for the signal x_{signal} was IMF, so that the noise components of the signal x_{signal} were IMF5-IMF6. The SG filtering was conducted for noise components. The filtered IMF components were reconstructed with the effective IMF components to obtain the denoised vibration signal as shown in Figure 13.

The vibration signal of a marine atomic gravimeter was measured during navigation, so that it was impossible to obtain a noise-free original vibration signal. For this reason, SNR and MSE could not be used to quantitatively analyze and compare the proposed method with other algorithms. Figure 13 shows the results of wavelet transform denoising by five layers of soft threshold with db5 and sym6 wavelets and the effects of denoising by EMD-PE-SG, respectively. As revealed in Figure 13, EMD-PE-SG achieved better denoising than db5 and sym6 wavelets and could retain more actual information. However, it still lost too much useful information compared with the proposed method, so it resulted in severe loss and distortion of signal information.

6. Conclusion

A vibration signal denoising method based on improved VMD is put forward in this paper. In this method, an improved GPSO based on PSO and GA is first adopted for the parametric optimization of VMD. Minimum PE is taken as the fitness function to adaptively search for the optimal parameters K and α in VMD. Based on the obtained parameters K and α , a noise-contained signal is decomposed into a number of IMF components. PE is utilized to calculate the proportion of noise-containing components in the signal components obtained by decomposition. A mutation point is found with PE of adjacent IMF components to classify these components into noise and signal components. The SG filter is carried out to denoise these noise components. At last, the denoised components are reconstructed with signal components to generate the denoised vibration signal. The reconstructed signal contains more physical information. The proposed method makes use of signal mode decomposition to adaptively extract noise but does not use any fixed priori threshold. In order to demonstrate its effectiveness, the proposed method is applied in denoising with the vibration data collected by vibration and measured by a marine atomic gravimeter. As proved in the test, the proposed method can effectively separate noise from vibration signals and achieve great denoising. Its potential has been

demonstrated in filtering noise and improving the quality of vibration data to provide the supporting data for the vibration compensation of a marine atomic gravimeter.

Data Availability

No data were used to support the findings of the study.

Conflicts of Interest

The authors declare that they have no conflicts of interest.

Acknowledgments

This research was funded by the National Natural Science Foundation of China under Grants (61873275), the Foundation of Basic Strengthening Technology of the Military Science and Technology Commission (2019JCQJ047), and the Natural Science Foundation of Hubei Provincial of China (2017CFB377).

References

- [1] P. Cheiney, L. Fouché, S. Templier et al., "Navigation-compatible hybrid quantum accelerometer using a Kalman filter," *Physical Review Applied*, vol. 10, no. 3, 2018.
- [2] Y. Bidel, N. Zahzam, C. Blanchard et al., "Absolute marine gravimetry with matter-wave interferometry," *Nature Communications*, vol. 9, no. 1, p. 627, 2018.
- [3] B. Cheng, Y. Zhou, P. J. Chen et al., "Absolute gravity measurement based on atomic gravimeter under mooring state of a ship," *Acta Physica Sinica*, vol. 70, no. 4, article 040304, 2021.
- [4] A. Li, H. Che, F. J. Qin, C. F. Huang, and W. B. Gong, "Development and prospect of cold atom interferometry gravimetry measurement," *Journal of Naval University of Engineering*, vol. 33, no. 6, pp. 1–7, 2021.
- [5] M. K. Zhou, X. Xiong, L. L. Chen, J. F. Cui, X. C. Duan, and Z. K. Hu, "Note: a three-dimension active vibration isolator for precision atom gravimeters," *The Review of Scientific Instruments*, vol. 86, no. 4, article 046108, 2015.
- [6] M. Hauth, C. Freier, V. Schkolnik, A. Senger, M. Schmidt, and A. Peters, "First gravity measurements using the mobile atom interferometer GAIN," *Applied Physics B*, vol. 113, no. 1, pp. 49–55, 2013.
- [7] V. Menoret, P. Vermeulen, N. Le Moigne et al., "Gravity measurements below 10(-9) g with a transportable absolute quantum gravimeter," *Scientific Reports*, vol. 8, no. 1, p. 12300, 2018.
- [8] A. P. Xu, D. L. Kong, Z. J. Fu, Z. Y. Wang, and Q. Lin, "Vibration compensation of an atom gravimeter," *Chinese Optics Letters*, vol. 17, no. 7, article 070201, 2019.
- [9] B. Barrett, L. Antoni-Micollier, L. Chichet et al., "Dual matter-wave inertial sensors in weightlessness," *Nature Communications*, vol. 7, no. 1, p. 13786, 2016.
- [10] X. B. Zhang, W. W. Ying, P. X. Yang, and M. Sun, "Parameter estimation of underwater impulsive noise with the class B model," *IET Radar, Sonar & Navigation*, vol. 14, no. 7, pp. 1055–1060, 2020.
- [11] X. B. Zhang, P. X. Yang, P. Huang, H. X. Sun, and W. W. Ying, "Wide-bandwidth signal-based multireceiver SAS imagery

- using extended chirp scaling algorithm,” *IET Radar, Sonar & Navigation*, vol. 16, pp. 531–541, 2022.
- [12] X. B. Zhang and P. X. Yang, “An improved imaging algorithm for multi-receiver SAS system with wide-bandwidth signal,” *Remote Sensing*, vol. 13, no. 24, p. 5008, 2021.
- [13] Q. J. Zhang, G. X. Lu, C. Y. Zhang, and Y. Xu, “Time–frequency analysis of torsional vibration signals based on the improved complete ensemble empirical mode decomposition with adaptive noise, robust independent component analysis, and Prony’s methods,” *Journal of Vibration and Control*, no. - article 10775463211038124, 2021.
- [14] X. B. Zhang, H. R. Wu, H. X. Sun, and W. W. Ying, “Multireceiver SAS imagery based on monostatic conversion,” *IEEE Journal of Selected Topics in Applied Earth Observations and Remote Sensing*, vol. 14, pp. 10835–10853, 2021.
- [15] W. B. Gong, A. Li, C. F. Huang, H. Che, C. X. Feng, and F. J. Qin, “Effects and prospects of the vibration isolation methods for an atomic interference gravimeter,” *Sensors*, vol. 22, no. 2, p. 583, 2022.
- [16] C. W. Shen, Z. Q. Wang, C. Liu et al., “Analysis of vehicle platform vibration based on empirical mode decomposition,” *Shock and Vibration*, vol. 2021, 13 pages, 2021.
- [17] Y. Kopsinis and S. McLaughlin, “Development of EMD-based denoising methods inspired by wavelet thresholding,” *IEEE Transactions on Signal Processing*, vol. 57, no. 4, pp. 1351–1362, 2009.
- [18] M. Rezaee and A. Taraghi Osguei, “Improving empirical mode decomposition for vibration signal analysis,” *Proceedings of the Institution of Mechanical Engineers, Part C: Journal of Mechanical Engineering Science*, vol. 231, no. 12, pp. 2223–2234, 2016.
- [19] Z. H. Wu and N. E. Huang, “Ensemble empirical mode decomposition: a noise-assisted data analysis method,” *Advances in Adaptive Data Analysis*, vol. 1, no. 1, pp. 1–41, 2011.
- [20] Y. C. Jia, G. L. Li, X. Dong, and K. He, “A novel denoising method for vibration signal of hob spindle based on EEMD and grey theory,” *Measurement*, vol. 169, p. 12, 2021.
- [21] K. Dragomiretskiy and D. Zosso, “Variational mode decomposition,” *IEEE Transactions on Signal Processing*, vol. 62, no. 3, pp. 531–544, 2014.
- [22] H. Yang, L. L. Li, and G. H. Li, “A new denoising method for underwater acoustic signal,” *IEEE Access*, vol. 8, pp. 201874–201888, 2020.
- [23] F. Y. Li, B. Zhang, S. Verma, and K. J. Marfurt, “Seismic signal denoising using thresholded variational mode decomposition,” *Exploration Geophysics*, vol. 49, no. 4, pp. 450–461, 2018.
- [24] J. X. Wang, Y. L. Zhang, F. Y. Zhang et al., “Accuracy-improved bearing fault diagnosis method based on AVMD theory and AWPSO-ELM model,” *Measurement*, vol. 181, p. 109666, 2021.
- [25] D. M. Wang, L. J. Zhu, J. K. Yue, J. Y. Lu, D. W. Li, and G. F. Li, “Application of variational mode decomposition based on particle swarm optimization in pipeline leak detection,” *Engineering Research Express*, vol. 2, no. 4, p. 15, 2020.
- [26] T. Liang, H. Lu, and H. Sun, “Application of parameter optimized variational mode decomposition method in fault feature extraction of rolling bearing,” *Entropy (Basel)*, vol. 23, no. 5, p. 520, 2021.
- [27] W. X. Wu, Z. J. Wang, J. P. Zhang, W. J. Ma, and J. Y. Wang, “Research of the method of determining k value in VMD based on kurtosis,” *Journal of Mechanical Transmission*, vol. 42, no. 8, pp. 153–157, 2018.
- [28] Y. Q. Song, S. C. Deng, and Y. G. Lu, “Application of K value optimized VMD in bearing fault diagnosis,” *Measurement & Control Technology*, vol. 38, no. 4, pp. 117–121, 2019.
- [29] A. Kumar, Y. Q. Zhou, and J. W. Xiang, “Optimization of VMD using kernel-based mutual information for the extraction of weak features to detect bearing defects,” *Measurement*, vol. 168, p. 108402, 2021.
- [30] G. R. Feng, H. R. Wei, T. Y. Qi, X. M. Pei, and H. Wang, “A transient electromagnetic signal denoising method based on an improved variational mode decomposition algorithm,” *Measurement*, vol. 184, p. 109815, 2021.
- [31] F. M. Zhou, X. Q. Yang, J. X. Shen, and W. Q. Liu, “Fault diagnosis of hydraulic pumps using PSO-VMD and refined composite multiscale fluctuation dispersion entropy,” *Shock and Vibration*, vol. 2020, 13 pages, 2020.
- [32] C. Bandt and B. Pompe, “Permutation entropy: a natural complexity measure for time series,” *Physical Review Letters*, vol. 88, no. 17, article 174102, 2002.
- [33] H. Yang, Y. X. Cheng, and G. H. Li, “A denoising method for ship radiated noise based on Spearman variational mode decomposition, spatial-dependence recurrence sample entropy, improved wavelet threshold denoising, and Savitzky-Golay filter,” *Alexandria Engineering Journal*, vol. 60, no. 3, pp. 3379–3400, 2021.
- [34] G. Ravizza, R. Ferrari, E. Rizzi, and V. Dertimanis, “On the denoising of structural vibration response records from low-cost sensors: a critical comparison and assessment,” *Journal of Civil Structural Health Monitoring*, vol. 11, no. 5, pp. 1201–1224, 2021.

Research Article

Supervised Contrastive Learning-Based Modulation Classification of Underwater Acoustic Communication

Daqing Gao , Wenhui Hua , Wei Su , Zehong Xu , and Keyu Chen 

Information and Communication Engineering, Xiamen University, Xiamen, China

Correspondence should be addressed to Wei Su; suweixiamen@xmu.edu.cn

Received 12 January 2022; Accepted 21 February 2022; Published 21 March 2022

Academic Editor: Hamada Esmaiel

Copyright © 2022 Daqing Gao et al. This is an open access article distributed under the Creative Commons Attribution License, which permits unrestricted use, distribution, and reproduction in any medium, provided the original work is properly cited.

Modulation parameters are very significant to underwater target recognition. But influenced by the severe and time-space varying channel, most currently proposed intelligent classification networks cannot work well under these large dynamic environments. Based on supervised contrastive learning, an underwater acoustic (UWA) communication modulation classifier named UMC-SCL is proposed. Firstly, the UMC-SCL uses a simply convolutional neural networks (CNN) to identify the presence of the UWA signals. Then, the UMC-SCL uses ResNet50 as an encoder and updates the network by supervised contrastive learning loss function, which can effectively use the category information and make the eigenvector distribution of the same category more concentrated. Then, the classifier uses the feature vector output by the encoder to distinguish the final modulation categories. Finally, extensive ocean, pool, and simulation experiments are done to verify the performance of the UMC-SCL. Without any prior information, the average classification accuracy for MPSK and MFSK can reach 98.6% at 0 dB and is increased by 6% compared to the benchmark algorithm under low SNR.

1. Introduction

With the development of UWA communication technology, more and more ocean applications have installed UWA communication equipments. Through modulation classification can explore the influence of ocean multipath and Doppler effect and more effectively assistant target identification, signal identification, interference identification, and spectrum management.

In general, conventional modulation classification algorithms can be divided into two categories: likelihood-based and feature-based methods [1]. The likelihood-based method requires a large amount of prior information and computation, which makes it unsuitable for harsh noncooperative UWA communication. On the contrary, feature-based method has gradually become the mainstream method due to its low computational complexity and no dependence on prior information.

Feature-based methods consist of two parts: feature extraction and classifier. In [2], multiscale reverse dispersion entropy and grey relational degree features are used to improve the classification performance of ship-radiated

noise. In [3–5], support vector machine (SVM) is used to distinguish wireless signals. In [6], high order cumulant features are put into SVM based on mixture kernel function to classify the digital signals. Wei et al. [7] use a SVM based on hybrid features, cyclostationary, and information entropy to classify the modulation types, including BPSK, QPSK, 2FSK, 4FSK, and MSK. By this means, the parameter extraction process is complicated, and the capacity is low. Even if more training data is added, the classification performance cannot always be improved [8]. For recent years, deep learning [9–16] has shown excellent performance in image feature extraction, speech recognition, and natural language processing and has been successfully used on acoustic signal sets [17, 18]. However, in modulation classification area, it is mainly used in the electromagnetic communication.

In [9], long-short term memory (LSTM) is used to classify the modulation schemes for a distributed wireless spectrum sensing network. Li et al. [10] use the I/Q data to classify signal directly through deep neural networks (DNN). In [11, 12], adaption of deep learning to the complex temporal signal domain is studied, and first proposed a CNN-based classifier to solve the problem of excessive

parameters in DNN. In [13], AlexNet and GoogLeNet are used to classify the constellation of the signal samples. Huang et al. [14] introduce a novel cascaded CNN that cascade two-block CNN to identify MPSK and MQAM hierarchically. Wang et al. [15] propose a hierarchical CNN scheme to more accurately classify the higher-order QAM signals. Liu et al. [16] combine CNN with long short-term memory (LSTM) architecture into DNN and increase the accuracy rate by 13.5% compared with original CNN. In these classic end-to-end neural networks, cross-entropy loss is the most widely used loss function to achieve the purpose of updating network weights. However, the cross-entropy loss function also lacks robustness to noisy tags [19, 20] and may have marginality [21, 22], leading to reduce generalization performance. The traditional end-to-end supervised training methods focus on the final classification accuracy rather than the quality of the features extracted from the UWA data. As a result, when the signal-to-noise ratio (SNR) becomes low, the accuracy of traditional methods will drop sharply and cannot work well. In recent years, the renaissance of contrastive learning has led to major advances in self-supervised performance learning [23–25]. When there is no available label, the data is augmented through its own cropping and flipping, and the encoder is updated through the self-supervised loss function. Although it can alleviate the disadvantages of traditional networks to a certain extent, it cannot learn from the other samples in the same category. As a result, self-supervised contrastive learning methods are not suitable for UWA data with different SNR.

In this paper, from the perspective of representation learning, we extract features with high discrimination through supervised contrastive learning [26] to support the normal classification tasks in harsh UWA channel and propose a novel classification framework named UMC-SCL. We first distinguish between valid signal and ocean noise through a simply CNN. Then, the supervised contrastive learning module will learn from the valid modulation signal and update the encoder network by supervised contrastive learning loss function. Go through this module, the features of the same category are as close as possible, and the features of different categories are as far away as possible. Therefore, we can achieve the purpose of classification only by using a fully connected layer. Finally, we verify the superiority of the proposed method through extensive ocean, pool, and simulation experiments and use principal component analysis (PCA) to visualize the output features for interpretability. Compared with the known traditional supervised networks, the proposed method greatly improves the classification accuracy under low SNR without any prior information and parameter extraction process.

2. System Model

2.1. Signal Model. The UWA communication channel is one of the most challenging wireless communication media known to human. The medium space of underwater sound propagation is very complicated, with high attenuation, long time delay, strong multipath, and high Doppler effect.

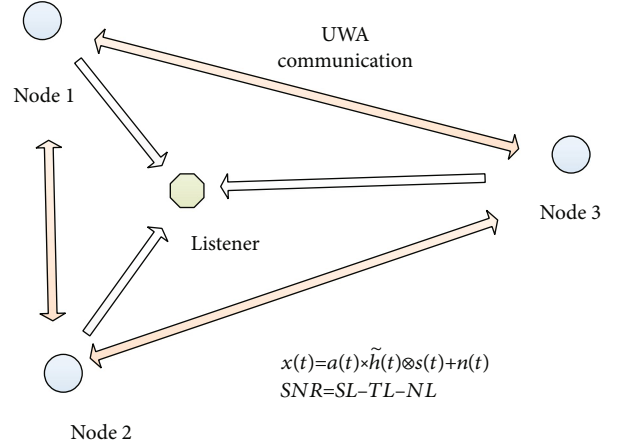


FIGURE 1: The progress of UWA communication.

Figure 1 shows the basic process of UWA communication. $\tilde{h}(t)$ is the energy normalized impulse response of UWA channel, $s(t)$ is the original signal, and $n(t)$ is the ocean noise. $a(t)$ is related to SNR. Node 1, Node 2, and Node 3 communicate with each other. The listener can intercept their communication signals from the sea water. SL is emitting sound source level, TL is propagation loss, and NL is the background noise level [27].

2.2. UWA Data Sources. In order to make the research result more applicable, we have constructed a complete data set through actual ocean experiments, pool experiments, and simulation experiments that are close to the reality.

2.2.1. Ocean Data. The ocean data are collected in Wuyuan Bay, Xiamen, China. As shown in Figure 2, the sound source T_{x1} and the receiving hydrophone R_{x1} are placed in the shallow sea near the footpath, with a depth of 5 m and a communication distance of 60 m.

We send and receive signals at four different times of the day. During the experiment, there are some activities such as yachts, fishing boats, and other activities that introduce a lot of man-made noise. Besides, dozens of plank road bridge piers between the sending and receiving ends make the reflection effect more significant.

2.2.2. Pool Data. Ocean experiments are costly, and the data acquisition is difficult. In order to increase the richness of the dataset, we further conduct pool experiments. The pool is located in UAC laboratory in Xiamen University. Figure 3(a) is the photo of the pool. The pool has a length of 25 m and a width of 5 m. It is divided into deep water area (depth = 1.5 m) and shallow water area (depth = 1.15 m). Figure 3(b) is the distribution of transmitter and receivers for pool experiment. T_x is the sound source, and R_x is the hydrophone. The distances between R_{x1} , R_{x2} , R_{x3} , and T_x are 3 m, 6 m, and 12 m, respectively, and the depth is 1 m. When T_x sends a signal, the sound rays will be attenuated by water and reflected on the pool wall.



FIGURE 2: The scene map of ocean experiment.

2.2.3. *Simulation Data.* Constructing a good simulation UWA channel is the basis for carrying out practical experiments. Figure 4 shows the sound ray propagation in a shallow sea channel. The sound ray will be reflected by the sea surface and bottom during propagation. Moreover, the speed of sound in seawater changes with temperature, salinity, and water depth, causing sound rays to be refracted. The speed of sound can be described according to the following formula [27].

$$c = 1449.2 + 4.6T - 0.055T^2 + 0.00029T^3 + (1.34 - 0.01T)(S - 35) + 0.016Z, \quad (1)$$

where T is temperature in, S is salinity in ppm, and Z is the depth of seawater in m.

In UWA communication, the impulse response can be assessed by beam tracing for typical acoustic communication frequencies. The basic path loss of the received signal that traveling through the UWA channel is given by [28].

$$A(l) = A_0 l^k \alpha^l, \quad (2)$$

where A_0 is a scaling constant, l is the traveling distance of sound ray, k is the spreading factor, and α is the absorption coefficient which is closely related to the frequency of sound waves and can be obtained by Thorp's empirical formula as

$$\alpha = \frac{0.11f^2}{1 + f^2} + \frac{44f^2}{4100 + f^2} + 2.75 \times 10^{-4}f^2 + 0.003, \quad (3)$$

where the units of α and f are dB/km and kHz, respectively. The impulse response of the multipath channel can be expressed as the summary of the transfer function of each path

$$\bar{H}(f) = \sum_p \bar{H}_p(f) e^{-j2\pi f \bar{\tau}_p} = \sum_p \frac{\Gamma_p}{\sqrt{A(\bar{l}_p)}} e^{-j2\pi f \bar{\tau}_p}, \quad (4)$$

where Γ_p , τ_p , and \bar{l}_p are, respectively, the cumulative reflection coefficient of the surface and bottom, propagation delay, and the propagation distance of the p -th path. Generally speaking, an ideal surface can be modeled by a reflection

coefficient $\gamma_s = -1$, while the bottom reflection can be modeled by

$$\gamma_b(\theta_p) = \begin{cases} \frac{\rho_p \sin \theta_p - \rho \sqrt{(c/c_b)^2 - (\cos^2 \theta_p)}}{\rho_p \sin \theta_p + \rho \sqrt{(c/c_b)^2 - (\cos^2 \theta_p)}}, & \cos \theta_p \leq \frac{c}{c_b}, \\ 1, & \text{otherwise} \end{cases} \quad (5)$$

where θ_p is the grazing angle associated with the p -th propagation path and ρ and c are the nominal density and the speed of sound in water ($\rho = 1000 \text{ kg/m}^3$ and $c = 1500 \text{ m/s}$). ρ_p and c_b (calculated by Equation (1)) are the density and the speed of sound in bottom. The propagation delay of p -th path can be simple calculated as

$$\bar{\tau}_p = \frac{\bar{l}_p - \bar{l}_0}{c}, \quad (6)$$

where \bar{l}_0 is the direct distance from the sender to the receiver. In order to get a tractable, simple channel model, we examine an approximation to the function. Taking $p = 0$ as the reference path and $\bar{H}_0(f)$ as the impulse function corresponding to \bar{l}_0 , the impulse function of the receiving end can be further expressed as

$$\bar{H}_p(f) = \frac{\Gamma_p}{\sqrt{(\bar{l}_p/\bar{l}_0)^k \alpha^{\bar{l}_p - \bar{l}_0}}} \bar{H}_0(f). \quad (7)$$

3. Supervised Contrastive Learning-Based Modulation Classification

A large number of studies have proved that DNN is superior to SVM. In the field of UWA modulation classification, the application of DNN is still scarce and all use end-to-end supervised methods. However, when the SNR becomes low, the accuracy will drop sharply. In response to this problem, we use supervised contrastive learning to narrow the feature distance between the same category and expand the distance between different categories, so as to improve the classification accuracy of modulation schemes under low SNR.

3.1. *Classification System Model.* As shown in Figure 5, in Step 1, the signals received by the receiver may be useful signal or useless ocean noise. In Step 2, the input signals are recognized through a simple two convolutional layers and a fully connected layer. Conv11 × 32 means the channel number is 32, and the size of convolutional kernels is 11 × 11.

If the input signal is useful signal, it will be transported to supervised contrastive learning module for further classification; if it is ocean noise, it will be discarded.

In Step 3, supervised contrastive learning loss function is used to update the backbone network (ResNet50) to extract features from UWA data and then put the features into

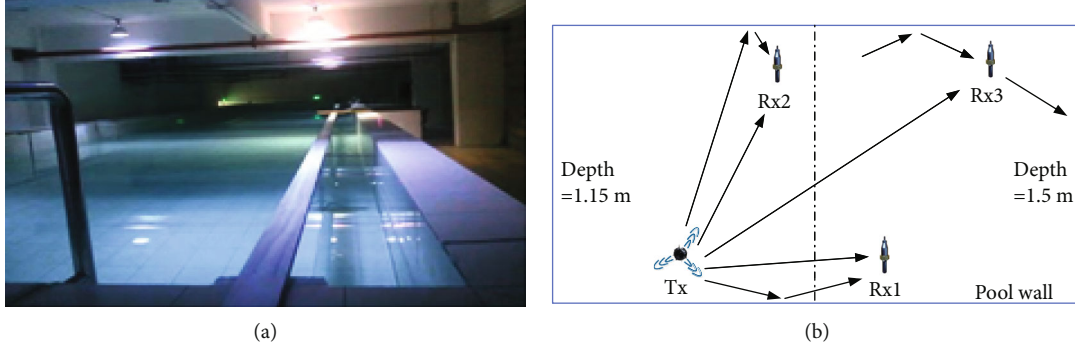


FIGURE 3: The real pool (a) vs. top view of equipment distribution for pool experiment (b).

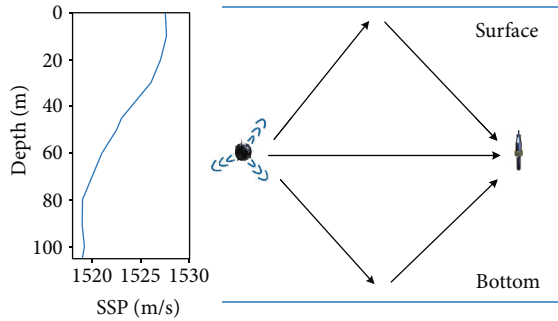


FIGURE 4: Sound ray propagation in shallow sea channel.

classifier for classification. By this means, the influence of ocean noise can be effectively eliminated, and the classification accuracy at low SNR will be significantly improved. In the following content, the specific network architecture will be given in details.

3.2. Backbone Network. The backbone network of supervised contrastive learning in this paper is ResNet50. ResNet50 is a residual CNN with 50 layers. It directly skips several layers and introduces the output of a certain layer into the input part of the following data layer, which overcomes the problems of low learning efficiency and ineffective improvement of accuracy due to the deepening of the network. Another two important operations in the network are batch normalization and ReLU. Batch normalization is aimed at converting the input data to an output data distribution with a variance of 1 and a mean of 0 to improve the speed of network optimization. ReLU is a nonlinear activation function. It makes the output of some neurons be 0, so as to improve the sparsity and avoid the overfitting phenomenon of the network.

In traditional supervised end-to-end CNN, as shown in Figure 6, the output of the classifier is used as the only indicator to update the network. The most widely used loss function is the cross-entropy loss function, and the expression is

$$L_{\text{oss}} = \frac{1}{N} \sum_i L_i = -\frac{1}{N} \sum_i \sum_{c=1}^M y_{ic} \log(p_{ic}), \quad (8)$$

where N is the number of samples and M is the number of label categories. If the true category of sample i is equal to

c , then $y_{ic} = 1$; otherwise, $y_{ic} = 0$. p_{ic} is the predicted probability that the sample i belongs to the corresponding category.

3.3. Supervised Contrastive Learning. Supervised contrastive learning effectively utilizes the category label information, making the feature points from the same category closer than the points from different categories. Different from self-supervised learning [24], the positive samples are other samples in the same category. As shown in Figure 7, the progress is divided into two training stages. The first stage focuses on the training of the encoder and uses the supervised contrastive learning loss function to update the encoder. The second stage focuses on the training of the classifier using the feature output by the encoder and using the cross-entropy loss function to update.

In self-supervision, the function of the two converters is to flip or crop the input picture so that the two newly generated images can be used as the positive samples. Due to the high complexity of UWA data, cropping or flipping the time domain signal will destroy its original characteristics. Since the label information is known, the supervised contrastive learning takes all the samples from the same class in the batch as positive samples and compares them with the negative samples in the rest of the batch. The loss function becomes

$$L^{\text{sup}} = \sum_{i=1}^{2N} L_i^{\text{sup}}, \quad (9)$$

where

$$L_i^{\text{sup}} = \frac{-1}{2N\hat{y}_i - 1} \sum_{j=1}^{2N} 1_{i \neq j} \cdot 1_{\hat{y}_i = \hat{y}_j} \cdot \log \frac{\exp(z_i \cdot z_j / \tau)}{\sum_{k=1}^{2N} 1_{i \neq k} \cdot \exp(z_i \cdot z_k / \tau)}, \quad (10)$$

where i is the blind UWA data and z_i represents the feature generated by the backbone network. z_j represents the feature that comes from the same category with data i , and z_k represents the feature generated by backbone network that is different from data i . τ is a scalar temperature parameter larger than 0. \hat{y}_i is the category label of i . To update the network parameters under the constraint of the loss function, the

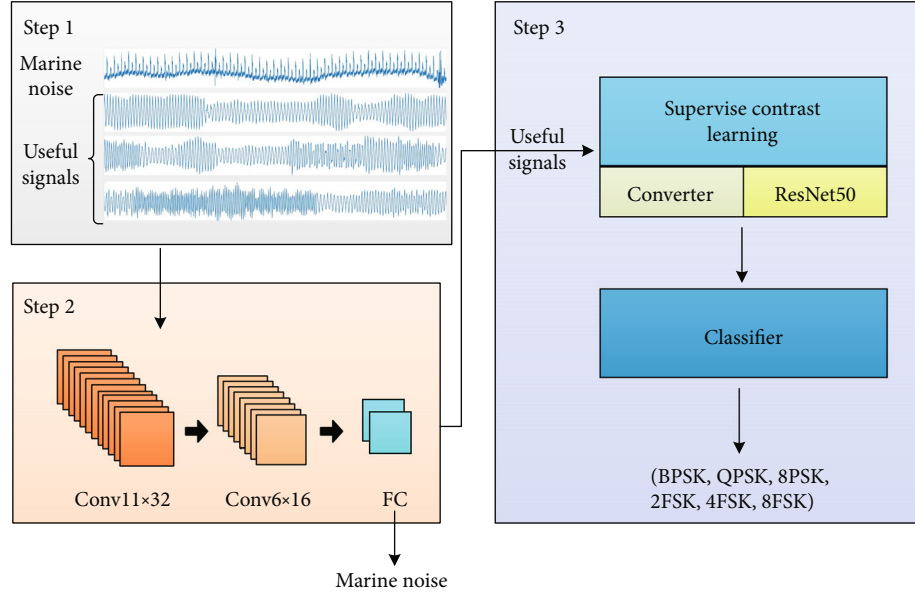


FIGURE 5: Flow chart of supervised contrastive learning-based modulation classification scheme.

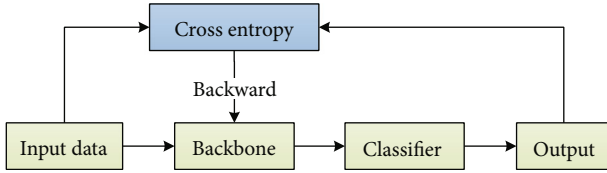


FIGURE 6: Schematic diagram of traditional supervised end-to-end training progress.

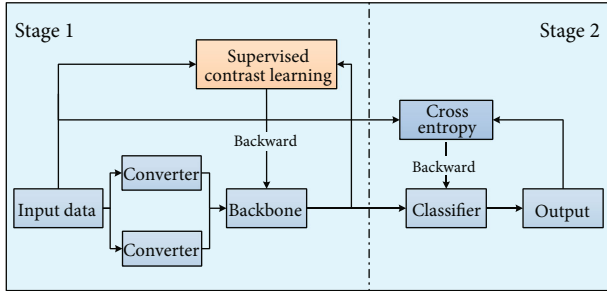


FIGURE 7: Schematic diagram of supervised contrastive learning structure.

feature output from backbone network will have the following characteristics:

- (1) The sum of the cosine distance between the feature vectors of all other samples in the same category and the feature vectors of the sample i , the larger the better
- (2) The sum of the cosine distance between the feature vectors of the sample in different categories and the feature vectors of the sample i , the smaller the better

The classifier in the second stage is a simple fully connected layer. It uses the 2048-dimensional standardized feature output by the encoder to classify the modulation

schemes. It should be mentioned that the parameters of the encoder are frozen in the second stage. Therefore, whether the encoder can obtain excellent features after training plays a decisive role.

Algorithm 1 describes the update process of the supervised contrastive learning.

4. Experiments and Results

In this section, the details of the experiments are explained. We also evaluate the modulation classification performance of the proposed method and compare it with the existing methods. In order to analyze the algorithm performance more intuitively, we use PCA to visualize the features to provide the interpretability of the proposed method.

4.1. Dataset Generation. The original modulation signals are generated through the MATLAB simulation platform. The candidate modulation set is given by

$$M = \{BPSK, QPSK, 8PSK, 2FSK, 4FSK, 8FSK\}. \quad (11)$$

Table 1 shows the parameter setting of different modulation schemes. The ocean noise is actually collected in the Wuyuan Bay sea area. After passing through the ocean channel, the pool channel, and the simulation channel, the data with the characteristics of multipath fading and Doppler frequency shift is obtained. On this basis, Gaussian white noise with different SNR is superimposed on the obtained data through MATLAB. In this paper, the intraband SNR is used to evaluate the performance of the proposed algorithm. It can be calculated as

$$SNR = 10 \log_{10} \left(\frac{F_s}{B_s} \right) + SNR_{\text{Gaussian}}(dB), \quad (12)$$

```

Input: Encoder training: batch size 32, initial learning rate  $\alpha=5e-2$ , epoch  $E_p=100$ ,  $\tau=0.07$ 
Classifier network training: batch size 128, initial learning rate  $\alpha'=1e-3$ , epoch  $E'_p=100$ 
Output: Backbone network parameter  $\theta$ , The Classifier network  $\Theta$ .
//Encoder training
1: for epoch =1: $E_p$ 
2: sample a batch of data, update  $\alpha$  as described in Section III – D
3: Backbone encodes  $m$  into  $F$ .
4: calculates loss  $L^{\text{sup}}$  (10)
5: update  $\theta$  with  $\theta \leftarrow \theta - \alpha \cdot \nabla_{\theta} L^{\text{sup}}$ 
6: end for
//Classifier network training
7: for epoch = 1: $E'_p$  do
8: Freeze encoder parameter, update  $\alpha'$  as described in Section III – D
9: Classifier network decodes  $F$  into result
10: calculates loss  $L_{\text{oss}}$  (8)
11: update  $\Theta$  with  $\Theta \leftarrow \Theta - \alpha' \cdot \nabla_{\Theta} L_{\text{oss}}$ 
12: end for
//Finish training
Return the parameter  $\theta$ ,  $\Theta$ 

```

ALGORITHM 1: Two-stage training of supervised contrastive learning.

TABLE 1: Parameter setting of the modulation signals.

Modulation type	2/4/8PSK	2/4/8FSK
Modulation point	$\theta_m = 2\pi m/M$ $m = 0, 1, \dots, M-1$	$f_m = 11 \text{ kHz} + 2 \text{ mkHz}$ $m = 0, 1, \dots, M-1$
Sample frequency	66 kHz	
Symbol width	1 ms	

where F_s is the sampling frequency and B_s is the bandwidth of the signal.

In Step 2, it is aimed at distinguishing the ocean noise and the useful signals. The train set consists of 2,000 ocean noise samples and 2,000 modulation signal samples with different SNR. The corresponding test set is 800 samples per category. In Step 3, the training set of supervised contrastive learning consists the data with different SNR after noise pollution. Among them, 550 samples of each modulated signal are generated from -9 dB to 9 dB every 2 dB, 250 samples of which are used as the training set and 300 samples are used as the test set. Therefore, the training set contains 15,000 samples with different SNR, and the test set of each SNR contains 1,800 samples.

4.2. Experimental Implements. In the ocean and pool experiments, NI USB-6259 Pinout capture card is used to convert the digital signal to analog signal at the transmitter and convert the analog signal to digital signal at the receiver. JYH500A power amplifier and Type-2692-0S2 charge amplifier are used to amplify the transmitted signal and the received signal, respectively. WBT22-1107 transducer which can convert the analog electrical signal to acoustic signal is used to send and receive signal in the water. Besides, the experiments are performed on computing server equipped with an Intel(R) Core(TM) i7-9700K 3.6GHz CPU, a NVIDIA GeForce RTX 2060 SUPER GPU, “Pytorch” and

“Python” programming language, the CUDA 10.1 and CUNDD software. The optimizer of ResNet50 is “Adam,” and the learning rate is 0.05 and decays to 10% of the original learning rate every 30 epochs.

4.3. Experiment Results

4.3.1. Simulation Results. The simulation experiment is carried out under the simulation UWA channel. In the noise distinction stage, the distinction between ocean noise and useful signals is obvious, especially in the frequency domain. Even when the SNR is -6 dB, the classification accuracy can still achieve 100%. Therefore, it can be explained that the simple convolutional network of Step 2 can well eliminate the influence of marine noise. In the Step 3, Figure 8 gives the classification accuracy of six modulation schemes. In general, the classification accuracy of six modulation signals increases with the increase of SNR and can achieve an average accuracy of 98.84% at 0 dB. When the SNR decreases to -6 dB, the recognition of 8PSK is the most difficult, and the confusion of modulation categories is mainly concentrated on QPSK and 8PSK.

4.3.2. Actual Ocean and Pool Experiment Results. Due to the difficulty and high cost of obtaining ocean data, in practical experiments, we mix pool data with the ocean data to increase the richness of training set, so that the trained encoder and classifier can better fit the distribution characteristics of UWA data. The result of Step 2 in practical experiments is the same as mentioned in the previous simulation part. In Step 3, using the feature output by the encoder, the classification accuracy of the single fully connected layer is shown in Figure 9. For MPSK, its information is modulated in phase, so its characteristics in the time domain are not as obvious as MFSK. When the SNR is -6 dB, the average accuracy of MPSK is 79.7%, while MFSK can achieve a high

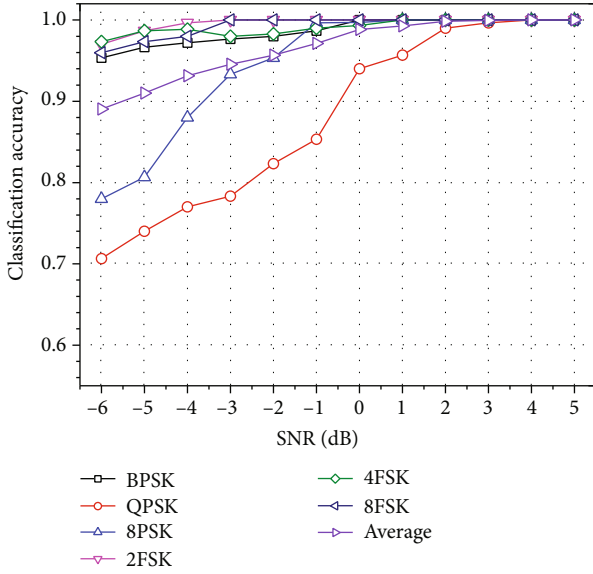


FIGURE 8: Classification accuracy of simulation experiments versus SNR.

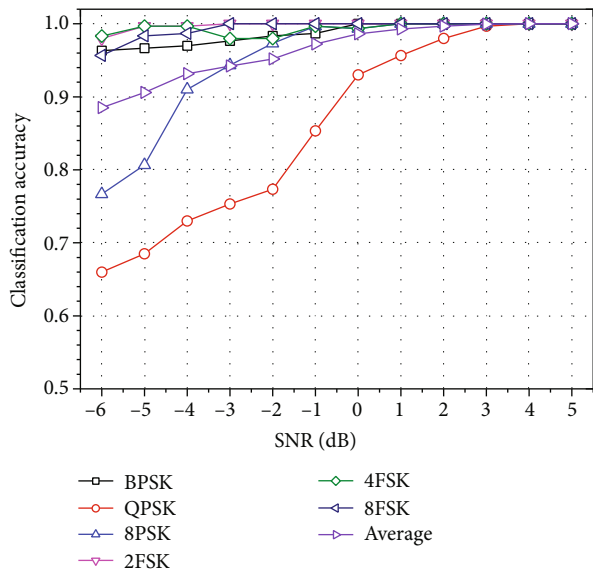


FIGURE 9: Classification accuracy of ocean and pool experiments versus SNR.

accuracy of 97.3%. When the SNR increases to 0 dB, the average accuracy of six types of modulation signals can reach 98.6%.

Classification performance results of six modulation categories at -6 dB and 0 dB are presented using confusion matrix in Figure 10. In each modulation category, 300 tests are implemented. When SNR is -6 dB, BPSK, 2FSK, 4FSK, and 8FSK have achieved high classification accuracy through supervised contrastive learning. However, since QPSK and 8PSK are relatively similar in modulation phase, they are easy to be confused. There are 102 QPSK samples that are mistaken for 8PSK and 70 8PSK samples that are mistaken for QPSK. When the SNR reaches 0 dB, except for the

slightly larger classification error of QPSK, the recognition accuracy of other modulation schemes almost reaches 100%.

4.3.3. Accuracy Comparison. To verify the superiority of the proposed method in this paper, the performance is investigated by making comparisons with four relevant algorithms in recent years; the comparison algorithms are as follows:

- (1) Algorithm 1 based on ResNet50 using constellation density as feature [29]
- (2) Algorithm 2 based on AlexNet using 3-channel image as feature [13]
- (3) Algorithm 3 based on VGGNet using original gray image as feature [30]
- (4) Algorithm 4 based on SE-Net using the features in time domain, frequency domain, and time-frequency domain [31]

Figure 11 presents the average classification accuracy of five algorithms versus SNR. The average accuracy is obtained by averaging the classification performance of six modulation categories. As shown in Figure 11, the following observations can be made.

- (1) For all five algorithms, the modulation classification performance improves with an increasing SNR value
- (2) Given the same SNR, in addition to the proposed algorithm, the other four algorithms will have a sharp decay on the classification accuracy when the SNR becomes low
- (3) The proposed supervised contrastive learning algorithm has strong adaptability to low SNR UWA modulation signals and outperform all other algorithms. When the SNR is -6 dB, the accuracy of our proposed method is 6% higher than the benchmark algorithm [29]

4.3.4. PCA for Interpretability. PCA can reduce a set of n -dimensional vectors to k -dimension through orthogonal transformation. That is, k unit orthogonal basis is selected, so that the original n -dimensional data is represented by this group of basis. For high-dimensional data, first make the mean of the input vector to 0 and then use the covariance to represent the correlation between vectors a and b . The covariance is calculated as

$$\text{Cov}(a, b) = \frac{1}{n} \sum_{i=1}^n (a_i - \mu_a)(b_i - \mu_b) = \frac{1}{n} \sum_{i=1}^n a_i b_i. \quad (13)$$

For mn -dimensional vectors $\{a_1, a_2, \dots, a_m\}$, the matrix X is composed of

$$X = \begin{bmatrix} a_{11} & \cdots & a_{1n} \\ \vdots & \ddots & \vdots \\ a_{m1} & \cdots & a_{mn} \end{bmatrix}. \quad (14)$$

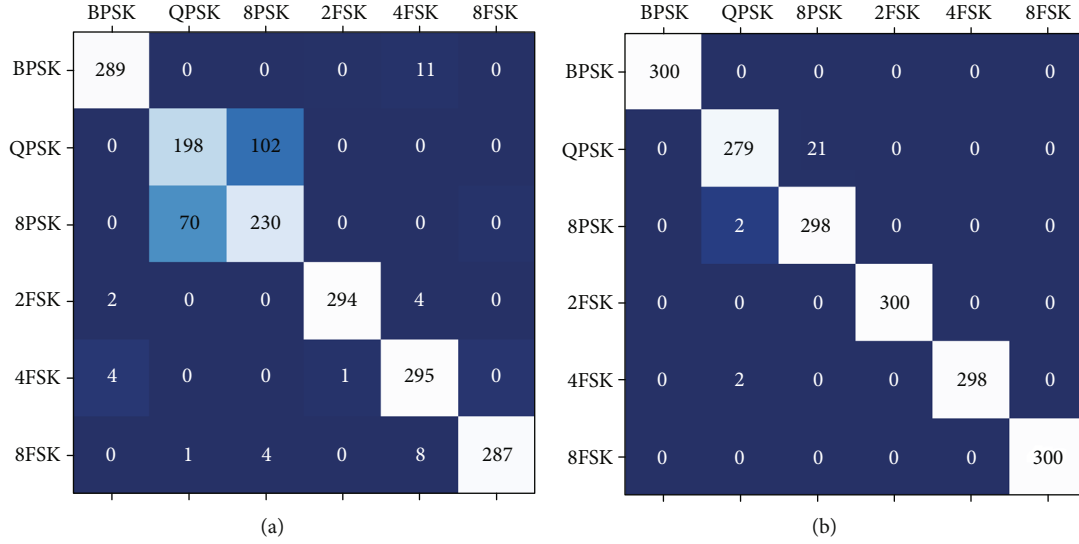


FIGURE 10: Confusion matrix under different SNR based on supervised contrastive learning.

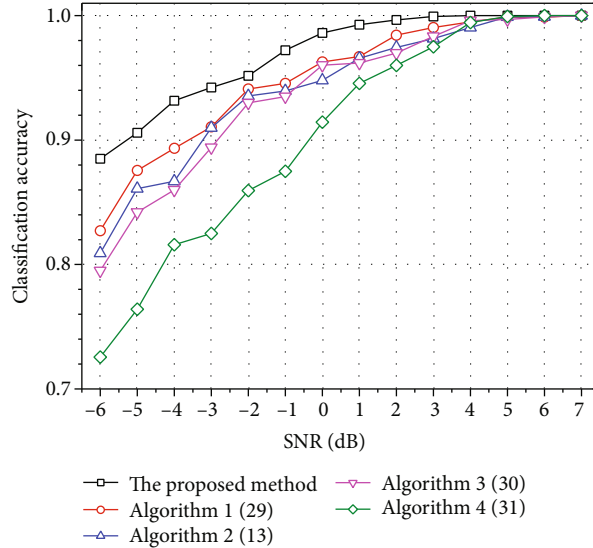


FIGURE 11: Classification accuracy of the proposed algorithm and the comparison algorithm versus SNR.

The covariance matrix C is

$$C = \frac{1}{n}XX^T, \quad (15)$$

$$= \begin{pmatrix} \frac{1}{n} \sum_{i=1}^n a_{1i}^2 & \cdots & \frac{1}{n} \sum_{i=1}^n a_{1i}a_{mi} \\ \vdots & \ddots & \vdots \\ \frac{1}{n} \sum_{i=1}^n a_{mi}a_{1i} & \cdots & \frac{1}{n} \sum_{i=1}^n a_{mi}^2 \end{pmatrix}.$$

It can be seen that the diagonal of the matrix C is the variance of the vectors, and the other elements are the covariances between different vectors. Supposing $Y = PX$ is the vector of the original data X projected to the low-

dimensional space, P is the transformation matrix, and D is the covariance matrix of Y , there is the following equation

$$D = \frac{1}{n}YY^T = \frac{1}{n}(PX)(PX)^T = PCP^T. \quad (16)$$

In order to enable the transformed low-dimensional vectors to represent more original information, we hope that they are not correlated with each other; that is, the covariance is equal to 0. Therefore, the matrix D should be a diagonal matrix. According to the relevant knowledge of linear algebra, the matrix P should be the eigenvector matrix of matrix C , and it should be arranged from top to bottom according to the size of the corresponding eigenvalues. Select the matrix P_k composed of the first k rows of matrix P , and obtain a matrix Y_k with k -dimensional vectors. Taking $k = 3$,

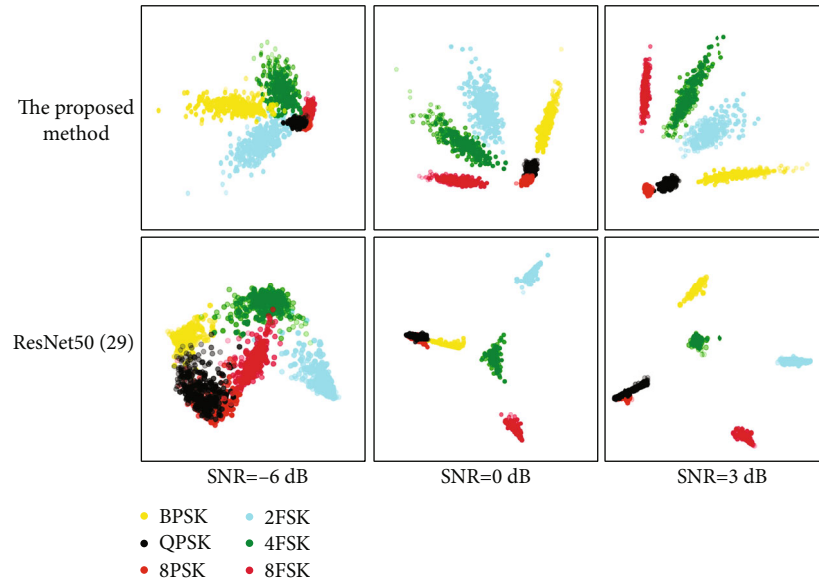


FIGURE 12: Feature point distribution after dimensionality reduction by PCA.

the high-dimensional feature outputs by the network are presented in a 3-dimensional plane. Figure 12 shows a 3-dimensional space cross-sectional view of the feature point distributions extracted by different networks.

It is easy to see that the features extracted by the supervised contrastive learning method have a higher degree of discrimination and better classification effect under low SNR. When SNR is -6 dB, the features extracted by ResNet50 [29] are overlapped. In contrast, the features extracted by the proposed method, except that the features of QPSK, 8PSK, and 8FSK, have some overlap; the feature distributions of the other three modulation signals are concentrated and easy to distinguish. What is more, with the increase of the SNR, the feature point distribution boundaries of different modulation schemes become clearer and clearer.

5. Conclusion

In this paper, we are the first to propose a novel modulation classification scheme based on supervised contrastive learning. Firstly, the useful signals and ocean noise will be distinguished in the first module. Secondly, the encoder ResNet50 in the supervised contrastive learning module will learn the input UWA data under the guidance of the supervised contrastive learning loss function to update the network. By this means, the distance between feature vectors in the same category but with different SNR will be minimized, and the distance between feature vectors of different categories will be expanded as much as possible. Then, the classifier recognizes the modulation scheme according to the feature output by the encoder. Finally, the ocean, pool, and simulation experimental results verify the superiority of the proposed method. Compared with the existing researches, the experimental verification in this paper is more complete. The proposed method eliminates the complex parameter extraction process and does not require any prior information. When the SNR is 0 dB, the average accuracy can achieve 98.6%. Com-

pared to the benchmark algorithm, the accuracy at -6 dB is improved by 6%. Moreover, we use PCA to visualize the feature distribution, which can intuitively analyze the superiority of the proposed algorithm.

Data Availability

The data used to support the findings of this study were supplied by Daqing Gao under license and so cannot be made freely available. Requests for access to these data should be made to Daqing Gao (dqgao@stu.xmu.edu.cn).

Conflicts of Interest

The authors declare that they have no conflicts of interest.

Acknowledgments

This work was supported by the National Natural Science Foundation of China (62071400, 62071402).

References

- [1] A. Ali and Y. Fan, "k-sparse autoencoder based automatic modulation classification with low complexity," *IEEE Communications Letters*, vol. 21, no. 10, pp. 2162–2165, 2017.
- [2] Y. Li, S. Jiao, and B. Geng, "A comparative study of four multi-scale entropies combined with grey relational degree in classification of ship-radiated noise," *Applied Acoustics*, vol. 176, no. 4, article 107865, 2021.
- [3] K. Tekbyk, Z. Akbunar, A. R. Ekti, G. K. Kurt, and A. Grin, "On the investigation of wireless signal identification using spectral correlation function and SVMs," in *2019 IEEE Wireless Communications and Networking Conference (WCNC)*, Marrakesh, Morocco, 2019.
- [4] S. Zhou, Z. Wu, Z. Yin, and Z. Yang, "Noise-robust feature combination method for modulation classification under

- fading channels,” in *2018 IEEE 88th Vehicular Technology Conference (VTC-Fall)*, Chicago, IL, USA, 2018.
- [5] J. Huang and R. Diamant, “Adaptive modulation for long-range underwater acoustic communication,” *IEEE Transactions on Wireless Communications*, vol. 19, no. 10, pp. 6844–6857, 2020.
 - [6] X. U. Wen and B. Wang, “A signal modulation classification method based on SVM,” *Computer Engineering*, vol. 8695, no. 1, pp. 117–136, 2013.
 - [7] Y. Wei, S. Fang, and X. Wang, “Automatic modulation classification of digital communication signals using svm based on hybrid features, cyclostationary, and information entropy,” *Entropy*, vol. 21, no. 8, p. 745, 2019.
 - [8] J. Fan, Y. Ren, X. Luo, and J. Joung, “Iterative carrier frequency offset estimation scheme for faster-than-nyquist signaling systems,” *IEEE Photonics Technology Letters*, vol. 32, no. 18, pp. 1203–1206, 2020.
 - [9] S. Rajendran, W. Meert, D. Giustiniano, V. Lenders, and S. Pollin, “Deep learning models for wireless signal classification with distributed low-cost spectrum sensors,” *IEEE Transactions on Cognitive Communications and Networking*, vol. 4, no. 3, pp. 433–445, 2018.
 - [10] W. Li, Z. Dou, C. Wang, and Y. Zhang, “Signal modulation classification based on deep belief network,” in *2019 IEEE Globecom Workshops (GC Wkshps)*, Waikoloa, HI, USA, 2019.
 - [11] T. J. O’Shea, J. Corgan, and T. C. Clancy, “Convolutional radio modulation recognition networks,” in *International Conference on Engineering Applications of Neural Networks*, Springer, 2016.
 - [12] T. O’Shea and J. Hoydis, “An introduction to deep learning for the physical layer,” *IEEE Transactions on Cognitive Communications and Networking*, vol. 3, no. 4, pp. 563–575, 2017.
 - [13] S. Peng, H. Jiang, H. Wang et al., “Modulation classification based on signal constellation diagrams and deep learning,” *IEEE Transactions on Neural Networks and Learning Systems*, vol. 30, no. 3, pp. 718–727, 2019.
 - [14] J. Huang, S. Huang, Y. Zeng, H. Chen, S. Chang, and Y. Zhang, “Hierarchical digital modulation classification using cascaded convolutional neural network,” *Journal of Communications and Information Networks*, vol. 6, no. 1, pp. 72–81, 2021.
 - [15] Y. Wang, M. Liu, J. Yang, and G. Gui, “Data-driven deep learning for automatic modulation recognition in cognitive radios,” *IEEE Transactions on Vehicular Technology*, vol. 68, no. 4, pp. 4074–4077, 2019.
 - [16] X. Liu, D. Yang, and A. E. Gamal, “Deep neural network architectures for modulation classification,” in *2017 51st Asilomar Conference on Signals, Systems, and Computers*, pp. 915–919, Pacific Grove, CA, USA, 2017.
 - [17] L. Zhang, D. Wang, C. Bao, Y. Wang, and K. Xu, “Large-scale whale-call classification by transfer learning on multi-scale waveforms and time-frequency features,” *Applied Sciences*, vol. 9, no. 5, p. 1020, 2019.
 - [18] S. Yu, K. J. Palmer, M. A. Roch, E. Fleishman, and H. Klinck, “Deep neural networks for automated detection of marine mammal species,” *Scientific Reports*, vol. 10, no. 1, p. 607, 2020.
 - [19] S. Sukhbaatar, J. Bruna, M. Paluri, L. Bourdev, and R. Fergus, *Training Convolutional Networks with Noisy Labels*, Computer Science, 2015.
 - [20] Z. Zhang and M. R. Sabuncu, “Generalized cross entropy loss for training deep neural networks with noisy labels,” *Advances in Neural Information Processing Systems*, vol. 31, 2018.
 - [21] G. Elsayed, D. Krishnan, H. Mobahi, K. Regan, and S. Bengio, “Large margin deep networks for classification,” 2018, <http://arxiv.org/abs/1803.05598>.
 - [22] W. Liu, Y. Wen, Z. Yu, and M. Yang, *Large-Margin Softmax Loss for Convolutional Neural Networks*, ICML, 2016.
 - [23] O. Henaff, “Data-efficient image recognition with contrastive predictive coding,” in *International Conference on Machine Learning*, pp. 4182–4192, PMLR, 2020.
 - [24] K. He, H. Fan, Y. Wu, S. Xie, and R. Girshick, “Momentum contrast for unsupervised visual representation learning,” in *Proceedings of the IEEE/CVF Conference on Computer Vision and Pattern Recognition*, pp. 9729–9738, Seattle, WA, USA, 2020.
 - [25] R. D. Hjelm, A. Fedorov, S. Lavoie-Marchildon et al., “Learning deep representations by mutual information estimation and maximization,” 2018, <http://arxiv.org/abs/1808.06670>.
 - [26] P. Khosla, P. Teterwak, C. Wang et al., “Supervised contrastive learning,” 2020, <http://arxiv.org/abs/2004.11362>.
 - [27] R. J. Urick, *Principles of Underwater Sound 3rd Edition*, McGraw-Hill Book Company, 1983.
 - [28] P. Qarabaqi and M. Stojanovic, “Statistical characterization and computationally efficient modeling of a class of underwater acoustic communication channels,” *IEEE Journal of Oceanic Engineering*, vol. 38, no. 4, pp. 701–717, 2013.
 - [29] Y. Kumar, M. Sheoran, G. Jajoo, and S. K. Yadav, “Automatic modulation classification based on constellation density using deep learning,” *IEEE Communications Letters*, vol. 24, no. 6, pp. 1275–1278, 2020.
 - [30] D. Sun, Y. Chen, J. Liu, Y. Li, and R. Ma, “Digital signal modulation recognition algorithm based on VGGNet model,” in *2019 IEEE 5th International Conference on Computer and Communications (ICCC)*, Chengdu, China, 2019.
 - [31] Q. Qu, S. Wei, H. Su, M. Wang, and X. Hao, “Radar signal recognition based on squeeze-and-excitation networks,” *IEEE International Conference on Signal, Information and Data Processing (ICSIDP)*, 2019, Chongqing, China, 2019, 2019.

Research Article

Underwater Localization Using Differential Doppler Scale and TDOA Measurements with Clock Imperfection

Bingbing Zhang,^{1,2} Jiahua Zhu ,^{1,2} Yanqun Wu,^{1,2} Weihua Zhang,^{1,2} and Min Zhu^{1,2}

¹College of Meteorology and Oceanography, National University of Defense Technology, Changsha 410073, China

²Hunan Key Laboratory for Marine Detection Technology, Changsha 410073, China

Correspondence should be addressed to Jiahua Zhu; zhujiahua1019@hotmail.com

Received 2 December 2021; Accepted 31 January 2022; Published 21 March 2022

Academic Editor: Xuebo Zhang

Copyright © 2022 Bingbing Zhang et al. This is an open access article distributed under the Creative Commons Attribution License, which permits unrestricted use, distribution, and reproduction in any medium, provided the original work is properly cited.

Underwater acoustic localization is an important, yet challenging problem: (1) node mobility issue, (2) Doppler effect, and (3) clock imperfection. To be specific, underwater nodes are not stationary in real-life due to unpredictable currents. Relative motion between a transmitter and a receiver causes the time scaling problem on the received signals, where the time scaling factor is termed as Doppler scale. Then, due to the slow acoustic signal propagation speed, the underwater Doppler scale becomes more severe compared with the one in terrestrial environments. Thus, the differential Doppler scale (DDS) measurements should also be collected, other than the time measurements like time-difference-of-arrival (TDOA), for enhancing the underwater localization. Since DDS/TDOA measurements and clock skew are tightly coupled, clock synchronization is essential for accurate localization. However, due to the stringent cost and power constraints of underwater nodes, low-cost clocks with relative low precision are normally employed, which makes it even more difficult to guarantee a perfect clock synchronization between transmitter/receiver pairs. In order to cope with those issues, we propose an algebraic underwater localization method using the hybrid DDS/TDOA measurements, which is particularly robust against the node clock imperfection. A new DDS/TDOA measurement model with clock imperfection is first presented by analyzing the received signals over underwater acoustic channels. Then, we devise a two-step weighted least square-based estimator, and the analytical study shows that our estimator can achieve the Cramer-Rao lower bound (CRLB) accuracy under small noise. Simulations corroborate the theoretical results and the good performance of the proposed method.

1. Introduction

Underwater localization has been an active area in recent years owing to its extensive applications such as data collection, environment monitoring, military surveillance, and assisted navigation [1–5]. Basically, the underwater localization process follows two steps, i.e., measurement collection and measurement fusion. To be specific, the measurements between the target and the predeployed anchors with *prior* known locations are first collected, from which we infer the target location. Since the Global Positioning System (GPS) signals are not available in underwater scenarios due to the severe power attenuation of electromagnetic waves, we can do nothing but collecting measurements from the acoustic signals [6]. For acoustic communication, there are

many modulation methods, such as frequency-shift keying (FSK), phase-shift keying (PSK), and orthogonal frequency-division multiplexing (OFDM) [7]. For the low complexity of receivers, which is required to deal with highly dispersive channels, in our study, we consider the OFDM scheme for data exchange [8]. There are different types of measurements that can be extracted from data exchanges, such as time-of-arrival (TOA), time-difference-of-arrival (TDOA) [9, 10], received signal strength (RSS), differential RSS, and angle-of-arrival (AOA) [11]. Among those, the TDOA-based method becomes the primary concern of most engineers in designing the underwater localization owing to its relative high-accuracy ranging results and the relaxation of clock synchronization requirements [12]. We should also mention here the kind of differential Doppler scale (DDS)

measurement, which results from the underwater nodes' relative motion that always exist in practice [13]. This kind of measurement will be explained in details later. With all the collected measurements, the target's position can be estimated by different families of measurement fusion methods, which are maximum likelihood (ML), semidefinite programming (SDP) based, least squares (LS) based, and alternating direction method of multipliers (ADMM) based [14, 15]. The ML method is asymptotically optimal, but the formed ML optimization problem is highly nonlinear and nonconvex, and thus, a closed-form solutions does not exist [16]. Although it can be solved approximately by iterative methods, they involve intensive computations and cannot guarantee the convergence to the correct solution unless the initial guess is close enough to it. The SDP-based method relaxes the nonconvex optimization problem to a convex one such that a global minimum can be effectively found [17, 18]. However, this method still requires a high complexity as well as a tight relaxation to guarantee an accurate estimate. To allow low complexity implementation as well as to ensure global convergence, (weighted) LS-based methods have been proposed in [19–21]. The LS-based method rearrange the nonlinear equations into a set of linear equations by introducing extra variables, which are functions of the target parameters (position and velocity). Furthermore, the relation between the extra variables and the unknown parameters of the target can also be utilized to improve the estimation accuracy, which reaches the Cramer-Rao lower bound (CRLB) under Gaussian noise at moderate to high signal-to-noise [19]. Therefore, due to the attractive advantages of the LS-based method over other methods, we choose it as our measurement fusion method.

Besides choosing the appropriate measurement fusion method, it is worth noting that when the target is moving, the DDS measurements can be explored together with the TDOA measurements to further improve the localization accuracy. Actually, underwater nodes can hardly maintain stationary due to the unpredictable ocean currents. A relative transmitter/receiver motion results into the time scaling problem on the received signals [22]. The time scaling factor is conventionally called as Doppler scale. Moreover, the low propagation speed of acoustic waves (about 1500 m/s) makes the acoustic signals very susceptible to the Doppler scale. Thus, the DDS measurements have to be effectively extracted from the received signals and exploited for underwater localization. It is worth noting that a similar kind of measurement called frequency-difference-of-arrival (FDOA) has been extensively studied for terrestrial localization problem [19–21]. One might ask what is the difference between the DDS and FDOA measurements. In fact, the DDS is the difference in received Doppler scales in time-domain, while the FDOA is the difference in received Doppler frequency offsets in frequency-domain, and both of them results from the Doppler effect. However, from the measurement point of view, narrowband signals will have more precise FDOA measurements compared with wideband signals [23]. Though underwater channels are wideband in nature because the signal bandwidth is not negligible compared to the carrier frequency [24]. To be specific, taking OFDM sig-

nals as an example, each subcarrier experiences a Doppler-induced frequency offset, which depends on the frequency of the subcarrier. This kind of Doppler shifts is called as nonuniform Doppler frequency offsets, and directly estimating it in frequency domain is intractable [6]. As a result, precisely estimating the Doppler frequency offsets in frequency-domain from the received signals over underwater channels might be difficult. Therefore, we alternatively choose to measure the time scaling factor of received signals in time-domain, which results in DDS measurements.

It is well known that time-based localization is very susceptible to the clock imperfection that always exists in practice. For example, due to the stringent cost and power constrains of underwater nodes, low-cost clocks are normally employed. This implies that the clock parameters of underwater nodes, i.e., clock skew and clock offset, might drift away over time. Although the anchor nodes can be synchronized with a reference clock by precalibration, the target node is usually very difficult to be guaranteed the same particularly for underwater scenarios. Even though the target is synchronized with the anchors, the clock imperfection might still exist due to the fact that the synchronization performance might significantly deteriorate in severe underwater communication environments. This will certainly incur the clock imperfection for the target node. Thus, taking into account the clock imperfection in underwater localization becomes an important task. In this work, we assume an independent clock for the target node and synchronized clocks among all the anchors. Traditionally, clock imperfection are usually considered while developing TOA- or TDOA-based localization algorithm [25, 26]. Compared with the TOA-based localization, TDOA technique resolves the clock offset ambiguity, though it can still suffer from the clock skew [27]. Other than the TDOA measurements, we also use the DDS measurements for enhancing the underwater localization. Obviously, the DDS measurement provides more information for localization. As a trade-off, when considering the clock imperfection, using the DDS is at price of a complicated measurement model since the measured DDS at the receiver is actually a combination of the Doppler effect and the clock skew between the transmitter/receiver pair, which will exacerbate the nonlinearity issue. However, the coupling nature between the DDS and clock skew is often overlooked in Doppler measurement based localization approaches. Recently, some pioneering research works noticed the potential coupling relationship between the Doppler scale measurement and clock skew [28–30]. However, they only explored the time synchronization problem in underwater sensor networks (UWSNs) using the clock skew-interfered Doppler scale measurements. In a nutshell, the clock imperfection will significantly degrade the DDS/TDOA-based localization performance, and hence, the localization methods that are robust against to this imperfection are urgently required.

To tackle the aforementioned clock imperfection problem, the first contribution of this work is proposing a new DDS/TDOA model with the clock imperfection by analyzing the received signals over underwater acoustic channels. Based on this model, we then contribute to localization

algorithm development by exploiting the linearization approach. Based on the pseudolinear equations with nuisance variables, two weighted least square (WLS) estimators are devised. The first one ignores the built-in relationships between the unknown parameters and gives a coarse solution. The second one improves the solution by exploiting the known relationships between the estimates resulted from the first WLS estimator. Since only two WLS estimators are involved, our proposed method is computationally attractive. We compare analytically the location accuracy of the proposed estimator to the Cramér-Rao lower bound (CRLB) for Gaussian measurement noise. We also conduct simulations to compare the performance of the proposed localization method with the corresponding CRLB and that of the WLS method assuming perfect clock [19] and the proposed method using a mismatched DDS model under different noise conditions. The numerical results verify the effectiveness of the proposed localization method.

1.1. Notations. Column vectors and matrices are denoted by bold lower- and uppercase letters, respectively; $\mathbf{a}(i)$ and $\mathbf{A}(i, j)$ are the i th element of \mathbf{a} and the (i, j) th element of \mathbf{A} , respectively; $\mathbf{a}(i : j)$ denotes a subvector with the i th to the j th elements of \mathbf{a} ; $\mathbf{A}(i, :)$ represents the i th row of \mathbf{A} ; $\|\cdot\|$ is the Euclidean distance norm; $\delta(\cdot)$ denotes the Dirac delta function; $*$ denotes the convolution operator; superscript T denotes the transpose of a matrix (vector); \odot denotes the element-wise multiplication; $\mathbf{1}$ and $\mathbf{0}$ are vectors (or matrixes) of 1 and 0, \mathbf{O} is zero matrix, \mathbf{I} denotes the identity matrix (size indicated in the subscript if necessary); $\text{diag}(\cdot)$ and $\text{blkdiag}(\cdot)$ represent the diagonal and the block-diagonal matrices; $\mathbb{E}(\cdot)$ denotes the expectation operator.

2. Problem Formulation and CRLB

In this section, we first show how the underwater acoustic channel and clock imperfection affect the DDS and TDOA measurement model, then the localization problem is formulated. The Cramér-Rao lower bound (CRLB) is also derived.

2.1. Problem Formulation. As depicted in Figure 1, consider a three-dimensional underwater localization scenario where N moving anchors are used to determine the position $\mathbf{u} = [x, y, z]^T$ and velocity $\dot{\mathbf{u}} = [\dot{x}, \dot{y}, \dot{z}]^T$ of a moving target using the DDS and TDOA measurements. The anchors are pre-deployed in the interested monitoring area, and their positions and velocities are known to the localization algorithm as $\mathbf{s}_i = [x_i, y_i, z_i]^T$ and $\dot{\mathbf{s}}_i = [\dot{x}_i, \dot{y}_i, \dot{z}_i]^T$, $i = 1, \dots, N$, respectively. Assume the anchors are synchronized and behave a common clock skew w and clock offset θ . Thus, the local time of the anchors with respect to (w.r.t.) a universal standard time t is given by [31].

$$c(t) = wt + \theta. \quad (1)$$

We assume the local time of the target is the universal standard time, i.e., clock skew is 1 and clock offset is 0.

To implement a DDS/TDOA information-based localization algorithm, it is necessary to transmit signals from

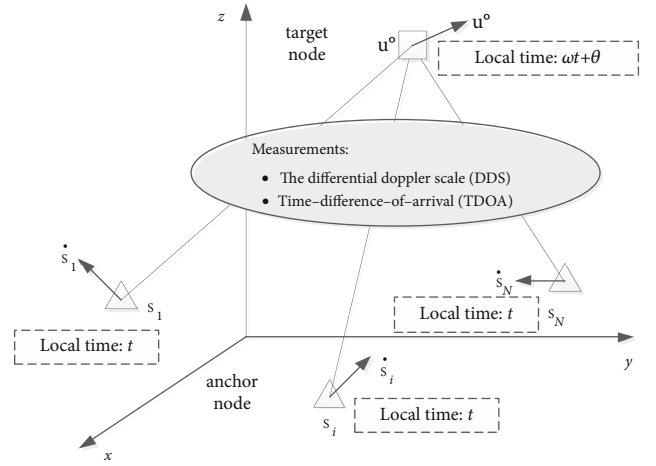


FIGURE 1: The underwater localization scenario.

the target to anchors and/or *vice versa*. For simplicity, we here assume that the target radiates a signal at a single time instant and received by each anchor after a propagation delay. Generally, some preprocessing steps including detection, synchronization, and Doppler scale estimation are required for underwater acoustic communication systems [24]. Several structures of the transmitted signal can be employed for the preprocessing steps, such as linear-frequency-modulated (LFM) signal, cyclic-prefixed (CP) OFDM signal, and m-sequence [32]. In this paper, as originally suggested in [33], we adopt an LFM preamble and an LFM postamble around each data frame to estimate the DDS and TDOA. The main reason for choosing an LFM signal rather than other signals is its robustness against the Doppler effect as well as its good cross-correlation performance in environments corrupted by white Gaussian noise.

Consider a multipath underwater channel between the target and the i th anchor that has the impulse response [6].

$$h_i(\tau, t) = \sum_{p=1}^M A_{i,p}(t) \delta(\tau - \tau_{i,p}(t)), \quad (2)$$

where M is the number of paths, $A_{i,p}(t)$ is the corresponding time-varying path attenuation, and $\tau_{i,p}(t)$ is the time-varying path delay. Assuming that the duration of transmitted signal is short enough, the relative movement between the target and anchor is small. Thus, the time variation of the path delay can be reasonably approximated by a Doppler scale $a_{i,p}$ as

$$\tau_{i,p}(t) = \tau_{i,p} - a_{i,p}t, \quad (3)$$

and the path attenuation are assumed constant $A_{i,p}(t) = A_{i,p}$. Moreover, we assume all paths have a similar Doppler scale a_i , which has already been justified in [6]. Finally, the underwater acoustic channel model is approximated as

$$h_i(\tau, t) = \sum_{p=1}^M A_{i,p} \delta(\tau - \tau_{i,p} + a_i t). \quad (4)$$

Let $s(t)$ be the transmitted passband signal at the target with duration T_0 , then the received passband signal at the i th anchor is given by

$$y_i(t) = s(t) * h_i(\tau, t) = \sum_{p=1}^M A_{i,p} s((1 + a_i)t - \tau_{i,p}) + \varepsilon_i(t), \quad (5)$$

where $\varepsilon_i(t)$ is additive noise. Sampling $y_i(t)$ yields its discrete time sequence which is used for extracting the DDS and TDOA measurements. Due to the clock imperfection, the actual sampling interval of the anchor is $T'_s = T_s/w$, where T_s is the reference sampling interval. Thus, the received signal at the i th anchor is discretized as

$$y_i[n] = y_i(t)|_{t=nT'_s/w} = \sum_{p=1}^M A_{i,p} s\left[\left(\frac{1 + a_i}{w}\right)n - \tau_{i,p}\right] + \varepsilon_i[n], \quad (6)$$

where $n = \lceil wt/T_s \rceil T_s$ is the time index and $\lceil \cdot \rceil$ denotes the upward rounding operator. From (6), we observe that the joint effect of Doppler scaling and clock skew manifests itself in scaling the signal duration from T_0 to $T_{i,r} = wT_0/(1 + a_i)$. The scaled signal duration can be estimated by cross-correlating the received signal with the known LFM preamble and postamble, denoted as $\hat{T}_{i,r}$. Then, by knowing the original signal duration T_0 , the Doppler scale measurement of the i th anchor is estimated as $\hat{a}_i = T_0/\hat{T}_{i,r} - 1$. Thus, the Doppler scale measurement model can be defined as

$$\hat{a}_i = \frac{1 + a_i}{w} - 1 + v_i, i = 1, \dots, N, \quad (7)$$

where a_i is modeled as the actual Doppler scale caused by the target/anchor motion and is given by

$$a_i = \frac{(u - s_i)^T (\dot{u} - \dot{s}_i)}{cr_i^o}. \quad (8)$$

c is the acoustic propagation speed, and $r_i^o = \|u - s_i\|$; v_i is the measurement noises, which are independent and identically distributed (i.i.d.) Gaussian random variables with zero-mean and variance $\sigma_{a_i}^2$. Furthermore, based on the LFM preamble that inserted in the transmitted signal, each anchor is able to measure the arrival time of the first path by using matched filtering [33]. Considering the clock model defined in (1), the TOA measurement for the signal transmitted from the target at the i th anchor

$$\hat{\tau}_i = w(t_0 + r_i^o/c) + \theta + n_i, i = 1, \dots, N, \quad (9)$$

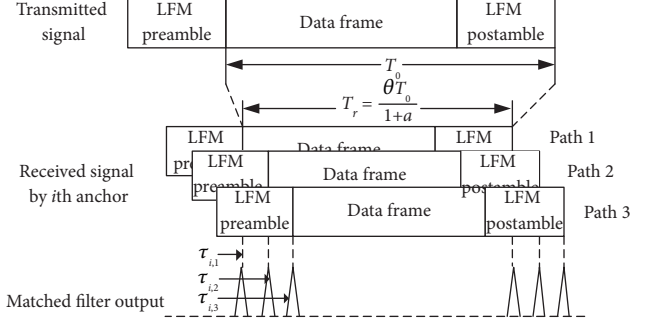


FIGURE 2: An example of extracting the Doppler scale and TOA measurements: T_0 is the signal duration, w is the clock skew, a_i is the Doppler scale, and the underwater acoustic channel has 3 paths with delay $\tau_{i,1}$, $\tau_{i,2}$, and $\tau_{i,3}$, respectively.

where t_0 is the unknown start transmission time of the target and n_i is TOA estimation error and modeled by i.i.d. Gaussian random variables with zero-mean and variance $\sigma_{\tau_i}^2$. Note that the ocean ambient noise is very complicated; and it is hard to model it accurately [34, 35]; we hence use the Gaussian noise model for the convenience of derivation. Without loss of generality, we choose $i = 1$ as the reference Doppler scale and TOA measurement and form the DDS and TDOA measurements, respectively, as

$$\Delta \hat{a}_{i1} = \hat{a}_i - \hat{a}_1 = \frac{1}{w} (a_i - a_1) + v_{i1}, \quad (10a)$$

$$\Delta \hat{\tau}_{i1} = \hat{\tau}_i - \hat{\tau}_1 = \frac{w}{c} (r_i^o - r_1^o) + n_{i1}, \quad (10b)$$

where $v_{i1} = v_i - v_1$, $n_{i1} = n_i - n_1$, and $i = 2, \dots, N$. It can be seen from (10b) that the parameters t_0 and θ are cancelled out by the TDOA calculation while the clock skew w still affects the TDOA measurements. So far, we have elaborated the method for extracting the DDS and TDOA measurements. For better understanding, this method is illustrated in Figure 2 in which an underwater acoustic channel example with 3 paths is used.

Stacking the DDS and TDOA measurements and fusing them into a $2(N - 1) \times 1$ vector, we obtain

$$m \triangleq [f^T, \boldsymbol{\tau}^T]^T, \quad (11)$$

where

$$f = \frac{1}{w} [a_2 - a_1, \dots, a_N - a_1]^T + [v_{21}, \dots, v_{N1}]^T \\ = f^o + \Gamma v, \text{ and } \Gamma = [-1_{N-1}, I_{N-1}],$$

$$v = [v_1, \dots, v_N]^T,$$

$$\boldsymbol{\tau} = \frac{w}{c} [(r_2^o - r_1^o), \dots, (r_N^o - r_1^o)]^T + [n_{21}, \dots, n_{N1}]^T \\ = \boldsymbol{\tau}^o + \Gamma n, \text{ and } n = [n_1, \dots, n_N]^T. \quad (12)$$

The measurement error vector is $\Delta m \triangleq [(\Gamma v)^T, (\Gamma n)^T]^T$, and its covariance matrix is $Q_m \triangleq \mathbb{E}[\Delta m \Delta m^T] = \text{blkdiag}(\Gamma Q_v \Gamma^T, \Gamma Q_n \Gamma^T)$, where $Q_v = \text{diag}([\sigma_{a,1}^2, \dots, \sigma_{a,N}^2]^T)$ and $Q_n = \text{diag}([\sigma_{\tau,1}^2, \dots, \sigma_{\tau,N}^2]^T)$. Note that the Doppler scale measurement noises \mathbf{v} are assumed to be independent of the TOA measurement noises \mathbf{n} . From (11), we can write the observed DDS and TDOA equation in matrix form as

$$m = m^o + \Delta m, \quad (13)$$

where $m^o = [f^o T, \boldsymbol{\tau}^o T]^T$. The goal of underwater localization is estimating u, \dot{u} , and w , from the noisy measurement vector \mathbf{m} . Under the mutually independent Gaussian noise condition, the ML estimator of u, \dot{u} , and w can be formulated as [36]

$$\left[\hat{u}^T, \hat{\dot{u}}^T, \hat{w} \right]^T = \min_{u, \dot{u}, w} (m - m^o)^T Q_m^{-1} (m - m^o). \quad (14)$$

The ML problem is nonconvex, implying that there exist multiple local minima, and the global minimum can hardly be obtained. We shall develop an efficient estimator by converting the nonconvex ML problem to a linear one.

2.2. CRLB. As observed in (13), the DDS/TDOA measurement vector \mathbf{m} is Gaussian distributed as $m \sim \mathcal{N}(m^o, Q_m)$. The CRLB is the lowest possible variance that an unbiased estimator can achieve. For the unknown vector $\boldsymbol{\varphi} = [u, \dot{u}, w]^T$, its CRLB is given by [36]

$$\text{CRLB}(\boldsymbol{\varphi}) = J(\boldsymbol{\varphi})^{-1}, \quad (15)$$

where $J(\boldsymbol{\varphi})$ is the Fisher information matrix (FIM). Using the notation $\nabla_b^a = \partial a / \partial b$, $J(\boldsymbol{\varphi})$ can be calculated as

$$J(\boldsymbol{\varphi}) = \left(\nabla_{\boldsymbol{\varphi}}^{m^o} \right)^T Q_m^{-1} \nabla_{\boldsymbol{\varphi}}^{m^o}. \quad (16)$$

The partial derivative in (16) can be expressed as

$$\nabla_{\boldsymbol{\varphi}}^{m^o} = \begin{bmatrix} \nabla_u^{f^o} & \nabla_{\dot{u}}^{f^o} & \nabla_w^{f^o} \\ \nabla_u^{\tau^o} & \nabla_{\dot{u}}^{\tau^o} & \nabla_w^{\tau^o} \end{bmatrix}, \quad (17)$$

where

$$\begin{aligned} \nabla_w^{f^o}(i-1) &= -w^{-2}(a_i - a_1), \\ \nabla_u^{f^o}(i-1) &= w^{-1} \left(\frac{(\dot{u} - \dot{s}_i)^T}{c r_i^o} - \frac{a_i(u - s_i)^T}{r_i^{o2}} - \frac{(\dot{u} - \dot{s}_1)^T}{c r_1^o} + \frac{a_1(u - s_1)^T}{r_1^{o2}} \right), \\ \nabla_{\dot{u}}^{f^o}(i-1) &= \frac{w^{-1}}{c} \left(\frac{(u - s_i)^T}{r_i^o} - \frac{(u - s_1)^T}{r_1^o} \right), \\ \nabla_w^{\tau^o}(i-1) &= \frac{r_i^o - r_1^o}{c}, \nabla_u^{\tau^o}(i-1) = w^2 \nabla_{\dot{u}}^{f^o}(i-1), \\ \nabla_{\dot{u}}^{\tau^o} &= O_{(N-1) \times 3}, i = 2, \dots, N. \end{aligned} \quad (18)$$

Based on the equations above, the FIM can be easily calculated, and hence, the CRLB is obtained.

3. Proposed Methods

The proposed method has two stages. The first stage creates a set of pseudolinear equations for the nonlinear DDS and TDOA measurements by introducing nuisance variables. Then, an initial solution is obtained through WLS optimization. The second stage utilizes the relationship between the nuisance variables and the interested parameters to refine the first stage solution.

3.1. First Stage: Transforming the Nonlinear Measurement Equation to a Pseudolinear One. To fuse the DDS and TDOA measurements, we start from transforming (10a) and (10b) as

$$\dot{r}_{i1} = \dot{r}_{i1}^o + \dot{\varepsilon}_{i1} = \frac{1}{w} (\dot{r}_i^o - \dot{r}_1^o) + \dot{\varepsilon}_{i1}, \quad (19a)$$

$$r_{i1} = r_{i1}^o + \varepsilon_{i1} = w(r_i^o - r_1^o) + \varepsilon_{i1}, \quad (19b)$$

where $\dot{r}_{i1} = c \Delta \hat{a}_{i1}$, $r_{i1} = c \Delta \hat{\tau}_{i1}$, $\dot{\varepsilon}_{i1} = c v_{i1}$, $\varepsilon_{i1} = c n_{i1}$, and

$$\dot{r}_i^o = \frac{(u - s_i)^T (\dot{u} - \dot{s}_i)}{r_i^o}. \quad (20)$$

Considering the noise free TDOA measurement in (19b), which can be written as

$$r_{i1}^o = w(r_i^o - r_1^o). \quad (21)$$

Upon rewriting (21) as $r_{i1}^o + w r_1^o = w r_i^o$, squaring both sides, and substituting $r_i^o = \|u - s_i\|$ for r_i^{o2} and r_1^{o2} , we have a set of TDOA equations for $i = 2, \dots, N$.

$$r_{i1}^{o2} + 2w r_{i1}^o r_1^o = w^2 \left(s_i^T s_i - s_1^T s_1 - 2(s_i - s_1)^T u \right). \quad (22)$$

Taking the time derivative of (22) results in a set of DDS equations for $i = 2, \dots, N$.

$$w r_{i1}^o \dot{r}_{i1}^o + w^2 \dot{r}_{i1}^o r_1^o + r_{i1}^o \dot{r}_1^o = w \left(s_i^T \dot{s}_i - s_1^T \dot{s}_1 - (\dot{s}_i - \dot{s}_1)^T u - (s_i - s_1)^T \dot{u} \right). \quad (23)$$

In terms of the noisy quantities by putting $r_{i1}^o = r_{i1} - \varepsilon_{i1}$ and $\dot{r}_{i1}^o = \dot{r}_{i1} - \dot{\varepsilon}_{i1}$ into (22) and (23) and ignoring the second-order error terms, we arrive at

$$e_1 = h_1 - G_1 \boldsymbol{\varphi}_1, \quad (24)$$

where $\boldsymbol{\varphi}_1 = [u, \eta_1, \eta_2, \dot{u}, \eta_3, w_1]^T$ is defined as the parameter vector, in which $\eta_1 = r_1^o w^{-1}$, $\eta_2 = w^{-2}$, $\eta_3 = \dot{r}_1^o w^{-1}$, and $w_1 =$

wr_1^o . The vector \mathbf{h}_1 and matrix \mathbf{G}_1 are defined as

$$\mathbf{h}_1 = \begin{bmatrix} s_1^T s_1 - s_2^T s_2 \\ \vdots \\ s_1^T s_1 - s_N^T s_N \\ 2(r_{21}\dot{r}_{21} + s_1^T \dot{s}_1 - s_2^T \dot{s}_2) \\ \vdots \\ 2(r_{N1}\dot{r}_{N1} + s_1^T \dot{s}_1 - s_N^T \dot{s}_N) \end{bmatrix},$$

$$\mathbf{G}_1(i-1, :) = -2 \left[(s_i - s_1)^T, r_{i1}, 0.5r_{i1}^2, \mathbf{0}_{1 \times 5} \right],$$

$$\mathbf{G}_1(i+N-2, :) = -2 \left[(\dot{s}_i - \dot{s}_1)^T, \mathbf{0}_{1 \times 2}, (s_i - s_1)^T, r_{i1}, \dot{r}_{i1} \right],$$

$$i = 2, \dots, N, \quad (25)$$

and the noise vector \mathbf{e}_1 is defined as

$$\mathbf{e}_1 = B_1 \begin{bmatrix} \boldsymbol{\varepsilon}_1 \\ \boldsymbol{\varepsilon}_2 \end{bmatrix}, B_1 = \begin{bmatrix} \mathbf{O} & \mathbf{B} \\ \mathbf{D} & \mathbf{C} \end{bmatrix},$$

$$\boldsymbol{\varepsilon}_1 = [\dot{\varepsilon}_{21}, \dots, \dot{\varepsilon}_{N1}]^T, \boldsymbol{\varepsilon}_2 = [\varepsilon_{21}, \dots, \varepsilon_{N1}]^T, \quad (26)$$

$$\mathbf{B} = 2w^{-1} \text{diag}([r_2^o, \dots, r_N^o]),$$

$$\mathbf{C} = 2w^{-1} \text{diag}([\dot{r}_2^o, \dots, \dot{r}_N^o]),$$

$$\mathbf{D} = 2w \text{diag}([r_2^o, \dots, r_N^o]).$$

Thanks to the nuisance variables η_1, η_2, η_3 , and w_1 introduced in the parameter vector $\boldsymbol{\varphi}_1$, it makes (24) become a set of linear equations with respect to $\boldsymbol{\varphi}_1$. As a result, $\boldsymbol{\varphi}_1$ can be estimated by the WLS method, whose solution is given as [36]

$$\widehat{\boldsymbol{\varphi}}_1 = (\mathbf{G}_1^T \mathbf{W}_1 \mathbf{G}_1)^{-1} \mathbf{G}_1^T \mathbf{W}_1 \mathbf{h}_1, \quad (27)$$

where \mathbf{W}_1 is the weighting matrix chosen as

$$\mathbf{W}_1 = \mathbb{E}[\mathbf{e}_1 \mathbf{e}_1^T]^{-1} = (\mathbf{B}_1 \mathbf{Q}_m \mathbf{B}_1^T)^{-1}, \quad (28)$$

where $\mathbf{Q}_m = c^2 \mathbf{Q}_m$. Note that the weighting matrix is dependent on the true values of clock skew, source position, and velocity through \mathbf{B}_1 . To cope with this, $\mathbf{W}_1 = \tilde{\mathbf{Q}}_m^{-1}$ is first employed to calculate an initial estimate from (27), which will be used back into (28) for an improved version of \mathbf{W}_1 , then leading to a better estimate of $\boldsymbol{\varphi}_1$. The estimation error in $\widehat{\boldsymbol{\varphi}}_1$ can be calculated as

$$\Delta \boldsymbol{\varphi}_1 = \widehat{\boldsymbol{\varphi}}_1 - \boldsymbol{\varphi}_1 = (\mathbf{G}_1^T \mathbf{W}_1 \mathbf{G}_1)^{-1} \mathbf{G}_1^T \mathbf{W}_1 \mathbf{e}_1. \quad (29)$$

The covariance matrix of $\widehat{\boldsymbol{\varphi}}_1$ is, therefore, assuming small measurement noise so that the noise in \mathbf{G}_1 can be ignored

[36].

$$\text{cov}(\widehat{\boldsymbol{\varphi}}_1) \approx (\mathbf{G}_1^T \mathbf{W}_1 \mathbf{G}_1)^{-1}. \quad (30)$$

3.2. Second Stage: Refining the Estimate Obtained in the First Stage. In this stage, we shall refine the estimate obtained in the first stage by utilizing the relationship between the parameters in $\boldsymbol{\varphi}_1$. In fact, they are related to each other through the following equations:

$$\eta_1 w_1 = r_1^{o2} = \|u - s_1\|^2, \quad (31a)$$

$$\eta_1^2 = \eta_2 r_1^{o2} = \eta_2 \|u - s_1\|^2, \quad (31b)$$

$$\eta_1 \eta_3 = \eta_2 \dot{r}_1^o r_1^o = \eta_2 (u - s_1)^T (\dot{u} - \dot{s}_1), \quad (31c)$$

$$\eta_3 w_1 = \dot{r}_1^o r_1^o = (u - s_1)^T (\dot{u} - \dot{s}_1). \quad (31d)$$

Note that there are only three independent equations among the equations in (31a), (31b), (31c), and (31d), since any one of the equations in (31a), (31b), (31c), and (31d) can be interpreted from the others. Without loss of generality, we use the relationships in (31a), (31b), and (31d) to perform the second stage estimation.

To start with, recall that the estimation error in $\widehat{\boldsymbol{\varphi}}_1$ is $\Delta \boldsymbol{\varphi}_1$. Expressing $\widehat{\boldsymbol{\varphi}}_1(1:3) = u + \Delta \boldsymbol{\varphi}_1(1:3)$ and subtracting both sides by s_1 , we have

$$\begin{aligned} (\widehat{\boldsymbol{\varphi}}_1(1:3) - s_1) \odot (\widehat{\boldsymbol{\varphi}}_1(1:3) - s_1) &\approx (u - s_1) \odot (u - s_1) \\ &+ 2(u - s_1) \odot \Delta \boldsymbol{\varphi}_1(1:3). \end{aligned} \quad (32)$$

where the second-order error terms are ignored. Similarly, expressing $\widehat{\boldsymbol{\varphi}}_1(6:8) = \dot{u} + \Delta \boldsymbol{\varphi}_1(6:8)$ and combining with the position estimates, we have

$$\begin{aligned} (\widehat{\boldsymbol{\varphi}}_1(1:3) - s_1) \odot (\widehat{\boldsymbol{\varphi}}_1(6:8) - \dot{s}_1) &\approx (u - s_1) \odot (\dot{u} - \dot{s}_1) \\ &+ (\dot{u} - \dot{s}_1) \odot \Delta \boldsymbol{\varphi}_1(1:3) + (u - s_1) \odot \Delta \boldsymbol{\varphi}_1(6:8). \end{aligned} \quad (33)$$

Substituting $\eta_1 = \widehat{\boldsymbol{\varphi}}_1(4) - \Delta \boldsymbol{\varphi}_1(4)$, $\eta_2 = \widehat{\boldsymbol{\varphi}}_1(5) - \Delta \boldsymbol{\varphi}_1(5)$, $\eta_3 = \widehat{\boldsymbol{\varphi}}_1(9) - \Delta \boldsymbol{\varphi}_1(9)$, and $w_1 = \widehat{\boldsymbol{\varphi}}_1(10) - \Delta \boldsymbol{\varphi}_1(10)$ into the equations (31a), (31b), and (31d), we obtain

$$\widehat{\boldsymbol{\varphi}}_1(10) \Delta \boldsymbol{\varphi}_1(4) + \widehat{\boldsymbol{\varphi}}_1(4) \Delta \boldsymbol{\varphi}_1(10) \approx \widehat{\boldsymbol{\varphi}}_1(4) \widehat{\boldsymbol{\varphi}}_1(10) - \|u - s_1\|^2, \quad (34a)$$

$$2\widehat{\boldsymbol{\varphi}}_1(4) \Delta \boldsymbol{\varphi}_1(4) - r_1^{o2} \Delta \boldsymbol{\varphi}_1(5) \approx \widehat{\boldsymbol{\varphi}}_1(4)^2 - \widehat{\boldsymbol{\varphi}}_1(5) \|u - s_1\|^2, \quad (34b)$$

$$\widehat{\boldsymbol{\varphi}}_1(10) \Delta \boldsymbol{\varphi}_1(9) + \widehat{\boldsymbol{\varphi}}_1(9) \Delta \boldsymbol{\varphi}_1(10) \approx \widehat{\boldsymbol{\varphi}}_1(9) \widehat{\boldsymbol{\varphi}}_1(10) - (u - s_1)^T (\dot{u} - \dot{s}_1). \quad (34c)$$

In order to provide an estimation of w in the second stage, we incorporate an additional equation

The proposed estimator

Input: Anchor's parameter, DDS/FDOA measurements, the measurement noise covariance.

First stage processing:

- 1: *Initialization:* $\mathbf{W}_1 = \tilde{\mathbf{Q}}_m^{-1}$.
- 2: **For** $l = 1$ to N_{iter} (N_{iter} is the number of iterations)
- 3: computing $\hat{\boldsymbol{\varphi}}_1$ from (27);
- 4: substituting $\hat{\boldsymbol{\varphi}}_1$ into (28) to update \mathbf{W}_1 ;

5: **end For**

Second stage processing:

- 6: Computing $\text{cov}(\hat{\boldsymbol{\varphi}}_1)$ using (30).
- 7: Using $\hat{\boldsymbol{\varphi}}_1$ to calculate \mathbf{B}_2 and obtaining \mathbf{W}_2 using (40).
- 8: **For** $l = 1$ to N_{iter}
- 9: computing $\hat{\boldsymbol{\varphi}}_2$ from (39);
- 10: applying (43a), (43b), and (43c) to generate the estimates;
- 11: substituting the estimates from (43a), (43b), and (43c) in \mathbf{B}_2 and updating \mathbf{W}_2 using (40) accordingly;
- 12: **end For**

Output: the target position and velocity, and the clock skew estimates.

ALGORITHM 1

$$\Delta\boldsymbol{\varphi}_1(5) = \hat{\boldsymbol{\varphi}}_1(5) - \boldsymbol{w}^{-2}. \quad (35)$$

Staking (32)–(35), we arrive at

$$\boldsymbol{e}_2 = \boldsymbol{h}_2 - \mathbf{G}_2\boldsymbol{\varphi}_2, \quad (36)$$

where

$$\boldsymbol{h}_2 = \begin{bmatrix} (\hat{\boldsymbol{\varphi}}_1(1:3) - s_1) \odot (\hat{\boldsymbol{\varphi}}_1(1:3) - s_1) \\ (\hat{\boldsymbol{\varphi}}_1(1:3) - s_1) \odot (\hat{\boldsymbol{\varphi}}_1(6:8) - \dot{s}_1) \\ \hat{\boldsymbol{\varphi}}_1(4)\hat{\boldsymbol{\varphi}}_1(10) \\ \hat{\boldsymbol{\varphi}}_1(4)^2 \\ \hat{\boldsymbol{\varphi}}_1(9)\hat{\boldsymbol{\varphi}}_1(10) \\ \hat{\boldsymbol{\varphi}}_1(5) \end{bmatrix}, \quad (37)$$

$$\mathbf{G}_2 = \begin{bmatrix} I_3 & O_{3 \times 3} & 0_{3 \times 1} \\ O_{3 \times 3} & I_3 & 0_{3 \times 1} \\ 1_{1 \times 3} & 0_{1 \times 3} & 0 \\ \hat{\boldsymbol{\varphi}}_1(5)1_{1 \times 3} & 0_{1 \times 3} & 0 \\ 0_{1 \times 3} & 1_{1 \times 3} & 0 \\ 0_{1 \times 3} & 0_{1 \times 3} & 1 \end{bmatrix},$$

$$\boldsymbol{\varphi}_2 = \begin{bmatrix} (u - s_1) & \odot & (u - s_1) \\ (u - s_1) & \odot & (\dot{u} - \dot{s}_1) \\ & & \boldsymbol{w}^{-2} \end{bmatrix}.$$

On the left side of (45), the noise vector \boldsymbol{e}_2 is defined as

$$\boldsymbol{e}_2 = \mathbf{B}_2\Delta\boldsymbol{\varphi}_1, \quad (38)$$

$$\mathbf{B}_2 = \begin{bmatrix} 2C_1 & O_{3 \times 2} & O_{3 \times 3} & O_{3 \times 2} \\ D_1 & O_{3 \times 2} & C_1 & O_{3 \times 2} \\ O_{4 \times 3} & E_1^T & O_{4 \times 3} & E_2^T \end{bmatrix},$$

$$C_1 = \text{diag}(u - s_1), D_1 = \text{diag}(\dot{u} - \dot{s}_1),$$

$$E_1 = \begin{bmatrix} wr_1^o & 2w^{-1}r_1^o & 0 & 0 \\ 0 & -r_1^{o2} & 0 & 1 \end{bmatrix},$$

$$E_2 = \begin{bmatrix} 0 & 0 & wr_1^o & 0 \\ w^{-1}r_1^o & 0 & w^{-1}r_1^o & 0 \end{bmatrix}.$$

Equation (36) is a set of linear equations with respect to $\boldsymbol{\varphi}_2$; its WLS solution is given by [36]

$$\hat{\boldsymbol{\varphi}}_2 = (\mathbf{G}_2^T \mathbf{W}_2 \mathbf{G}_2)^{-1} \mathbf{G}_2^T \mathbf{W}_2 \boldsymbol{h}_2, \quad (39)$$

where \mathbf{W}_2 is the weighting matrix, which is given as

$$\mathbf{W}_2 = \mathbb{E}[\boldsymbol{e}_2 \boldsymbol{e}_2^T]^{-1} = (\mathbf{B}_2 \text{cov}(\hat{\boldsymbol{\varphi}}_1) \mathbf{B}_2^T)^{-1}. \quad (40)$$

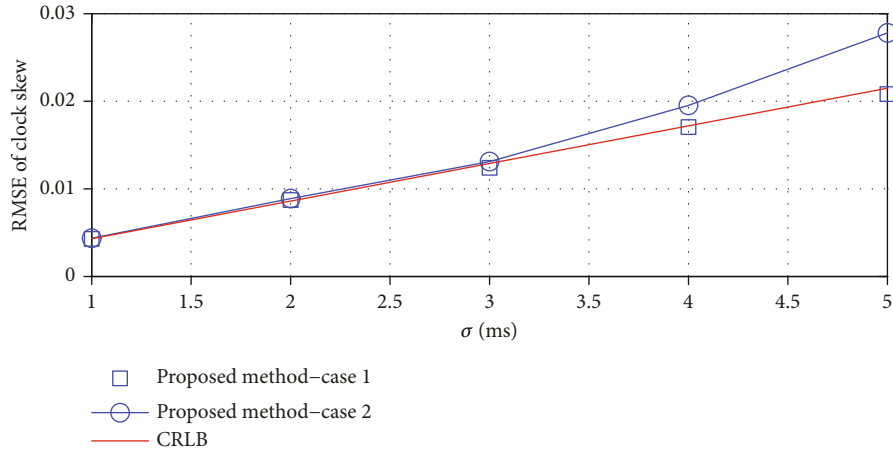
To examine the covariance of the second-stage solution $\hat{\boldsymbol{\varphi}}_2$, subtracting both sides of (39) by $\boldsymbol{\varphi}_2$ and using (36) gives

$$\Delta\boldsymbol{\varphi}_2 = \boldsymbol{\varphi}_2 - \hat{\boldsymbol{\varphi}}_2 = (\mathbf{G}_2^T \mathbf{W}_2 \mathbf{G}_2)^{-1} \mathbf{G}_2^T \mathbf{W}_2 \boldsymbol{e}_2. \quad (41)$$

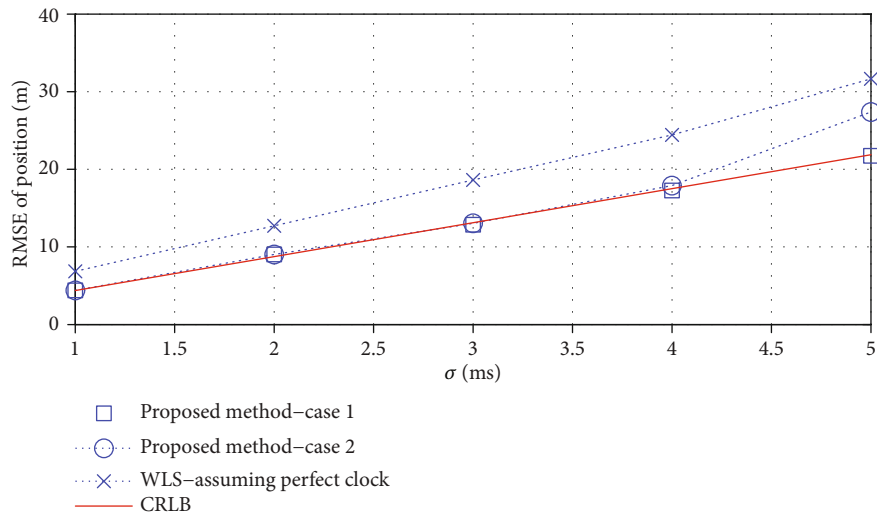
Hence, under small noise conditions, the covariance of the second stage solution $\hat{\boldsymbol{\varphi}}_2$ is given by [36]

$$\text{cov}(\hat{\boldsymbol{\varphi}}_2) \approx (\mathbf{G}_2^T \mathbf{W}_2 \mathbf{G}_2)^{-1}. \quad (42)$$

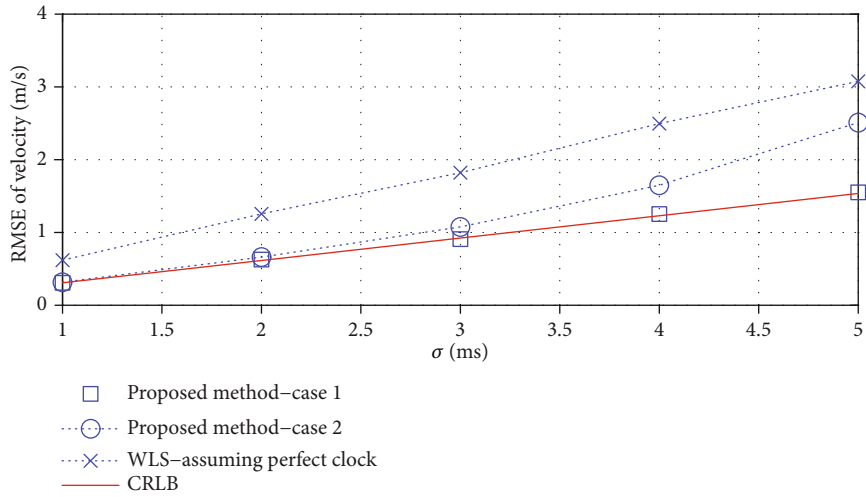
Finally, the clock skew, source position, and velocity



(a)

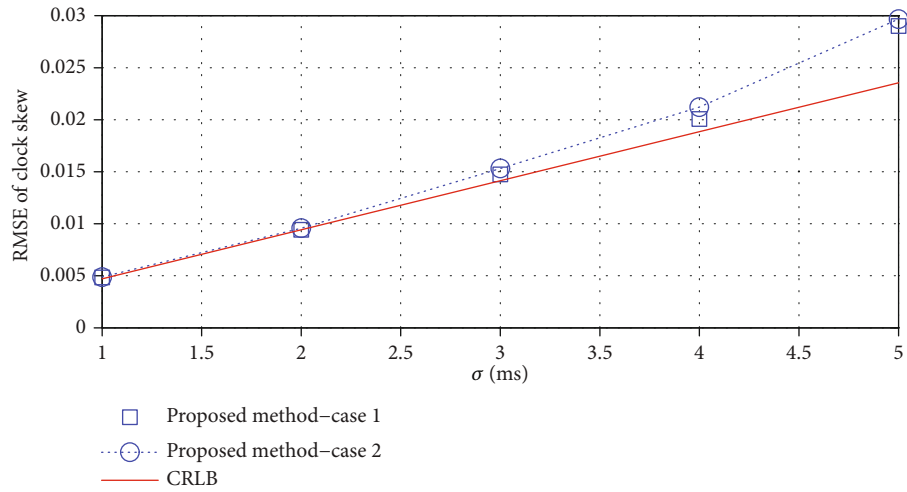


(b)

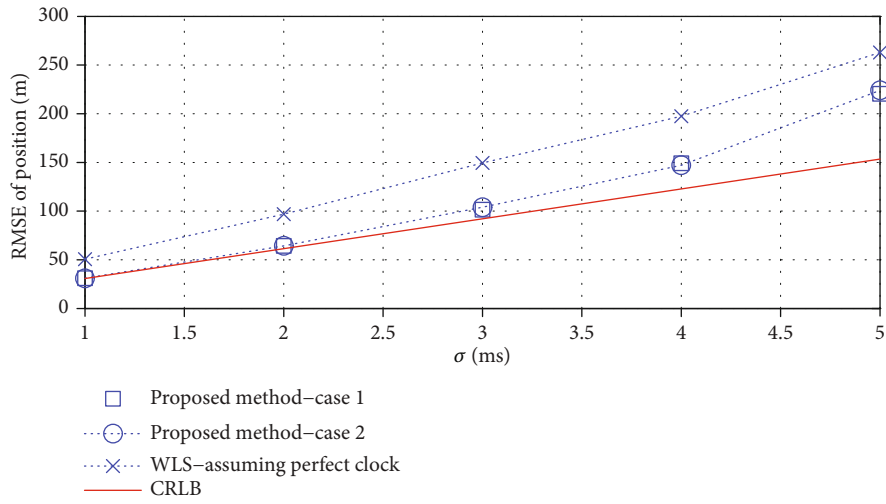


(c)

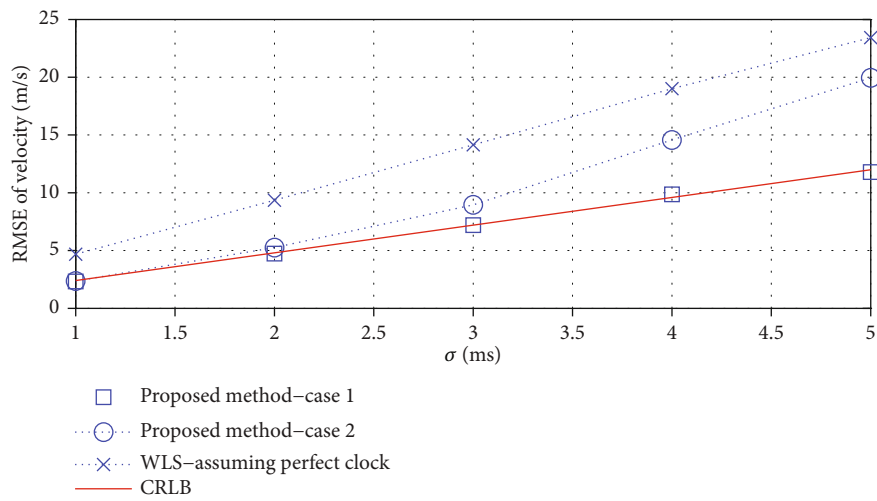
FIGURE 3: RMSE performance versus σ under scenario 1: (a) clock skew; (b) target position; (c) target velocity.



(a)



(b)



(c)

FIGURE 4: RMSE performance versus σ under scenario 2: (a) clock skew; (b) target position; (c) target velocity.

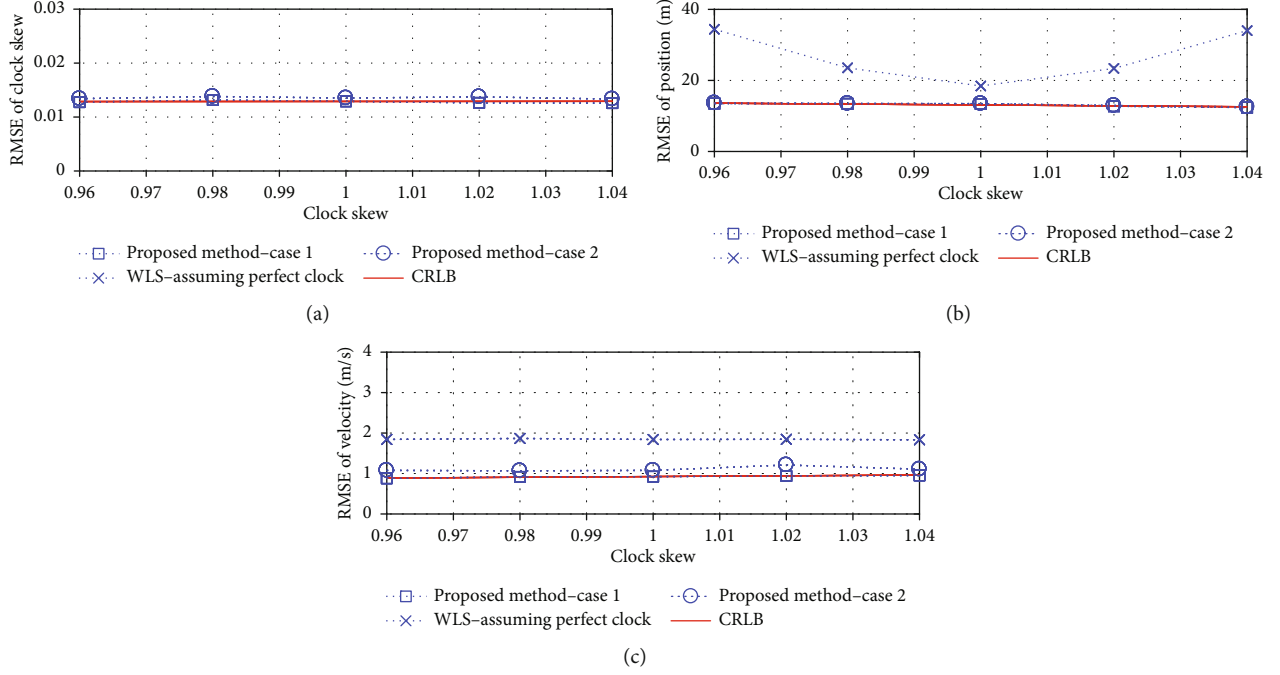


FIGURE 5: RMSE performance versus σ under scenario 2: (a) clock skew; (b) target position; (c) target velocity.

estimates can be deduced from the definition of $\hat{\boldsymbol{\varphi}}_2$.

$$\hat{\boldsymbol{u}} = \Pi \sqrt{\hat{\boldsymbol{\varphi}}_2(1:3)} + s_1, \quad (43a)$$

$$\hat{\dot{\boldsymbol{u}}} = \frac{\hat{\boldsymbol{\varphi}}_2(4:6)}{(u - s_1) + \dot{s}_1}, \quad (43b)$$

$$\hat{w} = \frac{1}{\sqrt{\hat{\boldsymbol{\varphi}}_2(7)}}, \quad (43c)$$

where $\Pi = \text{diag}(\text{sign}(\hat{\boldsymbol{\varphi}}_1(1:3) - s_1))$ is used to avoid the sign ambiguity caused by the square root operation.

Similar to \mathbf{W}_1 , the weighting matrix \mathbf{W}_2 is also dependent on the true values of clock skew, source position, and velocity through \mathbf{B}_2 . In practice, these true values can be substituted by the solution in $\hat{\boldsymbol{\varphi}}_1$ and then updated by the values in (43a), (43b), and (43c). We find that iterating one or two times leads to a good solution that meets the CRLB performance.

We summarize the prototype of our proposed estimator in Algorithm 1.

4. Performance Analysis

In this section, we shall analyze the theoretical covariance matrix of the proposed solution and compare it with the CRLB. By taking the differential of $\boldsymbol{\varphi}_2$ defined below (45), we can relate the estimation error of (43a), (43b), and

(43c) with that of $\hat{\boldsymbol{\varphi}}_2$ as

$$\begin{aligned} \Delta \boldsymbol{\varphi} &= [\Delta u, \Delta \dot{u}, \Delta w]^T = B_3^{-1} \Delta \boldsymbol{\varphi}_2, \\ B_3 &= \begin{bmatrix} 2 \text{diag}(u - s_1) & \mathbf{0}_{3 \times 3} & \mathbf{0}_{3 \times 1} \\ \text{diag}(\dot{u} - \dot{s}_1) & \text{diag}(u - s_1) & \mathbf{0}_{3 \times 1} \\ \mathbf{0}_{1 \times 3} & \mathbf{0}_{1 \times 3} & -2w^{-3} \end{bmatrix}. \end{aligned} \quad (44)$$

The bias of the final solution is given by taking expectation of $\Delta \boldsymbol{\varphi}$. Obviously, it can be seen that $\Delta \boldsymbol{\varphi}$ is linearly related to $[\boldsymbol{\varepsilon}_1, \boldsymbol{\varepsilon}_2]^T$ through the definitions of \mathbf{e}_1 , $\Delta \boldsymbol{\varphi}_1$, \mathbf{e}_2 , and $\Delta \boldsymbol{\varphi}_2$. Since $[\boldsymbol{\varepsilon}_1, \boldsymbol{\varepsilon}_2]^T$ is zero mean (when the noise is small), $\Delta \boldsymbol{\varphi}$ is also zero mean, which implies that the solution estimate is unbiased over a small noise region. Multiplying (44) by its transpose and taking expectation yields

$$\text{cov}(\hat{\boldsymbol{\varphi}}) = B_3^{-1} \text{cov}(\hat{\boldsymbol{\varphi}}_2) B_3^{-T}. \quad (45)$$

After substituting the corresponding covariance matrices in (30) and (42), (45) becomes

$$\text{cov}(\hat{\boldsymbol{\varphi}}) = (G_3^T Q_m^{-1} G_3)^{-1}, \quad (46)$$

where

$$G_3 = c^{-1} B_1^{-1} G_1 B_2^{-1} G_2 B_3. \quad (47)$$

Note that (46) has the same form as the CRLB given in (15) and (16). We shall compare $\text{cov}(\hat{\boldsymbol{\varphi}})$ with the CRLB under the case of far-field target. It has been shown that comparing $\text{cov}(\hat{\boldsymbol{\varphi}})$ with the CRLB for near-field target is not easy due to the tedious form of $\text{cov}(\hat{\boldsymbol{\varphi}})$; however, the

theoretical result drawn from the case of far-field target is also valid for near-field target in most cases [20]. For far-field target, we have the following two conditions

$$\begin{aligned} \text{(i)} \quad & r_1^o \approx r_2^o \approx \dots \approx r_N^o, \\ \text{(ii)} \quad & \dot{r}_i^o/r_i^o \approx 0, i = 1, \dots, N. \end{aligned} \quad (48)$$

The first condition indicates that the distances of the target to different receivers are approximately the same since the target is very far away from the anchors. The second condition implies that the velocities of underwater nodes are ignorable compared to the distances. This is valid due to two reasons: (1) the distances are large for far-field target; (2) underwater objects usually move slowly (several meters per second).

We now evaluate the matrix \mathbf{G}_3 . Substituting the relevant matrices into \mathbf{G}_3 , after some straightforward algebraic manipulation and appropriately using the conditions in (48), we can show that the elements of \mathbf{G}_3 can be approximated as

$$\begin{aligned} G_3(i-1, 1:3) &\approx w^{-1} \left(\frac{\dot{s}_1 - \dot{s}_i}{cr_i^o} - \frac{\dot{r}_i^o(s_1 - s_i)}{cr_i^{o2}} \right), \\ G_3(i-1, 4:6) &\approx \frac{w^{-1}(s_1 - s_i)}{c r_i^o}, \\ G_3(i-1, 7) &\approx -\frac{w^{-1} r_1^o \dot{r}_{i1}}{c r_i^o}, \\ G_3(N+i-2, 1:3) &\approx \frac{w(s_1 - s_i)}{c r_i^o}, \\ G_3(N+i-2, 4:6) &\approx 0_{1 \times 3}, \\ G_3(N+i-2, 7) &\approx \frac{w^{-1} r_1^o r_{i1}}{c r_i^o}, \end{aligned} \quad (49)$$

where $i = 2, \dots, N$. Then, using the variable relationships that $\dot{r}_i^o = ca_i$, $w\dot{r}_{i1}^o = \dot{r}_i^o - \dot{r}_1^o$, and $r_{i1}^o = w(r_i^o - r_1^o)$ and the approximations that $\dot{r}_{i1} \approx \dot{r}_{i1}^o$, $r_{i1} \approx r_{i1}^o$ and $r_i^o \approx r_1^o$, $i \neq 1$, we arrive at

$$\mathbf{G}_3 \approx \nabla_{\boldsymbol{\varphi}}^{m^o}. \quad (50)$$

This completes the proof that the proposed solution in Section 3 can attain the CRLB accuracy for small Gaussian noise and far-field target. Due to the tedious form of $\text{cov}(\hat{\boldsymbol{\varphi}})$, so far, we are not able to study the performance of the proposed solution under the case of near-field target. However, the simulation results in the next section show that the proposed solution can reach the CRLB for near-field target as well.

5. Numerical Examples

In this section, Matlab simulations are carried out to verify the effectiveness of the proposed localization algorithm (denoted by “proposed method-case 1”) by comparing with the CRLB, the WLS method assuming perfect clock [19],

and the proposed method considering the combination model of clock skew-free DDS model and clock skew-involved TDOA model (denoted by “proposed method-case 2”) (Note that the case of only considering the clock skew in DDS measurements is not included for comparison. This is because that the DDS measurement is much less than the TDOA measurement (about two orders of magnitude) so that the clock skew marginally affects the DDS measurement or even be overwhelmed by the noise. Thus, the estimates under this case is of poor accuracy as we observed in the simulations. As a result, the estimation performance of this case is not included.). The algorithm derivation of the proposed method, case 2, is similar to the procedure given in Section 3, and we would not repeat the derivation for simplicity. The performance criterion is the average root mean square error (RMSE), which can be expressed as

$\sqrt{1/N_{\text{exp}} \sum_{j=1}^{N_{\text{exp}}} \|\hat{\boldsymbol{\xi}}^{(j)} - \boldsymbol{\xi}\|^2}$, where $\hat{\boldsymbol{\xi}}^{(j)}$ is the estimate of $\boldsymbol{\xi} \in \{u, \dot{u}, w\}$ obtained in the j th trial. Each simulation result is averaged over $N_{\text{exp}} = 2000$ Monte Carlo trials. Two scenarios are considered in our simulation with the target being a near-field one and a far-field one. In scenario 1, 10 anchors and 1 target are randomly placed in a $1000 \times 1000 \times 1000$ cube centered at $[500, 500, 500]^T$, the velocities of the nodes are randomly drawn from $[-3, 3]$ m/s, and the clock skew is randomly drawn from $[0.995, 1.005]$. The sound propagation speed is set as 1500 m/s. The errors $\{\varepsilon_{i1}\}$ and $\{\dot{\varepsilon}_{i1}\}$ are zero-mean white Gaussian processes with identical variances of σ^2 and $0.01\sigma^2$, respectively. In scenario 2, the target is placed in $[-300, -300, -300]^T$ while the other settings are the same as scenario 1. Scenario 1 is a near-field target case while the scenario 2 is a far-field target case. Both scenarios are used to test the RMSE performance of the considered localization methods.

Figure 3 plots the RMSE of the considered localization algorithms versus $\sigma \in [1, 5]$ ms under scenario 1. It should be noted that perfect clock is assumed to be available in [19]. Therefore, only the clock skew estimation of our proposed method is presented in Figure 3(a). It is seen that the accuracy of the proposed method-case 1 approaches the CRLB in the whole noise range while the one that is using a mismatched DDS model (i.e., “proposed method-case 2”) is optimal only when $\sigma \leq 3$ ms. This corroborates the theoretical analysis in Section 4. As expected, the WLS method assuming a perfect clock yields the worst performance in the whole noise range. The performance gap between the WLS method assuming perfect clock and the proposed method-case 1 increases as the measurement noise increases. This demonstrates the significance of taking the clock imperfection into account. Regarding implementation complexity, the average computation times per trial for the proposed method-case 1, proposed method-case 2, and the WLS method assuming perfect clock [19] are measured as 8.9×10^{-4} s, 10×10^{-4} s, and 7.8×10^{-4} s, respectively. This indicates the computational attractiveness of the proposed method.

Figure 4 plots the RMSE of the considered localization algorithms versus $\sigma \in [1, 5]$ ms under scenario 2. We again see the superiority of our proposed method over the WLS

method without considering the clock imperfection. However, the location accuracy is generally worse for a far-field target than a near-field target as shown in Figures 4(a) and 4(b). To be specific, the proposed method reaches the CRLB only when $\sigma \leq 2$ ms. Despite the optimality, the RMSE of the target position and the velocity are larger than the one under scenario 1 by around 10 times as illustrated in Figures 4(b) and 4(c). This is because that the far-field target case implies a bad localization geometry, which leads to a significant decrease in target location accuracy. What is more, as shown in Figure 4(b), the position RMSEs of the proposed method-case 1 and proposed method-case 2 almost overlap. This indicates that the contribution of explicitly considering the clock skew in DDS model to the position estimation is marginal for a far-field target. To conclude the effect of the target position on the considered localization methods, a good localization geometry is very significant for all the methods. Although the RMSE performance of our proposed method is heavily deteriorated under a far-field target case, it still outperforms the localization method ignoring the clock imperfection.

Figure 5 plots the RMSE of the considered localization algorithms versus clock skew $\epsilon \in [0.96, 1.04]$ under scenario 1. The noise standard deviation σ is set to be 3 ms. In this simulation, we aim to study the impact of the value of clock skew on the considered algorithms. Note that the range of clock skew adopted here is based on the clock synchronization performance of widely used underwater acoustic modem (S2CR series) [37]. As it can be seen from Figure 5, along with the increase of the clock skew (both in positive or negative direction), the localization performance of the WLS method which have no regard for the clock skew gets worse. However, it has almost no effect on our proposed methods. This validates that the proposed localization algorithm is robust to the clock skew variation.

6. Conclusion

A new model for DDS/TDOA-based underwater localization with considering the clock imperfection has been proposed. Based on such a model, two WLS estimators are devised for underwater target parameters (position and velocity) and the clock skew estimation. The first one introduces nuisance variables to eliminate the coupling relationships between parameters; as a result, we obtain a pseudolinear estimation model for calculating a coarse estimate. The second WLS estimator refines the estimate by exploiting the coupling relationships between the target parameter, clock skew, and nuisance variables. The RMSE performances of the proposed estimator are compared with other competitive estimators by computer simulations. The performance of the proposed method is shown in theory and by simulations to reach the CRLB accuracy under sufficiently small noise conditions. As a future direction, we shall validate the performance of the proposed method using real underwater DDS/TDOA measurements.

With regard to the scalability issue, we notice that the proposed algorithm is designed to localize a single target node by using multiple anchor nodes. However, when there

presents multiple target nodes, the localization scheme proposed in this work may turn to be inapplicable. In the future work, we aim to develop a multistage underwater node localization scheme to achieve large-scale underwater network positioning. The key idea of multistage scheme lies in that the localized target nodes can be used as anchor nodes to localize other unlocated nodes. As performing iteratively, the localization range is gradually increasing.

Data Availability

All the data used to support the findings of this study are available in this paper.

Conflicts of Interest

The authors declare that there is no conflict of interest.

Acknowledgments

This work was supported in part by the National Nature Science Foundation of China under the grants 52101391, 62101573, and 62101578 and the Project of National University of Defense Technology under grant nos. ZK20-35 and ZK19-36.

References

- [1] M. Erol-Kantarci, H. T. Mouftah, and S. Oktug, "A survey of architectures and localization techniques for underwater acoustic sensor networks," *IEEE Communications Surveys and Tutorials*, vol. 13, no. 3, pp. 487–502, 2011.
- [2] C. Zheng, D. Sun, L. Cai, and X. Li, "Mobile node localization in underwater wireless networks," *IEEE Access*, vol. 6, pp. 17232–17244, 2018.
- [3] Z. Gong, C. Li, and F. Jiang, "AUV-aided joint localization and time synchronization for underwater acoustic sensor networks," *IEEE Signal Processing Letters*, vol. 25, no. 4, pp. 477–481, 2018.
- [4] L. Paull, S. Saeedi, M. Seto, and H. Li, "AUV navigation and localization: a review," *IEEE Journal of Oceanic Engineering*, vol. 39, no. 1, pp. 131–149, 2014.
- [5] J. Luo, Y. Yang, Z. Wang, and Y. Chen, "Localization algorithm for underwater sensor network: a review," *IEEE Internet of Things Journal*, vol. 8, no. 17, pp. 13126–13144, 2021.
- [6] B. Li, S. Zhou, M. Stojanovic, L. Freitag, and P. Willett, "Multi-carrier communication over underwater acoustic channels with nonuniform Doppler shifts," *IEEE Journal of Oceanic Engineering*, vol. 33, no. 2, pp. 198–209, 2008.
- [7] S. Zhou and Z. H. Wang, *OFDM for Underwater Acoustic Communications*, JohnWiley and Sons, 2014.
- [8] Z. Wang and G. B. Giannakis, "Wireless multicarrier communications," *IEEE Signal Processing Magazine*, vol. 17, no. 3, pp. 29–48, 2000.
- [9] S. Sun, X. Zhang, C. Zheng, J. Fu, and C. Zhao, "Underwater acoustical localization of the black box utilizing single autonomous underwater vehicle based on the second-order time difference of arrival," *IEEE Journal of Oceanic Engineering*, vol. 45, no. 4, pp. 1268–1279, 2020.
- [10] F. Liu, H. Chen, L. Zhang, and L. Xie, "Timedifference-of-arrival-based localization methods of underwater mobile

- nodes using multiple surface beacons,” *IEEE Access*, vol. 9, pp. 31712–31725, 2021.
- [11] N. Patwari, J. N. Ash, S. Kyperountas, A. O. Hero, R. L. Moses, and N. S. Correal, “Locating the nodes: cooperative localization in wireless sensor networks,” *IEEE Signal Processing Magazine*, vol. 22, no. 4, pp. 54–69, 2005.
- [12] Q. Liang, B. Zhang, C. Zhao, and Y. Pi, “TDOA for passive localization: underwater versus terrestrial environment,” *IEEE Transactions on Parallel and Distributed Systems*, vol. 24, no. 10, pp. 2100–2108, 2013.
- [13] J. Yan, D. Guo, X. Luo, and X. Guan, “AUV-aided localization for underwater acoustic sensor networks with current field estimation,” *IEEE Transactions on Vehicular Technology*, vol. 69, no. 8, pp. 8855–8870, 2020.
- [14] S. Zhang, Y. Liu, and X. Li, “Fast sparse aperture ISAR autofocusing and imaging via ADMM based sparse Bayesian learning,” *IEEE Transactions on Image Processing*, vol. 29, pp. 3213–3226, 2020.
- [15] R. Li, S. Zhang, C. Zhang, Y. Liu, and X. Li, “Deep learning approach for sparse aperture ISAR imaging and autofocusing based on complex-valued ADMM-Net,” *IEEE Sensors Journal*, vol. 21, no. 3, pp. 3437–3451, 2021.
- [16] N. Patwari, A. O. Hero, M. Perkins, N. S. Correal, and R. J. O’Dea, “Relative location estimation in wireless sensor networks,” *IEEE Transactions on Signal Processing*, vol. 51, no. 8, pp. 2137–2148, 2003.
- [17] P. Biswas, T. C. Liang, K. C. Toh, Y. Ye, and T. C. Wang, “Semidefinite programming approaches for sensor network localization with noisy distance measurements,” *IEEE Transactions on Automation Science and Engineering*, vol. 3, no. 4, pp. 360–371, 2006.
- [18] Y. Wang and Y. Wu, “An efficient semidefinite relaxation algorithm for moving source localization using TDOA and FDOA measurements,” *IEEE Communications Letters*, vol. 21, no. 1, pp. 80–83, 2017.
- [19] K. C. Ho and W. Xu, “An accurate algebraic solution for moving source location using TDOA and FDOA measurements,” *IEEE Transactions on Signal Processing*, vol. 52, no. 9, pp. 2453–2463, 2004.
- [20] K. C. Ho, X. Lu, and L. Kovavisaruch, “Source localization using TDOA and FDOA measurements in the presence of receiver location errors: analysis and solution,” *IEEE Transactions on Signal Processing*, vol. 55, no. 2, pp. 684–696, 2007.
- [21] M. Sun and K. C. Ho, “An asymptotically efficient estimator for TDOA and FDOA positioning of multiple disjoint sources in the presence of sensor location uncertainties,” *IEEE Transactions on Signal Processing*, vol. 59, no. 7, pp. 3434–3440, 2011.
- [22] Y. T. Chan and K. C. Ho, “Joint time-scale and TDOA estimation: analysis and fast approximation,” *IEEE Transactions on Signal Processing*, vol. 53, no. 8, pp. 2625–2634, 2005.
- [23] D. Musicki, R. Kaune, and W. Koch, “Mobile emitter geolocation and tracking using TDOA and FDOA measurements,” *IEEE Transactions on Signal Processing*, vol. 58, no. 3, pp. 1863–1874, 2010.
- [24] S. F. Mason, C. R. Berger, S. Zhou, and P. Willett, “Detection, synchronization, and Doppler scale estimation with multicarrier waveforms in underwater acoustic communication,” *IEEE Journal on Selected Areas in Communications*, vol. 26, no. 9, pp. 1638–1649, 2008.
- [25] J. Zheng and Y. C. Wu, “Joint time synchronization and localization of an unknown node in wireless sensor networks,” *IEEE Transactions on Signal Processing*, vol. 58, no. 3, pp. 1309–1320, 2010.
- [26] Y. Wang and K. C. Ho, “TDOA source localization in the presence of synchronization clock bias and sensor position errors,” *IEEE Transactions on Signal Processing*, vol. 61, no. 18, pp. 4532–4544, 2013.
- [27] M. R. Gholami, S. Gezici, and E. G. Strom, “TDOA based positioning in the presence of unknown clock skew,” *IEEE Transactions on Communications*, vol. 61, no. 6, pp. 2522–2534, 2013.
- [28] J. Liu, Z. Wang, M. Zuba, Z. Peng, J. H. Cui, and S. Zhou, “DA-Sync: a doppler-assisted time-synchronization scheme for mobile underwater sensor networks,” *IEEE Transactions on Mobile Computing*, vol. 13, no. 3, pp. 582–595, 2014.
- [29] O. Pallares, P. J. Bouvet, and J. del Rio, “TS-MUWSN: time synchronization for mobile underwater sensor networks,” *IEEE Journal of Oceanic Engineering*, vol. 41, no. 4, pp. 763–775, 2016.
- [30] F. Zhou, Q. Wang, D. Nie, and G. Qiao, “DE-sync: a Doppler-enhanced time synchronization for mobile underwater sensor networks,” *Sensors*, vol. 18, no. 6, pp. 1710–1715, 2018.
- [31] Y. C. Wu, Q. Chaudhari, and E. Serpedin, “Clock synchronization of wireless sensor networks,” *IEEE Signal Processing Magazine*, vol. 28, no. 1, pp. 124–138, 2011.
- [32] L. Wan, Z. Wang, S. Zhou, T. C. Yang, and Z. Shi, “Performance comparison of Doppler scale estimation methods for underwater acoustic OFDM,” *Journal of Electrical and Computer Engineering*, vol. 2012, 11 pages, 2012.
- [33] B. S. Sharif, J. Neasham, O. R. Hinton, and A. E. Adams, “A computationally efficient Doppler compensation system for underwater acoustic communications,” *IEEE Journal of Oceanic Engineering*, vol. 25, no. 1, pp. 52–61, 2000.
- [34] X. Zhang, W. Ying, P. Yang, and M. Sun, “Parameter estimation of underwater impulsive noise with the class b model,” *IET Radar, Sonar and Navigation*, vol. 14, no. 7, pp. 1055–1060, 2020.
- [35] X. Zhang, W. Ying, and B. Yang, “Parameter estimation for class a modeled ocean ambient noise,” *Journal of Engineering and Technological Sciences*, vol. 50, no. 3, pp. 330–345, 2018.
- [36] S. M. Kay, *Fundamentals of Statistical Signal Processing, Estimation Theory*, Prentice-Hall, Upper Saddle River, NJ, USA, 1993.
- [37] K. G. Kebkal, V. K. Kebkal, O. G. Kebkal, and R. Petroccia, “Underwater acoustic modems (s2cr series) for synchronization of underwater acoustic network clocks during payload data exchange,” *IEEE Journal of Oceanic Engineering*, vol. 41, no. 2, pp. 428–439, 2016.

Research Article

Precoded IM-OFDM-SS for Underwater Acoustic Communication

Zeyad A. H. Qasem ¹, Hussein A. Leftah ², Haixin Sun ¹, and Hamada Esmail ^{1,3}

¹Department of Information and Communication, School of Informatics, Xiamen University, Xiamen 316005, China

²Basrah Engineering Technical College, Southern Technical University, Iraq

³Electrical Engineering Department, Faculty of Engineering, Aswan University, Aswan 81542, Egypt

Correspondence should be addressed to Hamada Esmail; h.esmaiel@aswu.edu.eg

Received 16 December 2021; Revised 30 January 2022; Accepted 18 February 2022; Published 9 March 2022

Academic Editor: Abdul Basit

Copyright © 2022 Zeyad A. H. Qasem et al. This is an open access article distributed under the Creative Commons Attribution License, which permits unrestricted use, distribution, and reproduction in any medium, provided the original work is properly cited.

The nature of the multipath channel and the peak-to-average power ratio (PAPR) are regarded as the main challenges restricting the design of a multicarrier reliable underwater acoustic (UWA) communication. This paper proposes a new scheme, precoded index modulation orthogonal frequency division modulation spread spectrum (IM-OFDM-SS), for UWA communication. The precoded IM-OFDM-SS is proposed to increase the transmission efficiency and exploit the spreading and multipath diversities and, at the same time, reduce the PAPR to achieve a reliable communication system. Two different precoders, discrete Hartley transform (DHT) and discrete cosine transform (DCT), are utilized in the proposed scheme and compared with the conventional IM-OFDM-SS scheme. Simulation and real experimental results demonstrate the outperformance of the proposed precoded IM-OFDM-SS in comparison to the conventional benchmarks in terms of PAPR and bit error rate (BER) performance.

1. Introduction

An underwater acoustic (UWA) channel is regarded as one of the most complicated media in use due to its challenging effects. The main challenges of UWA channels are represented by the long-delay effect and doubly selective channel caused by the oceanic environment [1, 2]. As the receiver, the signal is superimposed due to the substantial multipath effect causing a superposition of the signal at the receiver side rising a severe intersymbol interference (ISI) in the ocean environment. Therefore, exhaustive processing must be employed at the receiving end for equalizing and estimating the channel to ensure the reliability of UWA communication.

As a result, researchers are working hard to establish a reliable UWA communication with an acceptable data rate in that environment using two main modulation techniques, which are single-carrier and multicarrier modulations. On the one hand, single-carrier modulation was proven to be capable of dealing with the ISI since the adaptive equalizer can be employed, e.g., a decision feedback equalizer with a recursive least squares algorithm [3]. Furthermore, the use of correcting coding can also provide communication with

better quality [4]. The main drawback of a single-carrier system is the high-complexity process required for recovering the channel's effects at the receiving end. On the other hand, multicarrier modulation is presented to avoid that concern; it can mitigate the delay spread and bandwidth limitation of the UWA channel with less required processing. A multicarrier modulation system is able to recover the channel using a significantly low-complexity equalizer, but unfortunately, the significant Doppler effect leads to severe intercarrier interference (ICI) [5, 6].

Orthogonal frequency division multiplexing (OFDM) can be considered the finest choice which can effectively overcome the UWA channel effects. That is due to its ability to deal with the long multipath spread UWA channel with low-complex frequency-domain equalization; this means that, different from signal carrier systems, OFDM does not require a complicated time-domain equalization [5, 7, 8]. Despite those advantages, OFDM still has a problem with the high peak-to-average power ratio (PAPR) in UWA communication, limited spectral efficiency, and performance deterioration in communication systems with harsh channels [9].

Consequently, to overcome the OFDM PAPR performance and increase its resilience to multipath fading channels, channel-independent unitary precoders were utilized in OFDM systems [10]. Intensive research on using different unitary precoders such as Walsh-Hadamard transforms (WHT), discrete Hartley transform (DHT) [11], and discrete cosine transform (DCT) [12, 13] showed that system complexity and PAPR reduction level are mainly determined by the used unitary precoder.

Recently, the index modulation OFDM (IM-OFDM) was proposed [14–17] to overcome the intercarrier interference (ICI) that existed in the conventional OFDM scheme as well as improve its spectral efficiency. Unlike OFDM, the subcarriers in OFDM-IM are classified to be active or idle, where the data is carried physically by digital modulation via the active subcarriers and, at the same time, the index of the active subcarriers conveys additional information bits. OFDM-IM can provide better BER performance in low-to-medium data rate systems compared to OFDM. The maximum likelihood (ML) detector, regarded as an optimal detector, is employed at the receiver for jointly detecting the index of active subcarriers and modulated data. Apart from the high computational complexity of the ML receiver, the channel estimation error leads to dramatic deterioration of the performance of the ML decoder [18]. That issue becomes exhaustive in such untrusted communication systems like UWA communication. That is because of the dependence between the detection of data symbols and active subcarriers. In other words, the erroneous detection of active subcarriers leads to the incorrect decision of the data symbols [19]. Therefore, detecting the varied index of active subcarriers must be guaranteed at the receiving end by having perfect knowledge on the channel, which is one of the main difficulties in UWA communication.

On the other hand, the index modulation OFDM spread spectrum (IM-OFDM-SS) [18] was presented to improve the diversity gain of OFDM-IM. Unlike OFDM-IM, IM-OFDM-SS activates all subcarriers to transmit the modulated data symbols, but it spreads each data symbol across different subcarriers using a predefined spreading code. Specifically, the information bits are divided into two parts: one part is transmitted via the index of that predefined spreading code and the other part is carried by the spread modulated data symbols. Therefore, additional diversity is gained as the data symbols are spread across different subcarriers. Additionally, the maximal ratio combining (MRC) detector can straightforwardly be employed at the receiving end for performing low-complex detection as well as avoiding the issues of the ML detector related to the channel estimation susceptibility [18]. Despite those advantages, IM-OFDM-SS and OFDM-IM inherit the high PAPR from conventional OFDM systems.

In order to overcome the PAPR issue of OFDM and harvest higher diversity gain, X-transform IM-OFDM-SS has been presented in [20]. The higher performance of PAPR in that scheme is acquired by the low-complex X-transform matrix, composed of the discrete Fourier transform (DFT) matrix and DHT matrix. The channel effects in that scheme are recovered in the time-domain pseudo-

noise (PN) packet inserted for estimation tasks as well as guard interval. The enhanced performance provided by X-transform IM-OFDM-SS can only be guaranteed when considering the slow-varied UWA channel as the overhead packets are inserted at the beginning and at the end of each symbol. Moreover, inserting additional overhead packets might lead to deteriorating the structure of the X-transform matrix.

Motivated by those advantages offered by IM-OFDM-SS and X-transform IM-OFDM-SS, the contribution of this paper is to propose a new scheme called precoded IM-OFDM-SS to maximize the efficiency of the limited bandwidth of the UWA channel, decrease the higher PAPR, and suppress the residual ICI. Discrete cosine transform (DCT) type II and Hartley transform (DHT) are used as a spreading matrix for the new precoded IM-OFDM-SS. Unlike X-transform IM-OFDM-SS [20], the proposed schemes insert the overhead packets in the frequency domain to track the fast-varied UWA channel effects. Although the PAPR performance is a little bit deteriorated compared to our proposed scheme in [20], we believe that the proposed schemes are environment dependent making them very attractive for the untrusted UWA communication systems. Thanks to the precoding and spreading techniques of the new schemes, the information symbols are distributed over all new scheme subcarriers; hence, the symbol of a highly attenuated subcarrier can be recovered from the other subcarriers. The new precoded IM-OFDM-SS uses the unequal attenuation effect over the spread subcarrier symbols to avoid the underwater burst error and improve the UWA communication reliability. The rest of this paper is structured as follows: the system model, including the transmitter and the receiver of the proposed schemes, is presented in Section 2. The system performance analysis is studied in Section 3. Simulation and experimental results are shown in Section 4, and the conclusion of this paper is presented in Section 5.

2. System Model

The proposed IM-OFDM-SS structure is shown in Figure 1, letting the input of the bit splitter be B data bits. The B bits are divided into G groups, and each group has m bits, $m = B/G$. Bit splitter divides bits of each group $g \in \{1, \dots, G\}$ into two subgroups $P_1^{(g)}$ and $P_2^{(g)}$. $P_1^{(g)}$ is transmitted via the index of the selected spreading code $\mathbf{c}_{i^{(g)}}$ out of the preconfigured code set $\mathcal{C} = \{\mathbf{c}_1, \dots, \mathbf{c}_n\}$, where $i^{(g)} \in \{1, \dots, n\}$ is the index of the g -th group spreading code. The $\mathbf{c}_{i^{(g)}}$ length is n . The other subgroup $P_2^{(g)}$ is mapped into the $s^{(g)} \in \chi$ symbol, χ is any M -ary digital modulation with a unit average power, and $P_2^{(g)} = \log_2(M)$. The modulated constellation symbols $s^{(g)}$ will be spread over the spreading code $\mathbf{c}_{i^{(g)}}$ selected using $P_1^{(g)}$ index bits as follows:

$$\mathbf{x}^g = \left[x_1^{(g)}, \dots, x_n^{(g)} \right]^T = \left[s^{(g)} c_{i^{(g)},1}, \dots, s^{(g)} c_{i^{(g)},n} \right]^T. \quad (1)$$

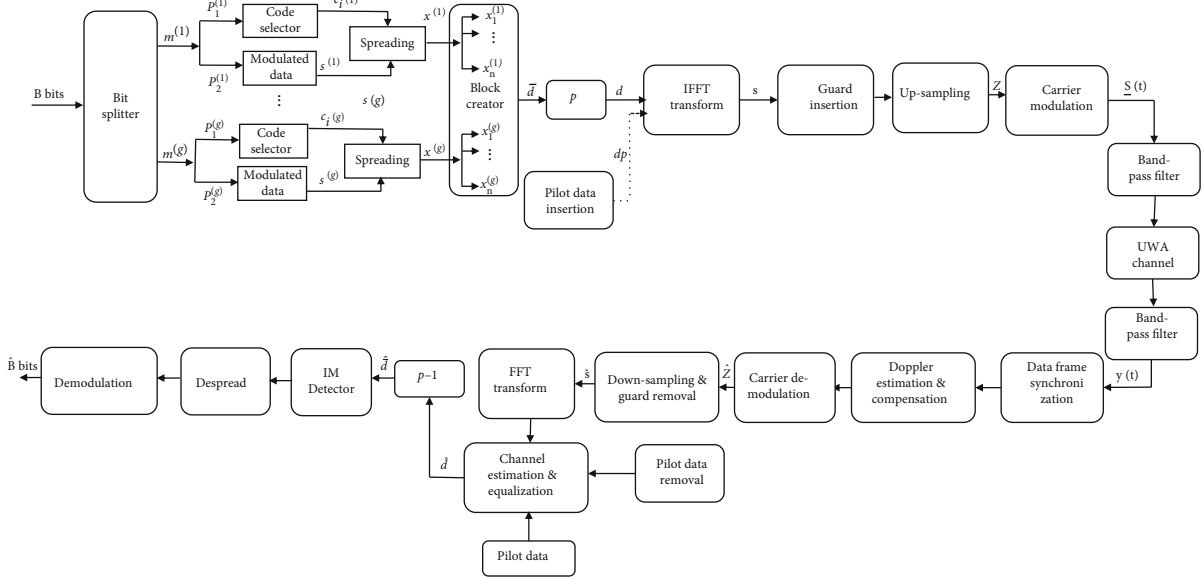


FIGURE 1: Structure of the UWA precoded IM-OFDM-SS system.

In this paper, to relax the receiver complexity, the maximum size of \mathcal{C} spreading codes is normally restricted to be n since it must be mutually orthogonal, and we can consider 5th orthogonal codes of Walsh or Zadoff-Chu (ZC) [18]. The data symbol vector $[\bar{\mathbf{d}}]_{\mathcal{M} \times 1} = [\mathbf{x}^1, \mathbf{x}^2, \dots, \mathbf{x}^G]$ is generated by concatenating \mathbf{x}^g of all groups, and the total transmitted bits via the new precoded IM-OFDM-SS can be written as

$$\mathcal{N} = G \times (\log_2(n) + \log_2(M)). \quad (2)$$

Unlike the conventional IM-OFDM-SS, the proposed precoded IM-OFDM-SS multiplies the vector of spread data symbol $\bar{\mathbf{d}}$ by a precoding matrix; \mathcal{P} resulting in the precoded data symbol noted \mathbf{d} , noted by $\mathbf{d} = \mathcal{P}\bar{\mathbf{d}}$. In this paper, DCT type II and DHT are considered precoding matrices $\mathcal{P}, \mathcal{P} \in \mathbb{R}^{\mathcal{M} \times \mathcal{M}}$; the (r, l) entries of DCT and DHT are given in (3) and (4), respectively. In both cases, the \mathcal{P} matrix is invertible and has a flexible size which can be any positive integer; its entries have the same magnitude. Consequently, all IM-OFDM-SS data symbols are equally spread over \mathcal{M} with significant diversity gain compared to the conventional IM-OFDM-SS.

$$\rho_{r,l} = \begin{cases} \sqrt{\frac{2}{\mathcal{M}}} \cos\left(\frac{(l-1)(2l-1)\pi}{2\mathcal{M}}\right), & r > 1, \\ \sqrt{\frac{1}{\mathcal{M}}} & r = 1, \end{cases} \quad (3)$$

$$\rho_{r,l} = \cos\left(\frac{2\pi r l}{\mathcal{M}}\right) + \sin\left(\frac{2\pi r l}{\mathcal{M}}\right). \quad (4)$$

For channel estimation purposes, pilot tones \mathbf{d}_p are multiplexed with the \mathbf{d} to estimate the doubly selective UWA channel. The resulted vector $\mathbf{d}_T \in \mathbb{C}^{\mathcal{N} \times 1}$ including

data, pilots, and null subcarriers is fed into the OFDM modulator as the inverse fast Fourier transform (IFFT) is used for modulating information symbols. Then, the cyclic prefix (CP) is inserted as a guard interval resulting in the transmitted baseband signal expressed as follows:

$$\mathbf{s}(t) = \sum_{n=-N/2}^{N/2-1} \mathbf{d}_T[n] e^{j2\pi n \Delta f t}, \quad (5)$$

where Δf is the OFDM subcarrier frequency spacing. Then, the baseband signal transmitted over the UWA channel will be processed by upconversion including upsampling and carrier modulation. The underwater channel can be written as [21]

$$\mathbf{h}(t, \tau) = \sum_{\rho=1}^L \alpha_{\rho}(t) \delta\left(\tau - \left(\tau_{\rho} - \beta_{\rho} t\right)\right), \quad (6)$$

where $\alpha_{\rho}(t)$, $\tau_{\rho}(t)$, $\delta(t)$, and β_{ρ} denote the time-varying amplitudes of the path ρ , delays of L multipath components, Dirac delta function, and Doppler scaling factor (DSF), respectively. The received passband signal is

$$\mathbf{y}(t) = \text{Re} \left\{ \sum_{\rho=1}^L \alpha_{\rho} \left[\sum_{n=-N/2}^{N/2-1} \mathbf{d}_T[n] e^{j2\pi n \Delta f (t + \beta t - \tau_{\rho})} \cdot p(t + \beta - \tau_{\rho}) \right] \times e^{j2\pi f_c (t + \beta t - \tau_{\rho})} \right\} + \mathbf{v}(t), \quad (7)$$

where $\mathbf{v}(t) \sim \mathcal{CN}(0, \sigma^2)$ is the passband additive white Gaussian noise (AWGN). f_c and $p(t)$ denote the carrier frequency and pulse shaping filter, respectively. Root-raised cosine-type pulse shaping filters are used in both the transmitter and the receiver. In (7), each path of the received

signal is scaled in $(T \sim T/(1 + \beta))$; T is the OFDM symbol duration. Also, a Doppler shift $e^{j2\pi\beta f_n t}$ is affecting every sub-carrier. The frequency-dependent Doppler shift causes a critical ICI in the UWAC. To mitigate the ICI effect, the two-step Doppler estimation and compensation in [21] are adopted in this paper where two low-frequency modulation (LFM) segments are used as preamble and postamble to coarsely estimate the DSF at the receiver end. The DSF is estimated by a cross-correlation between $\mathbf{y}(\mathbf{t})$ and those two known segments, preamble and postamble. Cross-correlation operation will give a signal with two peaks; the first one is utilized for synchronization. The difference between first and second cross-correlation peaks is used to find the length of the received signal \mathcal{B}' . By comparing \mathcal{B}' with the length of transmitted signal length \mathcal{B} which is supposed to be known, the DSF can be estimated as

$$\beta' = \frac{\mathcal{B}}{\mathcal{B}'} - 1. \quad (8)$$

The received signal is resampled at the receiving end as in (7) at $(1 + \beta')f_s$, where f_s is the original sampling frequency used at the transmitter side. The resampled received signal under a resampling factor β' is $\mathbf{z}(t) = \mathbf{y}(t/(1 + \beta'))$, $\mathbf{z}(\mathbf{t}) = \text{Re}(\mathbf{z}(\mathbf{t})e^{j2\pi f_c t})$. Considering $(1 + \beta)/(1 + \beta') = 1$, $\mathbf{z}(\mathbf{t})$ can be expressed as

$$\begin{aligned} \mathbf{z}(\mathbf{t}) &\approx e^{j2\pi\beta - \beta'/(1 + \beta')f_c t} \\ &\times \sum_{n=-N/2}^{N/2-1} \left\{ \mathcal{d}_T[n] e^{j2\pi n \Delta \text{ft}} \times \left[\sum_{\rho=1}^L \alpha_\rho e^{-j2\pi f_n \tau_\rho} p(t - \tau_\rho) \right] \right\} + \bar{\mathbf{v}}(\mathbf{t}), \end{aligned} \quad (9)$$

where $\bar{\mathbf{v}}(\mathbf{t}) \sim \mathcal{CN}(0, \sigma^2)$ is the AWGN in the baseband. The expression of the frequency-independent Doppler shift is given following (9) by

$$\mathcal{E} = \frac{\beta - \beta'}{1 + \beta'} f_c. \quad (10)$$

The ε term in (10) is called carrier frequency offset (CFO) when the narrowband is considered. The CFO is estimated by minimizing the null subcarriers' energy. To explain the CFO estimation in the precoded IM-OFDM-SS, we use the null subcarrier of the received data, after resampling each OFDM data block. Assume a vector \mathbf{f}_n of $(N + L) \times 1$, where $\mathbf{f}_n = [1, e^{j2\pi n/N}, \dots, e^{j2\pi n(N+L-1)/N}]^T$ and a $(N + L) \times (N + L)$ diagonal matrix $\zeta(\mathcal{E}) = \text{diag} \{ [1, e^{j2\pi T_n \mathcal{E}}, \dots, 1, e^{j2\pi T_n(N+L-1)\mathcal{E}}] \}$; \mathcal{E} is the residual CFO, and $T_n = T/N$ is the sample's duration. The energy of the null subcarrier whose locations are well known is used as a cost function, and the CFO can be obtained as

$$\hat{\mathcal{E}} = \arg \min_{\mathcal{E}} \left\{ \sum_{n \in \mathcal{S}_N} \left| \mathbf{f}_n^H \zeta(\mathcal{E}) \hat{\mathbf{z}} \right|^2 \right\}. \quad (11)$$

The collected $N + L$ samples after resampling of each block are $\hat{\mathbf{z}} = [\hat{z}(0), \dots, \hat{z}(N + L - 1)]^T$. After CFO estimation and compensation, the signal of the n -th subcarrier is given by

$$\hat{\mathbf{s}}[n] = \mathbf{f}_n^H \zeta(\hat{\mathcal{E}}) \hat{\mathbf{z}} = H(n) \hat{\mathbf{d}}_T[n] + \bar{\mathbf{v}}_n, \quad (12)$$

where $H = \sum_{\rho=1}^L \alpha_\rho e^{-j2\pi f_n \tau_\rho}$ is the channel frequency response, $\bar{\mathbf{v}}_n$ is the resulting noise of the n -th subcarrier, and $\mathcal{H}(\cdot)$ is the Hermitian transpose. Using $\hat{\mathbf{s}}[n]$, channel estimation is performed based on pilot symbols located as predefined. Without loss of generality, orthogonal matching pursuit (OMP) [22] is adopted in this paper for underwater channel estimation, and the minimum means square error (MMSE) is used for equalization. After removing the overhead packets from the MMSE equalizer output, the resultant signal $\hat{\mathbf{d}} \in \mathbb{C}^{M \times 1}$ is the received precoded estimated data. The IM-OFDM-SS demapping extracts the physically transmitted data encapsulated in the index of the spreading code. First, the despreading matrix $\mathcal{P}^{\mathcal{H}}$ is used to extract the transmitted data symbols $\hat{\mathbf{d}}$ (noted by $\hat{\mathbf{d}} = \mathcal{P}^{\mathcal{H}} \hat{\mathbf{d}}$).

The maximum ratio combining (MRC) detector is employed, as shown in Figure 2, for detecting the received information bits. Each vector $\hat{\mathbf{x}}^{(g)} \in \mathbb{C}^{n \times 1}$, picked from $\hat{\mathbf{d}}$, which is corresponding to the subgroup g , is despreading by all predefined spreading codes used at the transmitting end. Thus, the output of the l -th code, $l \in \{1, \dots, n\}$, can be expressed as follows:

$$\Delta_l = \sum_{k=1}^n \hat{\mathbf{x}}^{(g)} c_{l^{(g)}, k}. \quad (13)$$

Therefore, $P_1^{(g)}$ can be found using (13) as follows:

$$\hat{l}^{(g)} = \arg \max_l |\Delta_l|^2. \quad (14)$$

Finally, the output of despreading $\hat{\mathbf{x}}^{(g)}$ using $\hat{l}^{(g)}$ is corresponding to $P_2^{(g)}$.

3. Performance Analysis

This section evaluates the proposed precoded IM-OFDM-SS scheme in terms of pairwise error probability (PEP) and coding and diversity gains. The conditional PEP of the estimated $\hat{\mathbf{d}}$ data to the transmitted data \mathbf{d} is given by

$$P\left(\mathbf{d} \rightarrow \frac{\hat{\mathbf{d}}}{\mathbf{H}}\right) = Q\left(\sqrt{\frac{\|\mathbf{H}\mathcal{P}(\mathbf{d} - \hat{\mathbf{d}})\|^2}{2N_0}}\right), \quad (15)$$

where $Q(\cdot)$ is the Gaussian tail probability [23]. Using the Q -function, an alternative form of (15) can be expressed as

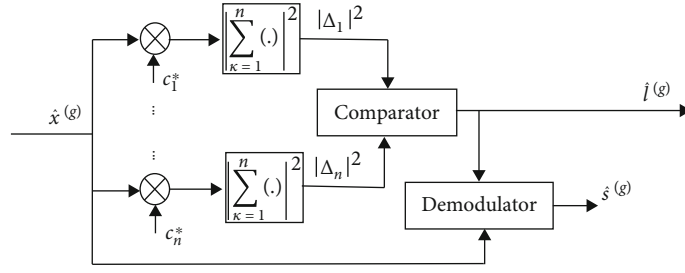


FIGURE 2: MRC detector of the precoded IM-OFDM-SS.

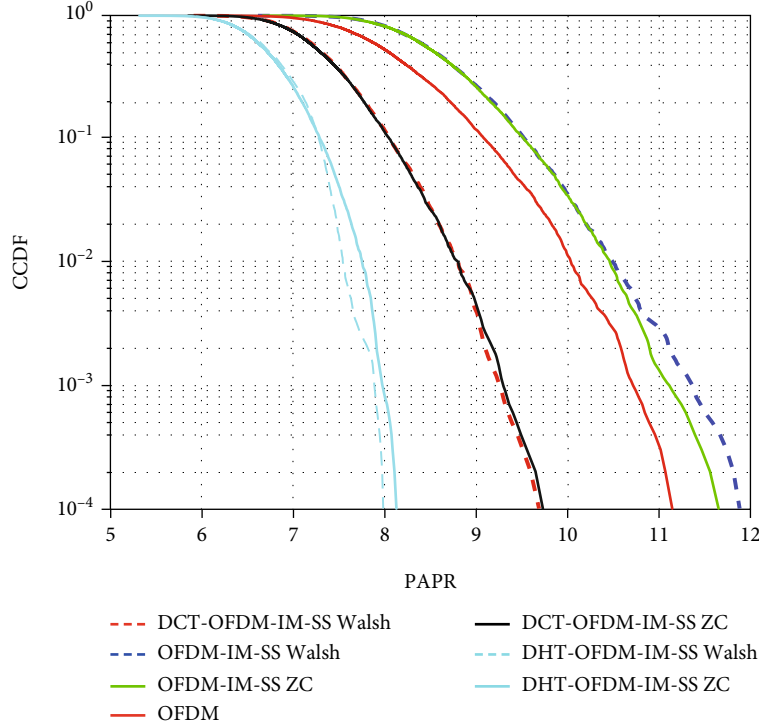


FIGURE 3: PAPR performance comparison.

follows [23]:

$$P(\mathbf{d} \rightarrow \hat{\mathbf{d}}) = \frac{1}{\pi} \int_0^{\pi/2} e^{-\frac{\mu}{4N_0 \sin^2 \varnothing}} d\varnothing, \quad (16)$$

where $\mu = \|\mathbf{H}\mathcal{P}(\mathbf{d} - \hat{\mathbf{d}})\|^2$ which can be rewritten as $\mu = \sum_{i=1}^M \sigma_i |h_i|^2$, $\sigma_i = |\mathbf{g}_i(\mathbf{d} - \hat{\mathbf{d}})|^2$, and \mathbf{g}_i is the i -th row of \mathcal{P} . The unconditional PEP is given by averaging (16) with respect to μ as follows:

$$P(\mathbf{d} \rightarrow \hat{\mathbf{d}}) = \frac{1}{\pi} \int_0^{\pi/2} \aleph_{\mu} \left(-\frac{1}{4N_0 \sin^2 \varnothing} \right) d\varnothing, \quad (17)$$

where \aleph_{μ} is the moment generating function (MGF) of μ . Due to the channel model, the MGF of $\Lambda_i = \sigma_i |h_i|^2$ of μ is $\aleph_{\Lambda_i}(t) = (1 - \sigma_i \varphi^2 t)^{-1}$ which

gives $\aleph_{\mu}(t) = \prod_{i=1}^M (1 - \sigma_i \varphi^2 t)^{-1}$. Therefore, (17) can be expressed as

$$P(\mathbf{d} \rightarrow \hat{\mathbf{d}}) = \frac{1}{\pi} \int_0^{\pi/2} \prod_{i=1}^M \frac{\sin^2 \varnothing}{\sin^2 \varnothing + (\sigma_i \varphi^2 / 4N_0)} d\varnothing. \quad (18)$$

For any precoding matrix \mathcal{P} , let us define $\Gamma_{\mathbf{d}, \hat{\mathbf{d}}}$ as the cardinality of a defined set $\mathcal{Q}_{\mathbf{d}, \hat{\mathbf{d}}} = \{i \mid \sigma_i \neq 0\}$, $\Gamma_{\mathbf{d}, \hat{\mathbf{d}}} = |\mathcal{Q}_{\mathbf{d}, \hat{\mathbf{d}}}|$, we can approximate $\sin^2 \varnothing (\sin^2 \varnothing + (\sigma_i \varphi^2 / 4N_0))^{-1} \leq (1 + (\sigma_i \varphi^2 / 4N_0))^{-1} \approx 4/\sigma_i \bar{\gamma}$ at high signal-to-noise ratios (SNRs) because $0 \leq \sin^2 \varnothing \leq 1$. The integrand of (18) can be approximated as

$$P(\mathbf{d} \rightarrow \hat{\mathbf{d}}) \approx \frac{(\bar{\gamma}/4)^{-\Gamma_{\mathbf{d}, \hat{\mathbf{d}}}}}{2 \prod_{i \in \mathcal{Q}_{\mathbf{d}, \hat{\mathbf{d}}}} \sigma_i}. \quad (19)$$

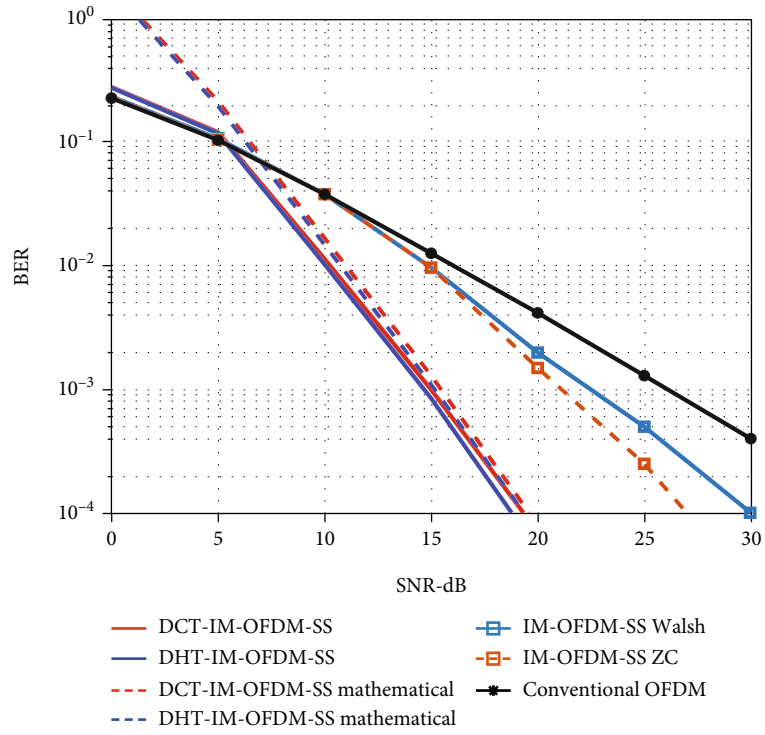


FIGURE 4: BER performance of the precoded IM-OFDM-SS with the Walsh code as $\mathbf{c}_{i(g)}$.

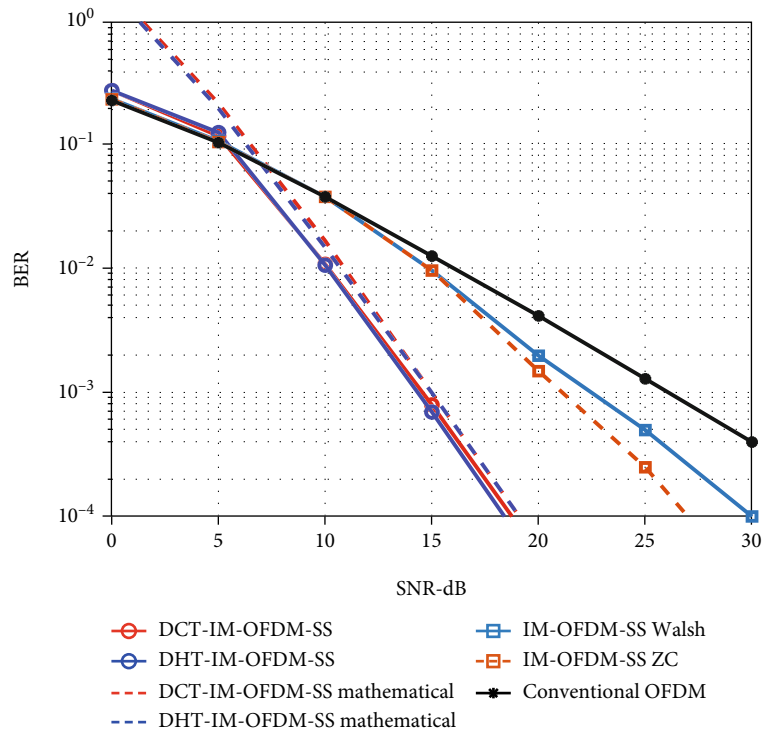
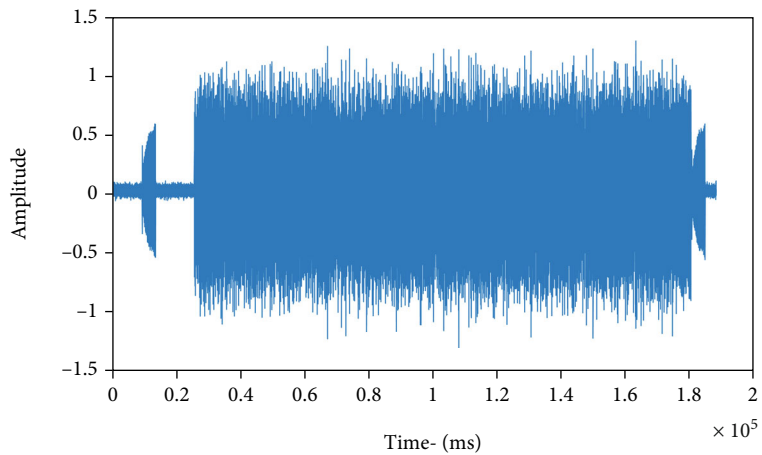


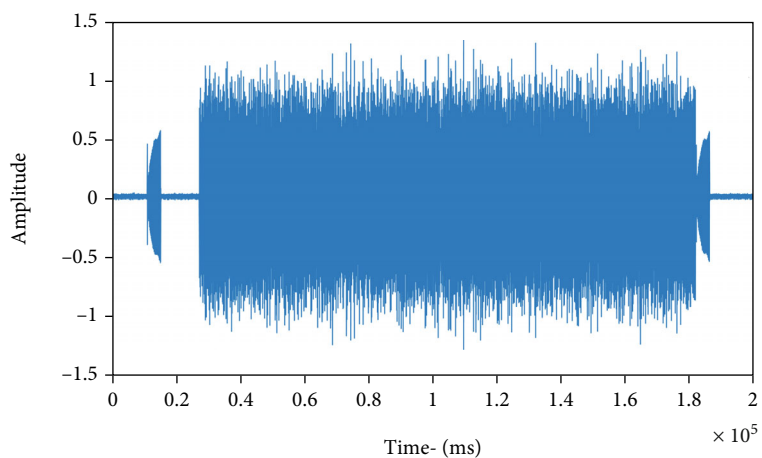
FIGURE 5: BER performance of the precoded IM-OFDM-SS with the ZC code as $\mathbf{c}_{i(g)}$.



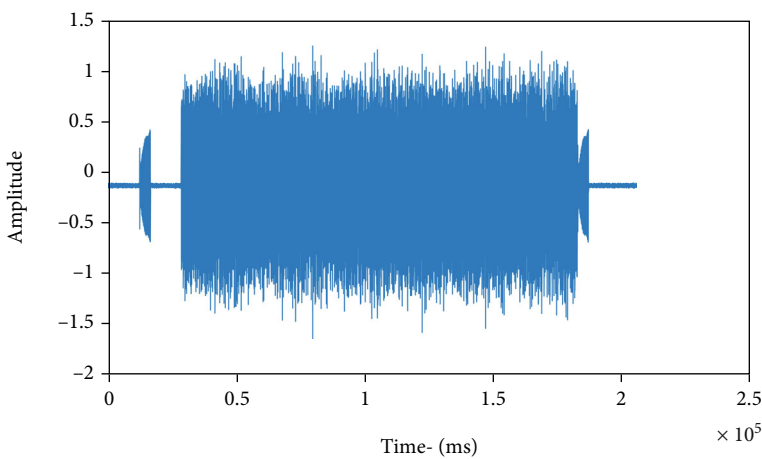
FIGURE 6: Packet structure.



(a)



(b)



(c)

FIGURE 7: Continued.

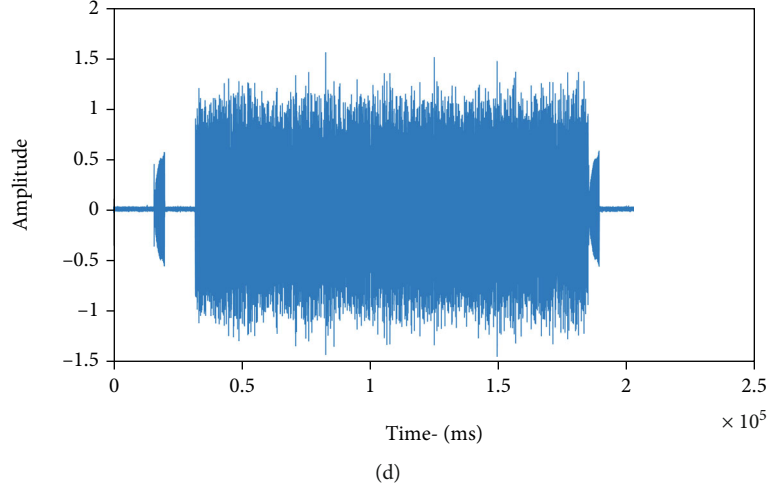


FIGURE 7: Received signal: (a) DCT-IM-OFDM-SS Walsh; (b) DCT-IM-OFDM-SS ZC; (c) DHT-IM-OFDM-SS Walsh; (d) DHT-IM-OFDM-SS ZC.

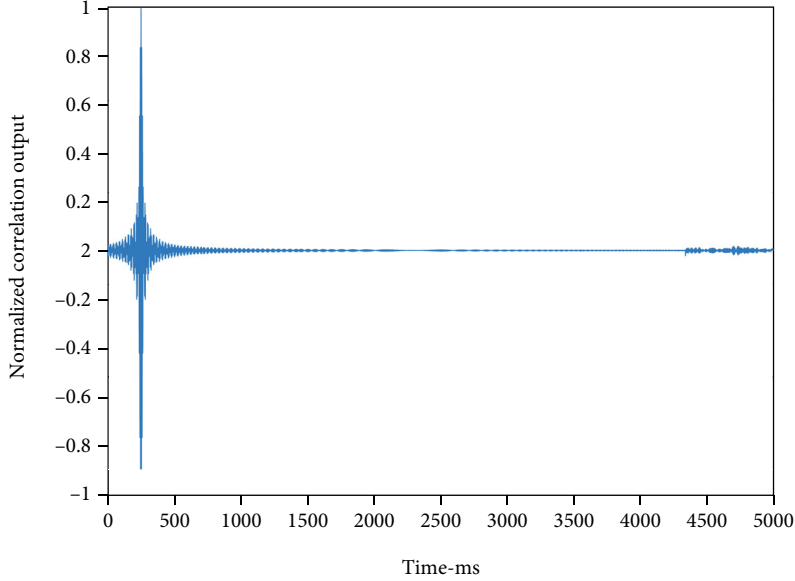


FIGURE 8: Estimated channel using the preamble correlation—pool experiments.

Therefore, the diversity and coding gains of the precoded IM-OFDM-SS are, respectively, given by

$$\mathcal{G}_e = \min_{\mathbf{d} \neq \hat{\mathbf{d}}} \Gamma_{\mathbf{d}, \hat{\mathbf{d}}}, \mathcal{G}_c = \min_{\mathbf{d} \neq \hat{\mathbf{d}}, \Gamma_{\mathbf{d}, \hat{\mathbf{d}}} = \mathcal{G}_e} \left(\prod_{i \in \mathcal{Q}_{\mathbf{d}, \hat{\mathbf{d}}}} \sigma_i \right)^{1/\mathcal{G}_e} \quad (20)$$

Finally, the upper bound BEP can be written based on $P(\mathbf{d} \rightarrow \hat{\mathbf{d}})$ evaluation using the union bound theory as follows:

$$P_b \leq \frac{1}{m^{nMG}} \sum_{\mathbf{d}} \sum_{\hat{\mathbf{d}}} \frac{\mathcal{U}(\mathbf{d}, \hat{\mathbf{d}}) (\bar{\gamma}/4)^{-\Gamma_{\mathbf{d}, \hat{\mathbf{d}}}}}{2 \prod_{i \in \mathcal{Q}_{\mathbf{d}, \hat{\mathbf{d}}}} \sigma_i} \quad (21)$$

Moreover, the use of IM-OFDM-SS instead of IM-OFDM offers additional diversity order since the data of each subcarrier is spread over many subcarriers. The formula of BER given by IM-OFDM-SS is calculated in [18].

4. Simulation and Experimental Results

The proposed precoded IM-OFDM-SS performance is evaluated in terms of BER and PAPR based on simulation and real experimental underwater channels.

4.1. Simulation Evaluation. For the simulation channel, the results are obtained over the 10^5 -symbol transmitter over a statistical underwater channel presented in [24]. The proposed precoded IM-OFDM-SS performances are compared with those of the conventional UWA-OFDM [21] and IM-

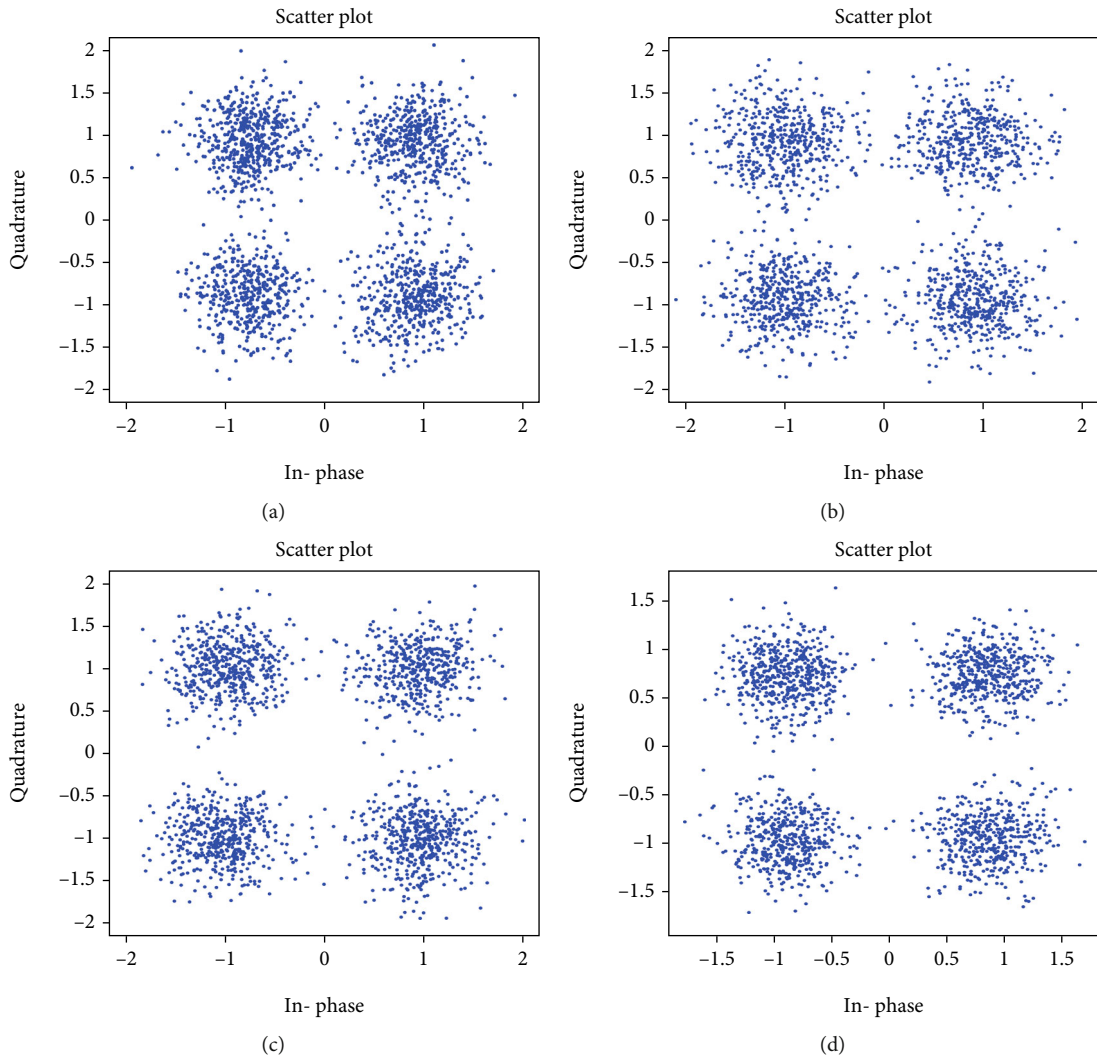


FIGURE 9: Constellation plot: (a) DCT-IM-OFDM-SS Walsh; (b) DCT-IM-OFDM-SS ZC; (c) DHT-IM-OFDM-SS Walsh; (d) DHT-IM-OFDM-SS ZC—pool experiments.

TABLE 1: Experimental pool results.

No.	OFDM	IM-OFDM-SS Walsh	IM-OFDM-SS ZC	Proposed DCT Walsh	Proposed DCT ZC	Proposed DHT Walsh	Proposed DHT ZC
1	0.018	0.020	0.020	0.0038	0.0031	0.0035	0.0031
2	0.0096	0.0072	0.0061	0.0021	0.0022	0.0021	0.0021
3	0.027	0.0041	0.0035	0.0035	0.0035	0.0030	0.0033
4	0.026	0.023	0.022	0.0091	0.009	0.0093	0.0088
5	0.0072	0.0061	0.0065	0.00054	0.00052	0.00053	0.00054
Average	0.0176	0.0121	0.0116	0.0038	0.0037	0.0037	0.0036

OFDM-SS [18]. In this simulation and without loss of generality, Walsh and ZC codes are used as spreading codes $c_{i(g)}$.

In simulation demonstration, each block contains $N = 1024$ with a guard interval of 256. For a fair comparison, all communication schemes have the same system data rate, $T = 0.25$ ms, and the bandwidth of 5 kHz; f_c and f_s are set to be 23 kHz and 122.8 kHz, respectively. To guarantee a similar transmitted rate for all communication schemes, the

binary phase-shift keying (BPSK) is used with the conventional OFDM and the quadrature amplitude modulation (QAM) is employed for the IM-OFDM-SS and precoded IM-OFDM-SS at $n = 4$. Both the transmitter and receiver are 10 m below the surface with a 0.2 km distance between them. The CFO = 0.02 and $\beta = 3e - 4$ are used. The RRC filter has been used at the transmitter and receiver with a roll-off of 0.55. Figure 3 shows the PAPR complementary cumulative

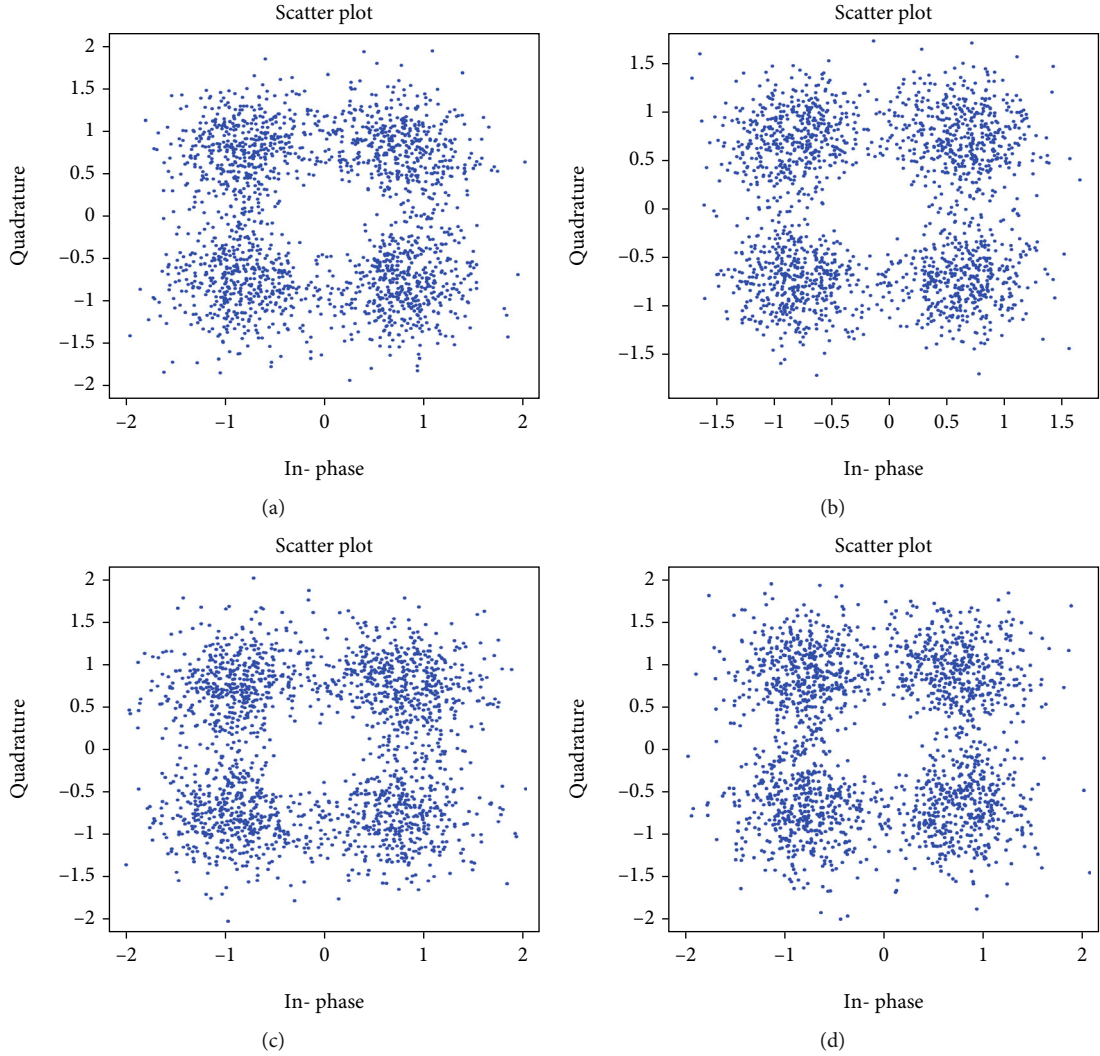


FIGURE 10: Constellation plot: (a) DCT-IM-OFDM-SS Walsh; (b) DCT-IM-OFDM-SS ZC; (c) DHT-IM-OFDM-SS Walsh; (d) DHT-IM-OFDM-SS ZC—shallow-water experiments.

TABLE 2: Experimental shallow water results.

No.	OFDM	IM-OFDM-SS Walsh	IM-OFDM-SS ZC	Proposed DCT Walsh	Proposed DCT ZC	Proposed DHT Walsh	Proposed DHT ZC
1	0.042	0.043	0.042	0.015	0.014	0.021	0.009
2	0.031	0.022	0.026	0.0083	0.0072	0.007	0.008
3	0.061	0.046	0.040	0.0091	0.0098	0.0084	0.0072
4	0.008	0.006	0.01	0.002	0.003	0.001	0.001
5	0.0096	0.0090	0.006	0.0079	0.0068	0.008	0.0085
Average	0.0303	0.0252	0.0248	0.0085	0.0082	0.0076	0.0067

distribution function (CCDF) performance. As shown, the IM-OFDM-SS when using $\mathbf{c}_{i(g)}$ Walsh or ZC is suffering from higher PAPR compared with the conventional OFDM, while the proposed schemes including both DCT-based precoding and DHT-based precoding offer about 1.5 dB and 3 dB superiority compared with the conventional schemes, respectively. The low PAPR of the precoded IM-OFDM-SS schemes is because the precoded schemes overcome the input informa-

tion symbol superposition which forms each OFDM sample. DHT-based precoding offers better PAPR than DCT-based precoding. This is because of the similarity of the IFFT and the DHT where some matrix kernels are canceling each one another leading to avoiding the superposition of the input data symbols due to the combined DHT-IFFT [11, 12, 20, 25]. Figures 4 and 5 show the BER performance of precoded schemes when using $\mathbf{c}_{i(g)}$ Walsh and ZC, respectively. The

proposed precoded IM-OFDM-SS in both cases offers more than 5~10 dB compared with IM-OFDM-SS and traditional UWA-OFDM. The BER improvement in the precoded IM-OFDM-SS is because of spreading symbol data vectors over all subcarriers enabling the recovery of highly attenuated symbols from the others which are well received. Both precoded IM-OFDM-SS using the Walsh code and ZC code achieve maximum diversity with slight superiority when using the ZC code due to the large Euclidean distance in ZC code vectors. Moreover, it is worth mentioning here that in low SNR, below 5 dB, there is a slightly small BER gain in the conventional scheme in comparison to the proposed scheme. This is because the power in the case of the proposed precoded system is spread over two transforms instead of a single transform in the case of a conventional scheme, making the system more susceptible to error in the case of extremely low SNR. However, this has no impact on the superiority of our proposed scheme in the practical scenarios as it achieves about 9 dB SNR gain at 10^{-4} BER in comparison to the conventional IM-OFDM-SS.

4.2. Pool Experimental Results. The proposed scheme's effectiveness is also evaluated over a UWA real channel. This experiment was carried out at Xiamen University, where a pool of size 18 m \times 5 m is used for transmitting a signal between one transmitting and one receiving hydrophone. The depth of the transmitter and the receiver is 1.2 m beneath the water's surface, and 7 m distance is separating them. The transmitted packet is shown in Figure 6, five packets with ten symbols in each frame have been transmitted with FFT size, guard interval, f_c , f_s , effective bandwidth, symbol duration, and data rate being set similar to parameters mentioned above in the case of the simulated channel Section 4.1. The used structure of the packet to be practically transmitted is shown in Figure 6 where two LFM segments are transmitted before and after the packet. Those two segments are used for synchronization and DSF estimation as explained in Section 2. A vector of zeros is inserted between the preamble and data vectors to prevent the inference while an optional zero vector can be inserted between the data vector and postamble too. The received data corresponding to $\mathbf{y}(\mathbf{t})$ in (6) is shown in Figure 7 including the DHT-based and DCT-based precoded IM-OFDM-SS for one frame based on $\mathbf{c}_{i(g)}$ of Walsh and ZC codes.

In practical real experiments, a cross-correlation between the received signal and the well-known preamble and postamble segments is first performed; the first resulted peak was used for synchronization while the difference between the first and the second peaks is utilized to evaluate the DSF as in (8). The output of cross-correlation is shown in Figure 8. After estimating and compensating the DSF, the signal shows the output of the correlator between the preamble and the received signal processed as explained in Section 2. Figure 9 shows the constellation of the received signal of the proposed precoded schemes after despreading the signal following (14). It is worth mentioning that IM-OFDM-SS is practically evaluated in this paper for underwater communication for the first time. Precoded IM-OFDM-SS offers better performance than conventional OFDM and

IM-OFDM-SS schemes in both cases of using the Walsh and ZC codes. The DHT-based precoded IM-OFDM-SS scheme slightly outperforms the DCT-based precoded IM-OFDM-SS scheme. In fact, under a perfect linear communication system that is completely free of nonlinear devices, all the aforementioned precoded systems should have the same diversity degree and ultimately the same BER performance. However, as the system is not perfectly linear, the DHT precoded IM-OFDM-SS has better BER performance than the other precoders as it has less PAPR as mentioned above, and consequently, the interference due to the performance of the nonlinear device is reduced. The proposed scheme is compared to the traditional UWA-OFDM in Table 1.

4.3. Shallow Water Experimental Results. The experiment took place in Xiamen, China, at the port of Xiamen. Five frames with ten symbols in each frame have been transmitted; the transmitter and receiver are separated by 106 meters, with depth of 5 meters beneath the sea surface. FFT size, guard interval, f_c , f_s , effective bandwidth, symbol duration, and data rate were set similar to the parameters mentioned above in Sections 4.1 and 4.2. The sea's channel is considered to be a harsh channel, so to guarantee communication reliability, conventional coding with the rate of 2/3 and interleaving are adopted. The received signal is processed similar to Section 4.2 where the constellation of the received signal after (14) is shown in Figure 10, and the experimental results are shown in Table 2. The performance of the proposed schemes confirms the effectiveness of the proposed schemes over the practical UWA channel.

5. Conclusion

This paper proposed a new scheme called precoded IM-OFDM-SS for UWA communication. The IM-OFDM-SS data symbols are spread over all other subcarriers; hence, the reliability of the UWA communication system can be improved. Thanks to the precoding and spreading scheme, the proposed IM-OFDM-SS increases the transmit diversity, domesticates the spreading and multipath diversities of the UWA channel, and reduces the PAPR. The performance of the proposed schemes has been evaluated over simulation and experimental results. The new scheme outperformed the conventional OFDM multicarrier modulation scheme currently used in the UWAC and the new conventional IM-OFDM-SS proposed for the next 5G mobile networks which are not previously practically evaluated over the UWA channel. Field measurements and simulation results clearly show how the proposed precoded IM-OFDM-SS is suitable for the UWAC.

Data Availability

The authors declare that the data used to support the findings of this study will be available from the corresponding author upon request.

Conflicts of Interest

The authors declare that they have no conflicts of interest.

Acknowledgments

This work is supported by the National Natural Science Foundation of China (61671394), the Fundamental Research Funds for the Central Universities (20720170044), and the Science and Technology Program of Shenzhen, China (JSGG20170414090428464).

References

- [1] M. E. Bayrakdar, "Cooperative communication based access technique for sensor networks," *International Journal of Electronics*, vol. 107, no. 2, pp. 212–225, 2020.
- [2] M. E. Bayrakdar, "A smart insect pest detection technique with qualified underground wireless sensor nodes for precision agriculture," *IEEE Sensors Journal*, vol. 19, no. 22, pp. 10892–10897, 2019.
- [3] M. Stojanovic, J. A. Catipovic, and J. G. Proakis, "Phase-coherent digital communications for underwater acoustic channels," *IEEE Journal of Oceanic Engineering*, vol. 19, no. 1, pp. 100–111, 1994.
- [4] E. Sozer, J. G. Proakis, and F. Blackmon, "Iterative equalization and decoding techniques for shallow water acoustic channels," in *MTS/IEEE Oceans 2001. An Ocean Odyssey. Conference Proceedings (IEEE Cat. No.01CH37295)*, vol. 4, pp. 2201–2208, Honolulu, HI, USA, December 2001.
- [5] Y. V. Zakharov and A. K. Morozov, "OFDM transmission without guard interval in fast-varying underwater acoustic channels," *IEEE Journal of Oceanic Engineering*, vol. 40, no. 1, pp. 144–158, 2015.
- [6] J. Li and Y. V. Zakharov, "Efficient use of space-time clustering for underwater acoustic communications," *IEEE Journal of Oceanic Engineering*, vol. 43, no. 1, pp. 173–183, 2017.
- [7] M. Stojanovic, "OFDM for underwater acoustic communications: adaptive synchronization and sparse channel estimation," in *2008 IEEE International Conference on Acoustics, Speech and Signal Processing*, vol. 1no. 6, pp. 5288–5291, Las Vegas, NV, USA, 2008.
- [8] B. Li, J. Huang, S. Zhou et al., "MIMO-OFDM for high-rate underwater acoustic communications," *IEEE Journal of Oceanic Engineering*, vol. 34, no. 4, pp. 634–644, 2009.
- [9] G. Rojo and M. Stojanovic, "Peak-to-average power ratio (PAR) reduction for acoustic OFDM systems," in *OCEANS 2009*, pp. 1–7, Biloxi, MS, USA, October 2009.
- [10] J. Tao, "DFT-precoded MIMO OFDM underwater acoustic communications," *IEEE Journal of Oceanic Engineering*, vol. 43, no. 3, pp. 805–819, 2017.
- [11] H. A. Leftah and S. Boussakta, "Efficient modulation scheme for OFDM system with ZP and MMSE equalizer," in *2013 IEEE International Conference on Communications (ICC)*, pp. 4703–4707, Budapest, Hungary, June 2013.
- [12] H. A. L. Al-Sodani, *New OFDM schemes based on orthogonal transforms for mobile communications systems*, Doctoral dissertation, Newcastle University, 2013.
- [13] H. A. Leftah and S. Boussakta, "Novel OFDM based on C-transform for improving multipath transmission," *IEEE Transactions on Signal Processing*, vol. 62, no. 23, pp. 6158–6170, 2014.
- [14] H. V. Poor, "Orthogonal frequency division multiplexing with index modulation," in *2012 IEEE Global Communications Conference (GLOBECOM)*, pp. 4741–4746, Anaheim, CA, USA, 2012.
- [15] E. Basar, "Index modulation techniques for 5G wireless networks," *IEEE Communications Magazine*, vol. 54, no. 7, pp. 168–175, 2016.
- [16] E. Basar, M. Wen, R. Mesleh, M. Di Renzo, Y. Xiao, and H. Haas, "Index modulation techniques for next-generation wireless networks," *IEEE Access*, vol. 5, pp. 16693–16746, 2017.
- [17] M. Wen, B. Zheng, K. J. Kim et al., "A survey on spatial modulation in emerging wireless systems: research progresses and applications," *IEEE Journal on Selected Areas in Communications*, vol. 37, no. 9, pp. 1949–1972, 2019.
- [18] Q. Li, M. Wen, E. Basar, and F. Chen, "Index modulated OFDM spread spectrum," *IEEE Transactions on Wireless Communications*, vol. 17, no. 4, pp. 2360–2374, 2018.
- [19] J. Choi, "Coded OFDM-IM with transmit diversity," *IEEE Transactions on Communications*, vol. 65, no. 7, pp. 3164–3171, 2017.
- [20] Z. A. Qasem, H. A. Leftah, H. Sun, J. Qi, and H. Esmail, "X-transform time-domain synchronous IM-OFDM-SS for underwater acoustic communication," *IEEE Systems Journal*, pp. 1–12, 2021.
- [21] B. Li, S. Zhou, M. Stojanovic, L. Freitag, and P. Willett, "Multi-carrier communication over underwater acoustic channels with nonuniform Doppler shifts," *IEEE Journal of Oceanic Engineering*, vol. 33, no. 2, pp. 198–209, 2008.
- [22] N. Lin, H. Sun, E. Cheng, J. Qi, X. Kuai, and J. Yan, "Prediction based sparse channel estimation for underwater acoustic OFDM," *Applied Acoustics*, vol. 96, pp. 94–100, 2015.
- [23] M. K. Simon and M.-S. Alouini, *Digital Communication over Fading Channels*, John Wiley & Sons, 2005.
- [24] P. Qarabaqi and M. Stojanovic, "Statistical characterization and computationally efficient modeling of a class of underwater acoustic communication channels," *IEEE Journal of Oceanic Engineering*, vol. 38, no. 4, pp. 701–717, 2013.
- [25] Z. A. Qasem, J. Wang, X. Kuai, H. Sun, and H. Esmail, "Enabling unique word OFDM for underwater acoustic communication," *IEEE Wireless Communications Letters*, vol. 10, no. 9, pp. 1886–1889, 2021.

Research Article

Time-Domain Channel Estimation Scheme for OFDM over Fast Fading Channels

Sami Asharjabi , Hefdhallah Sakran , and Azzam Al-nahari 

Department of Electrical Engineering, Faculty of Engineering, Ibb University, Ibb, Yemen

Correspondence should be addressed to Sami Asharjabi; sami.tarbosh@gmail.com

Received 5 January 2022; Accepted 5 February 2022; Published 27 February 2022

Academic Editor: Hamada Esmail

Copyright © 2022 Sami Asharjabi et al. This is an open access article distributed under the Creative Commons Attribution License, which permits unrestricted use, distribution, and reproduction in any medium, provided the original work is properly cited.

In high-mobility scenarios, the time variation of mobile radio channels leads to a loss of orthogonality among subcarriers in orthogonal frequency division multiplexing (OFDM) systems, resulting in intercarrier interference (ICI) and performance deterioration. Conventional channel estimation schemes are usually based on pilot tones, which are distributed in each OFDM symbol to estimate the channel variation. Hence, the channel estimator itself suffers from ICI. In this study, a new estimation scheme, which does not suffer from ICI, is proposed to estimate the channel variation within OFDM symbols. The main idea is to zero-pad (ZP) the OFDM symbol in the time domain. Then, in the middle of the ZP interval, an impulse signal is inserted as a pilot sample, which is used to estimate the channel at the pilot signal in the OFDM symbol. Finally, a linear model is used to estimate the channel variation over an OFDM symbol. Additionally, we derive the mean squared error (MSE) of the proposed estimation technique under the constraint that the channel varies linearly within OFDM symbols. Simulation results show that our scheme can achieve a substantial improvement in the bit error rate (BER) performance of OFDM, in spite of the OFDM symbol length being increased. Moreover, in many cases, the new scheme can achieve the same BER performance as the perfect knowledge of channel state information (CSI). Theoretical analysis and numerical simulations show that our scheme achieves excellent performance with much lower computational complexity.

1. Introduction

Due to the rapid deployment of high-speed vehicles, such as high-speed railway and low-altitude fly objects systems, during the past few years, wireless communication systems should be able to provide reliable service to the mobile devices in such high-mobility environment [1, 2]. Thus, high-mobility communications have become an integral part of the fifth generation (5G) of wireless systems standards, which first deployed in the year 2020 [3, 4]. The 5G communication systems are expected to support high speed up to 500 km/h and provide high data rate up to 150 Mb/s, simultaneously [5].

To achieve the 5G requirements, many technologies have been proposed, such as massive multiple-input multiple-output (MIMO) systems. Orthogonal frequency division multiplexing (OFDM) combined with massive MIMO is a promising technique for wideband massive MIMO

transmission [6]. OFDM is one of the most attractive modulation techniques due to its high spectral efficiency and its robustness against multipath delay. Recently, index modulation-OFDM-spread spectrum (IM-OFDM-SS) [7] and low-redundant energy UW-OFDM (LRE-UW-OFDM) [8] schemes have been proposed to improve the spectral and energy efficiencies, respectively, in OFDM systems. OFDM has been extensively used in wired and wireless application, digital audio/video broadcast (DAB/DVB), and many standards such as IEEE 802.16a and IEEE 802.11e [9, 10].

However, OFDM is vulnerable to the time variation of the channel, which is one of its main drawbacks. In high-mobility environments, the time variation of the channel destroys the orthogonality of the subcarriers severely, resulting in intercarrier interference (ICI) and performance degradation [11, 12]. Usually, the normalized maximum Doppler frequency, $\varepsilon = f_{d,\max} T_u$, is used to measure the time variation of the channel, where $f_{d,\max}$ is the maximum

Doppler spread, $T_u = 1/\Delta f$ is the useful OFDM symbol duration, and Δf is the subcarriers spacing.

2. Related Work

To estimate the channel variation over several OFDM symbols or within one OFDM symbol, different estimation techniques have been proposed. Most channel estimation techniques are based on pilots' (arrangement in OFDM) symbols [13, 14]. In fast time-varying channel environments, the channel variation during one OFDM symbol period exhibits high-order variation [15, 16]. Hence, the number of unknown channel coefficients to be estimated is very large. To reduce the number of estimated coefficients, various models have been developed to approximate the channel variation, such as a basis expansion model (BEM) [17, 18], a block-sparse Bayesian learning (BSBL) [19, 20], and a piecewise linear model (PLM) [21].

In this paper, a zero-padding (ZP) scheme is proposed to estimate the channel variation in OFDM systems, which can be summarized as follows. First, a cyclic prefixed OFDM symbol is zero-padded. After that, an impulse signal is inserted in the middle of these zeros, which is used in the receiver to estimate the channel at the pilot sample of each OFDM symbol. Lastly, a linear model is used to estimate the channel variation within the OFDM symbol period.

The remainder of this paper is organized as follows. First, the proposed model of an OFDM system is described briefly in Section 3. Then, the ICI due to time-varying channel is described in Section 4. The channel estimation is presented in Section 5. Simulation results are presented and discussed in Section 6. Finally, in Section 7, the conclusions of this paper are drawn.

Notations: superscripts $(\cdot)^{-1}$, $(\cdot)^H$, and $(\cdot)^T$ stand for inverse, conjugate transpose (Hermitian), and transpose operators, respectively. $[A]_P$, $\text{diag}(\cdot)$, $J_{M \times N}$, and I_Q denote a submatrix of A with row indices which correspond to the set P , a diagonal matrix is constructed from the vector-valued argument, an $M \times N$ is all-ones matrix, and $Q \times Q$ is identity matrix, respectively. $\|\cdot\|_F$ denotes the Frobenius matrix norm. The notation $\mathbb{C}^{M \times N}$ represents the set of $M \times N$ matrices in the complex field.

3. System Model

Figure 1 shows a discrete model of a baseband OFDM system with the proposed scheme (dashed line blocks). The OFDM system with the proposed scheme is different from conventional OFDM systems by adding and removing ZP blocks, after and before adding and removing a cyclic prefix (CP), respectively. After IDFT is performed, the i th time-domain OFDM signal can be expressed as

$$x_n^{(i)} = \frac{1}{\sqrt{N}} \sum_{k=0}^{N-1} X_k^{(i)} e^{j2\pi kn/N}, \quad 0 \leq n \leq N-1, \quad (1)$$

where N is the number of subcarriers and $X_k^{(i)}$ is the data symbol transmitted on the k th subcarrier.

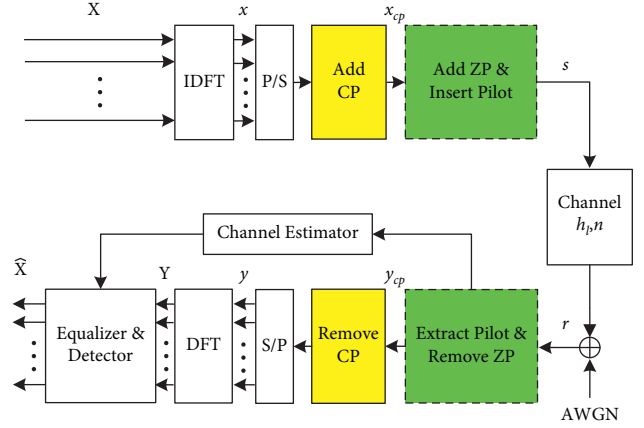


FIGURE 1: A baseband model of an OFDM system with the proposed scheme.

Let $\mathbf{x}_{cp}^{(i)} = [(\mathbf{x}_{N-N_g+1:N}^{(i)})^T \quad (\mathbf{x}^{(i)})^T]^T$ be the discrete time of i th OFDM symbol vector after adding the CP of length N_g , that is, longer than the maximum delay spread of the channel impulse responses (CIR), where $\mathbf{x}^{(i)} = [x_0^{(i)}, x_1^{(i)}, \dots, x_{N-1}^{(i)}]^T$. In our scheme, first, the cyclic prefixed symbol is extended by an interval (of zero samples) of total length $2N_g + 1$. Then, an impulse signal, $A\delta_{-(2N_g+1)}$, with amplitude A , is inserted in the middle of these zeros, which is served as a pilot. The guard interval on the left of the impulse signal is used for eliminating intersymbol interference (ISI) caused by multipath fading channels, whereas the guard interval on the right is used for channel estimation. Hence, the OFDM symbol with the time-domain pilot samples can be written as follows:

$$\mathbf{s}^{(i)} = \left[\underbrace{0, \dots, 0, A\delta_{N/2}, 0, \dots, 0}_{2N_g+1}, (\mathbf{x}_{cp}^{(i)})^T \right]^T, \quad (2)$$

where $\delta(\cdot)$ denotes the Kronecker delta function.

4. ICI Analysis

Assuming perfect synchronization of time, the received samples of the i th OFDM symbol, after transmitting over a time-varying multipath channel, can be expressed as (after discarding both ZP and CP samples)

$$y_n^{(i)} = \sum_{l=0}^{L-1} h_{l,n}^{(i)} x_{n-l}^{(i)} + w_n^{(i)}, \quad 0 \leq n \leq N-1, \quad (3)$$

where $h_{l,n}^{(i)}$ is the gain of l th time-domain channel path at the n th sample, L is the total number of propagation paths, and $w_n^{(i)}$ is the additive white Gaussian noise (AWGN). Let us define the DFT of $Y_k^{(i)}$ as

$$Y_k^{(i)} = \frac{1}{\sqrt{N}} \sum_{n=0}^{N-1} y_n^{(i)} e^{-j2\pi kn/N}, \quad 0 \leq k \leq N-1. \quad (4)$$

Substituting (3) into (4) and with some manipulations, the DFT of $y_n^{(i)}$ and $Y_k^{(i)}$ can be written as

$$Y_k^{(i)} = H_{k,k}^{(i)} X_k^{(i)} + \underbrace{\sum_{\substack{m=0 \\ m \neq k}}^{N-1} H_{k,m}^{(i)} X_m^{(i)}}_{ICI \text{ term}} + W_k^{(i)}, \quad 0 \leq k \leq N-1, \quad (5)$$

where

$$W_k^{(i)} = \frac{1}{\sqrt{N}} \sum_{n=0}^{N-1} w_n^{(i)} e^{-j2\pi kn/N}, \quad 0 \leq k \leq N-1, \quad (6)$$

$$H_{k,m}^{(i)} = \frac{1}{N} \sum_{n=0}^{N-1} \sum_{l=0}^{L-1} h_{n,l}^{(i)} e^{j2\pi n(m-k)/N} e^{j2\pi ml/N},$$

where $H_{k,m}^{(i)}$ is a channel coefficient, which represents the ICI interference, due to Doppler spread, from the m th subcarrier on k th subcarrier. Equation (5) can be written in the matrix form as follows:

$$\mathbf{Y}^{(i)} = \mathbf{H}^{(i)} \mathbf{X}^{(i)} + \mathbf{W}^{(i)}, \quad (7)$$

where $\mathbf{X}^{(i)} = [X_0^{(i)}, X_1^{(i)}, \dots, X_{N-1}^{(i)}]^T$, $\mathbf{Y}^{(i)} = [Y_0^{(i)}, Y_1^{(i)}, \dots, Y_{N-1}^{(i)}]^T$, $\mathbf{W}^{(i)} = [W_0^{(i)}, W_1^{(i)}, \dots, W_{N-1}^{(i)}]^T$, and $\mathbf{H}^{(i)}$ is the frequency-domain channel matrix, given by (for simplicity, the OFDM symbol index i is omitted)

$$\mathbf{H} = \begin{bmatrix} H_{0,0} & H_{0,1} & \dots & H_{0,N-1} \\ H_{1,0} & H_{1,1} & \dots & H_{1,N-1} \\ \vdots & \vdots & \ddots & \vdots \\ H_{N-1,0} & H_{N-1,1} & \dots & H_{N-1,N-1} \end{bmatrix}. \quad (8)$$

5. Channel Estimation

One should note that, in our proposed scheme, the received samples at $n_l = -2N_g - 1 + l$ ($0 \leq l \leq L-1$) comprise the CIR corresponding to the pilot sample in an OFDM symbol. Hence, the channel path's variation during one OFDM symbol can be estimated by using a linear model, as depicted in Figure 2.

Let $\mathbf{r}^{(i)}$ denote the i th received vector, where $\mathbf{r}^{(i)} = [r_{-(3N_g+1)}^{(i)}, r_{-3N_g}^{(i)}, \dots, r_{-1}^{(i)}, r_0^{(i)}, r_1^{(i)}, \dots, r_{N-1}^{(i)}]^T \in \mathbb{C}^{N_T \times 1}$, where $N_T = N + 3N_g + 1$.

The CIR through $\mathbf{r}^{(i)}$ can be extracted by using row selector matrix $\Psi = [\mathbf{I}_{N_T}]_{\mathcal{P}} \in \mathbb{C}^{L \times N_T}$, while $\mathcal{P} = \{n_0, n_1, \dots, n_{L-1}\}$ denotes the set of row indices corresponding to the time-domain pilot samples locations.

For symbol $\mathbf{r}^{(i)}$, the CIR can be written as

$$[\mathbf{r}^{(i)}]_{\mathcal{P}} = \Psi \mathbf{r}^{(i)}. \quad (9)$$

Then, the channel path gains at the pilot samples are obtained by using the conventional least-squares (LS) method. Let $\hat{h}_{l,n_l}^{(i)}$ and $\hat{h}_{l,n_l}^{(i+1)}$ denote, respectively, the LS estimated CIR corresponding to the pilot sample of the current $\mathbf{s}^{(i)}$ and the next $\mathbf{s}^{(i+1)}$ symbols of the l th path at n_l . Then, the time-domain variation of the l th path $\hat{\mathbf{h}}_l^{(i)} = [\hat{h}_{l,0}^{(i)}, \hat{h}_{l,1}^{(i)}, \dots, \hat{h}_{l,N-1}^{(i)}]^T$ in the current OFDM symbol can be estimated as follows:

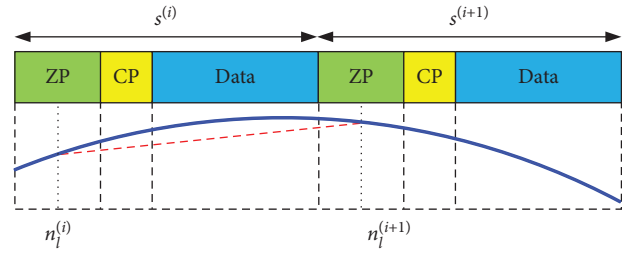


FIGURE 2: Channel approximation. Solid line: real or imaginary part of a channel path. Dashed line: linear model approximation of the channel path.

$$\hat{h}_{l,n}^{(i)} = \frac{(\hat{h}_{l,n_l}^{(i+1)} - \hat{h}_{l,n_l}^{(i)})(n - n_l^{(i)})}{N_T - 1} + \hat{h}_{l,n_l}^{(i)}, \quad (10)$$

where $n = 0, 1, \dots, N-1$, $i = 1, 2, \dots, l = 0, 1, \dots, L-1$, and $n_l < 0$.

After estimating the time-domain variation of all paths over an OFDM symbol period, the estimated channel matrix in time-domain ($\hat{\mathcal{H}}^*$) can be composed as follows (for simplicity, the OFDM symbol index i is omitted):

$$\hat{\mathcal{H}}^* = \begin{bmatrix} \hat{\mathbf{h}}_0 \\ \hat{\mathbf{h}}_1 \\ \vdots \\ \hat{\mathbf{h}}_{L-1} \end{bmatrix}^T = \begin{bmatrix} \hat{h}_{0,0} & \hat{h}_{0,1} & \dots & \hat{h}_{0,N-1} \\ \hat{h}_{1,0} & \hat{h}_{1,1} & \dots & \hat{h}_{1,N-1} \\ \vdots & \vdots & \ddots & \vdots \\ \hat{h}_{L-1,0} & \hat{h}_{L-1,1} & \dots & \hat{h}_{L-1,N-1} \end{bmatrix}, \quad (11)$$

where $\hat{\mathcal{H}}^* \in \mathbb{C}^{L \times N}$.

Combining (10) with (11), we can define the new linear interpolation model in a matrix form as

$$\hat{\mathcal{H}}^* = \frac{1}{N_T - 1} \text{diag}(\Psi[\mathbf{r}^{(i+1)} - \mathbf{r}^{(i)}])\mathbf{M} + \Psi \mathbf{r}^{(i)} \mathbf{J}_{1 \times N}, \quad (12)$$

in which

$$\mathbf{M} = \mathbf{J}_{L \times 1} \mathbf{V} - \mathbf{W} \mathbf{J}_{1 \times N} \in \mathbb{C}^{L \times N}, \quad (13)$$

where

$$\mathbf{V} = [0, 1, 2, \dots, N-1] \in \mathbb{C}^{1 \times N}$$

$$\mathbf{W} = [n_0, n_1, n_2, \dots, n_{L-1}]^T \in \mathbb{C}^{L \times 1}$$

In order to obtain the OFDM channel matrix, $\hat{\mathcal{H}}$, we rearrange the entries of $\hat{\mathcal{H}}^*$ as follows:

$$\hat{\mathcal{H}} = \begin{bmatrix} \hat{h}_{0,0} & 0 & \dots & 0 & \hat{h}_{L-1,0} & \dots & \hat{h}_{1,0} \\ \hat{h}_{1,1} & \hat{h}_{0,1} & 0 & \ddots & 0 & \ddots & \hat{h}_{2,0} \\ \vdots & \ddots & \ddots & \ddots & \ddots & \ddots & \vdots \\ \hat{h}_{L-1,L-1} & \vdots & \ddots & \ddots & \ddots & \ddots & 0 \\ 0 & \hat{h}_{L-1,L} & \ddots & \ddots & \ddots & \ddots & \vdots \\ \vdots & \ddots & \ddots & \ddots & \ddots & \ddots & 0 \\ 0 & \dots & 0 & \hat{h}_{L-1,N-1} & \dots & \hat{h}_{1,N-1} & \hat{h}_{0,N-1} \end{bmatrix}. \quad (14)$$

Finally, the received symbol, \mathbf{Y} , at the output of DFT is equalized (by multiplying the vector \mathbf{Y} by the inverse of estimated frequency-domain channel matrix $\hat{\mathbf{H}}$):

$$\hat{\mathbf{X}} = \hat{\mathbf{H}}^{-1} \mathbf{Y}, \quad (15)$$

in which

$$\hat{\mathbf{H}} = \mathbf{F} \hat{\mathcal{H}} \mathbf{F}^H, \quad (16)$$

where \mathbf{F}^H is the IDFT matrix.

5.1. Complexity and Noise Reduction (CNR) Criterion. In most cases, mobile communication channel has only a few dominant channel paths, compared to maximum delay spread (see Table 1 as an example). Hence, many samples of the CIR have little or no energy and comprise noise, removing these nondominant paths will reduce the estimator complexity, and it is expected to improve its performance. Therefore, to remove those nondominant paths and consequently reduce the noise effect, all paths are compared against a threshold.

The optimum threshold requires knowledge of the signal-to-noise ratio, which is not practically feasible for a very high Doppler scenario. Hence, we suggested a simple but effective method to remove most of those paths. The suggested threshold depends on the maximum absolute value of the CIR and also on its mean value as follows:

$$\text{Threshold} = \frac{\beta \mathbb{E} \left[\left| \hat{h}_{l,n_l}^{(i)} \right| \right]}{\max \left| \hat{h}_{l,n_l}^{(i)} \right|}, \quad 0 \leq \beta \leq 1, \quad 0 \leq l \leq L-1, \quad (17)$$

where the parameter β is used to set the threshold. If β is set to low, some noise components are treated as channel paths. On the contrary, if β is set high, some dominant channel paths are removed.

In our simulation in Section 6, we set $\beta = 0.50$, such that most of the dominant channel paths are preserved. Moreover, to reduce the probability of erroneously zeroing dominant channel paths, the final decision to set the current path to zero is based on both the current and next CIRs as follows:

$$\text{If both } \left| \hat{h}_{l,n_l}^{(i)} \right| \text{ and } \left| \hat{h}_{l,n_l}^{(i+1)} \right| \leq \text{Threshold} \implies \hat{h}_{l,n_l}^{(i)} = 0. \quad (18)$$

Therefore, by implementing the CNR criterion, instead of estimating numerous channel paths, only few dominant channel paths are estimated. Hence, the CNR criterion substantially reduces the computational complexity. Additionally, we expect better BER performance due to removing those noise perturbation paths.

5.2. Mean-Square Error Analysis. In this subsection, we derive an analytical expression for the mean-squared error (MSE) under some reasonable assumptions. In our scheme, the estimation errors come from linear interpolation and AWGN components in the received pilot samples. First, we assume the channel varies linearly within the OFDM symbol

TABLE 1: OFDM simulation parameters.

Parameters	Specifications
IFFT, FFT size (N)	1024
Subcarrier spacing (Δf)	10.94 kHz
Signal constellation	16 QAM, 64 QAM
Effective symbol duration (T_u)	91.40 μ s
Guard interval (T_g)	5.71 μ s
Sampling interval (T_s)	89.26 ns
Bandwidth	11.20 MHz
Number of OFDM symbols (I)	3000
Carrier frequency (f_c)	3 GHz

and is noiseless. Hence, in this case, the proposed scheme will estimate the channel perfectly without any error.

5.2.1. Noise-Free Case. Let the true value of the channel path at instant time n be $h_{l,n}^{(i)}$. Then, by using LS estimation, the estimated CIR at pilot samples for the l th path, $0 \leq l \leq L-1$, can be found as follows:

$$\hat{h}_{l,n_l}^{(i)} = \frac{A h_{l,n_l}^{(i)}}{A} = h_{l,n_l}^{(i)}, \quad (19)$$

$$\hat{h}_{l,n_l}^{(i+1)} = \frac{A h_{l,n_l}^{(i+1)}}{A} = h_{l,n_l}^{(i+1)}.$$

Substituting, $\hat{h}_{l,n_l}^{(i)}$ and $\hat{h}_{l,n_l}^{(i+1)}$ into (10), we have

$$\hat{h}_{l,n}^{(i)} = \frac{(h_{l,n_l}^{(i+1)} - h_{l,n_l}^{(i)})(n - n_l^{(i)})}{N_T - 1} + h_{l,n_l}^{(i)}, \quad 0 \leq n \leq N-1. \quad (20)$$

Equation (20) provides an error free estimate of the l th channel path.

5.2.2. Noise Case. In this case, we assume the channel varies linearly over an OFDM symbol and take into account the noise effect. Then, by using LS estimation, the estimated CIR at pilot samples can be found as follows:

$$\hat{h}_{l,n_l}^{(i)} = h_{l,n_l}^{(i)} + \frac{w_{l,n_l}^{(i)}}{A}, \quad (21)$$

$$\hat{h}_{l,n_l}^{(i+1)} = h_{l,n_l}^{(i+1)} + \frac{w_{l,n_l}^{(i+1)}}{A}.$$

Substituting $\hat{h}_{l,n_l}^{(i)}$ and $\hat{h}_{l,n_l}^{(i+1)}$ into (10) yields, after simple math manipulation,

$$\begin{aligned} \hat{h}_{l,n}^{(i)} &= \frac{(h_{l,n_l}^{(i+1)} - h_{l,n_l}^{(i)})(n - n_l^{(i)})}{N_T - 1} + h_{l,n_l}^{(i)} \\ &\quad + \frac{(w_{l,n_l}^{(i+1)} - w_{l,n_l}^{(i)})(n - n_l^{(i)})}{A(N_T - 1)} + \frac{w_{l,n_l}^{(i)}}{A}, \end{aligned} \quad 0 \leq n \leq N-1. \quad (22)$$

Considering (20), in the noise-free case, (22) can be rewritten in terms of $h_{l,n}^{(i)}$ as

$$\hat{h}_{l,n}^{(i)} = h_{l,n}^{(i)} + \frac{(w_{l,n_l}^{(i+1)} - w_{l,n_l}^{(i)})(n - n_l^{(i)})}{A(N_T - 1)} + \frac{w_{l,n_l}^{(i)}}{A}. \quad (23)$$

The MSE of the l th channel path during the i th OFDM symbol interval can be defined as

$$\text{MSE} = \mathbb{E} \left[\left| \hat{h}_{l,n}^{(i)} - h_{l,n}^{(i)} \right|^2 \right], \quad 0 \leq n \leq N - 1. \quad (24)$$

Substituting (23) into (24), after some manipulation, we have

$$\begin{aligned} \text{MSE} = & \mathbb{E} \left\{ \left[\frac{(w_{l,n_l}^{(i+1)})^2 - 2w_{l,n_l}^{(i+1)}w_{l,n_l}^{(i)} + (w_{l,n_l}^{(i)})^2}{A^2(N_T - 1)^2} \right] (n - n_l^{(i)})^2 \right\} \\ & + \mathbb{E} \left\{ \left[\frac{2w_{l,n_l}^{(i+1)}w_{l,n_l}^{(i)}}{A^2(N_T - 1)} - \frac{2(w_{l,n_l}^{(i)})^2}{A^2(N_T - 1)} \right] (n - n_l^{(i)}) \right\} \\ & + \mathbb{E} \left[\frac{(w_{l,n_l}^{(i)})^2}{A^2} \right]. \end{aligned} \quad (25)$$

Since the noise is modeled as complex AWGN with zero mean and unit variance, we can rewrite (25) as

$$\text{MSE} = \frac{\sigma_{w_{l,n_l}}^2}{A^2} \left\{ 2\mathbb{E} \left[\frac{(n - n_l^{(i)})^2}{(N_T - 1)^2} \right] - 2\mathbb{E} \left[\frac{n - n_l^{(i)}}{N_T - 1} \right] + 1 \right\}. \quad (26)$$

Then, we have the following approximations (derived in Appendixes A and B):

$$\begin{aligned} \mathbb{E} \left[\frac{(n - n_l^{(i)})^2}{(N_T - 1)^2} \right] & \approx \frac{1}{3}, \\ \mathbb{E} \left[\frac{n - n_l^{(i)}}{N_T - 1} \right] & \approx \frac{1}{2}. \end{aligned} \quad (27)$$

Thus, we have

$$\text{MSE} \approx \frac{2}{3A^2} \sigma_{w_{l,n_l}}^2. \quad (28)$$

Since the channel paths are statistically independent. Therefore, a general formula for the MSE of the proposed estimator with L channel paths can be written as follows:

$$\text{MSE} \approx \frac{2L}{3A^2} \sigma_w^2. \quad (29)$$

5.3. Complexity Comparison. Here, we briefly discuss the main complexity of the proposed estimator in terms of the required complex multiplications and additions/subtractions operations. In the proposed scheme, the channel path is obtained directly by extracting the CIR from the time-domain received signal. The complexity of our scheme mainly exists in the linear interpolation between CIRs.

According to (12) and (13), our analysis shows that the computational complexity of calculating M and $\hat{\mathcal{H}}^*$ are $\mathcal{O}(3L_{MDP}N)$ and $\mathcal{O}(L_{MDP}^2N + 3L_{MDP}N + N_T + L_{MDP}N_T) \approx \mathcal{O}(L_{MDP}^2N + 4L_{MDP}N)$, respectively. Therefore, the overall complexity of the proposed scheme is approximately equal to $\mathcal{O}(L_{MDP}^2N + 7L_{MDP}N)$, where L_{MDP} is the number of most dominant channel paths ($L_{MDP} \ll N_g$).

On the contrary, the complexity of the BSBL scheme, which is used for comparison, is given by $\mathcal{O}(Q^3L^2N_{iter} + Q^3N_g^3N_{iter})$ [19]. In addition to the direct complexity of BSBL scheme, the number of required iterations (N_{iter}) for convergence is another issue for complexity analysis. Furthermore, simulations (Section 6) show that the BSBL scheme can work with a significant large N_{iter} . However, the complexity of the BSBL estimator is usually too high for practical use.

Finally, both schemes need a matrix inversion to perform the equalization in the frequency domain, in which computational complexity is high, especially for large OFDM symbol sizes (N). It should be emphasized here that our scheme achieves better performance while providing dramatically lower complexity.

6. Simulation Results

To investigate the performance of our estimator, a comparison is made between the BER performance of OFDM with our scheme and BSBL scheme [19], which uses the pilot subcarriers to estimate the time-domain channel matrix. Additionally, a BER performance of OFDM with perfect channel state information (CSI) is considered. Furthermore, the performance of channel estimators is evaluated by using the normalized mean square error (NMSE), which is defined as

$$\text{NMSE} = \frac{1}{I} \sum_{i=1}^I \frac{\|\hat{\mathbf{H}}^{(i)} - \mathbf{H}^{(i)}\|_F^2}{\|\mathbf{H}^{(i)}\|_F^2}, \quad (30)$$

where I is the number of the channel realizations and $\hat{\mathbf{H}}^{(i)}$ is the estimated channel matrix of $\mathbf{H}^{(i)}$ at the i th realization.

In the simulation, an uncoded OFDM system with 16-quadrature amplitude modulation (QAM) is considered. Moreover, the new scheme is also tested with the higher-order modulation constellations of 64-QAM. The relevant OFDM system parameters are given in Table 1.

To verify the performance of the proposed scheme, two different channel models are considered. The power-delay profile (PDP) of channel #1 is the COST 207 typical urban six-path (TU6) model which is given in Table 2. However, the PDP of channel #2 has two paths with power profile [0.64 0.34], which are separated by 5.7 μ s. In addition, each channel path weight is simulated based on Jakes' Rayleigh model [22]. Also, two maximum normalized Doppler spreads of $\varepsilon = 0.02$ and 0.07 are considered, corresponding to a mobile terminal moving at maximum speeds of 78 and 276 km/h, respectively. Moreover, based on the simulation results, the amplitude of the pilot signal is set equal to 10, which gives the best results for our scheme. Furthermore, in

TABLE 2: Power-delay profile of channel #1.

Path index	1	2	3	4	5	6
Delay (μ s)	0.0	0.2	0.5	1.6	2.3	5.0
Average power (dB)	-3	0	-2	-6	-8	-10

the new scheme, the OFDM is zero-padded by $2N_g + 1$ samples; thus, the spectral efficiency is reduced. Hence, for fair comparison, 47 equally spaced subcarriers are allocated for pilot subcarriers in the BSBL scheme. Therefore, both schemes have approximately the same spectral efficiency. Moreover, the same transmitted power is used for both schemes.

Figure 3 shows a comparison of the analytical and simulation results of MSE for the proposed scheme. At high E_b/N_0 s (>20 dB), excellent agreement between the analytical and simulation results is observed. However, at low E_b/N_0 s (<20 dB), the difference between the analytical and simulation results decreases with increasing E_b/N_0 s. This can be explained as follows; according to (29), the MSE is directly proportional to the number of paths. At high E_b/N_0 s, the noise power is low. Hence, the CNR criterion removes most of the nondominant paths (noise perturbation paths), so the number of estimated paths is approximately equal to the actual number of channel paths. Hence, there is great agreement between the theoretical and simulation MSE.

On the contrary, at low E_b/N_0 s, the noise power is high. Hence, the CNR criterion removes few nondominant paths, so the number of estimated channel paths is very large compared with the actual channel paths. Hence, theoretical and simulation MSE results are not identical.

Figure 4 shows BER vs. E_b/N_0 for 16QAM-OFDM with the proposed and BSBL schemes over channel #1, for different values of normalized Doppler frequency ($\epsilon = 0.02$ and $\epsilon = 0.07$). In case of $\epsilon = 0.01$, at low E_b/N_0 s (<25 dB), it is clear that our scheme consistently outperforms BSBL scheme whereas, at high E_b/N_0 s (>25 dB), our scheme significantly outperforms the BSBL scheme. This is due to the fact that, at low E_b/N_0 s, the noise significantly affects the amplitude of the pilot sample, which severely degrades the performance of the proposed scheme. Furthermore, in case of $\epsilon = 0.07$, one can observe that our scheme effectively reduces the error floor. Moreover, in both cases, $\epsilon = 0.02$ and $\epsilon = 0.07$, the performance of the proposed scheme is very close to the performance of CSI. Also, one can observe, in case of $\epsilon = 0.02$, our scheme has a slight performance gain over CSI. This is not a surprising result, since LS estimate yields some noise reduction.

Figure 5 shows a BER performance comparison for 64-QAM-OFDM, over channel #1. In case $\epsilon = 0.07$, one can observe that, at low E_b/N_0 (<10 dB), the proposed scheme can only achieve a slight improvement in BER performance over the BSBL scheme. However, at high E_b/N_0 s, our scheme can achieve impressive BER performance compared with BSBL scheme, particularly, when E_b/N_0 s >20 dB.

Additionally, from Figure 5, in case of $\epsilon = 0.02$, the performance of our scheme shows a very good agreement

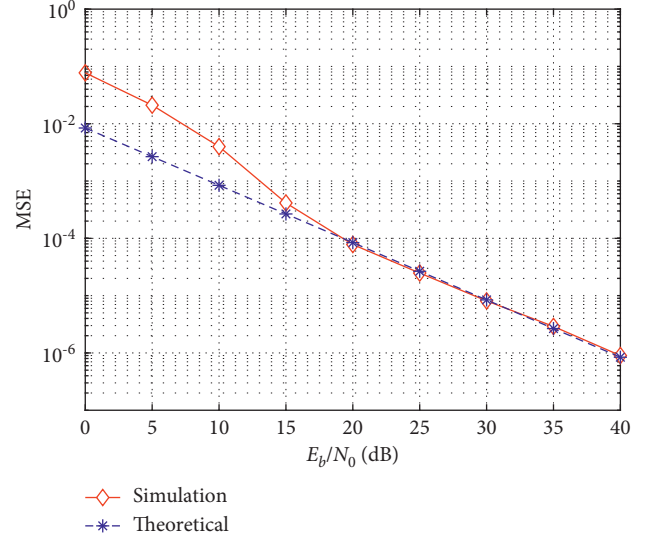


FIGURE 3: The MSE of the proposed estimator for 16QAM-OFDM over channel #1, with vehicle moving at 40 km/h.

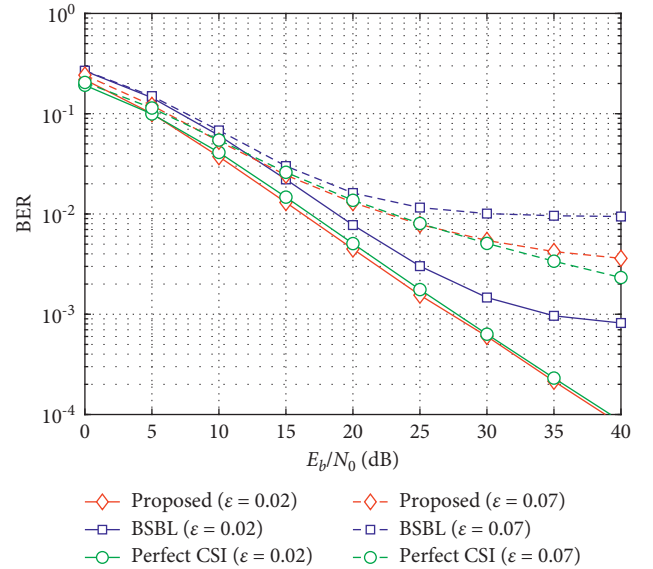


FIGURE 4: BER performance comparison among different channel estimators for 16QAM-OFDM over channel #1.

with the CSI. However, in case of $\epsilon = 0.07$, the proposed scheme and CSI have different performance when E_b/N_0 s >30 dB. A clear improvement in BER performance of the proposed scheme can be observed compared with the BSBL scheme. More specifically, the effect of ICI resulting in an error floor is significantly decreased. This can be explained by the fact that, in pilot subcarrier-based estimator (for example, BSBL scheme), the pilot itself suffers from ICI. Consequently, the channel estimator accuracy degrades as ICI increases. However, in pilot sample-based estimator (for example, the proposed scheme), the pilot is affected only by AWGN. Also, one can see from Figure 5, in case of $\epsilon = 0.02$, that the proposed scheme consistently outperforms BSBL scheme, and it can achieve a BER of 1.1×10^{-3} at

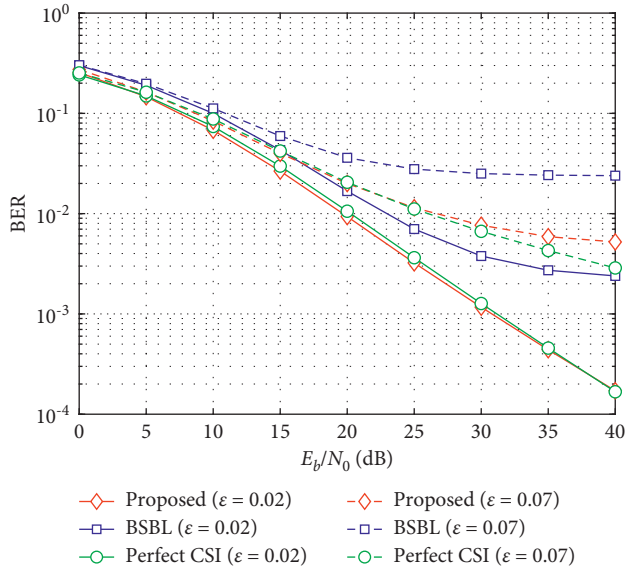


FIGURE 5: BER performance comparison among different channel estimators for 64-QAM-OFDM over channel #1.

$E_b/N_0 = 30$ dB. At a BER of 2×10^{-3} , our estimator outperforms the BSBL scheme by about 3 dB.

A BER performance comparison for 16QAM-OFDM with the proposed and BSBL schemes over channel #2 is shown in Figure 6. In case $\epsilon = 0.02$, one can observe that our scheme outperforms the BSBL scheme. However, $\epsilon = 0.07$, and our scheme significantly outperforms the BSBL scheme, particularly, at high E_b/N_0 s. This can be explained by noting that the channel has only two dominant paths, so the proposed scheme with CNR criterion removes many noise perturbation paths, which results in significant noise reduction. As a consequence, substantial performance improvement is compared with Figure 4. On the contrary, the BSBL scheme shows slight performance improvement compared with Figure 4.

Figure 7 illustrates a BER performance comparison as a function of $\epsilon\%$ for 16QAM-OFDM. In these comparisons, channel #1 is used and E_b/N_0 is set to 30 dB. In the same figure, one can see that the proposed scheme significantly outperforms the BSBL scheme in BER performance, particularly, when $\epsilon < 10\%$. Moreover, the BER performance of our estimator is very close to that with perfect channel knowledge, when $\epsilon < 7\%$. However, when $\epsilon > 7\%$, the gap between our estimator and CSI gradually increases with respect to ϵ . This can be explained that the channel variation within OFDM symbols is no longer linear, whereas the proposed scheme uses a linear model to approximate the channel variation.

Figure 8 shows NMSE comparison of the estimated frequency-domain channel for 16QAM-OFDM with the proposed and BSBL schemes over channel #1. When $\epsilon = 0.02$, our scheme estimates the channel perfectly; however, when $\epsilon = 0.07$, the proposed scheme fails to track channel variations within OFDM symbols, which is not surprising, since, in this case, the channel variation no longer linear. Hence, the linear approximation becomes ineffective,

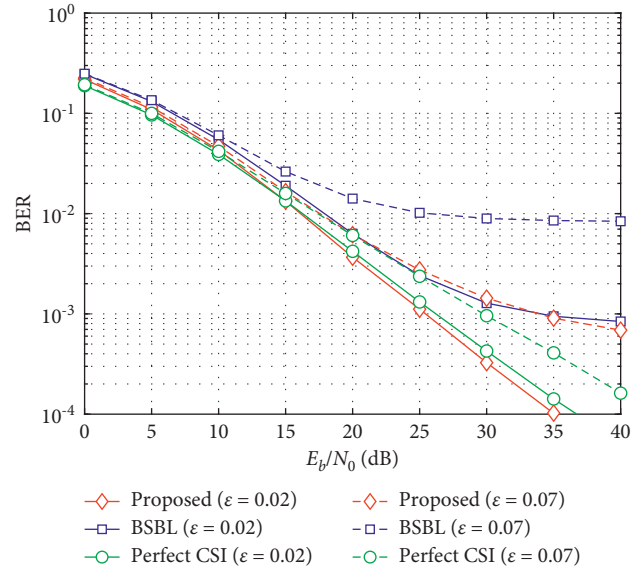


FIGURE 6: BER performance comparison among different channel estimators for 16QAM-OFDM over channel #2.

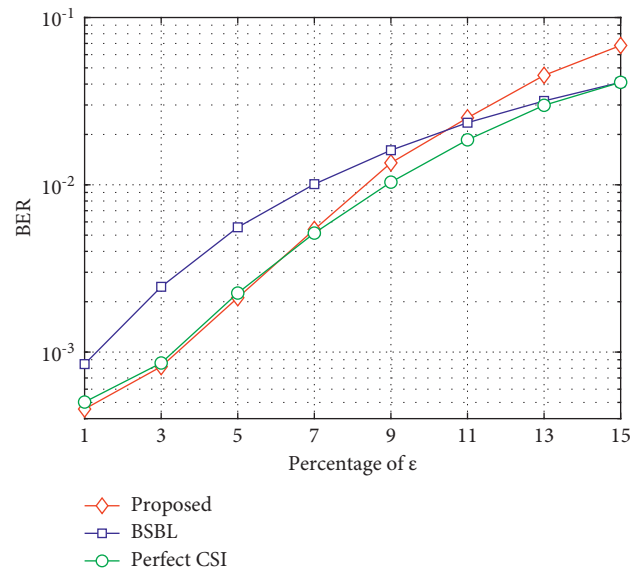


FIGURE 7: BER performance comparison as a function of ϵ among different channel estimators for 16QAM-OFDM over channel #1, with $E_b/N_0 = 30$ dB.

in this case, and leads to an error floor which cannot be overcome by increasing E_b/N_0 .

Figure 9 illustrates the BER performance for 16QAM-OFDM with the two estimation schemes versus E_b/N_0 and the maximum velocity over channel #1. It can be seen that the rate of the BER scheme increases as velocity increases for fixed values of E_b/N_0 . Also, in Figure 9, one can see that the proposed scheme can significantly improve the BER performance as compared to the BSBL scheme in the high E_b/N_0 and low-speed regions, especially when $E_b/N_0 > 20$ dB and the velocity < 400 km/h. However, in the

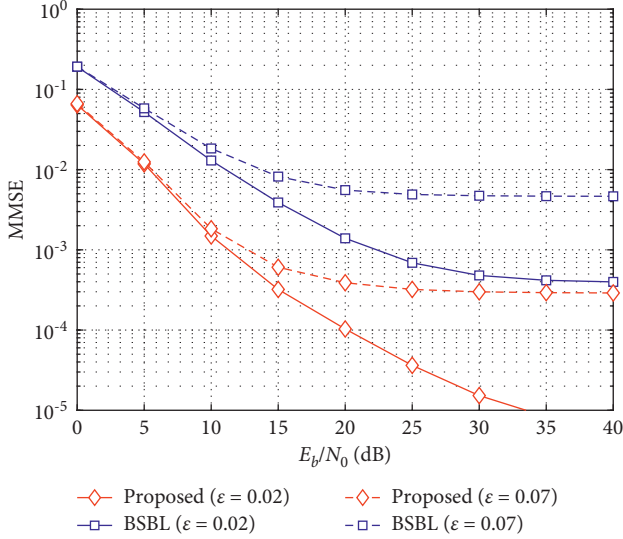


FIGURE 8: Mean square channel estimation error between the proposed and BSBL for 16QAM-OFDM over channel #1.

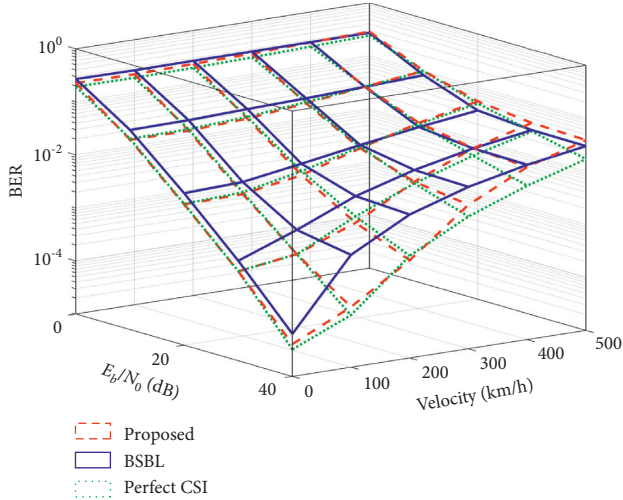


FIGURE 9: BER performance comparison among different channel estimators for 16QAM-OFDM over channel #1, at different speeds.

high-speed regions, both schemes suffer large estimation errors, which are due to the fact that, in high mobility, the channel paths show high-order time variation, whereas pilot subcarriers strongly suffer from ICI.

7. Conclusions

In this paper, a new scheme, which is mainly based on a sample pilot with ZP in the time domain, is proposed to estimate the channel variation over an OFDM symbol period. Simulation results of MSE, showing excellent agreement with theoretical analysis, confirm the validity of our MSE analysis. Also, simulation results demonstrate that the proposed scheme can greatly improve the BER performance of the OFDM system as compared with the BSBL scheme, in particular, at high E_b/N_0 s. Additionally, results show that

the error floor resulting from the effect of ICI is significantly decreased by implementing the new scheme. Furthermore, the BER performance of our scheme can nearly achieve the performance as good as the perfect knowledge of channel state information when $\epsilon < 0.02$. It is expected that our estimator will achieve best results when both the OFDM symbol duration and the channel delay spread are small, since, in this case, the separation between any two adjacent pilot signals is minimal. The complexity of the new estimator is significantly lower than BSBL, while showing a better performance.

Appendix

A. Analysis of the First Term in (20)

$$\mathbb{E} \left[\left(n - n_l^{(i)} \right)^2 \right] = \frac{1}{N} \sum_{n=0}^{N-1} \left(n - n_l^{(i)} \right)^2,$$

$$\mathbb{E} \left[\left(n - n_l^{(i)} \right)^2 \right] = \frac{2N^2 - 3N + 1 - 6n_l^{(i)}N + 6n_l^{(i)^2} + 6n_l^{(i)}}{6}. \quad (\text{A.1})$$

Then, we have the approximation:

$$\mathbb{E} \left[\left(n - n_l^{(i)} \right)^2 \right] \approx \frac{2N^2 - 6n_l^{(i)}N + 6n_l^{(i)^2}}{6}, \quad (\text{A.2})$$

$$\mathbb{E} \left[\frac{\left(n - n_l^{(i)} \right)^2}{(N_T - 1)^2} \right] \approx \frac{2N^2 - 6n_l^{(i)}N + 6n_l^{(i)^2}}{6(N_T - 1)^2}.$$

For large symbol duration and small delay spread, we obtain the approximation:

$$\mathbb{E} \left[\frac{\left(n - n_l^{(i)} \right)^2}{(N_T - 1)^2} \right] \approx \frac{1}{3}. \quad (\text{A.3})$$

B. Analysis of the Second Term in (20)

$$\mathbb{E} \left[n - n_l^{(i)} \right] = \frac{1}{N} \sum_{n=0}^{N-1} \left(n - n_l^{(i)} \right), \quad (\text{B.1})$$

$$\mathbb{E} \left[\frac{n - n_l^{(i)}}{N_T - 1} \right] = \frac{N - 2n_l^{(i)} - 1}{2(N_T - 1)}.$$

For large symbol duration and small delay spread, we have the approximation:

$$\mathbb{E} \left[\frac{n - n_l^{(i)}}{N_T - 1} \right] \approx \frac{1}{2}. \quad (\text{B.2})$$

Data Availability

No data were used to support this study.

Conflicts of Interest

The authors declare that they have no conflicts of interest.

References

- [1] Z. Sheng, H. D. Tuan, H. H. Nguyen, and Y. Fang, "Pilot optimization for estimation of high-mobility OFDM channels," *IEEE Transactions on Vehicular Technology*, vol. 66, no. 10, pp. 8795–8806, 2017.
- [2] Y. P. Wibawa, Iskandar, and I. Zakia, "Filtered-OFDM for high-speed railway communications," in *Proceedings of the 2020 6th International Conference on Wireless and Telematics (ICWT' 2020)*, pp. 1–5, Yogyakarta, Indonesia, September 2020.
- [3] G. Noh, B. Hui, and I. Kim, "High speed train communications in 5G: design elements to mitigate the impact of very high mobility," *IEEE Wireless Communications*, vol. 27, no. 6, pp. 98–106, 2020.
- [4] Z. Ma, Z. Zhang, Z. Ding, P. Fan, and H. Li, "Key techniques for 5G wireless communications: network architecture, physical layer, and MAC layer perspectives," *Science China Information Sciences*, vol. 58, no. 4, pp. 1–20, 2015.
- [5] T. Nakamura, "Requirements for further advancements for evolved universal terrestrial radio access (E-UTRA) (LTE-advanced) (release 14)," *Techrep Marketing*, vol. 36, p. 913, 2014.
- [6] X. Ma, F. Yang, S. Liu, J. Song, and Z. Han, "Sparse channel estimation for MIMO-OFDM systems in high-mobility situations," *IEEE Transactions on Vehicular Technology*, vol. 67, no. 7, pp. 6113–6124, J2018.
- [7] Z. A. H. Qasem, H. A. Leftah, H. Sun, J. Qi, and H. Esmail, "X-transform time-domain synchronous IM-OFDM-SS for underwater acoustic communication," *IEEE Systems Journal*, pp. 1–12, 2021.
- [8] Z. A. H. Qasem, J. Wang, X. Kuai, H. Sun, and H. Esmail, "Enabling unique word OFDM for underwater acoustic communication," *IEEE Wireless Communications Letters*, vol. 10, no. 9, pp. 1886–1889, 2021.
- [9] H. Senol, "Joint channel estimation and symbol detection for OFDM systems in rapidly time-varying sparse multipath channels," *Wireless Personal Communications*, vol. 82, no. 3, pp. 1161–1178, 2015.
- [10] L. Liang Zhang, Z. Zhihong Hong, L. Thibault, R. Boudreau, and Y. Yiyuan Wu, "A low-complexity robust OFDM receiver for fast fading channels," *IEEE Transactions on Broadcasting*, vol. 60, no. 2, pp. 347–357, 2014.
- [11] Y. Peng, W. Wang, and Y. il Kim, "Performance analysis of OFDM system over time-selective fading channels," in *Proceedings of the 2009 IEEE Wireless Communications and Networking Conference (WCNC' 2009)*, pp. 1–5, Budapest, Hungary, April 2009.
- [12] H.-C. Wu, "Analysis and characterization of intercarrier and interblock interferences for wireless mobile OFDM systems," *IEEE Transactions on Broadcasting*, vol. 52, no. 2, pp. 203–210, J2006.
- [13] Q. Tang, H. Long, H. Yang, and Y. Li, "An enhanced LMMSE channel estimation under high speed railway scenarios," in *Proceedings of the 2017 IEEE International Conference on Communications Workshops (ICC Workshops)*, pp. 999–1004, Paris, France, May 2017.
- [14] M. Almoneer, C. Rohde, K. Hassan, and W. H. Gerstacker, "Intercarrier interference-aware pilot-aided channel estimation in OFDM systems," *IEEE Transactions on Broadcasting*, vol. 63, no. 3, pp. 449–462, 2017.
- [15] P. Chen and H. Kobayashi, "Maximum likelihood channel estimation and signal detection for OFDM systems," in *Proceedings of the 2002 IEEE International Conference on Communications*, vol. 3, pp. 1640–1645, New York, NY, USA, April 2002.
- [16] Y.-H. Yeh and S.-G. Chen, "Reduction of Doppler-induced ICI by interference prediction," in *Proceedings of the 2004 IEEE 15th International Symposium on Personal, Indoor and Mobile Radio Communications (IEEE Cat. No.04TH8754)*, vol. 1, pp. 653–657, Helsinki, Finland, September 2004.
- [17] A. Baouni and A. Farrouki, "Channel estimation using a reduced rate of pilot subcarriers for OFDM systems over doubly-selective channels," *IET Communications*, vol. 12, no. 14, pp. 1714–1721, 2018.
- [18] A. N. Uwaechia and N. M. Mahyuddin, "Spectrum-efficient distributed compressed sensing based channel estimation for OFDM systems over doubly selective channels," *IEEE Access*, vol. 7, pp. 35 072–135 088, 2019.
- [19] X. Wang, J. Wang, L. He, and J. Song, "Doubly selective underwater acoustic channel estimation with basis expansion model," in *Proceedings of the 2017 IEEE International Conference on Communications (ICC' 2017)*, pp. 1–6, Paris, France, May 2017.
- [20] O. Barbu, C. Navarro Manchón, C. Rom, T. Balercia, and B. H. Fleury, "OFDM receiver for fast time-varying channels using block-sparse bayesian learning," *IEEE Transactions on Vehicular Technology*, vol. 65, no. 12, pp. 10 053–10 057, 2016.
- [21] S. S. Tarbosh, T. A. Rahman, and N. Seman, "General pilot-aided scheme for OFDM reception in fast varying channels," in *Proceedings of the 2012 International Conference on Computer and Communication Engineering (ICCCCE)*, pp. 932–935, Kuala Lumpur, Malaysia, July 2012.
- [22] M. F. Pop and N. C. Beaulieu, "Limitations of sum-of-sinusoids fading channel simulators," *IEEE Transactions on Communications*, vol. 49, no. 4, pp. 699–708, 2001.

Research Article

Reinforcement Learning for Distributed Energy Efficiency Optimization in Underwater Acoustic Communication Networks

Liejun Yang,¹ Hui Wang ,² Yexian Fan,¹ Fang Luo,¹ and Wei Feng¹

¹College of Information and Mechanical & Electrical Engineering, Ningde Normal University, Ningde 352000, China

²College of Physics and Information Engineering, Minnan Normal University, Zhangzhou 363000, China

Correspondence should be addressed to Hui Wang; wangh0802@163.com

Received 9 December 2021; Revised 28 January 2022; Accepted 31 January 2022; Published 24 February 2022

Academic Editor: Xuebo Zhang

Copyright © 2022 Liejun Yang et al. This is an open access article distributed under the Creative Commons Attribution License, which permits unrestricted use, distribution, and reproduction in any medium, provided the original work is properly cited.

To solve the problems of poor quality of service and low energy efficiency of nodes in underwater multinode communication networks, a distributed power allocation algorithm based on reinforcement learning is proposed. The transmitter with reinforcement learning capability can select the power level autonomously to achieve the goal of getting higher user experience quality with lower power consumption. Firstly, we propose a distributed power optimization model based on the Markov decision process. Secondly, we further give a reward function suitable for multiobjective optimization. Finally, we present a distributed power allocation algorithm based on Q-learning and use it as an adaptive mechanism to enable each transmitter in the network to adjust the transmit power according to its own environment. The simulation results show that the proposed algorithm not only increases the total channel capacity of the system but also improves the energy efficiency of each transmitter.

1. Introduction

Marine information technology not only plays an important role in the fields of marine environment monitoring, exploration and resource development, marine disaster warning, and underwater target location tracking but also is a hot direction for information science research [1, 2]. The primary problem to be solved in the development of marine information technology is the construction of underwater sensor networks and the allocation of resources for network communication; otherwise, marine information technology is not possible [3–5]. With the increasing exploitation of underwater resources, the variety and number of communication nodes deployed underwater are becoming more and more abundant, and there will even be multiple types of underwater communication networks deployed in the same sea area. For example, in Ref. [6], a two-dimensional underwater sensing network structure was developed in which the sensor nodes were anchored to the seafloor. This means that the sensors can only detect a range of data on the seafloor. However, many other important 3D data, such as the flow rate and salinity of seawater, which are crucial for

one to study the characteristics of the marine environment, are not detectable. Correspondingly, this paper proposes an autonomous underwater vehicle (AUV) to monitor and collect important 3D data, and uses different types of sensors to detect a range of data on the seafloor.

Unlike wireless electromagnetic wave communication networks, most acoustic modems in underwater acoustic communication networks (UACNs) are battery-powered, but in an underwater environment, battery replacement and charging are extremely difficult [7]. Meanwhile, there are many types of nodes deployed in UACNs, including multiple types of nodes such as master nodes, sub-nodes, AUVs, and so on. Normally, different types of nodes hope to transmit data with greater power to obtain a higher quality of service [8]. In this case, if proper interference control is not performed, there will be increased interference between nodes and a huge waste of transmit power. So it can be seen that, because of the complex underwater acoustic communication environment, the proposed resource allocation algorithm needs to have strong adaptive characteristics to counter the dynamic underwater acoustic communication environment. The low transmission rate of

orthogonal frequency-division multiplexing (OFDM) technology has obvious advantages in combating the complex communication environment of underwater acoustics. Its low transmission rate effectively reduces multipath reflection interference [9], and it is also extremely resistant to inter-code interference [10]. Motivated by previous analysis, based on the modeling of OFDM underwater heterogeneous communication networks, we consider how to find a balance between power consumption and interference level to achieve optimal system performance.

To summarize, we consider the issue of energy efficiency optimization in cooperative UACNs. Since the resource allocation process can be considered as a Markov decision process (MDP), reinforcement learning (RL) is applied to solve the above problems [11]. Specifically, RL methods are used to find the equilibrium between power consumption and interference level, i.e., to select the appropriate transmit power for each node to obtain a high quality of service within the interference allowable range. To this end, this paper seeks the global optimal strategy by constructing a global MDP. The main contributions of this work are summarized as follows:

- (i) We propose a learning framework suitable for communication nodes. The framework realizes the transformation of resource allocation problem like the Markov decision model, which defines the state space and action set in the environment according to the actual problem that needs to be solved.
- (ii) We propose a systematic reward function design method based on the multiobjective optimization problem and the nature of RL, which is used to guide the training method of the transmitter. The designed reward function takes into account the network environment and node energy which are uncontrollable factors, and achieves maximization of quality of service (QoS) of communication nodes with relatively small energy consumption. We further show that the proposed reward function can achieve significant improvements in energy efficiency.
- (iii) We propose a resource allocation strategy for underwater transmitters based on Q-learning, which is distributed and scalable. The simulation results show that, compared with the greedy algorithm, the resource allocation strategy based on Q-learning achieves a higher system capacity and a longer life cycle.

The rest of this paper is organized as follows. Section 2 reviews the work related to resource allocation in UACNs. Section 3 introduces the multisectional cooperative communication network model and describes the problems related to resource allocation. Section 4 proposes a resource allocation strategy based on Q-learning and proves the effectiveness of the designed scheme theoretically, and Section 5 compares the proposed algorithm with the greedy algorithm. Finally, Section 6 concludes the paper.

2. Related Work

Compared to the channel bandwidth on land, the available bandwidth underwater is very narrow, only a few kilohertz. When there are more underwater communication nodes, many nodes will communicate in similar frequency bands, which will generate large interference between nodes and affect the communication quality of underwater nodes. Facing the complicated underwater communication environment, many scholars have improved the communication quality of underwater sensor networks by rationally allocating resources such as channels and power.

The problem of resource allocation has been extensively studied in UACNs. Aiming at the energy limitation and throughput problems in UACNs, the linear Gaussian relay channel (LGRC) model is used in Ref. [12] to optimize the power spectral density of the input power, effectively expanding the transmission capacity of UACNs. In a similar study, For the MQAM-OFDM underwater acoustic communication system, a joint power-rate allocation algorithm is proposed in Ref. [13], which optimizes the transmission power of the node and improves the transmission rate of the system. In Ref. [14], the authors proposed an efficient spectrum management system receiver-initiated spectrum management (RISM) for underwater acoustic cognitive networks and aimed to maximize the node channel capacity for power allocation, which effectively avoids conflicts in data transmission and improves the data transmission rate. However, the centralized optimization algorithm proposed by the abovementioned study only optimizes the transmission rate of the node, and does not consider the quality of service of the network. In order to improve its own throughput, each transmitting node usually chooses a larger transmitting power, which causes more serious network interference and further reduces the life cycle of the node. In Ref. [15], a joint frequency-power allocation-based algorithm is proposed for UACNs, which effectively extends the life cycle of nodes by setting the power level according to the distance between nodes. The disadvantage is that this algorithm is only suitable for environments with dense network nodes. Meanwhile, considering the complex underwater communication environment, it is difficult to deploy a centralized control center underwater, so the abovementioned centralized power algorithm cannot meet the strong distributed application requirements of the UACNs.

RL has been developed to continuously optimize its own strategies through continuous interaction with unknown environments, and can be used in a distributed manner to achieve better results in many scenarios [16, 17]. For example, in order to solve the multinode interference problem in UACNs, in Ref. [5], the authors converted the resource allocation problem into a Markov decision model and proposed a cooperative Q-learning optimization scheme. However, Ref. [6] did not consider the node energy consumption. Furthermore, an anti-interference relay selection scheme for deep Q network (DQN) is proposed in Ref. [18], which selects the node position based on the interference level of the node on the one hand, and adjusts the node

transmit power according to the magnitude of the BER on the other hand. The disadvantage is that the algorithm only considers a network composed of a few nodes and lacks scalability. Therefore, in order to balance node energy consumption and network interference level, and at the same time, considering the scalability of the algorithm, this paper regards the communication node as an agent, and transforms the resource allocation problem into the Q-learning algorithm model to obtain the optimized strategy result.

3. System Model and Problem Formulation

3.1. System Model. In this paper, we consider the UACNs OFDM system composed of multiple transmitter-receiver pairs. In UACNs, the transmitting nodes collect environmental information, and the receiving nodes are relay nodes or data fusion centers. According to application needs, there are many types of transmitting nodes, including sensor nodes, Autonomous Underwater Vehicle (AUV), Unmanned Underwater Vehicle (UUV), and many others. Different types of transmitter-receiver pairs have different communication requirements and priority levels. The bandwidth of the OFDM system is equally divided into L orthogonal sub-channels, whose set is denoted as $L = [1, 2, \dots, L]$. For convenience, we assume that the bandwidth of each sub-channel is the unit bandwidth. All orthogonal channels are shared channels that can be freely accessed by all transmitter-receiver pairs. Meanwhile, suppose that there are N pairs of sensor nodes and 1 pair of AUV pairs in the network, where $\mathbf{N} = [1, 2, \dots, N]$ represents the index of the sensor node. The overall network configuration is shown in Figure 1. Please note that although

we consider each transmitter to serve a single receiver, the proposed method can be easily adapted to serve more transmitter-receiver pairs.

From the above text, the received signal of node $n_i^R, \forall i \in \mathbf{N}$ includes interference from node $n_j^R (j \neq i, j \in \mathbf{N})$ and thermal noise; then the signal-to-interference-to-noise ratio (SINR) at node $n_i^R, \forall i \in \mathbf{N}$ can be expressed as Ref. [19]

$$\eta_i = \frac{p_i h_{ii}}{\sum_{k=1, k \neq i}^N p_k h_{ki} + p_j h_{ji} + \sigma^2}, \quad (1)$$

where p_j is the transmit power of AUV j ; h_{ji} denotes the channel gain from the AUV j to node n_i^R ; p_i indicates the transmit power of node n_i^T ; h_{ii} is the channel gain from node n_i^T to node n_i^R ; p_k is the transmit power of node n_k^T ; and h_{ki} denotes the channel gain from node n_k^T to node n_i^R . σ^2 denotes the noise power of the underwater acoustic channel. Underwater acoustic channel noise is an important topic in the application practice of UACNs, as hydrostatic pressure effects (tides, waves, etc., caused by wind, rain, and seismic disturbances) and industrial behavior (e.g., surface sailing) remain one of the main reasons hindering the development of underwater acoustic communication [20–22]. Calculating the noise power σ^2 is a very complex challenge, because of the significant time-space-frequency variability of underwater acoustic channel noise [23, 24]. Fortunately, σ^2 can be calculated from the corresponding power spectral density [15, 25], which can be described as follows:

$$\varphi(f) = N_\tau(f) + N_w(f) + N_{th}(f) + N_t(f), \quad (2)$$

where

$$\begin{aligned} 10 \log N_\tau(f) &= 40 + 20(\tau - 0.5) + 26 \log_{10}(f) - 60 \log_{10}(f + 3), \\ 10 \log N_w(f) &= 50 + 7.5\sqrt{w} + 20 \log_{10}(f) - 40 \log_{10}(f + 0.4), \\ 10 \log N_{th}(f) &= -15 + 20 \log_{10}(f), \\ 10 \log N_t(f) &= 17 - 30 \log_{10}(f), \end{aligned} \quad (3)$$

where $N_\tau(f)$, $N_w(f)$, $N_{th}(f)$, and $N_t(f)$ denote ocean turbulence, ship activity, wind and waves, and thermal movement of molecules in the water, respectively. In addition, w and τ represent the influencing factor of sea surface wind speed and ship activity, respectively.

In the underwater acoustic communication system, the channel gain h can be expressed as Ref. [25]

$$h = A_0^{-1} d^{-sp} (\alpha(f))^{-d}, \quad (4)$$

where A_0 is the normalization coefficient, d denotes the transmission distance (km), f indicates the communication frequency (Hz), d^{-sp} is the expansion loss, which describes the channel characteristics of underwater acoustic propagation, sp denotes the expansion coefficient, with a value of 1.5, and $\alpha(f)$ is the absorption coefficient, which can be expressed by Thorp empirical formula as [26]

$$10\alpha(f) = \frac{0.11f^2}{1+f^2} + \frac{44f^2}{4100+f^2} + 2.75 \times 10^{-4} f^2 + 0.003. \quad (5)$$

Assume that all channel parameters are known by the transmitting node, which is consistent with previous work such as Refs. [3, 5]. In fact, this is reasonable, because the channel information can be fed back to each transmitting node through the backhaul network. Thus, the normalized capacity of any receiver can be expressed as follows:

$$C_i = \log_2(1 + \eta_i), \quad \forall i \in \mathbf{N}. \quad (6)$$

3.2. Problem Formulation. During the operation of UACNs, when the noise conditions of the underwater acoustic channel are given, each transmitter hopes to transmit data with a larger power in order to obtain a higher quality of

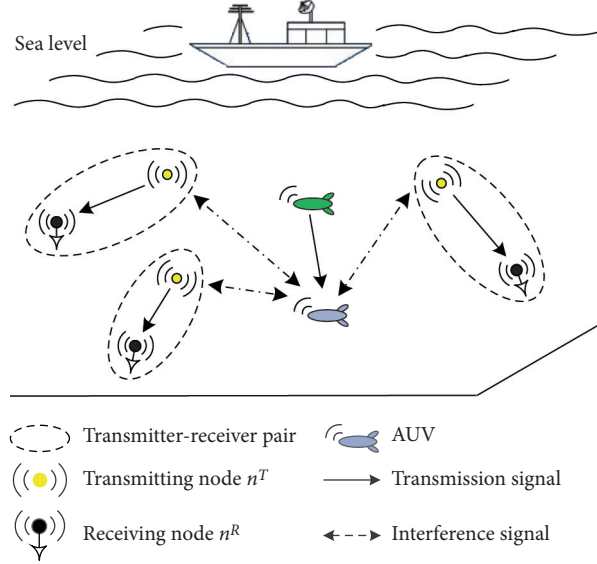


FIGURE 1: Underwater acoustic communication network model.

service. However, excessive transmission of power will increase the level of network interference, which will greatly reduce the communication quality. Besides this, transmitter usually uses battery power when working underwater, and excessive transmitting power will accelerate the energy consumption of the transmitter. Therefore, the main goal of our work is to solve the energy optimization problem, i.e., to maximize the service quality of the receiver with a smaller energy consumption.

As mentioned previously, if we assume that the transmitting power of the transmitting node n^T is $\mathbf{P} = [p_1, p_2, \dots, p_N]$, then the optimization goal can be expressed as follows:

$$\max \left\{ \sum_{i=1}^N C_i, - \sum_{i=1}^N p_i \right\}, \quad (7)$$

$$\text{s.t. } p_{\min} \leq p_i \leq p_{\max}, \quad i = 1, 2, \dots, N, \quad (8)$$

$$\eta_i \geq \eta_{\text{th}}, \quad i = 1, 2, \dots, N, \quad (9)$$

$$\eta_{\text{AUV}} \geq \eta'_{\text{th}}, \quad (10)$$

where the objective (7) indicates the maximization of the network capacity with relatively small energy consumption. C_i denotes the information transmission capacity between the i -th transmitter-receiver pair, and p_i is the transmit power of the i -th transmitter node. The first constraint (8) denotes the power limit of the transmitting node $n_i^T, \forall i \in \mathbf{N}$. The η_{th} in (9) and η'_{th} in (10), respectively, denote the minimum SINR of node $n_i^R, \forall i \in \mathbf{N}$ and the AUV when meeting application requirements. In other words, constraints (9) and (10) ensure that all receivers have sufficient quality of service. Considering (8)–(10), it can be concluded that the optimization in (7) is not only a multiobjective optimization problem but also a nonconvex problem of UACNs. This is mainly because of the SINR expression in (1)

and the optimization goal of (7). In the next section, a method based on reinforcement learning is proposed to solve the above problems.

4. Resource Allocation Based on Reinforcement Learning

4.1. Markov Decision Process. The environment that interacts with the agent is usually called a Markov Decision Process (MDP) with a finite state. We assume that S represents the discrete set of environmental states, A is the discrete set of actions that the agent can perform, r represents the reward value of the agent performing action $a, a \in A$ in state $s, s \in S$, and g be the state transition function. At each time t , the agent interacts with the environment to obtain the current state $s^t = s$, and selects an action $a^t = a$ from the action set A to execute. According to the probability distribution relation $g(s'|s, a)$, the environment is thus changed, shifting from state $s^t = s$ to $s^{(t+1)} = s'$ and generating feedback on the choice of action of the intelligence, that is, the reward value $r(s, a)$. The whole process is iterated and optimized until convergence.

The goal of the RL method is to continuously optimize the agent's decision strategy π in the iterative process. Formally, strategy π describes the mapping relationship from environmental state to action selection. The task of the intelligence is to obtain the optimal policy during the learning process so that the total expected discounted return reaches the maximum in a finite number of steps, that is

$$V^\pi(s) = E \left[\sum_{t=0}^{+\infty} \gamma^t r(s^t, \pi(s^t)) | s^0 = s_0 \right], \quad (11)$$

where γ^t is the reward discount factor at the moment; s_0 is the initial state of the system; and r is the immediate reward obtained by executing the action strategy. $V^\pi(s)$ is often referred to as the value function of the intelligence at state s .

The process of RL can be described as an MDP, which has Markov properties. In other words, the state of the

environment is only related to the state of the previous moment, and not related to the state of the earlier time. Therefore, the value function can be simplified to

$$V^\pi(s) = E[r(s, \pi(s))] + \gamma \sum_{s' \in S} g(s' | s, \pi(s)) V^\pi(s'). \quad (12)$$

Therefore, the optimal strategy satisfies the Bellman equation as [9]

$$V^*(s) = \max_{a \in A} \left\{ E[r(s, a)] + \gamma \sum_{s' \in S} g(s' | s, a) V^*(s') \right\}. \quad (13)$$

However, in the actual systems, the state transition function is generally unknown. The agent cannot model the quadruple $\langle S, A, r, g \rangle$ of reinforcement learning. Therefore, it is necessary to use model-free RL algorithms. Q-learning is the most representative of these algorithms. The Q-function is defined as

$$Q^*(s, a) = E[r(s, a)] + \gamma \sum_{s' \in S} g(s' | s, a) V^*(s'), \quad (14)$$

where $Q^*(s, a)$ denotes the cumulative discount reward obtained by selecting action a at state s and choosing the optimal policy all the way through the subsequent policy selection process. Combining equations (12) and (13), the relationship between the value function and the state-action value function can be obtained as follows:

$$V^*(s) = \max_{a \in A} Q^*(s, a). \quad (15)$$

Therefore, the optimal value function $V^*(s)$ can be obtained from $Q^*(s, a)$. Then, (14) can be expressed as follows:

$$Q^*(s, a) = E[r(s, a)] + \gamma \sum_{s' \in S} \left\{ g(s' | s, a) \max_{b \in A} Q^*(s', b) \right\}. \quad (16)$$

From the above equation, the update rule of the predicted Q function is provided as [5]

$$Q^{t+1}(s, a) = (1 - \alpha_t) Q^t(s, a) + \alpha_t \left[r^t + \gamma \max_{b \in A} Q^*(s', b) \right], \quad (17)$$

where Q^{t+1} and Q^t denote the Q values before and after the update, respectively; $\alpha_t \in [0, 1]$ is the learning rate, and a larger α_t value indicates that the update of rewards depends more on immediate rewards than on the accumulation of past experience. It can be seen that the Q value is updated using the optimal Q value of the immediate reward and the next state to which it is transferred, and the basic idea is to estimate the Q function by incrementally summing the Q values of the previous state action pairs.

4.2. Reinforcement Learning-Based Power Allocation Approach. In this paper, each emitter is considered as an intelligent body with RL capability. Next, the most important thing is to transform the resource optimization problem

in UACNs into a RL algorithm model and use it to obtain optimal decision results. The existing problem scenario is modeled based on the four elements of reinforcement learning.

4.2.1. Action Space A. According to the optimization goal described in (7), the action of the agent is to select the power. Generally speaking, the Q function is stored in a look-up table. For this, we first discretize the power selection. Assuming the transmit power of the i -th agent, the selection range is $[P_{\min}, P_{\max}]$, which can be discretized as follows:

$$p_i(a_i) = p_{\min} + \frac{a_i}{Y_i} (p_{\max} - p_{\min}), \quad y_i = 0, 1, \dots, Y_i, \quad (18)$$

where Y_i is the number of discretized powers.

4.2.2. State Space S. The state of the environment should be defined based on local observations. The key to the problem of UACNs resource allocation is to determine the level of interference around each receiver and the energy consumption of the transmitter. Therefore, at time t , we can define the state observed by transmitter i as follows:

$$s_i^t = (i, \psi_i, p_i(a_i)), \quad (19)$$

where $\psi_i \in \{0, 1\}$ indicates whether the SINR η_i received by receiver i is greater than or lower than its threshold η_i^* , that is,

$$\psi_i = \begin{cases} 1, & \text{if } \eta_i(a_i, a_{-i}) \geq \eta_i^*, \\ 0, & \text{otherwise,} \end{cases} \quad (20)$$

where $a_{-i} = (a_1, a_2, \dots, a_{i-1}, a_{i+1}, \dots, a_N) \in A_{-i}$ represents the action vector of other receivers. In this paper, we use s_i to represent the discrete set of environmental states related to receiver i .

4.2.3. Reward Function. The reward value of the agent's RL indicates the degree of satisfaction of the agent with the strategy choice. In the current scenario, the optimization goal is to maximize the QoS of the receiver device with less power consumption, which is essentially a multiobjective optimization problem. In this paper, we transform the multiobjective problem into a single-objective problem by the weight coefficient method, and transform the optimization goal setting into the reward value, denoted as follows:

$$r_i^t(a_i, a_{-i}) = \frac{\beta_i}{P_i} C_i^2 C_H - \frac{1}{\beta_i} (C_H - \Gamma_{\text{th}})^2 - (C_i - \Gamma'_{\text{th}})^2. \quad (21)$$

This is based on the following points. In (21), C_H and C_i , respectively, denote the capacity of AUV and node n_i^R , $i \in \mathbf{N}$ at time t . Γ_{th} and Γ'_{th} are equal to $\log_2(1 + \Gamma_{\text{th}})$ and $\log_2(1 + \Gamma'_{\text{th}})$, respectively. If there is a higher SINR at the receiver, a lower bit error rate will usually be obtained, which in turn will have a higher throughput. However, an excessively high SINR requires the transmitter to transmit at a high-power level, which in turn will cause more energy consumption and increase interference to other users. To

avoid this, we consider energy efficiency, i.e., (21) select the correct number of received bits per unit of energy consumption as part of the reward function. Simultaneously, (21) also considers the deviation of AUV and node $n_i^R, i \in \mathbf{N}$ from their required capacity thresholds, that is, $(C_H - \Gamma_{th})^2$ and $(C_i - \Gamma_{th})^2$ are reduced from (21) to decrease the value of the reward. In addition, the parameter β_i ensures the fairness of the algorithm. β_i represents the distance between the node $n_i^R, i \in \mathbf{N}$ and the AUV normalized to d_{th} . d_{th} is a constant, indicating whether the node $n_i^R, i \in \mathbf{N}$ is near an AUV. For example, if the distance between the node $n_i^R, i \in \mathbf{N}$ and the AUV is less than d_{th} , the node $n_i^R, i \in \mathbf{N}$ will be affected by the AUV more than any other transmitter with a distance greater than d_{th} . Then, the node $n_i^T, i \in \mathbf{N}$ should give less reward, which means that the first and third terms in (21) are multiplied by the inverse of β_i and β_i to reduce the reward, respectively.

Due to the independent selection of power levels by devices, different devices may interfere greatly with other devices in order to maximize their own profits. In other words, incorrect action selection may cause the SINR of some receivers to fall below its threshold, so the reward value is redefined as

$$R_i(s_i, a_i, a_{-i}) = \begin{cases} r_i(a_i, a_{-i}), & \text{if } \psi_i = 1, \\ 0, & \text{if } \psi_i = 0. \end{cases} \quad (22)$$

Specifically, if the SINR in the current channel is greater than the predefined threshold η_{th} (see (9)), i.e., the QoS is greater than the minimum requirement, the reward value is calculated from (21); otherwise, the reward value is 0. Overall, (22) is the payoff for choosing the power p_i under state s_i^t to ensure the quality of service of the transmission, as well as to achieve energy efficiency.

The convergence of the Q-learning algorithm mainly depends on the convergence of the Q-value function [27]. Next, we will analyze the convergence of the proposed algorithm.

Theorem 1. *The value of the reward function r formulated according to formula (22) is bounded in different system states.*

Proof. From (22),

$$R_i(s_i, a_i, a_{-i}) = \begin{cases} r_i(a_i, a_{-i}), & \text{if } \psi_i = 1, \\ 0, & \text{if } \psi_i = 0, \end{cases} \quad (23)$$

we need to prove that the reward function $R_i(s_i, a_i, a_{-i})$ is bounded in different system states when $\psi_i = 1$.

From (21), $r_i(a_i, a_{-i})$ consists of three components, which are the energy efficiency $\beta_i C_i^2 C_H / p_i$, the deviation of the communication capacity of the AUV from the corresponding capacity threshold $(C_H - \Gamma_{th})^2 / \beta_i$, and the deviation of the communication capacity of the sensor node from the corresponding capacity threshold $(C_i - \Gamma_{th})^2$. Here, $\beta_i, \Gamma_{th} = \log_2(1 + \eta_{th})$ and $\Gamma_{th}' = \log_2(1 + \eta_{th}')$ are constant.

Consider that the action space A defined by power discretization is a discrete finite value, i.e.,

$A = \{p_0, p_1, \dots, p_{Y_i}\}$, the communication capacity C_H of the AUV and the communication capacity $C_i, i \in \mathbf{N}$ of the sensor node are bounded in any state.

Furthermore, the product form composed of the capacity value C_H , the capacity value $C_i, i \in \mathbf{N}$, and the power value p_i must also be a discrete finite value, i.e., the energy efficiency value $\beta_i C_i^2 C_H / p_i$ is bounded. Meanwhile, $(C_i - \Gamma_{th})^2$ and $(C_H - \Gamma_{th}')^2$ are bounded. So $r_i(a_i, a_{-i})$ must be bounded. \square

Theorem 2. *In the iteration of the Q-value of a bounded reward function $r(s, a)$, the learn factor $0 < \lambda \leq 1$ and satisfies*

$$\sum_{t=1}^{\infty} \lambda_t = \infty, \sum_{t=1}^{\infty} \lambda_t^2 < \infty, \quad \forall s, a. \quad (24)$$

If the optimal Q-value is denoted as $Q^*(s, a)$, then when $t \rightarrow \infty$, we have

$$\lim_{t \rightarrow \infty} Q_t(s_t, a_t) = Q^*(s_t, a_t). \quad (25)$$

The conclusion exhibited in Theorem 2 has a detailed proof process in Ref. [28], which will not be repeated here.

4.3. Algorithm Description. Based on the above preparatory work, the Q-learning-based resource allocation algorithm for UACNs can be described as follows. Algorithm 1 first initializes the relevant parameters, and then uses the greedy method [29] to guide the behavior selection of the intelligent Q-Agent, and updates the Q-value function based on equation (17), and iterates until the Q-value function converges to make a decision on the resource allocation scheme of UACNs.

5. Numerical Results

In order to verify the effectiveness of the proposed algorithm, the next objective of this section is to evaluate the performance in two different scenarios, i.e., a sparse network consisting of four transmitter-receiver pairs and a dense network with dynamic access consisting of multiple transmitter-receiver pairs. The network model of this paper is shown in Figure 1, and the simulation parameters are set according to Refs. [19, 30]. The maximum transmit power of the transmitter $P_{max} = 11$ W, system bandwidth $W = 1$ MHz, propagation coefficient $\varepsilon = 1.5$, carrier frequency $f = 20$ kHz, noise power $\sigma^2 = 1.5 \times 10^{-7}$ W. In addition, we consider the random nonstationary characteristics of the underwater signal, and use δ to reflect the influence of the underwater uncertainty factors on the underwater acoustic channel, where $\delta = h \times \vartheta$ and ϑ obeys the Rayleigh distribution with a mean value of 0.1. Therefore, $h + \delta$ is used for the gain of the hydroacoustic channel in the simulation.

The minimum SINR requirement for node $n_i^R, i \in \mathbf{N}$ and AUV is defined in terms of the rate required to support its corresponding receiver. In the simulation, we assume that the minimum transmission rate required to satisfy QoS for

Initialization:

- (1) Set $\gamma = 0.9$, $\lambda = 0.5$.
- (2) Initialize $Q(s, a) = 0$, $s \in S$, $a \in A$.

Repeated Learning: (for each episode)

- (3) Looks up the Q-table and selects the state s , i.e.,

$$s = \operatorname{argmax}_{s \in S} Q(s, a).$$
- (4) Execute the ϵ -greedy [29] method to select the action a

$$\pi(a|s) \leftarrow \begin{cases} 1 - \epsilon + (\epsilon/|A(s)|), & \text{if } a = \operatorname{argmax}_a Q(s, a), \\ (\epsilon/|A(s)|), & \text{if } a \neq \operatorname{argmax}_a Q(s, a) \end{cases}$$
- (5) Calculate the reward function $r(s, a)$ based on equation (22).
- (6) Calculate the current Q-value function.
- (7) Update the Q-table according to equation (17).
- (8) Update the state $s \leftarrow s'$.
- (9) Go back to 3 until the state s is the final state.

ALGORITHM 1: Q-learning-based UACNs resource allocation algorithm for node $n_i^T, i \in \mathbf{N}$.

node $n_i^T, i \in \mathbf{N}$ is 0.4 b/s/Hz, i.e. $\log_2(1 + \eta_{\text{th}}) = 0.4$ (b/s/Hz). In addition, for AUV, the minimum rate required is set to 1 b/s/Hz, i.e. $\log_2(1 + \eta'_{\text{th}}) = 1$ (b/s/Hz). It is important to note that by knowing the media access control (MAC) layer parameters, the value of the channel transmission rate can be calculated using (Ref. [21], equations (20) and (21)). The parameters associated with performing Q-learning are set as follows: learning rate $\lambda = 0.5$, discount factor $\gamma = 0.9$. ϵ -greedy algorithm is used for the first 80% of iterations, random $e = 0.2$, and the maximum number of iterations is set to 50,000. Besides, in order to achieve noncooperative power allocation in UACNs, one of the most important issues is the definition of the receiving reward. In this paper, the concept of energy efficiency is introduced in (11), which will be used as one of the metrics for numerical evaluation.

We first consider a sparse network consisting of four transmitter-receiver pairs. Assume that the four transmitters and four receivers are randomly distributed in a region that is 1.5 km deep, 1.5 km long, and 1 km wide, and the coordinate information of the nodes is shown in Table 1. Figure 2 shows the effect of the transmit power of the AUV on the other three node $n_i^T, i \in \{1, 2, 3\}$. As a whole, the SINR of the three nodes $n_i^R, i \in \{1, 2, 3\}$ gradually decreases as the transmit power of the AUV increases and the network environment interference enhances, which makes the transmission capacity of the three nodes decrease continuously. Further, when the AUV is a certain fixed value, node n_1^R is closest to the AUV and suffers the strongest interference, i.e., the smallest SINR, and thus its acquired capacity is the smallest among the three links. Conversely, node n_3^R is farthest from the AUV and its acquired capacity is the largest.

Figure 3 shows the results of the proposed learning algorithm in this paper compared with the greedy algorithm. In order to make a fair comparison between the two algorithms, we choose energy efficiency as the evaluation index. The results are shown in Figure 3, which indicates that as the power of AUV increases, the network energy efficiency of the proposed learning algorithm, although gradually decreasing, is significantly better than that of the greedy

algorithm. It should be noted that, as shown in Figure 2, the decrease in network energy efficiency is a reasonable phenomenon. In fact, in the greedy algorithm, each transmitting node always chooses the maximum power for transmission, which keeps the energy in a high consumption state, but the transmission capacity does not increase significantly.

Figure 4 illustrates the curve of AUV transmission capacity variation with transmit power. From the figure, it can be seen that the proposed algorithm can make the transmission capacity of AUV better than the greedy algorithm. This is mainly because the proposed algorithm can better balance the energy consumption and network interference level, so that the transmit power of each node in the network can be adjusted adaptively to achieve a win-win situation.

Next, we further consider a dynamic access dense network consisting of multiple transmitter-receiver pairs. Assume that the transmitting power of the AUV is 8 W, while the number of sensor nodes in the network increases continuously from 1 to 20 with random distribution. The simulation starts with one transmitter-receiver pair. After convergence, the next transmitter-receiver pair is added to the network and so on. Figure 5 shows the state of the node capacity distribution as the number of nodes in the network increases. As can be seen from the figure, under the same conditions, compared to the greedy algorithm, the learning algorithm proposed in this paper is able to maintain a better network quality of service by adaptively adjusting the node transmitting power according to the changes in the network environment. At the same time, it should be noted that as the number of nodes increases, the level of network interference increases, which makes the overall energy efficiency of nodes show a decreasing trend.

Figure 6 shows the graph of network energy efficiency with increasing number of nodes. It is obvious from the graphs that the proposed algorithm can well balance the network transmission capacity and energy consumption, which greatly improves the network service quality. In the greedy algorithm, all nodes choose the maximum transmission power for the pursuit of higher transmission

TABLE 1: Location information of the four transmitting receiver pairs.

Location information (km)	n_1^T	n_2^T	n_3^T	AUV
x	0.25	0.5	0.75	0.3
y	-0.2	-0.4	-0.8	-0.3
z	0	0	0	100
Location information (km)	n_1^R	n_2^R	n_3^R	AUV
x	0.25	0.5	0.75	0.3
y	-0.2	-0.4	-0.8	-0.1
z	100	100	100	100

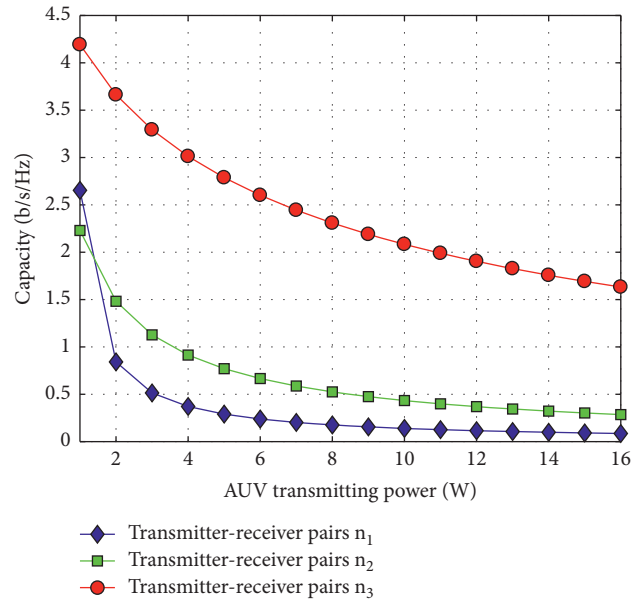


FIGURE 2: The graph of the change of node capacity with the transmitting power of AUV.

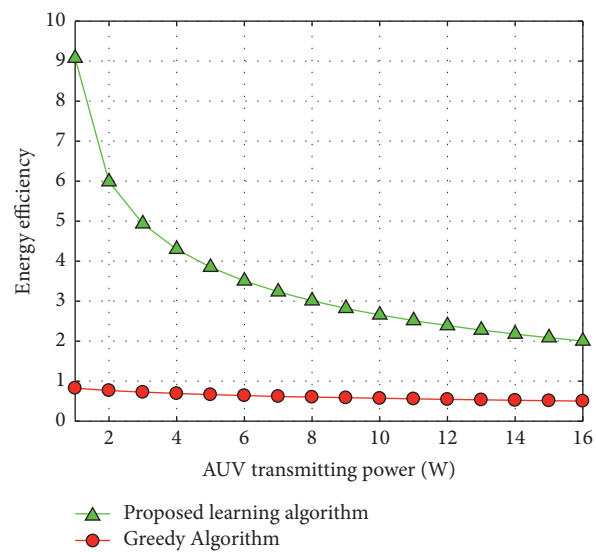


FIGURE 3: The graph of the change of network energy efficiency with the transmitting power of AUV.

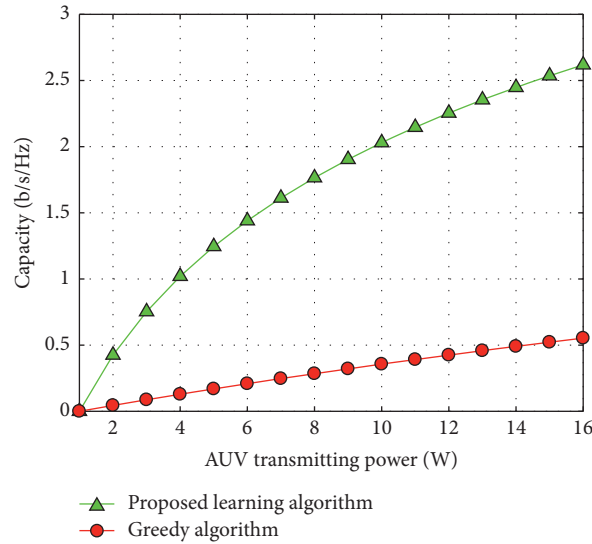


FIGURE 4: Curve diagram of AUV transmission capacity changing with transmitting power.

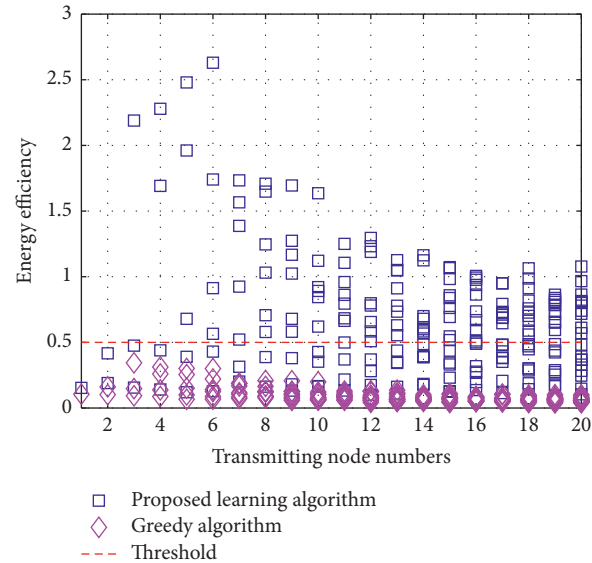


FIGURE 5: Distribution of energy efficiency as the number of nodes increases.

capacity, which not only causes energy waste but also enhances the interference between networks, and finally makes the network energy efficiency maintain at a low level.

Finally, we perform the convergence and complexity analysis of the algorithm. The maximum number of iterations of the proposed learning algorithm is set to 50,000, and the average number of iterations for the convergence of the algorithm in the two scenarios is shown in Figure 7. From the figure, it can be found that the proposed algorithm requires approximately equal number of iterations in the two different scenarios. In other words, the mathematical expectation and the variance of the number of iterations required for the proposed algorithm to converge are 41,200 and 35.6, respectively, in the underwater sparse scenario when the firing power of the heterogeneous nodes varies

between 0 and 15, and 41236 and 49.1, respectively, in the underwater dense scenario when the number of nodes varies between 1 and 20. The stability of the proposed algorithm is thus demonstrated.

To better understand the running time of the proposed algorithm, Figure 8 shows the actual running time of the proposed algorithm on a conventional processor. Specifically, in the underwater sparse scenario, when the transmit power of the heterogeneous nodes varies between 0 and 15, the mathematical expectation and variance of the running time required for the proposed algorithm to converge are 5.65 and 0.51, respectively. In the underwater dense scenario, when the number of nodes varies between 1 and 20, the running time required for the proposed algorithm to converge gradually increases. This is mainly because when the

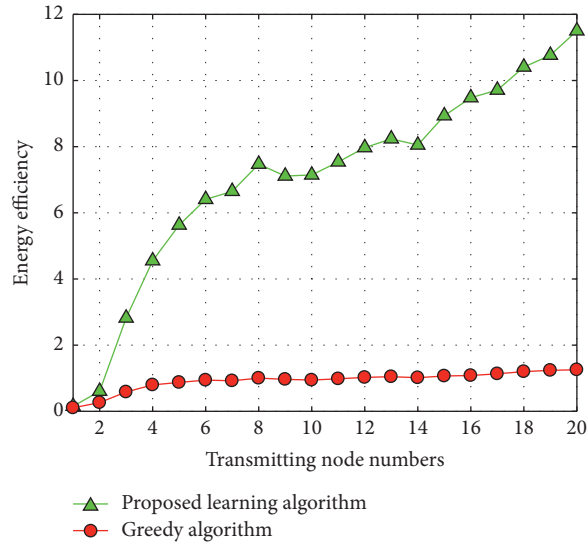


FIGURE 6: Distribution of energy efficiency as the number of nodes increases.

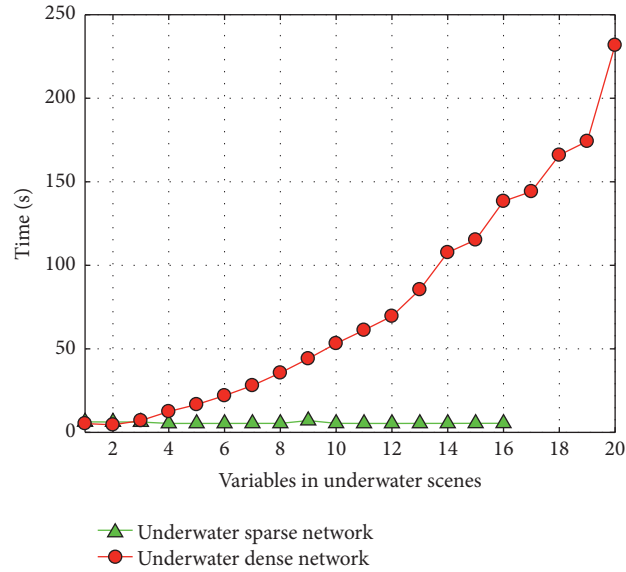


FIGURE 7: The average number of iterations for the algorithm to converge.

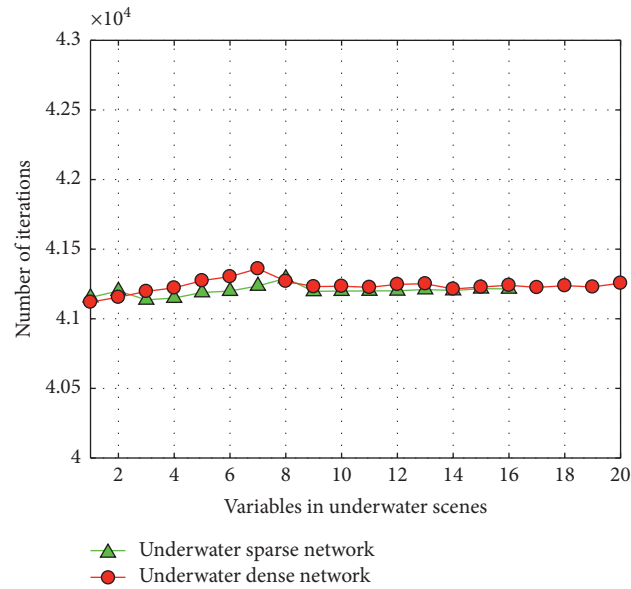


FIGURE 8: The average running time of algorithm convergence.

number of nodes increases, a lot of time is needed to find the equilibrium between communication capacity and energy consumption.

6. Conclusion

This paper proposes a power allocation scheme based on Q-learning. This scheme considers the interference problem in UACNs composed of multiple transmitter-receiver pairs and the energy efficiency of each transmitter, while each transmitter (sensor node, AUV) is able to train itself to select the appropriate transmit power to support its service nodes while protecting other nodes in the network. In addition, the learning algorithm proposed in this paper, as a distributed method, can solve the power optimization problem for networks with dynamic access of sensor nodes while having low complexity. The scheme is scalable and has a clear advantage in energy efficiency compared to the greedy algorithm. In future work, we design function approximators for neural networks to solve the problem of large state space and action space.

Data Availability

The data used to support the findings of this study are included within the article.

Conflicts of Interest

The authors declare that they have no conflicts of interest.

Acknowledgments

This work was funded by the National Natural Science Foundation of China, under grant no. 62001199, the Fujian Province Natural Science Foundation of China, under grant no. 2019J01842, the President's Fund of Minnan Normal

University, under grant no. KJ2020003, the Scientific Research Fund of Fujian Provincial Education Department, under grant no. JT180596, and the Ningde Science and Technology Project, under grant nos. 20140157 and 20160044.

References

- [1] I. F. Akyildiz, D. Pompili, and T. Melodia, "Underwater acoustic sensor networks: research challenges," *Ad Hoc Networks*, vol. 3, no. 3, pp. 257–279, 2005.
- [2] T. Archana, P. Rishi, and D. Sanjoy, "Localization schemes for underwater acoustic sensor networks –A review," *Computer Science Review*, vol. 37, pp. 1–18, 2020.
- [3] A. Doosti-Aref and A. Ebrahimzadeh, "Adaptive relay selection and power allocation for OFDM cooperative underwater acoustic systems," *IEEE Transactions on Mobile Computing*, vol. 17, no. 1, pp. 1–15, 2018.
- [4] G. Zhou, Y. Li, Y. C. He, X. Wang, and M. Yu, "Artificial fish swarm based power allocation algorithm for MIMO-OFDM relay underwater acoustic communication," *IET Communications*, vol. 12, no. 9, pp. 1079–1085, 2018.
- [5] H. Wang, Y. Li, and J. Qian, "Self-adaptive resource allocation in underwater acoustic interference channel: a reinforcement learning approach," *IEEE Internet of Things Journal*, vol. 7, no. 4, pp. 2816–2827, 2020.
- [6] V. Ravelomanana, "Extremal properties of three-dimensional sensor networks with applications," *IEEE Transactions on Mobile Computing*, vol. 3, no. 3, pp. 246–257, 2004.
- [7] Y. Luo, L. Pu, M. Zuba, Z. Peng, and J.-H. Cui, "Challenges and opportunities of underwater cognitive acoustic networks," *IEEE Transactions on Emerging Topics in Computing*, vol. 2, no. 2, pp. 198–211, 2014.
- [8] P. Casari and M. Zorzi, "Protocol design issues in underwater acoustic networks," *Computer Communications*, vol. 34, no. 17, pp. 2013–2025, 2011.
- [9] J. Zhang, H. Gharavi, and B. Hu, "Impact of cooperative space-time/frequency diversity in OFDM-based wireless

- sensor systems over mobile multipath channels,” *IET Wireless Sensor Systems*, vol. 6, no. 4, pp. 138–143, 2016.
- [10] S. Han, X. Li, L. Yan, J. Xu, Z. Liu, and X. Guan, “Joint resource allocation in underwater acoustic communication networks: a game-based hierarchical adversarial multiplayer multiarmed bandit algorithm,” *Information Sciences*, vol. 454–455, pp. 382–400, 2018.
- [11] X. Shen, X. Zhang, Y. Huang, S. Chen, and Y. Wang, “Task learning over multi-day recording via internally rewarded reinforcement learning based brain machine interfaces,” *IEEE Transactions on Neural Systems and Rehabilitation Engineering*, vol. 28, no. 12, pp. 3089–3099, 2020.
- [12] C. Choudhuri and U. Mitra, “Capacity bounds and power allocation for underwater acoustic relay channels with ISI,” in *Proceedings of the Fourth ACM International Workshop on UnderWater Networks*, New York, NY, USA, November 2009.
- [13] K. Nehra and M. Shikh-Bahaei, “Spectral efficiency of adaptive MQAM/OFDM systems with CFO over fading channels,” *IEEE Transactions on Vehicular Technology*, vol. 60, no. 3, pp. 1240–1247, 2011.
- [14] Y. Luo, L. Pu, H. Mo, Y. Zhu, Z. Peng, and J.-H. Cui, “Receiver-initiated spectrum management for underwater cognitive acoustic network,” *IEEE Transactions on Mobile Computing*, vol. 16, no. 1, pp. 198–212, 2017.
- [15] J. M. Jornet, M. Stojanovic, and M. Zorzi, “On joint frequency and power allocation in a cross-layer protocol for underwater acoustic networks,” *IEEE Journal of Oceanic Engineering*, vol. 35, no. 4, pp. 936–947, 2010.
- [16] H. Yang, Z. Xiong, J. Zhao, D. Niyato, C. Yuen, and R. Deng, “Deep reinforcement learning based massive access management for ultra-reliable low-latency communications,” *IEEE Transactions on Wireless Communications*, vol. 20, no. 5, pp. 2977–2990, 2021.
- [17] X. Qiu, L. Liu, W. Chen, Z. Hong, and Z. Zheng, “Online deep reinforcement learning for computation offloading in blockchain-empowered mobile edge computing,” *IEEE Transactions on Vehicular Technology*, vol. 68, no. 8, pp. 8050–8062, 2019.
- [18] L. Xiao, D. Jiang, Y. Chen, W. Su, and Y. Tang, “Reinforcement-learning-based relay mobility and power allocation for underwater sensor networks against jamming,” *IEEE Journal of Oceanic Engineering*, vol. 45, no. 3, pp. 1148–1156, 2020.
- [19] Y. Su, Y. Zhu, H. Mo, J.-H. Cui, and Z. Jin, “A joint power control and rate adaptation MAC protocol for underwater sensor networks,” *Ad Hoc Networks*, vol. 26, pp. 36–49, 2015.
- [20] M. A. Chitre, J. R. Potter, and S. H. Ong, “Viterbi decoding of convolutional codes in symmetric α -stable noise,” *IEEE Transactions on Communications*, vol. 55, no. 12, pp. 2230–2233, 2007.
- [21] A. Mahmood, M. Chitre, and M. A. Armand, “PSK communication with passband Additive symmetric α -stable noise,” *IEEE Transactions on Communications*, vol. 60, no. 10, pp. 2990–3000, 2012.
- [22] J. Wang, J. Li, S. Yan et al., “A novel underwater acoustic signal denoising algorithm for Gaussian/non-Gaussian impulsive noise,” *IEEE Transactions on Vehicular Technology*, vol. 70, no. 1, pp. 429–445, 2021.
- [23] X. Zhang, W. Ying, P. Yang, and M. Sun, “Parameter estimation of underwater impulsive noise with the Class B model,” *IET Radar, Sonar & Navigation*, vol. 14, no. 7, pp. 1055–1060, 2020.
- [24] X. Zhang, W. W. Ying, W. Ying, and B. Yang, “Parameter estimation for class a modeled ocean ambient noise,” *Journal of Engineering and Technological Sciences*, vol. 50, no. 3, pp. 330–345, 2018.
- [25] M. Stojanovic, “On the relationship between capacity and distance in an underwater acoustic communication channel,” *ACM SIGMOBILE-Mobile Computing and Communications Review*, vol. 11, no. 4, pp. 34–43, 2007.
- [26] V. T. Vakily and M. Jannati, “A new method to improve performance of cooperative underwater acoustic wireless sensor networks via frequency controlled transmission based on length of data links,” *Wireless Sensor Network*, vol. 2, Article ID 381, 2010.
- [27] C. J. C. H. Watkins and P. Dayan, “Q-learning,” *Machine Learning*, vol. 8, no. 3, pp. 279–292, 1992.
- [28] Q. Wei, F. L. Lewis, Q. Sun, P. Yan, and R. Song, “Discrete-time deterministic Q-learning: a novel convergence analysis,” *IEEE Transactions on Cybernetics*, vol. 47, no. 5, pp. 1224–1237, 2017.
- [29] Q. Zhang, M. Lin, L. T. Yang, Z. Chen, and P. Li, “Energy-efficient scheduling for real-time systems based on deep Q-learning model,” *IEEE Transactions on Sustainable Computing*, vol. 4, no. 1, pp. 132–141, 2019.
- [30] B. Wang, Z. Han, and K. J. R. Liu, “Distributed relay selection and power control for multiuser cooperative communication networks using stackelberg game,” *IEEE Transactions on Mobile Computing*, vol. 8, no. 7, pp. 975–990, 2009.

Research Article

A Directional Selective Power Routing Protocol for the Internet of Underwater Things

Manal Al-Bzoor ¹, Ahmed Musa ², Khawla Alzoubi ³, and Taha Gharaibeh ¹

¹Department of Computer Engineering, Yarmouk University, Irbid, Jordan

²Department of Communication Engineering, Yarmouk University, Irbid, Jordan

³Department of Engineering Technology, Community College of Qatar, Doha, Qatar

Correspondence should be addressed to Manal Al-Bzoor; mbzoor@yu.edu.jo

Received 21 December 2021; Revised 14 January 2022; Accepted 17 January 2022; Published 8 February 2022

Academic Editor: Hamada Esmail

Copyright © 2022 Manal Al-Bzoor et al. This is an open access article distributed under the Creative Commons Attribution License, which permits unrestricted use, distribution, and reproduction in any medium, provided the original work is properly cited.

The Internet of Underwater Things (IoUT) has lately gained popularity as a means of facilitating a wide range of underwater applications. In the IoUT, underwater communication is best accomplished by the usage of acoustic waves, whereas the terrestrial communication between the surface sinks and the on-shore control stations is typically achieved using radio waves. As a result, the greatest portion of an IoUT is enabled by the underwater acoustic sensor network (UASN), where the specific issues provided by the use of acoustic waves, the underwater node mobility, and the localization difficulties have yet to be addressed. In this paper, we discuss the challenges faced by the IoUT in terms of the currently proposed routing protocols and propose a Directional Selective Power Routing Protocol (DSPR) to cope with most of these challenges. The proposed protocol (i.e., DSPR) uses the angle of arrival and the sender depth information to find the best direction to the surface sink. In addition, the DSPR uses selective power control to enhance the delivery ratio and ensure connectivity while reducing energy consumption. To testify the performance of the proposed protocol, intensive simulation experiments have been conducted. The simulation results show that the proposed DSPR protocol outperforms two variations of the fixed directional routing (DR) protocol and the variable power depth-based routing (VDBR) protocol in terms of energy consumption and delivery ratio. For instance, the proposed DSPR protocol achieves at least 8 times enhancement in energy consumption compared with VDBR. In addition, DSPR saves around 30% of energy consumption over the DR protocols when the network is mobile. Moreover, the DSPR protocol acquires a delivery ratio above 90% for static/dynamic scenarios in both sparse and dense networks.

1. Introduction

Recent years have witnessed a rise in the usage of Internet of things (IoT), where smart devices from different heterogeneous systems are connected to exchange data and form one homogeneous large system. The IoTs have been extended to include the underwater networks deployed in submarine environment such as oceans, seas, etc. This extension is uniquely identified as the Internet of underwater things (IoUT). The IoUT is a promising technology that connects around 72% of the Earth surface with the land-connected Internet. In addition, this promising technology will serve many potential applications such as environmental monitoring, undersea explorations, disaster prevention, military

submarine tracking, and oil industry [1]. These applications require the deployment of smart underwater system which uses a mishmash of acoustic, radio, and optical waves for communications. It is worth mentioning that the optical waves suffer severe attenuation in the underwater environment. Henceforth, it can only be utilized at extremely high frequencies in the range of THz or in shallow water applications. Furthermore, the optical waves mandate a clear and precise Line of Sight (LOS), which is hard to achieve in marine environment [2]. In addition, the optical wave characteristics varies according to the water content, the temporal changes produced by turbulence, and other environmental variables. However, the underwater radio communication often operates at frequencies ranging from a

few kHz to hundreds of MHz, providing high data rates and low propagation delays [3]. Nevertheless, the radio waves suffer from significant attenuation at high frequencies and require the use of large and expensive antennas at low frequencies. As a result, the radio waves have been investigated in the communication between the surface sinks, buoys, and the offshore infrastructure. Additionally, the radio waves have been utilized in the shallow regions for real-time underwater applications, which require short latency and large bandwidth. Another communication technology called magneto inductive (MI) has been proposed as a carrier for data communication in underwater wireless sensor networks. Albeit the MI technology does not suffer from multipath fading, scattering, and signal propagation delay, it is only efficient for shallow water applications at distances up to 40 m [4].

According to the aforementioned limitations of radio, optical, and MI systems, acoustic waves are extensively employed as an alternative carrier for data communication in deep underwater environments. The key characteristics of acoustic waves include the low attenuation that allows signals to travel long distances without losing data. However, the main drawback of acoustic waves is long propagation delays and limited bandwidth. Fortunately, most underwater networks are used to send small sized packets to the surface or to the on-land Internet that represent the sensory data. Thus, the limited bandwidth imposed by the acoustic waves is no longer a significant communication barrier.

The key contribution of this work is twofold. Firstly, we highlight the challenges imposed by acoustic waves usage in IoUT communication. In addition, we discourse the effect of underwater nodes mobility patterns on the design of successful routing protocols [5, 6]. Secondly, we propose a reliable and energy-efficient routing protocol named directional selective power (DSPR) to combat the challenges of IoUT. In the DSPR protocol, the underwater nodes do not need the three-dimensional position of themselves or other nodes within the network. The underwater nodes communicate their sensed data in the direction of the nearest sink by employing the arrival angle of the acoustic signal [7, 8]. Furthermore, we combine the directional approach by a selective power control to maintain the network connectivity [9]. Thus, we increase the delivery ratio and enhance the overall network reliability. Moreover, the DSPR protocol is applicable for both sparse and dense networks as it can cope with the mobility of underwater nodes.

The rest of this paper is organized as follows. Section 2 presents the main features of the Internet of underwater things and the key issues that result from the acoustic wave utilization, the nodes mobility, and the difficulty of localization within the three-dimensional underwater architecture. Section 3 summarizes the main locations unaware routing techniques used for underwater acoustic sensor network (UASN) and the IoUT. Section 4 presents and analyzes the proposed routing protocol. Section 5 presents and illustrates the simulation results. Finally, Section 6 concludes the paper and gives directions for future work.

2. Challenges for Efficient Communication in Internet of Underwater Things

As was previously mentioned, an IoUT is enabled mainly by the use of UASN. In this type of network, smart underwater sensor nodes, autonomous underwater vehicles (AUV), and remotely operated vehicles (ROV) have been introduced to the research and industry communities to facilitate various underwater applications [10]. The smart underwater sensor nodes are often equipped with several types of sensors, an acoustic modem, and other smart features. These nodes may record various observed data and selectively send them to a surface sink. In general, the surface sink is equipped with both acoustic and radio modems to connect the undersea world to the terrestrial Internet and hence forms the IoUT. Figure 1 illustrates an example of an IoUT where acoustic wireless links are used as a communication medium between a surface sink, a set of underwater nodes, and an autonomous underwater vehicle [1]. The communicated data are then relayed by the surface sink to a satellite station or to on-shore control centers using radio links. The upcoming subsections present the challenges and crucial issues for efficient communication in the IoUT.

Like IoT, the performance metrics such as reduced energy consumption, reliability, and shorter end-to-end delays are the main concerns for designers of the IoUT protocols. Unfortunately, there are different communication challenges in the underwater environment than that of the terrestrial environment. Therefore, to improve the overall network performance, different performance and special design factors are to be considered. These metrics include the unique characteristics of acoustic waves, the deployment architecture, the high energy requirements, the mobility of underwater nodes, and the localization difficulty [1, 11]. Table 1 compares the unique characteristics and challenges experienced by the designers of IoUT with those experienced by IoT. The next subsections elaborate more on each of these challenges.

2.1. Acoustic Wave Communication. The acoustic waves compromise the largest part of communications in the underwater world. The radio waves are still the dominant medium for communication between surface sinks and the on-land control stations. Needless to say, the acoustic waves have their own set of challenges, such as the limited bandwidth and the slow propagation speed (1500 m/s). This speed is five times slower than that of radio waves. The acoustic signal speed is also affected by different water characteristics such as salinity, depth, and temperature. The effect of these characteristics is more noticeable near the shore or in the shallow water, where salinity and temperature vary greatly. In deep oceans, these variations are limited and hence the acoustic signal speed is almost fixed. The depth of water is another factor that impacts the sound speed where it increases by the increase in water pressure. Therefore, in deep underwater communications where the acoustic waves are required to travel for distances up to a few kilometers, the slow speed of sound results in huge

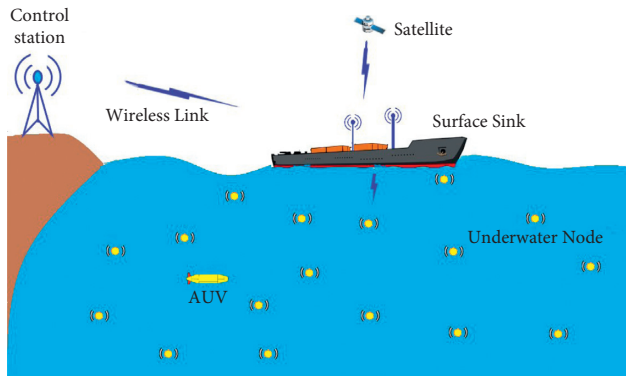


FIGURE 1: An architecture for IoUT.

TABLE 1: IoUT vs IoT features and challenges.

Feature	IoUT	IoT
Communication medium	Acoustic waves	Radio wave
Propagation speed	1500 m/s	2×10^8 m/s
Transmission range	100–10 000 meters	10–100 meters
Localization	Expensive algorithms	Cheap with GPS
Modem	Expensive large/acoustic	Cheap small/radio
Transmission power	Up to 10 s of watts	In milliwatts
Data rate	In 10's of kbps	In Mbps
Deployment architecture	Mostly 3D	Mostly 2D
Mobility	Affected by water current	Easily tracked

propagation delays [3, 12]. Hence, for time sensitive IoUT applications, optimized delivery techniques in the presence of such long delays are required. It is either done by reducing the control packet exchange in multihop routing or by using one or more AUVs for data collection in a timely manner [13].

The acoustic waves suffer from absorption loss that is directly affected by the imperfections of the water medium, the frequency used by acoustic transceivers, and the distance traveled by the acoustics signal. The absorption loss of both radio and optical waves is much higher than that for acoustic waves [12]. Moreover, the multipath propagation can severely affect the acoustic based communication in underwater medium. For instance, in the shallow water environment, the multipath arrivals of reflected signals are caused by the surface or bottom of the deployment region. In deep water, the multipath propagation can occur due to the refraction induced by changing the acoustic wave speed [3]. These challenges are usually overcome by the modem designs according to the physical layer level. However, the effect of multipath propagation may be mitigated at other protocol layers [14].

2.2. Deployment Architecture and Energy Efficiency. The deployment architecture of underwater sensor networks is inextricably coupled with the application requirements. For example, in some applications, the sensor nodes are

deployed in a two-dimensional centralized topology at the seabed. A highly efficient node (gateways) collects data from sensor nodes and forwards it to the surface sink directly via a single hop. Other applications might use multihop communication to interact with one or more surface sinks that require the deployment of sensor nodes in a three-dimensional architecture at various depths. This will lead to categorizing the UASN deployments into either a two-dimensional or a three-dimensional architecture. The deployment strategies can also be classified as static if it is performed once at the network setup or dynamic/adaptive if a redeployment decision is made during the network operation. Pompili et al. in [15] discussed the two architectures and investigated the problem of achieving maximal coverage with the lowest sensor count. These architectures were combined with multiple sink architecture to efficiently reduce delay, decrease energy consumption, and alleviate the limited bandwidth problem in acoustic communications [16]. The static deployment was illustrated by many frameworks and thus, many solutions were proposed for the underwater sensor network deployment. The dynamic node deployment strategies, on the other hand, are required to encounter the mobility of underwater nodes [11, 17, 18]. Nevertheless, dynamic deployment necessitates physical relocation of nodes and continuous update of nodes positions. Therefore, the mobility handling at the protocol layer stack is less expensive than dealing with it via dynamic deployment.

It is worth noting that the underwater nodes are battery powered. Henceforth, conserving their energy is a crucial requirement. This requirement has risen since most underwater node' deployment is done in remote underwater regions. Thus, replacing the battery of these nodes is difficult or infeasible. Furthermore, the acoustic modems require higher power than the radio modems, which can be in the order of watts compared to milliwatts for the radio modems. As a result, an underwater network protocol should prioritize energy efficiency while maintaining reliable connectivity.

2.3. Mobility and Localization. In the underwater settings, the node movement is unavoidable, negating the benefits of static-based methods proposed for terrestrial WSN. As a result, resilience to mobility should always be considered while designing efficient routing protocols [19]. In the AUVs and remotely operated vehicles (ROVs), mobility is supervised and controlled. On the other hand, the floating underwater sensor nodes are affected by uncontrolled mobility due to the water currents and dispersion that is also influenced by water temperature and varies with depth. In the UASN, simulating and predicting the performance of a given protocol requires precise modeling of nodes' mobility. This is because the node movement in a particular undersea environment is not completely random. Thus, customized mobility models such as the meandering model and the tidal mobility model have been used for modeling the movement of the underwater nodes [20, 21]. The tidal model is better suited in offshore locations where tides are the primary

driver of water movement, whereas the meandering one is used in the deepwater environments. Nonetheless, more precise prediction models based on the spatial and temporal correlation of movement patterns in UASN are still needed [22–25].

When compared to other routing categories, geographic-based routing protocols have been found to be the most scalable and efficient for UASN [26]. Nevertheless, the majority of these protocols need that nodes be aware of their three-dimensional position [27]. However, in the presence of mobility, locating nodes in large-scale mobile underwater sensor networks is a challenge. This is because the typical GPS-based approaches cannot operate in the water medium. Therefore, the localization is typically accomplished using expensive algorithms, which might cost additional energy expenditure and time [6, 28]. As a result, location unaware routing protocols are favored by the UASN.

3. Routing Protocols for the IoUT

According to the aforementioned challenges of underwater communication, the location unaware routing protocols are best suited for communication in the underwater part of the IoUT network. There have been various efficient location unaware routing protocols proposed [29]. However, only a few discussed the successful data delivery while maintaining the network connectivity and saving energy expenditure in the presence of nodes mobility in the IoUT communication.

One of the location unaware routing protocols proposed for underwater communication is depth-based routing (DBR) [30]. In the DBR protocol, the depth information collected by the pressure sensors is the only dimension used by the network nodes for data forwarding. The nodes forward data if the depth of the current node is less than that of the previous node. The DBR protocol improves the performance of the dynamic scenarios. However, it still suffers from void region handling and redundant forwarding with high energy consumption. To overcome the problem of energy efficiency in the DBR protocol, an Enhanced Energy Depth-Based Routing (EEDBR) protocol was proposed in [31]. In this protocol, a residual energy indicator is used to achieve energy balancing and efficiency. The authors of [32] proposed two variants to enhance the DBR protocol. The first variation (or protocol) is an energy efficient one that is developed to decrease the redundancy of forwarding in the multiple paths. The second variation is the directional depth which is developed to enhance the end-to-end delay. In the first protocol, energy efficiency is achieved by prohibiting the nodes in the void region from performing the forwarding process. Instead, these nodes use the time of arrival ranging technique to decide on nodes in void regions. Surely, this will add extra overhead. In the directional DBR protocol, the nodes use the depth and angle metrics in the holding time calculations to guide the packets forwarding toward a surface sink via an optimal route. Thus, the end-to-end delays are drastically decreased and the delivery ratio is enhanced as well. However, in both protocols, the redundancy is reduced but not eliminated and void region formation is handled via

expensive ranging technique in only one enhancement of the DBR protocol.

In [33], Adaptive Mobility of Courier nodes in Threshold-Optimized DBR (AMCTD) protocol is proposed. To reduce the number of forwarders, the AMCTD sets a predefined depth threshold for numerous nodes based on the network density. In addition, the AMCTD relies on a motorized movement of a set of courier nodes to handle void regions. Therefore, this protocol was not appropriate for data-sensitive applications. Hence, an Improved-AMCTD (I-AMCTD) protocol is developed in [34]. The I-AMCTD protocol minimizes the end-to-end delay by optimizing the mobility pattern of the sink. It also varies the depth threshold in order to increase the number of forwarders to minimize data loss and enhance the delivery ratio for delay-sensitive applications. However, like the AMCTD, the locations of courier nodes are mechanically adjusted and thus, extra overhead will take place.

A Delay-Sensitive Depth-Based Routing (DSDBR) protocol was proposed to solve the delay problem in the depth based routing schemes [35]. Here, the authors implement a delay sensitive holding time and a delay efficient priority factor. These factors reduce the end-to-end delay at an expense of lowering the throughput. Unfortunately, the DSDBR protocol was demonstrated only for static scenarios. In these scenarios, a time-consuming mechanical movement of courier nodes is used to bypass the void region.

Moreover, an Enhanced location unaware Channel Aware Routing Protocol (ECARP) was specifically proposed for the IoUT [36]. This protocol is an enhancement of the channel aware routing protocol [37]. The ECARP protocol uses the previously collected information to aid forwarders in the decision whether to forward the incoming packets or not. Forwarders in ECARP might select a previous-hop forwarder even if this hop is not the best. This selection is performed to cope with the mobility of the nodes. This protocol efficiently forwards useful packets and reduces energy consumption. In ECARP, the nodes are assumed to store sensory data and make a comparison before forwarding decisions. This comparison will add extra storage cost and processing overhead. Furthermore, the network nodes are expected to switch between two power levels to achieve the same bit error ratio for both control and data packets.

A localization-Free Interference and Energy Holes Minimization (LF-IEHM) routing protocol was proposed to overcome the energy hole problem in multihop routing [38]. The authors of [38] used the holding time to limit the interference between consecutive *Hello* packets for forwarders discovery. Further, a variable transmission range is used by the sensor node to select forwarders. However, this selection process relies on the sound pressure value. According to this value, a forwarder that is not in the direction of the surface sink might be selected. In addition, it is not clear how the transmission range of nodes varies. Needless to say, this range should be directly related to the acoustic modem power.

In [8], a shortest path routing protocol based on the vertical angle (SPRVA) is proposed. This protocol improves

both energy efficiency and the end-to-end delay by using the directional approach. This protocol is similar to the protocol we proposed as both use the directional approach. In the SPRVA protocol, the best forwarder is chosen according to the main priority which is indicated by the residual energy and the vertical angle between the propagation and the depth orientations. An alternative priority is utilized when the main priorities of the candidate nodes are equal. Reduced delivery ration in a sparse deployment is mitigated by implementing a recovery algorithm to bypass the nodes in void regions from participating in the forwarding process.

In an energy efficient routing approach for the IoUTs, researchers have used terrestrial based adaptive clustering protocols to enhance the delivery ratio and to reduce the energy consumption [39]. Here, an extension of a lifetime is achieved compared with the depth based routing. In general, the clustering approach provides energy balance, but it comes at a high cost in terms of communication overhead, especially, in mobile scenarios.

Authors in [40] introduced an opportunistic routing for optoacoustic IoUTs. They used the directional nature of light to guide the packet forwarding toward the surface sink. Unlike our proposed protocol, this protocol is applicable only for shallow and clear underwater communication.

The most recent proposed enhancement for the DBR protocol suggests using the variable power control protocol to bypass the routing voids [41]. However, the high energy consumption of this protocol has not been solved yet.

Taking routing decisions based on predicting mobility is proposed in [25, 42, 43]. However, in order to reduce the prediction error and obtain high efficiency, a huge input data should be recorded and analyzed by time consuming algorithms.

In our work, we consider the unique challenges of underwater environment while focusing on the application requirements for IoUTs. These requirements include increasing the delivery ratio and reducing the energy expenditure in both dense and sparse deployment. The proposed protocol is location unaware. In addition, it combines the directional and the selective power routing approaches in a three-dimensional mobile network to handle the void regions and maintain the connectivity.

4. A Directional Selective Power Routing Protocol for IoUT

The multihop routing protocols are the best candidate for an Underwater acoustic sensor network. They are usually developed based on geographical information [5]. In this kind of routing protocol, the exact location of nodes is a requirement. However, in the underwater environment, nodes location is obtained by running costly localization techniques [6]. The cost grows exponentially when the process of finding a location is frequently performed. For instance, in a dynamic environment, the nodes are susceptible to constant movement with water currents and thus finding their exact location at a certain moment seems difficult. In the proposed location unaware directional selective power routing the network connectivity is maintained by using the power

control and an optimized shortest path is selected based on the angle of arrival of acoustic signal.

4.1. Network Architecture. In the proposed protocol, we assume that an underwater network consists of one or N surface sinks: S_1, S_2, \dots, S_N . The surface sinks and the underwater nodes are both assumed to be equipped with an acoustic modem that is capable of switching to a set of k power levels. For instance, the power level of node i can be characterized as $Pl_i^k \in 1, 2, \dots, k$. At each power level, the acoustic signal can be correctly received and detected within a range specified by the acoustic modem characteristics and channel equations. All nodes are equipped with on-board arrays of multiple microphones to determine the arrival angle of the received acoustic signal [44].

The proposed routing protocol is subdivided into two phases; (1) the network setup phase where nodes assign themselves to a certain sink and select the minimum power level to choose a set of possible forwarders. (2) The network operation phase where the nodes use the initial settings and can switch back to renew their possible forwarders if the network is disconnected due to mobility or node failure.

4.2. Network Setup. During network setup, the sink node will broadcast a *Hello* packet using its maximum transmission power. A surface sink is usually equipped with an acoustic transmitter that can send at maximum transmission power to a distance of up to a few kilometers. The underwater nodes which received the *Hello* packet will record the angle of arrival (sinkAoA) of each received sink's along with its sinkID. Using this information, the underwater nodes will determine the relative directions toward each of the surface sinks. Consequently, the underwater nodes will use this information to determine the directional path toward the closest sink S_i that has the lowest vertical angle of arrival such as

$$S_i = \arg \min_{(t)} \|\theta_i - 90\|. \quad (1)$$

Figure 2 shows an illustration of the sink selection process. Here, a source node S receives two *Hello* packets from sink1 and sink2. Accordingly, it will select sink1 as its final destination since it has a lower arrival angle (i.e., $\theta_1 < \theta_2$).

4.3. Forwarder Discovery. The forwarder discovery step is performed initially after the network setup. This step will be repeated when a sender receive no acknowledgments (Acks) for data packets due to the network topology change. In this step, the sender nodes send *Hello* packets to select the best forwarders using their minimum transmission power and sets a timer to receive the acknowledgments. The timer is selected to slightly exceed the round trip time required for the acoustic signal to reach the furthest node in its range. The waiting time (wt_i) for each power level is defined by the following:

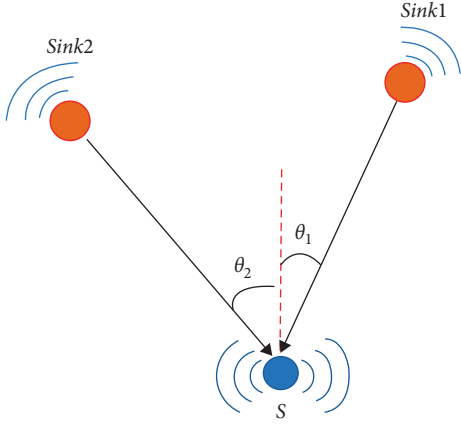


FIGURE 2: The source node S selects its destination as sink1.

$$wt_i = \frac{2R_i}{c} + \delta, \quad (2)$$

where R_i is the maximum distance at which an acoustic signal at a power level P_i can be correctly received and detected, c is the sound speed (1500 m/s), and δ is a marginal time added to slightly exceed the *Hello* packet transmission time.

Nodes receiving this *Hello* packet will reply with an Ack packet that includes the potential forwarder ID, its sinkAoA, and residual energy level. Each forwarder holds an indicator to the residual energy level. These levels range from 1 to 5 where 1 indicates the least power level, whereas 5 indicates the maximum. A sender node will calculate the Ack angle of arrival (ackAoA) and compare it with its sinkAoA. The senders will select the best possible forwarders based on two metrics: the angle of arrival difference for the Ack packet and the sink identification packet and the residual energy level of potential forwarders. If no Ack is received before the timer expires, the sender switch to a higher power level to find forwarders and will again select the best forwarders based on sinkAoA and ackAoA. This step is repeated until the nodes find the correct power level needed to find the candidate forwarders or until the maximum power level is reached. Figure 3 shows a sender S finds two possible forwarders when switching to the power level associated with range r_2 . S will then select between n_1 and n_2 based on the angle of arrival values and the residual energy level. It is worth mentioning that nodes will be disconnected if it cannot find neighbors at the highest available power level. Therefore, the number of power levels should be carefully selected.

4.4. Forwarder Selection. After the forwarder discovery step, each sender will maintain a table of possible forwarders with information extracted from the Ack packet including the forwarder ID, its ackAoA, and a residual energy indicator. The later information consists of multiple values where 1 and 5 values indicate very low and very high, respectively. When a sender has data to send, it will only look for forwarders

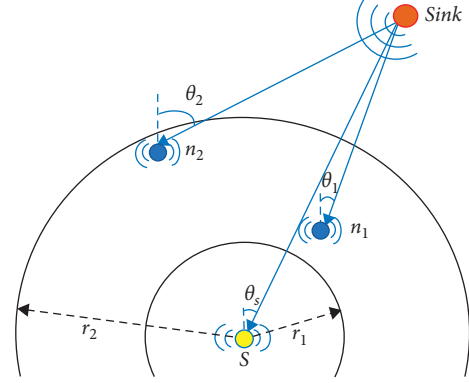


FIGURE 3: Two possible forwarders for node S at power range r_2 .

with residual energy indicators above 1. In addition, it will select the forwarder with the least difference between the possible forwarder ackAoA and the sender sinkAoA. This ensures the minimum directional path toward the sink. The residual energy indicator in the forwarder table will be updated with the forwarders information of the received Ack packets. If the residual energy of all forwarders is very low (say at 1), the discovery procedure will be triggered to look for another set of possible forwarders using a higher transmission power level.

4.5. Power Control Implementation. To obtain the relative power values for the selected communication ranges used by the underwater nodes, we used the acoustics path loss model presented in [45, 46]. The relation between the power level $P(l)$ values and the power spectral density (psd) of a transmitted acoustic signal $S_l(f)$ over the frequency bandwidth $B(l)$ is defined by the following:

$$P(l) = \int_{B(l)} S_l(f) df. \quad (3)$$

To simplify the calculation of the proposed protocol, we consider that $S_l(f)$ are flat over a narrow band bandwidth $B(l)$. So equation (3) becomes as follows:

$$P(l) = B(l)S_l(f). \quad (4)$$

In order for a signal to be correctly received and detected by an acoustics modem, the signal-to-noise ratio $\text{SNR}(l, f)$ should be greater than a modem specified threshold SNR_0 . This value is affected by the noise level $N(f)$, the attenuation level $A(l, f)$, and the psd of the signal level $S_l(f)$ that can be derived from equation (4). Therefore, $\text{SNR}(l, f)$ at a distance l and frequency f can be written as follows:

$$\text{SNR}(l, f) = \frac{P(l)}{(N(f)A(l, f)B(l))}. \quad (5)$$

The attenuation $A(l, f)$ can be obtained by applying equation (6) as follows:

$$A(l, f) = 10 \log\left(\frac{A(l, f)}{A_0}\right) = k.10 \log l + l.10 \log a(f), \quad (6)$$

where A_0 is a unit normalizing factor that represents fixed losses, $a(f)$ is the absorption coefficient, and k is the spreading factor defined as 1 for cylindrical, 2 for spherical, and 1.5 for practical spreading. The absorption coefficient is expressed using Thorp's formula that returns $a(f)$ in dB/km for f in kHz as follows:

$$a(f) = \frac{0.11f^2}{1 + f^2} + \frac{44f^2}{4100 + f^2} + \frac{2.75f^2}{1000 + f^2} + 0.003. \quad (7)$$

Additionally, the noise level $N(f)$ is a combination of different kind of noise such as the ambient noise which is caused by shipping $N_s(f)$, the waves noise which is caused by wind $N_w(f)$, the turbulence noise $N_t(f)$, and the thermal noise $N_{th}(f)$. Equations (8) to (11) listed below calculate each individual noise as follows:

$$10 \log_{10} N_s(f) = 40 + 20(s - 0.5) + 26 \log_{10} f + 60 \log_{10}(f + 0.03), \quad (8)$$

$$10 \log_{10} N_w(f) = 50 + 7.5\sqrt{w} + 20 \log_{10} f - 40 \log_{10}(f + 0.4), \quad (9)$$

$$10 \log_{10} N_t(f) = 17 - 30 \log_{10} f, \quad (10)$$

$$10 \log_{10} N_{th}(f) = -15 + 20 \log_{10} f. \quad (11)$$

The $N(f)$ noise can now be computed in log scale by adding equations (8) to (11). It is worth noting that, for the deep marine environment, the $N(f)$ noise can be approximated as follows:

$$10 \log_{10} N(f) = 50 - 18 \log_{10} f. \quad (12)$$

As we are interested in finding the required power level needed to be detected at a distance l , we can rewrite equation (4) in the following form:

$$P(l) = \text{SNR}(l, f)N(f)A(l, f)B(l). \quad (13)$$

The signal-to-noise ratio should be greater than an acoustic modem specified threshold SNR_0 to detect and decode correctly. Substituting $S_l(f)$ from equation (13) into (4) gives the required acoustic power as follows:

$$P(l) \approx \text{SNR}_0 B_3(l) \frac{N(f)}{A^{-1}(l, f)}. \quad (14)$$

In acoustic communication, the transducer of an acoustic modem changes the electrical power Pt in watt to an acoustic sound power in micro-Pascal (μPa). The electrical power of an acoustic modem is a function of the modem efficiency and the acoustic power $P(l)$ needed to cover a distance l . Since no transducer is 100% efficient, the acoustic power is reduced by the transducer efficiency η . The relationship between the electrical power and the acoustic power needed to cover a distance l is defined by the following:

$$10 \log(\eta Pt(l)) = 170.8 - 10 \log P(l) + \text{DI}, \quad (15)$$

where 170.8 is a conversion factor between electric power and acoustic power. DI is the directivity index of the antenna, which is equal to zero for the omnidirectional antenna.

5. Performance Evaluation

To evaluate the proposed routing strategy, we have conducted extensive simulations for different static and mobile scenarios. In all simulation scenarios, the nodes are assumed to be uniformly distributed within $1 \text{ km} \times 1 \text{ km} \times 1 \text{ km}$ three dimensional topology. We also adopted the power settings used in EvoLogic acoustic modem [47]. Nodes are able to set their transmission power P_{tx} to a set of values between 5.5 watt and 10.2 watt that is associated with a set of four communication ranges 250 m, 350 m, 500 m, and 650 m. Equation (14) is used to find the transmission power used at each range. The power value for receiving one bit of information has been set to $P_{rx} = 0.8$ watt. The bit error ratio of acoustic modem has also been set to 10^{-9} . The data packet size is 512 bits and the data rate is 30 kbps. The receiver minimum signal-to-noise ratio is $\text{SNR}_0 = 30$ dB. The underlying MAC protocol has been used as the underwater broadcast MAC. We measured the average end-to-end delays of all packets generated throughout the whole simulation time which was fixed at 1200 s. The per bit energy consumption is defined by the total consumed power over the total number of delivered data bits. In addition, the total energy consumption is the sum of all energy dissipated by all nodes. The delivery ratio is calculated as the total number of packets submitted successfully to the sink node over the total number of packets generated by all source nodes.

5.1. Static Scenarios. Here, we evaluate the performance of the proposed directional selective power protocol. A comparison between the performance of the proposed protocol and that of the VDBR protocol is performed. We also compare the performance of the proposed protocol with that of the other two versions of a directional fixed power routing using two ranges (500 m and 250 m). The two aforementioned ranges represent two cases where a low range at 250 m is suitable for dense networks, and the 500 m works best to maintain connectivity for the sparse networks. Figure 4 shows the delivery ratio for the fixed directional routing at the range of 250 m (DR250). Here, one can see that the delivery ratio is between 20% and 45%. In addition, the achieved ration almost doubled to that of RD250 when increasing the power range to 500 m (DR500). A fixed low communication range (i.e., DR250) requires a dense network to maintain the network connectivity and hence achieves a high delivery ratio. However, the VDBR and DSPR protocols have a very high delivery ratio above 92% for all node densities. Furthermore, the VDBR protocol achieves a slightly better delivery ratio than the DSPR one. This is due to the nature of the depth based routing, which allows multiple forwarders at each step to acquire higher delivery probability. As a result, the power consumption is drastically increased.

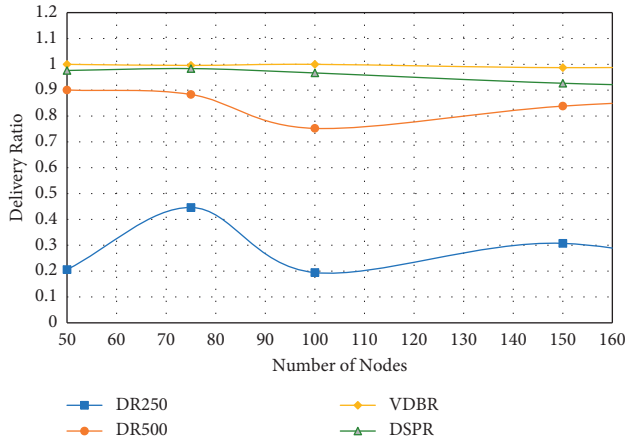


FIGURE 4: Delivery ratio, one sink, static scenario.

Figure 5 shows the end-to-end delays for one sink with varying nodes density. The data packets in the DBR250 and VDBR reach the surface sinks in less time than that of DR500 and DSPR by about 0.2 seconds. This is due to the fact that the depth based routing protocols do not employ retransmissions for dropped packets and hence data is delivered faster with no delays. In the DR250, the delivery is scarce, and it happens only when a sender finds one forwarder within 250 m. Therefore, the probability of collisions that triggers the time-consuming retransmissions in DR500 is lowered in DR250. In the DSPR, the extra delay is due to the time needed to exchange the control packet for the forwarder and the power range selection. As a result, for the time sensitive applications, the VDBR protocol is rather to be used in favour of the DSPR protocol.

Although the VDBR protocol shows a relatively low end-to-end delay and high delivery ratio, the energy expenditure is extremely high. Table 2 shows that the energy consumption by the VDBR protocol is around 8 times higher than that of the DSPR protocol when the number of nodes is 50. Moreover, the energy consumption is 15.7 times higher than that at 200 nodes. This excessive energy expenditure is due to the flooding of multiple copies of the same packet when the number of nodes in the network increases. In the directional scenarios, we limit the maximum number of nodes that can participate in the forwarding process to two nodes. Each node keeps a record of the forwarded packet IDs to forbid forwarding the same packet twice. Thus, the unnecessary forwarding is reduced in the DBR protocol.

Figure 6 also shows that using the selective power routing achieves considerably better energy savings than that of both fixed case scenarios at the 250 m range for both high and low node densities with more than 40% savings. The per bit energy saving achieved by the DSPR protocol is more than 25% compared to the DR500 when the node densities get high.

The proposed routing protocol has also been illustrated with four sinks. Similarly, the proposed protocol achieves a noticeable enhancement in both energy and delivery ratios. Figure 7 shows that the DR500, VDBR, and DSPR protocols delivery ratios are always above 90%. However, the DR250

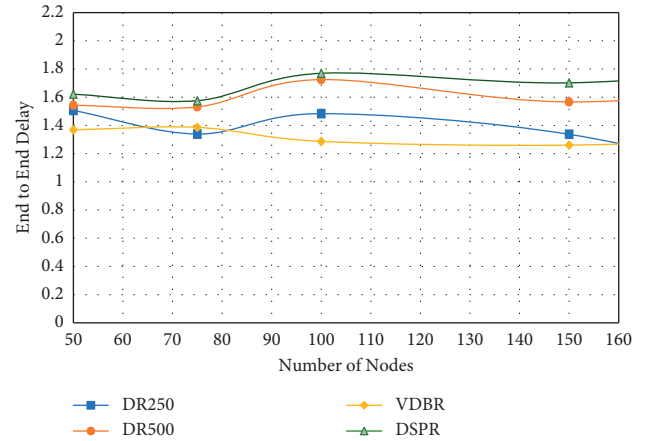


FIGURE 5: The end-to-end delay, one sink, static scenario.

TABLE 2: Per bit energy consumption VDBR vs DSPR.

Routing scheme	Per bit energy 10^{-3} joule		
	at 50 node	at 100 node	at 200 node
VDBR	18.50	32.47	51.04
DSPR	2.22	2.44	3.23

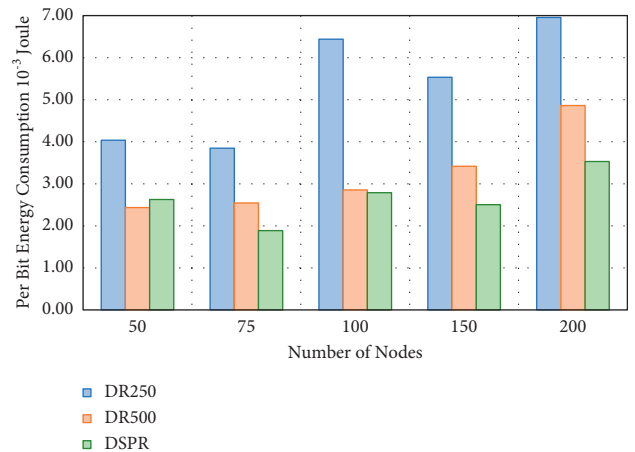


FIGURE 6: Per bit energy consumption, one sink, static scenario.

protocol achieves a very low delivery ratio. This is because of the limited communication range where the senders can rarely find forwarders. When we increase the number of nodes (i.e., higher nodes densities), the probability of finding forwarders increases, and hence the delivery ratio increases to 46% at 150 nodes.

Figure 8 shows the end-to-end delay with four sinks. One can see that the end-to-end delay is slightly less than that for one sink architecture. This is because having more sinks will lead to shortening the distances from the underwater nodes to the surface and thus reducing the propagation delays. The other forms of delay are a result of control message exchange and packet retransmissions that slows the directional routing protocol compared to the VDBR.

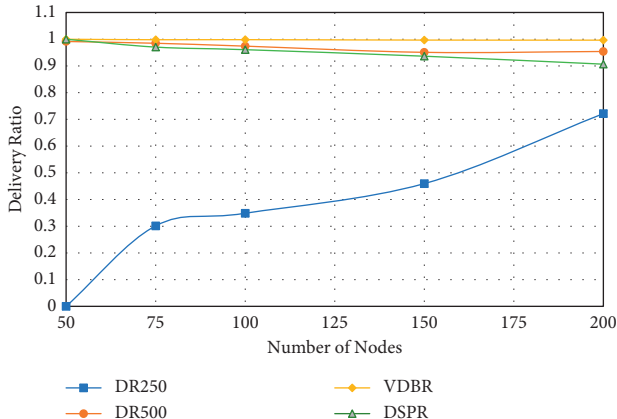


FIGURE 7: Delivery ratio, four sinks, static scenario.

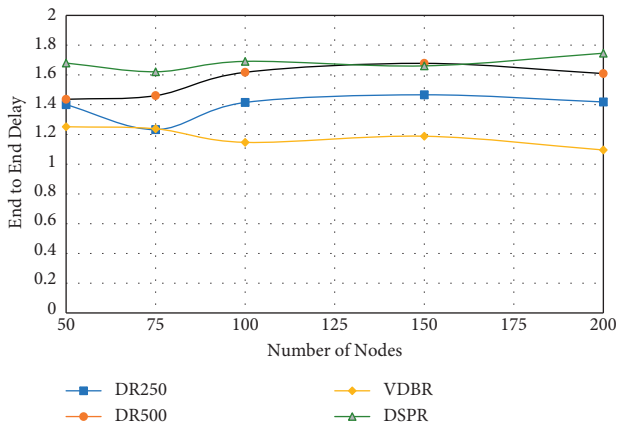


FIGURE 8: The end-to-end delay, four sinks, static scenario.

The energy expenditure is reduced when using multiple sinks architecture as shown in Figure 9. DSPR is also shown to outperforms both fixed directional routing techniques at DR250 and DR500. More than 20% saving is obtained when number of nodes greater than 150. This results from the fact that in DSPR, nodes tends to use lowest power level needed to reach forwarders. At low densities energy saving in DR500 is almost the same as in DSPR since both strategies tend to use the same power range at 500 m and hence will consume same amount of power.

5.2. Mobility Consideration. We ran a set of more experiments to test our technique against directional routing in dynamic scenarios. For modeling the node mobility, we adopted the a tidal mobility model where tidal and residual current fields are used for determining the composite current field. The residual current field is assumed to be an infinite sequence of clockwise and anticlockwise spinning eddies, and the tidal field is assumed to be a spatially uniform oscillating current in one direction [23]. In this model, the velocity fields in the x and y directions field are approximated by using the kinematic model as follows:

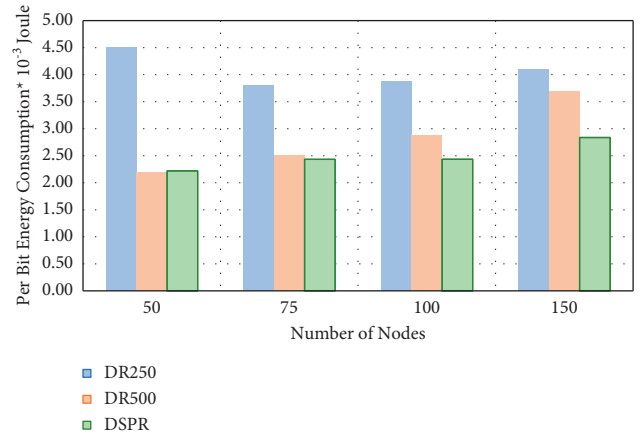


FIGURE 9: Per bit energy consumption, four sinks, static scenario.

$$\begin{aligned}
 V_x &= k_1 \lambda v \sin e(k_2 x) \cos(k_3 y) + k_1 \lambda \cos(2k_1 t) + k_4, \\
 V_y &= -\lambda v \cos(k_2 x) \sin(k_3 y) + k_5,
 \end{aligned}
 \tag{16}$$

where V_x and V_y are the speed in the x and y directions. k_1, k_2, k_3, k_4, k_5 and λ are parameters related to water environment factors including bathymetry and tides. In our simulations, we used the settings for deep underwater environments as in [22] with an underwater node speed in the range of 1–5 m/s. In DR250 and due to limited communication range, senders can rarely find forwarders at low node densities. In fixed scenarios delivery ratio is less than 46% when the number of nodes is less than 150. When the network is mobile, forwarders keep moving and get out of senders’ range. Senders with fixed low power range will suffer updating their forwarding list and the delivery ration will drop more. Figure 10 shows that for a mobile network, the delivery ratio in fixed directional power cases is less than 10% at the 250 m range and is less than 68% when using the 500 m range. On the other hand, the delivery ratio in DSPR is just slightly lower than that found in a static network situation and remains over 90% when varying node density. As a result, DSPR is best suited for mobile scenarios since it improves network connectivity significantly compared to fixed directional routing strategies.

The energy consumption is also advantageous in the DSPR protocol with more than 80% and 30% saving compared to the DR250 and the DR500, respectively, as shown in Figure 11. The extra energy expenditure in the DR250 protocol results from increasing the number of hops. Thus, more nodes use lower power levels to participate in the data packet forwarding. In the DR500 protocol, the collision domain is high and the extra energy is consumed because of the retransmissions. Therefore, selecting the best power level shows an advantage over the other two variations of directional routing. This is because the usage of the correct power level is chosen in accordance with forwarders availability.

The advantage of DSPR over other tested static strategies and the VDBR was also clear when finding total energy consumption by nodes. Our simulation results showed a much higher energy expenditure of dynamic case VDBR

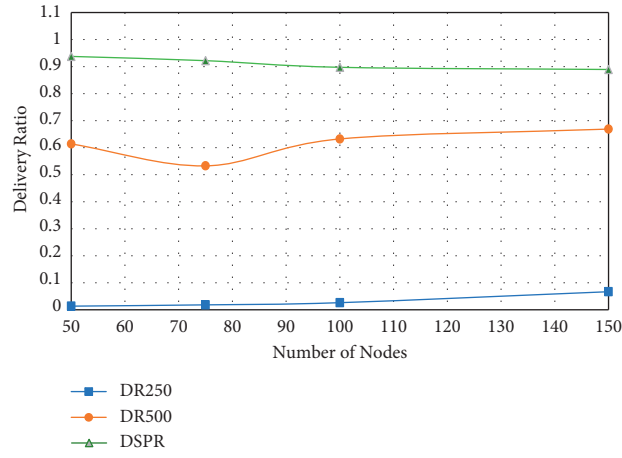


FIGURE 10: Delivery ratio, mobile scenario.

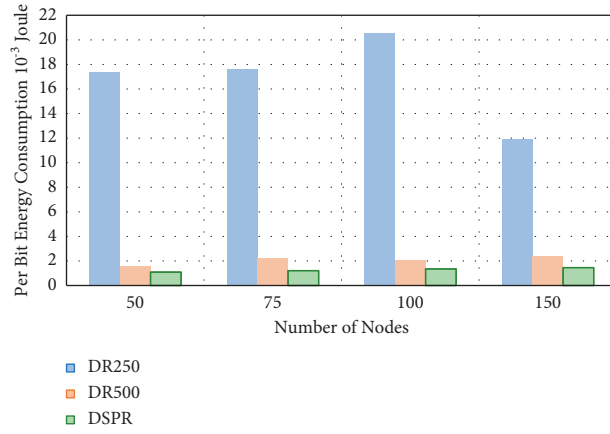


FIGURE 11: Per bit energy consumption, mobile scenario.

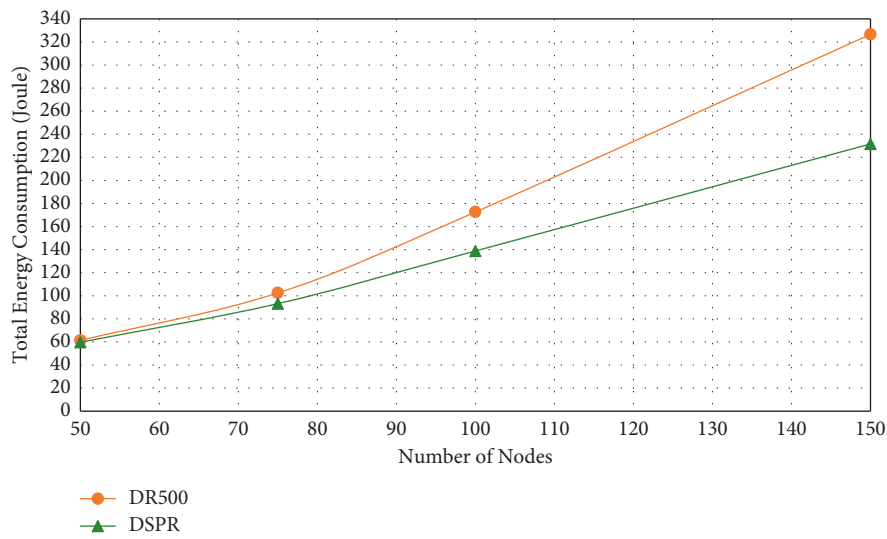


FIGURE 12: Total energy consumption, mobile scenario.

than that for the static case VDBR as shown previously in Table 2. The energy expenditure, in this case, was at least 20 times more than the dynamic case of our proposed DSPR. On the other hand, very low energy consumption was found with fixed directional routing DR250. This is due to the fact no energy is consumed in sending data packets as forwarders are not actually found at this low range. Therefore, in this case, we only compare DSPR with DR500 since they tend to have a comparable delivery ratio. Figure 12 shows that the total energy expenditure is reduced when the network becomes denser as nodes tend to use lower power levels to reach forwarders. Therefore, collisions and retransmissions are reduced and the network lifetime is enhanced.

6. Conclusion

In this paper, we focused our attention on the issues and challenges that affect the protocol design for the underwater part of IoUT network. Increasing reliability by maintaining connectivity and conserving energy are of the most important requirements for efficient communication in a dynamic underwater environment. The unique challenges imposed by the characteristics of the underwater communication channel have impacted the underwater routing performance. To overcome these challenges, we proposed a directional selective power technique that is location-free, robust to mobility, and energy efficient. In the proposed technique, we acquire the simplicity of sender-based angle of arrival forwarding decision with a practical power control implementation of an acoustic modem. The senders in the proposed protocol select the best forwarder in the direction of the nearest sink via directional routing. In addition, the sender nodes can switch to use a higher power level when the network is sparse. This will help the acoustic signal to traverse higher distances to locate the most suited forwarders. Hence, a forwarder is guaranteed to be found with the least possible power level to reduce the energy expenditure and maintain network connectivity. Extensive simulations show enhancements over other protocols regarding energy expenditure and delivery ratio for both static and mobile scenarios, dense or sparse networks, and with one or multiple surface sink architectures. However, a slight increase in the end-to-end delays is observed as an overhead of switching to the correct power level and increasing the number of hops. In future work, an optimization of the number of power levels is to be conducted to further reduce energy expenditure and to avoid transmission delay overhead.

Data Availability

The data used to support the findings of this study are included within the article.

Conflicts of Interest

The authors declare that they have no conflicts of interest.

References

- [1] C.-C. Kao, Y.-S. Lin, G.-D. Wu, and C.-J. Huang, "A comprehensive study on the internet of underwater things: applications, challenges, and channel models," *Sensors*, vol. 17, no. 7, p. 1477, 2017.

- [2] D. Anguita, D. Brizzolara, and G. Parodi, "Building an underwater wireless sensor network based on optical: communication: research challenges and current results," in *Proceedings of the 2009 Third International Conference on Sensor Technologies and Applications*, Athens, Greece, June 2009.
- [3] L. Liu, S. Zhou, and J.-H. Cui, "Prospects and problems of wireless communication for underwater sensor networks. wiley wcmc special issue on underwater sensor networks," *Wireless Communications and Mobile Computing*, vol. 8, pp. 977–994, 2008.
- [4] M. C. Domingo, "Magnetic induction for underwater wireless communication networks," *IEEE Transactions on Antennas and Propagation*, vol. 60, no. 6, pp. 2929–2939, 2012.
- [5] D. E. Lucani, M. Stojanovic, and M. Medard, "On the relationship between transmission power and capacity of an underwater acoustic communication channel," in *Proceedings of the OCEANS 2008 - MTS/IEEE Kobe Techno-Ocean*, April 2008.
- [6] G. Tuna and V. C. Gungor, "A survey on deployment techniques, localization algorithms, and research challenges for underwater acoustic sensor networks," *International Journal of Communication Systems*, vol. 30, no. 17, Article ID e3350, 2017.
- [7] P. Xu, B. Yan, and S. Hu, "DOA estimation of multiple sources in sparse space with an extended array technique," *Cluster Computing*, vol. 19, no. 3, pp. 1437–1447, 2016.
- [8] M. Li, X. Du, X. Liu, and C. Li, "Shortest path routing protocol based on the vertical angle for underwater acoustic networks," *Journal of Sensors*, vol. 2019, pp. 1–14, 2019.
- [9] M. A. Bzoor, Y. Zhu, J. Liu, R. Ammar, J. H. Cui, and S. Rajasekaran, "An adaptive power controlled routing protocol for underwater sensor network," *International Journal of Sensor Networks*, vol. 18, no. 3/4, pp. 238–249, 2015.
- [10] Z. Fang, J. Wang, J. Du, X. Hou, Y. Ren, and Z. Han, "Stochastic optimization aided energy-efficient information collection in internet of underwater things networks," *IEEE Internet of Things Journal*, vol. 9, no. 3, pp. 1775–1789, 2022.
- [11] Z. Hong, X. Pan, P. Chen, X. Su, N. Wang, and W. Lu, "A topology control with energy balance in underwater wireless sensor networks for iot-based application," *Sensors*, vol. 18, no. 7, p. 2306, 2018.
- [12] M. Barbeau, J. Garcia-Alfaro, E. Kranakis, and S. Porretta, "The sound of communication in underwater acoustic sensor networks," in *Ad Hoc Networks*, pp. 13–23, Springer International Publishing, Berlin, Germany, 2018.
- [13] Z. Fang, J. Wang, C. Jiang, Q. Zhang, and Y. Ren, "AoI-inspired collaborative information collection for AUV-assisted internet of underwater things," *IEEE Internet of Things Journal*, vol. 8, no. 19, pp. 14559–14571, 2021.
- [14] N. Iruthayanathan, V. K. Srinivasan, V. Rajendran, and R. Palanimurugan, "Mitigating ambient noise and multipath propagation in underwater communication using the DSTTD-OFDM system," *Computers & Electrical Engineering*, vol. 53, pp. 409–417, 2016.
- [15] D. Pompili, T. Melodia, and I. F. Akyildiz, "Deployment analysis in underwater acoustic wireless sensor networks," in *Proceedings of the 1st ACM International Workshop on Underwater Networks*, ser. WUWNet '06, ACM International Workshop on Underwater Networks, pp. 48–55, Association for Computing Machinery, New York, NY, USA, 2006.
- [16] S. Ibrahim, M. Al-Bzoor, J. Liu, R. Ammar, S. Rajasekaran, and J.-H. Cui, "General optimization framework for surface

- gateway deployment problem in underwater sensor networks,” *EURASIP Journal on Wireless Communications and Networking*, vol. 2013, no. 1, p. 128, 2013.
- [17] B. Liu, F. Ren, C. Lin, Y. Yang, R. Zeng, and H. Wen, “The redeployment issue in underwater sensor networks,” in *Proceedings of the Global Telecommunications Conference, 2008. IEEE GLOBECOM 2008*, pp. 1–6, IEEE, New Orleans, LA, USA, December 2008.
 - [18] J. Liu, W. Guan, G. Han, J. H. Cui, L. Fiondella, and M. Al-Bzoor, “A dynamic surface gateway placement scheme for mobile underwater networks,” *Sensors*, vol. 19, no. 9, 2019.
 - [19] A. Serhani, N. Naja, and A. Jamali, “AQ-routing: mobility-, stability-aware adaptive routing protocol for data routing in MANET-IoT systems,” *Cluster Computing*, vol. 23, no. 1, pp. 13–27, 2020.
 - [20] S. Beerens, H. Ridderinkhof, and J. Zimmerman, “An analytical study of chaotic stirring in tidal areas,” *Chaos, Solitons & Fractals*, vol. 4, no. 6, pp. 1011–1029, 1994.
 - [21] A. Caruso, F. Paparella, L. F. M. Vieira, M. Erol, and M. Gerla, “The meandering current mobility model and its impact on underwater mobile sensor networks,” in *Proceedings of the IEEE INFOCOM 2008 - The 27th Conference on Computer Communications, ser. IEEE INFOCOM 2008, The 27th Conference on Computer Communications*, pp. 221–225, IEEE, Phoenix, AZ, USA, April 2008.
 - [22] Z. Zhou, Z. Peng, J.-H. Cui, Z. Shi, and A. Bagtzoglou, “Scalable localization with mobility prediction for underwater sensor networks,” *IEEE Transactions on Mobile Computing*, vol. 10, no. 3, pp. 335–348, 2011.
 - [23] Y. Zhang, J. Liang, S. Jiang, and W. Chen, “A localization method for underwater wireless sensor networks based on mobility prediction and particle swarm optimization algorithms,” *Sensors*, vol. 16, no. 2, p. 212, 2016.
 - [24] M. Dong, H. Li, R. Yin, Y. Qin, and Y. Hu, “Scalable asynchronous localization algorithm with mobility prediction for underwater wireless sensor networks,” *Chaos, Solitons & Fractals*, vol. 143, Article ID 110588, 2021.
 - [25] G. J. Alqahtani and F. Bouabdallah, “Energy-efficient mobility prediction routing protocol for freely floating underwater acoustic sensor networks,” *Frontiers in Communications and Networks*, vol. 2, 2021.
 - [26] Z. Wan, S. Liu, W. Ni, and Z. Xu, “An energy-efficient multi-level adaptive clustering routing algorithm for underwater wireless sensor networks,” *Cluster Computing*, vol. 22, no. 56, pp. 14651–14660, 2019.
 - [27] R. Coutinho and A. Boukerche, “Data collection in underwater wireless sensor networks: research challenges and potential approaches,” in *Proceedings of the 20th ACM International Conference on Modelling, Analysis and Simulation of Wireless and Mobile Systems*, vol. 11, pp. 5–8, Miami, FL, USA, 2017.
 - [28] M. Jouhari, K. Ibrahim, H. Tembine, and J. Ben-Othman, “Underwater wireless sensor networks: a survey on enabling technologies, localization protocols, and internet of underwater things,” *IEEE Access*, vol. 7, pp. 96879–96899, 2019.
 - [29] K. M. Awan, P. A. Shah, K. Iqbal, S. Gillani, W. Ahmad, and Y. Nam, “Underwater wireless sensor networks: a review of recent issues and challenges,” *Wireless Communications and Mobile Computing*, vol. 2019, Article ID 6470359, 20 pages, 2019.
 - [30] H. Yan, Z. J. Shi, and J.-H. Cui, “Dbr: depth-based routing for underwater sensor networks,” in *Networking 2008 Ad Hoc and Sensor Networks, Wireless Networks, Next Generation Internet, ser. Lecture Notes Computer Science*, vol. 4982, pp. 72–86, Springer, Berlin, Heidelberg, 2008.
 - [31] A. Wahid, S. Lee, H.-J. Jeong, and D. Kim, “EEDBR: energy-efficient depth-based routing protocol for underwater wireless sensor networks,” in *Communications in Computer and Information Science*, pp. 223–234, Springer, Berlin, Heidelberg, 2011.
 - [32] B. Diao, Y. Xu, Z. An, F. Wang, and C. Li, “Improving both energy and time efficiency of depth-based routing for underwater sensor networks,” *International Journal of Distributed Sensor Networks*, vol. 2015, Article ID 781932, 9 pages, 2015.
 - [33] M. Jafri, S. Ahmed, N. Javaid, Z. Ahmad, and R. Qureshi, “Adaptive mobility of courier nodes in threshold-optimized DBR protocol for underwater wireless sensor networks,” in *Proceedings of the 2013 Eighth International Conference on Broadband and Wireless Computing, Communication and Applications*, October 2013.
 - [34] N. Javaid, M. R. Jafri, Z. A. Khan, U. Qasim, T. A. Alghamdi, and M. Ali, “iAMCTD: improved adaptive mobility of courier nodes in threshold-optimized DBR protocol for underwater wireless sensor networks,” *International Journal of Distributed Sensor Networks*, vol. 10, no. 11, Article ID 213012, 2014.
 - [35] N. Javaid, M. R. Jafri, S. Ahmed et al., “Delay-sensitive routing schemes for underwater acoustic sensor networks,” *International Journal of Distributed Sensor Networks*, vol. 11, no. 3, Article ID 532676, 2015.
 - [36] Z. Zhou, B. Yao, R. Xing, L. Shu, and S. Bu, “E-carp: an energy efficient routing protocol for uwsns in the internet of underwater things,” *IEEE Sensors Journal*, vol. 16, no. 11, pp. 4072–4082, 2016.
 - [37] S. Basagni, C. Petrioli, R. Petrocchia, and D. Spaccini, “CARP: a Channel-aware routing protocol for underwater acoustic wireless networks,” *Ad Hoc Networks*, vol. 34, pp. 92–104, 2015.
 - [38] A. Khan, I. Ahmedy, M. Anisi et al., “A localization-free interference and energy holes minimization routing for underwater wireless sensor networks,” *Sensors*, vol. 18, no. 2, p. 165, 2018.
 - [39] N. Usman, O. Alfandi, S. Usman et al., “An energy efficient routing approach for IoT enabled underwater WSNs in smart cities,” *Sensors*, vol. 20, no. 15, p. 4116, 2020.
 - [40] A. Celik, N. Saeed, B. Shihada, T. Y. Al-Naffouri, and M.-S. Alouini, “Opportunistic routing for opto-acoustic internet of underwater things,” *IEEE Internet of Things Journal*, vol. 9, no. 3, pp. 2165–2179, 2022.
 - [41] M. Al-Bzoor, T. Gharaibeh, and O. Ai-Ta’ani, “Avoiding routing voids with selective transmission power in underwater wireless sensor networks,” in *Proceedings of the 2021 IEEE Jordan International Joint Conference on Electrical Engineering and Information Technology (JEEIT)*, November 2022.
 - [42] M. R. Jafri, M. M. Sandhu, K. Latif, Z. A. Khan, A. U. H. Yasar, and N. Javaid, “Towards delay-sensitive routing in underwater wireless sensor networks,” *Procedia Computer Science*, vol. 37, pp. 228–235, 2014.
 - [43] A. Umar, N. Javaid, A. Ahmad et al., “DEADS: depth and energy aware dominating set based algorithm for cooperative routing along with sink mobility in underwater WSNs,” *Sensors*, vol. 15, no. 6, pp. 14458–14486, 2015.
 - [44] E. Dubrovinskaya, V. Kebkal, O. Kebkal, K. Kebkal, and P. Casari, “Underwater localization via wideband direction-of-arrival estimation using acoustic arrays of arbitrary shape,” *Sensors*, vol. 20, no. 14, p. 3862, 2020.
 - [45] M. Stojanovic, “On the relationship between capacity and distance in an underwater acoustic communication channel,” *ACM Sigmobile-Mobile Computing and Communications Review*, vol. 11, no. 4, pp. 34–43, 2007.

- [46] H. U. Yildiz, V. C. Gungor, and B. Tavli, "Packet size optimization for lifetime maximization in underwater acoustic sensor networks," *IEEE Transactions on Industrial Informatics*, vol. 15, no. 2, pp. 719–729, 2019.
- [47] Evologic, "Evologics underwater acoustic modems," 2021, <https://evologics.de/acoustic-modems>.

Research Article

MuLSi-Co: Multilayer Sinks and Cooperation-Based Data Routing Techniques for Underwater Acoustic Wireless Sensor Networks (UA-WSNs)

Munsif Ali,¹ Sahar Shah ,² Mahnoor Khan ,³ Ihsan Ali ,⁴ Roobaea Alroobaea ,⁵ Abdullah M. Baqasah,⁶ and Muneer Ahmad ⁷

¹Department of Information Technologies, University of Parma, Italy

²School of Physics and Electronics, Central South University, Changsha, China

³Department of Physics, Government Post Graduate College Nowshera, Pakistan

⁴Department of Computer System and Technology Faculty of Computer Science and Information Technology Universiti Malaya, Kuala Lumpur, Malaysia

⁵Department of Computer Science, College of Computers and Information Technology, Taif University, P. O. Box 11099, Taif 21944, Saudi Arabia

⁶Department of Information Technology, College of Computers and Information Technology, Taif University, P. O. Box 11099, Taif 21944, Saudi Arabia

⁷School of Electrical Engineering and Computer Science (SECS), National University of Sciences and Technology (NUST), Sector H-12, Islamabad, Pakistan

Correspondence should be addressed to Ihsan Ali; ihsanalichd@siswa.um.edu.my

Received 14 October 2021; Revised 15 December 2021; Accepted 20 December 2021; Published 15 January 2022

Academic Editor: Hamada Esmail

Copyright © 2022 Munsif Ali et al. This is an open access article distributed under the Creative Commons Attribution License, which permits unrestricted use, distribution, and reproduction in any medium, provided the original work is properly cited.

Designing an efficient, reliable, and stable algorithm for underwater acoustic wireless sensor networks (UA-WSNs) needs immense attention. It is due to their notable and distinctive challenges. To address the difficulties and challenges, the article introduces two algorithms: the multilayer sink (MuLSi) algorithm and its reliable version MuLSi-Co using the cooperation technique. The first algorithm proposes a multilayered network structure instead of a solid single structure and sinks placement at the optimal position, which reduces multiple hops communication. Moreover, the best forwarder selection amongst the nodes based on nodes' closeness to the sink is a good choice. As a result, it makes the network perform better. Unlike the traditional algorithms, the proposed scheme does not need location information about nodes. However, the MuLSi algorithm does not fulfill the requirement of reliable operation due to a single link. Therefore, the MuLSi-Co algorithm utilizes nodes' collaborative behavior for reliable information. In cooperation, the receiver has multiple copies of the same data. Then, it combines these packets for the purpose of correct data reception. The data forwarding by the relay without any latency eliminates the synchronization problem. Moreover, the overhearing of the data gets rid of duplicate transmissions. The proposed schemes are superior in energy cost and reliable exchanging of data and have more alive and less dead nodes.

1. Introduction

The network structure, reliability, and energy efficiency play an important role in the algorithm designing for UA-WSNs due to its tremendous applications and crucial challenges. A reliable, stable, and efficient algorithm with good network formation is used for many applications, such as military

operations, mission, time, and data critical situations, locating and directing submarines and examining oil pipelines and cables [1, 2]. Moreover, addressing the unique and critical challenges during designing such an algorithm gets stringent attention of the researchers and academia. The acoustic communication amongst nodes tends to extreme latency than the optical and radio communication [3]. But

optical and radio communication is not feasible for these networks. It is because of the scattering and absorption of these waves [4]. Attaining the location information of the nodes is also challenging due to the constraint of the global position system (GPS) in the water. It is due to the working of GPS on radio waves [5, 6]. Another way of getting location information is complex simulations. However, this is time and energy consuming, which also introduces computational complexity [7]. Moreover, nodes' movement with water waves degrades the reliable and efficient operation of the algorithm [8]. Furthermore, energy-efficient operations are required due to the constraint of energy. The replacement and energizing of the nodes are hard [9]. The noisy environment in these networks also reduces reliable data exchanging between nodes. These challenges are given in Figure 1. Due to the mentioned reasons, limitations, and challenges, a good algorithm is required for operation of these networks.

Cooperative communication is the best solution in these networks to achieve reliable communication amongst the nodes and reduces data failure. The data advancement through multiple paths towards the destination for increasing the chances of correct data reception is called cooperation [10]. The data advancement every time by the relay for data reliability is called fixed cooperation. While in the incremental cooperation, the delivery is done when the receiver demands from it. Before advancing data to the forwarder/receiver, either it is boosted or decoded by the relay. Based on relay behavior, it is named as amplify forward (AF) and decode forward (DF) [11]. The DF is complex in computation than AF. The cooperative algorithms obtain greater data reception and less packet drop. However, excessive energy and time consumption make these challenging and difficult. In the case of acoustic waves, it is more challenging because of energy resources and the low speed of communication.

In noncooperative algorithms, delivery through a single link consumes less energy and time than cooperative techniques. However, these algorithms are not reliable and have greater chances of packets loss [12]. A small obstacle may lead to data loss and failure. Moreover, noise sources also cause data corruption and have greater effects on data loss in noncooperative algorithms. The retransmission mechanism is not a suitable choice for data reception again over the same noisy link. Also, multiple antennas are costly and not feasible in underwater [13]. Cooperation is the best choice to achieve reliable and good communication in UA-WSNs.

The network structure has greater effects on routing performance, especially in UA-WSNs. Poorly designed network leads to bad performance, while a well-designed network structure improves the results and performance. Furthermore, sink placement plays an important role in algorithm efficiency. Sink placement at the best position tends to perform enhancement. Many algorithms such as [14–17] designed network in a single solid structure and placed the sink on the top. Placement of the sink on such positions leads to high and imbalance data load. The high load tends to traffic congestion and data collision. The collision causes

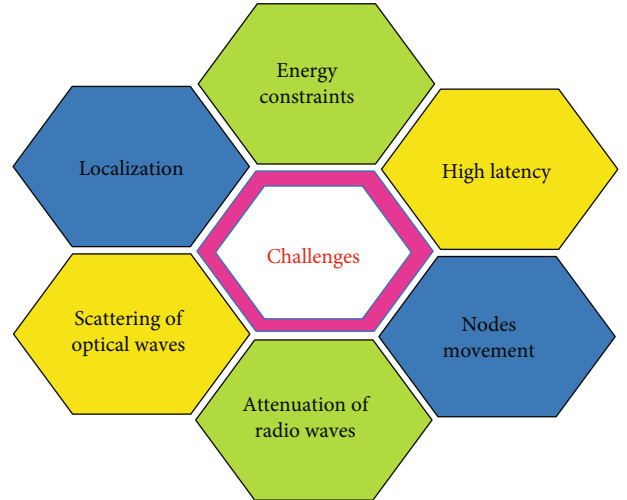


FIGURE 1: Challenges in UA-WSNs.

the packets to drop and forwards data with greater latency. Moreover, the life of the nodes near to the sink is less compared to the other nodes which are far away from the sink.

Many cooperative algorithms exist in the literature [18–24]. Some of the existing cooperative algorithms, such as [25–27], are reliable but they compromise on energy, which leads to less stability and reduces the life of the network. In the case of poorly designed network architecture in cooperative algorithms, its stability is further reduced. Data and time synchronization are other issues in these algorithms. The nodes near to the sink have the highest data traffic. This traffic creates issues, like data collision, a greater amount of energy cost, and high time consumption.

Considering the aforementioned challenges and difficulties, the article proposes two carefully designed algorithms. The first one is the MuLSi algorithm, and the second one is its extended version using the cooperation methodology for reliability enhancement of the MuLSi algorithm. The MuLSi technique proposes a network structure in layers instead of a single solid structure. The sinks are placed in the middle of each layer to reduce the multihop communication between nodes and sinks. Such placement of sinks also reduces the path length between the nodes and the final destination. Reduction in the path length tends to minimize the effects on the data. The next stage consists of data exchanging. The data is delivered to the sink using multihop communication. Therefore, the next forwarder selection is made upon the distance of the nodes from the sink. The node which is the nearest is selected as the next forwarder. In MuLSi algorithm, the data exchanges with the receiver/forwarder on a single link. The single link does not achieve the best and reliable results. Therefore, cooperation is one of the best solutions to intensify a reliable operation. The article proposes the extended version of the MuLSi algorithm named as MuLSi-Co algorithm. The MuLSi-Co algorithm provides reliable operation by utilizing the broadcast behavior of nodes. The relay forwards data to the destination without any latency. As a result, the forwarder/receiver receives the data along two paths and then combines the

data to minimize the channel effects and ensure its reliable operation. The overall contributions of the article are summarized as follows:

- (i) The network structure plays an important role in network performance improvement. Therefore, the suggested MuLSi algorithm in this article proposes the network structure in layers instead of a single solid structure. Moreover, the layered structure decreases the dependency on other nodes as compared to a single solid structure. Then in each layer, a sink is positioned in the top center. This reduces the multi-hop communication between nodes and tends to reliable and energy-efficient operation. Then instead of the receiver-based approach, the proposed scheme prefers the sender-based approach due to latency, synchronization between nodes, and reduction in computational cost. The sender decides its next forwarder upon nodes' distance from the destination. Instead of complete information about the distance, a simple distance formula is utilized to reduce the computational complexity and cost. Moreover, the knowledge acquisition stage is designed in such a way that reduces the data overhead, traffic congestion, data overload, and energy expenses
- (ii) Due to the high effects of the channel on a single link data in the MuLSi algorithm, the chance of data corruption is high. The single link breaking has high chances which affect the reliable transmission and sometimes leads to loss of data. So, this motivation leads to the extended version of the MuLSi algorithm termed as MuLSi-Co. In this, the cooperative behavior of the nodes makes the network reliable. The relay forwards the data to the forwarder/receiver and combines the copy and original packets to reduce its chances of being dropped
- (iii) The redundant packet transmission and synchronization between nodes, sender, receiver, and forwarder, are two of the most important aspects of the cooperative techniques. In order to improve synchronization, a fixed cooperative behavior of the relay tends to eliminate such issues. The relay advances the data as it receives it without any time-wasting. The other nodes in the proximity of the sender discard the data after analyzing it, which leads to a reduction in duplicate data transmission. The suppression of such packets improves efficiency in terms of energy and data collision

2. Related Work

The two most important parameters, the power of sensor nodes and less noisy links to transmit data in the harsh environment of the UA-WSNs, are addressed in [28] by proposing two routing protocols. The first scheme "energy effective and reliable delivery (EERD)" deals with the battery consumption parameter, and the second scheme "cooperative

energy effective and reliable delivery (CoEERD)" incorporates the noisy link issue. The EERD consists of only one single path, in order to deliver the data from one state to the next higher state. Initially, the source node generates information and advances it. Every source has its own transmission range. All those nodes which come in the range of transmitter receive the data. The source nominates a node (forwarder) amongst the nodes which are around the source for further transmission. The nominating criteria for the forwarder node depends on a weight function. The weight function includes the information of residual energy, bit error rate (BER), and distance. In other words, the node is selected as a forwarder that has maximum residual energy, less BER, and the lowest distance to the sink node. Due to a single link for data transmission, it has the maximum probability of data corruption. To avoid and tackle such issues, an extended version of the EERD is proposed, called CoEERD. In CoEERD, along with the forwarder, a relay is also selected for data advancement to the next stage. The selection criteria of the forwarder and relay nodes are similar as in the EERD mechanism. If the BER increases from the threshold value, then the relay node sends the data. This way improves data exchanging over the noisy links, and the original data is transmitted in a safe mode. The discussed routing schemes outperform, in terms of alive and dead nodes, the successful packet reception with the lowest a lower energy cost.

A "reliable multipath energy-efficient routing protocol (RMEER)" is presented in [29]. This research work targets to enhance the network lifetime and set an optimal route to deliver the information to the desired target. The whole network is divided into five different and equal layers. The final destination node is placed at the top of the water surface, and static powerful carriers are deployed in the remaining layers. The last layer of the network contains ordinary sensor nodes. The multipath data routing mechanism is followed to deliver the information. In order to improve the packet delivery ratio multisinks with the multipath disjoint algorithm are used. In this algorithm, if any node dies, then an alternate route selection bypasses the died node route. The data forwarding process is defined by a routing table. A hello packet is sent by the courier node; after receiving this packet, every source node updates its routing table. This table contains the residual energy, link quality, and node ID. By analyzing all these parameters, an optimal forwarder node is selected for the data transmission towards the sink.

Once the battery of sensor nodes dies, it is impossible to change it in a harsh environment. In addition, the noise degrades the quality of the information packets. These two major problems are incorporated in [30]. For these two problems, two different routing protocols are designed. One deals with a power consumption problem called SRSPR: "stable and reliable short-path routing", and the second deals with the successful transmission of the data called Co-SRSPR. Initially, all the sensor nodes are not familiar with the basic information of the neighbor nodes. So, the hello packet is a method to collect records, all the necessary and basic information of the nodes like residual energy,

signal to noise ratio, Euclidean distance, and a minimum number of hops. Information in the form of packets is generated and is not sent directly to the sink because of maximum energy consumption and noise. However, it is sent through a multihop mechanism. The best forwarder selection depends on the maximum residual energy, signal to noise ratio, the lowest Euclidean distance to the sink, and minimum hops. The whole purpose of the mentioned article is to minimize energy consumption. However, this protocol is not able to enhance reliable operation; to do so, a new routing scheme is developed by adding the cooperation to the SRSPR protocol called Co-SRSPR. In Co-SRSPR, one extranode called relay takes part in data transmission in delivery. The relay is selected on the basis of the second largest value of the weight function. If the link is noisy and the BER crosses the limit, then the relay transmits the packet to the final destination. This mechanism minimizes the packet drop ratio and hence increases the successful transmission of the data. Experimental outcomes clearly indicate the best performance of the presented protocol in energy consumption and maximum packet delivery ratio.

In [31], cooperation and multihop energy-efficient routing schemes are introduced for UA-WSNs. The information is generated by the nodes and directs this information towards the sinks through a multihop algorithm. To enhance the reliability of the network, a cooperation scheme is introduced to the one-hop communication. The data forwarding stage is accomplished in two phases. In the first phase, the forwarder node receives the information, and in the second phase, along with the forwarder node, one relay node is set to transmit the data. When both forwarders receive the information, then MRC technique is used which merges these two packets to make one reliable packet. To find the relative distance between nodes, the RSS algorithm is used. The outcomes of the proposed scheme show the best responses in terms of energy and stability of the network.

The fuzzy vector technique is determined in [32] which copes with the delay minimization and battery life issues. This is an advanced version in which fuzzy logic technique (FLT) is utilized. The source generates information and then directs it towards the sink through a multihop mechanism and considers the maximum residual energy for data advancement. The best forwarder selection depends on the residual energy along with the node position. When the data packet generated by the source is broadcasted, all its neighbors receive the packet. Amongst all neighbors, one optimal node is chosen to deliver data to the next node. The residual energy of the selected node should be maximum so that it does not die soon and the position of this node should be minimum to sink node. The experimental results show the best responses in terms of fast data transmission and the network have maximum alive nodes.

In [33], a new mechanism is introduced called “multimedia- and multiband-based adaptation layer techniques” which deals with the bandwidth limitation, propagation delay, and power constraint problems in UA-WSNs. In this routing scheme, the information is collected and transmitted in an effective way. The delivery of data to the sink is accomplished in a hierarchical manner. In order to choose the

path, this task is divided into two different phases. The Manhattan approach determines the nodes which are nearer and away from the final destination and selects the medium for data exchanging. The RSSI technique also determines the distance. The modem used for multimedia is developed which supports the bandwidth of acoustic wave range from 70 to 140 KHz. Only one single bandwidth is used for infrared wavelength ranges from 700 nm to 1 mm. For visible light communication, the blue light with 450 to 485 nm wavelength is used. In the simulation results, the proposed scheme seems better in propagation delay, bandwidth, and energy consumption.

To reduce the interference and undesired signals to the information signal and to use minimum energy by the nodes for transmission and reception of data are proposed in [34]. Multiple datasets are received with minimum or no interference. To control the power parameter of the nodes, a frequency-selective interference channel based on a noncooperative game-theoretic approach is discussed in which the uniqueness and existence of Nash equilibrium are proved. The throughput and cost function of the proposed network is defined by the utility function, in which the cost function indicates the power consumption record of the nodes. The utility function of the nodes changes with the noncooperative mechanism. Hence, increase the throughput and reduce the energy usage of nodes.

Energy-efficient clustering algorithm is proposed in [35], to deal with the balancing and energy problems of the nodes in UWSNs. To reduce the overhead of energy problem during rotation in cluster heads (CHs), leomna, a dual cluster head mechanism, is introduced. To manage the energy of network nodes, a noncooperative game model is also discussed. In this approach, the whole workload in terms of energy is measured first. Then, equal distribution is carried out for each node in terms of energy. In this game model, the Nash equilibrium point is carried out and justified with solid proof. This means a single average value of the energy is defined which every node uses in transmission. Transmission of information amongst intracluster and intercluster domains is carried out in an efficient way to reduce energy usage; to do so, cluster-combined game theory and dual cluster head are proposed, which distribute the energy in an effective way. As a result, the overall network in balancing and energy consumption is optimal compared to existing techniques as shown in the simulation result section.

In [36], network stability and noise awareness are the main concern. This routing called depth-based noise aware scheme targets these two parameters. Initially, the network is idle and knows nothing about nodes. Hello packet is issued from the sink and channel reciprocity obeys in this routing mechanism. By receiving this hello packet, every node puts its ID number, depth, and noise information. By doing this, all nodes become familiar with each other. When the source generates the information signal, every node in the source transmission range will receive this. If all nodes send this data to the final destination node called sink node, then there is huge energy crisis within the network. For this purpose, only one node has been selected to transmit the packet. This node selects the lowest depth and lowest noise

parameters. Such node is selected up to complete successfully transferring of data to sink node. Hence, the selection of such node reduces the energy consumption, optimizing the path quality of the signal. Moreover, the reliability of the network increases, alive nodes increase, and dead nodes decrease.

Due to the harsh and unpredictable atmosphere of the underwater networks, it hits the overall performance of the network in the aspect of packet delivery, battery life, and the error rate of data. In order to cope with these issues, new ideas have been presented in [37]. This protocol divided the whole network into 4 different regions based on the depth of the nodes. Three different depth-based regions are classified on the base of the depth of the sensor nodes, which are the lowest depth node region, medium depth node region, and highest depth node region. At the top of each region, a sink node is placed which directly communicates with the offshore sink node. Every region has different random nodes amongst which only one node is chosen to transmit the data towards the sink node of each region, respectively. The one forwarder node is selected on the base of the highest residual energy and the lowest depth value. This whole arrangement increases the network time and increases the throughput and reliability of the network.

Due to the most frequent use of top nodes, the energy of those nodes ends which stops further transmission of data; this is called hole generation. The work in [38] avoids the hole generation. Sink nodes are placed far away from the region of interest; therefore, two routing schemes are discussed here, called distributed energy-efficient and connectivity-aware routing protocols. These schemes avoid the mostly used of overhead lowest depth nodes which are responsible to create a hole as a result of which blockage of data transmission in the underwater network takes place. In this protocol, the route changes to multihop. Although the burden of data transmission on the lowest depth nodes minimizes as the output of which the probability of dead ratio in upper surface nodes is reduced, the simulation result shows that the lifespan of the lowest depth nodes increases from 50 to 70 percent. Dead node ratio minimizes, and alive nodes are in maximum number.

In [39], different issues are highlighted and tried to fix them when someone deals with underwater wireless sensor networks. These issues include delay in data processing, more energy usage, and noisy links. However, the most dominant problems are energy consumption and network reliability. An opportunistic energy-efficient routing scheme (EECOR) is proposed here to tackle these problems. In the opportunistic scheme, relay node is selected in cooperative mode with the forwarder node to deliver the data packet in an efficient way. With EECOR, fuzzy logic-based relay is chosen for energy usage and maximum data delivery probability. This scheme avoids the collision of the data packets which reduces the most energy usage of the nodes. The timer mechanism is fixed which notes the time of the already transmitted data packet, and after a fixed time, it sends another packet; in this way, the collision is controlled. The experimental graph shows that the average packet transmission ratio, average delay, and average network lifetime are

optimal for the presented protocol compared to the rest schemes.

A multilayer multipath data forwarding scheme is proposed in [40]. Three phases are defined to forwarding the data from bottom to top of the water surface. The first phase explain the network architecture, and in this model, nodes are randomly deployed. In the second phase, the whole routing mechanism is explained, how the data is forwarded to the next higher state nodes. In this phase, the seabed sources initialize the information signal; acoustic powerful nodes are fixed in the upper layer of the surface. The transmitter node is responsible to transmit the data to the acoustic powerful nodes from which the data is directed towards the sink nodes placed on the water surface. The forwarder node selects with lowest depth information; once the forwarder node is selected, this will receive and transmit the information data to powerful acoustic nodes. The RREQ/RREP algorithm is used to choose the best route for multipath transmission. The last phase clearly verifies the shortest distance node selection which sends the data from the source to the sink node. The outcomes show the best performance and maximum improvement in network lifetime, throughput.

DIEER routing is proposed in [41]; it is a delay intolerant energy-efficient algorithm. This protocol can avoid the collision in data packet propagation delay and increase the PDR. No one routing protocol deals with all these problems except the DIEER protocol. The retransmission of data minimizes which reduces the energy usage of the network and hence decreases the delay of the network. The joint optimization framework for sink mobility, hold, and forwarding mechanism is introduced. To reduce the network delay, maximum data delivery, enhancing network life, minimizing energy usage, and the adaptive value of the threshold is fixed with data aggregation and pattern matching schemes. Three-dimensional underwater environment is designed with sink mobility and dense deployment of the nodes with varying communication radii. There is no retransmission of the data that occurs by the adaptation of the presented protocol.

In [42], deep learning-coded index modulation-spread spectrum (DL-CIM-SS) technique is adopted to overcome the data rate issue for multiusers and hence remove the flaw that exists in multiuser direct sequence spread spectrum (DSSS). This mechanism sends the data via index of spreading code instead of sending data to all users physically. In this way, the energy usage is reduced, and the maximum data is transmitted. The algorithm proposed in [43] transmits data at a high rate which is the key parameter of underwater communication systems in order to reduce battery power, spreading, and scattering phenomena. The experimental results show the advancement in energy and spectral efficiency.

Secure energy efficiency with cooperation setup is introduced in [18]. The security parameter is not only important for terrestrial networks but also for underwater networks. The security of the data is analyzed for combatting attacks. At the bottom of the network, information has been generated; the main task of the proposed scheme is how to make secure the generated data while transmitting it to the water surface. Along with this, to consume minimum energy in

transmission and reception, a hello packet is transmitted to all nodes; every node can add the path loss, residual energy, and depth information to this hello packet. The depth threshold from 20 m to 40 m is included to avoid the flooding process in the underwater network. Attack of unauthentic signals is checking mechanism to secure the information packet. A duplicate copy of the data packet is already sent to the minisink. When the original data is sent to the sink by multihop process, this original data packet and already sent duplicate copy have been compared. In this way, this protocol ensures the security of the data. This protocol was best performed in terms of security network lifespan. Tables 1 and 2 show the analysis of these algorithms.

3. The Proposed Scheme

3.1. Multilayer Sink Algorithm

3.1.1. Proposed Network Structure. The network structure has tremendous effects on the performance parameters, such as reliability, stability, scalability, delay, and energy efficiency. The poorly designed network model reduces the overall performance and does not complete the main objectives and aims of the network. So, the network structure plays an important and fundamental role in precise operation to achieve fair and worthy performances. On account of this, a multilayer network structure is proposed as shown in Figure 2. The proposed network is partitioned into five equal layers called a multilayer network. The intention behind the multilayer network structure is to place the sinks on the optimal position, which motive is to accumulate data more efficiently and conveniently. The network comprises of a set $S = S_n \cup S_s$ of sensor nodes and sinks, where the set of sensor and sink nodes is represented by S_n and S_s , respectively.

The set of nodes $S_n = n_1, n_2, n_3, \dots, n_n$ is arranged irregularly in the network. These nodes have different sensors for monitoring and investigation of different environmental factors. For transmission of data, each node is equipped with an acoustic modem. The energy at the initial stage of every node is E_0 . Therefore, the total energy of the network is $n \times E_0$, where n represents the total number of nodes. Two nodes x and y are neighbors if their transmission range r_t is less than its Euclidean distance. All nodes are identical in all aspects, such as energy consumption, data rate, and battery power.

Nodes' random distribution has a negligible effect on performance of the network, while the positioning of the sinks is very important and crucial for performance enhancement, improvement, and data accumulation. So, the sinks $S_s = s_1, s_2, s_3, s_4, s_5$ are placed in the middle top of each layer. The position of the first sink is given as

$$s_1(x, y) = x_c, y_o, \quad (1)$$

where the y_o is the value of y coordinate, and it is 0 for the first sink, while x_c represents the center point of the x coordinate

TABLE 1: Related work comparison.

Protocol	Energy cost	PDR	Packet drops	Delay
Co-EERD	High	High	Low	High
RMEER	Low	Low	High	Low
Co-RSPR	Low	High	Low	Low
CAEEC	Low	High	Low	Low
FLVB	Low	Low	High	Low
MMMBB	Low	Low	High	Low
PCNC	Low	High	Low	Low
EECA	Low	High	Low	High
EBLFCN	Low	High	Low	Low
DEADS	Low	High	Low	Low
EEPEH	Low	Low	High	High
EECOR	Low	High	Low	Low
MLMP	Low	High	High	Low
DIEER	Low	High	Low	Low
SEECR	Low	High	Low	Low

TABLE 2: Related work information.

Protocol	Location information	Cooperation	Energy efficient	Multilayers
Co-EERD	No	Yes	Yes	No
RMEER	No	No	Yes	Yes
Co-RSPR	No	Yes	Yes	No
CAEEC	Yes	Yes	Yes	No
FLVB	No	No	Yes	No
MMMBB	No	No	Yes	Yes
PCNC	No	No	Yes	No
EECA	No	No	Yes	No
EBLFCN	Yes	Yes	Yes	No
DEADS	Yes	Yes	Yes	Yes
EEPEH	No	No	Yes	No
EECOR	No	Yes	Yes	No
MLMP	No	No	Yes	Yes
DIEER	No	No	Yes	No
SEECR	No	Yes	Yes	No

dinate in the network and is obtained as

$$x_c = \frac{\text{total length of } x - \text{axis}}{2}. \quad (2)$$

The positions of the second, third, fourth, and fifth sinks are

$$s_2(x, y) = x_c, y_o + a, \quad (3)$$

$$s_3(x, y) = x_c, y_o + 2a, \quad (4)$$

$$s_4(x, y) = x_c, y_o + 3a, \quad (5)$$

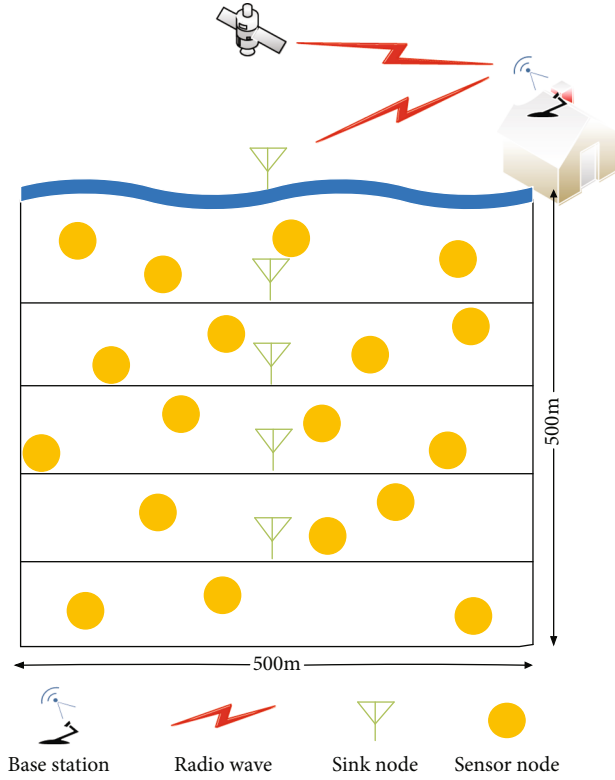


FIGURE 2: Proposed multilayer network structure.

$$s_5(x, y) = x_c, y_o + 4a, \quad (6)$$

where $a = 100$. The sink has a greater energy resource than the other nodes. The nodes communicate with each other or sink through acoustic waves with a data rate of m bit/sec and frequency f KHz. The base station collects all the data from the sinks for further processing and analysis as considered in [16].

3.1.2. Knowledge Acquisition. After sinks' and nodes' placement, information about the nodes and sinks are exchanged with each other. In order to minimize the data overhead, traffic congestion, and energy expenditure, information acquisition takes place in parts. The purpose of information or knowledge acquisition is to find the distance of nodes from the sink and their neighbors to select the best candidates for data forwarding. In the first part, the sink broadcasts data of one bit in order to inform the nodes in its transmission area. The node within the transmission area of the sink receives the data. In response to this data, each node transmits INFO PACKET, which contains the ID of that node. As the node broadcasts the INFO PACKET, it set a timer and starts measuring the time. When the sink receives the INFO PACKET, it updates the INFO PACKET by embedding its own information and transmits it towards that node. When the node receives the updated INFO PACKET, it stops the timer and notes its one-way transmission time t . The node finds its distance d from the sink by $d = vt$, where v denotes the acoustic wave speed.

In the second part, the other nodes send INFO PACKET and start time counting. In response to this, the nodes which have calculated their distance now respond to other nodes. The node then calculates its distance from each respondent node and its distance from the sink. The sink distance is added to nodes' mutual distance. The INFO PACKET format is given in Figure 3.

In order to enhance network performances, further, updating of information is not done very frequently. However, information acquisition occurred after some interval of time. The updating process is necessary to find its recent and most suitable neighbor for data forwarding.

3.1.3. Data Forwarding. To enhance the network performance, the sender-based approach is a preferred choice in the proposed algorithm. In a sender-based approach, the sender decides its next forwarder which reduces the data forwarding time and computational cost. The reduction of computational cost leads to less energy cost. The nodes near to the sink and lying in sink's transmission area directly communicate with it as shown in Figure 4. These nodes do not need any further route for data delivery. The nodes which are far away from the sink and cannot exchange data with the sink directly follow a multihop communication.

In order to deliver the data quickly, the proposed algorithms follow the shortest route towards the sink by using distance from the destination. Before broadcasting of the data from the sender, it arranges all its neighbours in descending order based on distance information to assign priority to each neighbour. Another word, the nodes having the nearest to the sink, is assigned the first priority for data delivery. When the sender arrange all its neighbours, then it forwards the data packet. Figure 5 depicts and elaborates the packet forwarding scenario. The packet header contains the complete information of the forwarder, final sink, and its own information. The header contains the sender ID, forwarder ID, and the sink ID. After the header data is appended with, they analyze the packet and look for its own ID. When the neighbour ID matches with the ID in the packet, then forward the data packet towards the next stage using the same procedure. The other nodes which receive the data from the sender holds the data for a while, because this data held by the nodes will be utilized in it improved cooperative version of the proposed MuLSi.

The nodes are far away from the sink and follow path to the sink. There are two scenarios of possible position of the neighbours. When these are at different distance from the same, then the sender gives priority to the node which is near to the sink. On another hand, when the nodes are the same distance from the sink, then the sender is free to select anyone of these nodes. Although the second scenario has low chances to occur, it is considered in the proposed algorithm.

It is considered that each sink communicates and forwards its data to the sink placed in the upper layer. The sink placed at the top of the network communicates with the base station. It exchanges all its data with the base station for further processing and analyzing.

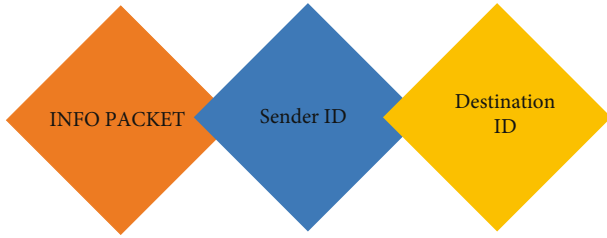


FIGURE 3: Structure of INFO PACKET.

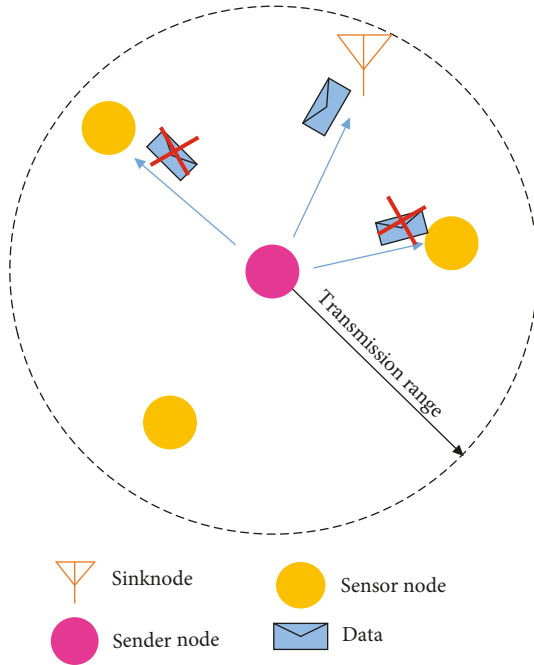


FIGURE 4: Data exchanging directly with sink.

3.1.4. Suppression of Redundant Packets and Acknowledgment. The proposed algorithm tries to control the redundant packet transmission by utilizing the broadcast nature of the nodes. When these nodes overhear the same packet, then they delete the packet from its memory. They consider that the data is delivered to the next destination. In order to reduce the traffic congestion, data overhead, and energy cost, the acknowledgment is not considered in the proposed algorithm.

3.2. MULSI-Co: Multilayer Sink Algorithm with Cooperation. In the unpredictable and high noise availability in the underwater, a single link is not feasible for communication. The retransmission of the data through the same link is not a good choice, because the data reception through the same link has high chances of data corruption again, which will tend to waste energy and high latency in the data exchanging. The proposed MuLSi algorithm follows a single link for exchanging of data. In order to increase the reliable data reception at the destination of the proposed MuLSi algorithm, the cooperation technique is added to it. Delivery of the same data over many paths towards the destination is known as cooperation. This increases the correct reception

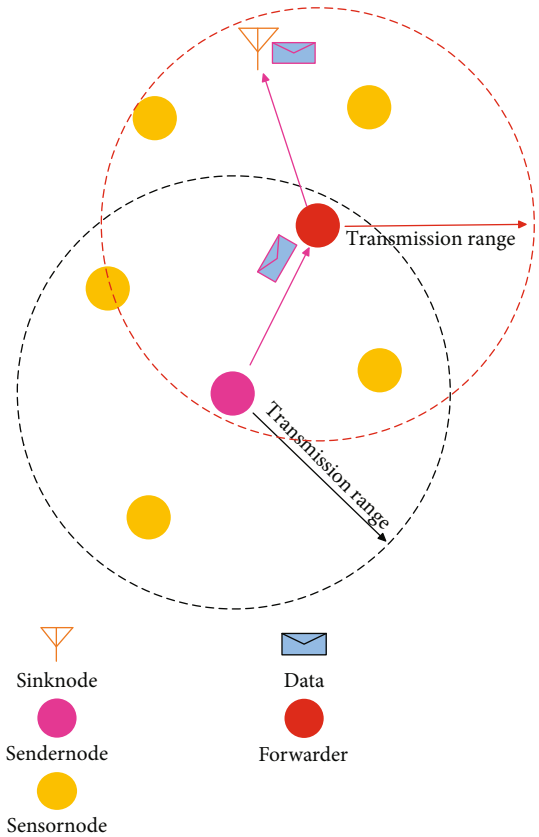


FIGURE 5: Data exchanging with sink through forwarder.

of the data with a cost of more energy and latency than the noncooperative methods. This section gives the details of the proposed MuLSi-Co algorithm.

3.2.1. Cooperative Relay Identification. The important step in cooperation is the relay selection. The best relay selection amongst the neighbors tends to improve the performance. The cooperation technique is reliable, but its cost in terms of energy and delay are greater. So, to minimize the delay and reduce the channel effects, the proposed MuLSi-Co selects the relay which is the nearest to the final destination.

During the knowledge acquisition phase in the MuLSi algorithm, each node has its neighbours list along with their distance information. If the sink is not reachable by the sender directly, then amongst these neighbours, the node which is the nearest to the sink is considered as the forwarder, and the nearer node is selected as relay by the sender. If the sender can exchange its data directly with the sink, then the nearest node is selected as the relay. These relays cooperate with forwarders and destinations to improve reliability.

3.2.2. Data Exchanging and Synchronization. After identification of the relay and forwarder/destination by the sender, the next phase is about data exchanging. Whenever the sender wants to deliver its packet, it appends the information of the relay and forwarder/destination. The sender, relay, and forwarder/destination IDs are appended with the

data. In case of the direct communication with the sink, the sender appends the ID to it. Otherwise, the node nearest to the sink works as a forwarder, and the sender declares it as a forwarder and appends its ID. And the next node ID is appended as a relay.

Whenever the data is received by any node from any sender, then the node searches for its own ID in the packet. If it finds its own ID in the data as forwarder, this node can work as a forwarder for that sender. The relay also searches for its own ID and works as a relay. When the forwarder receives a packet, it waits for a while to receive its copy from the relay. The data received by the relay is delivered to the forwarder as it is received. The other nodes which hear the data ignore it and become silent. Whenever there is no relay, the forwarder does not wait and deliver it to the next stage without cooperation. The forwarder knows the relay by analyzing the packet.

The time and data synchronization are one of the most challenging stage in cooperation. The delivery of the data by the relay in the exact time is important to improve performance. Therefore, for simplicity, the proposed MuLSi-Co routing is designed in a manner to handle the time synchronization between the relay and forwarder. Whenever the relay receives the data, it forwards it without any wait and holding. Due to the broadcast nature of the nodes, all neighbours hear the data. These neighbors check for its own ID in the data. If they do not find its ID, then they ignore the data. This reduces the duplicate packet transmission and improves the energy cost.

3.2.3. Cooperation and Data Combining Model. In the proposed cooperative algorithm, the data advancement occurs in three steps. In the first step, the sender advances its data to the forwarder and relay. In the second step, the forwarder holds the data for a while and waits for the relay data. As the relay receives data, it sends it to the forwarder. In the third state, two copies of the same data are merged to make one reliable data packet from these.

Considering three nodes, sender j , receiver or forwarder k , and relay l are depicted in Figure 6. In the first stage, the j broadcasts the generated data T_j towards the k and l . The received signal R_{jk} at k is given as

$$R_{jk} = g_{jk}T_j + n_{jk}. \quad (7)$$

The channel noise n_{jk} and the fading g_{jk} affects the data when transmitting from the j to k . Likewise, putting a subscript j_l to n and g indicates the noise and fading between j and l . The received data R_{jl} is represented as

$$R_{jl} = g_{jl}T_j + n_{jl}. \quad (8)$$

In the second stage, the forwarder/receiver k waits for the copy of the same data packet from the l . As l receives the data in the first stage, it analyze it. In case the l finds himself eligible for data forwarding, it forwards the data T_l to the k without any holding. The factors which influence the data transmission between l and k are the channel noise

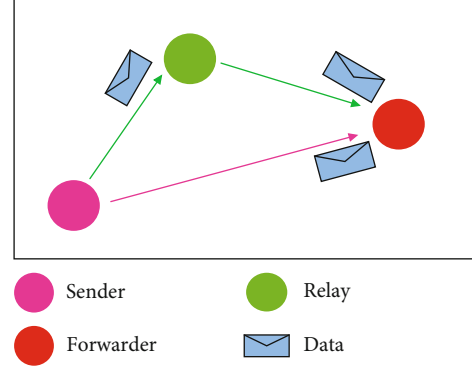


FIGURE 6: Cooperation model.

TABLE 3: Analysis of the proposed and counterpart algorithms.

Protocol	Routing parameter	Routing	Network structure
DBR	Depth	Multihop	Single
CoDBR	Depth	Multihop cooperation	Single
MuLSi	Distance	Multihop	Multi layers
MuLSi-Co	Distance	Multihop cooperation	Multi layers

n_{lk} and fading g_{lk} . The l receives the data R_{lk} and is given as

$$R_{lk} = g_{lk}T_l + n_{lk}. \quad (9)$$

In the third stage, k has a direct received packet R_{jk} and its copy R_{lk} received through l . Now, the k combines these data using maximal ratio combining. The combined data is given as

$$R_k = R_{jk} + \frac{R_{jl}R_{lk}}{1 + R_{jl} + R_{lk}}. \quad (10)$$

4. Analysis and Simulation Results

Validation of the results and network implementation of the proposed schemes are accomplished using MATLAB simulations. The dimension of the network is taken 500 m. The network is further split into five layers having an equal size of 100 m^2 . The purpose of making such layers is to collect data with easiness and quickly. Moreover, it increases the stability and reliability of these networks. The sink at the top of every layer is placed for data collection and information acquisition of the nodes. The nodes are homogeneous in all aspects scattered randomly in the networks. The total amount of energy on each node is 20 J. These nodes are capable of detecting different environment parameters, for example, temperature and pressures. The LinkQuest UMW 2000 cite modem is coupled with every node for data exchanging. The energy expenditure according to the modem used is considered for transmission and reception are 2 W and 0.8 W, respectively, while the idle state or sleep

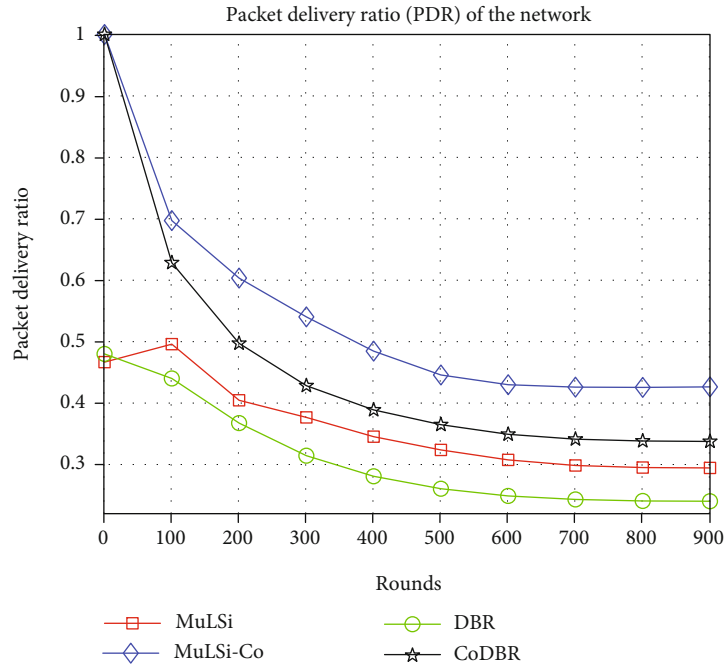


FIGURE 7: Packet delivery ratio (PDR).

TABLE 4: PDR.

Protocol	PDR at round 1	PDR at round 100	PDR at round 200	PDR at round 300	PDR at round 400	PDR at round 500	PDR at round 600	PDR at round 700	PDR at round 800	PDR at round 900
MuLSi-Co	1.0000	0.6971	0.6035	0.5403	0.4846	0.4457	0.4299	0.4260	0.4255	0.4264
MuLSi	0.4667	0.4959	0.4045	0.3767	0.3453	0.3237	0.3075	0.2984	0.2951	0.2944
CoDBR	1.0000	0.6285	0.4972	0.4283	0.3889	0.3649	0.3492	0.3412	0.3383	0.3375
DBR	0.4800	0.4401	0.3674	0.3144	0.2808	0.2606	0.2488	0.2432	0.2407	0.2402

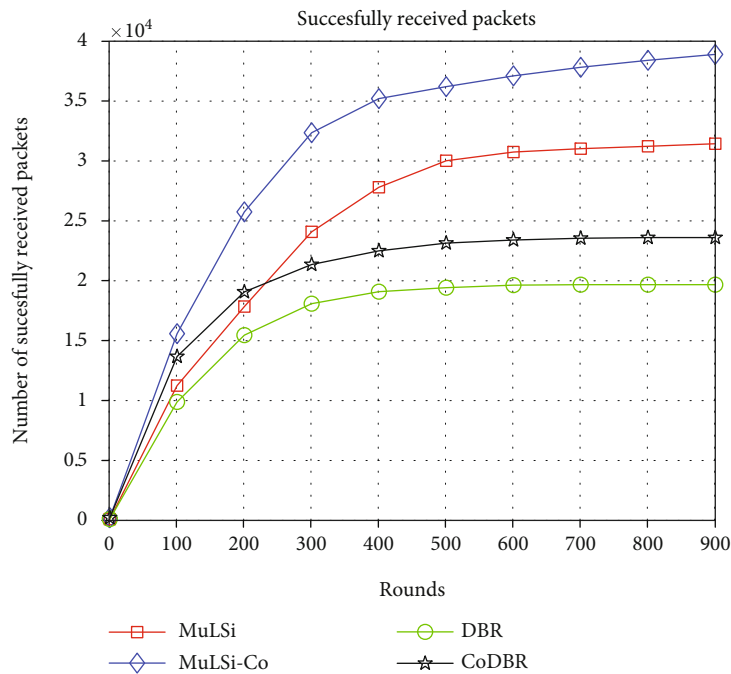


FIGURE 8: Received packets.

TABLE 5: Received packet analysis.

Protocol	Received packets at round 1	Received packets at round 100	Received packets at round 200	Received packets at round 300	Received packets at round 400	Received packets at round 500	Received packets at round 600	Received packets at round 700	Received packets at round 800	Received packets at round 900
MuLSi-Co	225	15589	25755	32361	35210	36208	37108	37824	38406	38902
MuLSi	105	11252	17850	24087	27809	30021	30750	31030	31229	31442
CoDBR	225	13682	19076	21361	22502	23148	23405	23553	23610	23610
DBR	108	9889	15465	18092	19093	19426	19638	19678	19678	19678

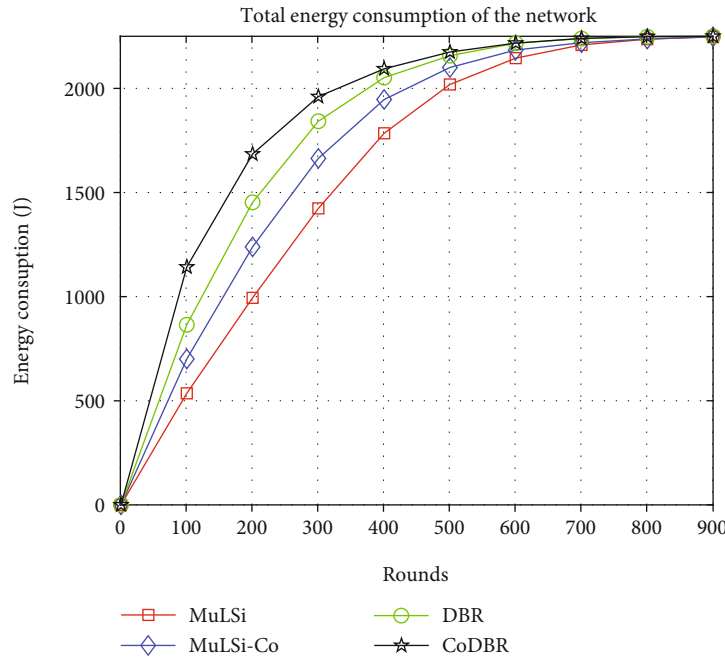


FIGURE 9: Energy consumption.

TABLE 6: Residual energy analysis.

Protocol	Residual energy at round 1	Residual energy at round 100	Residual energy at round 200	Residual energy at round 300	Residual energy at round 400	Residual energy at round 500	Residual energy at round 600	Residual energy at round 700	Residual energy at round 800	Residual energy at round 900
MuLSi-Co	2.2499×10^3	1.5577×10^3	1.0187×10^3	592.5394	307.6515	151.7722	66.7701	30.8496	13.0675	2.4202
MuLSi	2.2499×10^3	1.7196×10^3	1.2608×10^3	831.2838	469.9592	234.0915	106.1561	41.8966	14.0033	2.8491
CoDBR	2.2499×10^3	1.1205×10^3	572.6635	293.6711	157.3787	76.1240	33.0757	10.1817	1.7483	0
DBR	2.2499×10^3	1.3937×10^3	804.4937	412.6768	200.1105	93.9679	33.8725	10.9521	1.8618	0.1186

mode energy exhaustion is 8 mW. Moreover, the data transmission rate is 9600 bps. For the sake of reducing the computational complexity, the data is considered dropped when the channel is busy. The proposed MuLSi and MuLSi-Co schemes are compared with some existing techniques DBR and CoDBR from the literature. The motivation behind choosing these competitive algorithms is the same

network architecture, topology, and cooperative behavior of the nodes. An overview of all these algorithms are given in Table 3.

4.1. Packet Delivery Ratio (PDR) or Packet Acceptance Ration (PAR). The ratio of the number of correct packet reception to the total sent packets is termed as PDR or PAR. The

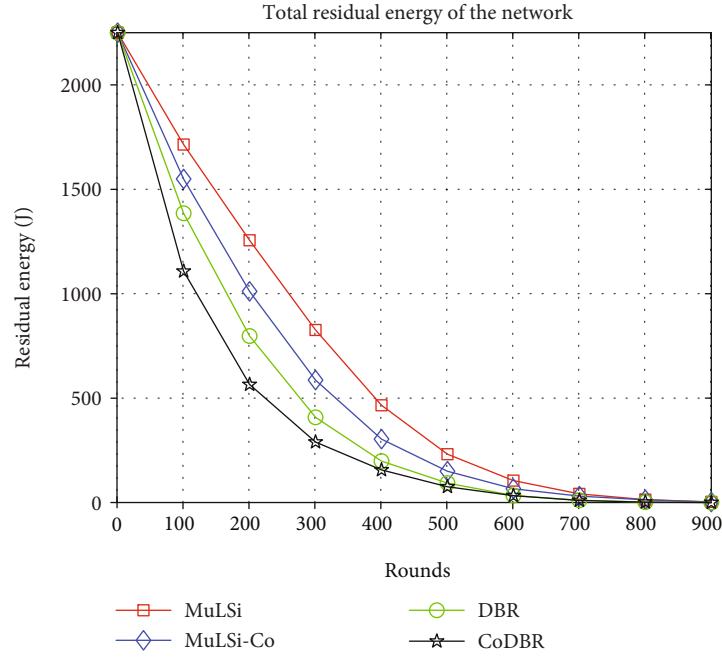


FIGURE 10: Residual energy.

PDR performance is given in Figure 7. The order of algorithm based on PDR performance from highest to the lowest is MuLSi-Co, CoDBR, MuLSi, and then, DBR. The highest PDR of the proposed MuLSi-Co is due to the sink placement and cooperation. The sink placement in every layer ensures the data reception with the lowest delay than the other schemes, which tends to less effect of the data. Both the MuLSi-Co and CoDBR are cooperative schemes. However, the sink placement in the proposed cooperative algorithm reduces the path losses and improves the packet reception. In result, the proposed cooperative technique has the highest PDR. Moreover, the best destination and cooperative node selection is another reason of the highest PDR in MuLSi-Co algorithm. The second reason behind the highest performance is the cooperation. Incorrect data are exchanged with the retransmitted data by the cooperative node, which makes sure the correct packet reception at the destination.

The CoDBR algorithm PDR has the best performance than the noncooperative schemes, MuLSi and DBR, due to the cooperation and multiple paths are followed for data delivery. The same packets received through many paths are then combined to improve the packet reception and lead to the highest PDR than the noncooperative algorithms.

The MuLSi has the higher PDR than the competitor scheme DBR. It is because of the network topology and node selection using distance parameter for data advancement towards the final destination. The sink placement in each layer and the distance parameter reduce the path for data delivery. This tends to reduce the effects of the channel attributes and increases the probability of correct data reception, while in DBR, the depth is utilized for data forwarding, and the sinks are at the top which are far away from the bottom nodes. Therefore, this increases the channel effect on the data and degrades the packet reception and tends to the lowest PDR. More detail PDR performance is given in Table 4.

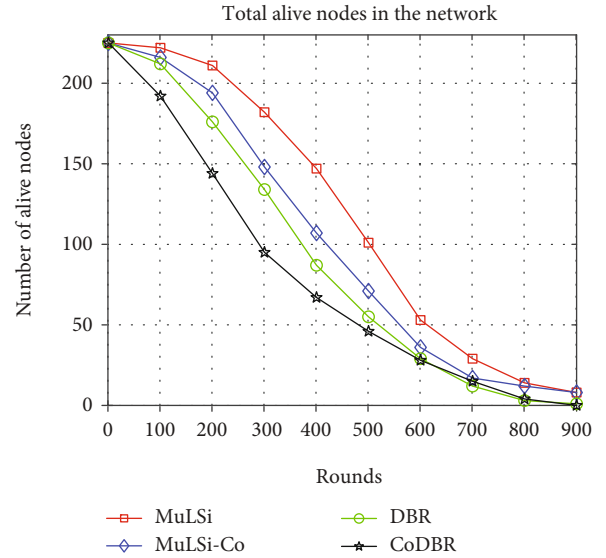


FIGURE 11: Alive nodes.

4.2. *Correct Received Packets.* The successful received packet results are shown in Figure 8. The proposed cooperative algorithm has the highest number of received packets. It is due to the data forwarding on multiple paths towards the sink node. The same packet is received through multiple paths and then combined, which increases the probability of correct data reception. Moreover, the sink placement also enhances the probability of correct data reception. Most of the nodes are directly exchange data with the sink. All these parameters lead to the highest data packet reception.

TABLE 7: Dead node analysis.

Protocol	Dead nodes at round 1	Dead nodes at round 100	Dead nodes at round 200	Dead nodes at round 300	Dead nodes at round 400	Dead nodes at round 500	Dead nodes at round 600	Dead nodes at round 700	Dead nodes at round 800	Dead nodes at round 900
MuLSi-Co	0	9	31	77	118	154	189	208	213	217
MuLSi	0	3	14	43	78	124	172	196	211	217
CoDBR	0	33	81	130	158	179	197	210	221	225
DBR	0	13	49	91	138	170	196	213	222	224

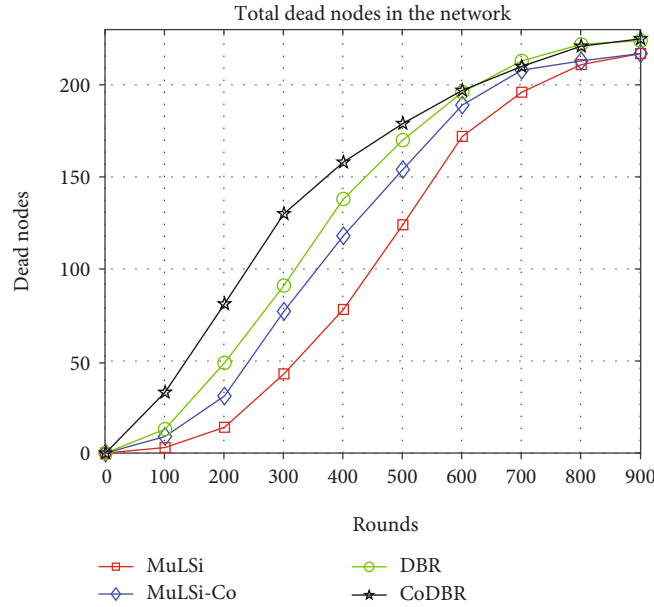


FIGURE 12: Dead nodes.

The proposed MuLSi algorithm has the highest packet reception than the counterpart algorithms after 230 rounds, although it is a noncooperative algorithm due to well placement of sink nodes and the node selection for data forwarding. The sinks are near to the nodes which exchange data easily, and the channel effects are less on the data. Also, the distance parameter chooses the nearest node to destination. All these factors lead to the highest packet reception.

The CoDBR has the highest packet reception up to 230 rounds. Due to the cooperation of the nodes, the packet reception probability is the highest at the start. Onward, the death ratio of the nodes in CoDBR is high due to the multiple forwards for a single-packet delivery. The multiple forwarders lead to excessive energy consumption and have less chance of cooperation at the end. Therefore, the packet reception becomes lower than the proposed MuLSi algorithm. On the other hand, the DBR has the lowest packet reception due the noncooperative algorithm. The analysis of the packet reception of all these schemes is shown in Table 5.

4.3. Energy Expenditure and Residual Energy Analysis. The energy expenditure is one of the most important parameter for performance evaluation especially in UA-WSNs. The

corresponding results are given in Figure 9. Due to the cooperation mechanism, the consumption of energy in CoDBR is the highest than all other schemes. In cooperation, the data is delivered through multiple paths to the destination. The multipath transmission of the same data tends to consume excessive energy and leads to increase the overall expenditure in terms of energy.

The DBR consumes the highest amount of energy than the remaining algorithms, due the involvement of many nodes for data advancement towards the sink leads to more energy consumption. Another reason of such high-energy expenditure is of the data burden on the top nodes in the network. The top nodes are selected again and again by the lowest nodes to deliver the data. In result, the consumption is the highest than MuLSi-Co and MuLSi. Although MuLSi-Co is a cooperative algorithm, its energy expenditure is lower than the noncooperative algorithm DBR. It is due to the longest route followed for data transmission, and sinks are far away from the bottom nodes in DBR.

The MuLSi-Co has the higher energy consumption than MuLSi algorithm. In MuLSi-Co, for increasing the reliability of the network, the cooperative behaviour of the node is utilised. The cooperation of the nodes tends to consume excessive energy and leads to less network lifetime, while in

MuLSi, the multilayer network structure and sink placement at the optimal position reduce the path length and node involvement in the data forwarding. Therefore, the resultant energy expenditure of the proposed MuLSi algorithm is the lowest than all other algorithms. The energy performance evaluation is given in detail in Table 6. The above discussion is conversely true for the residual energy and is shown in Figure 10.

4.4. Alive and Dead Node Analysis. The analysis of these algorithms with reference to dead nodes is shown in Figure 11, also with more details in Table 7. The dead nodes in CoDBR algorithm are the highest than the rest of algorithms. As discussed, the network energy expenditure is the highest due to cooperation, and many nodes take part in single-packet delivery. Therefore, in the result, it is concluded that the nodes are spending high amount of energy and tends to greatest number of dead nodes. So, the overall performance of the dead nodes is the highest than the rest of the algorithms.

The DBR has the highest number of dead nodes than the proposed algorithm. For a single-packet delivery, many nodes participate. Due to the involvement of many nodes, they consume a greater amount of energy and tend to increase its death ratio. Therefore, the resultant dead node in DBR is the highest than the proposed algorithm.

On another hand, both the proposed algorithms have the lowest number of dead nodes than the competitor. Due to the well management of network architecture, sink placement and best node selection during data transmission lead to less energy consumption. The less amount of energy consumption also decreased the number of dead nodes in the network. Therefore, the resultant dead nodes are the highest than the counterpart, while, comparing the proposed noncooperative MuLSi with cooperative MuLSi-Co algorithm, the cooperative algorithm has the higher number of dead nodes. It is because of the greater number of forwarder nodes in the MuLSi-Co algorithm. This discussion is true conversely for the alive nodes and is shown in Figure 12.

5. Conclusion

To design and configure an efficient, reliable, and stable algorithm for underwater acoustic wireless sensor networks (UA-WSNs) needs great attention on account of its notable and distinctive challenges and amazing applications. The energy-efficient operation of these networks takes care of their working and running for a longer time and tends to have more stability. The best network structure reduces the number of multiple hops between the sender and destination; this leads to less energy cost and minimized effects of the channel on data. To increase the reliable data exchanging, the cooperation is the best and suitable choice instead of other costly and complex techniques. However, in cooperative techniques, the excessive expenditure of energy makes it challenging. Moreover, the time and data synchronization are also crucial issues in cooperation. To address these difficulties, the article introduces two algorithms: multilayer sink (MuLSi) algorithm and its reliable version MuLSi-Co using

the cooperation technique. The first algorithm proposes a multiple-layered network structure instead of a solid single structure and sink placement at the optimal position. This reduces the multiple hops between the sender and sink. Moreover, the best forwarder selection amongst nodes based on the node closeness to sink makes the network performances more better and valuable. The node closest to the sink is a good choice for choosing the best forwarder. However, the MuLSi algorithm does not fulfil the requirement of reliable operation due to a single link for data exchanging. Unlike the traditional algorithms, the proposed scheme does not need the location information about nodes.

Data Availability

The data used to support the findings of this study are available from the corresponding author upon request.

Conflicts of Interest

The authors declare that they have no conflicts of interest.

Acknowledgments

The authors are grateful to the Taif University Researchers Supporting Project (number TURSP-2020/36), Taif University, Taif, Saudi Arabia. This research work was partially supported by the Faculty of Computer Science and Information Technology, University of Malaya, under Postgraduate Research Grant (PG035-2016A).

References

- [1] A. Davis and H. Chang, "Underwater wireless sensor networks," in *In 2012 Oceans*, pp. 1–5, IEEE, 2012.
- [2] R. W. L. Coutinho, A. Boukerche, L. F. M. Vieira, and A. A. F. Loureiro, "Underwater wireless sensor networks," *ACM Computing Surveys (CSUR)*, vol. 51, no. 1, pp. 1–36, 2018.
- [3] S. Chafale and N. Dhande, *Opportunistic Routing and Monitoring of Packet Data in Underwater Wireless Sensor Network*, Tech. Rep, 2018.
- [4] J.-H. Cui, J. Kong, M. Gerla, and S. Zhou, "The challenges of building scalable mobile underwater wireless sensor networks for aquatic applications," *IEEE Network*, vol. 20, no. 3, pp. 12–18, 2006.
- [5] A.-K. Othman, "GPS-less localization protocol for underwater acoustic networks," in *In 2008 5th IFIP International Conference on Wireless and Optical Communications Networks (WOCN'08)*, pp. 1–6, IEEE, 2008.
- [6] K. Chen, Y. Zhou, and J. He, "A localization scheme for underwater wireless sensor networks," *International Journal of Advanced Science and Technology*, vol. 4, 2009.
- [7] G. Han, J. Jiang, L. Shu, X. Yongjun, and F. Wang, "Localization algorithms of underwater wireless sensor networks: a survey," *Sensors*, vol. 12, no. 2, pp. 2026–2061, 2012.
- [8] M. Ayaz, A. Abdullah, I. Faye, and Y. Batira, "An efficient dynamic addressing based routing protocol for underwater wireless sensor networks," *Computer Communications*, vol. 35, no. 4, pp. 475–486, 2012.

- [9] A. Wahid, S. Lee, H.-J. Jeong, and D. Kim, "Eedbr: energy-efficient depth-based routing protocol for underwater wireless sensor networks," in *In International Conference on Advanced Computer Science and Information Technology*, pp. 223–234, Springer, Berlin, Heidelberg, 2011.
- [10] S. I. Aldharrab, *Cooperative Communication Over Underwater Acoustic Channels*, 2013.
- [11] M. J. Jannati, A. D. Aref, and V. T. Vakily, "Implementation of cooperative virtual MISO communication in underwater acoustic wireless sensor networks," *International Journal of Computer Science Issues (IJCSI)*, vol. 8, no. 4, 2011.
- [12] A. Ahmad, S. Ahmed, M. Imran, M. Alam, I. A. Niaz, and N. Javaid, "On energy efficiency in underwater wireless sensor networks with cooperative routing," *Annals of Telecommunications*, vol. 72, no. 3-4, pp. 173–188, 2017.
- [13] L. Lanbo, Z. Shengli, and C. J. Hong, "Prospects and problems of wireless communication for underwater sensor networks," *Wireless Communications and Mobile Computing*, vol. 8, no. 8, p. 994, 2008.
- [14] H. Yan, Z. J. Shi, and J.-H. Cui, "DBR: depth-based routing for underwater sensor networks," in *In International conference on research in networking*, pp. 72–86, Springer, Berlin, Heidelberg, 2008.
- [15] U. Lee, P. Wang, Y. Noh, L. F. M. Vieira, M. Gerla, and J.-H. Cui, Eds., "Pressure routing for underwater sensor networks," in *2010 Proceedings IEEE INFOCOM*, pp. 1–9, IEEE, 2010.
- [16] J. Qadar, A. Khan, and H. Mahmood, "DNAR: depth and noise aware routing for underwater wireless sensor networks," in *In Conference on Complex, Intelligent, and Software Intensive Systems*, pp. 240–251, Springer, Cham, 2018.
- [17] Y. Lu, R. He, X. Chen, B. Lin, and Y. Cunqian, "Energy-efficient depth-based opportunistic routing with Q-learning for underwater wireless sensor networks," *Sensors*, vol. 20, no. 4, p. 1025, 2020.
- [18] K. Saeed, W. Khalil, S. Ahmed, I. Ahmad, and M. N. K. Khatkhat, "SEECR: secure energy efficient and cooperative routing protocol for underwater wireless sensor networks," *IEEE Access*, vol. 8, pp. 107419–107433, 2020.
- [19] Y. Chen, J. Zhu, L. Wan, S. Huang, X. Zhang, and X. Xiaomei, "ACOA-AFSA fusion dynamic coded cooperation routing for different scale multi-hop underwater acoustic sensor networks," *IEEE Access*, vol. 8, pp. 186773–186788, 2020.
- [20] Y. Su, Y. Zhang, R. Bai, Y. Liu, B. Wang, and Y. Sun, Eds., "Q-learning based dynamic cooperative communication in time varying underwater acoustic channels," in *In 2021 IEEE/CIC International Conference on Communications in China (ICCC Workshops)*, pp. 293–298, IEEE, 2021.
- [21] S. Karim, F. K. Shaikh, B. S. Chowdhry et al., "GCORP: geographic and cooperative opportunistic routing protocol for underwater sensor networks," *IEEE Access*, vol. 9, pp. 27650–27667, 2021.
- [22] H. Zhao, X. Li, S. Han, L. Yan, and Y. Junzhi, "Adaptive relay selection strategy in underwater acoustic cooperative networks: a hierarchical adversarial bandit learning approach," *IEEE Transactions on Mobile Computing*, p. 1, 2021.
- [23] Y. Chen, K. Zheng, X. Fang, L. Wan, and X. Xiaomei, "QMCR: a Q-learning-based multi-hop cooperative routing protocol for underwater acoustic sensor networks," *China Communications*, vol. 18, no. 8, pp. 224–236, 2021.
- [24] R. Arul, R. Alroobaea, S. Mechti et al., "Intelligent data analytics in energy optimization for the internet of underwater things," *Soft Computing*, vol. 25, no. 18, pp. 12507–12519, 2021.
- [25] J. Qadir, U. Ullah, B. Sainz-De-Abajo, B. G. Zapirain, G. Marques, and I. de la Torre Diez, "Energy-aware and reliability-based localization-free cooperative acoustic wireless sensor networks," *IEEE Access*, vol. 8, pp. 121366–121384, 2020.
- [26] A. Khan, I. Ali, A. U. Rahman, M. Imran, and H. Mahmood, "Co-EEORS: cooperative energy efficient optimal relay selection protocol for underwater wireless sensor networks," *IEEE Access*, vol. 6, pp. 28777–28789, 2018.
- [27] H. Nasir, N. Javaid, S. Hifsa Ashraf, Z. A. Manzoor, U. Q. Khan, and M. Sher, "CoDBR: cooperative depth based routing for underwater wireless sensor networks," in *In 2014 Ninth International Conference on Broadband and Wireless Computing, Communication and Applications*, pp. 52–57, IEEE, 2014.
- [28] U. Ullah, A. Khan, M. Zareei, I. Ali, H. A. Khattak, and I. U. Din, "Energy-effective cooperative and reliable delivery routing protocols for underwater wireless sensor networks," *Energies*, vol. 12, no. 13, p. 2630, 2019.
- [29] M. Ahmed, M. Mazleena Salleh, I. Channa, and M. F. Rohani, "RMEER: reliable multi-path energy efficient routing protocol for underwater wireless sensor network," *International Journal of Electrical Computer Engineering*, vol. 8, no. 6, p. 4366, 2018.
- [30] U. Ullah, A. R. Shahid, M. Irfan, J. Qadir, M. Nawaz, and R. Qureshi, "A stable and reliable short-path routing scheme for efficient acoustic wireless sensor networks (AWSNs)," *IEEE Access*, vol. 8, pp. 1458–1474, 2020.
- [31] H. Tran-Dang and D.-S. Kim, "Channel-aware energy-efficient two-hop cooperative routing protocol for underwater acoustic sensor networks," *IEEE Access*, vol. 7, pp. 63181–63194, 2019.
- [32] R. Bu, S. Wang, and H. Wang, "Fuzzy logic vector based forwarding routing protocol for underwater acoustic sensor networks," *Transactions on Emerging Telecommunications Technologies*, vol. 29, no. 3, article e3252, 2018.
- [33] D. R. KM, S.-H. Yum, E. Ko, S.-Y. Shin, J.-I. Namgung, and S.-H. Park, "Multi-media and multi-band based adaptation layer techniques for underwater sensor networks," *Applied Sciences*, vol. 9, no. 15, p. 3187, 2019.
- [34] R. Sun, Z. Wei, X. Zengwei Lyu, L. S. Ding, and H. Songhua, "Power control algorithm based on non-cooperative game theory in successive interference cancellation," *Wireless Networks*, vol. 25, no. 6, pp. 3297–3305, 2019.
- [35] D. Lin and Q. Wang, "An energy-efficient clustering algorithm combined game theory and dual-cluster-head mechanism for WSNs," *IEEE Access*, vol. 7, pp. 49894–49905, 2019.
- [36] J. Qadir, A. Khan, M. Zareei, and C. Vargas-Rosales, "Energy balanced localization-free cooperative noise-aware routing protocols for underwater wireless sensor networks," *Energies*, vol. 12, no. 22, p. 4263, 2019.
- [37] A. Umar, N. Javaid, A. Ahmad et al., "DEADS: depth and energy aware dominating set based algorithm for cooperative routing along with sink mobility in underwater WSNs," *Sensors*, vol. 15, no. 6, pp. 14458–14486, 2015.
- [38] R. E. Mohamed, A. I. Saleh, M. Abdelrazzak, and A. S. Samra, "Energy-efficient routing protocols for solving energy hole problem in wireless sensor networks," *Computer Networks*, vol. 114, pp. 51–66, 2017.
- [39] R., M. Arifur, Y. Lee, and I. Koo, "EECOR: an energy-efficient cooperative opportunistic routing protocol for underwater acoustic sensor networks," *Access*, vol. 5, pp. 14119–14132, 2017.

- [40] M. Ahmed, N. Naeem, S. Parveen, N. Hussain, and R. Malookani, "M2DFR: multi-layer multipath data forwarding routing protocol for underwater wireless sensor network," *Indian Journal of Science and Technology*, vol. 12, no. 1, pp. 1–6, 2019.
- [41] K. Latif, N. Javaid, I. Ullah, Z. Kaleem, Z. Abbas, and L. D. Nguyen, "DIEER: delay-intolerant energy-efficient routing with sink mobility in underwater wireless sensor networks," *Sensors*, vol. 20, no. 12, p. 3467, 2020.
- [42] Z. A. H. Qasem and H. A. Leftah, "Deep learning-based code indexed modulation for autonomous underwater vehicles systems," *Communications*, vol. 28, article 100314, 2021.
- [43] Z. A. H. Qasem, H. Esmail, H. Sun, J. Wang, Y. Miao, and S. Anwar, "Enhanced fully generalized spatial modulation for the internet of underwater things," *Sensors*, vol. 19, no. 7, p. 1519, 2019.

Review Article

Analysis of Security Attacks and Taxonomy in Underwater Wireless Sensor Networks

Irfan Ahmad ¹, Taj Rahman ¹, Asim Zeb ², Inayat Khan ³, Inam Ullah ⁴,
Habib Hamam ^{5,6,7} and Omar Cheikhrouhou ⁸

¹Qurtuba University of Science & Technology Peshawar, Peshawar 25000, Pakistan

²Department of Computer Science, Abbottabad University of Science and Technology, Abbottabad 22500, Pakistan

³Department of Computer Science, University of Buner, Buner 19290, Pakistan

⁴College of Internet of Things (IoT) Engineering, Hohai University (HHU), Changzhou Campus, China

⁵Faculty of Engineering, Uni de Moncton, Moncton, NB, Canada E1A3E9

⁶Spectrum of Knowledge Production & Skills Development, Sfax 3027, Tunisia

⁷School of Electrical Engineering, Dept. of Electrical and Electronic Eng. Science, University of Johannesburg, Johannesburg 2006, South Africa

⁸CES Laboratory, National School of Engineers of Sfax, University of Sfax, Sfax 3038, Tunisia

Correspondence should be addressed to Omar Cheikhrouhou; omar.cheikhrouhou@isetsf.rnu.tn

Received 23 September 2021; Revised 30 October 2021; Accepted 3 November 2021; Published 24 December 2021

Academic Editor: Hamada Esmaiel

Copyright © 2021 Irfan Ahmad et al. This is an open access article distributed under the Creative Commons Attribution License, which permits unrestricted use, distribution, and reproduction in any medium, provided the original work is properly cited.

Underwater Wireless Sensor Networks (UWSN) have gained more attention from researchers in recent years due to their advancement in marine monitoring, deployment of various applications, and ocean surveillance. The UWSN is an attractive field for both researchers and the industrial side. Due to the harsh underwater environment, own capabilities, and open acoustic channel, it is also vulnerable to malicious attacks and threats. Attackers can easily take advantage of these characteristics to steal the data between the source and destination. Many review articles are addressed some of the security attacks and taxonomy of the Underwater Wireless Sensor Networks. In this study, we have briefly addressed the taxonomy of the UWSNs from the most recent research articles related to the well-known research databases. This paper also discussed the security threats on each layer of the Underwater Wireless sensor networks. This study will help the researchers design the routing protocols to cover the known security threats and help industries manufacture the devices to observe these threats and security issues.

1. Introduction

Underwater Wireless Sensor Networks (UWSNs) are commonly used nowadays to detect and monitor the underwater environment. It contains several sensors and vehicles placed in a selected area to perform specific tasks. These networks are further connected with base stations and satellites to process the detected data for further processing. UWSNs support several applications such as river and sea pollution discovery, a compilation of oceanographic data, resource exploration, disaster prevention, monitoring, and marine surveillance [1]. Due to the attenuation of radio signals in an underwater environment, the global positioning system

(GPS) cannot be used to locate sensor nodes. Therefore, UWSNs use an acoustic method of communication to send and receive the data between the source and destination. Terrestrial wireless sensor networks (TWSN) and UWSNs have distinct characteristics and functionalities. These variations can be observed in a variety of ways. To begin, UWSNs communicate by acoustic signals rather than radio transmissions like TWSNs do. TWSNs have more static networks, whereas UWSNs have more dynamic networks.

Third, compared to TWSNs, the underwater placement is unmanaged and limited. Node localization is more difficult in UWSNs than TWSNs. In addition, underwater sensor devices have more expensive hardware and are constrained

by resources (i.e., memory and energy). It is also difficult to repair or recharge the batteries once they have been deployed [2]. In underwater sensor networks, the speed of sound is assumed to be constant. However, acoustic signals have distinct characteristics from radio waves. Underwater, acoustic signals travel at around 1500 m/s, which is five times a magnitude slower than radio waves. The speed is changeable and is determined by the water's temperature, pressure, and salinity. These variables cause changes in the speed of sound in underwater situations. Different applications rely on wireless sensor networks (WSNs), which serve as a key link between the physical environment and the Internet of Things [3]. WSNs are widely used in the industry for continuous object boundary detection, which is essential for WSNs [4]. Improper packet size determination degrades network performance in terms of latency, resource utilization, throughput efficiency, and energy consumption in multihop underwater networks. Still, using the optimum packet size will increase [5].

Underwater wireless sensor networks are made up of nodes deployed both on the underwater and surface of the water. All nodes must communicate and share data with other devices in the same network and the ground station. Sensor network communication methods feature data transmission via acoustic, electromagnetic, or optical wave mediums. Because of the attenuation properties of water, acoustic communication is the most common and widely utilized approach among various types of media. The poor transmission factor is generated from the conversion of energy and absorption into temperature in the water. On the other hand, acoustic signals operate at low frequencies, allowing them to be broadcast and received over great distances. Figure 1 shows the Underwater Wireless Sensor Network environment.

2. UWSNS Taxonomy

This article suggests a taxonomy based on trend analysis and surveys of reliable published articles over the last few years. Before developing the thematic taxonomy, the utmost frequently discussed issues in the related work are also considered. Figure 2 depicts a UWSN thematic taxonomy to help realize its features. It divides the vital elements into Communication, Architectural Elements, Security, Applications, Routing Protocols, and Standards. These characteristics are discussed in the sections that follow:

2.1. Architectural Elements. The underwater wireless sensor network architecture types are categorized based on the network's three-dimensional area of the applications and sensor nodes.

2.1.1. Sensors. Smart things in IoT networks, also known as sensor nodes in Wireless Sensor Networks (WSN), are required to sense configuration parameters on a regular basis, collect and route received data packets to the middle, similar to the mobile sink in WSN, for anomalous investigation and source persistence [6]. For maximizing the network abilities for data collection, the mobile node requires two transceivers. Remotely operated underwater vehicles

(ROVs), autonomous underwater vehicles (AUVs), and sea gliders are examples of such vehicles. The third type of hybrid architecture consolidates mobile and static sensor nodes to carry out particular tasks. Mobile nodes can act as routers or controllers in a hybrid system to interact with static or basic data sensors. The sensor nodes in the dynamic architecture can move freely, allowing the network topology to change dynamically. Finally, ocean depth anchors are used in two-dimensional UWSN architecture to collect data from sensor devices.

Underwater sink-node can gather data from deep-sea sensors and transfer it to offshore base stations via surface channels. Underwater sinks are provided for this purpose, along with vertically and horizontally acoustic transmitters. Sensor nodes communicate with horizontal transceivers to collect data or provide instructions received by the offshore base station, whereas vertical transceivers send data to the base station. Through the use of various planned underwater sink nodes, a surface sink equipped with acoustic transceivers is capable of managing parallel communication [7]. The ocean floor is used to anchor sensor nodes in the architecture of underwater three-dimensional sensor networks. The depth of these sensor nodes is adjusted via wires attached to these anchors. However, the marine ecosystems' existing properties impact a significant obstacle to such a network.

2.1.2. Network Operations. The underwater sensor network operation goals are to maintain and enhance various functions, attributes, and specific requirements for improved functionality. As per recent publications, we conclude that the critical application development trends favour a greater emphasis on implementation and localization responsibilities that have made the foundation for UWSN architecture to improve full network functionality. As a result, this section contextualizes each job's strategies and features that enhance the network's performance.

(i) Localization

Localization methods have been extensively investigated in underwater sensor networks and are crucial for providing information about the location of sensor nodes in typical applications. We classified localization methods into three broad branches: mobile, hybrid, and stationary algorithms based on research articles. Classification is contingent upon sensor node movement in UWSNs. According to these categories, the majority of researchers concentrated on techniques for the localization of stationary nodes. For the static localization process, all sensor nodes are permanent and constant in the particular selected area, either tethered to sea floats or secured on the seafloor. The position of stationary nodes can be determined using a variety of methods. A recent approach [8] advocated using conventional ray equations to handle uncertainty in the anchor node position based on the rigidity theory. Some new research, such as [9], has supported that energy usage is reduced by minimizing the communication burden in the transmission process. To support near real-time decision making, an accurate border identification of continuous objects is an essential

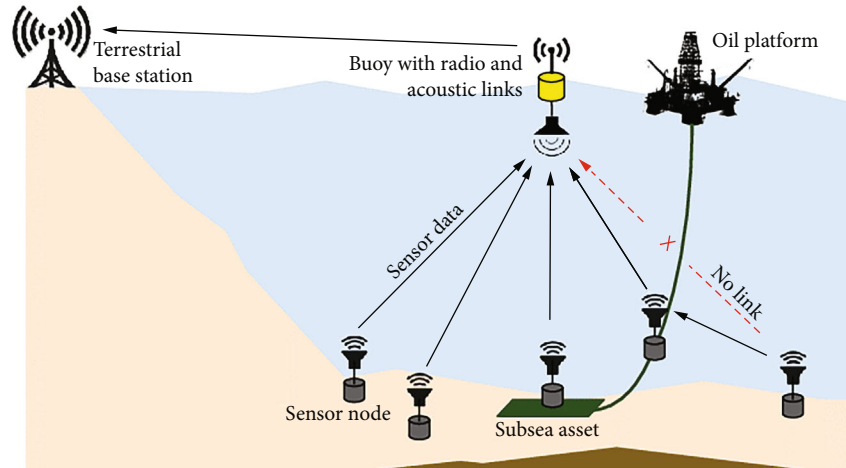


FIGURE 1: Environment of UWSNs.

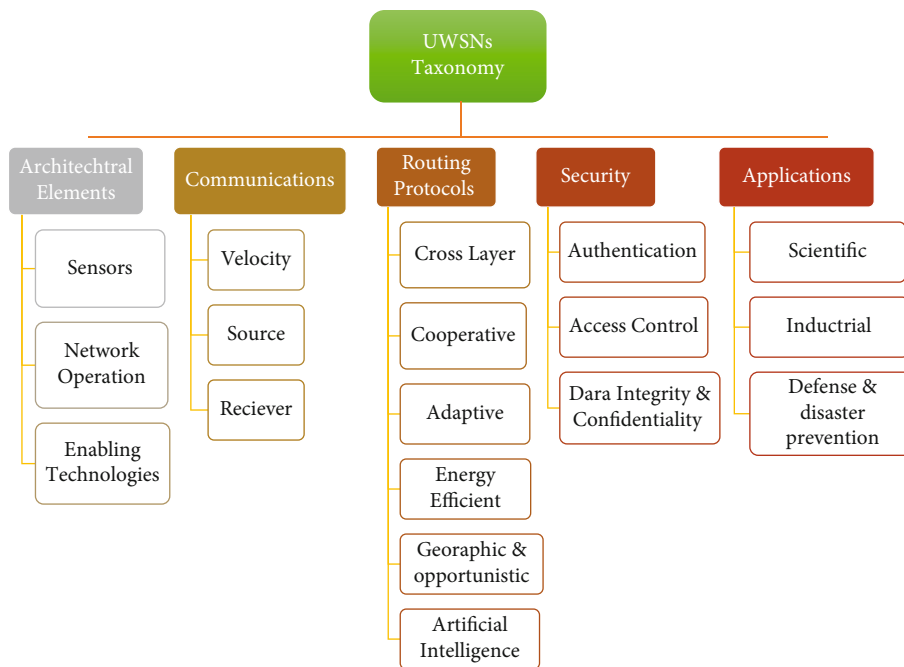


FIGURE 2: Underwater wireless sensor networks taxonomy.

research topic that relies on wireless sensor networks (WSNs) installed inside the geographical region to be monitored [10]. The researchers discovered that the unpredictability of sound speed made distance estimate for node identification less reliable.

(ii) Deployment

UWSNs are made up of hops placed underwater and nodes deployed on the water’s surface, and they perform their jobs in specific locations. Underwater sensors that occupy a sparse area must be deployed optimally to make the best use of the low power consumption. Based on the ability to support different critical activities, such as localization, network topology, and routing protocol, which substantially affect net performance, node placement is a

crucial step in underwater sensor networks. According to [11], there are three types of node deployment in UWSNs: limited mobility or self-adjusted, movement-assisted or accessible mobility, and static or fixed placement. All nodes are moored on the seafloor or affixed to surface buoys in a specific region of interest in the static node deployment. A disturbance in the sensor node area, according to [12], is an approach for achieving a final predicted configuration. To report their detection status, the nodes exchange control messages with each other and with the sink node. Nodes at the phenomenon boundary must be carefully selected for accurate tracking and detection [13]. After some network modifications have happened, such as node failure or target/event detection, reorganization or redeployment is required. The authors predicted that mobile sensor nodes would adjust their existing location actively to facilitate

ultimate connectivity and stabilize the network coverage. Moreover, refs. [14] enhanced detection rates in mobile sensor nodes compared to the static and hybrid sensor nodes.

2.1.3. Enabling Technologies. In industry 4.0, this novelty has developed the driving force for deploying the Internet of Things industry (IIoT). Data from various sensor devices can be securely forwarded to the cloud network and updated regularly, thanks to IIoT. According to [15], IIoT combines IoT technologies and industrial wireless connections into a unified system comprising terminals, cloud networks, equipment, and machines. As a result, recent advancements in IoT and UWSNs have rekindled interest in the Internet of Underwater Things (IoUT). Aside from the greenhouse effect, underwater nodes and vehicles consume a lot of power, which can cause critical missions or applications to fail rashly. This problem prompted the authors in [16] to develop a new design based on energy efficiency for UWSNs, precisely discovering offshore oil and gas environments. In the coming years, communication in underwater systems will face some threats, including complex architectural design, integrating underwater vehicles or heterogeneous nodes, and various other underwater applications. SDN IIoT architecture incorporates 3 layers model [15]. Node data is transferred to the control layer from the physical layer via a southbound edge, and then through the northbound interface, data are transferred to the application layer. Relationships of SDN, IIoT, IoUT, and industry 4.0 among enabling technologies are shown in Figure 3.

2.2. Communication. Over the last half-century, there has been a substantial increase in acoustic study and development, mainly marine acoustics. Commercially, an auditory method is used to disclose ocean mammals and even submarines. The army sector is also similar to public acoustic communication, especially in ocean surveillance applications. As a result, this section covers the fundamentals of underwater acoustic communication, such as sources, receivers, and sound velocity properties. Furthermore, all aspects influence the sound speed and affect the network functioning or devices installed in the network.

2.2.1. Sound Velocity. The acoustic waveform in the sea is affected by sound velocity and the surrounding environment. Through actual investigation, [17] discovered that many main elements influence the excellent speed in water: salinity, temperature, and hydrostatic pressure. The following sections discuss the key points of these aspects.

(i) Temperature

The sound intensity and climate of the water are strongly associated when the water temperature rises. The velocity increases as well. When near the water's surface, the temperature increases, the sound velocity is also increasing.

(ii) Salinity

The salinity ratio is the second component that affects the sound velocity in water. However, as compared to temperature, salinity has a more negligible effect on sound speed.

Sound speed is affected by the concentration of solidified salts in pure water. The ocean average level salinity is 35 Pascal. However, this figure fluctuates based on soil and qualities of water, atmosphere, and rock. Another aspect is affecting the level of salinity that they change with the depth of water.

(iii) Hydrostatic pressure

The sound speed of the water is also being affected by hydrostatic factors. Hydrostatic pressure enhances sound speed and depth [18]. This is because the increase in the center of the hydrostatic pressure is directly proportional.

(iv) Sound velocity profile

Based on ocean depth, the ocean is divided into two major zones. Each degree of profound results in distinctive sound velocity changes referred to as sound velocity profiles.

(v) Ocean depth below 200 m

The ocean consists of two main ocean-depth areas. Each depth causes various variations in sound speeds, known as sound velocity profiles. The top surface (0–100 m) is liable to wind, temperature, and environmental change. This layer can be mixed, and wind power converted into isothermic energy. The sound speed is significantly reduced when the wind is more than seven m/s because of the dominance of balloons at a distance of 10 m lower than the water's surface. The temperature varies seasonally in the seasonal thermocline region (100–200 m); the temperature decreases depending on the water depth. As a result, the thermocline is weak in winter, as the water surface is always excellent.

(vi) Ocean depth of more than 200 meters

The primary thermocline is located at depths of 200–100 m and has the lowest sound speed. The temperature of the water begins to rise at this depth. Temperature features in the deep isothermal layer are determined by water density and salinity. However, the temperature and salinity are considerably less significant than the hydrostatic pressure on sound velocity.

(vii) Ray bending

The amount of ray bending is determined by the difference in sound velocity, defined by salinity changes, pressure, and water temperature. The sound speed increases with depth in qualitative ray bending, paralleling the growing number of bubble populations. With improved routes at the sea surface, the number of bubbles reduces. A reflection occurs near the surface when acoustic energy concentrates within a layer. It does not transmit on all sides because it reduces the sound speed when the wave fronts propel toward the ocean depth. The SOFAR (Sound Fixing and Ranging) channel is named after this velocity profile.

(viii) Extended distance propagation

In the SOFAR channel geometry, attenuation and thermometry all impact sound reduction in signal-to-noise

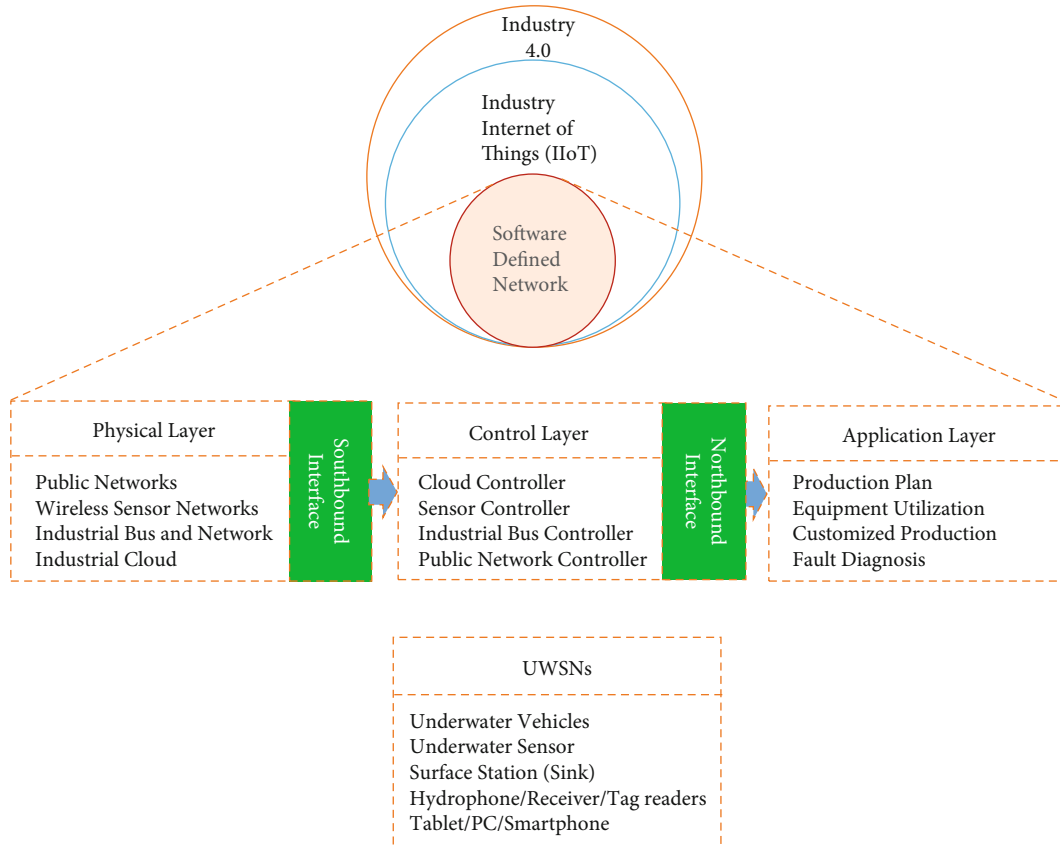


FIGURE 3: Relationship of IIoT, SDN, IoUT, and industry 4.0.

amplitude caused by long-distance transmission. However, the action on the SOFAR channel is slightly various. The rays do not bend spherically but instead spread in the form of a cylinder symmetry from a line source. The geometric spreading can decrease the power of acoustic waves as distance decreases based on inverse-square law.

Finally, noise, low variable speed, frequency-dependent absorption, and the architecture of communications in underwater networks are significantly affected. As a result of the considerable delays in spreading submarine transmission, spatial uncertainty and spatial unfairness also affect the networks [19]. As the reception time of the packet relies on the distance from the transmitter, the emitter first and then the receiver will be free.

(ix) Sea surface

There are varied proportions to the sound velocity parameters in various regions, such as at the frontier, bottom, and sea interface. Factors affecting the increase or decrease of sonority are the density and composition of rocks and trash in the sea bottom. Moreover, another factor influencing the sound speed is the bubble population near the surface of the sea. Average water density rises due to the presence of bubbles. As demonstrated in formulations and experiments, the speed of sound reduces the incidence of bubbles.

2.3. Routing Protocols. The routing protocol made a critical scheme challenge inside a network layer to identify and support network routes by providing different needs for acoustic communication. Several protocols to boost the network performance for underwater sensor networks have been developed and examined in the past and the present. The authors examined the previous study on UWSN routing protocols and identified that energy efficiency is the primary goal of most routing protocols (see Table 1—routing table). The main issue is to keep the limited amount of energy when using the UWSNs.

Underwater Acoustic communications use more energy than terrestrial radiofrequency. Static sink would suffer from battery power if the sensors located one hope away, potentially resulting in energy holes. In addition, it may result in preventing messages from reaching the sink node and network disconnectivity. In designing a routing protocol, the unique component of the underwater situation should be taken into account by using a time-varying channel. Most current studies on the network layer focused on minimizing latency while producing energy-efficient communication. But neglected to account for essential propagation factors such as bottom surface reflections, the Doppler effect and frequency-dependent attenuation, all of which, significantly impact energy consumption via rate and power.

Furthermore, modern routing protocols stress the usage of opportunistic routing, adaptive routing, cooperative,

TABLE 1: Shows the current routing protocols based on its features.

Protocols	Concentration points	Sink (multiple/ single)	Mobility	Multihop	Location known	Void avoidance
BLOAD [20]	Balanced energy consumption, energy holes avoidance	Single	Yes	No	Yes	No
EMGGR [21]	Void avoidance, reliability	Single	Yes	Yes	Yes	Yes
ECBCCP [22]	Reliability, energy conservation	Multiple	Yes	Yes	Yes	No
EULC [23]	Balanced energy dissipation, improved network lifetime, hot spot mitigation	Single	Yes	Yes	Yes	Yes
iAMCTD [24]	Packet delivery ratio, energy efficiency	Multiple	Yes	No	No	No
SACRP [25]	Packet delivery ratio, energy efficiency, clustering	Single	No	Yes	Yes	No
QL-EEBDG [26]	Packet delivery ratio, energy efficiency, clustering	Multiple	Yes	No	Yes	No
EnOR [27]	Packet delivery ratio, energy efficiency, improved network lifetime	Single	No	Yes	Yes	No
EECAR-AC [28]	Network lifetime, void avoidance	Multiple	Yes	Yes	Yes	Yes
QERP [29]	End-to-end delay, improve network energy consumption, and packet delivery ratio (PDR)	Single	Yes	No	Yes	Yes
EEDC-AA [30]	Prolong underwater network lifetime, and balance energy consumption	Multiple	Yes	No	Yes	No
JREM [31]	Energy holes and balancing energy consumption, and increase network lifetime by avoiding	Single	No	Yes	Yes	Yes
PCR [32]	Energy efficient data, opportunistic routing, and reliability	Multiple	No	Yes	Yes	Yes
EBOR [33]	Network lifetime, reliability, PDR, energy consumption	Multiple	No	Yes	Yes	No
RBCRP [34]	Reduce outage probability, load balancing	Multiple	Yes	Yes	Yes	No
CSQSR [35]	Network lifetime, application-specific QoS	N/A	No	No	Yes	No
AREP [36]	Link asymmetry, void handling	Single	Yes	No	Yes	Yes
VA-GMPR [37]	Void avoidance, load balancing, reliability	Single	Yes	Yes	Yes	Yes
P-AUV [38]	Low latency, energy efficiency	Multiple	Yes	Yes	Yes	No
RPO [39]	Reliability, energy efficiency	Multiple	No	N/A	Yes	N/A

artificial intelligence-related, and cross-layer routing protocols to meet the various requirements of UWSNs. The underwater environment is, by definition, unreliable and scant and hostile. As a result, these inconsistent states uncover UWSNs to the natural division caused by sensor mobility, decreasing the accuracy of data transmission from sender to receiver. As a result, routing protocol designs and approaches are necessary to address these difficulties.

2.4. Security. UWSN sensor nodes are often infrequently installed in harsh and dangerous conditions. As a result, they are susceptible to network attacks. One of the most important factors of UWSNs is security to ensure that an application smoothly functions and generates secure data. Internal and external attacks have been made against UWSNs due to their characteristics (e.g., limited bandwidth, high propagation latency, computational capability limitations, and high bit error rates).

2.4.1. Authentication. As previously stated, the acoustic channel is open; further, without encryption, a malicious attacker can readily grab manipulate their content. As a result, to filter malicious attacks, the receiving node must identify the data source, services, and channels, to access and share the applications and data on that network, nodes must be authorized. A trust management system and intrusion detection can be used to recognize aberrant behaviour and remove rogue nodes from the web. These procedures confirm that only verify nodes have access to the system's resources [40]. During transmission, all of the nodes connected with the network must have the authorization or permission of the network services. After the completion of the authentication process, the devices will be ready to carry out any duties that have been allocated to them using the encoded procedures. As a result, in UWSN, the implementation of a robust authentication technique is critical.

2.4.2. Access Control. The data access limitation is used in the access control process to protect the data (front-end and back end), resources, and services of underwater sensor networks. Intelligent devices or adaptive methods can help avoid or reduce the risk of malicious nodes and unauthorized data vulnerability. The two kinds of access methods are present: distributed and centralized. To permit a connection, all control access inquiries must process through the server in a centralized approach. However, with the distributed control access technique, an entity is designated by the access control server to authorize access to UWSN resources. Services that are used by the system should always be present in the system to reduce any communication problems in UWSNs.

2.4.3. Confidentiality and Data Integrity. In addition, integrity is a critical security requirement. During data transmission, each node must maintain the confidentiality of the data. The packet's header must also be encrypted in some security techniques to protect each node's identity. The node can ensure that the messages must be newly generated, and information that is already stored from previous broadcasts is not received or transferred by utilizing the difference time

approach. If a node has older communicated data, then the mentioned node cannot refuse the completed transmission. Nonrepudiation is the legal term for this process.

More work is undertaken to discover the existing techniques of attacks. According to the researchers, the invasion in UWSNs happened through data transfer in physical node attacks, denial of service (DoS), and impersonation and replication. According to [41], DoS attacks are common in UWSNs due to their challenges, low operational costs, and high effectiveness. [42, 43] have conducted a more profound study of DoS attacks on the physical layer. They put the results to the test in a real-world environment. A data assault is another common security concern with UWSNs. One way for protecting data from DoS assaults is data management utilizing information-centric architecture. Attacks from innovative DoS types are still capable of damaging the data. As a result, ref. [44] detected different types of mobile attackers by the use of machine learning in information-centric architecture.

According to prior investigations, security challenges in underwater sensor networks are focused primarily on routing, data aggregation, localization, and intrusion detection models. Five methods, including the secure localization and trust model, are proposed in the evaluation process [45]. The authors in [46] refined the implementation of the mentioned trust model by establishing a single point of trust management in underwater sensor networks by utilizing a cloud paradigm. The mentioned management methodology aims to govern each sensor node's trustworthiness using a mathematical technique to gather trust proof.

Multiple experiments are conducted in [47] and discovered that the effective encryption technique could maintain the integrity and secrecy of the data. Furthermore, the method has the potential to decrease communication overhead on the upper layer. The authors in [48] developed a crucial model to generate more helpful hash bits for underwater sensor networks secure acoustic communications.

2.5. Applications. The technology used in underwater wireless sensor networks can replace conventional methods by remote control of underwater appliances and onshore systems, advanced data recording devices, and real-time monitoring. Underwater wireless sensor network applications are typically classified into three branches: commercial, military and security, and scientific (see Figure 4). Sensor devices are utilized in the military to sense the enemy's activity and position. It can be used to monitor ports and harbors, detect enemy submarines, identify underwater mine locations, and conduct border surveillance. In addition, sensor nodes can see marine environments in advance of natural disasters by performing seismic monitoring.

2.5.1. Scientific. UWSNs have diverse applications in science, including ocean sampling, environmental monitoring, and most importantly, Great Barrier Reef activities. For example, the ecological monitoring application is used to track the amount of trash, both biological and chemical, accumulated on the sea-bed [8]. Furthermore, in [49], a robotic model

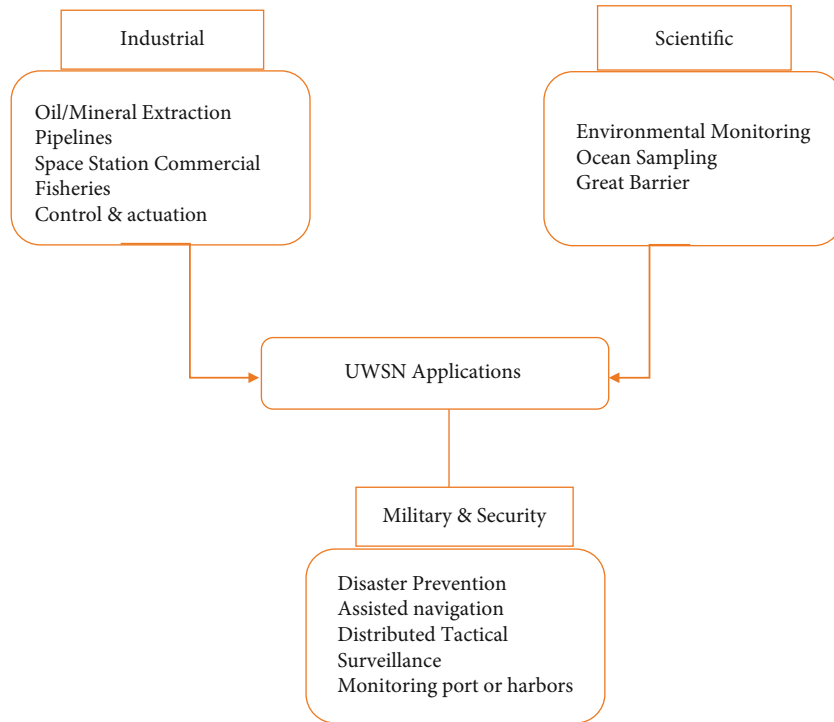


FIGURE 4: Application of UWSNs.

was used to evaluate the level of oxygen in the water and track temperature and pressure [50]. The authors in [51] present a coral reefs application that integrates big data, IoT, and sensor networks to assess the impact of humidity, pressure, ocean temperature, marine ecosystems, and salinity on coral bleaching. Deep maritime conditional surveillance can also be accomplished by using a variety of agents and communication methods.

2.5.2. Commercial. UWSN industrial applications have an important effect on commercial activity facilitation. Underwater sensor network monitors applications such as underwater gas and oil pipeline monitoring. The researchers in [52] have been developed a model for underwater tracking of gas and oil pipelines. The network was created to provide facts on the health of channels that are linked across large environments. Additionally, [53] developed a monitoring system for underwater gas and oil pipelines, including the desired components requiring control.

One of the most labour-intensive industries that help in a healthy economy is referred to as fish farming. Moreover, it necessitates a rigorous monitoring system to assess the fish's environmental conditions. In [54] proposed a Zigbee-based underwater sensor network observation system for big fish farms that can be accessed through remote control for interested users. Additionally, the system can monitor fish farms based on pH values, water level, humidity temperature, and dissolved oxygen. Further, wireless cameras are interconnected with the design and the Internet to enable remote monitoring from any location in the world. Additionally, the researchers of [55] built a comparable commer-

cial fishery monitoring system that communicates via acoustic waves.

2.5.3. Disaster Prevention and Defense Application. Underwater sensor networks are used for military and defense applications to detect possible enemies before ports and port surveillance and control in [56]. Sea mines discovery in [57], border protection against illegal fighting ships in [58]. In addition, underwater sensors network advanced technologies such as the mobile UWSNs provide warning alerts prior to the natural disasters, such as seismic and seafloor activities [59].

The network settings are classified by the characteristics of the application, the region, the network's size and frequency of communication, the distance among hops, the sensor types, and the total number of sensor devices. In general, the overall communication among the hops is accomplished through acoustic waves or a combination of radiofrequency and acoustic signals. Therefore, it is difficult to detect and prevent a malicious node disguised as a valid user from disturbing the network. Even worse, internal threats may be initiated by hacked nodes that were previously correct.

The network settings are classified by the characteristics of the application, the region, the network's size and frequency of communication, the distance among hops, the sensor types, and the total number of sensor devices. In general, the overall communication among the hops is accomplished through acoustic waves or a combination of radiofrequency and acoustic signals. Therefore, it is difficult to detect and prevent a malicious node disguised as a valid user from disturbing the network. Even worse, internal threats may be initiated by hacked nodes that were previously correct.

3. Security Threats and Attacks

Many limitations exist in underwater acoustic channels and UWSNs, causing potential security risks. As a result, UWSNs are subject to a variety of risks, including malicious attacks. These challenges and attacks were thoroughly examined and evaluated in this work. These attacks can be passive or active, depending on the behaviour of the malicious attacker. As illustrated in Figure 5, these challenges and attacks are classified broadly into active and passive attacks.

3.1. Passive Attacks. Passive attacks are attempts performed by effected devices to detect the activities and gather data transferred in the network without interfering with its functioning, such as interference, eavesdropping, impersonation, message distortion, message replay, and secret information leakage. The acoustic channels are open channels and easily come under attack.

Using a hydrophone or underwater microphone, malicious attackers can capture packets transmitted in the data channel. Furthermore, the attacker can determine the nature of communication by evaluating packet flow, detecting packet exchange, identifying the data transferring hosts, and determining the position of nodes. Unfortunately, it is challenging to determine the mentioned attacks because the network functionality is unaffected. So, the efficient solution is to use encryption technologies that make it difficult for eavesdroppers to obtain any information. Unfortunately, the current encryption algorithms used in wireless networks cannot be immediately translated into UWSNs due to the high energy consumption and massive overhead. The encryption techniques utilized by UWSNs will be discussed in further detail in the following sections.

3.1.1. Eavesdropping. Additionally, eavesdropping is referred to as “passive information collecting.” Eavesdropping on confidential data is possible through the tapping of communication cables. As a result, wireless networks are much more vulnerable to passive attacks than wireless connections. Because UWSNs use short-range transmissions, an attacker must be nearby to eavesdrop on important information, making UWSNs less vulnerable to tapping than lengthy wireless communication technologies. Interception of messages transmitted by UWSNs may expose valuable information such as gateways, the physical location of specific nodes, key distribution centers, timestamps, message identifiers (IDs), and other fields, even nearly everything that was not secured. Using a mathematical model that takes underwater acoustic channel characteristics, including ambient noise and signal attenuation in [60], the authors looked into the possibility of eavesdropping attempts. Underwater acoustic signal channels are shown to be related to an intercept’s success condition. According to the authors, both isotropic and array eavesdroppers are considered when calculating the eavesdropping probability. To make matters even more complicated, node density and wind speed all impact the probability of a collision.

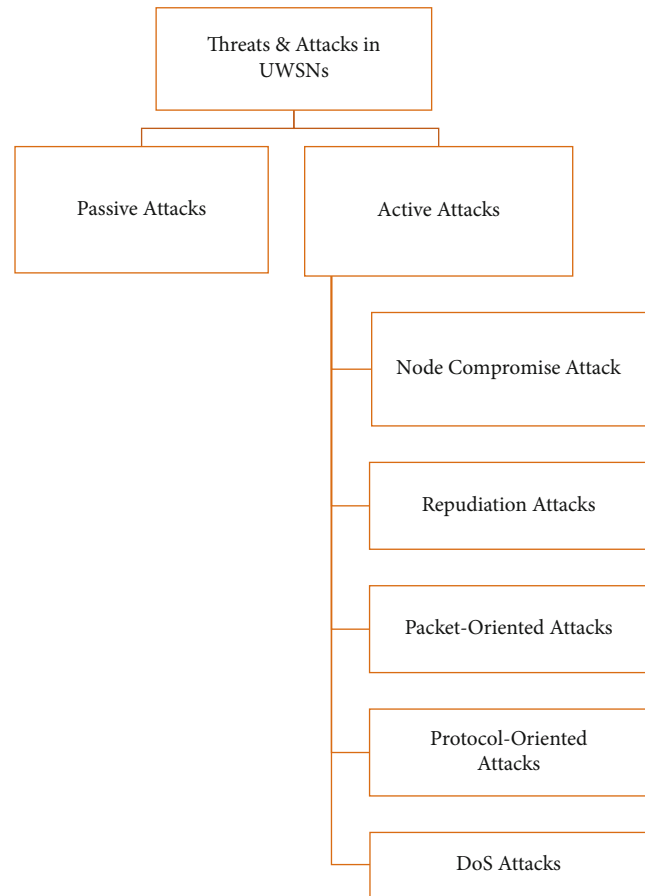


FIGURE 5: Security threats and attacks.

3.1.2. Node Malfunctioning. It can occur for many reasons, including defective sensors or energy depletion due to sensor overloading or other denial-of-service attacks.

3.1.3. Node Destruction. Physically destroying a node (by using an electrical surge, physical force, or gunfire) in any way possible so that the node is rendered inoperable.

3.1.4. Traffic Analysis. For attackers, the traffic pattern of a network may be as helpful as the substance of data packets. By examining traffic patterns, sensitive data about the networking infrastructure can be gleaned. In UWSNs, the nodes closest to the access point, i.e., the sink, transmit more packets than the other nodes because they relay more packets. Similarly, clustering is a critical component of UWSN stability.

3.1.5. Node Outage. Such a threat happens if a node’s standard functionality is compromised. For instance, if a central node in a heterogeneous network fails to operate normally, the WSN protocols must be robust enough to offset the negative consequences of such node outages by choosing new cluster heads and offering alternate network channels.

3.2. Active Attacks. Active attacks aim to inject, change, destroy, or delete data carried over a network. Active cyber-attacks may capture network data and attempt to alter or

destroy packets to disturb network communication and operation. Both internal and external attackers can carry out active attacks if the attacks are conducted out by hops that are not part of the network, and they are classified as external attacks, which are capable of finding and protecting. If an attempt is launched from an insider node, it is classified as an inside threat, which can cause significant harm to the network. According to the results of the prior research, interior attacks are harder to trace and may cause more danger than outside ones. The possible answer to this problem is to use security techniques such as encryption, trust management, and authentication.

3.3. Attacks Occur on Physical Layer

3.3.1. Node Capture. An attacker seizes control of the sensor node using a physical attack, such as connecting wires to its circuit board and accessing both stored data and continuous communication in the UWSN [61]. Capturing a node may disclose vital data, most notably cryptographic keys, compromising the entire UWSN. Additionally, attackers can tamper with the actual wiring of the electronic board or the content of the nodes' memory, allowing them to utilize the seized slave node in any way they like. Two issues occur in this instance:

- (i) The hijacked node can make unlimited requests on behalf of the attacker
- (ii) Hijacked nodes may offer erroneous information to genuine users

3.3.2. Jamming DoS. According to [62], a hostile machine may lead to jam its transmission in case of sending information with same frequency. The jamming signal adds to the carrier's noise. Its intensity is sufficient to drop the SNR below the threshold required for the nodes utilizing that channel to receive data effectively. Constant jamming can be carried out in a region, effectively preventing all nodes in that zone from communicating. However, temporary jamming using random time intervals can be used to disrupt signals successfully. There are a limited number of antijamming devices available for UWSNs that can be used to defend against WSN jamming attacks. Acoustic communication underwater frequently makes use of spread-spectrum techniques. Frequency-hopping spread spectrum (FHSS) and direct sequence spread spectrum (DSSS) are two of these approaches gaining popularity because of their superior performance in noisy environments and dealing with multipath interference. FHSS and DSSS approaches can withstand interference from jammers to a certain extent. If FHSS is employed, the jamming attacker will still jam a large portion of the spectrum. Even worse, a powerful jamming signal can compromise the DSSS system.

3.4. Attacks Occur on Data Link Layer. Algorithms at the data link layer, particularly MAC address techniques, provide numerous options for exploitation. For example, continuous channel jamming via DoS assaults or more complicated cases depending on MAC layer addressing tech-

niques. Collision, Dos, weariness, spoofing, desynchronization, link-layer jamming, flooding, and unfairness are all examples of data link layer attacks.

3.4.1. Denial of Sleep (Sleep Deprivation Torture). A denial of sleep attack will result in energy depletion for battery-powered devices [63]. This attack can be carried out by collision threats or repetitive handshaking, which involves repeatedly manipulating the clear to send (CTS) and request to send (RTS) flow control signals, thereby preventing the node from entering the sleep state.

3.4.2. Collision. During this type of attack, an attacker communicates on the same frequency as a legitimate network node. As a result, the two broadcasts collide, rendering the data received unintelligible to the recipient. At some point, the receiver will request retransmission of the same packet [64]. A single byte of a message colliding would result in a CRC (cyclic redundancy check) error, rendering the entire message unusable. This assault is more advantageous for an attacker than jamming, as it consumes less transmission energy and has a lower risk of detection [65]. A colluding collision attack can be mitigated via a mitigating colluding collision strategy. The error-correcting code, in a sense, is a practical method of preventing collisions.

3.4.3. Jamming Attack. A datalink layer jamming attack is similar to a physical layer jamming attack, but it is more intelligent and effective. The potential hacker can accomplish this purpose by sending a request to send (RTS) packets continuously. The valid nodes are denied access to the channel. The potential hacker can assign the highest priority to himself and constantly utilize the medium regarding MAC protocols. As a result, scheduled MAC protocols can protect against the exploit. These attacks can be mitigated with antireplay prevention and link-layer verification. Consequently, receiving a significant number of RTS packets costs energy and utilizes channels on a node [66].

3.4.4. Exhaustion Attack. This type of attack can be used to keep the communication line busy and drain the device's energy by hosting a malicious node into the network. It can be triggered by the attacker or by a hijacked node with the attacker's internal program code. Another type of exhaustion attack is when the hijacked node sends RTS/CTS messages or requests to join to push the receiver node to transmit and receive. A strategy proposed by [58] is based on fuzzy logic for defending against dispersed node exhaustion attacks. Rate limiting on each node of the network is a reasonable solution. [58] proposes a fuzzy logic-based antidistributed-node-exhaustion solution.

3.4.5. Unfairness. It is a weak type of DoS attempt in which the attacker decreases the network's performance rather than entirely blocking authorized sensor nodes from using the communication channel. A minor frames method is utilized to cut down on time. It is vulnerable to further disparity. An attacker, for example, may resend at a faster rate instead of just randomly stopping [67]. Most of the DoS attacks on the data link layer listed above can be

mitigated by utilizing error detection code, limiting transmission speed, and splitting packets into short frames. To lower the amount of time required, consider using a small frames approach. Utilizing this strategy results in a smaller impact at the sacrifice of effectiveness. In addition, it is open to future exploitation. Instead of randomly delaying, an attacker might retransmit at a higher speed.

Most datalink layer denial-of-service attacks described above can be mitigated using rate limiter, error detection code, and packet slicing.

3.5. Network Layer Attacks. Routing the packets from source to destination is the main task of the network layer. Due to the particular features, the network layer is subject to various threats and attacks that disrupt the network's routing, including selective forwarding, replay, misdirection, neglect and greed, sinkhole, Sybil, wormhole, blackhole/gray hole, homing, and hello flooding attacks.

3.5.1. Selective Forwarding Attack. There is a possibility that the adjacent node will locate different routes to the destination node. As a result, to avoid detection, it intentionally transmits and drops specific packets. The attacker who is focused on overwhelming and changing a packet created from a few source nodes can effectively transfer the rest packets while minimizing suspicion of misbehaviour [68].

Evidential assessment is used in [69] to discover node capture attacks that employ the Dempster–Shafer theory of integrated numerous facts. These attacks can be detected and isolated from the network using trust management and reputation methods based on behaviour evaluation [46].

3.5.2. Misdirection Attack. In this type of attack, the attacker redirects packets to invalid paths, modifies the routes, or redirects the packets to a hijacked node. This attack can be mitigated by changing the route path, including the source route in each packet.

3.5.3. Greed and Neglect. This type of attack is a variation of the selective forwarding threat. The attacker may drop incoming packets at random while still acknowledging the source node or giving high precedence to its packets [70, 71]. Declaring alternate routing paths is a feasible solution to this type of attack by sending repeated messages. But in conversation, more power would be required, and UWSNs would face the most serious energy shortage.

3.5.4. Gray Hole/Black Hole Attack. In this type of attack, the attacker broadcasts fake routing information with the shortest path or lowest cost toward the receiver. The hijacked nodes would choose this path as the best option, even though it passes over the adversary computer. Furthermore, the adversary can evaluate, change, or even destroy packets at will. A black hole attack occurs when the attacker drops all data packets. If the attacker removes some crucial packets, then it is called a gray hole attack.

This form of attack damages those sensor nodes located a long distance away from the sink node. In a more sophisticated manner, the adversary may drop necessary packets at

a specific period or a specified percentage, proving it more challenging to detect.

3.5.5. Sybil Attack. An attacker can use the Sybil attack to create many identities and appear in multiple locations simultaneously. The primary purpose of these fake identities is to prevent the information transmission operation from taking place. These numerous identities can be taken by inventing defects or hijacking legitimate node IDs. As a result, the Sybil attack can severely harm distance-based or location-based routing schemes. Furthermore, the attacker can act as a base station or recipient, sending acknowledgment packets to sensor nodes to prevent retransmission. In [72, 73], the researchers provided a lightweight and robust scheme based on the received signal strength indicator for detecting the Sybil attacks. Also, the authors in [74] designed the random key predistribution method for protecting the Sybil attacks.

3.5.6. Homing Attack. A potential hacker may monitor the traffic in a homing attack to identify and target nodes with individual responsibility, such as sinkhole nodes or cluster heads. Furthermore, the attacker may execute additional DoS operations to block or disable these specific nodes. The use of “dummy packets” in an antitraffic analysis method helps hide the location of the base station from observers [75]. It is unfortunate that these dummy packets use up a lot of nodes' energy, particularly for UWSNs. As a result, it should only be utilized when preventing traffic analysis is absolutely necessary.

3.6. Attacks on Transport Layer. The UWSN transport layer has the responsibility for source to destination reliable communication of data. This layer of common attacks contains the synchronization flooding attack and desynchronization attack.

3.6.1. Synchronization Flooding Attack. An intruder may create new user request indefinitely until the resources required by each connection are consumed or reach the highest limit. A popular type of DoS attack includes delivering a large number of common packets, such as internet control message protocol (ICMP), transmission control protocol (TCP), and user datagram protocol (UDP), all intended at the exact location. Because of the large data flood created by these packets, the network can no longer differentiate between authentic and fraudulent traffic in [76].

3.6.2. Desynchronization Attack. A desynchronization attack occurs when a malicious user disrupts existing connections between nodes by sending faked packets with faked sequence numbers or control signals that desynchronize destinations. Synchronization is critical and challenging for UWSNs; additionally, the global positioning system (GPS) is ineffective [77].

4. Open Issues and Challenges

UWSNs have a wide range of uses, including civic, military, and a variety of others. UWSN research and

implementation have been increasingly popular in both academia and industry. Following a study of existing developments and investigations, various problems remain to be explored to progress further.

4.1. Reliability. In order to ensure reliability in all aspects, such as hop-by-hop, data, and end-to-end reliability, reliability is essential. The ability to successfully convey and transfer data between participating sensor nodes in the UWSNs is critical to its stability. Reliability ensures that packets are delivered successfully between sensor nodes involved in joint operations [78]. Therefore, proposing a cooperation method that takes this reliability into account and solves it.

4.2. Propagation Delay. The MAC or retransmission timeout (RTO) waiting time directly impacts throughput. The authors of [79] discovered that the current fixed RTO is not efficient. Furthermore, because of the lengthy propagation delay in UWSNs, a handshaking method that enables all nodes to share a channel costs a lot more than in a terrestrial sensor network. It will gradually result in high handshaking overheads, resulting in a limited bandwidth.

4.3. Variance Delay. Variance delay is a factor that leads to erroneous round-trip time (RTT) estimates and makes measuring the waiting time in the MAC protocol challenges. However, according to [80], most MAC protocol studies did not account for the variable delay in their findings.

4.4. Mobility of Nodes. While nodes in terrestrial networks are likely to remain static, underwater vertices will certainly wander due to underwater shipping activity, currents, winds, and other factors. Because the oceanic current is spatially dependent, nodes may drift in different directions. While GPS updates can pinpoint reference nodes tied to surface buoys, maintaining submerged underwater nodes at precise positions is problematic. It may have an impact on the accuracy of the localization.

4.5. Efficiency. Efficiency is essential for providing a cooperative mechanism and making communication easier between nodes in a communication network. Underwater localization collaborative control tasks necessitate a reliable means for transferring and receiving data. In order to use resources that enable efficient delivery of information, cooperative gaming strategies must include efficiency; otherwise, the cost of such information distribution will rise, i.e., delays and throughput will grow.

4.6. Privacy and Security. The authors of [81] explained how security assaults might affect underwater localization and countermeasures and how privacy is affected. For the sensor node to be localized, it must show specific information, leading to privacy gaps. When gathering location-related information, location privacy is a topic that is discussed. DoS attacks, range-based assaults, no range estimation attacks, noncooperation, and deceptive advertising information are some examples of these types of attacks.

4.7. Communication Range. In the underwater environment, a signal's absorption depends on the water's depth, one of the distinctive characteristics. Signal absorption can be minimized by lowering the frequency. Even nevertheless, when the transmission range expands, new issues arise regarding interruption probability and high data collision rates.

4.8. Hardware Dependent. Sensor nodes in the water, such as autonomous underwater vehicles (AUVs), wheels, or unscrewed aircraft, use battery power and are difficult to change once in place. As a result, customizing another system is difficult because different applications have distinct data formats, protocols, and service constraints.

4.9. Reliability of Link. High delivery rates in real-time scenarios require good link reliability as well. The sensor nodes in the network's link dependability factor might affect the delivery rates and, as a result, the transmission loss, which lowers the aggregated strength of the waveform's propagation from sender to the receiver. Data transmission reliability can be harmed by noise in the underwater environment, resulting in dropped transmissions. If the link is unreliable, continuous transmission of data will increase node energy consumption and bandwidth utilization. Data transmission efficiency must be taken into account to prevent using unreliable connections.

5. Conclusion and Future Directions

Wireless sensor networks are a great area nowadays for researchers. As advancements are made in technology, this field is also growing faster than other fields. As the nature of the network, it broadcast the signals in an open environment. Underwater Wireless Sensor Networks is one of the branches of this network that operates underwater to monitor the marine environment and collect data for different purposes. This study first investigated the Underwater Wireless Sensor Network taxonomy from the latest research articles and well-known databases. This paper also indicates and analyses the current security threats for Underwater Wireless Sensor Networks on each layer. UWSNs have come a long way in recent years, but there is still more to be done, especially when it comes to building large-scale systems. There is room for improvement in a future study on node mobility with high monitoring area to explore the impact on the network connection, energy consumption, network longevity, and coverage resulting from these findings. Studies should focus on creating cooperative control among a few underwater vehicles to raise the efficiencies of UWSNs and improve their performance. Future research should improve the cars' ability to communicate cooperatively by increasing the channel capacity and autonomy level. Future studies could look at environmental factors and underwater vehicle designs simultaneously, extending the algorithm's usefulness. A high-level planning layer follows this that the researchers construct to specify the ideal vehicle configurations or strategic regions of interest for the vehicle to investigate. Complex network scenarios such as mobility,

multipath fading, and shadowing could potentially be addressed in the research.

Data Availability

Data will be available upon request from the corresponding author.

Conflicts of Interest

The authors declare no conflict of interest.

References

- [1] X. Xiao, H. Huang, and W. Wang, "Underwater wireless sensor networks: an energy-efficient clustering routing protocol based on data fusion and genetic algorithms," *Applied Sciences*, vol. 11, no. 1, p. 312, 2021.
- [2] R. Mhemed, F. Comeau, W. Phillips, and N. Aslam, "Void avoidance opportunistic routing protocol for underwater wireless sensor networks," *Sensors*, vol. 21, no. 6, p. 1942, 2021.
- [3] S. Khisa and S. Moh, "Survey on recent advancements in energy-efficient routing protocols for underwater wireless sensor networks," *IEEE Access*, vol. 9, pp. 55045–55062, 2021.
- [4] J. Xiang, Z. Zhou, L. Shu, T. Rahman, and Q. Wang, "A mechanism filling sensing holes for detecting the boundary of continuous objects in hybrid sparse wireless sensor networks," *IEEE Access*, vol. 5, pp. 7922–7935, 2017.
- [5] D. Zhao, G. Lun, R. Xue, and Y. Sun, "Cross-layer-aided opportunistic routing for sparse underwater wireless sensor networks," *Sensors*, vol. 21, no. 9, p. 3205, 2021.
- [6] X. Du, Z. Zhou, Y. Zhang, and T. Rahman, "Energy-efficient sensory data gathering based on compressed sensing in IoT networks," *Journal of Cloud Computing*, vol. 9, pp. 1–16, 2020.
- [7] D. B. Kilfoyle and A. B. Baggeroer, "The state of the art in underwater acoustic telemetry," *IEEE Journal of Oceanic Engineering*, vol. 25, no. 1, pp. 4–27, 2000.
- [8] M. Stojanovic, "Acoustic (underwater) communications," in *Encyclopedia of Telecommunications*, Wiley, Hoboken, NJ, USA, 2019.
- [9] K. M. Awan, P. A. Shah, K. Iqbal, S. Gillani, W. Ahmad, and Y. Nam, "Underwater wireless sensor networks: a review of recent issues and challenges," *Wireless Communications and Mobile Computing*, vol. 2019, Article ID 6470359, 20 pages, 2019.
- [10] H. Ping, Z. Zhou, T. Rahman, and Y. Duan, "Localization and tracking of continuous objects boundary area leveraging planarization algorithms in duty-cycled wireless sensor networks," in *43rd Annual Conference of the IEEE Industrial Electronics Society*, Beijing, China, 2017.
- [11] G. Han, C. Zhang, L. Shu, N. Sun, and Q. Li, "A survey on deployment algorithms in underwater acoustic sensor networks," *International Journal of Distributed Sensor Networks*, vol. 9, no. 12, Article ID 314049, 2013.
- [12] J. Vilela, Z. Kashino, R. Ly, G. Nejat, and B. A. Benhabib, "A dynamic approach to sensor network deployment for mobile-target detection in unstructured, expanding search areas," *IEEE Sensors Journal*, vol. 16, no. 11, pp. 4405–4417, 2016.
- [13] T. Rahman, Z. Zhou, and H. Ning, "Energy efficient and accurate tracking and detection of continuous objects in wireless sensor networks," in *IEEE International Conference on Smart Internet of Things (SmartIoT)*, Xi'an, China, 2018.
- [14] B. Wang, *Coverage Control in Sensor Networks*, Springer Science & Business Media, Berlin, Germany, 2010.
- [15] J. Wan, S. Tang, Z. Shu, S. W. Di Li, M. Imran, and A. V. Vasilakos, "Software-defined industrial internet of things in the context of industry 4.0," *IEEE Sensors Journal*, vol. 16, pp. 7373–7380, 2016.
- [16] R. W. Coutinho, A. Boukerche, L. F. Vieira, and A. A. Loureiro, "On the design of green protocols for underwater sensor networks," *IEEE Communications Magazine*, vol. 54, no. 10, pp. 67–73, 2016.
- [17] T. G. Leighton, *The Acoustic Bubble*, vol. 96, no. 4, 1994, Academic Press, London, UK, 1994.
- [18] Y. Yang, W. Zhao, and X. Xiao, "The upper temperature limit of life under high hydrostatic pressure in the deep biosphere," in *Deep Sea Research Part I*, vol. 176, Oceanographic Research Papers, 2021.
- [19] A. A. Syed, W. Ye, J. Heidemann, and B. Krishnamachari, "Understanding spatio-temporal uncertainty in medium access with ALOHA protocols," in *Proceedings of the Second Workshop on Underwater Networks*, pp. 41–48, Montréal, QC, Canada, September 2007.
- [20] I. Azam, N. Javaid, A. Ahmad, W. Abdul, A. Almogren, and A. Alamri, "Balanced load distribution with energy hole avoidance in underwater WSNs," *IEEE Access*, vol. 5, pp. 15206–15221, 2017.
- [21] F. Al Salti, N. Alzeidi, and B. R. Arafeh, "EMGGR: an energy-efficient multipath grid-based geographic routing protocol for underwater wireless sensor networks," *Wireless Networks*, vol. 23, no. 4, pp. 1301–1314, 2017.
- [22] S. Rani, S. H. Ahmed, J. Malhotra, and R. Talwar, "Energy efficient chain based routing protocol for underwater wireless sensor networks," *Journal of Network and Computer Applications*, vol. 92, pp. 42–50, 2017.
- [23] R. Hou, L. He, S. Hu, and J. Luo, "Energy-balanced unequal layering clustering in underwater acoustic sensor networks," *IEEE Access*, vol. 6, pp. 39685–39691, 2018.
- [24] N. Javaid, M. R. Jafri, Z. A. Khan, U. Qasim, T. A. Alghamdi, and M. Ali, "IAMCTD: improved adaptive mobility of courier nodes in threshold-optimized dbr protocol for underwater wireless sensor networks," *International Journal of Distributed Sensor Networks*, vol. 10, no. 11, 2014.
- [25] Y. D. Chen, D. R. Wu, W. Chen, and K. P. Shih, "A self-adaptive cooperative routing protocol for underwater acoustic sensor networks," in *Proceedings of the OCEANS'15 MTS/IEEE Washington*, pp. 1–5, Washington, DC, USA, October 2015.
- [26] Z. Jin, Y. Ma, Y. Su, S. Li, and X. Fu, "A Q-learning-based delay-aware routing algorithm to extend the lifetime of underwater sensor networks," *Sensors*, vol. 17, no. 7, p. 1660, 2017.
- [27] R. W. Coutinho, A. Boukerche, L. F. Vieira, and A. A. Loureiro, "EnOR: energy balancing routing protocol for underwater sensor networks," in *Proceedings of the IEEE International Conference on Communications (ICC)*, pp. 1–6, Paris, France, May 2017.
- [28] M. R. Bharamagoudra, S. S. Manvi, and B. Gonen, "Event driven energy depth and channel aware routing for underwater acoustic sensor networks: agent oriented clustering based approach," *Computers and Electrical Engineering*, vol. 58, pp. 1–19, 2017.

- [29] F. Muhammad, G. Tuna, and V. C. Gungor, "QERP: quality-of-service (QoS) aware evolutionary routing protocol for underwater wireless sensor networks," *IEEE Systems Journal*, vol. 12, pp. 2066–2073, 2018.
- [30] Y. Jing, X. Yang, X. Luo, and C. Chen, "Energy-efficient data collection over AUV-assisted underwater acoustic sensor network," *IEEE Systems Journal*, vol. 99, pp. 1–12, 2018.
- [31] B. Fatma, C. Zidi, and R. Boutaba, "Joint routing and energy management in underwater acoustic sensor networks," *IEEE Transactions on Network and Service Management*, vol. 14, no. 2, pp. 456–471, 2017.
- [32] R. W. L. Coutinho, A. Boukerche, and A. A. F. Loureiro, "PCR: a power control-based opportunistic routing for underwater sensor networks," in *Proceedings of the 21st ACM International Conference on Modeling, Analysis and Simulation of Wireless and Mobile Systems*, pp. 173–180, Montreal, QC, Canada, November 2018.
- [33] Z. Jin, Z. Ji, and Y. Su, "An evidence theory based opportunistic routing protocol for underwater acoustic sensor networks," *IEEE Access*, vol. 6, pp. 71038–71047, 2018.
- [34] N. Javaid, S. Hussain, A. Ahmad, M. Imran, A. Khan, and M. Guizani, "Region based cooperative routing in underwater wireless sensor networks," *Journal of Network and Computer Applications*, vol. 92, pp. 31–41, 2017.
- [35] L. E. Emokpae, Z. Liu, G. F. Edelman, and M. A. Younis, "Cross-stack QoS routing approach for underwater acoustic sensor networks," in *Proceedings of the 2018 Fourth Underwater Communications and Networking Conference (UComms)*, pp. 1–5, Lercici, Italy, August 2018.
- [36] G. Han, L. Liu, N. Bao, J. Jiang, W. Zhang, and J. J. P. C. Rodrigues, "Arep: an asymmetric link-based reverse routing protocol for underwater acoustic sensor networks," *Journal of Network and Computer Applications*, vol. 92, pp. 51–58, 2017.
- [37] T. Al-Subhi, B. Arafeh, N. Alzeidi, K. Day, and A. Touzene, "A void avoidance scheme for grid-based multipath routing in underwater wireless sensor networks," *Wireless Sensor Network*, vol. 10, no. 7, pp. 131–156, 2018.
- [38] A. Bereketli, M. Tümcakır, and B. Yeni, "P-AUV: position aware routing and medium access for ad hoc AUV networks," *Journal of Network and Computer Applications*, vol. 125, pp. 146–154, 2019.
- [39] M. Ali, A. Khan, K. Aurangzeb et al., "CoSiM-RPO: cooperative routing with sink mobility for reliable and persistent operation in underwater acoustic wireless sensor networks," *Sensors*, vol. 19, no. 5, p. 1101, 2019.
- [40] E. Felemban, F. K. Shaikh, U. M. Qureshi, A. A. Sheikh, and S. B. Qaisar, "Underwater sensor network applications: a comprehensive survey," *International Journal of Distributed Sensor Networks*, vol. 11, no. 11, Article ID 896832, 2015.
- [41] Y. W. Law, M. Palaniswami, L. V. Hoesel, J. Doumen, P. Hartel, and P. Havinga, "Energy-efficient link-layer jamming attacks against wireless sensor network MAC protocols," *ACM Transactions on Sensor Networks (TOSN)*, vol. 5, no. 1, pp. 1–38, 2009.
- [42] S. Misra, M. Dash, A. V. Khatua, and M. S. O. Vasilakos, "Jamming in underwater sensor networks: detection and mitigation," *IET Communications*, vol. 6, no. 14, pp. 2178–2188, 2012.
- [43] M. Zuba, Z. Shi, Z. Peng, J. H. Cui, and S. Zhou, "Vulnerabilities of underwater acoustic networks to denial-of-service jamming attacks," *Security and Communication Networks*, vol. 8, no. 16, 2645 pages, 2015.
- [44] R. Martin and S. Rajasekaran, "Data centric approach to analyzing security threats in underwater sensor networks," in *Proceedings of the OCEANS 2016 MTS/IEEE Monterey*, pp. 1–6, Monterey, CA, USA, September 2016.
- [45] G. Han, L. Liu, J. Jiang, L. Shu, and J. J. Rodrigues, "A collaborative secure localization algorithm based on trust model in underwater wireless sensor networks," *Sensors*, vol. 16, p. 229, 2016.
- [46] J. Jiang, G. Han, C. Zhu, S. Chan, and J. J. Rodrigues, "A trust cloud model for underwater wireless sensor networks," *IEEE Communications Magazine*, vol. 55, no. 3, pp. 110–116, 2017.
- [47] C. Peng, X. Du, K. Li, and M. Li, "An ultra-lightweight encryption scheme in underwater acoustic networks," *Journal of Sensors*, vol. 2016, Article ID 8763528, 10 pages, 2016.
- [48] Y. Luo, L. Pu, Z. Peng, and Z. Shi, "RSS-based secret key generation in underwater acoustic networks: advantages, challenges, and performance improvements," *IEEE Communications Magazine*, vol. 54, no. 2, pp. 32–38, 2016.
- [49] A. G. Lazaropoulos, "Designing the undersea internet of things (IoT) and machine-to-machine (M2M) communications using underwater acoustic MIMO networks," *Trends Renew. Energy*, vol. 2, pp. 13–50, 2016.
- [50] A. Majid, I. Azam, A. Waheed et al., "An energy efficient and balanced energy consumption cluster based routing protocol for underwater wireless sensor networks," in *Proceedings of the IEEE 30th International Conference on Advanced Information Networking and Applications (AINA)*, pp. 324–333, Crans-Montana, Switzerland, March 2016.
- [51] W. Lin, D. Li, Y. Tan, J. Chen, and T. Sun, "Architecture of underwater acoustic sensor networks: a survey," in *Proceedings of the First International Conference on Intelligent Networks and Intelligent Systems*, pp. 155–159, Wuhan, China, November 2008.
- [52] H. Saeed, S. Ali, S. Rashid, S. Qaisar, and E. Felemban, "Reliable monitoring of oil and gas pipelines using wireless sensor network (WSN)—REMONG," in *Proceedings of the 2014 9th International Conference on System of Systems Engineering (SOSE)*, pp. 230–235, Adelaide, Australia, June 2014.
- [53] M. Z. Abbas, K. A. Bakar, M. A. Arshad, M. Tayyab, and M. H. Mohamed, "Scalable nodes deployment algorithm for the monitoring of underwater pipeline," *Telkomnika*, vol. 14, no. 3, pp. 1183–1191, 2016.
- [54] L. A. Abdul-Rahaim and A. M. A. Ali, "Remote wireless automation and monitoring of large farm using wireless sensors networks and internet," *International Journal of Computer Science & Engineering Technology (IJCSET)*, vol. 6, pp. 118–137, 2015.
- [55] Y. Taniguchi, "Experimental evaluation of effect of turbidity on the performance of visible light communication in an underwater environment," *International Journal of Simulation: Systems, Science and Technology*, vol. 17, pp. 1–4, 2016.
- [56] G. Antonelli, A. Caffaz, G. Casalino et al., "The widely scalable mobile underwater sonar technology (WiMUST) H2020 project: first year status," in *Proceedings of the OCEANS 2016-Shanghai*, pp. 1–8, Shanghai, China, April 2016.
- [57] S. Kumar, A. Perry, C. Moeller et al., "Real-time tracking magnetic gradiometer for underwater mine detection," in *Int*

- Proceedings of the Oceans'04 MTS/IEEE Techno-Ocean'04*, vol. 2, pp. 874–878, Kobe, Japan, November 2004.
- [58] S. Kamalesh and P. G. Kumar, “Fuzzy based secure intrusion detection system for authentication in wireless sensor networks,” *Journal of Computational and Theoretical Nanoscience*, vol. 14, no. 5, pp. 2465–2472, 2017.
- [59] S. Kemna, M. J. Hamilton, D. T. Hughes, and K. D. LePage, “Adaptive autonomous underwater vehicles for littoral surveillance,” *Intelligent Service Robotics*, vol. 4, no. 4, pp. 245–258, 2011.
- [60] Q. Wang, H. N. Dai, X. Li, and H. Wang, “On modeling eavesdropping attacks in underwater acoustic sensor networks,” *Sensors*, vol. 16, no. 5, p. 721, 2016.
- [61] I. Butun, *Prevention and Detection of Intrusions in Wireless Sensor Networks*, [Ph.D. thesis], University of South Florida, 2013.
- [62] F. Hu and N. K. Sharma, “Security considerations in ad hoc sensor networks,” *Ad Hoc Networks*, vol. 3, no. 1, pp. 69–89, 2005.
- [63] F. Stajano and R. Anderson, “The resurrecting duckling: security issues for ubiquitous computing,” *Computer*, vol. 35, no. 4, pp. suppl22–supl26, 2002.
- [64] T. Borgohain, U. Kumar, and S. Sanyal, “Survey of security and privacy issues of internet of things,” 2015, <https://arxiv.org/abs/1501.02211>.
- [65] W. Znaidi, M. Minier, and J.-P. Babau, *An Ontology for Attacks in Wireless Sensor Networks*, [Ph.D. Thesis], INRIA, 2008.
- [66] C. Pu, S. Lim, B. Jung, and M. Min, “Mitigating stealthy collision attack in energy harvesting motivated networks,” in *Proceedings of the 2017 IEEE Military Communications Conference (MILCOM 2017)*, pp. 539–544, Baltimore, MD, USA, October 2017.
- [67] F. Stajano and R. J. Anderson, “The resurrecting duckling,” in *Proceedings of the 7th International Workshop on Security Protocols*, Cambridge, UK, April 1999.
- [68] P. Pandarinath, “Secure localization with defense against selective forwarding attacks in wireless sensor networks,” in *Proceedings of the 2011 IEEE 3rd International Conference on Electronics Computer Technology (ICECT)*, vol. 5, pp. 112–117, Kanyakumari, India, April 2011.
- [69] M. R. Ahmed, M. Aseeri, M. S. Kaiser, N. Z. Zenia, and Z. I. Chowdhury, “A novel algorithm for malicious attack detection in uwsn,” in *Proceedings of the 2015 IEEE International Conference on Electrical Engineering and Information Communication Technology (ICEEICT)*, pp. 1–6, Dhaka, Bangladesh, May 2015.
- [70] C. Ioannou and V. Vassiliou, “The impact of network layer attacks in wireless sensor networks,” in *Proceedings of the 2016 IEEE International Workshop on Secure Internet of Things (SIoT)*, pp. 20–28, Heraklion, Greece, September 2016.
- [71] I. Khan, M. A. Khan, S. Khusro, and M. Naeem, “Vehicular lifelogging: issues, challenges, and research opportunities,” *Journal of Information Communication Technologies and Robotics Applications*, vol. 8, no. 2, pp. 30–37, 2017.
- [72] M. Demirbas and Y. Song, “An RSSI-based scheme for Sybil attack detection in wireless sensor networks,” in *Proceedings of the 2006 International Symposium on World of Wireless, Mobile and Multimedia Networks*, pp. 564–570, Washington, DC, USA, January 2006.
- [73] I. Khan and S. Khusro, “Towards the design of context-aware adaptive user interfaces to minimize drivers’ distractions,” *Mobile Information Systems*, vol. 2020, 23 pages, 2020.
- [74] F. Yavuz, J. Zhao, O. Yagan, and V. Gligor, “On secure and reliable communications in wireless sensor networks: towards k-connectivity under a random pairwise key pre-distribution scheme,” in *Proceedings of the 2014 IEEE International Symposium on Information Theory (ISIT)*, pp. 2381–2385, Honolulu, HI, USA, July 2014.
- [75] H. Chen and W. Lou, “On protecting end-to-end location privacy against local eavesdropper in wireless sensor networks,” *Pervasive and Mobile Computing*, vol. 16, pp. 36–50, 2015.
- [76] I. Ahmad, M. S. Niazy, R. A. Ziar, and S. Khan, “Survey on IoT: security threats and applications,” *Journal of Robotics and Control (JRC)*, vol. 2, no. 1, pp. 42–46, 2021.
- [77] I. F. Akyildiz, D. Pompili, and T. Melodia, “Underwater acoustic sensor networks: research challenges,” *Ad Hoc Networks*, vol. 3, no. 3, pp. 257–279, 2005.
- [78] D. Muhammed, M. Anisi, M. Zareei, C. Vargas-Rosales, and A. Khan, “Game theory-based cooperation for underwater acoustic sensor networks: taxonomy, review, research challenges and directions,” *Sensors*, vol. 18, no. 2, p. 425, 2018.
- [79] Y. Chen, F. Ji, Q. Guan, Y. Wang, F. Chen, and H. Yu, “Adaptive RTO for handshaking-based MAC protocols in underwater acoustic networks,” *Future Generation Computer Systems*, vol. 86, pp. 1185–1192, 2017.
- [80] H. Li, Y. He, X. Cheng, H. Zhu, and L. Sun, “Security and privacy in localization for underwater sensor networks,” *IEEE Communications Magazine*, vol. 53, no. 11, pp. 56–62, 2015.
- [81] I. Khan, S. Khusro, N. Ullah, and S. Ali, “AutoLog: toward the design of a vehicular lifelogging framework for capturing, storing, and visualizing LifeBits,” *IEEE Access*, vol. 8, pp. 136546–136559, 2020.